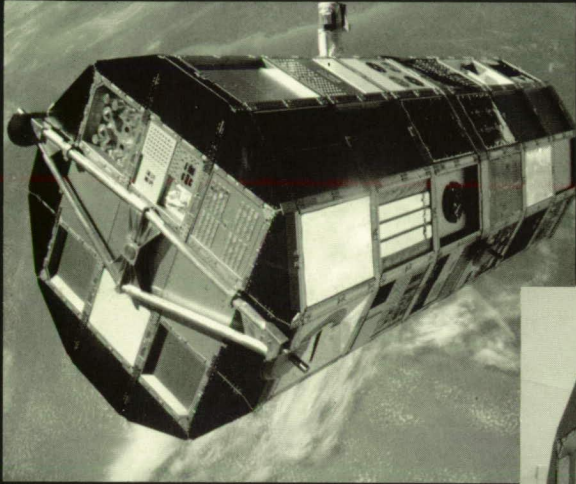
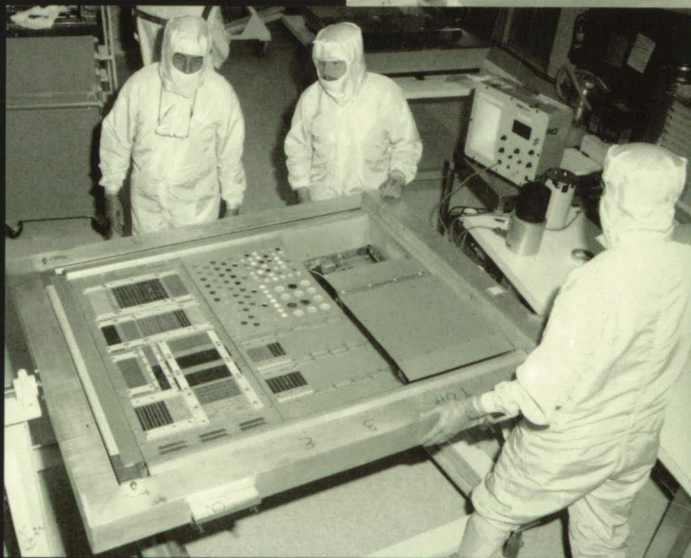


Research and Technology



1990



Langley Research Center
NASA Technical Memorandum 4243

Research and Technology

1990

ORIGINAL CONTAINS
COLOR ILLUSTRATIONS



National Aeronautics and
Space Administration

Langley Research Center
Hampton, Virginia 23665-5225

Langley Research Center
NASA Technical Memorandum 4243

Foreword

The mission of the NASA Langley Research Center is to increase the knowledge and capability of the United States in a full range of aeronautics disciplines and in selected space disciplines. This mission will be accomplished by performing innovative research relevant to national needs and Agency goals, transferring technology to users in a timely manner, and providing development support to other United States Government agencies, industry, and other NASA centers. This report contains highlights of the major accomplishments and applications that have been made during the past year. The highlights illustrate both the broad range of the research and technology activities at NASA Langley Research Center and the contributions of this work toward maintaining United States leadership in aeronautics and space research. For further information concerning the report, contact the Chief Scientist, Mail Stop 105-A, NASA Langley Research Center, Hampton, Virginia 23665, (804) 864-6062.



Richard H. Petersen
Director

Availability Information

The NASA program office and the corresponding Agency-wide Research and Technology Objectives and Plans (RTOP's) work breakdown structures are listed in the Contents for each research and technology accomplishment. OAET designates the Office of Aeronautics, Exploration and Technology; OSSA designates the Office of Space Science and Applications; AA designates the Associate Administrator; OCE designates the Office of the Chief Engineer; OCP designates the Office of Commercial Programs; and OSF designates the Office of Space Flight.

The accomplishments are grouped in 12 strategic thrusts including contributions in Fundamental Knowledge, Subsonic Aircraft, High-Speed Civil Transport, High-Performance Military Aircraft, Hypersonic and Transatmospheric Vehicles, Space Transportation, Space Station, Space Technology, Exploration, Global Change, Facilities, and Technology Utilization. For ease of reference, an index is provided at the end of this report.

For additional information on any summary, contact the individual identified with the highlight. This individual is generally either a member or a leader of the research group submitting the highlight. Commercial telephone users may dial the listed extension preceded by (804) 86. Telephone users with access to the Federal Telecommunications System (FTS) may dial the extension preceded by 928.

Contents

Foreword.....	iii
Availability Information.....	iv

Fundamental Knowledge

Scanning Electron Acoustic Microscopy	1
(OCE 323-51-66)	
Impact Damage Assessment in Thick Composite Plates With Through-the-Thickness Reinforcements	2
(OCE 323-51-66 and 505-63-01)	
Prediction and Control of Asymmetric Flow Around Cones	3
(OAET 505-60-01)	
Navier-Stokes Solutions of Three-Dimensional Leading-Edge Vortex Flow	4
(OAET 505-60-01)	
Adaptive Grid Calculations for Two-Dimensional Euler Equations	5
(OAET 505-60-01)	
Development of Matrix-Valued Dissipation Model for Central-Difference Schemes	5
(OAET 505-60-01)	
Navier-Stokes Calculations for Boeing 747 Wing/Fuselage Configuration	6
(OAET 505-60-01)	
Numerical Study on Use of Sulfur Hexafluoride in Wind Tunnels	7
(OAET 505-60-01)	
Numerical Predictions of Jet Exhaust Plume Flows Using Multiblock Multigrid Euler Solver	8
(OAET 505-60-01)	
Reynolds-Stress Modeling for Compressible Turbulence	8
(OAET 505-60-01)	
Three-Component Laser Velocimeter Surveys of Flow Over Rearward Facing Step	10
(OAET 505-60-11)	
New Method for Handling Artificial Computational Boundaries	10
(OAET 505-61-11)	
Complete Package for Analysis of 3-D Flows Using Unstructured Grids	11
(OAET 505-61-21)	
Elimination of Nacelle Interference Using DISC Design Method	12
(OAET 505-61-21)	
Design of Advanced Slow-Expansion, Slotted Nozzle for Quiet Operation of Mach 8 Variable Density Tunnel	13
(OAET 505-61-31)	
Multiple Paths to Laminar Breakdown in Boundary Layer	13
(OAET 505-61-31)	
Visualization of Traveling Wave Packet on Rotating Disk	14
(OAET 505-61-31)	

Navier-Stokes Simulation of Transonic Afterbody Flows With Jet Exhaust (OAET 505-62-71)	15
Faster Analysis of Space Shuttle Solid Rocket Booster Using PVSOLVE (OAET 505-63-01)	16
Accurate Global/Local Stress Analysis Procedure for Detailed Stress Distribution Calculations (OAET 505-63-01)	16
Identification of Commonality in Failure Behavior for Metal and Composite Aircraft Structures Under Crash Loads (OAET 505-63-01)	17
Combined Effect of Matrix Cracking and Free Edge on Delamination (OAET 505-63-01)	18
Relationship Between Constituent and Composite Fatigue Behavior for Titanium Matrix Composites (OAET 505-63-01)	19
Energy-Absorption Capability of Composite Tubes and Beams (OAET 505-63-01)	20
Equivalent Domain Integral Method and Applications (OAET 505-63-01)	21
Elimination of Stiffener/Skin Separation Failure Mode by Integrally Woven Hat-Stiffener Preform (OAET 505-63-01)	22
Prediction of Static and Resultant Dynamic Aeroelastic Behavior by Nonlinear Method (OAET 505-63-21)	23
Demonstration of Flutter Control Using Active Flexible Wing Wind Tunnel Model (OAET 505-63-21)	24
Validation of Tire Analysis Codes With Experimental Measurements of Space Shuttle Nose Gear Tire (OAET 505-63-41)	26
Validation of Unstructured-Grid Euler Algorithm (OAET 505-63-50)	26
Demonstration of Euler Flutter Analysis of Airfoils Using Unstructured Dynamic Meshes (OAET 505-63-50)	27
Conical Euler Method to Study Unsteady Vortical Flows About Rolling Delta Wings (OAET 505-63-50)	28
p-Version, Tapered, Beam Finite Element for Vibrations Analysis (OAET 505-63-51)	29
Identification of Anomaly in Damping Treatments for Reducing Vibrations (OAET 505-63-51)	31
Pressure-Instrumented Main Rotor Noise Test (OAET 505-63-51)	32
Performance Optimization of Helicopter Rotor Blades (OAET 505-63-53)	32
Object-Oriented Design and Analysis of Application Specific Architectures (OAET 505-65-11)	33
Experimental Evaluation of Software Redundancy for Improving Reliability (OAET 505-65-11)	34

Reliability/Availability Integrated Workstation	35
(OAET 505-66-21)	
Conditional Factoring Approach to Network Analysis	36
(OAET 505-66-21)	
Multicolor Electroluminescent Display Fabrication Using Ion Implantation	36
(OAET 505-67-01)	
Improvement in Depth-Viewing Volume of Collimated Stereo 3-D Graphic Displays	37
(OAET 505-67-01)	
Improved Tracking and Monitoring Performance Using Stereopsis and Color Cueing	38
(OAET 505-67-01)	
Effect of Exposure to Heads-Down Stereoscopic Flight Displays on Real-World Depth Perception	39
(OAET 505-67-01)	
Transition of Work Load Brain Wave Measures From Laboratory to Simulators	39
(OAET 505-67-11)	
Work Load Demands (Drop-Offs Over Time) by Voice Amplitude Measure	40
(OAET 505-67-11)	
Gigaflop Performance Modeling of Taylor-Couette Flow	41
(OAET 505-90-21)	
Prediction of Radiation for 10-km/s Flows With DSMC	42
(OAET 506-40-91)	
Integrated Controls-Structures Optimization	43
(OAET 506-43-41)	
Development of Advanced Modal Method for Transient Structural Analysis (Force Derivative Method)	44
(OAET 506-80-31)	
Improving Damage Tolerance of Carbon/Epoxy Composites by Stitching	44
(OAET 510-02-11)	
Helicopter Far-Field Noise Reduction	45
(OAET 532-06-01)	
Blade Deformation Effects on Aerodynamics and Noise of Advanced Propellers	46
(OAET 535-03-11)	
Noise Control in Fuselage Structures Using Piezoceramic Actuators	47
(OAET 535-03-11)	

Subsonic Aircraft

Implementation of Stochastic Control for Two-Axis Skin-Friction Balance	49
(OAET 505-61-01)	
Video Support of Vortex Interaction Studies	50
(OAET 505-61-05)	
Onboard Station for Researchers	50
(OAET 505-61-41)	
Transition Physics Flight Research Experiments	51
(OAET 505-61-41)	
Airborne Wake Vortex Detection	52
(OAET 505-61-41)	

Hybrid Laminar-Flow Control Flight Program (OAET 505-61-41)	52
Thermographic Detection of Cracks in Thin Sheets (OAET 505-63-01)	53
Active Control of Multimodal Random Sound in Ducts (OAET 505-63-01)	54
Thermographic Characterization of Back-Surface Geometry (OAET 505-63-01)	55
Response and Failure Characteristics of Composite Shear Webs With Cutouts Described by Experiments (OAET 505-63-01)	55
Powder-Coated Prepreg (OAET 505-63-01)	56
Expanded Aeromechanical Stability Data Base for Parametric Hingeless Rotor (OAET 505-63-51)	57
Adaptive Failure Detection and Isolation System (OAET 505-66-01)	58
Benefits of Forward-Look Wind Shear Detection (OAET 505-66-11)	58
Aircraft Digital-Packet Up/Down Radio Communications Link (OAET 505-66-41)	59
Airborne 4-D Flight Management in Time-Based ATC Environment (OAET 505-66-41)	60
Aircraft ATC Data-Link Information Transfer Simulation (OAET 505-66-41)	61
Interactive Management of Large Screen Displays (OAET 505-67-01)	61
Transport Landing Approach Alternate Pathways and Stereo 3-D Presentation (OAET 505-67-01)	62
Fault-Monitoring Concept for Application to Aircraft Subsystems (OAET 505-67-21)	63
Heavy Rain Research (OAET 505-68-01)	64
Influence of Design Concept on Composite Wing Structure Weight and Cost (OAET 510-02-21)	64
Superior Compression-After-Impact Performance by Commingled Graphite/Thermoplastic Composite (OAET 510-02-21)	65
Development of Euler Method for Turboprop Integration (OAET 535-03-01)	66

High-Speed Civil Transport

Supersonic Aerodynamic Characteristics of High-Speed Civil Transport (OAET 505-61-61)	69
--	----

Evaluation of Pressure Proof Test Concept	69
(OAET 505-63-01)	
Determination of Leading-Edge Curvature Effects on Flutter	70
(OAET 505-63-21)	
Grid Generation on and About HSCT Configurations	71
(OAET 505-90-21)	
ANOPP Jet Noise Predictions for HSCT	72
(OAET 537-03-11)	
Wind Tunnel Models for Low Sonic Boom Concepts	73
(OAET 537-03-21)	
Producing More Acceptable Sonic Booms	74
(OAET 537-03-21)	
Numerical Analysis of F-16XL Laminar-Flow Control Configuration	75
(OAET 541-03-41)	

High-Performance Military Aircraft

Acoustics of ASTOVL Aircraft in Ground Effect	77
(OAET 505-61-11)	
Static and Dynamic Ground Effects	78
(OAET 505-61-71)	
Tail Buffet Research	79
(OAET 505-61-71)	
Ignitability Test Method	79
(OAET 505-63-01)	
Polyamic Acid and Polyimide Fibers	80
(OAET 505-63-91)	
Optimal Input Design for Aircraft Parameter Estimation	81
(OAET 505-66-01)	
Flutter Suppression on Active Flexible Wing	81
(OAET 505-66-71)	
Candidate Control Design Metrics for Agile Fighter	82
(OAET 505-68-71)	
Simulation Study of High-Angle-of-Attack Nose-Down Pitch Control Requirements	83
(OAET 505-68-71)	
Interference Flows About Missile-Sting Assemblies Near and Inside Cavities	84
(OAET 505-68-91)	
Forebody Controls Research	85
(OAET 533-02-01)	

Hypersonic and Transatmospheric Vehicles

Low-Energy Gamma Ray System for Monitoring Slush Hydrogen	89
(AA 307-50-09)	

Large Thin-Film Heat-Transfer Sensor Arrays (OAET 505-60-11)	89
Transonic Numerical Calculations for Nozzle Drag Reduction (OAET 505-61-31)	90
Fuel-Air Mixing Enhancement in Supersonic Combustor (OAET 505-62-31)	91
Flow Establishment in Generic Scramjet Combustor (OAET 505-62-31)	92
Dynamic Response of Initially Deformed Composite Plates Using Finite Elements (OAET 505-63-01)	93
Reduction of Thermal Heating Effects on Flutter by Aeroservoelasticity Method (OAET 505-63-21)	93
Analysis of Carbon-Carbon/Heat-Pipe Wing Leading Edge (OAET 505-63-31)	94
Guidance Analysis of Aeroglide Orbital Plane Change Maneuver (OAET 505-66-01)	95
Regulator Designs for Hypersonic Vehicles (OAET 505-66-31)	96
Direct-Deposit Thin-Film Sensors for 3-D Surfaces (OAET 505-61-01)	97
Update and Improvement of Finite-Element Weight Prediction Code (OAET 505-69-31)	97
Degradation of Film Cooling Effectiveness by Incident Shocks (OAET 506-40-21)	98
Experimental Investigation of Transatmospheric Vehicle Concept With Minimum-Drag Forebody (OAET 506-40-41)	99
Surface Pressure and Shock-Layer Pitot-Pressure Profiles for 6°/12° Cone/Flare at Mach 6 in Air (OAET 506-40-41)	99
High-Purity Silica Ceramics for Casting Wind Tunnel Heat-Transfer Test Models (OAET 506-40-41)	100
Application of LAURA Code for Slender-Vehicle Aerothermodynamics (OAET 506-40-71)	101
Potential of Ti-1100 Matrix Composites for Hypersonic Vehicle Applications (OAET 506-43-01)	102
New Low-Toxicity, High-Temperature Nadimide End-Capped Thermosetting Polyimide: LaRC-RP46 (OAET 506-43-11)	102
Improved Processability of LARC-CPI Semicrystalline Polyimide (OAET 506-43-11)	103
Study of Morphological Changes in PEEK at Cryogenic Temperatures (OAST 506-43-21)	104
Integrated Thermal-Structural Analysis With Adaptive Unstructured Meshes (OAET 506-43-31 and OAET 506-40-21)	105
Fabrication, Test, and Analysis of Blade-Stiffened Carbon-Carbon Compression Panels (OAET 506-43-31)	105

Improved Mechanical Properties of 2-D Carbon-Carbon Composites	106
(OAET 506-43-71)	
Cost-Effective Three-Dimensional Analysis of Scramjet Combustors.....	107
(OAET 763-01-21)	
Mixing Enhancement and Flow Losses for Scramjet Combustors	107
(OAET 763-01-21)	
Scramjet Inlet Testing at Mach 6	108
(OAET 763-01-31)	
Analysis and Design of Scramjet Nozzle-Afterbody Using Sensitivity Coefficients	109
(OAET 763-01-31)	
Generic Scramjet Nozzle/Afterbody Studies	110
(OAET 763-01-31)	
Ineffectiveness of Moderate Transpiration Cooling to Reduce Type IV Shock-on-Lip Heat Flux	111
(OAET 763-01-41)	
Hydrogen Transport Properties of NASP Materials	111
(OAET 763-01-41)	
Analysis of Liquid-Metal-Cooled NASP Engine Cowl Leading Edge	112
(OAET 763-01-41)	
Acoustic Testing of High-Temperature Panels	113
(OAET 763-01-41)	
Demonstration of High Structural Efficiency in Honeycomb Core Structure Using Enhanced Diffusion Bonding	113
(OAET 763-01-41)	
Thermal Management for Hypersonics	114
(OAET 763-01-61)	
NIST Large Temperature Difference Boil-Off Calorimeter	115
(OSF 946-01-00)	

Space Transportation

Magnetoacoustic Residual Stress Characterization of SRM D6AC Steel	117
(OCE 323-51-66)	
Measurement and Analysis of Structural Adhesive Bond Strength	118
(OCE 323-51-66)	
Ground Wind Loads Characteristics for Atlas II	119
(OAET 505-63-21)	
Surface Temperature/Heat-Transfer Measurements Using Optical Fluorescence Thermography System	120
(OAET 506-40-41)	
Evaluation of Infrared Thermography for Hypersonic Heat-Transfer Measurements.....	121
(OAET 506-40-41)	
Aerothermodynamic and Aerodynamic Testing of Propulsion/Avionics Module	122
(OAET 506-40-41)	
Flow Field Calibration of 15-Inch Mach 6 High-Temperature Tunnel	122
(OAET 506-40-41)	

Assessment of Two Heat-Transfer Measurement Techniques	123
(OAET 506-40-41)	
Aerothermodynamic Measurements on Proposed Personnel Launch System Vehicle	124
(OAET 506-40-41)	
Experimental Aerodynamic Characteristics of Proposed PLS Lifting-Body Concept	125
(OAET 506-40-41)	
New Three-Dimensional DSMC Code	125
(OAET 506-40-91)	
Shuttle Infrared Leeside Temperature Sensing Experiment	126
(OAET 506-48-11)	
Lifting-Body Personnel Launch System Flyability Analysis	127
(OAET 506-49-11)	
Aircraft Electronic Subsystem for Acquisition of Loran-C Navigation Data	128
(OSF 560-01-00)	
Built-up Structure for Cryogenic Tanks Using Superplastic Forming	129
(OSF 946-01-00)	

Space Station

Noncontacting Motion Monitoring System	131
(OSF 472-47-12)	
Predicted Torque Equilibrium Attitude Utilization for Space Station <i>Freedom</i> Attitude Control	131
(OSF 476-14-07)	
Space Station <i>Freedom</i> Power Growth Study	133
(OSF 488-11-02)	
Space Station <i>Freedom</i> Evolution to Accommodate Space Exploration Initiative	134
(OSF 488-11-02)	
Space Operations Data Base and Analysis System	135
(OSF 488-30-01)	
Smart Structures Research	137
(OAET 506-43-11)	
Modal Identification Experiment	137
(OAET 506-48-91)	
In-Space Experiments Data Base	138
(OAET 506-49-31)	
Demonstration of Flexible Mini-Mast Control by Guest Investigators	138
(OAET 585-01-21)	
Middeck 0-Gravity Dynamics Experiment	139
(OAET 589-01-21)	
Closed-Loop Control Test on Mini-Mast	140
(OAET 590-14-11)	
Development and Application of Learning Control Method in Flexible Panel Slewing Analysis	141
(OAET 590-14-21)	
Improved Estimator Performance for Active Control by New Adaptive Modal State Estimator	142
(OAET 590-14-21)	

Integrated Control-Structure Design Methodology Development for Class of Flexible Spacecraft	143
(OAET 590-14-51)	
Enhanced Multiprocessor Performance Model	144
(OAET 590-32-31)	
Fabrication of Space Crane Articulating Joint Test Bed	145
(OAET 591-22-21)	

Space Technology

Experimental Aerodynamics of General-Purpose Heat Source Modules	149
(OAET 506-40-41)	
Precision Signal Processing for Micro-Level Flight Measurements	149
(OAET 506-40-71)	
Laser Beam Profile Calculations	150
(OAET 506-41-41)	
Lidar Boresight Alignment Using Four-Quadrant Microchannel Plate Photomultiplier Tube.....	151
(OAET 506-48-01)	
LDEF Retrieval Mission	151
(OAET 506-48-71)	
Spaceflight Optical Disk Drive	152
(OAET 584-02-21)	
Spaceflight Optical Disk Recorder Controller Development	153
(OAET 584-02-21)	
Multiple Architecture Space Technology 1750A Computer	153
(OAET 585-01-91)	
Precision-Segmented Reflector Support Truss	154
(OAET 585-02-31)	
Local Intensity Adaptive Imaging	155
(OAET 590-11-21)	
Thermal Analysis of Solid-State Lasers for DIAL and Doppler Lidar	156
(OAET 590-31-31)	
Modeling of Multiple-Ion-Doped Eye-Safe Solid-State Lasers for DIAL and Doppler Lidar.....	156
(OAET 590-31-31)	
Spectroscopic Measurements of Energy Transfer Processes in 2- μ m Laser Materials.....	157
(OAET 590-31-31)	
CO-O ₂ Recombination Catalyst for CO ₂ Lasers.....	158
(OAET 590-31-31 and OSSA 146-74-06)	
Development of Composite Materials for Precision Reflector Panels.....	158
(OAET 590-33-21)	
Functional Margin Demonstration for Pyrotechnics.....	159
(OSSA 678-12-04)	
Structural Life Assessment of Fasteners Via Test.....	160
(OSSA 678-12-04)	

Nonvolatile Residue (NVR) Cleanliness of Clean Room Wipes, Swabs, and Gloves.....	161
(OSSA 678-12-04)	
Organic-Film Cleanliness Certification of Environmental Chambers and Clean Rooms.....	162
(OSSA 678-12-04)	

Exploration

Reevaluation of Magnetic Radiation Shielding for Manned Mars Missions.....	165
(OSSA 199-04-16)	
Radiation Dose Estimates for 500-Day Manned Mars Mission	166
(OAET 326-83-10)	
Surface Heating Distributions on Aerobrake-Carrier-Payload Assemblies.....	166
(OAET 506-40-91)	
Thermochemical Nonequilibrium for Mars Aerobraking Entry	167
(OAET 506-40-91)	
Thermochemical Nonequilibrium Issues for Earth Reentry of Mars Mission Vehicles	168
(OAET 506-40-91)	
Aerodynamic Requirements of Manned Mars Aerobraking Transfer Vehicle	168
(OAET 591-42-11)	
Coupled Radiation Solutions for Earth Aerobraking	169
(OAET 591-42-21)	
New Bridging Formula for Calculating Rarefied-Flow Aerodynamics of Blunt Bodies	170
(OAET 592-01-11)	
Experimental Investigation of Aerobrake Near Wakes	171
(OAET 592-01-11)	
Lateral-Directional Stability Characteristics of Aeroassist Flight Experiment (AFE) Vehicle Configuration	172
(OAET 592-01-11)	

Global Change

Airborne Lidar Measurements of Atmospheric Water Vapor Distributions.....	175
(OSSA 146-74-01)	
Ground-Based Microwave Monitoring of Stratospheric Ozone	176
(OSSA 147-13-19)	
Laboratory Measurements of Ozone Infrared Spectrum	176
(OSSA 147-23-11)	
Infrared Spectroscopy of Stratosphere: Recent Results of Relevance to Global Change.....	177
(OSSA 147-44-02)	
CITE-3: Airborne Intercomparison of Tropospheric Instrumentation.....	178
(OSSA 176-20-13)	
Satellite Estimates of Gases Produced From Biomass Burning	178
(OSSA 199-30-76)	

Global Ozone Changes During 1980's	179
(AA 307-51-09)	
Gas Filter Correlation Radiometer Concept Utilizing Photo-Elastic Modulator	180
(AA 307-51-09)	
SAGE III	181
(OSSA 413-18-06)	
Spaceborne CO and CH ₄ Mapper	182
(OSSA 413-18-06)	
CERES Instrument Definition Studies	182
(OSSA 413-18-06)	
Design, Analysis, and Evaluation of Optical Systems	183
(OAET 506-45-31)	
Sensor Research for Lidar Applications	184
(OAET 506-48-01)	
High-Speed Data Acquisition for Lidar Applications	185
(OAET 506-48-01)	
Global Climate Change Technology Architecture Trades	186
(OAET 506-49-21)	
Large Platform Pointing	187
(OAET 506-49-21)	
Structural-Dynamic Behavior of Earth-Observing Large-Diameter Antenna	188
(OAET 506-49-21)	
Narrowband, High-Power, Ti:Al ₂ O ₃ Laser Development for DIAL Applications	189
(OAET 590-31-31)	
Mid-Infrared Optical Parametric Oscillator	189
(OAET 590-31-31)	
Earth Radiation Budget Experiment Movies	190
(OSSA 665-45-20)	
Validation of Earth Radiation Budget Measurements	191
(OSSA 665-45-30)	
Global Water Vapor Climatology From SAGE II	192
(OSSA 665-45-30)	
Tropospheric Measurements From Space With Solar Occultation Technique	193
(OSSA 665-45-30)	
Antarctic Ozone Loss Variability Linked to Polar Stratospheric Cloud Abundance	193
(OSSA 665-45-30 and OSSA 665-10-40)	
SAGE II Observations of Polar Stratospheric Clouds Near 50°N	194
(OSSA 665-45-30)	
Verification of Satellite Measurements of Stratocumulus Clouds	195
(OSSA 672-22-04)	
Determination of Tropical Cirrus Particle Size From Space	195
(OSSA 672-22-12)	

Estimation of Synoptic Fields of Middle Atmosphere Parameters Obtained From Satellite Data Sets.....	196
(OSSA 673-41-10)	
Mesopause Region Heating by Exothermic Chemical Reactions.....	197
(OSSA 673-41-10)	
Discovery of QBO Signal in SAGE II NO ₂ Data.....	198
(OSSA 673-41-13)	
Global Change of Total Column Ozone Through Solar Forcing.....	198
(OSSA 673-56-05)	
Heterogeneous Chemical Processes and Polar Ozone.....	199
(OSSA 673-64-02)	
Spike Detection Algorithm for HALOE Test Data Analysis.....	200
(OSSA 678-12-04)	
HALOE Quick-Look System.....	201
(OSSA 678-12-04)	
Venus Cooling Mechanism Isolated-Impact on Mars and Earth.....	201
(OSSA 889-50-48)	

Facilities

Bolt Tension Monitor.....	205
(OCE 323-51-66)	
Technology Developments for Advanced Hypervelocity Aerophysics Facility (AHAF).....	206
(OAET 504-40-71)	
Development of Particle Image Velocimeter for Rapid Global Flow Field Mapping.....	207
(OAET 505-60-11)	
Calibration and Characterization of Solid-State Cameras.....	208
(OAET 505-61-01)	
Thermal/Structural Analysis of Shaft Disk Region of National Transonic Facility.....	208
(OAET 505-61-85)	
Use of Oxygen-Free Contact Tip in GMAW Applications.....	209
(OAET 505-63-01)	
Addition of Automated Wetness System to Aircraft Landing Dynamics Facility.....	210
(OAET 505-63-41)	
Experimental Test Range.....	211
(OAET 505-66-91)	

Technology Utilization

Ultrasonic Tissue Thermometry System.....	215
(OCP 141-20-40)	
Contact Lens Quality Monitoring System.....	216
(OCP 141-20-10)	

Diaphragmatic Function Monitor	216
(OCP 141-20-40)	
Ultrasonic Monitor of Composite Porosity During Pultrusion	217
(OCE 323-51-66)	
Custom Cranial Patches	218

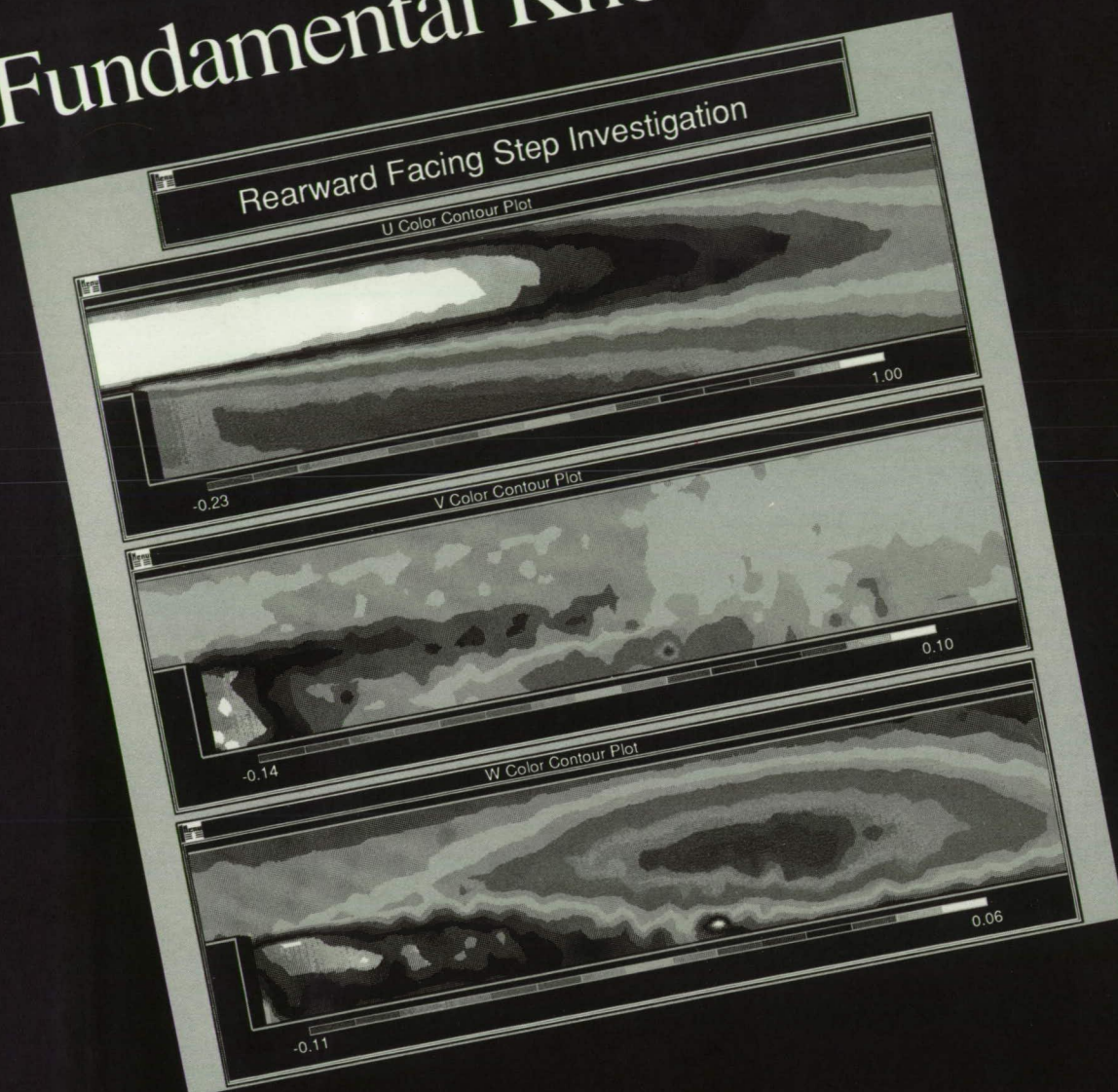
Contributing Organizations

Aeronautics Directorate	220
Electronics Directorate	221
Flight Systems Directorate	222
Space Directorate	223
Structures Directorate	223
Systems Engineering and Operations Directorate	224
Technology Utilization	225

Index

Index.....	226
------------	-----

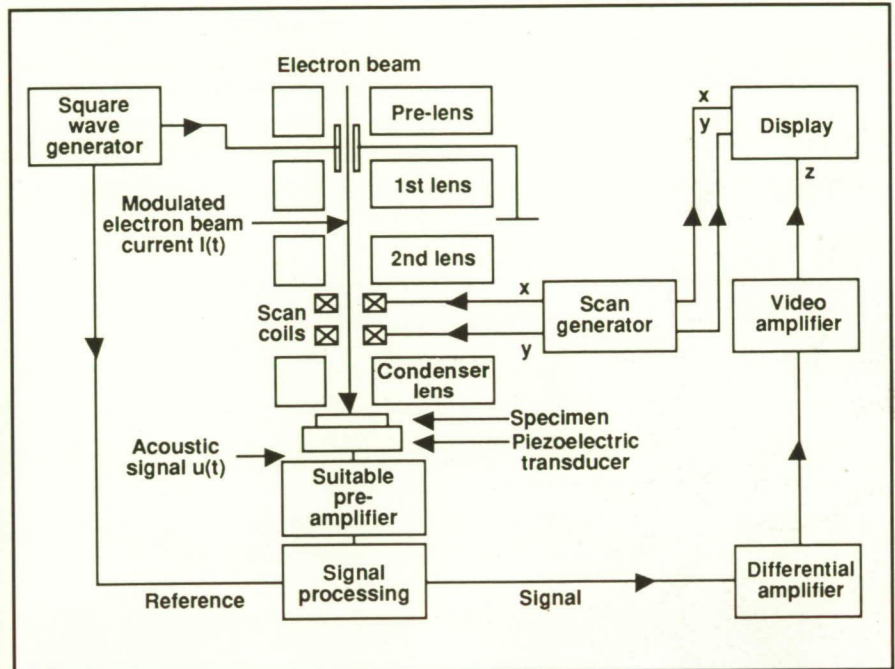
Fundamental Knowledge



Scanning Electron Acoustic Microscopy

The capability to assess the microstructural features of materials is important not only in fundamental studies of material properties but also in identifying those microstructural features that most directly influence

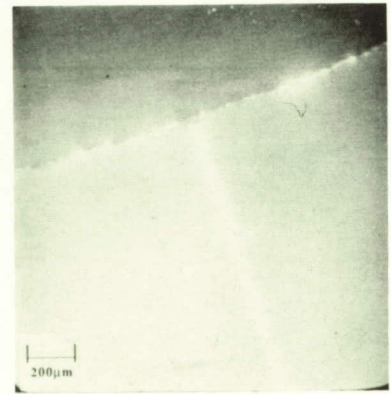
nondestructive measurements. Traditionally, the primary tools for microstructural studies have been optical and electron microscopes. Except for transmission microscopes, which require extensive and often elaborate specimen preparation, most microstructural images are topographical. Scanning electron acoustic microscopy (SEAM), a



Schematic of SEAM system.



(A)



(B)

($f = 305.43 \text{ kHz}$)

Comparative SEM (A) and SEAM (B) micrographs of flaws in alumina specimen.

novel microscopic imaging technology developed at Cambridge University, England, and now transferred to Langley Research Center, offers a new and often unique capability in imaging subsurface features of materials. J. H. Cantrell, as a participant in the NASA-National Space Club Dryden Fellowship program at Cambridge, has codeveloped and experimentally verified the first complete three-dimensional model of electron-acoustic signal generation in SEAM in which the factors defining and influencing contrast and spatial resolution of the images have been obtained.

The SEAM technology utilizes acoustic waves generated by modulating or chopping the electron beam in a conventional scanning electron microscope (SEM). The energy lost by the modulated electron beam in

colliding with the atoms of the specimen is converted in part to an acoustic wave at the modulation frequency. The acoustic energy is typically detected by a piezoelectric transducer attached to the specimen surface (as shown in the first figure). The signal from the transducer is fed into the input of a lock-in amplifier, the reference signal of which is obtained from the chopping frequency generator. The output from the lock-in is differentially amplified and fed to the z-axis of a cathode-ray oscilloscope. As the electron beam forms a raster on the specimen surface, an electron-acoustic image of the specimen is generated on the display.

A particularly important advantage of SEAM over conventional SEM is the ability to image not only topographical features of specimen microstructure but also subsurface

features. As an illustration, the second figure shows comparative SEAM and SEM micrographs of flaws in a ceramic material. The subsurface flaw that runs perpendicular to the surface breaking crack is revealed only in the SEAM micrograph.

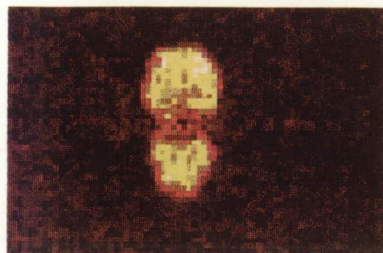
(J. H. Cantrell, 44989)

Electronics Directorate

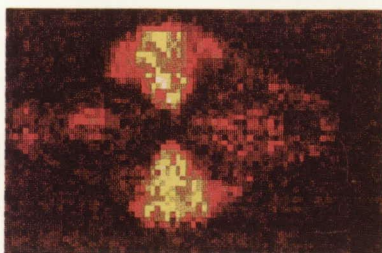
Impact Damage Assessment in Thick Composite Plates With Through-the-Thickness Reinforcements

One of the principal design requirements of aerospace structures fabricated from composite materials is the compression strength that remains after impact damage in these

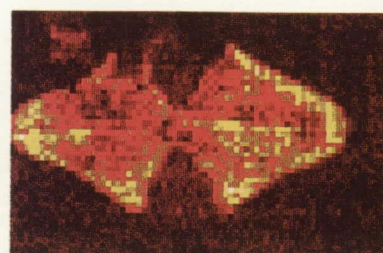
Uni-woven



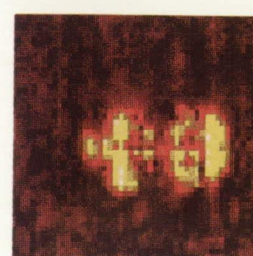
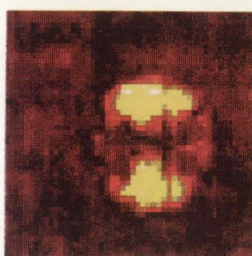
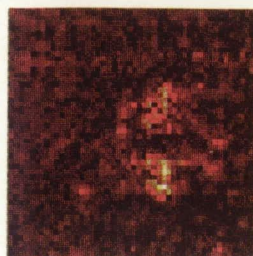
Interface 1



7



8



No crimp 3-D weave

Damage characterization of woven composite panels.

new emerging materials. Recent advances in textile technology and resin transfer molding techniques have produced composite structures that are equivalent to the cost of conventional metallic structures and which offer properties that are superior to those used in expensive damage tolerant prepreg systems. Research is needed to verify the promising attributes of these materials. Nondestructive testing methods can be cost effective for this verification as well as for application to maintenance and operational requirements.

Five nine-layer [0/90] AS-4-3501-6 graphite/epoxy panels (approximately 0.25 in. thick) have been evaluated. Two panels were fabricated using a lock stitch, and two panels were fabricated using an integral weave. One of the stitched and one of the integrally woven panels incorporated Kevlar, and the

other panel utilized graphite through-the-thickness fibers. A fifth panel was fabricated with no through-the-thickness reinforcements. All of the panels were impacted with an 0.5-in.-diameter aluminum ball traveling at 550 ft/s, which produced an impact energy of approximately 30 ft-lb. These panels first were nondestructively tested and then destructively tested for comparison.

The nondestructive evaluation (NDE) consisted of ultrasonically scanning to determine the location and extent of the damage. The signals were digitized and signal processed using Fourier deconvolution and analytic signal magnitude methods to produce volumetric views of the samples at any depth inside the panels. Shown in the figure are the quantitative NDE images of the impact-generated delaminations for three representative interfaces for a uniwoven and no-

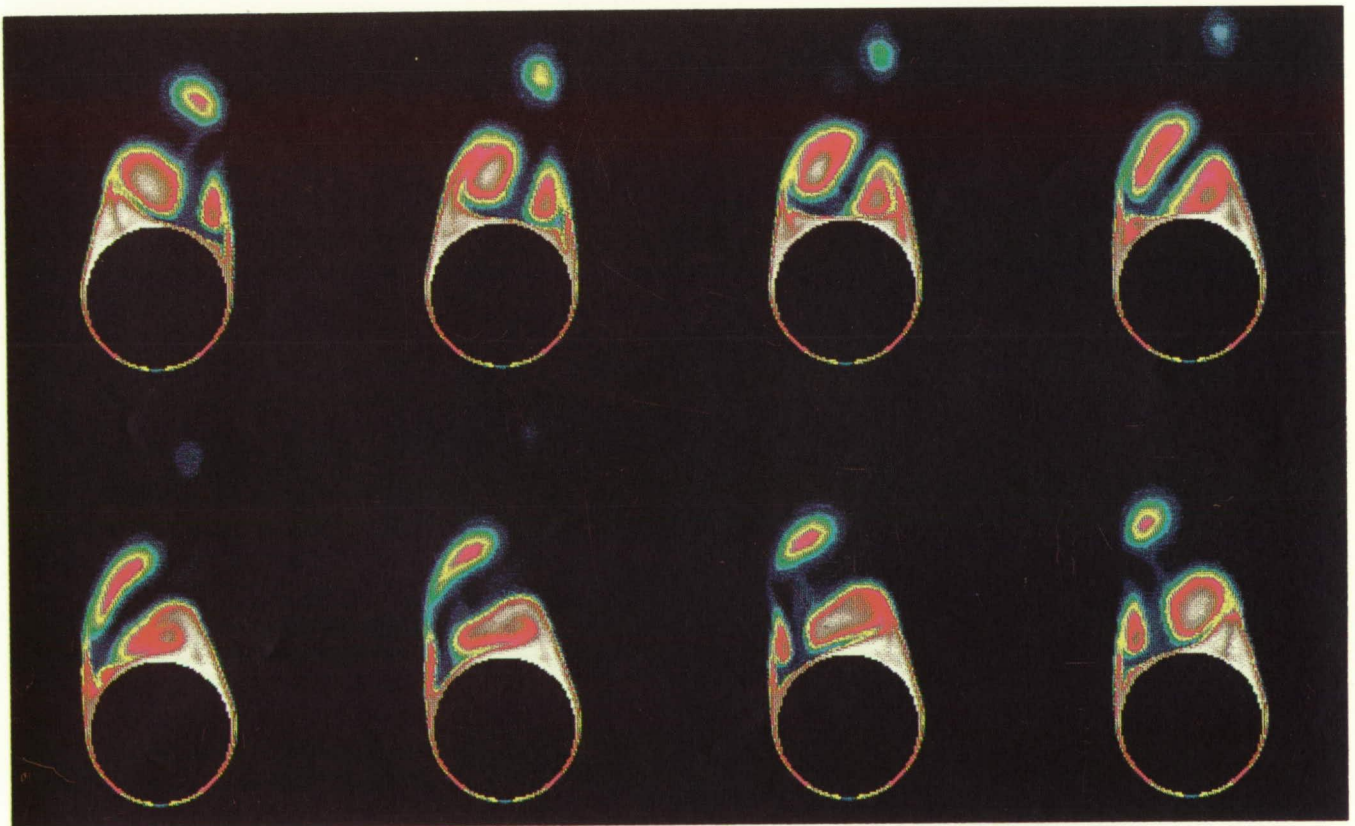
crimp three-dimensional (3-D) weave sample. The NDE images subsequently were verified by destructive testing. The images in the top part of the figure indicate larger delaminations as compared to the lower part of the figure. Both figures indicate progressively more damage deeper into the samples (from left to right). The data in the figure indicate the potential for this technique to assess impact damage in individual layers in these complex materials.

(Barry Smith, 44790, and Gary Farley)

Electronics Directorate

Prediction and Control of Asymmetric Flow Around Cones

The problem of asymmetric vortex flow about slender bodies in



Unsteady asymmetric flow with $\alpha = 30^\circ$, $M = 1.8$, and $Re = 100\,000$ (total-pressure-loss contours).

the high angle-of-attack α range is of vital importance to the dynamic stability and controllability of fighter aircraft and missiles. The onset of flow asymmetry occurs when the relative incidence (the ratio of angle of attack to the nose semiapex angle) of pointed forebodies exceeds a certain critical value. Flow asymmetry also is dependent upon the free-stream Mach number M , Reynolds number Re , and body-cross-section shape. The unsteady, compressible, thin-layer Navier-Stokes equations are used to computationally study asymmetric supersonic flows and their control around cones. Two computational schemes are used to solve the equations. The first, which is the primary scheme, is an implicit, upwind, flux-difference splitting, finite-volume scheme. The second, which is used to validate certain solutions of the upwind scheme, is an implicit, approximately factored, central-difference finite-volume scheme. Locally conical flow solutions are considered at a chord station of unity, and time-accurate stepping is used for unsteady-flow solutions. The implicit, upwind, flux-vector-splitting, finite-volume scheme also has been used to solve a few unsteady asymmetric flow cases for validation with the solutions of the flux-difference-splitting scheme. Several unsteady asymmetric flow cases have been computed; these cases show periodic asymmetric vortex shedding.

This study has shown that, for the same flow conditions, circular-section cones produce the strongest flow asymmetry, and diamond-section cones produce the weakest flow asymmetry. The study also has shown that flow asymmetry decreases as the Mach number increases and increases as the Reynolds number increases. Passive control of flow asymmetry also has been studied using vertical fins of different heights and side strakes of different orientations; side strakes were found to be

superior to vertical fins for controlling flow asymmetry over a wide range of relative incidence.

(Osama A. Kandil, 42278, Tin-Chee Wong, and Chen-Huei Liu)
Aeronautics Directorate

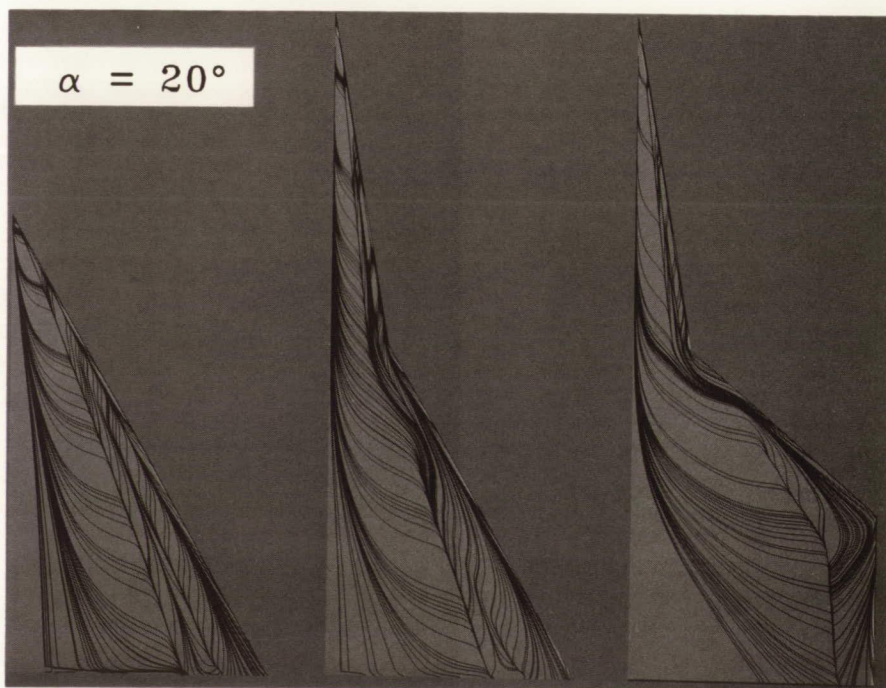
Navier-Stokes Solutions of Three-Dimensional Leading-Edge Vortex Flow

The computer code VOR3DI has been developed for computing low-speed viscous flows, such as three-dimensional (3-D) vortical flows over delta wings. The code uses the implicit upwind-relaxation finite-difference algorithm with a nonsingular eigensystem to solve the preconditioned, 3-D incompressible Navier-Stokes equations in curvilinear coordinates.

Navier-Stokes computations for 3-D leading-edge vortex flows over a delta wing of 60° , a double-delta

wing of 80° - 60° , and a cropped double-delta wing of 80° - 40° have been carried out. Steady-state solutions of these three low-aspect-ratio wings with rounded edges were compared with low-speed wind tunnel data. Good qualitative and quantitative comparisons were obtained.

Computed surface particle traces (equivalent to streamlines in the steady state) at an angle of attack α of 20° are shown in the figure. The flow is from the top. The complex flow fields of vortical interactions between the primary vortices of the wing, strake, and tip vortices are well simulated. Also, the secondary and tertiary vortices are clearly captured. The study has demonstrated that the code is capable of predicting accurately the complicated vortical flows over delta and double-delta wings.
(C.-H. Hsu, 42153, and C. H. Liu)
Aeronautics Directorate



Leading-edge vortex flows.

Adaptive Grid Calculations for Two-Dimensional Euler Equations

A two-dimensional upwind Euler code has been developed which employs adaptive grid embedding. The use of adaptive grid embedding produces irregularly shaped grid topologies, and, therefore, an unstructured data set is used. Each embedded grid is treated as a separate level so that a multigrid algorithm can be implemented to accelerate convergence. The fluxes, obtained using van Leer flux vector splitting, are computed in a conservative manner across grid levels. The solution is advanced in time using an explicit two-stage scheme.

The adaptive Euler code has been applied to several transonic airfoil cases. Results are shown for an

NACA 0012 airfoil at a free-stream Mach number of 0.95. The final adapted grid, which was adapted to the velocity difference across cells, consists of 29 243 cells and 8 levels of refinement in which the finest level of refinement is equivalent to a structured grid containing 1 572 864 cells. Excellent resolution of the shock structure is shown.

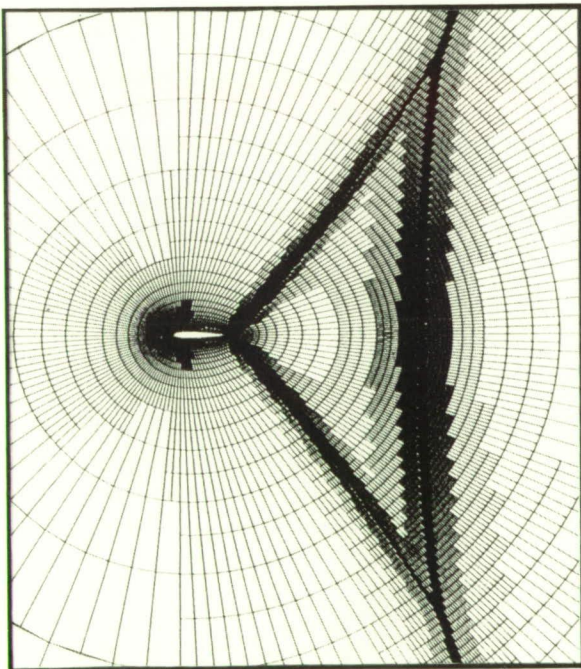
The capability to resolve flow features with significantly fewer grid points than the comparable structured grid has been demonstrated. The increased resolution of the calculations allows the investigation of shock structures that are difficult or impossible to examine experimentally.

The two-dimensional adaptive Euler code implementation is complete, and an extension to three dimensions is planned. Research is continuing to evaluate the effect of adaptation criteria on the reduction of

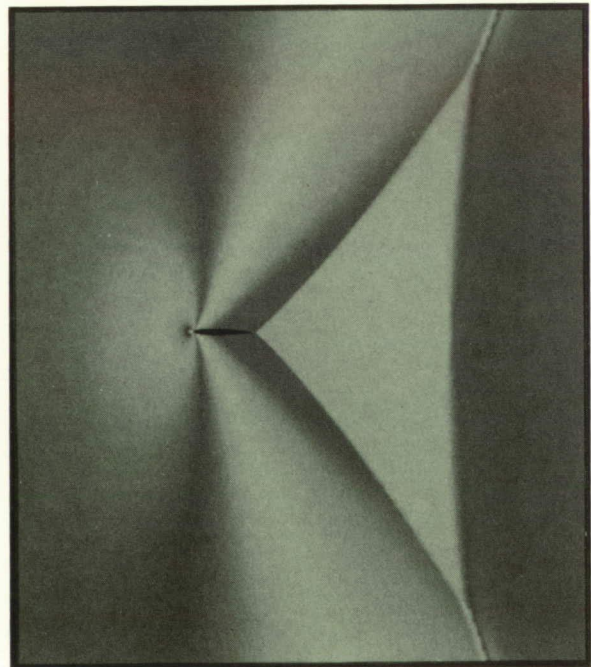
local and global truncation errors.
(Gary P. Warren, 42162)
Aeronautics Directorate

Development of Matrix-Valued Dissipation Model for Central-Difference Schemes

Numerical methods for solving the Navier-Stokes equations which are based on central finite differences have certain advantages in simplicity and speed of convergence over other more complex schemes, such as upwind-difference schemes. However, the artificial numerical dissipation inherent with the central differences is generally greater than that in the best upwind schemes. Artificial dissipation is a major source of numerical error on a given computational mesh. The rule of thumb has



Final adapted grid
(29,243 cells)



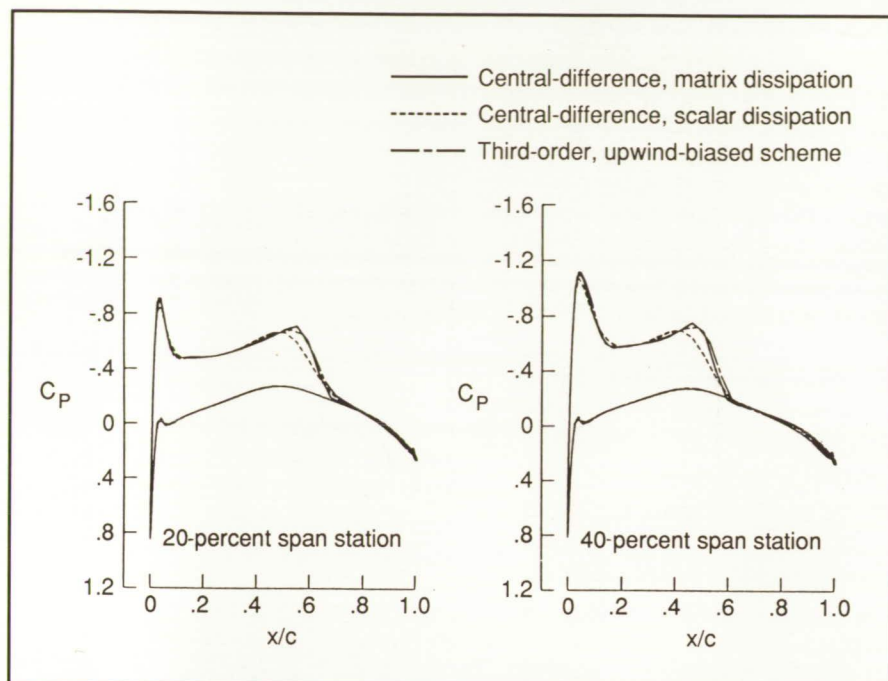
Pressure contours

Adaptive grid algorithm for NACA 0012 airfoil ($M = 0.95$ and $\alpha = 0^\circ$).

Navier-Stokes Calculations for Boeing 747 Wing/Fuselage Configuration

The availability of current-generation supercomputers coupled with recent advances in numerical algorithms has made it feasible to compute viscous flows over realistic aircraft configurations. A very efficient numerical code, TLNS3D, using a multistage Runge-Kutta time-stepping scheme, has been developed at Langley Research Center for computing high Reynolds number, viscous, transonic flows. The governing equations employed in the TLNS3D code are the thin-layer form of the Reynolds-averaged equations. A three-dimensional version of the Johnson-King turbulence model is used for improving the accuracy of the solutions for separated flow cases. The efficiency of the TLNS3D code is enhanced significantly via a multigrid acceleration technique.

The Navier-Stokes computations for flow over a Boeing 747 wing/fuselage configuration have been performed over a large range of test conditions. Approximately 3000 s of central processing unit (CPU) time is required to obtain a converged solution for a given test condition on the Boeing Cray-Y-MP supercomputer on a mesh consisting of over 600 000 grid points. The computed pressure distributions compare well with the experimental data; a typical comparison is shown in the figure for an angle of attack α of 5.73° at a Mach number M of 0.855. Similar agreement with the experimental data is obtained for the complete range of angle of attack, including the cruise and maximum-lift conditions. Based on such comparisons, it is concluded that the TLNS3D code can predict accurately the transonic flow over these types of configurations for test conditions of practical interest. This code is being



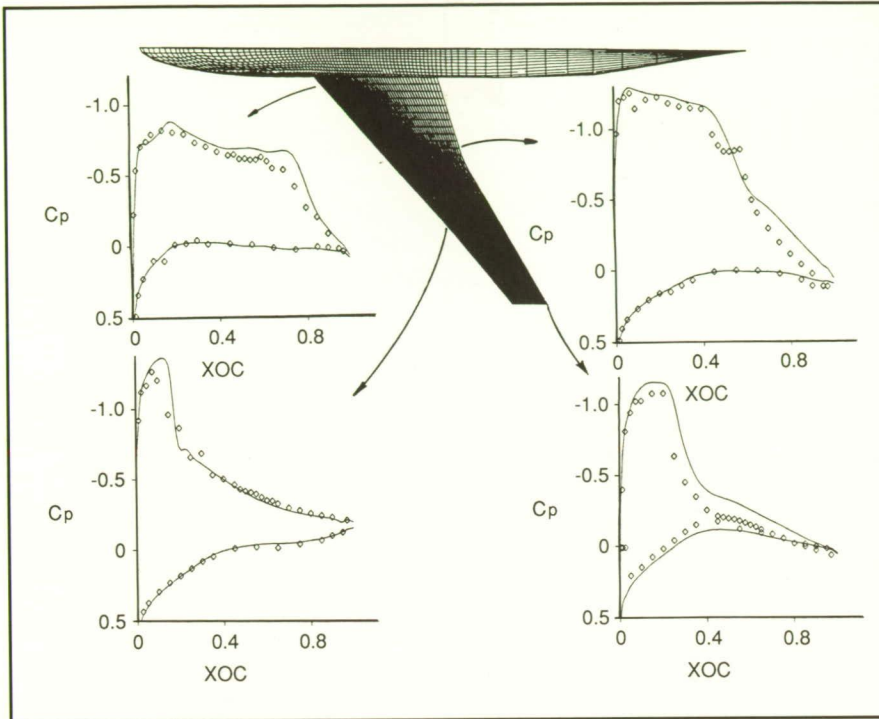
Comparison of central- and upwind-difference results for ONERA M-6 wing ($M_\infty = 0.84$, $\alpha = 3.06^\circ$, $Re_c = 11.7 \times 10^6$) with $97 \times 25 \times 17$ grid computations.

been that when solving high Reynolds number viscous flow fields with the central-difference scheme, one needs a finer mesh by a factor of 2 in each coordinate direction to achieve the same accuracy as the upwind scheme. Thus, some of the speed advantages of the central-difference schemes are lost when compared to upwind schemes on the basis of equal accuracy.

In principal, it is possible to improve the accuracy of central-difference schemes by reducing the dissipation in a fashion that mimics the dissipation inherent in the best upwind-difference schemes. This procedure leads to a matrix-dissipation model for the central-difference scheme, as opposed to the usual, simpler, scalar-valued dissipation model. A newly developed matrix-dissipation model is incorporated in the central-difference Navier-Stokes code, TLNS3D, which is a very efficient code for solving high Reynolds number, viscous, transonic flows. Based on the pressure distri-

butions for transonic flows over the ONERA (Office National d'Etudes et de Recherches Aérospatiales) M-6 wing shown in the figure, the accuracy of the new TLNS3D code is seen to be enhanced significantly, especially in the vicinity of the three-dimensional shock waves; this accuracy appears to be comparable to one of the best upwind-difference codes, CFL3D. Furthermore, only a small degradation was observed in the convergence rate of the TLNS3D code due to the matrix dissipation model. The increased accuracy thus allows engineering accuracy to be obtained on relatively coarser meshes and results in significant savings in computer resources and improved turnaround of computer runs in a design environment.

(Veer N. Vatsa, 42236)
Aeronautics Directorate



Test/theory comparisons for Boeing 747-200 configuration ($M = 0.855$, $\alpha = 5.73^\circ$, and $Re = 2.09 \text{ m/ft}$).

used at the Boeing Commercial Airplane Company for analyzing the newer wing designs.
(Veer N. Vatsa, 42236)
Aeronautics Directorate

Numerical Study on Use of Sulfur Hexafluoride in Wind Tunnels

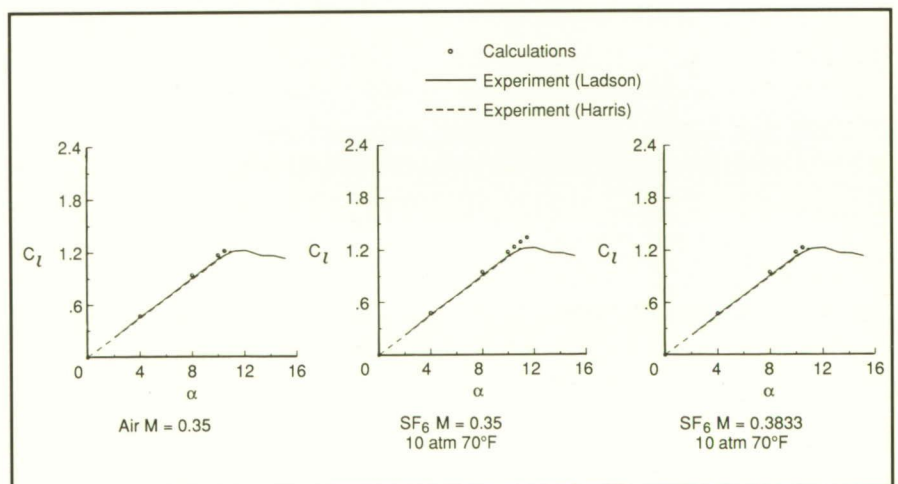
To attain higher Reynolds numbers for wind tunnel testing of high-lift devices, alternative test gases are being considered. One such gas is sulfur hexafluoride, SF_6 ; the high molecular weight of this gas makes it attractive as an air substitute in order to achieve high Reynolds numbers. However, unlike air, SF_6 is a nonideal gas with properties (such as internal energy and speed of sound) which are dependent on both pressure and temperature. While this is of little consequence for incompressible flows, compressibility effects at higher speeds (such as the variation

of shock locations and boundary-layer properties with Mach number) are not the same between the two gases.

The purpose of this study is to present numerical results for the inviscid Euler and viscous Navier-Stokes equations for several flow fields as an aid in determining the

suitability of SF_6 as a possible substitute for air in wind tunnels. Nonideal gas thermodynamics for SF_6 are included in both inviscid and viscous calculations.

Inviscid results for airfoils indicate that for transonic cases the shock locations calculated for SF_6 are different from those in air, and they move progressively forward on the airfoil as the free-stream pressure is increased and the real-gas effects become pronounced. However, a simple scaling procedure can be used which provides a different free-stream Mach number for SF_6 which results in good correlation with air. Subsonic turbulent flows over an NACA 0012 airfoil have been obtained using both air and SF_6 . The calculations were extended upward in angle of attack until steady solutions were no longer obtainable, thus indicating the onset of stall. The figure shows three curves of the lift coefficient C_l versus angle of attack α comparing the calculations with experiments in air. Higher angles of attack for stall were obtained for SF_6 than for air. The application of the Mach number correction ($M = 0.3833$) to the SF_6 calculations shows that the agreement with the air calculations is substantially improved. Although not shown, the



Lift comparison for air and SF_6 for NACA 0012 airfoil with $M = 0.35$ (air) and $Re = 6 \times 10^6$.

study indicates that as the Mach number increases, thermodynamic differences between air and SF₆ result in significant differences in boundary-layer properties which may make correlations between air and SF₆ difficult.

(W. Kyle Anderson, 42164)
Aeronautics Directorate

Numerical Predictions of Jet Exhaust Plume Flows Using Multiblock Multigrid Euler Solver

The proposed use of nonaxisymmetric nozzles for thrust vectoring in high-performance fighters has created a need for numerical tools to predict the flow fields associated with the jet exhaust plumes. These configurations can have very complex geometries that can make the grid generation quite difficult for a numerical method. To relieve this difficulty, a multiblock strategy was incorporated

into an existing three-dimensional, explicit, upwind Euler solver. Because the original code had multigrid acceleration to speed convergence, the data structure of multigrid was used to incorporate the multiblock structure. The marriage of multigrid acceleration and a multiblock structure creates a very useful code.

The multiblock structure provides a computer program that is independent of grid topology. This independence allows the same computer program to be used to solve internal flows (such as nozzle flows that have an H-H grid topology) and external flows (such as flows over a wing which have a C-H, C-O, or an O-O grid topology) without making changes to the program. This characteristic provides sufficient flexibility to calculate geometrically complex nozzle flow configurations.

As an example of its capability, the program was used to compute the two-nozzle flow shown in the figure.

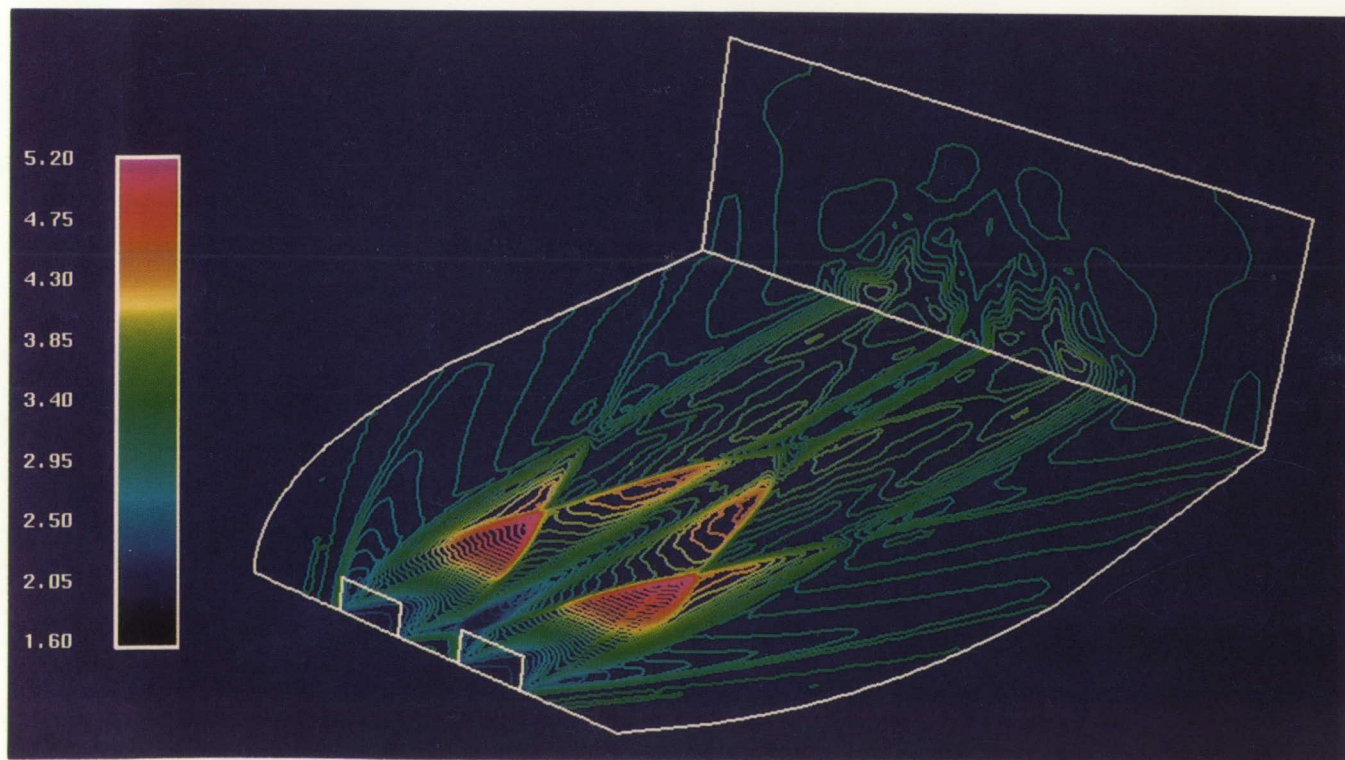
The flow conditions were $M_\infty = 3.0$, $M_{jet} = 1.99$, $p_{jet}/p_\infty = 8.96$, and $T_{jet}/T_\infty = 3.55$. The exit of nozzles is at the left with flow from left to right across a symmetry plane. The Mach contours of the predicted flow field are shown on the symmetry plane and the outflow boundary of the computational domain.

Future plans include improving the computational efficiency of the computer program by investigating various types of residual smoothing and including viscous terms in the governing equations.

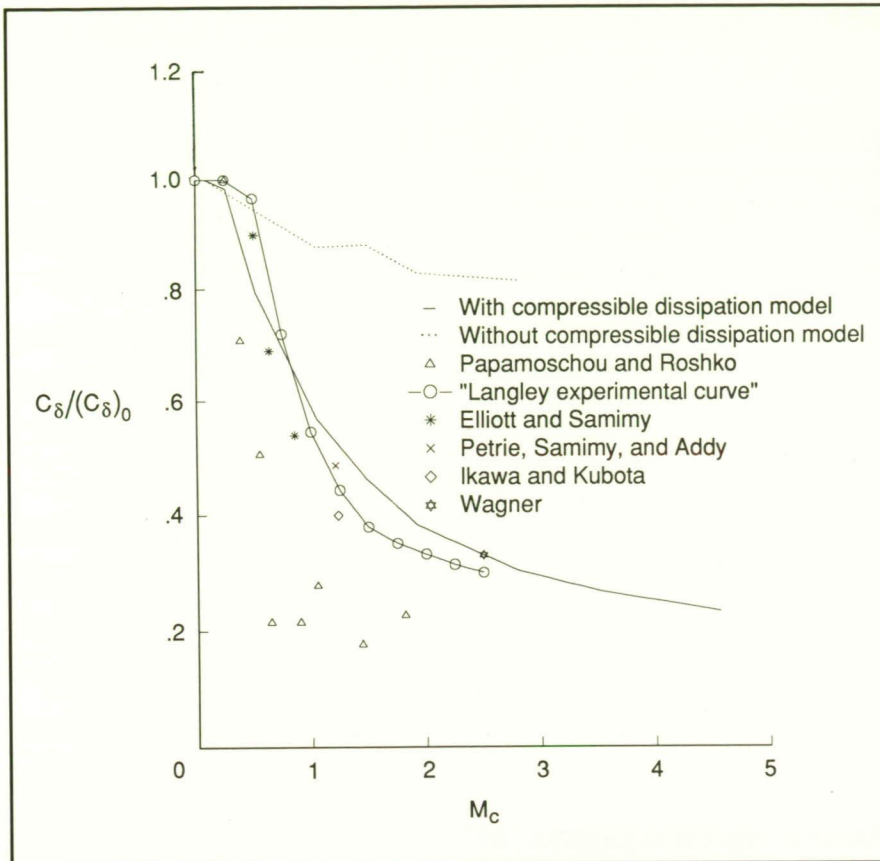
(N. Duane Melson, 42227)
Aeronautics Directorate

Reynolds-Stress Modeling for Compressible Turbulence

The primary objective of this project was the development and implementation of a Reynolds-stress



Interaction of multiple plumes and Mach contours ($M_{jet} = 1.99$, $M_\infty = 3.0$, $p_{jet}/p_\infty = 8.96$, and $T_{jet}/T_\infty = 3.55$).



Variation of growth rate of compressible shear layer with convective Mach number.

turbulence closure for high-speed compressible flows. Theoretical analyses and direct numerical simulations of compressible, homogeneous turbulence were used to develop turbulence models relevant to supersonic and hypersonic flows. Transport equations were formulated for the Favre-averaged Reynolds-stress tensor and the turbulent dissipation rate. The turbulent dissipation rate was decomposed into a solenoidal, incompressible part ϵ_s , and a compressible part ϵ_c . The compressible dissipation was shown to depend on the turbulent Mach number M_t by using both asymptotic analysis and direct numerical simulation of homogeneous turbulence. The following model was proposed for the compressible dissipation rate $\epsilon_c = \alpha_1 \epsilon_s M_t^2$, where the model constant $\alpha_1 = 1$ was obtained by calibrating against simulations.

The high-speed shear layer is a flow that shows strong compressibility effects because its growth rate is significantly lower than that of its low-speed counterpart. However, the prediction of this phenomenon of reduced mixing has been a major, unresolved issue in theoretically based turbulence modeling. The turbulence closure model in combination with the compressible Navier-Stokes equations was applied to the compressible shear layer. The figure compares model performance with experimental data regarding the variation of the normalized spreading rate $C_\delta/(C_\delta)_0$, as a function of the convective Mach number M_c . The Langley Research Center experimental curve in the figure is a consensus representation of various experimental investigations prior to 1972, while the symbols denote data obtained

from later experiments. The poor performance of a variable-density generalization of a standard incompressible Reynolds-stress closure (see the dotted curve in the figure) indicated the need for incorporating explicitly the mechanisms associated with turbulence compressibility. Inclusion of the new model of the compressible dissipation ϵ_c into the Reynolds-stress closure leads to agreement with the following critical trends in the experimental data. The first trend is the significant decrease in the spreading rate when the Mach number is increased, and the second trend is the relative insensitivity of the spreading rate, after its initial decrease, to further increases in the relative Mach number.

The need for incorporating the physics of compressible turbulence in order to capture strong compressibility effects (such as the dramatic reduction of growth in the high-speed shear layer) has been unequivocally established. A turbulence model based on asymptotic analysis and validated against direct numerical simulations has successfully captured the reduction in growth rate of the compressible shear layer. Reynolds-stress modeling along with direct simulations seems to be a promising approach in the study of compressible turbulence.

Direct numerical simulations will continue to be conducted in order to gain more insight into the turbulence processes in high-speed flows. The Reynolds-stress closure will be applied to other compressible flows such as perturbed as well as unperturbed turbulent boundary layers. Additional compressibility effects (such as large thermodynamic fluctuations) and the presence of shocks will be modeled.

(S. Sarkar, ICASE, 42194)
Aeronautics Directorate

Three-Component Laser Velocimeter Surveys of Flow Over Rearward Facing Step

A cooperative research program between Langley Research Center and Ames Research Center has been established to develop and validate direct turbulence simulations (DTS), large eddy simulations (LES), and closure models for the Reynolds-averaged Navier-Stokes equations. As part of the program, Langley is conducting an investigation to provide detailed flow field measurements of the flow over a rearward facing step. This investigation measured the instantaneous velocities throughout the flow field using a three-component laser velocimeter. The mean velocities and normal and

Reynolds stresses were calculated from these velocity measurements.

The investigation was conducted on a rearward facing step with a 2:1 expansion ratio at a Reynolds number based on a step height of 26 000. Two 700-point flow field surveys were conducted along the centerline of the facility, and detailed boundary-layer surveys were made at 27 locations. Over 6 million individual measurements of velocity were made at 4000 locations in the flow. The figure presents the nondimensionalized mean velocity components for one of the 700-point surveys of the flow over the step. The longitudinal component u shows a reversed flow of 20 percent of the free-stream velocity in the recirculation zone. The out-of-plane flow is shown by the v component; this component indicates that the flow is essentially

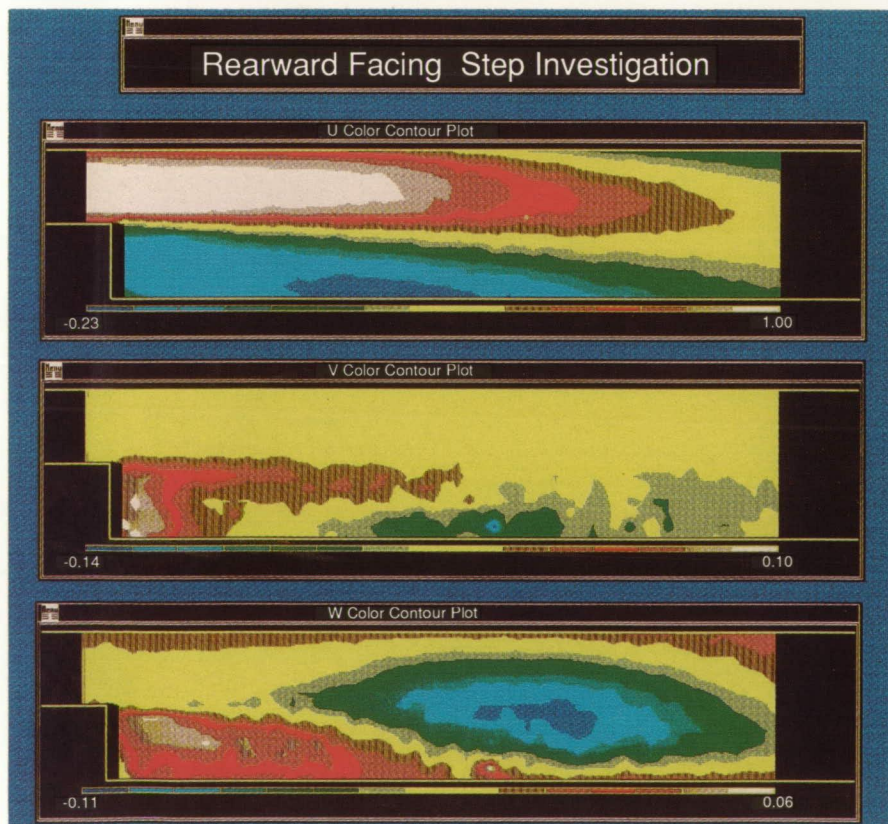
two dimensional except in the recirculation region. The w component shows the downwash of the flow to fill the expanding duct. These data are the first three-component measurements of the flow over a rearward facing step, and they provide a unique data base for the development and validation of DTS, LES, and closure models.

(Scott O. Kjeldaard, 42160)
Aeronautics Directorate

New Method for Handling Artificial Computational Boundaries

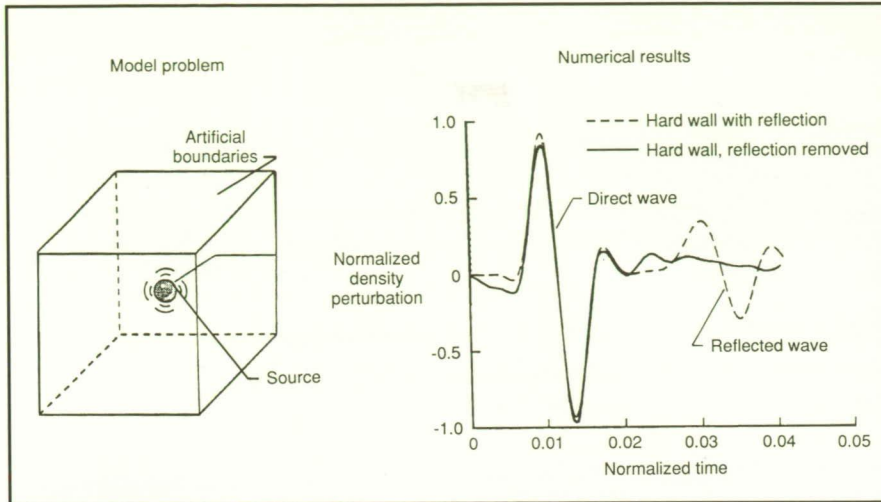
One difficulty in applying numerical methods to many unsteady, multidimensional problems is developing and implementing non-reflecting boundary conditions for artificial computational boundaries. Artificial boundaries do not exist in the physical problem, but they must be imposed to make the problem finite so that it may be solved on a computer. Perfectly nonreflecting boundary conditions allow information to travel unimpeded through the artificial boundaries and not to reflect back into the computational domain. Because successful development of nonreflecting boundary conditions has been limited, recent work done at Langley Research Center has focused on a new approach for handling artificial computational boundaries. Instead of attempting to derive nonreflecting boundary conditions, the approach taken is to allow reflections from the artificial computational boundaries and then to remove the reflections from the solution with a digital signal-processing technique known as Cepstrum analysis.

The results of the research show that Cepstrum analysis may be used to effectively remove reflections from



Color contours of mean velocity components in flow over rearward facing step.

ORIGINAL PAGE
COLOR PHOTOGRAPH



Removing reflections from artificial boundaries with Cepstrum analysis.

artificial computational boundaries. As an example, the model problem of a time-dependent simple acoustic source in infinite space is considered. In order to solve this problem on a computer, artificial boundaries are imposed as illustrated in the figure. The approach taken is to prescribe simple hard wall conditions at these artificial boundaries and to remove the resulting reflections from the solution with Cepstrum analysis.

The Euler equations are solved in three dimensions on a uniform Cartesian grid. The source at the center of the computational domain is perturbed resulting in a wave that travels to the artificial boundaries and reflects back. The normalized density perturbation time history at a grid point located midway between the source and boundary is shown by the dashed line in the figure. The first pulse, consisting of expansion and compression regions, is the initial source wave. The second pulse is the wave reflected from the hard wall boundary. Cepstrum analysis is applied to the time sequence, and most of the reflection is removed from the solution, as illustrated by the solid line in the figure. The Cepstrum analysis procedure may be similarly applied to each grid point in the numerical domain, thus resulting

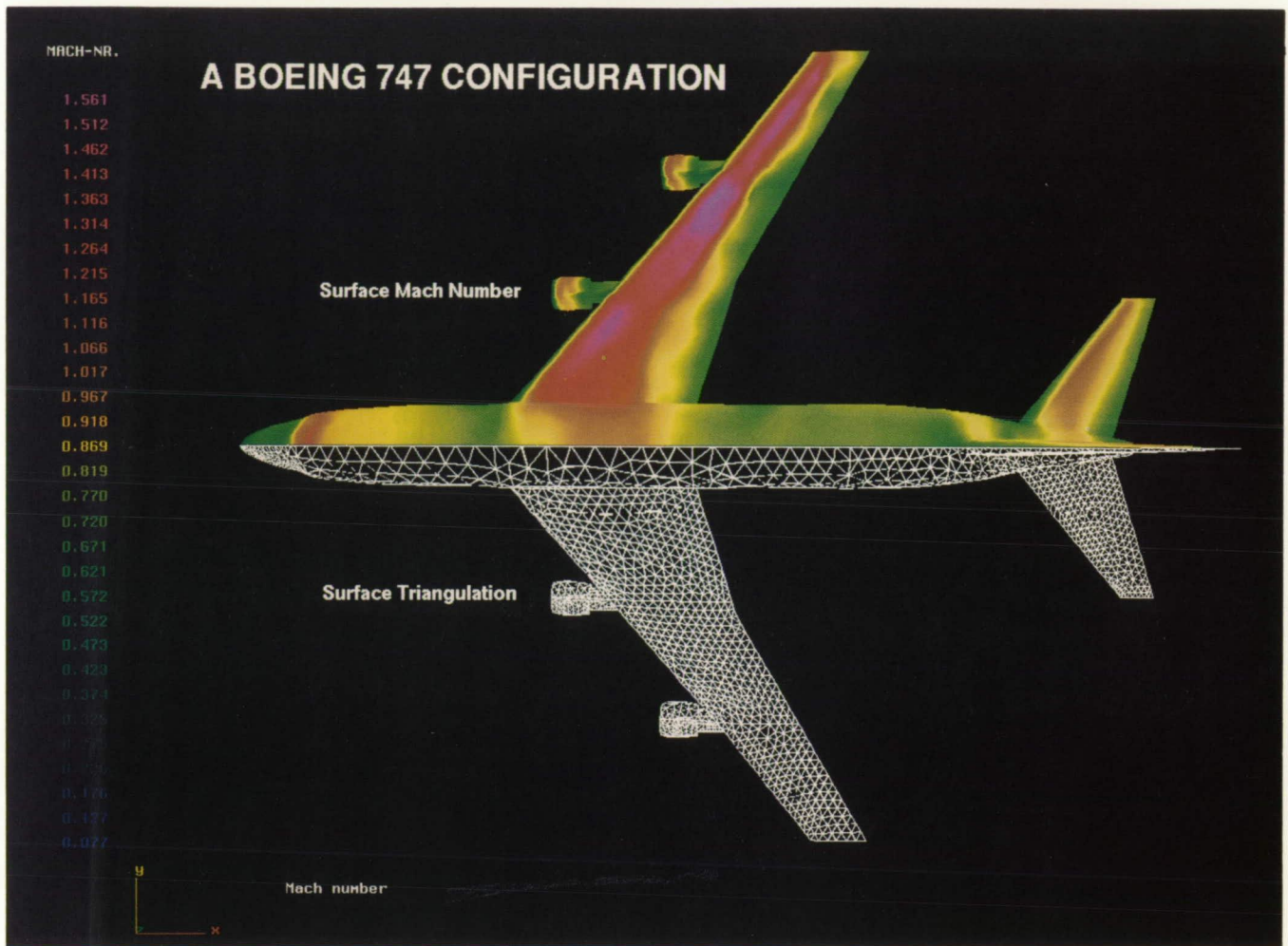
in a solution free of reflections from the artificial computational boundaries.

(Kristine R. Meadows, 43624)
Structures Directorate

Complete Package for Analysis of 3-D Flows Using Unstructured Grids

A complete, reliable package has been developed for analyzing in a timely manner the transonic flow field about complex configurations. This package contains an unstructured grid generator, an Euler equation solver, and a postprocessor graphics visualization program. Unstructured grids are generated and refined using VGRID3D, which applies the advancing front technique to construct tetrahedral cells and their connectivity. A transonic inviscid flow solution is obtained on the grid using a new, efficient upwind flow solver, USM3D. The results are analyzed and plotted using an interactive, graphics postprocessor program, VPLO3D.

Besides their inherent capability of handling complex configurations with ease, unstructured grids offer better control over the grid size and point clustering and are apt to efficiently incorporate adaptive refinement techniques. A tetrahedral grid has been generated from a surface patch definition of a Boeing 747-200 configuration with flow-through nacelles using VGRID3D. The grid consists of 105 372 cells and 19 698 nodes. An inviscid solution has been obtained on this grid using USM3D. The converged result is portrayed in the figure, which shows both the surface grid as well as the shaded Mach contours for a free-stream Mach number 0.84 and an angle of attack of 2.73° . The red contours on the wing indicate a region of supersonic flow that is terminated by a shock wave where the contours change to yellow. This solution was obtained with a Courant-Friedrichs-Lewy (CFL) number of 3 in 1600 cycles for a decrease in the residual error of 3.7 orders of magnitude. The solution required approximately 100 min of Cray-2S



Mach contours and surface grid for Boeing 747-200 configuration ($M_\infty = 0.84$ and $\alpha = 2.73^\circ$).

time and used less than 8 MW of memory. The presented results, which were readily obtained on the first attempt, thus demonstrate the robustness of the code in computing a complex flow field about a full aircraft configuration.

(P. Parikh, S. Pirzadeh (ViGYAN, Inc.), and N. T. Frink, 42244) Aeronautics Directorate

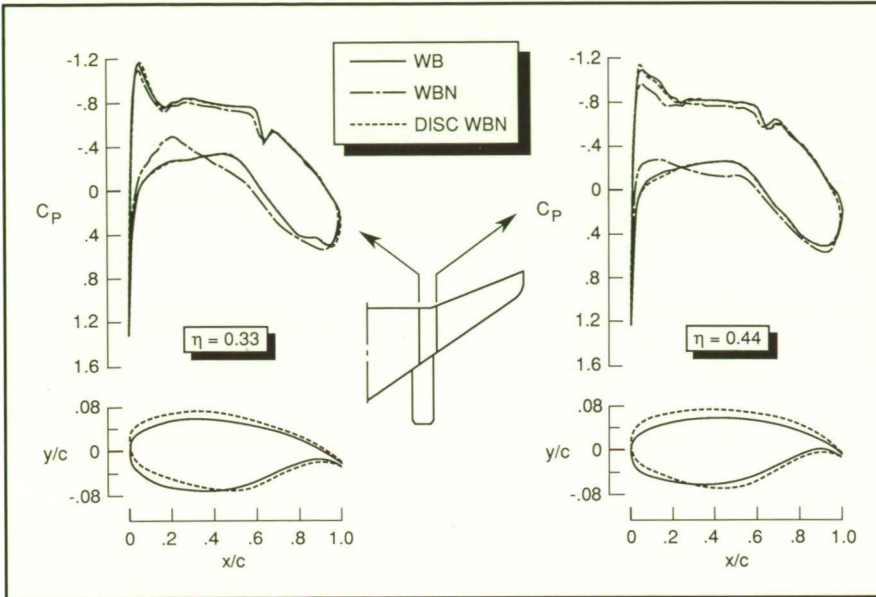
Elimination of Nacelle Interference Using DISC Design Method

A study has been conducted to explore the use of the Direct Iterative

Surface Curvature (DISC) design method in recontouring a wing to eliminate nacelle interference. The DISC method is a technique that modifies surface curvatures and slopes of an initial geometry so that a target pressure distribution is matched. This method has been coupled with various codes, including the Wing/Body/Pod/Pylon/Winglet (WBPPW) code developed by Charles Boppe of Grumman Corporation. For this exercise, the combined DISC and WBPPW methods were applied to a high-wing transport configuration with nacelles. By specifying wing/body-only pressures as target pressure distributions, a new

wing shape was obtained for the nacelle-on case.

The figure shows pressure distributions and airfoils for stations both slightly inboard and slightly outboard of the nacelle centerline at a cruise Mach number of 0.8. Computed pressure coefficients (C_p) are shown for the original wing and body (WB) and the original wing/body with the nacelle added (WBN). The DISC curves show the results for the new wing coupled with the body and nacelle. Thus, the finished wing design when analyzed with nacelles on yields the previous clean-wing pressures. This observation holds true for both design and off-design Mach numbers.



Comparison of original and redesigned pressures and airfoil sections ($M = 0.8$).

This exercise demonstrates the ability of the DISC design method to eliminate nacelle interference. The ability to design to a specific pressure distribution with the nacelles on should help maintain elliptical spanloads for reduced induced drag and limit other undesirable effects of nacelle-on wing performance, such as early separation and lift loss.

(Leigh Ann Smith, 42878)
Aeronautics Directorate

laminar nozzle wall flow. A new, slow-expansion nozzle contour with a radial flow section was implemented to increase the length of the quiet flow region by delaying the onset of the Görtler instability mode. The nozzle design was completed using the Method of Characteristics with displacement thickness corrections. Linear stability analysis was used to predict nozzle wall transition locations as shown in the figure.

Computations show that a quiet region of uniform Mach 8 flow up to

90 in. in length may be realized at the total pressure and temperature conditions shown. This performance, however, requires an exceptionally high-quality polish in the throat region which will endure the corrosive, high-temperature conditions required for Mach 8 operation. Employing a roughness Reynolds number of 12 based on pilot tunnel experience, the maximum allowable roughness height is 30×10^{-6} in.

If the nozzle can be fabricated to design tolerances and polished to the required finish and can maintain these under high-temperature run conditions, it will be a unique facility that allows, for the first time, hypersonic instability and transition testing in a disturbance-free environment.

The engineering design of the nozzle is complete using Inconel 601 (a high-temperature, corrosion-resistant steel) as the nozzle material.

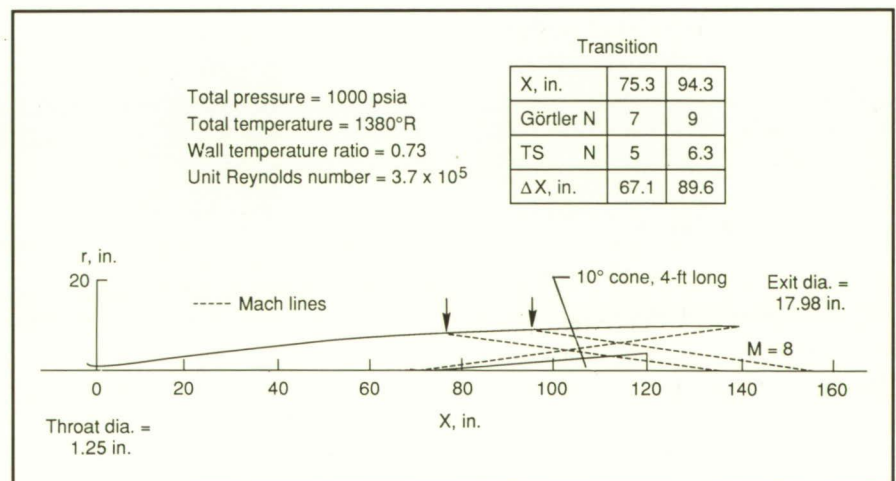
(Stephen P. Wilkinson, 45733)
Aeronautics Directorate

Multiple Paths to Laminar Breakdown in Boundary Layer

The classical boundary-layer transition experiments of the early

Design of Advanced Slow-Expansion, Slotted Nozzle for Quiet Operation of Mach 8 Variable Density Tunnel

A Mach 8 axisymmetric nozzle has been designed for conversion of the Mach 8 Variable Density Tunnel to a quiet-flow facility. The new design is based on experience obtained in the Supersonic Low-Disturbance Pilot Tunnel which showed that a highly polished nozzle preceded by slots to remove the settling-chamber boundary layer along with settling-chamber free-stream turbulence/noise management was sufficient to produce quiet,



Mach 8 quiet nozzle.

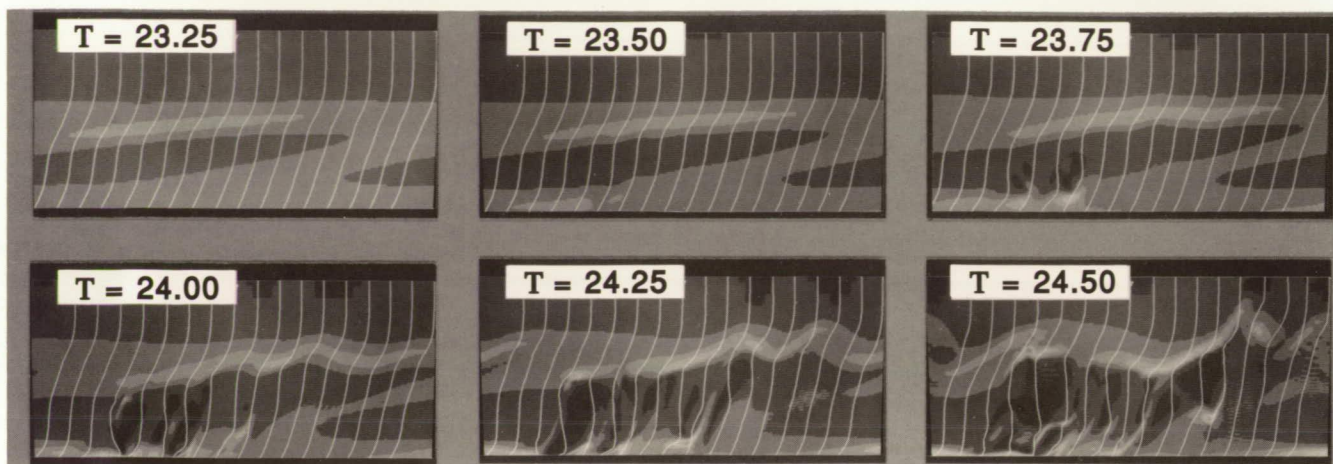


Illustration of subharmonic small-scale laminar breakdown triggered by wall bursts with low-amplitude Kachanov-Levchenko conditions (normal shear in peak plane).

1960's led to the scenario that the breakdown of laminar flow into turbulent flow was triggered by large-scale vortices (known as detached shear layers) which were generated near the edge of the boundary layer. However, in several recent transition experiments, laminar breakdown was observed to occur without such detached shear layers.

High-resolution numerical simulations based upon the three-dimensional, time-dependent, nonlinear Navier-Stokes equations have been employed to study the laminar breakdown stage and to clarify the distinctions between these two experimentally observed types of laminar breakdown. Some of these numerical simulations have reproduced the classical type of breakdown in which the detached shear layers appear. The laminar breakdown process in other simulations has been characterized by much weaker detached shear layers but with very strong wall bursts. The simulations indicate that the key parameters determining the type of breakdown are the initial amplitudes of the disturbances. Large initial amplitudes produce large-scale detached shear layers, whereas small initial amplitudes are connected with laminar breakdown triggered by wall bursts.

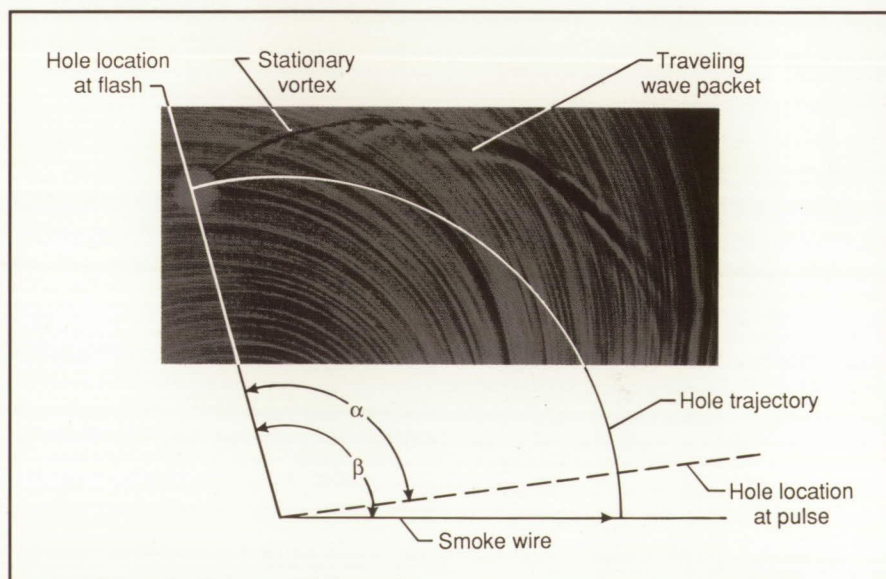
The key features of the breakdown process are best observed in the so-called peak plane, which is that cross section in the streamwise and wall normal directions in which the detached shear layer is most prominent. The figure shows the evolution in time of the normal shear (essentially the spanwise vorticity) in the peak plane. The detached shear layer is quite weak, and the strongest vorticity originates at the wall (at $T = 23.75$ and later). These wall bursts trigger the breakdown of the entire flow,

including the weak detached shear layer.

(T. A. Zang, 42307, and M. Y. Hussaini, ICASE)
Aeronautics Directorate

Visualization of Traveling Wave Packet on Rotating Disk

The laminar boundary layer on a rotating disk is a fully three-dimen-



Smoke streak lines showing traveling wave packet.

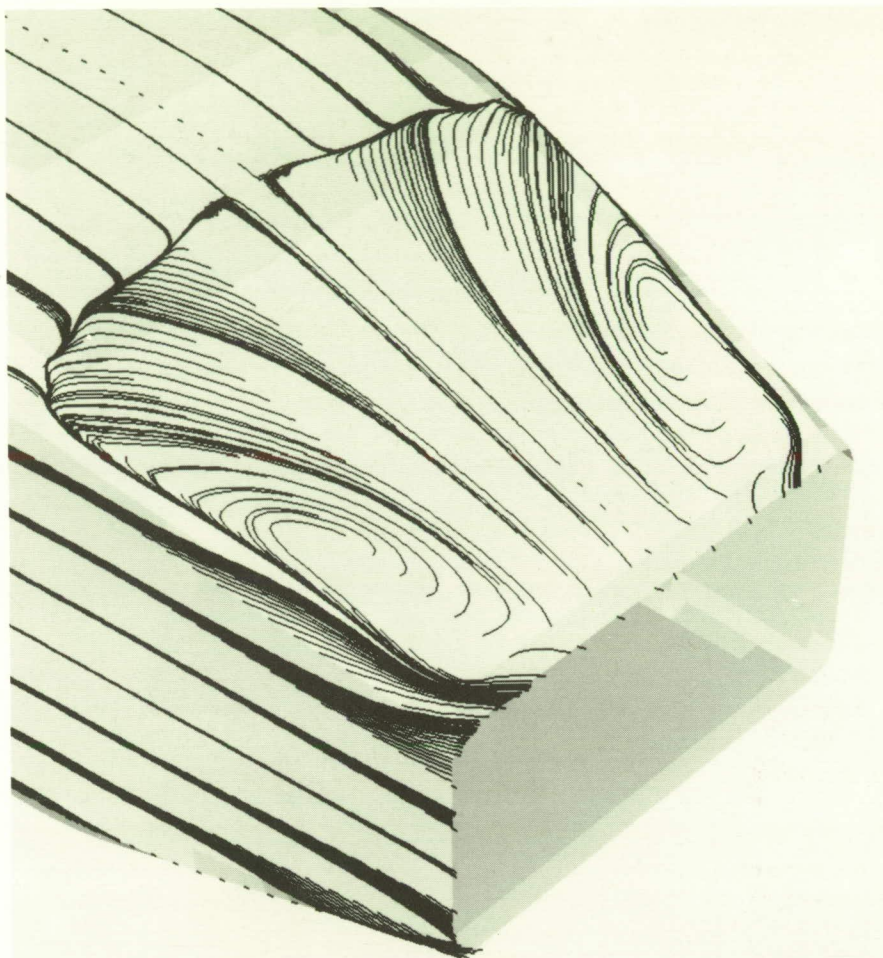
sional, cross-flow-dominated flow similar to flow over swept wings. Although the dominant transition mode on a rotating disk is the breakdown of stationary cross flow vortices, linear stability theory admits other nonstationary disturbance modes. As a first step toward developing experimental capabilities to study such nonstationary modes, a demonstration was set up to visualize the effect of a single, short-duration pulse of air through a small orifice in the disk surface. This setup is known to generate a traveling wave packet in a two-dimensional flow. Using a traditional smoke-wire flow visualization technique, the pulsed disturbance also was observed to produce a traveling wave packet in the three-dimensional disk flow (in addition to the stationary vortex caused by the orifice itself, as shown in the figure).

This result is significant for several reasons. First, it shows that the presence of the smoke wire in the disk boundary layer did not introduce unacceptable disturbances of its own. Second, it opens up a new avenue for research into the nature and behavior of nonstationary, three-dimensional instability modes on the disk. Image analysis techniques applied to a series of photos (such as that shown along with conventional hot-wire velocity measurements) will allow reconstruction of flow structures for comparison with companion computational fluid dynamics (CFD) efforts.

(Stephen P. Wilkinson, 45733)
Aeronautics Directorate

Navier-Stokes Simulation of Transonic Afterbody Flows With Jet Exhaust

Three-dimensional Navier-Stokes simulations have been made for the transonic flow past a nonaxisymmetric nozzle typical of those advocated for advanced fighter



Computed oil flows on afterbody (calculated jet, free-stream Mach number = 0.94, angle of attack = 0° , and Reynolds number = 20×10^6 using Goldberg turbulence model).

airplanes. Jet exhaust simulation is evaluated as are the Baldwin-Lomax and Goldberg turbulence models. Solutions were obtained with the CFL3D and PAB3D codes for Mach numbers of 0.80 and 0.94, an angle of attack of 0° , and a Reynolds number of 20×10^6 based on the model length. The results are compared to wind tunnel data.

At a free-stream Mach number of 0.80 where the separation is minimally thick, the calculations all correlated well with the wind tunnel data over the forward one-half of the nozzle. These calculations capture the suction pressure peak exceptionally well as the flow expands around the boattail shoulder.

At this Mach number, including the jet exhaust in the calculations gives the most accurate solution near the nozzle exit. As expected, a solution with a sting plume simulator does not predict well the flow near the exit. This result reiterates the well-established fact that a solid-plume simulator does not adequately represent the jet exhaust.

At a free-stream Mach number of 0.94, where massive separation exists on the nozzle, the pressure distributions calculated with both turbulence models agree well with the data up to the point of shock-induced separation. Behind this point, the models give considerably different flow fields. The Goldberg model predicts the location of the shock-induced

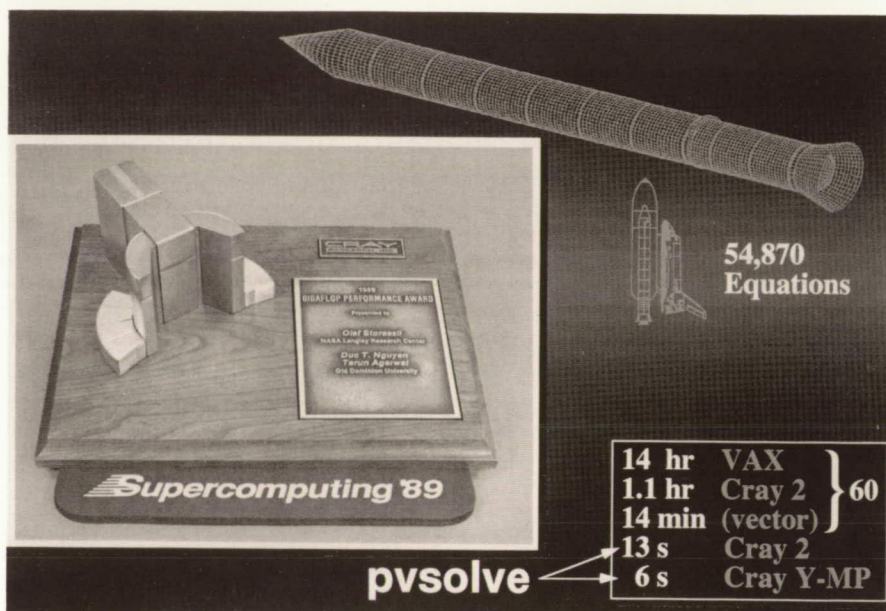
separation better than the Baldwin-Lomax model, gives a more accurate pressure rise after the shock, and also produces a much thicker separated region than the Baldwin-Lomax model. The figure depicts particle traces on the afterbody surface computed with the Goldberg turbulence model at a free-stream Mach number of 0.94.

(William B. Compton III, 43048, and Khaled S. Abdol-Hamid)
Aeronautics Directorate

Faster Analysis of Space Shuttle Solid Rocket Booster Using PVSOLVE

Predicting the mechanical response of complex aerospace structures under operational environments can be a computationally intensive task, even using current structural analysis codes on supercomputers. Solving the simultaneous equations resulting from the structural finite-element model dominates the computational time, particularly for large-scale problems. New methods are needed which minimize structural analysis time by exploiting both the parallel (multiple processors) and vector capability of supercomputers.

Computational mechanics research at Langley Research Center has resulted in a general-purpose parallel-vector equation solver, PVSOLVE, which reduces computational time in proportion to the number of processors used. This reduction is achieved by performing Cholesky factorization with parallel computation at the outermost loop and vector computation at the innermost loop in addition to optimizing vector performance. A variable-band storage scheme yields optimal vector efficiency with simultaneous addition and multiplication operations using all eight processors of the Cray Y-MP supercomputer.



Tabulated times and Cray award.

L-89-14315

A 54 870-equation structural model of the Space Shuttle Solid Rocket Booster (SRB), developed to investigate the effects of local bending in the neighborhood of the O-ring seals, exceeds 14 hr for a typical finite-element code on a VAX 11/780 computer. The same analysis takes 66 min on a Cray-2 and reduces to 14 min when fully vectorized; this is a sixtyfold speedup due to hardware. In addition, using PVSOLVE requires only 13 and 6 elapsed seconds to obtain solutions of equivalent accuracy on the Cray-2 and Cray Y-MP supercomputers, respectively. This additional speedup of up to 140 times is essentially due to the PVSOLVE algorithm, giving a total speedup of 8400 times the original VAX 11/780 solution. The 9.2×10^9 floating-point operations required for the matrix factorization with 6 elapsed seconds results in a rate of 1.517 gigaflops. This rate is the highest performance achieved for equation solution and is recognized by the 1989 Cray Gigaflop Performance Award (see the figure) presented during the Supercomputing '89 Conference in November 1989.

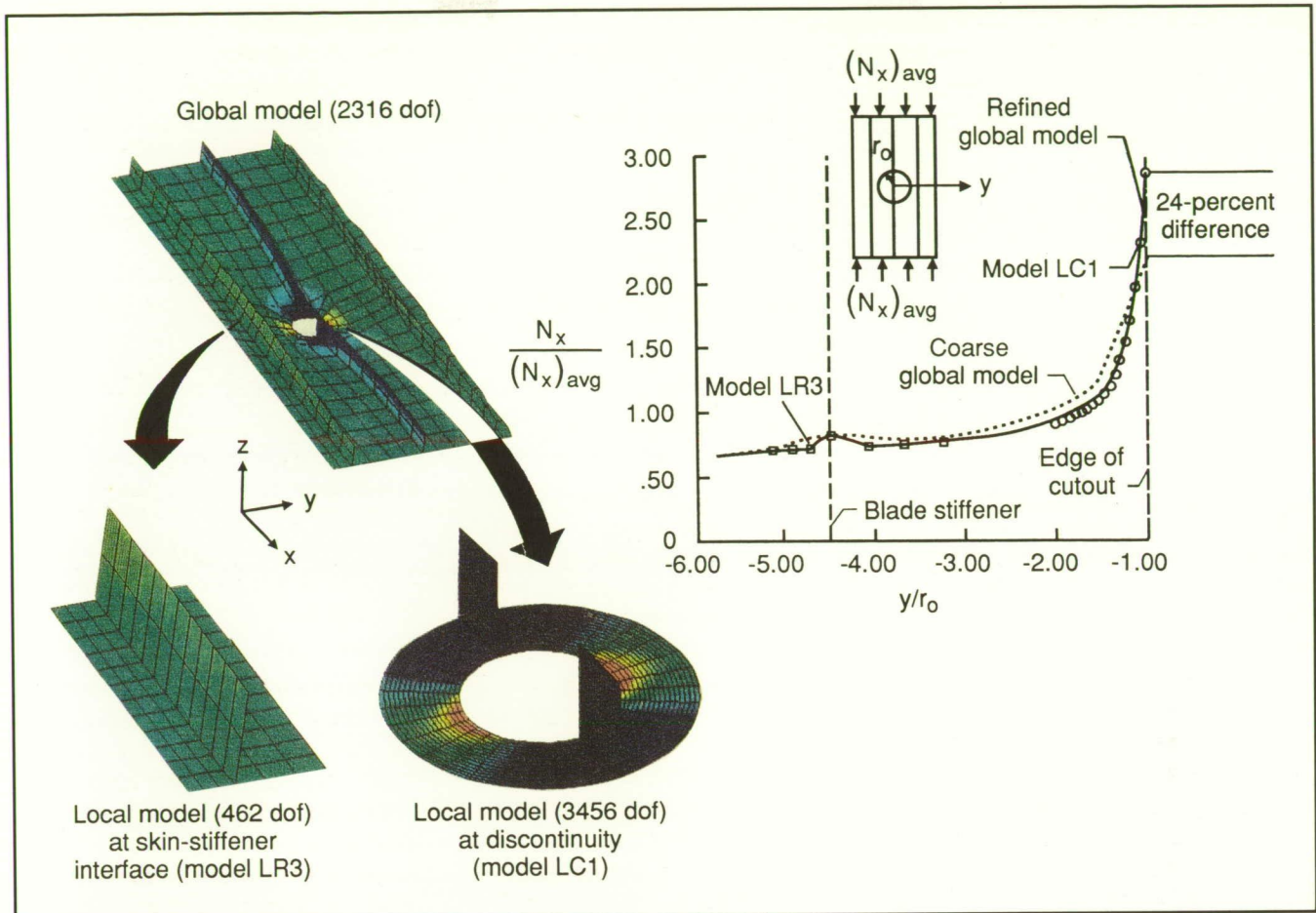
The PVSOLVE solver functions both as a stand-alone code and as part

of the Computational Mechanics Testbed (COMET) code and has the option to solve structural analysis matrix equations of very large size for static, dynamic, and nonlinear problems.

(Olaf O. Storaasli, 42927)
Structures Directorate

Accurate Global/Local Stress Analysis Procedure for Detailed Stress Distribution Calculations

Discontinuities and eccentricities, which are common in actual structures, increase the difficulty in accurately predicting detailed local stress distributions, as required in the design and certification process for aerospace structures. This difficulty is true especially when the component is built of a graphite/epoxy material. A global finite-element model of an entire airframe structure with embedded detailed local refinement may have too many degrees of freedom (dof) to be computationally practical. Hence, a global/local procedure has been developed at



Global/local models and analysis results.

Langley Research Center to enhance significantly the computational efficiency and to give accurate results.

The global/local procedure requires only a single coarse global analysis that provides the boundary conditions for the local regions. In general, the global and local models will not have coincident mesh grid points, and spline interpolation is used to interpolate the generalized displacements from the global model to the boundary of the local model. The key to smooth transition between the global and local models is the use of functions based on the linear plate bending equation.

A global linear stress analysis of a flat blade-stiffened graphite/epoxy panel loaded in axial compression

demonstrates the procedure. The stress-resultant contours and the distribution of the normalized longitudinal stress resultant N_x in the panel skin are shown in the figure. The coarse global-model solution (represented by the dashed curve) provides good agreement away from the cutout, but it underestimates the stress concentration at the edge of the cutout by 24 percent. A local-model analysis of the region around the cutout calculated normalized stress resultants (represented by the open circles) within 1.4 percent of a refined global model, generated for comparison purposes. Similar agreement also is found for the skin/stiffener interface region.

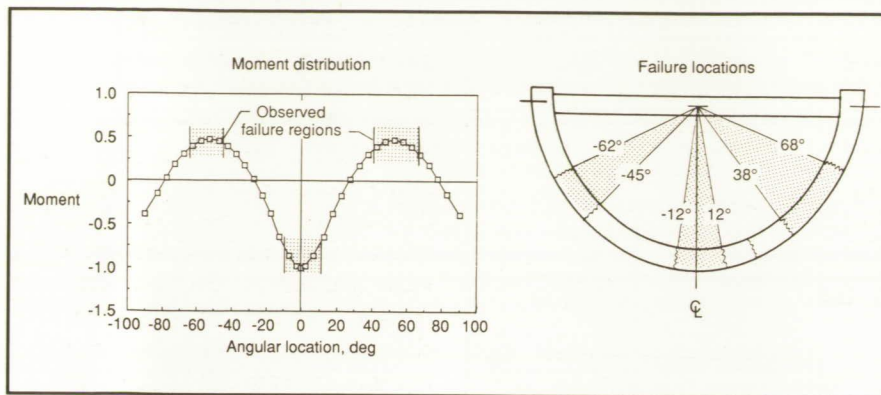
Thus, the global/local stress analysis procedure produces stress distributions with the same level of

accuracy as a more costly refined global model of the entire structural component. This method has been implemented in the Langley Research Center COMET code.

(Jonathan B. Ransom, 42924, and Norman F. Knight, Jr.)
Structures Directorate

Identification of Commonality in Failure Behavior for Metal and Composite Aircraft Structures Under Crash Loads

Experimental and analytical studies are part of the composite impact dynamics research and



Illustrative failure results.

generation of a data base on the behavior of composite structures under crash loads. Part of the effort has been the assessment of the failure and response behavior of generic metal and composite aircraft structures under crash loading. This research is aimed at providing the basic knowledge needed to provide airframe designs with better crash-worthy characteristics and, thus, to contribute significantly to crash survivability.

Static and dynamic tests have been conducted on a variety of metal and composite aircraft structures and components to determine their response and failure behavior. Nonlinear finite-element models have been used to predict behavior and to provide insight into the fundamental physics of the behavior of the structures under crash loads. Static loads were applied to the structural simulations to determine the load-deflection response. Failure loads and strain distributions were determined using the models for comparison to experimental data.

Some illustrative results are shown in the figure. On the left is a normalized analytical moment (strain) distribution for a typical composite fuselage frame under vertical load. Superimposed on the distribution is the location of the observed experimental failure positions for metal and/or composite full-scale panels,

aircraft sections, frames, and subfloors. A commonality exists in the location of the failures for the various aircraft structures which coincides with the maximums in the moment distribution of the typical frame under vertical loading. As shown on the sketch at the right, the angular locations occur at the point of initial contact or impact with the ground and at approximately 50° to 60° up both sides of the structure. As indicated at the left, these locations correspond to the points of maximum moment or strain for the loaded structure.

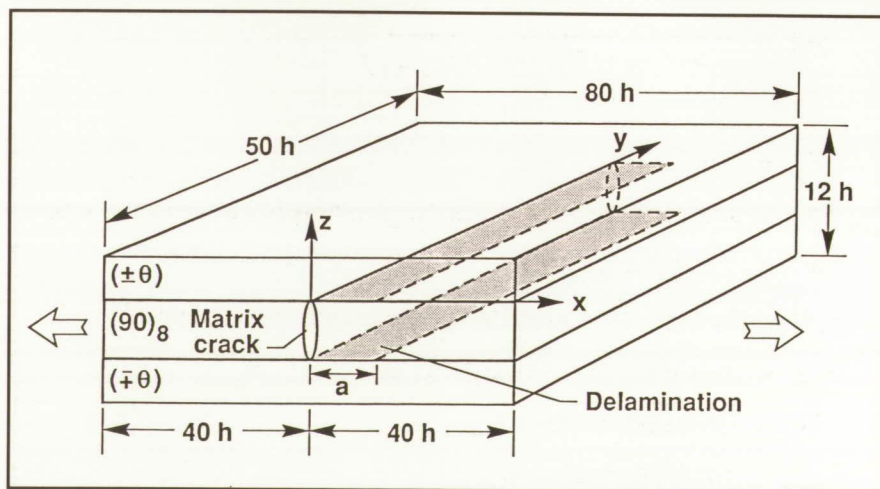
With the discrete failure locations noted for cylindrical structures under vertical loads, energy absorption decreases dramatically, thus empha-

sizing the need to provide structural concepts that are designed to provide some energy-absorbing mechanism in the design. Additionally, knowing that these aircraft structures have a commonality in failure behavior may provide designers, dynamists, and analysts with useful information to allow newer, more energy-absorbing structures to be designed, provide knowledge of where failures most probably will occur, and allow better analytical models to be formulated for analysis and prediction.

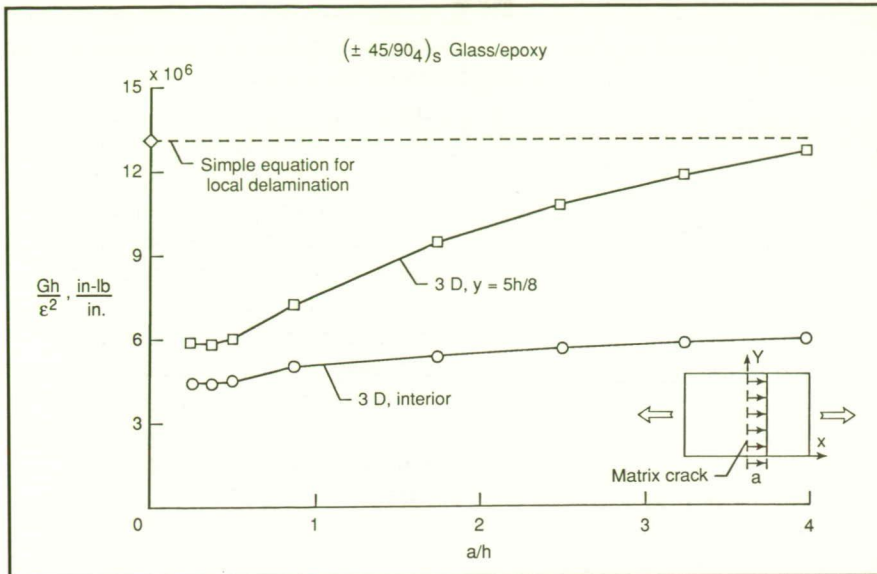
(Huey D. Carden, 44151)
Structures Directorate

Combined Effect of Matrix Cracking and Free Edge on Delamination

With the increased use of composite materials in primary aircraft structures, a need exists for understanding their failure mechanisms to better predict service life. Composite laminates subjected to monotonic tension and tension fatigue loading undergo a succession of various forms of damage before complete failure. These damage mechanisms include matrix ply cracking, edge delamination, and local delaminations



Schematic of uniform through-width delamination growing from 90° matrix crack.



Change in normalized G due to uniform delamination growth in cross-ply laminate.

arising from matrix ply cracks. These local delaminations give rise to strain concentrations through the laminate thickness and lead to laminate failure.

In this study, the $(0_2/90_4)_s$ and $(\pm 45/90)_s$ glass/epoxy laminates were analyzed using the finite-element method. These layouts were chosen to study the effect of cracking in the 90° plies on the strain energy release

rate G for local delamination near the free edge (see the first figure). A three-dimensional analysis was required to determine the G distribution across the delamination front and the change in G with delamination growth. The virtual crack closure technique was used to calculate the strain energy release rates.

As shown in the second figure, the three-dimensional (3-D) analysis

revealed that the magnitude of G is much larger near the edge ($y = 5h/8$) than in the interior of the laminate width. Therefore, delaminations are most likely to form at the intersection of the matrix crack and the edge of the laminate. Furthermore, G results near the edge reach an asymptotic value that agrees with a previously derived simple equation (see the second figure). Hence, this simple equation (see the third figure) may be used with confidence in fatigue life prediction models to account for local delaminations generated by matrix cracks.

(S. A. Salpekar, 43464, and T. K. O'Brien)

Structures Directorate

Relationship Between Constituent and Composite Fatigue Behavior for Titanium Matrix Composites

Titanium matrix composites are leading candidates for high-temperature structural applications on proposed supersonic and hypersonic aircraft. Because these materials are projected for use in highly loaded, stiffness-critical parts, a complete understanding of their mechanical behavior is a necessity.

Because the development of the optimum composite material involves many potential matrix/fiber combinations, it is important to develop an understanding of the role that each constituent plays in the overall behavior of the composite. To this end, fatigue tests were conducted on a Ti-15-3 matrix material at both room and elevated temperature (650°C). Because the elastic high-modulus fibers essentially control the strain in the matrix, the matrix material was fatigue cycled in strain control. The number of cycles to failure versus cyclic strain range is

$$G_T = \frac{P^2}{2mw^2} \left(\frac{1}{t_{LD} E_{LD}} - \frac{1}{t E_{LAM}} \right)$$

P = axial load

m = number of delaminations growing from matrix crack

w = laminate width

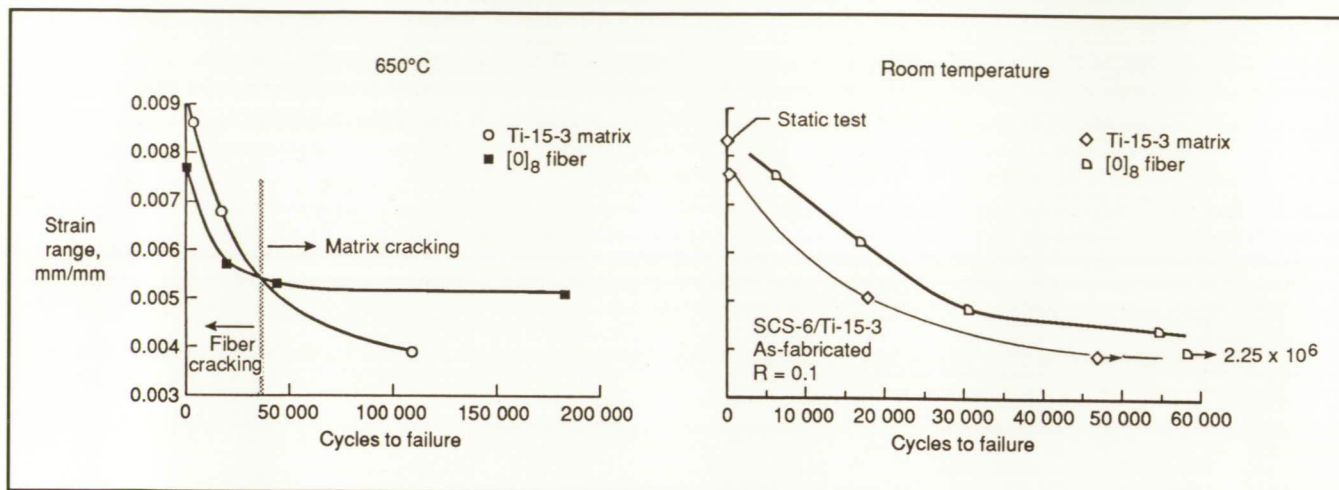
t_{LD} = thickness of load carrying (uncracked) plies

E_{LD} = modulus of uncracked plies

t = laminate thickness

E_{lam} = laminate modulus

Equation for total strain-energy-release rate.



Constituent fatigue behavior that can be used to predict composite failure modes.

plotted for the matrix material at both temperatures in the figure.

Also shown in the figure is the strain range versus number of cycles to failure for silicon-carbide fibers (SCS-6) as derived from in situ composite tests. At room temperature, for a given strain level, the fibers always fail before the matrix fatigue cracks in unidirectional laminates. This failure has been confirmed by examination of the failure surfaces from a variety of fatigue tests on this SCS-6/Ti-15-3 system at several stress levels. However, at elevated temperatures, the matrix fatigue curve crosses that of the fibers. This crossing implies that the fibers would fail before matrix cracking at high strain levels and short life, but the matrix would crack before the fibers failed at lower strains and longer life. This failure behavior was confirmed by fractographic examination of specimens tested at several different cyclic load levels. These results are significant because they demonstrate that the fatigue properties determined for the matrix material can be used to predict the in situ behavior of the matrix in the composite.

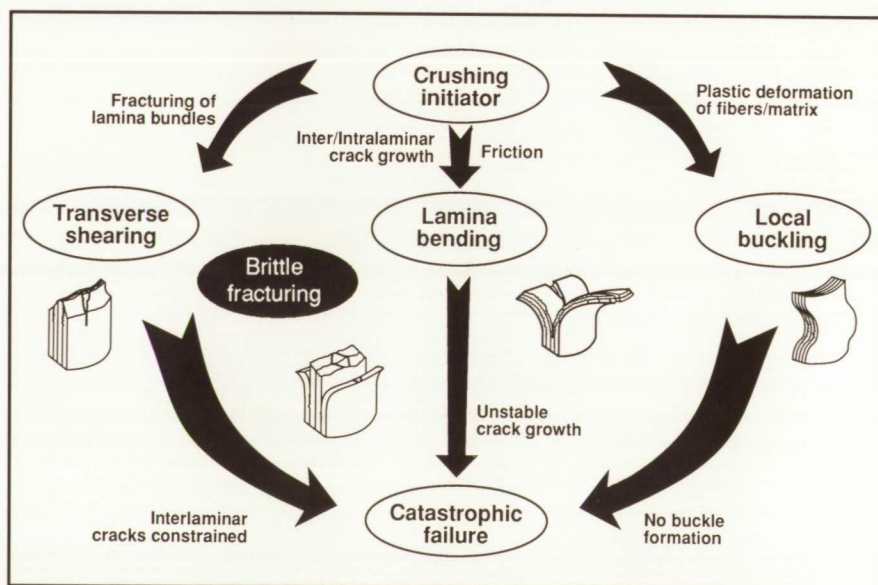
(W. S. Johnson, 43463, W. D. Pollock, and B. M. Hillberry)
Structures Directorate

Energy-Absorption Capability of Composite Tubes and Beams

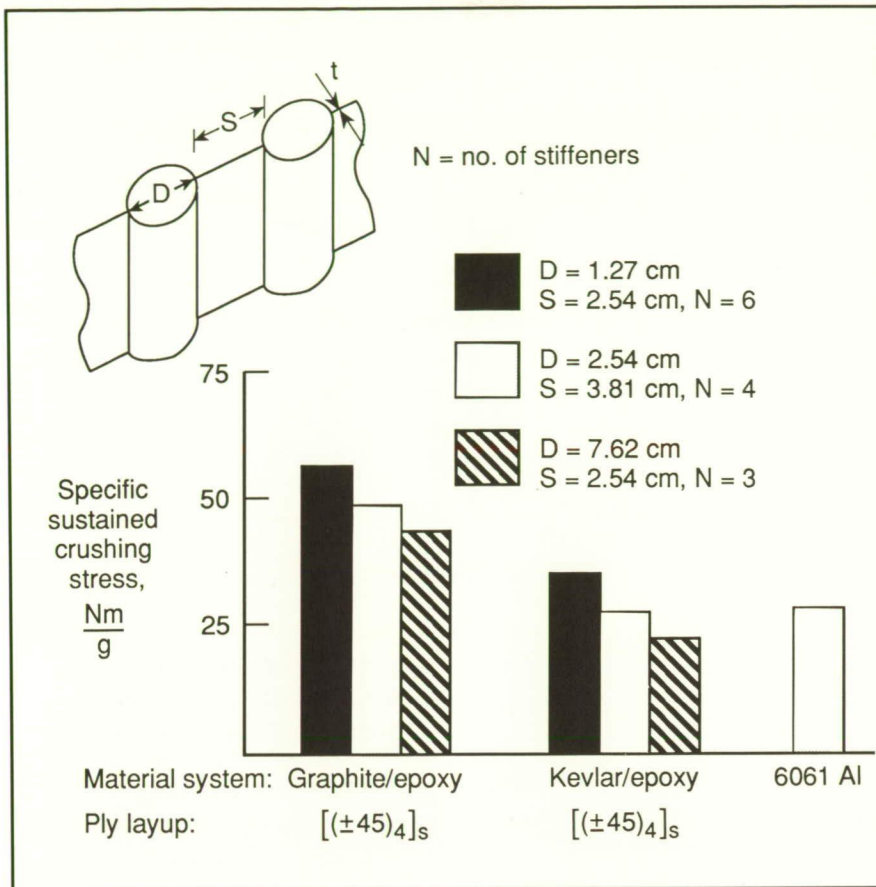
The cause and effect relationship between the mechanical properties of the constituent materials and geometrical parameters of a composite structure, on the one hand, and its crushing response on the other, are complex. This investigation sought to develop a fundamental understanding of how the numerous material and geometrical parameters affect the

crushing characteristics of composite tubes and beams. Circular and square cross-section tubes and sine-wave, integrally stiffened, and sandwich beam specimens were crushed in this investigation to develop an understanding of this relationship. After an understanding of the physics of the problem was established, analytical tools to predict this behavior were developed.

A unified understanding of how the mechanical properties of the constituent material, specimen geometry, and crushing rate affect the



Crushing process of continuous fiber-reinforced composite tubes.



Energy-absorption capability of circular tube stiffened beams.

energy-absorption capability has been developed. Three unique crushing modes have been experimentally observed and categorized (as shown in the first figure), and the mechanisms that control these modes have been identified and described. The fourth mode, brittle fracturing, is a combination of the transverse shearing and lamina bending modes. A simple prediction method has been developed to qualitatively predict change in energy-absorption capability due to changes in material properties and specimen geometry. The crushing process also has been successfully modeled using a geometric and material nonlinear finite-element model. A simple yet accurate analysis was developed to predict the energy-absorption capability of beams. Energy-absorption trends obtained from the tubular specimen tests were consistent with trends

obtained from beam specimens. On a specific energy-absorption basis, the energy-absorption capability of composite beams can be more than twice that of comparable aluminum alloy beams, as shown in the second figure.

(G. L. Farley, 43091)
Structures Directorate

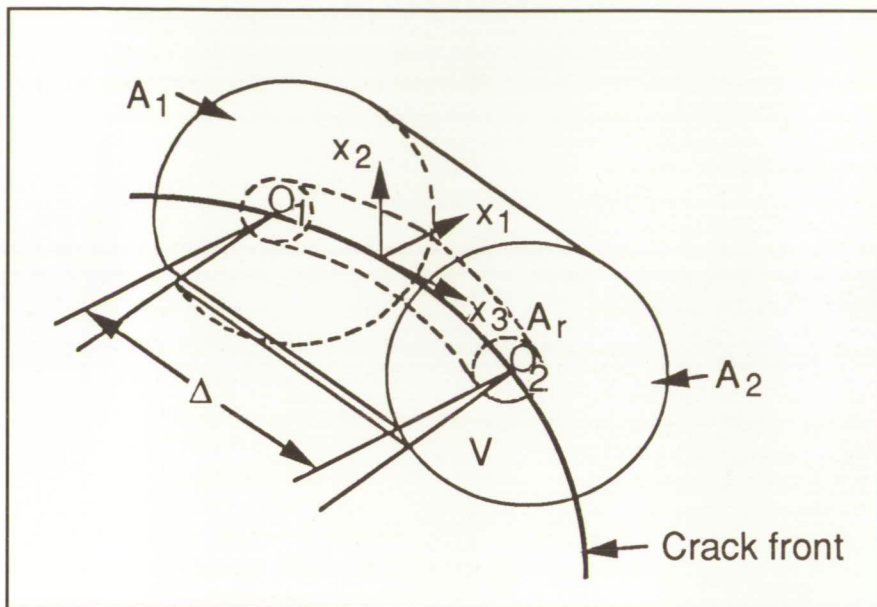
Equivalent Domain Integral Method and Applications

As the quest for developing newer, stronger, lighter, and tougher materials for aerospace applications continues, their fracture characteristics are becoming more complex. These characteristics pose challenges in developing new techniques to calculate fracture mechanics param-

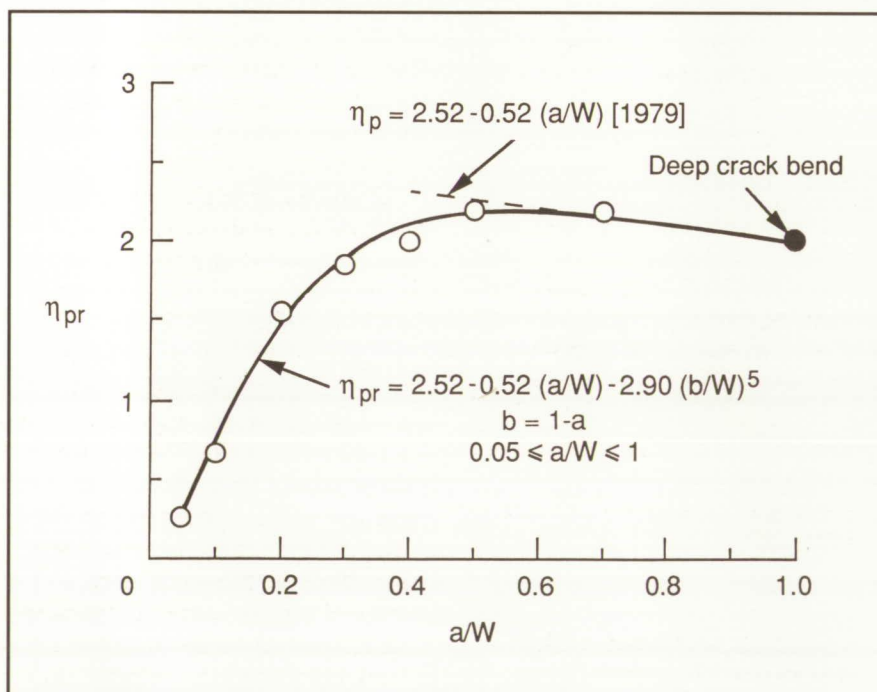
eters, which are fundamental in predicting strength and life of structural components. The new materials may have inelastic, anisotropic, and time-temperature deformation properties. In the literature, virtual crack extension and J-integral methods also have been used widely to analyze cracked bodies. These methods, however, have restricted applications (namely, to planar cracks, elastic, or nonlinear elastic materials) and evaluate only the total fracture mechanics parameter in nonlinear materials.

A method that has much broader applications to elastic, inelastic, and anisotropic materials and has the potential to address time-dependent materials, yet is simple to use in any finite-element analysis, is based on the equivalent domain integral (EDI). This method has been enhanced for mixed-mode fracture and nonsingular elements and has been incorporated into the Langley Research Center fracture mechanics codes.

The method is an extension of the classical J-integral method for cracked two-dimensional bodies to general crack configurations in three-dimensional bodies. In this method, an integral of the stress-strain potential on a surface enclosing the crack front is transformed into a volume integral by the divergence theorem, hence the name domain integral. Further, an arbitrary crack extension is introduced by the virtual crack extension concept. The equivalent domain integral is defined as an integral of the stress-strain potential in the volume of material between the two cylinders around the crack front as shown in the first figure. The second figure shows an equation for the elastic-plastic eta factor η_{pr} for a single-edge-crack-tension specimen developed from the results of the EDI method. The η_{pr} is used to calculate the J-integral from the measured load-displacement record in a fracture test. Thus, the



Domain V around crack front.



Deformation independent elastic-plastic eta-factor.

versatility of the EDI method to elastic and inelastic materials is demonstrated.

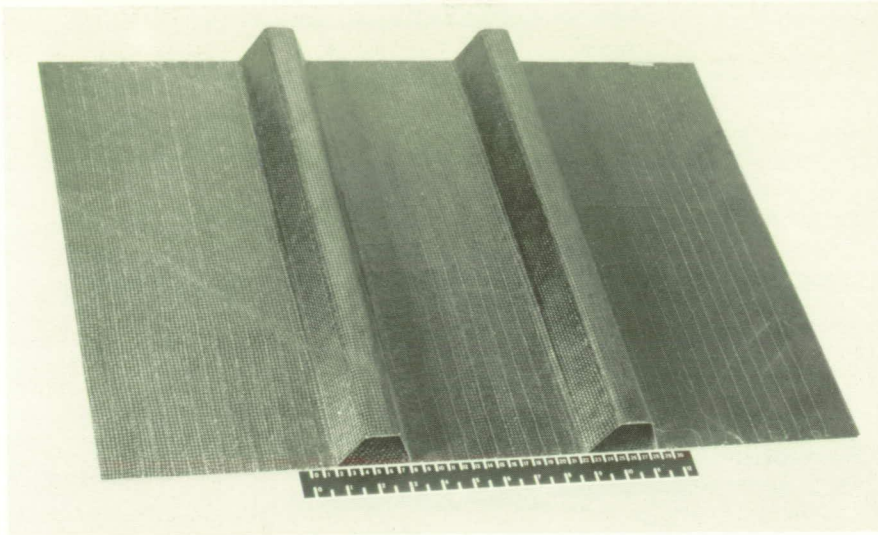
(K. N. Shivakumar, 43469, J. C. Newman, Jr.)
Structures Directorate

Elimination of Stiffener/Skin Separation Failure Mode by Integrally Woven Hat-Stiffener Preform

Textile processes have the potential to reduce fabrication costs of advanced composite materials for aircraft structures by reducing part count and assembly time. An example of such a textile-reinforced composite element is shown in the first figure. The center ply of the hat-stiffened panel was a plain-weave fabric woven on a standard loom using Hercules AS-4 graphite fiber with the fabric coming off the loom in the direction of the hat stiffeners. Two additional $\pm 45^\circ$ plies of plain weave AS-4 graphite fabric then were stitched to the upper and lower preform surfaces with eight plies of unidirectional graphite tape material inserted at the top of the hats, between the preform layer and the $\pm 45^\circ$ surface layer. The panel was resin transfer molded (RTM) with Hercules 3501-6 epoxy resin and cured at 350°F under vacuum only.

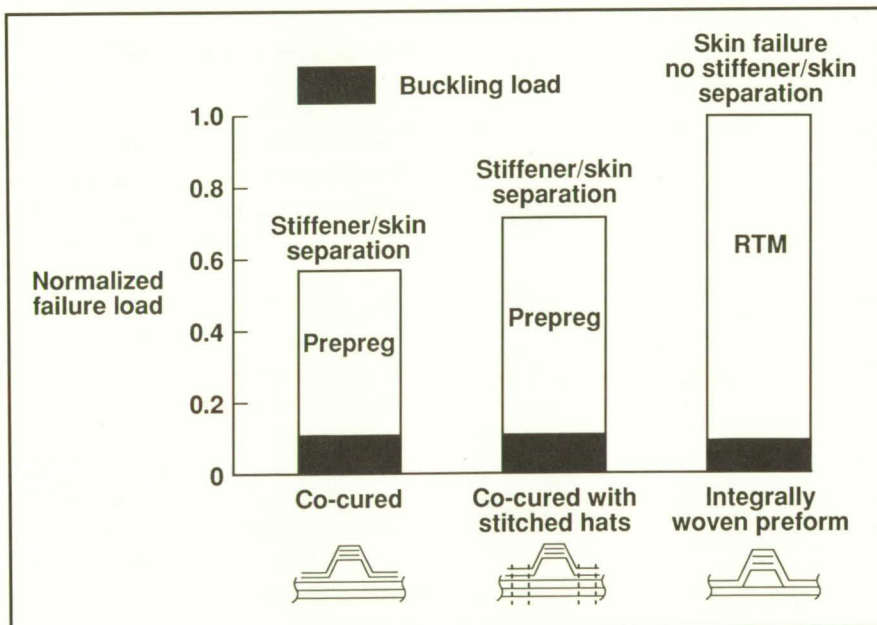
Panel performance was evaluated under shear loading and compared with the performance of two other panels fabricated from identical AS-4/3501-6 prepreg fabric and conventional manufacturing procedures. The bar chart in the second figure shows the relative shear load-carrying capability for each panel normalized with respect to the integrally woven preform panel results. All of these panels buckled at the same load, but the failure load of the integrally woven preform panel exceeded the failure loads of the other two panels by as much as 40 percent. The integrally woven preform panel failed through the skin under the hat, whereas the other two panels failed by stiffener/skin separation.

(J. W. Deaton, 43087)
Structures Directorate



Integrally woven hat-stiffened panel.

L-89-8047

Graphite/epoxy fabric hat-stiffened shear panel results ($\pm 45/0/90/\pm 45$).

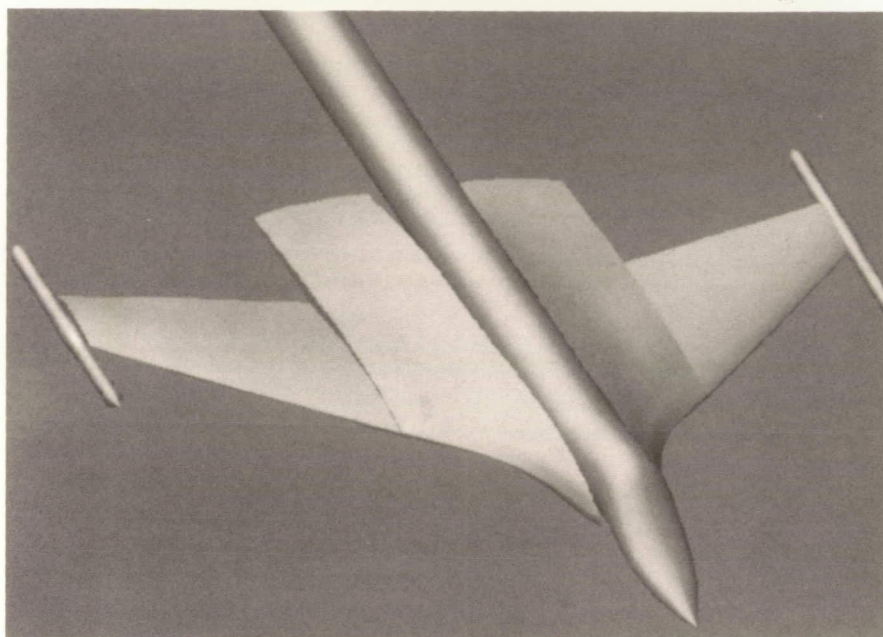
Prediction of Static and Resultant Dynamic Aeroelastic Behavior by Nonlinear Method

The inability to predict accurately the transonic flutter boundary of realistic aircraft configurations is well-known. The objective of the present work is to develop a methodology for determining the effects of

nonlinear transonic aerodynamics on the combined static and dynamic aeroelastic behavior of complex flight vehicles.

A computational model (including wing, wing-tip-mounted store, and fuselage) of a wind tunnel model representative of a high-performance military airplane has been developed for the Computational Aeroelasticity Program-Transonic Small Disturbance (CAP-TSD) code. The computational model is shown in the first figure. The analysis procedure first determines the static aeroelastic shape of the configuration resulting for certain flight (Mach number and dynamic pressure) and model (angle of attack and control surface angles) conditions. This change in shape is illustrated schematically at the top of the second figure. Dynamic perturbation analyses then are performed about the deformed shape to obtain the flutter characteristics, as illustrated by the sketch at the bottom of the figure.

A procedure was developed to analyze situations in which static aeroelasticity is important (nonsymmetric airfoils or symmetric airfoils at nonzero angles of attack) in determining the dynamic stability at transonic flight conditions. For example, the steady-state aerodynamics of a nonsymmetric airfoil produces a transient response that, if not handled properly, can yield misleading dynamic response results. As part of the analysis procedure, artificially large values of damping are used to accelerate the convergence to the static aeroelastic shape. Transonic flutter calculations about this static aeroelastic shape were made for the configuration studied here at an angle of attack of 1.5° . These results, not shown in the figure, indicate the presence of a steep transonic flutter dip near $M = 0.95$. A comparison of linear and nonlinear CAP-TSD results at $M = 0.9$ reveals a difference in flutter



dynamic pressure due to the effects of nonlinear aerodynamics. The existence of a shock at $M = 0.95$ limits the use of linear aerodynamic theories to Mach numbers not much greater than $M = 0.9$.

This study identified the importance of static aeroelasticity on the dynamic aeroelastic behavior of flight vehicles at transonic speeds. The study also addressed the important nonlinear aerodynamic effects of vehicle components, such as the fuselage and wing-tip stores, on aeroelastic characteristics.

(Walter A. Silva and Robert M. Bennett, 42834)

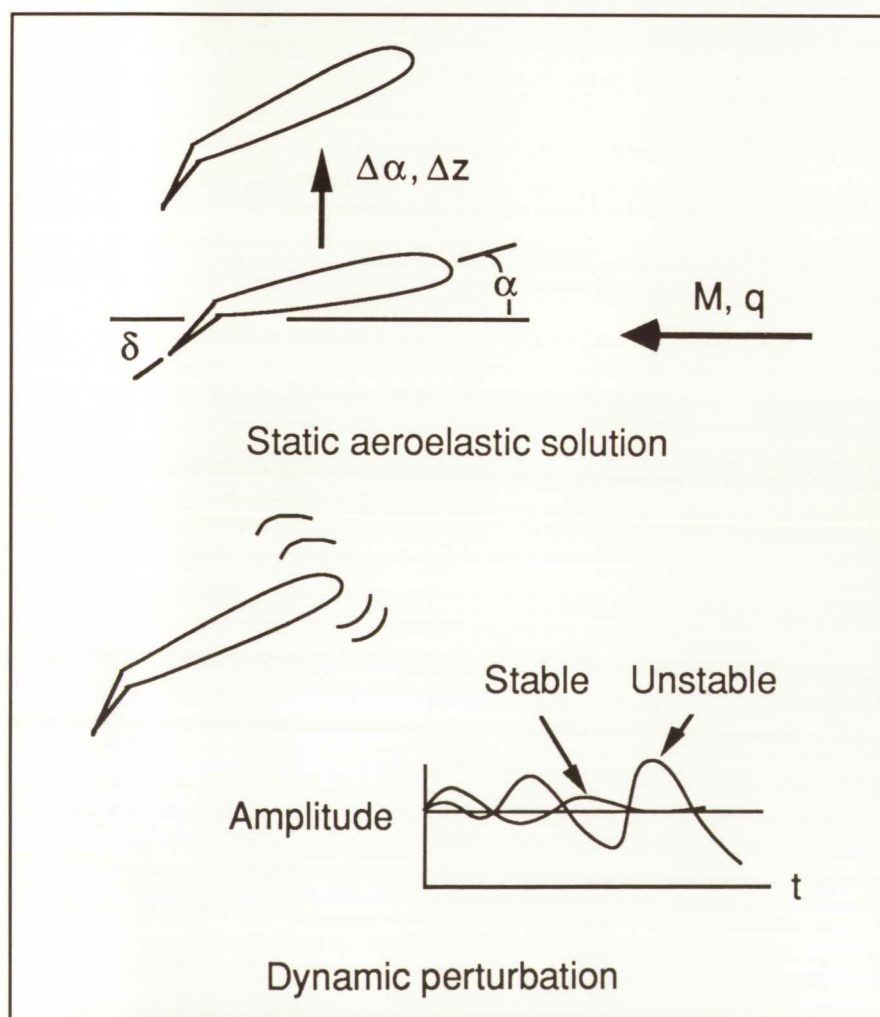
Structures Directorate

Computational model.

Demonstration of Flutter Control Using Active Flexible Wing Wind Tunnel Model

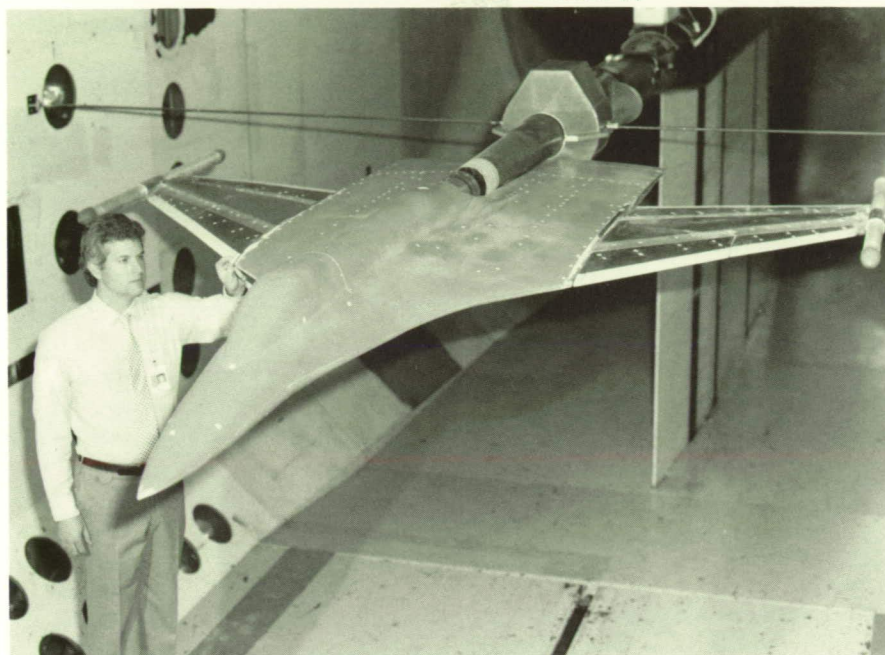
The Active Flexible Wing (AFW) Project is a joint Langley Research Center/Rockwell International Corporation program with the overall goal of demonstrating multi-input/multioutput (MIMO), multifunction digital control of a sophisticated aeroelastic wind tunnel model representative of high-performance airplane design. The research objectives of the project are to validate the analysis, synthesis, simulation, and test methodologies necessary to perform such a demonstration.

In the first figure, the AFW wind tunnel model is shown mounted in the test section of the Transonic Dynamics Tunnel (TDT) in preparation for a recently completed active flutter suppression (FS) study. Each wing of the model was equipped with four remotely controlled aerodynamic control surfaces, two on the leading edge and two on the trailing edge.



Schematic illustrations of analysis process ($\Delta\alpha$ is twist angle and Δz is change in vertical deflection).

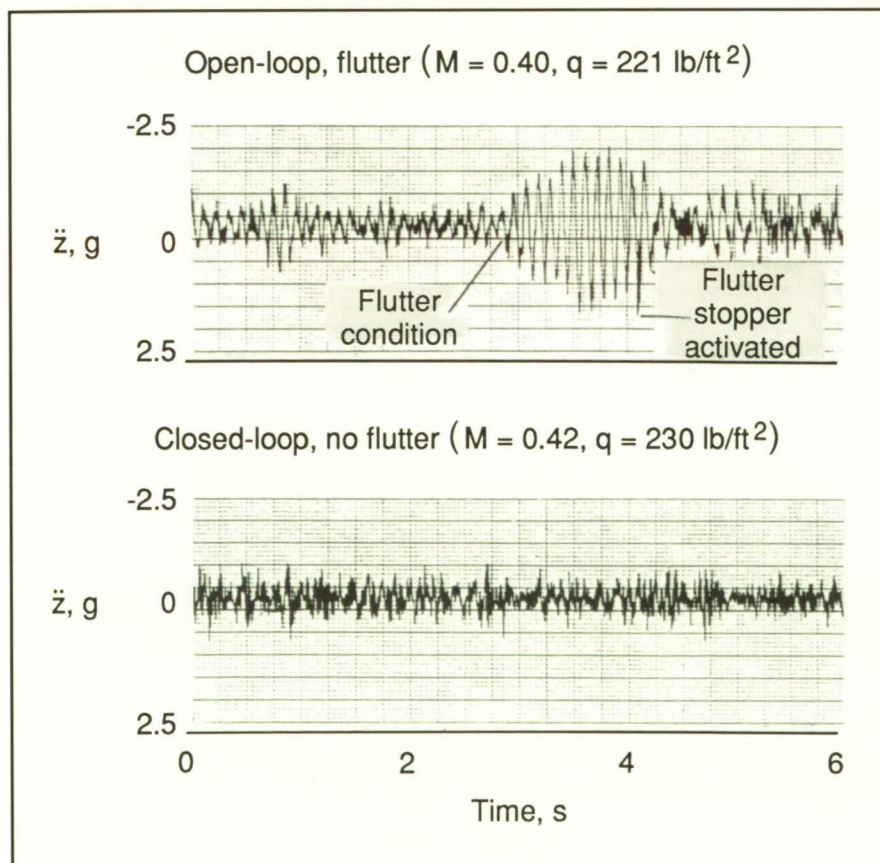
ORIGINAL PAGE
BLACK AND WHITE PHOTOGRAPH



Photograph of AFW model in TDT.

L-89-12442

Several accelerometers were mounted in each wing for use in sensing vibratory motion. The control surfaces were actuated by command signals generated by an FS control law, which was implemented on a digital computer. This test had four specific objectives; the first two objectives were to determine the basic unaugmented (open-loop, flutter suppression system off) flutter boundary of the model and to verify the operation of a flutter-stopper device (a decoupler pylon-like wing-tip store) which had been incorporated into the model design. The last two objectives were to verify the capabilities of the digital controller on which the flutter suppression control laws were implemented and to evaluate three different active flutter suppression concepts specifically designed for this model.



Active flutter suppression results (test time histories).

The data shown in the second figure collectively illustrate the results in achieving these specific objectives. The top plot in the second figure is a time history of a wing accelerometer measured during open-loop testing at the tunnel conditions indicated in parentheses. At approximately 3 s into the time history, an open-loop flutter condition was encountered, as indicated by the increasing acceleration amplitudes. After approximately 1 s of increasing amplitudes, the flutter stopper was activated, and the wind tunnel model was returned to a flutter-free condition, as indicated by the decreasing acceleration amplitudes. The bottom plot is a time history of the same wing accelerometer measured during closed-loop testing of one of the three FS control laws at a dynamic pressure 9 lb/ft² above the open-loop flutter boundary. This FS control law was successful in taking the model to a dynamic pressure 51 lb/ft² above the open-loop flutter boundary.

The knowledge and insight gained from this test to validate analysis, synthesis, simulation, and test

methodologies provide a valuable addition to active flutter suppression research and development capabilities.

(Boyd Perry III and Stanley R. Cole, 42840)

Structures Directorate

Validation of Tire Analysis Codes With Experimental Measurements of Space Shuttle Nose Gear Tire

Numerical modeling of the response characteristics of aircraft tires remains one of the most challenging applications of computational mechanics because the tire is a composite structure composed of rubber, textile, and steel constituents that exhibit anisotropic and non-homogeneous material properties. Furthermore, all the forces developed by the tire during takeoff and landing operations are developed through the tire-runway interface. These facts emphasize the need to develop modeling strategies and analysis methods that are both powerful and efficient. Two codes that have been

developed for tire analysis include a semianalytic model (which employs finite elements in the tire cross section which are expanded in a Fourier series around the tire circumference) and a two-dimensional shell finite-element model (which includes a frictionless contact algorithm). The analytical results obtained by using these two models have been compared with experimental measurements of the Space Shuttle nose gear tire. Some illustrative results are shown in the figure.

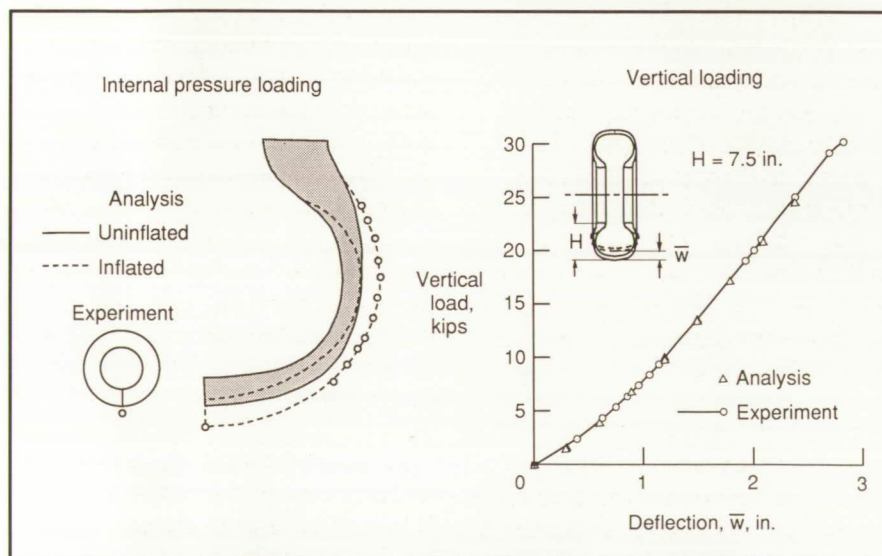
The carcass of the Space Shuttle nose gear tire was treated as an anisotropic material, and the properties of the different layers were obtained using the mechanics of materials approach. Because of symmetry, only one-half of the tire cross section was modeled. The one-half tire was divided into seven segments. Each segment contained a different number of layers, different material properties corresponding to different textile cord content in the carcass, and different fiber orientations. Shown on the left in the figure is a comparison of experimental and analytical results for the Space Shuttle tire that has been inflated to an internal pressure of 300 lb/in².

The data are given along a meridional line for this axisymmetric loading case. The figure illustrates the change in tire cross-section geometry for this pressure loading condition and demonstrates excellent agreement between the model and the experiment. The two-dimensional shell finite element with a frictionless contact algorithm was used to model the load-deflection characteristics of the inflated tire vertically loaded against a rigid plate. The load-deflection data shown on the right in the figure clearly illustrate the ability of the finite-element model to predict accurately the nonlinear response of the Space Shuttle nose gear tire to this loading condition. The excellent agreement between the finite-element model predictions and the experimental measurements validates these two tire analysis codes that form the core for the family of analysis tools under development.

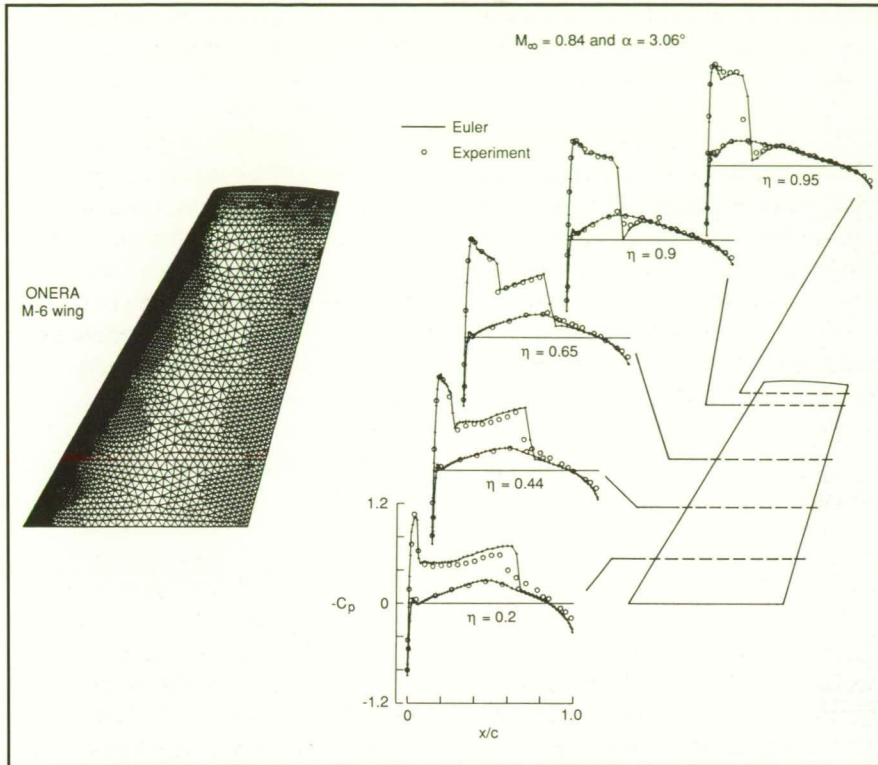
(Ahmed K. Noor, Kyun O. Kim, and John A. Tanner, 41302)
Structures Directorate

Validation of Unstructured-Grid Euler Algorithm

New algorithms are being developed for the solution of the three-dimensional unsteady Euler equations based on the use of unstructured grids. These algorithms require validation before they may be used with confidence for general applications. Research was undertaken, therefore, to determine the accuracy of a new flux-split method of solving the Euler equations on an unstructured grid of tetrahedra. The new algorithm involves improvements that have been developed recently to the spatial and temporal discretizations used by unstructured grid flow solvers. The spatial discretization now involves a flux-split approach that is naturally



Comparison of calculated and experimental tire characteristics.



Surface grid topology and correlation of computational and experimental pressure coefficients.

dissipative and captures shock waves sharply with only one grid point within the shock structure. The temporal discretization involves either explicit or implicit time marching. The explicit time marching is a four-stage Runge-Kutta integration, and the implicit time marching is a two-sweep Gauss-Seidel relaxation procedure.

To assess the accuracy of the new three-dimensional flux-split Euler solver, calculations were performed for the ONERA M-6 wing. The M-6 wing has a leading-edge sweep angle of 30° , an aspect ratio of 3.8, and a taper ratio of 0.562. The results were obtained using a grid that had 154 134 nodes and 869 056 tetrahedra. The surface grid topology for the upper surface of the wing is shown in the left part of the figure. Results were obtained for the M-6 wing at a free-stream Mach number

$M_\infty = 0.84$ and an angle of attack $\alpha = 3.06^\circ$. These conditions were chosen for comparison with experimental pressure coefficient C_p data plotted versus fractional chord x/c for five values of fractional semispan η , as shown in the right part of the figure. The results indicate that a weak supersonic-to-supersonic shock wave exists near the leading edge on the inboard portion of the wing. The primary, supersonic-to-subsonic shock that occurs in the midchord region coalesces with the first shock in the outboard direction toward the wing tip. Near the tip, the two shocks merge to form a single, strong, supersonic-to-subsonic shock wave.

The Euler results are in good agreement with the experimental pressure data, especially in predicting the strength and location of the shock waves; this agreement tends to verify the new Euler algorithm. The shocks

are sharply captured with only one grid point within the shock structure, and no overshoots or undershoots exist.

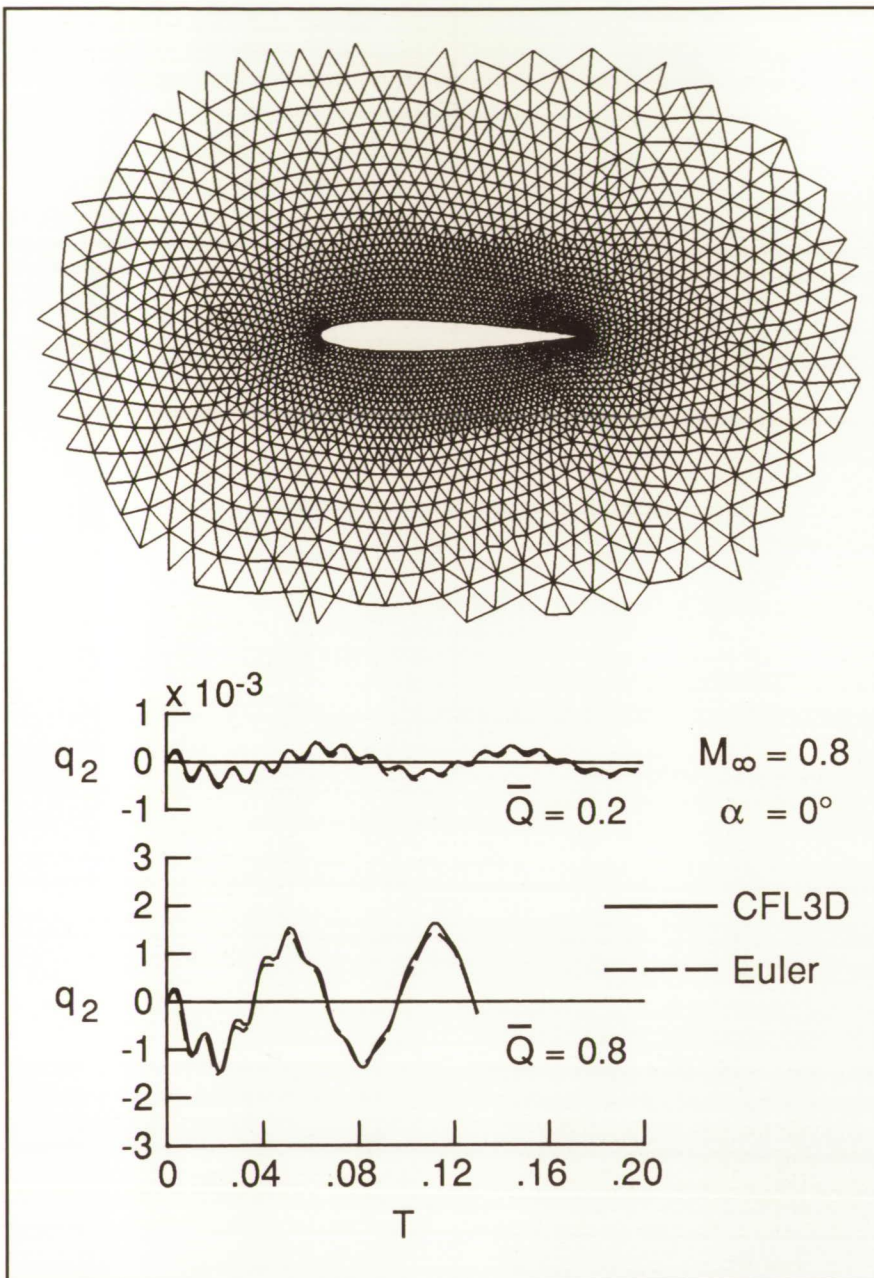
(John T. Batina, 42268)
Structures Directorate

Demonstration of Euler Flutter Analysis of Airfoils Using Unstructured Dynamic Meshes

For steady flow analysis, unstructured grid methods have been shown to have advantages over structured grid methods such as the ability to treat very complicated geometries and the ability to adaptively refine the grid for maximum accuracy and computational efficiency. This suggests that the methodology may also have advantages for unsteady aerodynamic and aeroelastic analysis. Consequently, a study has been undertaken to assess the accuracy of the unstructured grid methodology for flutter analysis of airfoils as a first step toward aeroelastic analysis of complete aircraft configurations.

Modifications were made to a two-dimensional (2-D) unsteady Euler code involving unstructured grids of triangles to include the structural equations of motion for their simultaneous time-integration with the governing fluid flow equations. Detailed comparisons of results obtained from a structured grid Euler code (the CFL3D code run in a 2-D mode) with the results obtained from the present Euler code are used to determine the accuracy of the unstructured grid methodology for flutter applications.

To assess the accuracy, aeroelastic analyses were performed for the NACA 0012 airfoil. The top part of the figure contains a partial view of the unstructured grid of triangles



Partial view of unstructured grid and comparison of generalized displacements.

used. For a comparison of the aeroelastic results, a similar structured mesh of quadrilateral cells was generated. Aeroelastic results were obtained using these grids for a two degree-of-freedom (pitch and plunge) NACA 0012 airfoil at a free-stream Mach number $M_\infty = 0.8$. Initial modal velocities were used to perturb the airfoil from an angle of attack $\alpha = 0^\circ$. Comparisons of second-

mode generalized displacement q_2 versus time T are shown in the lower part of the figure for two values of nondimensional dynamic pressure \bar{Q} which bracket the flutter point.

The generalized displacements agree well with the structured grid (CFL3D) solution that verifies the unstructured grid methodology for aeroelastic analysis. The flutter

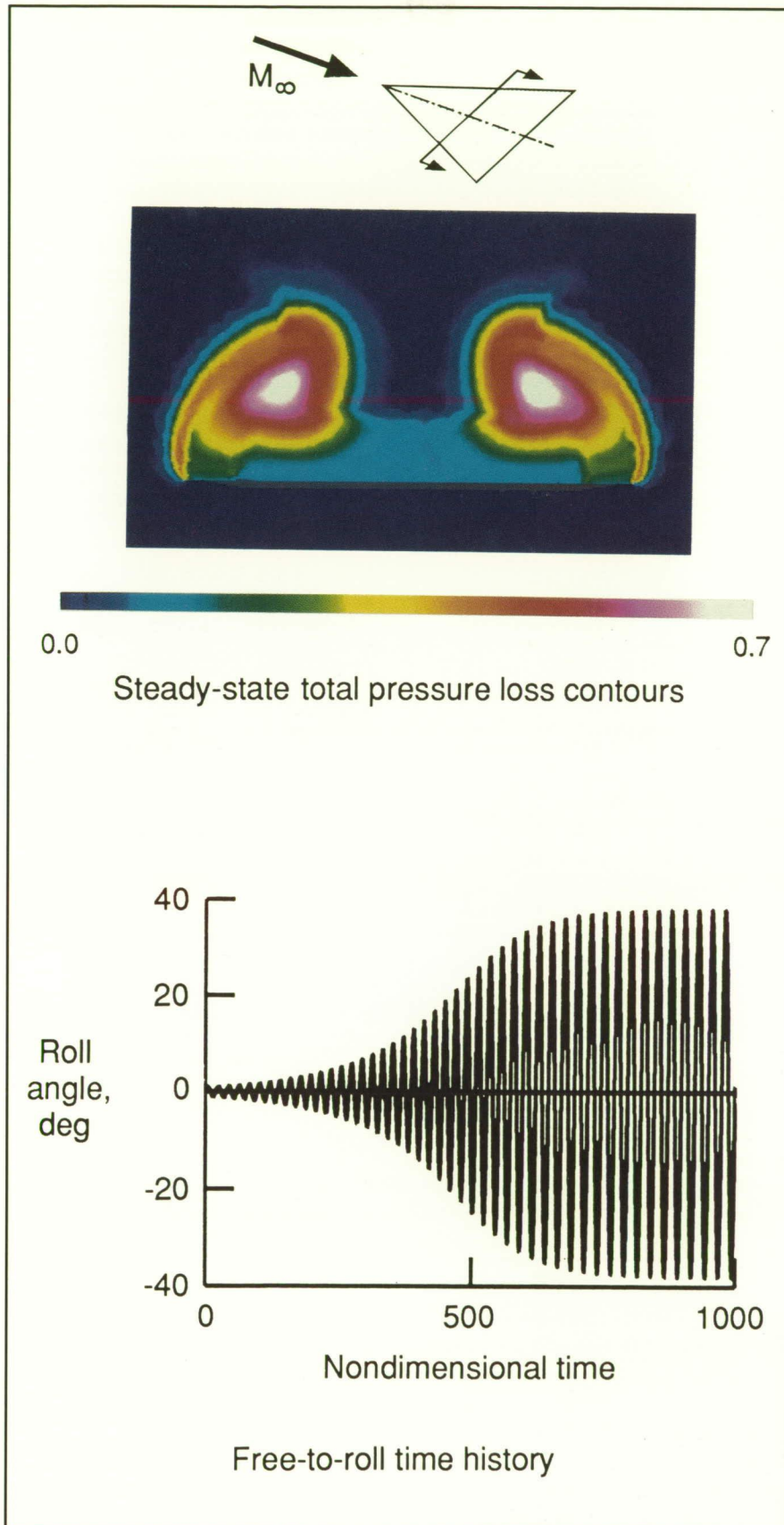
speed for this case also agrees to within 2 percent of the value predicted by using the CFL3D code. (Russ D. Rausch and John T. Batina, 42268) Structures Directorate

Conical Euler Method to Study Unsteady Vortical Flows About Rolling Delta Wings

Recently, a growing interest has existed in high angle-of-attack fighter capability for increased maneuverability. Typically, these high-performance aircraft have thin, highly swept lifting surfaces that produce a vortical flow over the leeward side of the vehicle at high angle of attack. In order to gain a more complete understanding of these types of flows, a conical Euler methodology has been developed to efficiently investigate unsteady vortical flows about highly swept delta wings undergoing forced and free-to-roll motions. These analyses aid in the determination of the aerodynamic response characteristics of such wings, including one type of wing-rock phenomena.

Modifications were made to an existing conical Euler code to allow for the additional analysis of the free-to-roll motions of a delta wing. The current code employs a multistage Runge-Kutta time-stepping scheme and a finite-volume spatial discretization of the Euler equations on an unstructured mesh of triangles. The free-to-roll motion is determined by including the rigid-body equation of motion for its simultaneous time integration with the governing flow equations.

Calculations were performed for a sharp-leading-edge delta wing swept 75° at a free-stream Mach number $M_\infty = 1.2$ and an angle of attack $\alpha =$

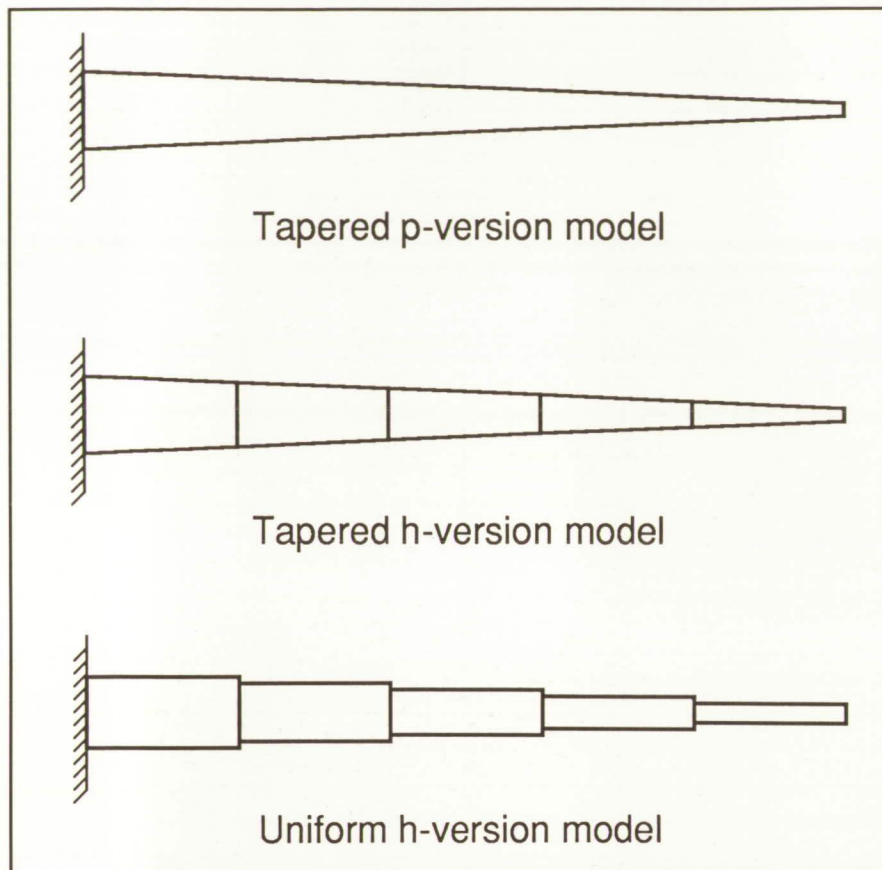


Vortical-flow results for rolling delta wing $M_\infty = 1.2$ and $\alpha = 30^\circ$.

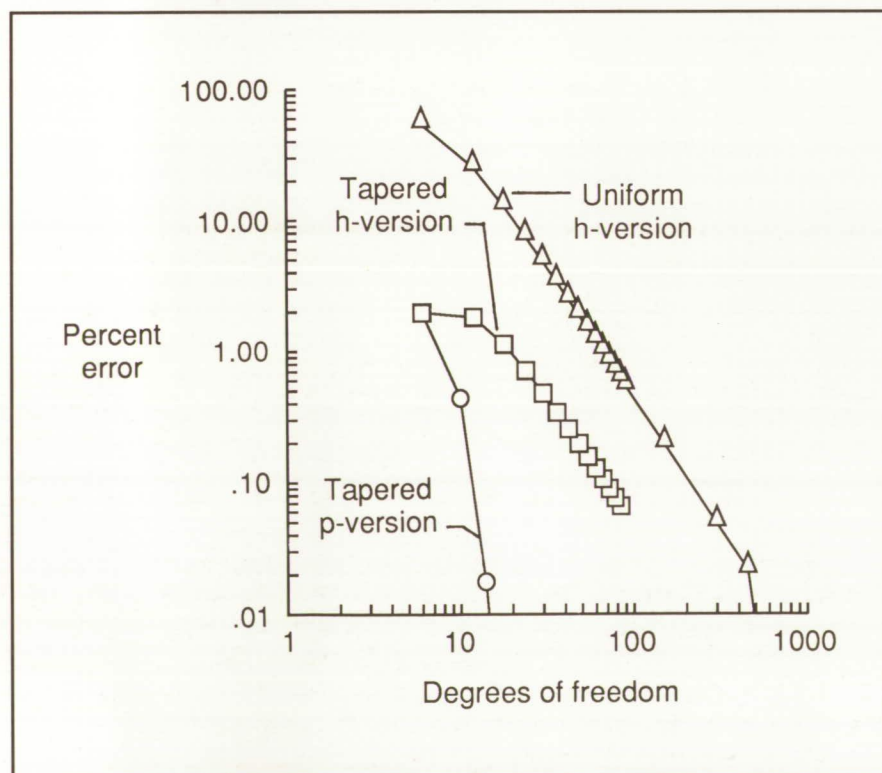
30° . Steady-state results were first obtained to determine the basic character of the vortical flow. A cross-sectional view of the total pressure loss contours from this calculation, shown in the figure, indicates that the flow separates from each of the leading edges producing two large circular vortices. An unsteady, forced harmonic analysis at these conditions showed that for small amplitudes of roll motion the aerodynamic loads will have a destabilizing effect on the free response. However, at larger roll amplitudes, the analysis showed that nonlinear aerodynamic effects will provide a stabilizing influence on the free response. The results of the forced harmonic analysis were verified in a free-to-roll calculation. The roll angle time history, shown in the figure, indicates that initially the oscillatory response diverges for small values of roll angle. As the amplitude of motion grows with time, however, the response changes to a limit cycle oscillation. This type of limit cycle oscillation is indicative of a phenomenon called wing rock. These results demonstrate the ability of the conical Euler methodology to predict this type of a vortical-flow phenomenon for supersonic speeds. (Elizabeth M. Lee and John T. Batina, 42269)
Structures Directorate

p-Version, Tapered, Beam Finite Element for Vibrations Analysis

The reduction of rotorcraft vibrations is one of the most pressing and difficult problems facing the structural dynamicist today. To have a significant impact on reducing vibration, without attendant weight or performance penalties, it is becoming increasingly important for vibration reduction to be considered during



Sample finite-element models of tapered, cantilevered beam.



Relative efficiencies of three different types of finite-element models. (Percent error versus number of degrees of freedom for first torsional frequency.)

design. However, current finite-element-based dynamic analyses are not accurate enough to be used with confidence during design. This research was undertaken to develop finite-element dynamic analysis methodologies that are more accurate, easier to use, and computationally more efficient than present methods.

Although several possible reasons exist for the lack of correlation with experiment, one that has recently attracted attention is the accuracy of the elements themselves. Most finite-element codes in use today employ what are commonly referred to as h-version elements. An h-version element uses fixed-order shape functions to relate the discrete nodal displacements of the element to the continuous displacements within the element. The p-version element is different from the h-version element in that the user may select the order of the shape functions defining the displacement behavior of the element. Increasing the order of the shape functions is analogous to increasing the number of elements for a comparable h-version model.

A p-version, tapered, beam finite element has been derived. Three finite-element models of a truncated, conical beam were then formed. One model used a single p-version tapered beam element; the second model used the h-version tapered beam elements. The third version used the h-version uniform beam elements. Convergence studies then were performed by varying the number of elements used in the h-version models and by increasing the order of the shape functions in the p-version model. As shown by the data in the figure, the model using the p-version, tapered, beam element produces more accurate frequencies for a given number of degrees of freedom than the models using the tapered h-version elements or uniform h-version elements. This relationship is a

general indication of the computational efficiency of the finite element. The most valuable characteristic of p-version elements is the relative ease of increasing the accuracy of the finite-element model. This is difficult with large h-version models because of the need to generate new, refined mesh. With p-version finite elements, however, the existing mesh does not need to be altered; the order of the shape functions used for the elements is increased instead, which is a relatively trivial task.

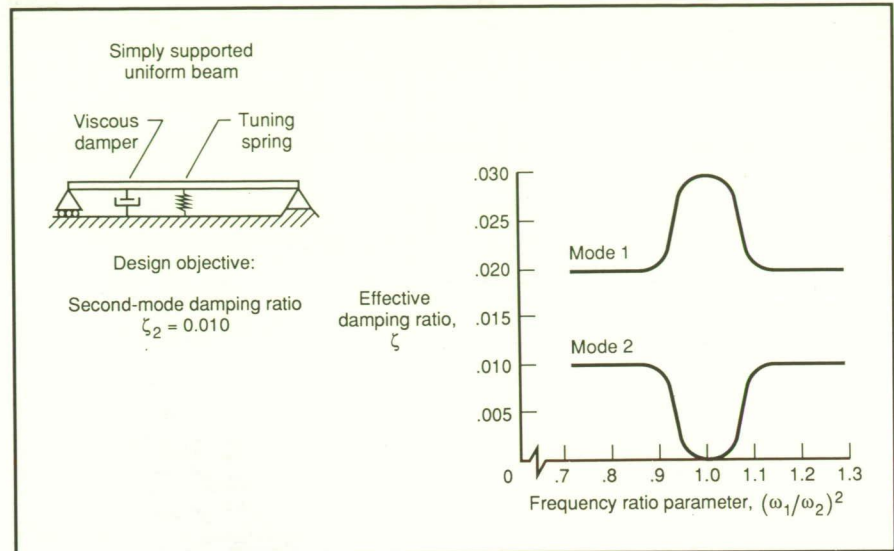
The development of an efficient, well-behaved, p-version, tapered, beam element is an important demonstration of the type of technology that might be used to improve the effectiveness of current finite-element dynamic analyses.

(Howard E. Hinnant, 41227)
Structures Directorate

Identification of Anomaly in Damping Treatments for Reducing Vibrations

In aerospace vehicle applications it is often desirable to achieve up to an order-of-magnitude reduction in resonant or near-resonant structural forced vibrations by the addition of one or more localized and concentrated damping treatments and devices. Such large reductions are possible because these types of structures are inherently lightly damped and because small additional amounts of damping will yield large reductions in forced vibratory responses.

A simplified analytical preliminary design method has been developed which will predict accurately the effect of localized, concentrated, and other types of damping treatments in increasing the various modal vibration ratios of equivalent viscous critical damping. An energy quotient



Damping anomaly results.

analogous to Rayleigh's quotient for predicting undamped, natural frequencies of vibration for the various modes of complex structures is employed. This energy quotient utilizes the known structural mass, stiffness, and undamped modes of vibration and permits a straightforward evaluation of the effect of damping treatment types, locations, and magnitudes on the modal damping ratios ζ_i . Application of this energy quotient for ζ_i is followed by an interaction analysis to account for a modal resonance effect when two modes have the same or nearly the same natural frequency. The simplified analytical preliminary design method followed by the interaction analysis yields predictions of ζ_i within 1 percent or less of the values obtained by using more rigorous methods when the damping ratios are less than 10 percent of critical.

An illustrative example of the method is given in the figure for a uniform simply supported beam with a tuning spring at the center. A viscous damper is employed with a view toward damping the second (antisymmetrical) bending mode. The first (symmetrical) bending mode is tuned so that its natural frequency

matches that of the second mode. As the frequency ratio (ω_1/ω_2) increases from its normal ratio of one-fourth with increasing tuning spring stiffness, the effective damping ratio of the second mode progressively decreases from its design objective to zero. As the frequency ratio increases beyond unity, the effective damping ratio of the second mode recovers to its design objective. The first mode, in effect, steals damping intended for the second mode when their natural frequencies match or nearly match.

The anomaly of a resonating structure not benefiting from a damping treatment to reduce its vibratory response has been identified. An analytical method has been developed which computes the effectiveness of the damping treatment when two different modes of vibration have matching or nearly matching natural frequencies. This method permits the structural designer to better employ damping treatments in conjunction with structural mass and stiffness considerations that influence natural frequency placement.

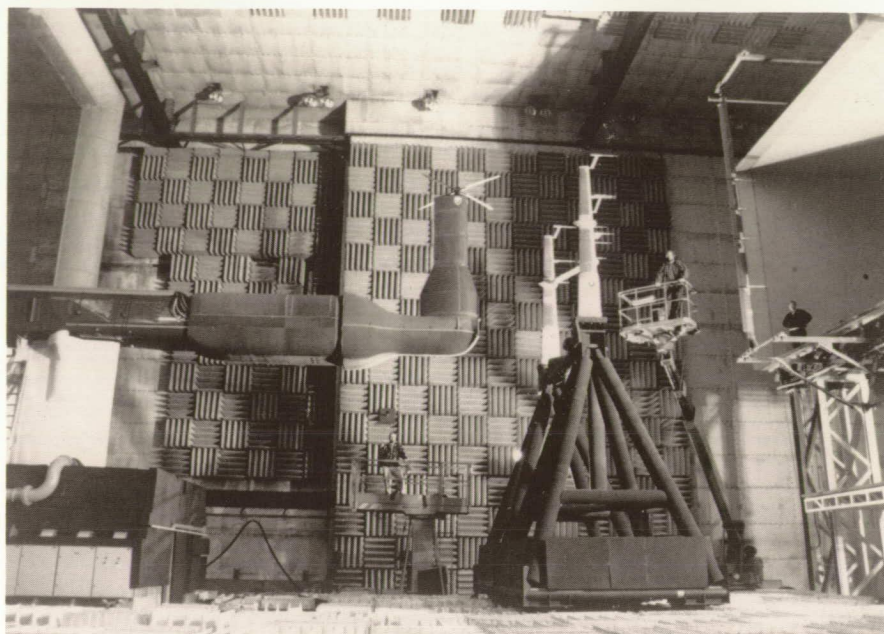
(Maurice I. Young, 41232)
Structures Directorate

Pressure-Instrumented Main Rotor Noise Test

Blade-vortex interaction (BVI) noise is a highly impulsive noise source that can be a major problem in helicopter noise certification. The BVI noise occurs when a helicopter rotor blade strikes, or passes very close to, a tip vortex that has been shed into the wake of the rotor. The interaction of the vortex with the blade produces a large, unsteady pressure pulse on the blade surface, which produces the BVI noise pulse.

In order to investigate this interaction process more closely, simultaneous measurement of blade pressures and far-field acoustics is required. To obtain these data, a test was performed on a United Technologies model rotor with 176 pressure transducers on the blades. This test was done as part of the Aerodynamic and Acoustic Testing of Model Rotors (AATMR) program, and it was a cooperative effort between the Aeroflightdynamics Directorate of the Army, United Technologies Research Center, Sikorsky Aircraft, Ames Research Center, and Langley Research Center. Although AATMR is an Army Aeroflightdynamics Directorate program, the United Technologies Research Center program owns the blades. The test was performed in the Duits-Nederlandse Windtunnel/Deutsch Niederlandischer Windkanal (DNW), which is the large German/Dutch Acoustic Wind Tunnel in the Netherlands. The figure shows the model rotor in the open-jet acoustic test section of the DNW.

The simultaneous acoustic and pressure data serve several purposes. The unsteady pressure fluctuations due to BVI can be directly compared to the measured BVI noise, which has provided a great deal of insight into the BVI noise mechanism. In addition, the surface pressures are



*United Technologies Research Center model rotor in DNW (flow is from right to left).
L-90-7805*

being directly input into the rotor noise prediction program WOPWOP, which is the computer code for Farassat's formulation 1A. This program predicts rotor thickness and loading noise in the time domain, given the unsteady pressure distribution around the rotor. These data are being used to validate the prediction technique, and they serve as a bridge between measured noise data and a noise prediction from purely theoretical/computational means.

**(Michael A. Marcolini, 43629, and Ruth M. Martin)
Structures Directorate**

Performance Optimization of Helicopter Rotor Blades

As part of a Center-wide activity at Langley Research Center to improve helicopter rotor blade design procedures by accounting for discipline interactions, a performance design optimization procedure has been developed. The procedure optimizes the aerodynamic performance of rotor

blades in both hover and forward flight by selecting the point of taper initiation, root chord, taper ratio, and maximum twist that minimizes hover horsepower while not degrading forward flight performance. The procedure uses HOVT (a strip theory momentum analysis) to compute hover horsepower and the comprehensive helicopter analysis program CAMRAD for forward flight and maneuver. The optimization algorithm consists of the general-purpose optimization program CONMIN and approximate analyses. Sensitivity analyses consisting of derivatives of the objective function and constraints are carried out by finite differences. Satisfactory aerodynamic performance is defined by the following requirements that must hold for any part of the mission scenario. These requirements include that the required horsepower must be less than the available horsepower, the airfoil section stall along the rotor blade must be avoided, and the helicopter must be trimmed.

This procedure has been applied to a test problem that is a wind tunnel model of the UH60-A Growth Black Hawk rotor blade. Results in the

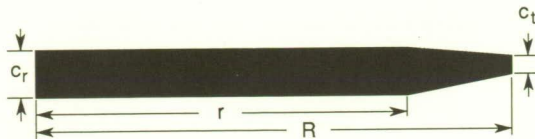
Design requirements

Minimum hover horsepower (hp)
 $hp_{req'd} \leq hp_{avail}$
 No airfoil stall
 Blade must be trimmed

} For 3 flight conditions

Design requirements

Point of taper initiation, r/R
 Blade root chord, c_r
 Taper ratio, c_r/c_t
 Maximum twist, τ_{max}



	Initial	Final
r/R	0.8	0.472
c_r	5.4 in.	5.0 in.
c_r/c_t	3	5.0
τ_{max}	-16°	-15.5°
Hover hp	11.27	10.57
Forward flight hp	8.95	8.0
Maneuver hp	12.0	9.87

Performance optimization for model rotor blade.

figure indicate that the optimized design has moved the point of taper initiation significantly inboard, reduced the root chord, and increased the taper ratio. The maximum twist changed slightly. A very significant decrease in the hover horsepower was obtained, and the horsepower for the other flight conditions decreased as well. Specifically, the optimized design has a decrease of 7 percent in hover horsepower, 12 percent in forward flight horsepower, and 22 percent in maneuver horsepower. (Joanne L. Walsh, 42806) Structures Directorate

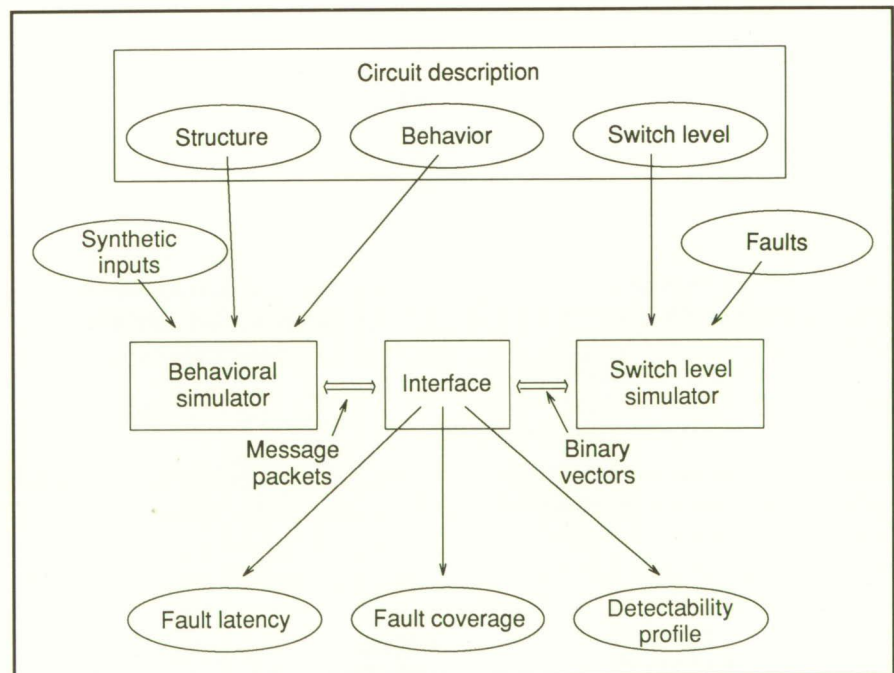
Object-Oriented Design and Analysis of Application Specific Architectures

The objective of this research was to develop computer-aided analysis and design tools for evaluating

tures. This work focused on the development of an object-oriented workbench that provides for combined performance, reliability, and yield evaluation of message-passing application-specific architectures. An initial version of the Object-Oriented Design/Analysis of Reliable/Reconfigurable Architectures (OODRA) workbench was completed during 1989. The work was performed at the University of Illinois Urbana-Champaign under partial funding by the Illinois Computer Laboratory for Aerospace Systems and Software (ICLASS) block grant and the Semiconductor Research Corporation.

The OODRA workbench provides for graphical description and architectural simulation of restructurable message-passing architectures. Concurrency is modeled using communicating sequential process constructs implemented in C++; these constructs utilize an object-oriented class library for C++ programs, InterViews libraries, and iDraw with X-windows. The OODRA workbench also has been interfaced with

performance and reliability of application-specific reconfigurable message-passing parallel architec-



OODRA fault simulation environment.

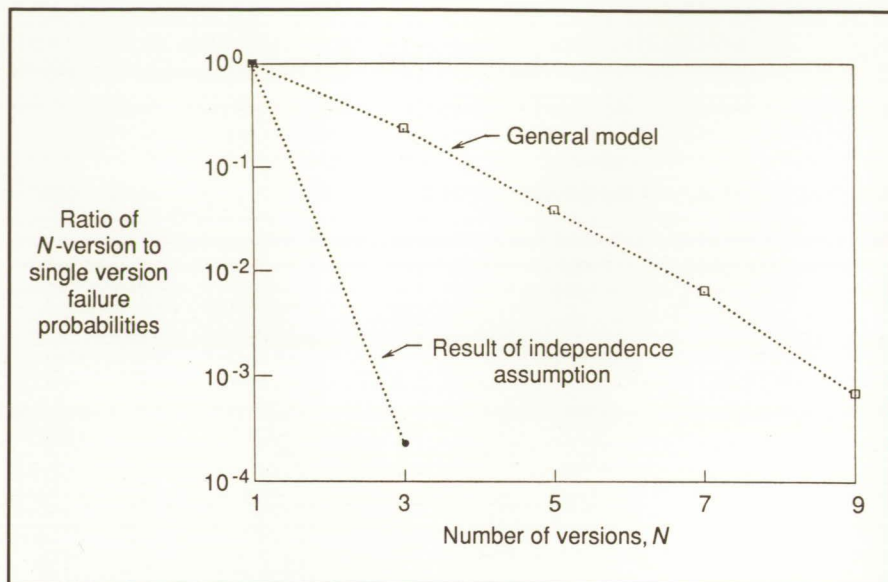
the Concurrent Hierarchical and Multilevel Program for Simulation (CHAMPS) of VLSI (very large-scale integrated) circuits. CHAMPS is a concurrent hierarchical, switch-level fault simulator developed at the University of Illinois. The figure illustrates the architectural fault simulation environment. The combined visually oriented fault simulation environment has been used to evaluate the fault coverage for various testing schemes and error propagation effects in message-passing digital adaptive beam-forming architectures.

The computer-aided analysis and design software developed is unique in that it provides for ease in architectural description and simulation by using message-passing concurrency, object-oriented C++ descriptions, and reconfiguration and reliability analysis.

(Kathryn A. Smith, 41699)
Flight Systems Directorate

Experimental Evaluation of Software Redundancy for Improving Reliability

The use of redundant software for tolerating software failures is suggested by the success of hardware redundancy for tolerating hardware failures. In both approaches, the degree to which faults result in independent failures determines the effectiveness of redundancy as a method for improving reliability. Interest in redundant software centers on whether it provides an adequate measure of increased reliability to warrant its use in critical applications. In a large-scale study, multiple versions of independently developed software configured in a fault-tolerant structure are studied by comparing estimates of the failure probabilities of these systems with estimates of the



Ratio of failure probability of N-version systems to failure probability of single-version systems.

failure probabilities of the individual versions. Forty programmers from 4 universities (University of Virginia, University of California, University of Illinois, and North Carolina State University) independently produced, in teams of 2, 20 versions of software for a complex aerospace application (the sensor redundancy management task for a Redundant-Strapped-Down-Inertial-Measurement Unit). An additional 20 programmers performed independent certifications of the versions. The versions then were subjected to long-term testing in an operational setting. Estimates of failure probability are obtained using a general model of software redundancy developed by NASA researchers. Estimates also are obtained using the classical model of hardware redundancy which assumes that failure behavior is independent.

The general model does not require an assumption that failures are independent but, rather, suggests analytical arguments that the failures of functionally equivalent component versions will be dependent. However, the nature of failures of independently developed software is a

matter of considerable controversy. For the 20 versions in this experiment, coincident failures of the redundant versions occurred at rates that greatly exceed the rates expected by chance under the assumption of independence.

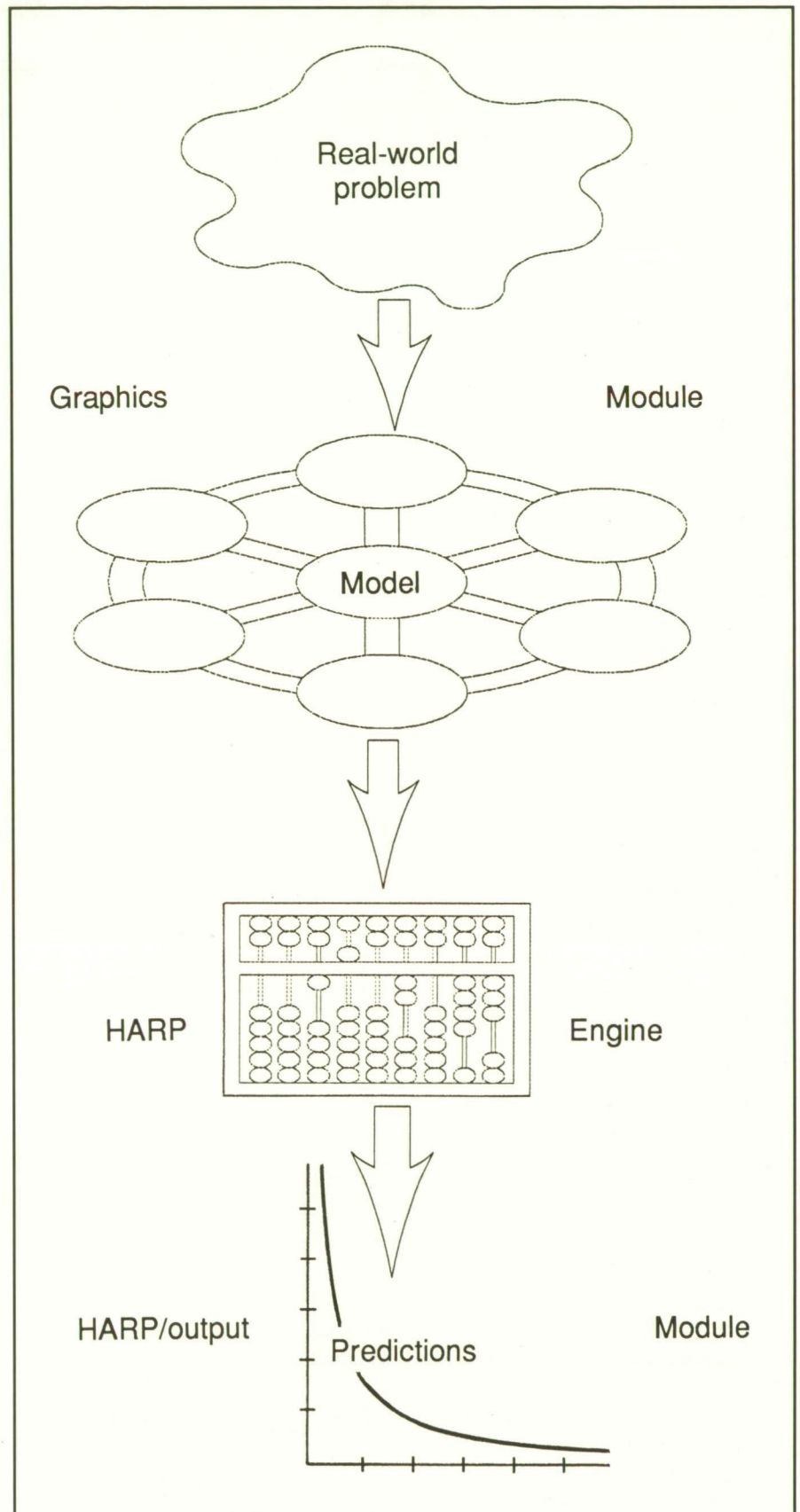
The results show a reduction in the failures of redundant software systems as the level of redundancy increases; however, this reduction does not occur to the degree indicated when the failures are assumed to be independent. For example, when independence is assumed, a representative case (shown in the figure) indicates that the failure probability for a three-version system will be a small fraction (0.0002) of the failure probability of a single version. However, the failure data applied to the general model indicate that this ratio is three orders of magnitude (0.2) higher. For this study, independent development in itself was not sufficient to achieve ultrahigh reliability gains over using a single version.

(Dave E. Eckhardt, 41698)
Flight Systems Directorate

Reliability/Availability Integrated Workstation

The HARP (Hybrid Automated Reliability Predictor) integrated workstation tool system marks another accomplishment toward the goal of producing a totally integrated workstation design capability. Because reliability engineers generally graphically represent a reliability model before they can solve it, the use of a graphical input description language will increase productivity and decrease the incidence of error. The captured image displayed on a cathode-ray tube serves as a documented copy of the model (a hard copy can be made by the push of a button) and the data for automatic input to the reliability model solver. In addition, the PC (IBM-compatible personal computer), Sun, and VAXstation versions create files that are 100 percent compatible with all versions; therefore, the PC can be used strictly as a reliability model input device and can have its files transferred to a VAX, Sun, or some other mini- or maxi-computer for solution (for very large models), or the entire model can be solved on the PC (for small models). Very large models can be worked completely on a Sun or VAXstation.

Preprocessor and postprocessor computer programs generate files for the HARP program to provide an input language with a graphical reliability modeling description. A graphical output tradeoff analysis capability was defined and implemented in a portable ANSI standard graphics language, a GKS (Graphics Kernel System) for the PC, a Sun workstation, and a VAXstation workstation. As part of the description language, a new fault tree notational language also was defined and implemented. In addition to the standard AND and OR gates commonly found in combinatorial fault trees, four new dependency gates



HARP integrated tool system.

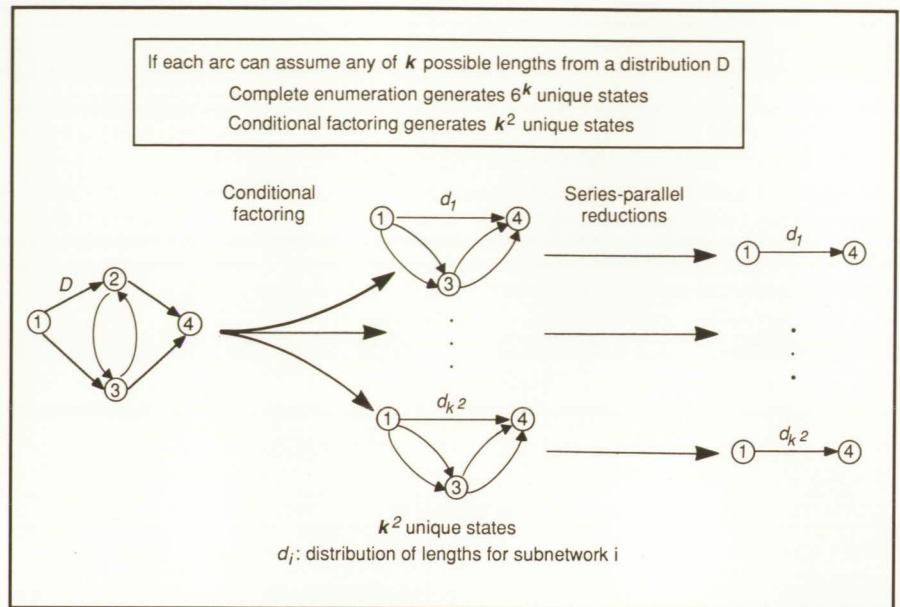
have been identified for the modeling of fault-tolerant systems. The postprocessor provides the user with a very powerful graphical data manipulation capability required for detailed tradeoff analyses. The user can display multiple reliability/availability data as a function of several important design parameters. In a few short minutes, the user can review and analyze massive amounts of HARP-generated data.

(Salvatore J. Bavuso, 46189)
Flight Systems Directorate

Conditional Factoring Approach to Network Analysis

Shortest path calculations are valuable in the analysis of various distribution networks such as those utilized in complex telecommunications processes and distributed computer architectures. To reflect uncertainties commonly present in many distribution systems, a stochastic model is often more realistic. However, most existing methods for determining the distribution of the shortest path length for a stochastic network rely on complete enumeration of each possible state of the network. Even for relatively small networks, this approach is computationally infeasible. Consequently, current analysis methods have been largely confined to approximation, simulation, and bounding techniques.

To avoid complete enumeration, a simple but powerful graph-theoretic approach, called conditional factoring, has been developed. With this new approach, a directed, stochastic network is decomposed into a set of smaller, less complex networks that can be solved for the exact shortest path distribution without complete enumeration. Several network constructs were identified and



Decomposition of simple loop construct using conditional factoring.

exploited such that the application of conditional factoring to these constructs significantly reduces the computational effort needed to solve the problem. The figure shows the decomposition of one such construct, the simple loop, into a set of series-parallel subnetworks.

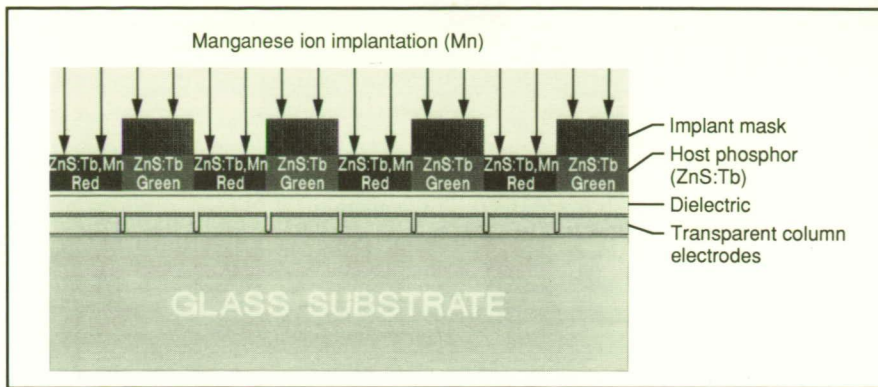
Conditional factoring extends the computational range for network problems, especially in the case of cyclic networks, to larger and more complex networks than have been solved previously. In addition, this approach applies to two important classes of problems (determining the critical path distribution for acyclic networks and the exact two-terminal reliability for probabilistic networks). Computational experience with the algorithm has been encouraging and has allowed the exact solution of networks that previously had been analyzed only by approximation techniques.

(Kelly J. Hayhurst, 46215)
Flight Systems Directorate

Multicolor Electro-luminescent Display Fabrication Using Ion Implantation

Electroluminescent (EL) display technology is a candidate flat-panel display technology for future use in aircraft and spacecraft cockpits. Recently, full-color capability has been achieved in EL displays through contractual research sponsored by NASA and the U.S. Army. However, the present method for fabricating full-color EL displays is highly complex in that it requires three separate phosphor deposition steps and three separate etching steps. The chemical etching is difficult to control and leads to low yields. The objective of this research has been to develop and evaluate a new method of EL color display fabrication which will eliminate all of the etching and two of the deposition steps, thereby, resulting in a simpler fabrication method with higher yields.

A new method for the fabrication of multicolor EL displays has been conceived and documented in the



Multicolor TFEL fabrication by ion implantation.

L-89-10438

form of a U.S. patent application (NASA Case No. LAR 13616-1). To establish the feasibility of the fabrication method, which uses a single-phosphor layer in conjunction with ion implantation, a simplified test cell approach was utilized. The EL test cell was a single-phosphor-layer display having a 1-in. by 1-in. active area with 16 columns (as defined by addressing column electrodes). The single-phosphor layer was a thin film of ZnS:TbF_3 (zinc sulfide with 1 percent terbium fluoride), which is a green-emitting EL phosphor. Alternate columns of the test cell display were masked, and Mn (manganese) ions were implanted into the unmasked columns (as shown in the figure). The regions receiving the ion implant become $\text{ZnS:TbF}_3 + \text{Mn}$, which is a red-emitting phosphor. Following the implantation, the test cell was made into a functional thin-film electroluminescent (TFEL) display for testing through the addition of 16 row electrodes and an insulating (dielectric) layer.

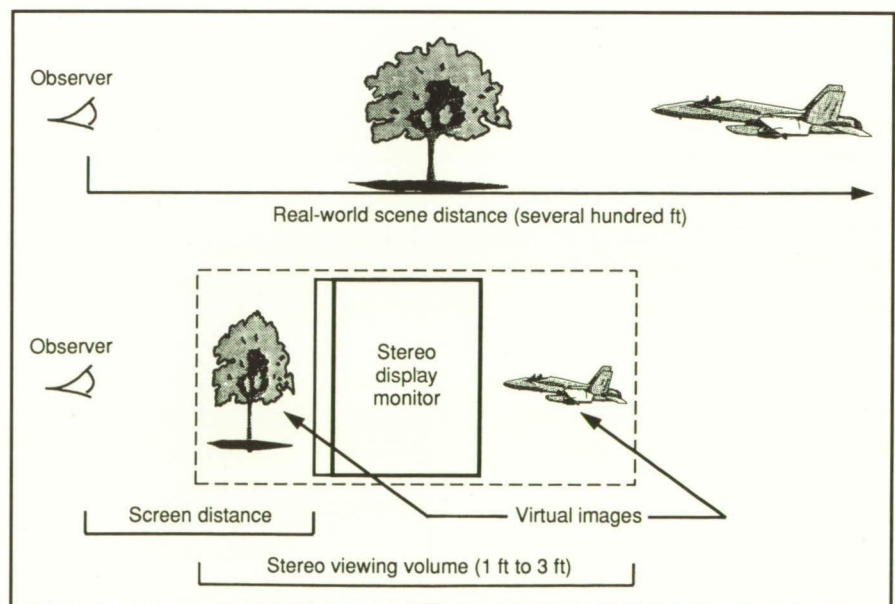
Testing revealed that a two-color (red plus green) TFEL display was produced successfully using a single deposition layer of host phosphor material and ion implantation in alternate columns. The ZnS:TbF_3 host phosphor, as deposited, emitted green light. The areas receiving the Mn ion implant emitted red-orange light. The resulting display device

had eight green and eight red-orange stripes. The results of this experiment are proof of the concept of using ion implantation to produce multicolor EL displays having a single-deposition phosphor layer. This concept offers the possibility of a simpler fabrication process with higher yields than the currently used process by eliminating the difficult-to-control etching steps.

(James B. Robertson, 46654)
Flight Systems Directorate

Improvement in Depth-Viewing Volume of Collimated Stereo 3-D Graphic Displays

Recent research in the application of stereopsis to real-world, three-dimensional (3-D), pictorial flight displays has demonstrated gains in pilot situational awareness and improved task performance. This research also has documented the preference of pilots for stereo versions of these displays. These encouraging results have occurred despite the use of conventional directly viewed (noncollimated) stereo display technology that severely limits the stereo depth-viewing volume. It is well-known from psychophysical research that the effective range of human stereo vision is several hundred feet. Constraints are imposed by the limited depth-viewing volumes of conventional directly viewed stereo 3-D display hardware, in which the real-world depth cues of hundreds of feet are mapped into a virtual volume with only several feet of depth. The objective of this proof-of-concept



Scene-to-screen mapping problems using conventional stereo display technology.

effort was to investigate whether or not a dramatic increase in depth-volume for stereo 3-D displays would be provided by the application of collimated optics to the stereo display source.

Recent experiments at Langley Research Center discovered that the effective region of stereopsis cueing (i.e., the depth-viewing volume) increased when the viewer-screen distance was increased. However, this increase was accompanied by a decrease in the field of view of the system. Collimation of the display source would move the effective accommodation distance to near infinity while maintaining the field of view at required levels. A dramatic increase in the depth-viewing volume was postulated due to relaxed accommodation/convergence restrictions. The conventional stereo 3-D monitor was mounted on a collimation system, and subjective determinations of the viewing-volume were made, which revealed a one hundred-fold increase in depth compared to the conventional system. Thus, a depth-viewing volume more commensurate with that of natural human vision was achieved. This dramatic increase in depth-viewing volume, which is a breakthrough in heads-down stereo display technology, will contribute to the full exploitation of stereopsis cueing in advanced display concepts (particularly in advanced applications such as a High-Speed Civil Transport (HSCT) which may require virtual windows and/or a see-through-the-nose pictorial display capability).

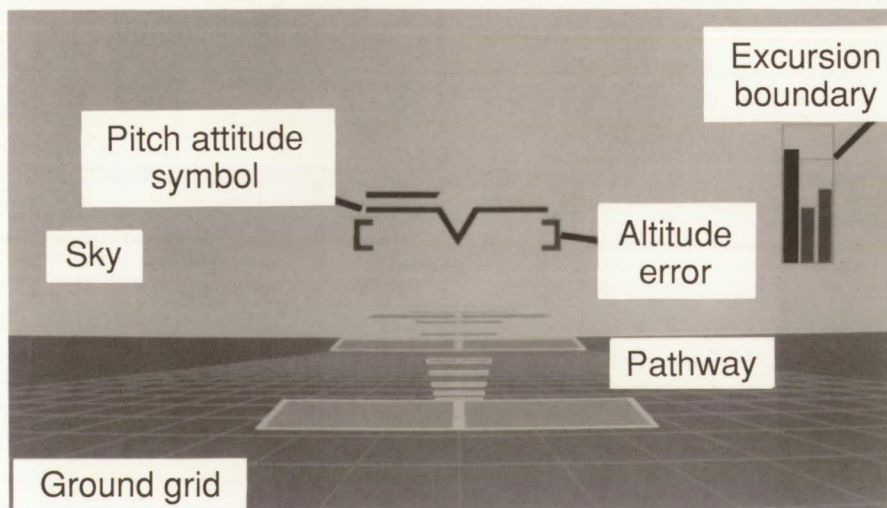
(Russell V. Parrish, Anthony M. Busquets, and Steven P. Williams, 46649)
Flight Systems Directorate

Improved Tracking and Monitoring Performance Using Stereopsis and Color Cueing

The use of monochrome helmet mounted display (HMD) systems is becoming prevalent in today's complex fighter flight mission environment. These HMD systems can provide stereopsis cueing as an almost natural byproduct for binocular helmet systems. The application of stereopsis (true depth) cueing to heads-down flight display concepts has demonstrated gains in pilot situational awareness and improved task performance. The issue of the use of color in information displays is somewhat similar to the use of stereopsis cueing; the advantages in its use seem obvious and intuitive, and yet its inclusion sometimes has been debated because of the additional costs. Unlike stereopsis, the technology for color is not yet available with the HMD flight systems of today. The goal of this research has been to assess the use of color cueing in peripheral monitoring displays and of stereopsis cueing in the foveal display of tracking information as may be encountered in future HMD systems.

A single-axis vertical tracking task for a rotorcraft, using a "pathway-in-the-sky" format, was chosen as the primary task for the pilot-in-the-loop experiment. A monitoring task (detection of boundary excursions) was presented in the periphery of the display. Because current HMD's cannot provide the capabilities of nonstereo and stereo cueing with color capability, a heads-up color cathode-ray tube stereo monitor configuration was used to emulate the HMD. The total field-of-view of 40° was partitioned into a foveal area of 20° and left- and right-peripheral areas of 10°. The primary tracking task was presented as a nonstereo/stereo pathway in the foveal area, while the monitoring task was presented in the peripheral area, with the presence and absence of color cueing.

The addition of color cueing to the monitoring task resulted in improvements in the primary tracking task, but only when using a nonstereo pathway. The addition of stereopsis cueing to the pathway display resulted in improvements in the primary tracking task, with or without color in the monitoring task display. The addition of color cueing in the monitoring task display resulted in an



Display format and associated tasks.

L-89-13515

increase in the number of correct boundary excursions detected by the pilots and a decrease in the number of extraneous (false) detections. In future HMD systems, the inclusion of both stereopsis cueing in the foveal area (to provide enhanced situational awareness in precision tasks) and color cueing in peripheral monitoring tasks (to enhance alerting functions) is desirable.

(Russell V. Parrish and Steven P. Williams, 46649)

Flight Systems Directorate

Effect of Exposure to Heads-Down Stereoscopic Flight Displays on Real-World Depth Perception

Current electronic technology can provide high-fidelity pictorial displays under flicker-free conditions that incorporate depth in the display elements. The application of stereopsis (true depth) cueing to advanced

heads-down flight display concepts offers potential gains in pilot situational awareness and improved task performance; however, little attention has been focused on a fundamental issue involving its use. The goal of this effort has been to resolve the question of whether short-term use of heads-down stereoscopic displays in flight applications would degrade the real-world depth perception of pilots using such displays.

Stereoacuity tests traditionally are used to measure the real-world depth perception of a subject. Stereoacuity is the smallest resolvable difference in depth and is determined from the measurement of attempted placements to the same depth of two targets originally positioned at different distances from the observer. Eight transport pilots flew repeated simulated landing approaches using both nonstereo and stereo three-dimensional heads-down "pathway-in-the-sky" displays. At the decision height of each approach, the pilots began a transition to a stereoacuity

test using real objects rather than a two-dimensional target test apparatus (as shown in the figure).

Statistical analysis of stereoacuity measures that compared a control condition of no exposure to any electronic flight display with the transition data from nonstereo displays and stereopsis displays revealed no significant differences for any of the conditions. Tests for statistical significance for the individual data did reveal some differences. In only one instance was depth perception degraded from the control condition, and that case was significant only for the transition from nonstereo displays. In all other cases, there were either no differences or the acuity was improved over the control condition. Clearly, beginning a transition from a heads-down stereopsis display has no more effect on real-world depth perception than changing from a nonstereo display.

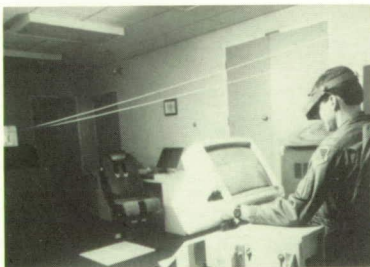
A fundamental issue challenging the application of stereoscopic displays in heads-down flight applications has been addressed with the determination that real-world depth perception is unaffected by the short-term use of stereo three-dimensional displays.

(Anthony M. Busquets, Steven P. Williams, and Russell V. Parrish, 46649)

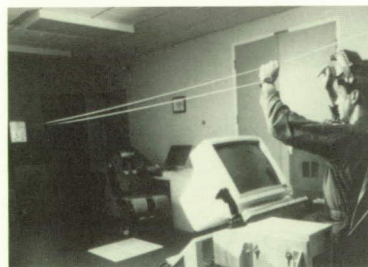
Flight Systems Directorate

Transition of Work Load Brain Wave Measures From Laboratory to Simulators

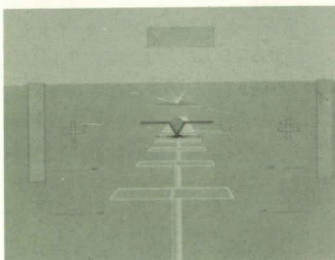
Most previous investigations that have addressed the relationship between evoked electrical brain potentials (EP's) and mental work load have focused on responses elicited by a secondary task. To be



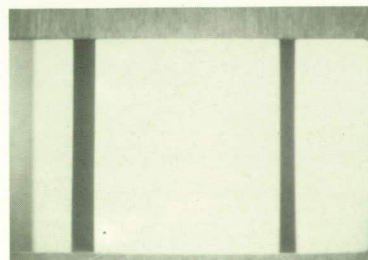
Flying the landing approach



Transition to real world



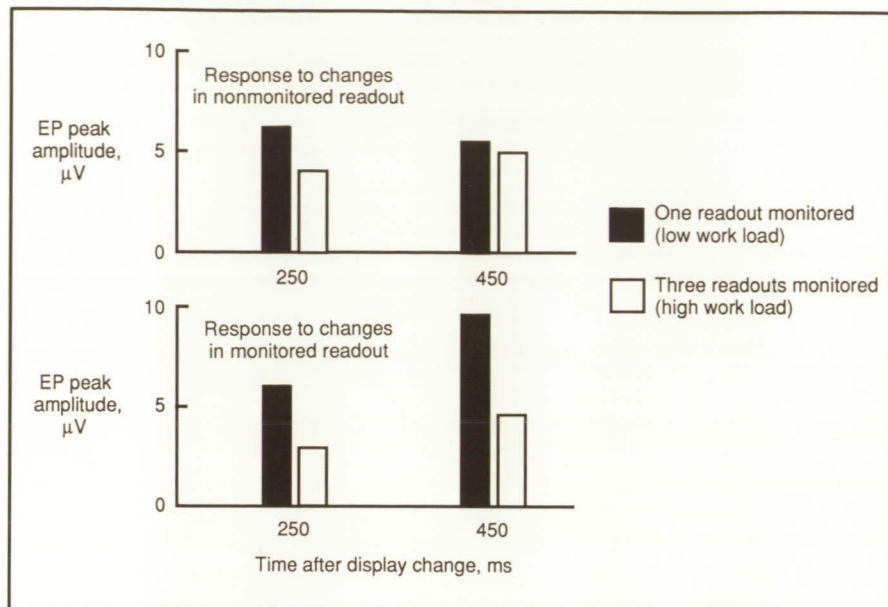
"Pathway-in-the-sky" display



Howard-Dohlman stereo depth test

Stereoacuity experiment.

L-89-10439



Work load effects on evoked potential peaks (averages of 12 subjects).

useful in evaluating the work load of human operators in real-world systems, EP methodology must avoid the use of contrived and possibly interfering secondary tasks. The objective of this study has been to determine the extent to which EP's elicited by stimuli, as they are processed naturalistically, reflect the cognitive work load demands of a complex task.

A laboratory task was designed which provided discrete stimuli to elicit EP's, allowed for the manipulation of mental work load, but yet was analogous in many ways to the types of monitoring activities which are performed in operational aircraft flight deck environments. In this task, 12 subjects monitored a circular arrangement of 6 2-digit readouts (as shown in the figure). On each trial, the value of one of the readouts was changed. Only a subset of the display was salient to subjects in that they were instructed to monitor either one or three of the six readouts and to report critical readout changes (readout changes that exceeded prespecified boundaries). The EP's were obtained by recording the brain

electrical activity that followed each display change.

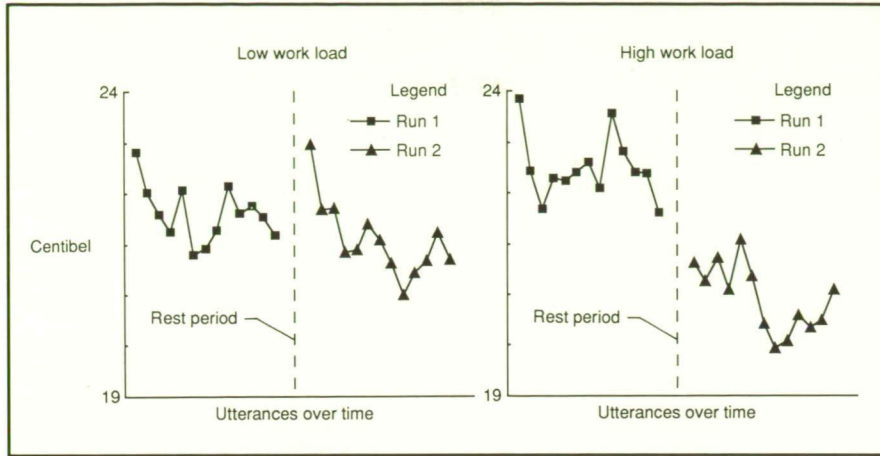
Two components of the EP, which reflected cognitive work load, were discovered at 250 ms and 450 ms obtained in response to only the critical readout changes in both monitored and nonmonitored readouts. The results at 250 ms reveal differences between EP's due to the number of readouts being monitored, regardless of whether the changing (and eliciting) readout was being monitored or not. The results at 450 ms reveal differences between EP's only when the monitored readout is changing. These findings appear promising to provide a way of distinguishing background events (not monitored) from foreground events (monitored) and to assess work load on the basis of EP responses to either event type. The results demonstrate the usefulness of EP's as indicants of mental work load in any setting that offers the ability to time-lock recordings to a discrete eliciting stimulus.

(Alan T. Pope and Richard L. Horst, 46642)
Flight Systems Directorate

Work Load Demands (Drop-Offs Over Time) by Voice Amplitude Measure

A series of studies were undertaken to determine the relationship between the acoustical properties of the voice and the work load demands placed on the speaker. Such measures of work load would be less obtrusive and better tolerated by pilots than present measures that involve electrodes (such as the electrocardiogram) or which involve questionnaires. In the present study, subjects repeatedly spoke short, imperative sentences just as pilots would do on an advanced flight deck that employed voice recognition systems. This task elicited speech samples. A simultaneous loading task was used to manipulate work load. The time pressure of the loading task was great in a high-work-load condition and less in a low-work-load condition. The voice samples were subjected to a computer analysis used in previous mental-state studies of psychiatric patients.

The results indicated that during both the high- and the low-work-load conditions, the amplitude of the voice fell over the course of the tasks. This drop-off occurred more quickly in the high-work-load condition. In the low-work-load condition, the amplitude recovered to earlier, higher levels following rest periods. In the high-work-load condition, this recovery did not occur. These results suggest that work load may not be best revealed by calculating the means of the acoustical parameters of the voice. Instead, work load may be best assessed by the strain that it induces in the operator over time. Performing a high-work-load task over a period of time may cause strain, which in turn may reveal itself as a loss in the energy of the voice over time (that is, a reduction in loudness). Increased strain makes it



Relationship between voice amplitude over time and work load demands (mean amplitude of 14 subjects).

less likely that the voice will regain its energy following rest periods. These findings were essentially replicated in follow-on tests in the Transport Systems Research Vehicle Simulator.

The results suggest that voice measures of work load could play a role in assessing the demands placed by new technology on operators. However, as results with pilots revealed, that role is limited by the variability among operators, and even within a single operator, of the effects of task demands on the voice. Increased mean amplitude may reflect heightened effort devoted to a task. Faster drop-offs in amplitude may reflect the fatigue resulting from sustained effort. In this way, the acoustical parameters of the voice may reveal the strategy that an operator uses for allocating effort during demanding situations.

(Alan T. Pope, 46642)
Flight Systems Directorate

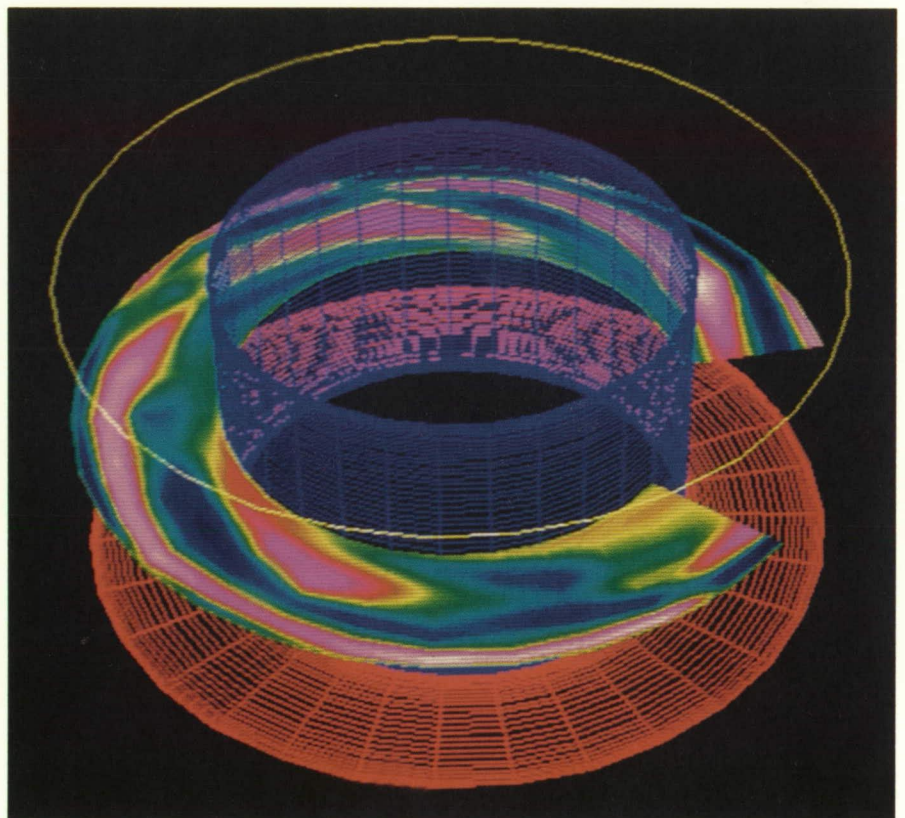
Gigaflop Performance Modeling of Taylor-Couette Flow

A researcher can bring the power of all the vector processors in a Cray

supercomputer to bear on a particular problem through the process of multitasking, or "parallelization" of the computer code. Described here is the "parallelization" of a production computational fluid dynamics (CFD) code on Cray Research, Incorporated (CRI) supercomputers.

The CRI product, microtasking, implements "parallelization" through compiler directives, which leave the code in standard FORTRAN that is portable to other architectures. This method of "parallelization" was used on the NSCYL3D code that models Taylor-Couette flow (the flow between two concentric cylinders which is induced by rotating one with respect to the other). This flow has been investigated for over a century as a model for the instability of curved and rotating shear flows.

The CFD problem is solved on a grid of 137 280 points, with four



Contours of axial velocity component on plane midway between apparatus end plates.

equations to be solved at each grid point. A sustained computational rate of 1.012 gigaflops or 1.012×10^9 floating point operations per second was achieved on Voyager (the four-processor Cray-2S at Langley Research Center). A rate of 1.586 gigaflops was achieved on Reynolds (the eight-processor Cray Y-MP at Ames Research Center).

Achieving these higher computational rates involved more than just placing compiler directives. First, the code was analyzed and optimized for execution on a single Cray CPU because it was initially executing at less than 250×10^6 operations per second on Voyager. Most of the computations were done in highly optimized Cray Assembly language routines that performed matrix multiplications and fast-Fourier transforms. In order to perform alternative but equivalent parallel matrix multiplications and transforms, the code and calling sequences to these routines needed modification.

This work resulted in a Gigaflop Performance Award presented at the Supercomputing '89 Conference. Although significantly more effort was placed on the optimization and "parallelization" of this code to reach the gigaflop performance level on the Cray-2S than the typical researcher has time to implement, just a few of the optimization and "parallelization" techniques had a major impact on the final performance. Thus, a substantially less intense effort would have netted a significant performance increase as well.

(Geoffrey M. Tennille, 45786, and Andrea L. Overman)
Electronics Directorate

Prediction of Radiation for 10-km/s Flows With DSMC

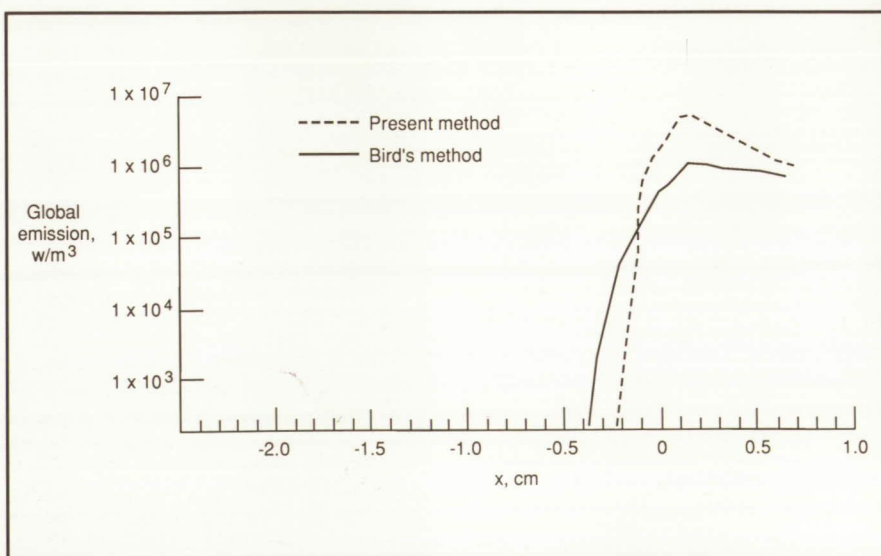
The Direct Simulation Monte Carlo (DSMC) method has been used to predict radiation from a shock at 10 km/s and 0.1 torr. This condition is representative of flows that might be experienced by the Aeroassist Flight Experiment, for which the prediction of radiation will be an important calculation.

The modeling of radiation with DSMC involves assumptions and approximations that require further investigation. The current research has been in the area of electronic excitation. The values of the electronic excitation number, which were used by Graeme Bird (the developer of the DSMC method) at the University of Sydney, Australia, are estimates based on typical cross sections and refined to reproduce measurements. A new method, which is based on available excitation rate data, has been developed for calculating these numbers. The method determines temperature, density, and species-dependent excitation numbers

that should be valid over a wider range of flow field conditions than the numbers that were used previously.

The predictions for global emission of radiation through a one-dimensional shock are shown in the figure. The radiation is plotted against distance measured from the center of the shock. For the current purposes, the shock center is defined as the point at which the density is six times the free-stream density. Both predictions are within the range of values currently being generated with other methods for AFE flows. However, the present method shows significantly more radiation from the center of the shock. This occurrence would have a large effect on the radiative heating on the surface of the vehicle during upper atmospheric maneuvers. The more conservative predictions must be considered in determining the amount of thermal protection used for the vehicle.

(Ann B. Carlson, 47050)
Systems Engineering and Operations Directorate



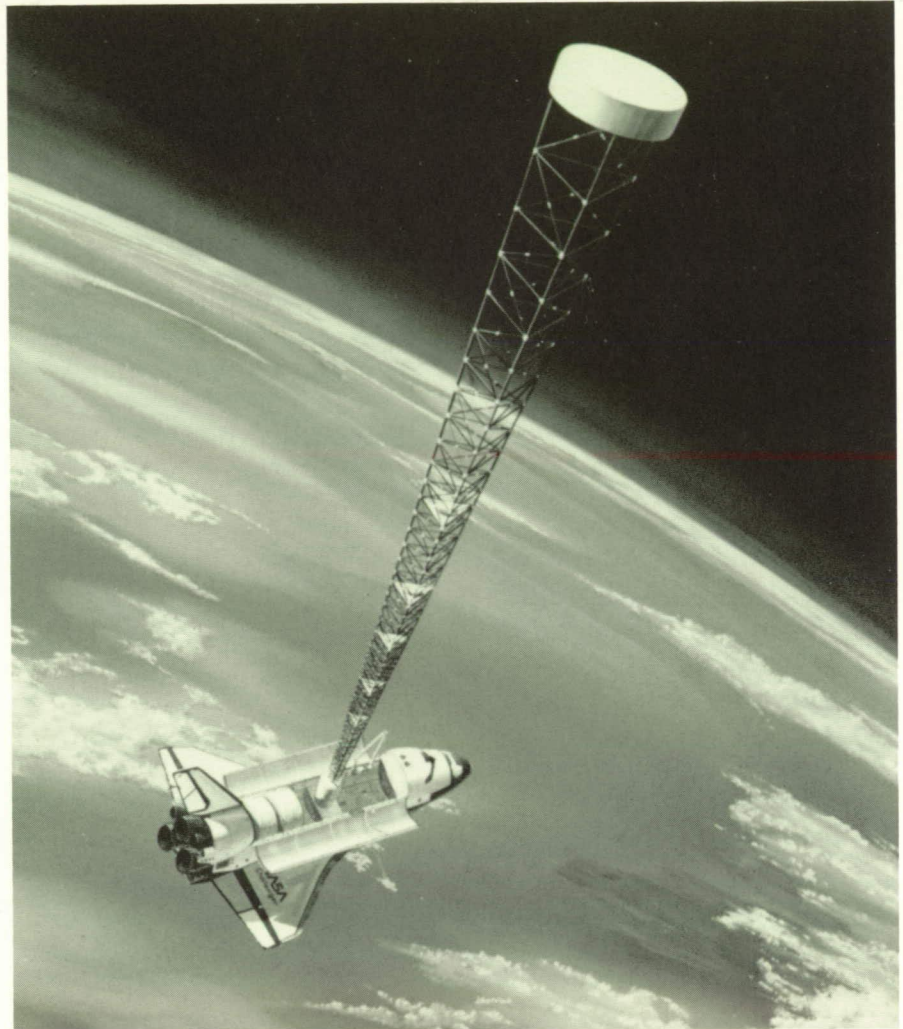
Comparison of radiation predictions for two methods of determining excitation collision number.

Integrated Controls-Structures Optimization

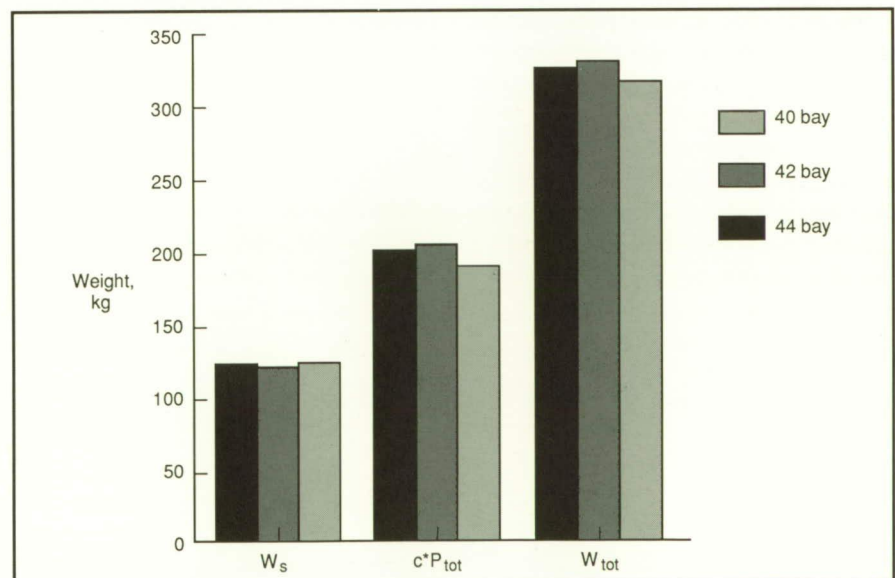
Future NASA missions (such as Mission to Planet Earth) envision large space structures that will require control systems to damp vibrations due to excitations (such as the motion of articulated payloads and pointing maneuvers). Strong evidence exists that an optimized design that accounts for controls-structures interaction (CSI) effects will have significant cost and performance benefits not possible if the control system and structure are designed separately.

A method for CSI optimization was developed and tested by application to the COFS-I mast flight system (MFS). The method consists of three computational steps. The first step performs a structural optimization to find the best compromise among all the design requirements, given the current weight budget. The optimal control step finds the best control settings, given the reduced model of the optimized structure, and calculates the total power requirements. The final step predicts whether changes in the weight budget or control strategy could reduce the total system weight (i.e., structural weight plus power-generating equipment weight). If improvement is possible, system parameters are reset, and the three steps are repeated.

The method was applied to a study of three configurations of the COFS-I MFS, which differed by the number of bays in the mast. In each case, the method successfully reduced the total weight of the system by approximately 20 percent. The graph indicates that the 42-bay configuration had the smallest structural weight W_s but had the largest power requirements P_{tot} and thus the largest total weight W_{tot} . Conversely, the 40-bay case had the largest structural weight but the lowest total weight.



COFS-I mast flight system.



Comparison of final weights.

This fact emphasizes the need for integrated controls-structures optimization.

The project is the first CSI optimization to use general-purpose controls and structures software and one of the first applied to a design problem with a significant number of degrees of freedom and with realistic design constraints.

(Sharon L. Padula, 42807, and Joanne L. Walsh)
Structures Directorate

Development of Advanced Modal Method for Transient Structural Analysis (Force Derivative Method)

Calculating the transient response of complex aerospace structures that are approximated by large, discrete finite-element models can be computationally expensive. The mode-displacement method (MDM) and the mode-acceleration method

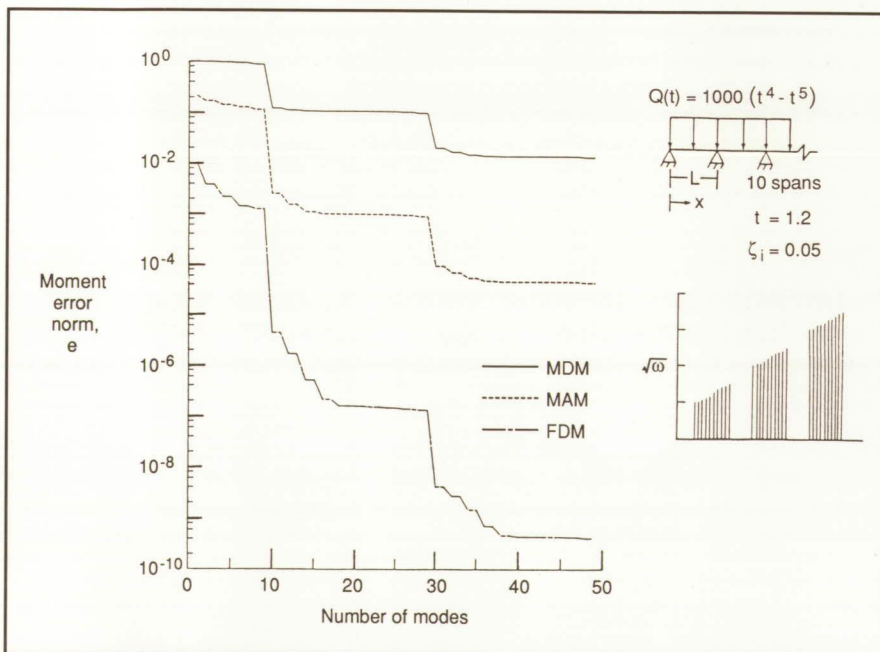
(MAM) are two popular methods to reduce the size of the problem by using the natural vibration modes as a set of reduced basis vectors. For structural problems that have closely spaced frequencies (e.g., large-area truss-like space structures), convergence of the solution is typically very slow using either of these two methods. A new, higher order, faster converging, modal method has been developed.

This new method successively integrates by parts the convolution integral form of the response and is called the force-derivative method (FDM) because it produces terms that are related to the forcing function and its time derivatives. The FDM is a unified method for developing higher order modal methods, beginning with the zeroth- and first-order methods (MDM and MAM, respectively) and continuing as high as necessary, providing that a suitable analytical description of the forcing function is available. The FDM is found to be more accurate than either the MDM or MAM methods. In particular,

where there are a large number of closely spaced frequencies, the FDM is very effective in representing the important, but otherwise neglected, higher modes. A uniform load distribution, which has a magnitude that varies as a quintic function of time, is applied to a 10-span, simply supported beam with proportional damping (as shown in the figure). The multispan beam has closely spaced frequencies occurring in groups of 10. As shown, the moment error for the FDM method is two orders of magnitude less than the MDM method and one order of magnitude less than the MAM method. The FDM converged to an accurate solution using only 1 mode as compared to 10 modes for the MAM and 49 modes for the MDM.

The FDM can reduce the computational effort of very large, complex dynamic problems to enable efficient solutions for displacements and stresses. Coupling this reduction technique with new methods for sensitivity calculations can greatly reduce the computational expense for transient structural optimization.

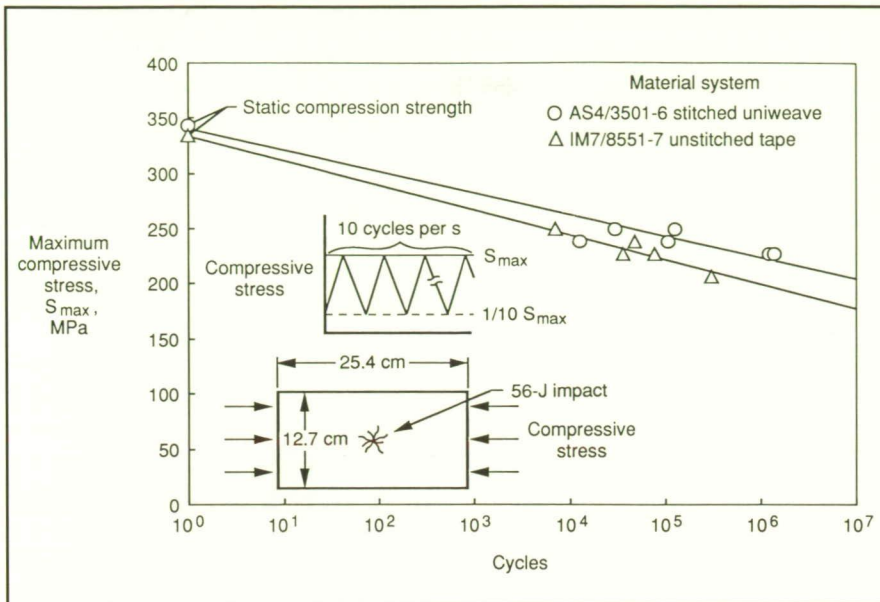
(Charles J. Camarda, 45436)
Structures Directorate



FDM that shows improvement over lower order methods. (Multispan beam has uniform load distribution.)

Improving Damage Tolerance of Carbon/Epoxy Composites by Stitching

Laminated carbon/epoxy composites are damaged more easily than metals when struck by tools and debris. This damage consists of disbonded layers and broken fibers. When loaded in compression, the disbonded layers buckle, thus causing the composites to fail prematurely. The disbonds can be eliminated or reduced in size by using stronger and tougher resins or by stitching the composite, thereby strengthening the interface between layers. Because



Gross compressive stress versus cycles to failure for postimpact specimens.

the tough resins are expensive, cheap resins with stitching have a potential cost advantage.

Although the stitched laminates performed well for single applications of compression load, some concern existed that the stitch sites might cause high local stresses and premature fatigue damage. To determine whether or not fatigue loading was a problem, stitched and toughened (unstitched) carbon/epoxy composites were impacted and then fatigue tested. The maximum compressive stress was 10 times the minimum. A sketch of the specimen, a schematic of the fatigue loading, and a graph of the maximum compressive stress versus number of cycles to failure are shown in the figure. The strengths for a single application of load are plotted on the ordinate. The stitched composite was not only stronger than the toughened composite for a single application of load, but also its fatigue strengths were greater in general than those of the toughened composite.

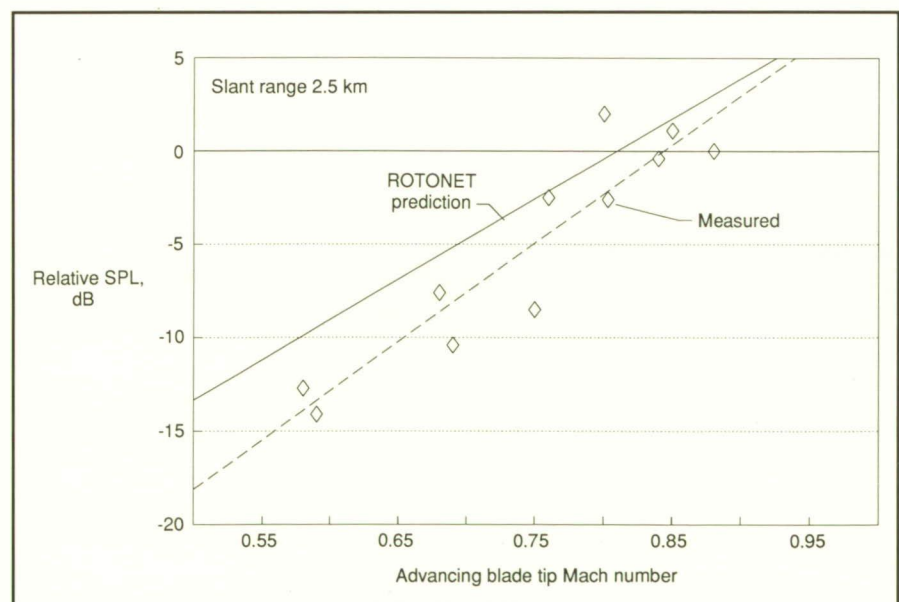
The layers of carbon fabric were stitched using a heavy fiberglass

thread (approximately 12 percent by weight) and then impregnated with resin. The fabric also contained fiberglass fill yarn, approximately 5 percent by weight. The stitched and unstitched laminates contained the same amount of carbon fiber, but because of the additional fiberglass, the stitched laminates were approximately 20 percent thicker than the

unstitched laminates. Without the increase in thickness, the stresses for the stitched composites would have been 20 percent greater, making the stitched composite even stronger. Future activities will develop the methodology to maximize the efficiency of stitched composites. (C. C. Poe, Jr., 43467, and M. A. Portanova)
Structures Directorate

Helicopter Far-Field Noise Reduction

Helicopter noise theory predicts that far-field noise decreases as the main-rotor speed decreases. This noise, which is in the plane of the main rotor, is a function of the advancing blade-tip Mach number, M_{AT} . However, until recently, comparing experimentally obtained flight data with predicted results has met with limited success. This limited success is because past flight tests have produced only a few experimental data points due to aircraft operational limits.



Comparison of relative measured and predicted far-field narrowband SPL's of main-rotor tone of Sikorsky S76-A helicopter.

The objective of this experiment was to study the relationship between measured and predicted noise over a wide range of M_{AT} . The experiment was successfully conducted using a Sikorsky S-76A helicopter that is certified by the Federal Aviation Administration to operate at more than one main-rotor speed during flight. A time signal was recorded simultaneously with measurements of the helicopter noise, operations parameters, and position along its flight track. Weather data also were taken at two sites separated by a distance of 8 km and to the side of the helicopter flight track.

Shown in the figure is a comparison of measured and predicted noise of the Sikorsky S-76A helicopter as a function of the M_{AT} . Measured narrowband sound pressure levels (SPL's) were obtained with the helicopter at a slant range of 2.5 km. These SPL's at the main-rotor fundamental acoustic frequency are relative to the measured SPL at the largest M_{AT} . The predictions are from the helicopter noise prediction program ROTONET. At the larger M_{AT} , agreement with ROTONET predictions is good. Data diverge from theory at the lower values of M_{AT} , but they continue the downward trend.

This experiment shows that helicopter design can be effective in reducing far-field noise and suggests that dual-mode operations are desirable, one for cruise and one with a lower M_{AT} for low-noise levels over populated areas.
(Arnold W. Mueller, 45277)
Structures Directorate

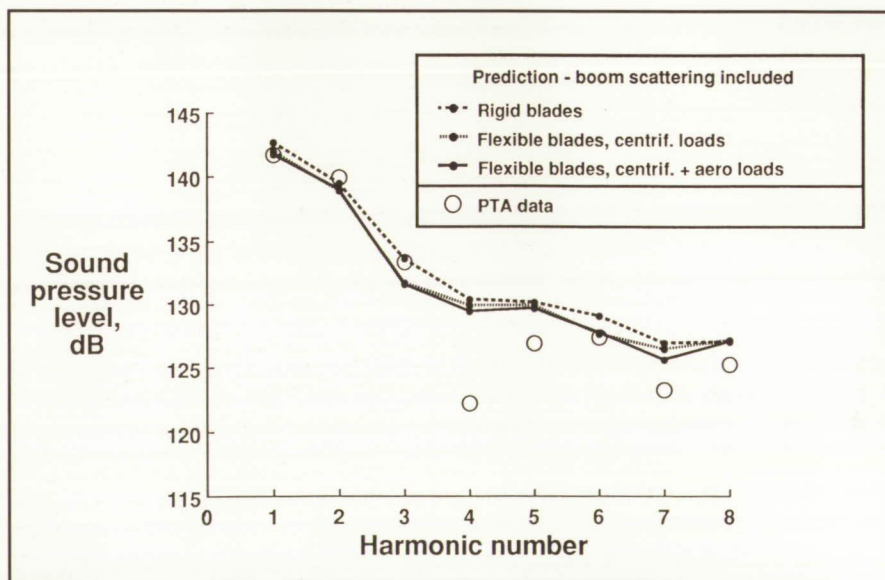
Blade Deformation Effects on Aerodynamics and Noise of Advanced Propellers

Modern advanced propellers have lightweight composite blades that deform during operation. Deformation is caused by centrifugal and aerodynamic forces. This deflection can have significant effects on propeller aerodynamics and noise. The objective of the research reported here is to quantify these effects for a full-scale advanced propeller (SR-7L) with a diameter of 2.74 m (9 ft) operating at the design condition. This propeller was tested in flight by Lockheed Georgia in 1988 for the NASA Lewis Research Center in the Propeller Technology Assessment (PTA) program. Considerable data were gathered from this program. In particular, acoustic measurements from microphones on a wing-mounted boom and on the fuselage are available, in addition to the power absorbed by the propeller.

Because blade deflection depends on blade loads, and the blade loads (i.e., aerodynamics) in turn depend on

deflection, the deflection and aerodynamics need to be calculated iteratively. In this work, blade deflection was calculated from the aeroelastic code NASTRAN, and blade pressure was calculated from a computational fluid dynamics code by Adamczyk (Lewis Research Center). The iteration between these codes is carried out automatically on a Langley Research Center Cray-2. The deflected blade shape and surface pressure then are used as input to the propeller acoustic code (DFP-ATP) developed by Dunn, Farassat, and Padula. The resulting acoustic output is compared with measured boom microphone data or used as input to the fuselage boundary-layer propagation code MRS-BLP developed by McAninch, Rawls, and Spence for comparison with fuselage microphone noise data.

Complete aeroelastic, aerodynamic, and noise calculations were performed for the SR-7L propeller operating at a flight Mach number $M_{A/C}$ of 0.81 and a helical tip Mach number $M_{H_{TIP}}$ of 1.15 (blade passage frequency of 226 Hz) at an altitude of 10.7 km (35 000 ft). The measured power of the propeller was known and used in the aeroelastic-aerody-



Example of noise spectrum of propeller with rigid and flexible blades operating at measured horsepower (PTA aircraft boom microphone 3 spectra).

ORIGINAL PAGE
BLACK AND WHITE PHOTOGRAPH

namic iteration. The results of these calculations show that the blade camber shape and twist are influenced by elastic deformation and that the outboard region of the blade is primarily affected. The centrifugal effect is more important than are blade loads in blade deformation. Blade deformation significantly affects propeller power and blade surface pressure. Again, the surface pressure of the outboard region of the blade is affected more by the blade deformation. The figure shows the effects of blade deformation on the noise spectrum for boom microphone 3 (1.12 diameters from propeller axis and 0.5 radius behind the propeller disc). The boom scattering correction is included in the predictions, and the propeller power is the same for all cases. Inclusion of blade deformation is seen to affect predicted noise. Deformation by centrifugal forces accounts for most of the changes in the noise spectrum. In particular, up to a 2.5-dB change is observed in some harmonics, and agreement between measured and predicted noise spectra is improved by the inclusion of the blade deformation. Further propeller noise predictions and comparison with measured data at different operating conditions of PTA aircraft are planned. The predictions will include both boom and fuselage microphones.

(F. Farassat, 43626, and Mark H. Dunn)

Structures Directorate

Noise Control in Fuselage Structures Using Piezoceramic Actuators

Active control techniques have attracted a great deal of attention stemming from their potential for low-frequency noise control in aerospace vehicles. This potential has been demonstrated in ground as well as flight tests. Most evaluations



Fuselage model with piezoceramic actuator used for active interior noise control.

L-90-7804

have focused on the use of acoustic control sources located within the cabin cavity. An alternative technique with additional potential is the use of force actuators inputting control directly to the fuselage structure. This technique has the significant advantage that the source distribution of the control source is identical to the offending noise source. Global noise control has been demonstrated in the laboratory with fewer control sources. However, concern arises from the local stress concentrations as well as the wide range of modes generated by the use of point forces on structures.

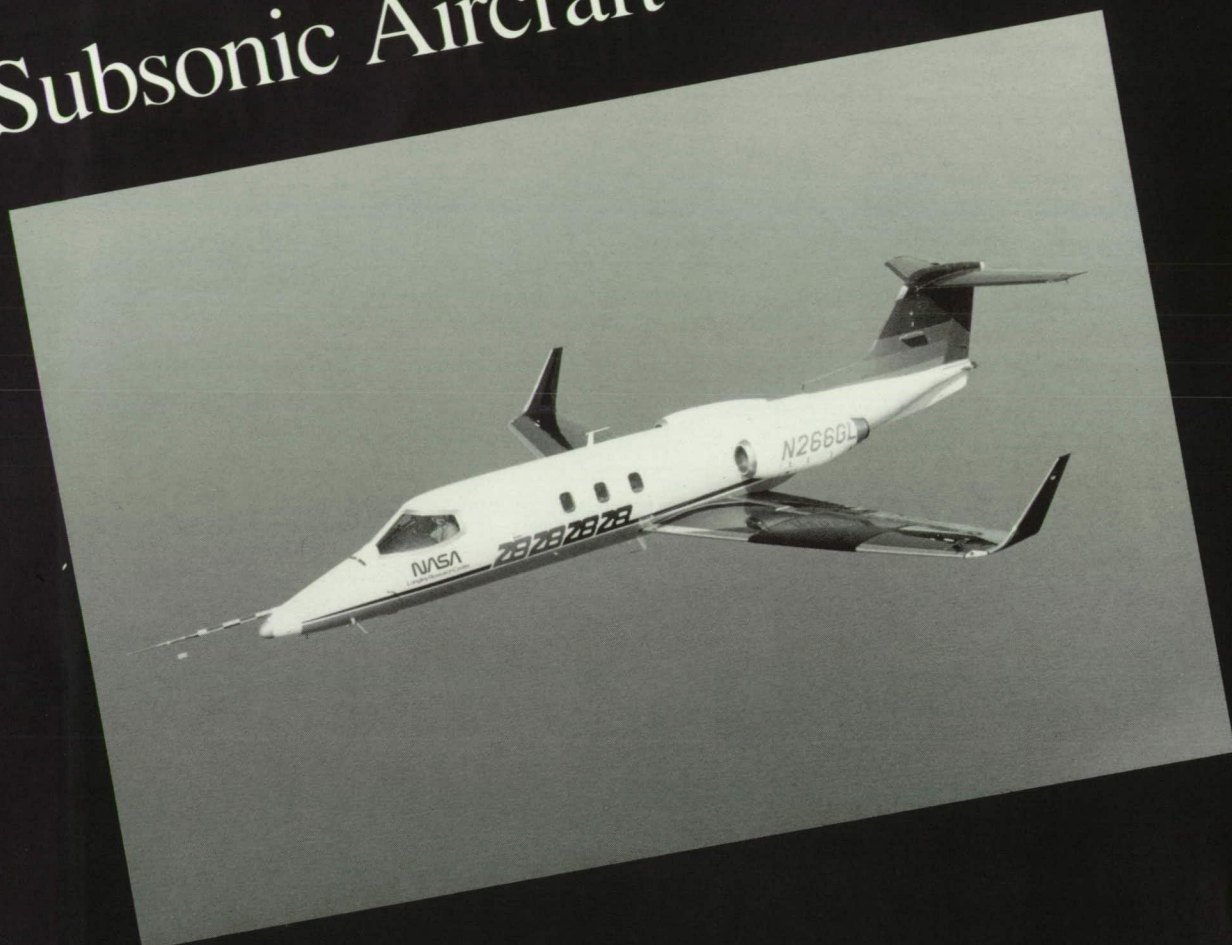
One alternative to the use of conventional shaker inputs is the use of piezoceramic patches bonded or embedded on the structure. These actuators work by expanding and contracting their planar surface when a voltage is applied to conducting upper and lower surfaces. One such actuator is shown (in the inset of the figure) bonded to the surface of a cylinder. The dimensions of this actuator are 0.5 in. by 2 in. This actuator is a two-layer assembly that will input a bending moment directly

to the structure. Single-layer actuator configurations strain the surface to which they are bonded, and, due to the actuator being displaced from the neutral axis, input both extensional forces and bending moments. These actuators have been found to exercise surprising authority in inputting energy into structural systems, especially in frequency ranges in which interior noise is of concern.

A preliminary evaluation of this test concept was implemented on the structural cylinder shown in the figure. The aluminum cylinder has a 20-in. diameter, is 48 in. long, and is 0.062 in. thick with interior rings and an attached floor. Interior noise fields were generated by an acoustic noise source adjacent to the cylinder. Control over this structurally transmitted noise was exercised with either one or two piezoceramic actuators, one of which is shown in detail. Interior sound pressure levels up to 85 dB were controlled with overall reductions of 8 dB to 15 dB for frequencies from 240 Hz to 700 Hz.

(Richard J. Silcox, 43590)
Structures Directorate

Subsonic Aircraft



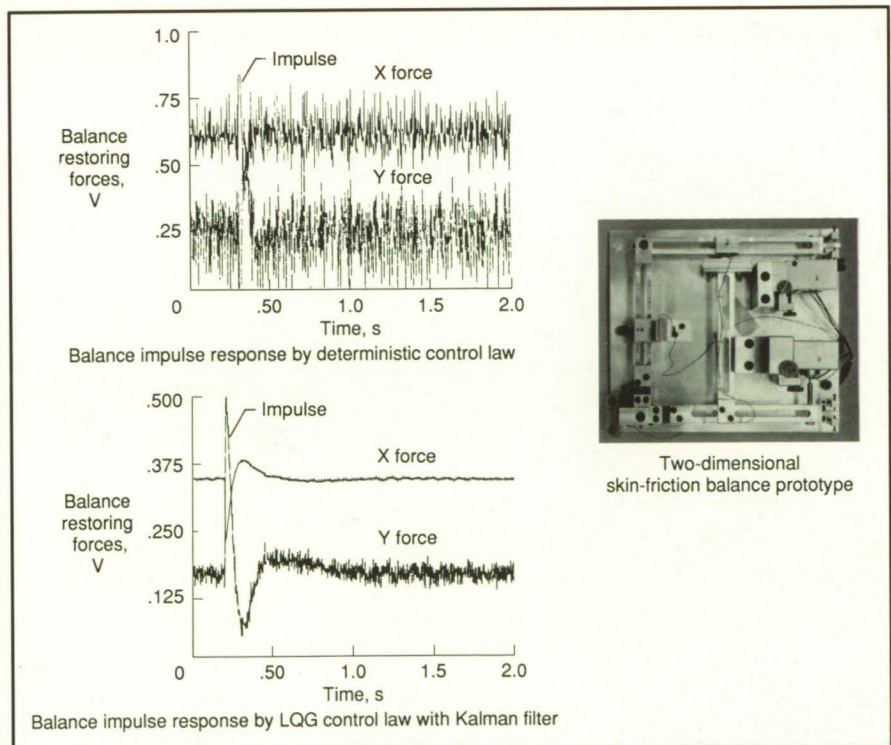
Implementation of Stochastic Control for Two-Axis Skin-Friction Balance

The two-axis skin-friction balance, developed at Langley Research Center to measure a two-dimensional (2-D) skin-friction force at a single point, requires the use of a feedback circuit. The objective of this research has been to apply the optimal state estimation theory (Kalman filtering) and the stochastic (LQG or linear quadratic Gaussian) control theory to develop a noise-resistant control law for the balance with adequate transient response for use in the noisy wind tunnel environment. An optimal state estimator and optimal linear regulator control gains were generated by simulation studies. Operation of the controller, which requires real-time computation of a six-state-variable, discrete-time linear system for state estimation, was implemented on an ADSP-2100 digital signal processing (DSP) microcomputer. A special ADC

(analog-to-digital converter) and DAC (digital-to-analog converter) interface board was developed to provide balance displacement measurements and restoring force feedback voltages at 3000 updates per second between the microcomputer and the prototype balance.

Performance comparisons of the LQG stochastic control law with an earlier deterministic control law showed a 13-dB improvement in noise rejection with good transient performance. This work represents a unique application of modern stochastic control theory and Kalman filtering to an instrument design. In addition, this research, which demonstrates the utility of high-speed digital signal processing hardware for Kalman filtering and multivariable control application, is one of the first applications of DSP technology to instrument design at Langley Research Center.

(John S. Tripp, 44711, and Stephen D. Patek)
Electronics Directorate



Two-dimensional skin-friction balance prototype and performance data.

Video Support of Vortex Interaction Studies

Trailing vortices pose a hazard to the aircraft that follow them, especially during landing when the longitudinal separation is small. A simple system that warns against vortex encounters and that uses a combination of instrumentation available on general-aviation craft may be feasible.

In order to test the proposed theoretical model for vortex detection, a flight experiment was performed using state-of-the-art flow direction, accelerometer, and roll rate sensors. The tests required continuous measurement of the distance between an instrumented PA-28 probe aircraft and the smoke-demarcated trailing vortex generated by a Lockheed P-3. Time-encoded video data, shown in the figure, were acquired using miniature solid-state

cameras mounted in the wing tips of a Beech T-34 aircraft.

The miniature video cameras were calibrated using analytical photogrammetry techniques to correct for sizable electronic and optical distortions. A personal-computer-controlled frame grabber system with customized software was used to acquire and process selected video sequences for which flight sensor data were available. The wingspan of the PA-28 was used to scale the photographs. The unique application of analytic photogrammetric techniques for calibrating miniature video cameras made this separation measurement possible with an estimated accuracy of 5 percent.

(W. L. Snow and B. A. Childers, 44636)

Electronics Directorate

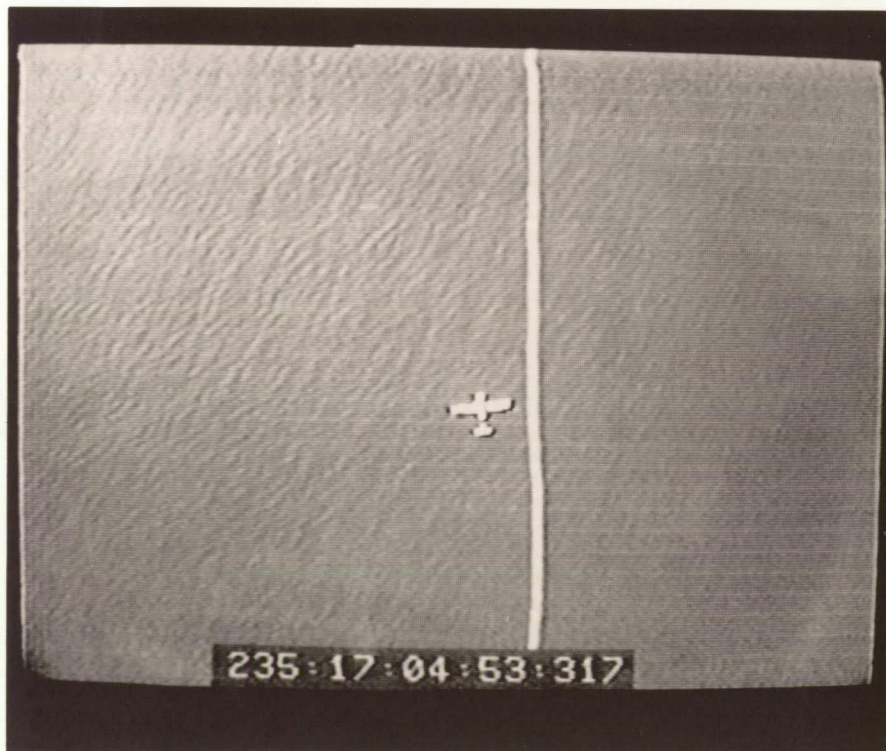
Onboard Station for Researchers

An onboard data analysis station for researchers was developed and utilized on the Learjet aircraft to determine if research test objectives were achieved while the aircraft was still in flight. This development allowed experimenters to take maximum advantage of good weather conditions and reduce expensive flight hours.

This station performs real-time analysis and displays flight experiment data. The system consists of a flight-hardened computer that includes a central processing unit with floppy disc storage, an electroluminescent flat panel display, a sampling and switching system, oscilloscopes, and a time code generator. The three dual-channel oscilloscopes permitted real-time simultaneous viewing of six hot-film signals selected via the switching system. From the computer, the onboard researcher could select a display of the surface pressure distribution or a power spectral density analysis (PSD) of a particular hot-film signal. Pertinent flight parameter data also were selected from the aircraft data system and shown on the display screen. Flight parameters computed and displayed included angle of attack (alpha), angle of sideslip (beta), airspeed, Mach number, altitude, outside air temperature, as well as time, date, and the amount of storage used on the current floppy disc.

(Daniel R. Norfolk and F. Keith Harris, 43820)

Electronics Directorate



PA-28 encounter with marked trailing vortex.

L-89-14731

ORIGINAL PAGE
BLACK AND WHITE PHOTOGRAPH



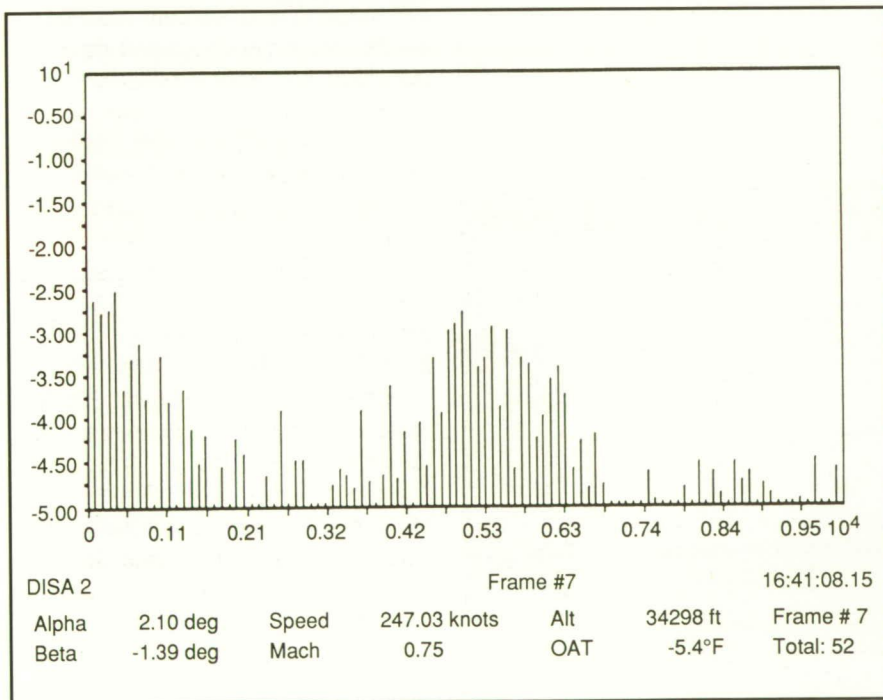
Experimenter's station onboard Learjet.

L-89-7681

Transition Physics Flight Research Experiments

Current laminar-flow research conducted by NASA is focused on understanding the dominant instability modes responsible for initiating the transition process from laminar to turbulent flow. Recently, flight experiments were conducted on a gloved surface of a Lear Model 28/29 airplane (as shown in the figure) to study in detail the growth of Tollmien-Schlichting (T-S) instabilities in the laminar boundary layer. The purpose of these experiments was to help validate computational fluid dynamics (CFD) compressible linear stability theory through measurement of the instability mechanisms. These experiments incorporated a fiberglass and foam glove section attached to the left-wing surface. The 0.25-in.-thick glove incorporated nonintrusive instrumentation for streamwise measurement of the growth of T-S instability frequencies (via hot-film and microphone sensors), temperature distributions, and pressure distributions.

These experiments were the first of their kind to measure streamwise T-S growth patterns along the wing chord at a specific spanwise location. In addition, these were the first experiments to obtain temperature distribution information that can be used as input to the compressible CFD codes. The flight tests were conducted over a range of conditions including altitudes up to 48 000 ft, Mach numbers up to 0.81, and Reynolds numbers up to 20×10^6 . The tests have demonstrated the ability to move transition from the leading edge to 60 percent chord by varying the flight conditions. Results have shown the ability to detect T-S wave frequencies from analysis of the hot-film signals. Compressible linear stability calculations predict comparable frequencies for the maximum amplification of the T-S waves. This



Power spectral density display onboard Learjet (Lear 28 DISA fast Fourier transform, power in dBu).

ORIGINAL PAGE
BLACK AND WHITE PHOTOGRAPH



Lear 28/29 transition physics research aircraft.

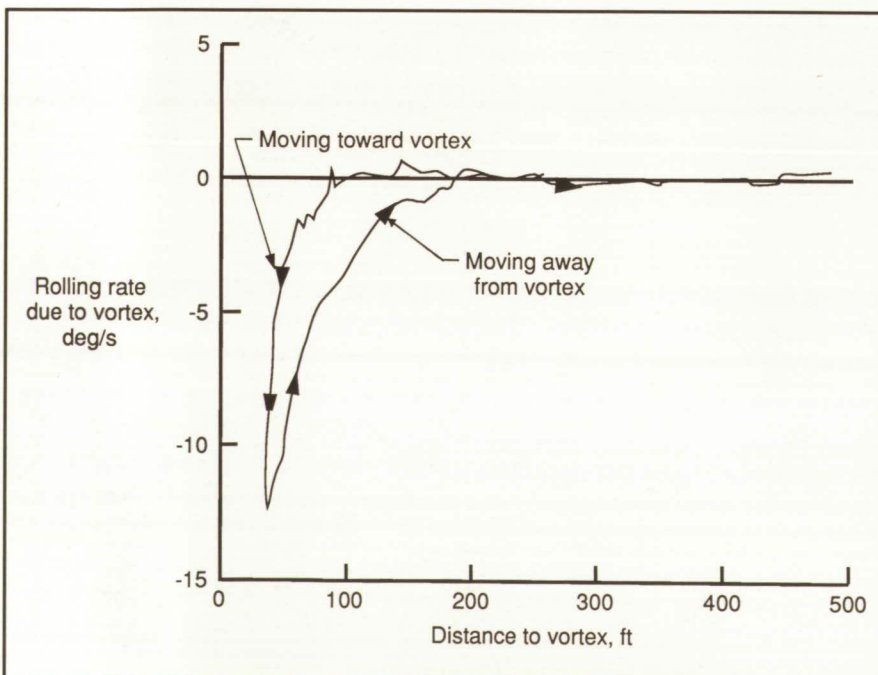
L-89-2828

research will provide information on the disturbance growth and transition mode which is essential to the understanding of design limits for applications of laminar-flow technology. (Cynthia C. Lee, Clifford J. Obara, and Michael S. Wusk, 43858) Aeronautics Directorate

Airborne Wake Vortex Detection

One way to increase airport capacity is to reduce the spacing

between airplanes that are approaching to land on a runway. The spacing requirements are presently dictated by the hazard due to the sometimes violent motions of an airplane encountering the trailing vortices from a preceding airplane. If the wake vortex could be detected far enough away for the pilot to avoid the hazard, the spacing requirements might be reduced and airport capacity increased. In order to determine the distance at which a wake vortex could be detected using conventional, airborne instrumentation, an explor-



Detection of presence of vortex with rolling rate parameter.

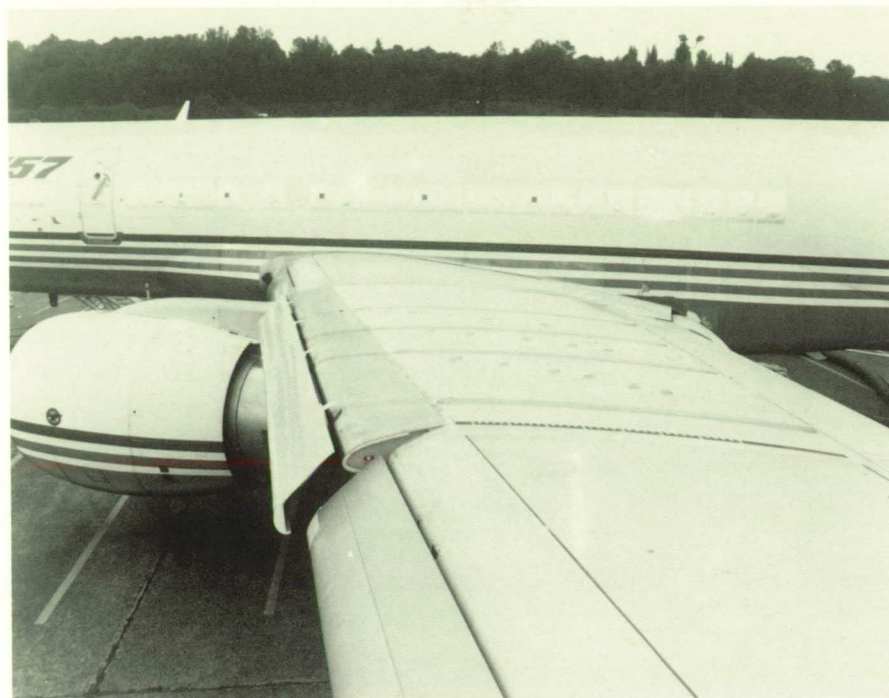
atory flight experiment was conducted.

A 90 000-lb, four-engine turboprop transport airplane was used to generate the wake vortex. Smoke produced by a smoke generator that was mounted near the wing tip of the transport airplane was used to make the wing-tip vortex visible. Instrumentation carried on a light, single-engine airplane was used to measure the airplane responses and pilot inputs needed to detect the wake vortex. A third airplane flying above the other two airplanes was used to photograph and measure the relative horizontal distance between the wake vortex and the detecting airplane. Algorithms were developed to remove the effects of pilot control inputs from the measured airplane responses and produce parameters due solely to the presence of the vortex. One of the most promising parameters developed was a simulated rolling rate due to the vortex. The figure presents this parameter as a function of the horizontal displacement from the vortex for a maneuver toward and then away from the vortex. The data indicate that the vortex can, in this case, be detected at a substantial distance.

(Eric C. Stewart, 43939) Aeronautics Directorate

Hybrid Laminar-Flow Control Flight Program

One of the most significant events in the history of boundary-layer control occurred in June 1990, when a Boeing 757 aircraft achieved laminar boundary-layer flow to 65 percent wing chord through the use of a Hybrid Laminar-Flow Control (HLFC) system (as shown in the figure). This event demonstrated the feasibility of the HLFC concept in flight for the first time. The HLFC



Boeing 757 Hybrid Laminar-Flow Control research aircraft. L-90-7975

system provides suction boundary-layer control in the leading edge (i.e., to the front spar) to control the initial, highly three-dimensional laminar boundary layer. Over the wing box (i.e., downstream of the front spar), the surface pressure distribution is relied upon to stabilize the boundary-layer flow and maintain laminar flow to the wing shock or aft pressure rise. A 22-ft span section of the Boeing 757 wing outboard of the left-engine pylon was modified for the flight test. The suction surface in the leading edge was a microperforated titanium skin with over 15×10^6 tiny (0.0016-in. nominal diameter) laser-drilled, closely spaced holes. A leading-edge Krueger flap is integrated into the wing high-lift system and also serves as an insect shield. The design incorporated innovations made in earlier NASA laminar-flow programs, such as the JetStar Leading-Edge Flight Test Program (which first used perforated titanium skin) and also made use of the detailed natural laminar-flow data base gathered during the NASA F-14 Variable Sweep Transition Flight

Experiment and the 757 Natural Laminar Flow and Wing Noise Program. Flight tests were conducted

over a 5-month period to altitudes of 40 000 ft, Mach numbers to 0.82, and chord Reynolds numbers to 30×10^6 . The program is jointly funded by NASA, the U.S. Air Force, and the Boeing Commercial Airplane Company. (Dal V. Maddalon, 41909, and Richard D. Wagner) Aeronautics Directorate

Thermographic Detection of Cracks in Thin Sheets

A method for the detection of through-the-thickness cracks in thin metal sheets has been developed using thermographic techniques. This technique has advantages over other techniques in that it is able to remotely inspect a large area in a short period of time. An approximate line source of heat is used to produce an inplane flow of heat in the thin



Aging aircraft sample with closed fatigue cracks.

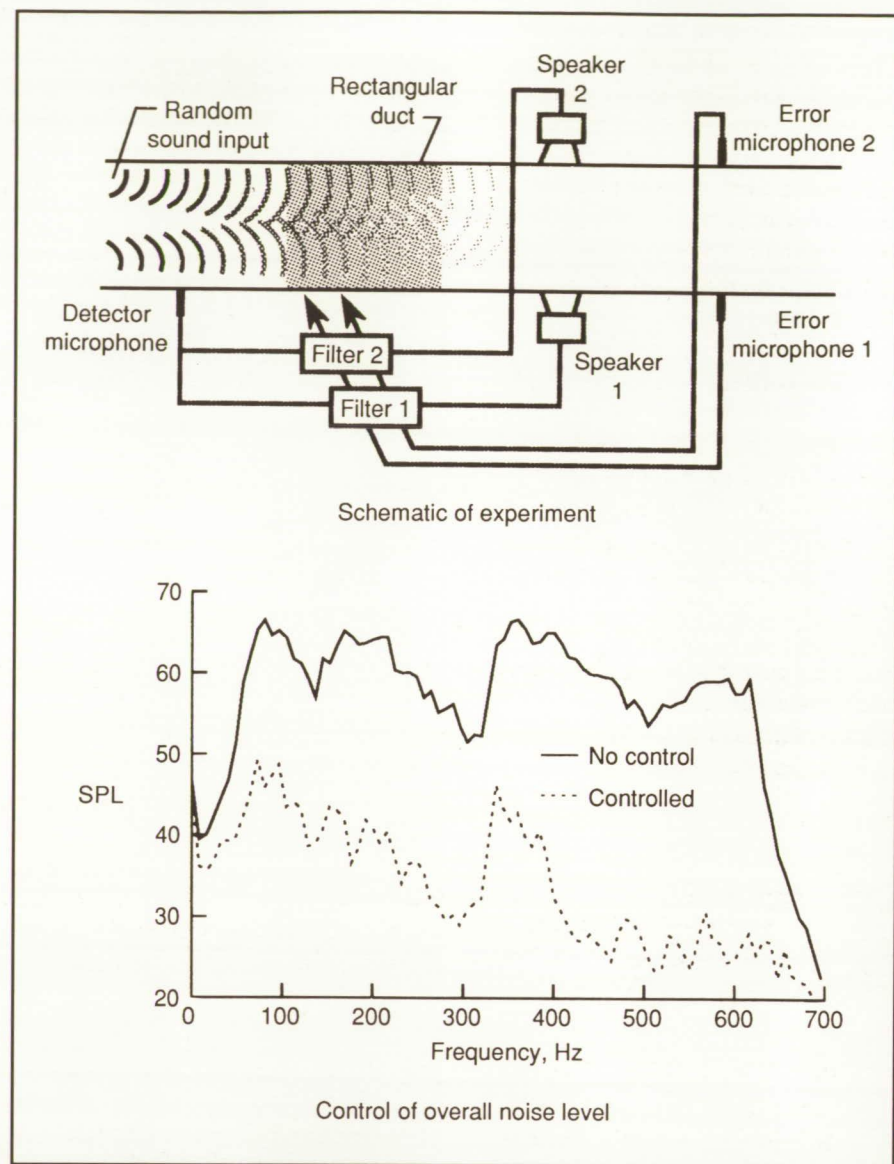
sheet. The presence of a crack disrupts the inplane heat flow, which can be seen in an image of the surface temperature of the sheet. An analysis technique has been developed which reduces the surface temperature image to an image of variations in the inplane heat flow and greatly increases the detectability of cracks.

The application of this technique to the detection of Electrical Discharge Machine (EDM) notches and closed fatigue cracks has shown that cracks can be detected down to the resolution limits of the imaging device. Electrical Discharge Machine notches as small as 0.050 in. have been detected using a full-field infrared imager. Additionally, closed fatigue cracks growing out of rivet holes on laboratory samples have been detected (as shown in the figure). The technique also has been applied to the detection of partially penetrating cracks around welds in thin sheets and has been able to detect cracks that penetrate halfway through the sheet.

(K. Elliott Cramer, 47945)
Electronics Directorate

Active Control of Multimodal Random Sound in Ducts

The problem of controlling random noise in ducts is an important application problem that also has taken the role of a benchmark in the development of active control systems. As an indicator of control system development, this problem requires the inclusion of feedforward and feedback elements as well as the development of a broadband controller. Systems and commercial products for flow systems have been developed which provide significant attenuations (i.e., 20 dB or greater) in the frequency range where only plane waves propagate. The purpose of this



Schematic and effectiveness of active system for control of sound in ducts.

work is to extend active control to suppress the noise of higher-order modes in ducts by applying multivariate control principles.

For the duct with cross-sectional dimensions of 21 in. by 9 in. (shown in the figure), the frequency below which only plane waves propagate is 325 Hz. The control system consisted of a single detector microphone, two loudspeakers mounted on opposite sides of the duct, similarly mounted error microphones, and two digital filters. The controller function is to optimize the parameters of the

digital filters and drive the two loudspeakers so that the outputs of the error microphones are minimized.

The sound pressure level (SPL) at one of the error microphones with no control is indicated by the solid line. The peak at 325 Hz is due to the cut-on of the (1,0) mode. Below this frequency, the plane wave dominates the spectra as all higher-order modes exponentially decay. Above 325 Hz, the pressure spectra are made up of a combination of the plane wave and the (1,0) mode. The reduced SPL as a function of frequency due to the

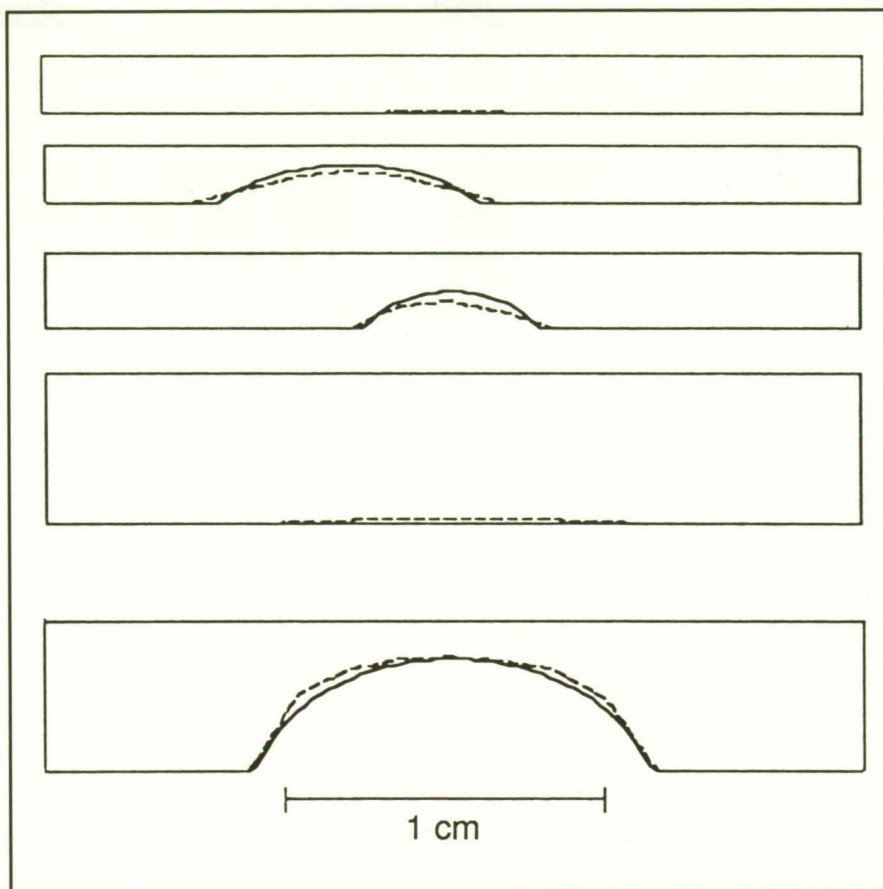
active control system is indicated by the dashed line. Reductions of 15 dB to 30 dB from 50 Hz to 600 Hz were achieved. Overall reductions of 19.1 dB for the plane and 22.6 dB for the (1,0) mode were recorded. The residual peak at 325 Hz for the higher-order (1,0) mode was due to restrictions on the length of the digital filters.

This work is the first to extend the concept of active control of sound fields in ducts to multimodal propagation. The work extends the usefulness of this technology to a broader frequency range, eliminates the necessity of redundant passive techniques, and will provide (in many flow systems) a lower lifetime operating cost than passive mufflers due to lower losses.

(Richard J. Silcox, 43590)
Structures Directorate

Thermographic Characterization of Back-Surface Geometry

A thermographic technique has been developed for the characterization of back-surface geometry for a single-layer system. The technique involves infrared heating of the front surface of the layer and subsequent infrared detection of the time evolution of its temperature. A numerical technique has been developed for mapping the heat flow equation in these irregular geometries into a space in which the structure exists as a simpler geometry. This decreased complexity in the geometry leads to an increased complexity in the partial differential equation that describes the heat flow in this new space; however, computationally, the complexity of finding a solution to the entire problem is reduced. This mapping technique is used in combination with a parameter estimation algorithm to reduce the thermo-



Comparison of true back-surface profiles (solid lines) to those estimated from thermographic data (dashed lines).

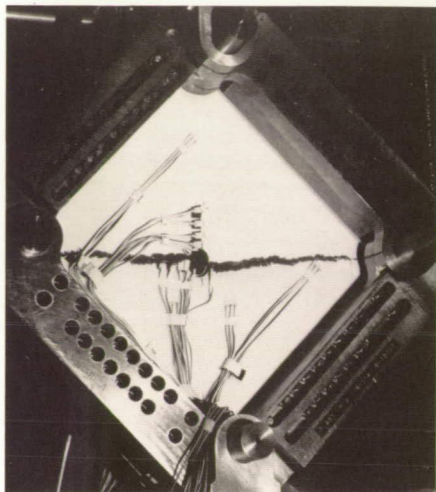
graphic data to give an estimate of the back-surface shape of the layer for two-dimensional geometries.

The technique was tested on steel samples with fabricated variations in the back-surface shape. The results shown in the figure indicate that the back-surface shape can be estimated to within 12 percent of the true shape using the thermographic data. The technique has possible application to the detection of corrosion or erosion in single-layer systems.

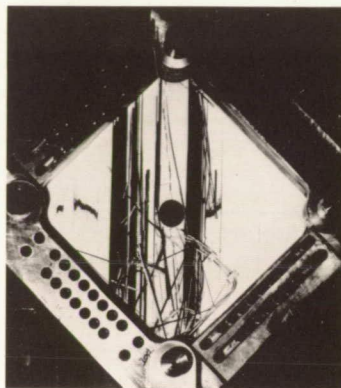
(William P. Winfree, 44963)
Electronics Directorate

Response and Failure Characteristics of Composite Shear Webs With Cutouts Described by Experiments

Advanced composite materials offer an attractive potential to reduce the mass of modern aircraft structural components. One aspect of the composite structural components design is the influence of local effects such as cutouts on the response and failure characteristics of composite shear webs. Experimental results were obtained which describe the response and failure characteristics of graphite/epoxy and graphite/thermoplastic plates loaded in shear with a centrally located circular cutout. Orthotropic and quasi-



Cracked graphite/epoxy



Shattered graphite/thermoplastic

Cracked and shattered specimens.

L-90-2742

isotropic specimens were fabricated having various laminate thicknesses. The specimens had a 12-in. by 12-in. test section, and the cutout diameters ranged from 0 in. to 3 in.

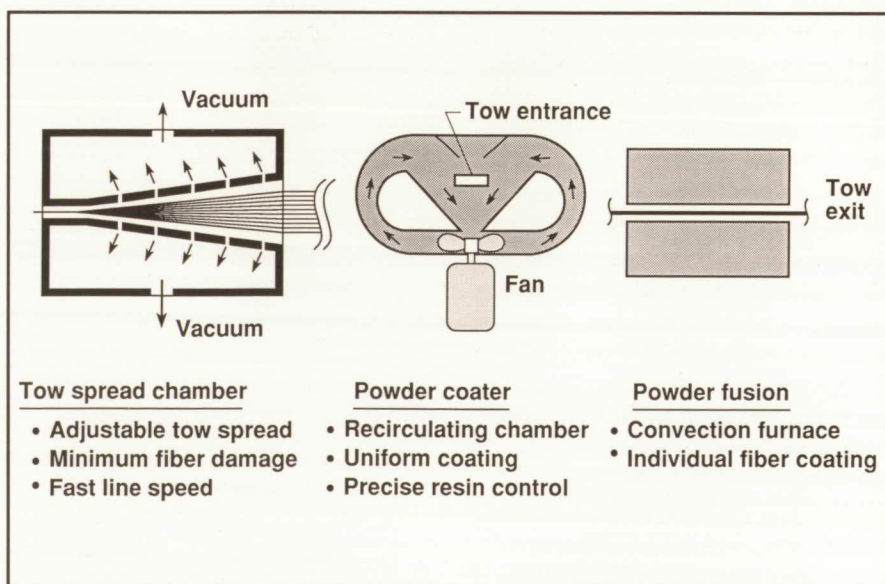
The graphite/thermoplastic specimens had approximately the same initial buckling mode shape as similar graphite/epoxy plates, but the buckling and failure strains for the graphite/thermoplastic plates were higher than the corresponding strains for similar graphite/epoxy plates. Also, the failure mode for the graphite/thermoplastic plates was different from the failure mode for the graphite/epoxy plates. The typical specimens shown by the photographs in the figure are 24-ply quasi-isotropic, and they have a circular cutout. The failure mode of the graphite/epoxy specimen (left photograph) is characterized by a tension crack that originated at the edge of the cutout and propagated diagonally across the specimen. The photograph also shows that a delamination has occurred at the boundary of the cutout. By contrast, the

graphite/thermoplastic specimen (right photograph) has a sudden overall shattering failure mode and several vertical splits, and appears significantly different from the graphite/epoxy specimen.

Graphite/thermoplastic shear webs may have improved buckling and failure strains when compared to similar graphite/epoxy shear webs, but the sudden failure characteristic of the graphite/thermoplastic shear webs still needs to be understood in order to develop fail-safe designs for graphite/thermoplastic shear webs. (Marshall Rouse, 43182) Structures Directorate

Powder-Coated Prepreg

High-performance thermoset and thermoplastic polymers are under extensive evaluation for use as matrix materials for advanced composite material systems. Conventional methods for the introduction of the matrix polymers into carbon fiber tows are not adequate to yield high-quality prepreg for many polymer/fiber combinations. Dry powder coating of carbon-fiber tows overcomes many inherent difficulties associated with melt, solution, and slurry methods for prepreg fabrication.



Fluidized bed powder coating.

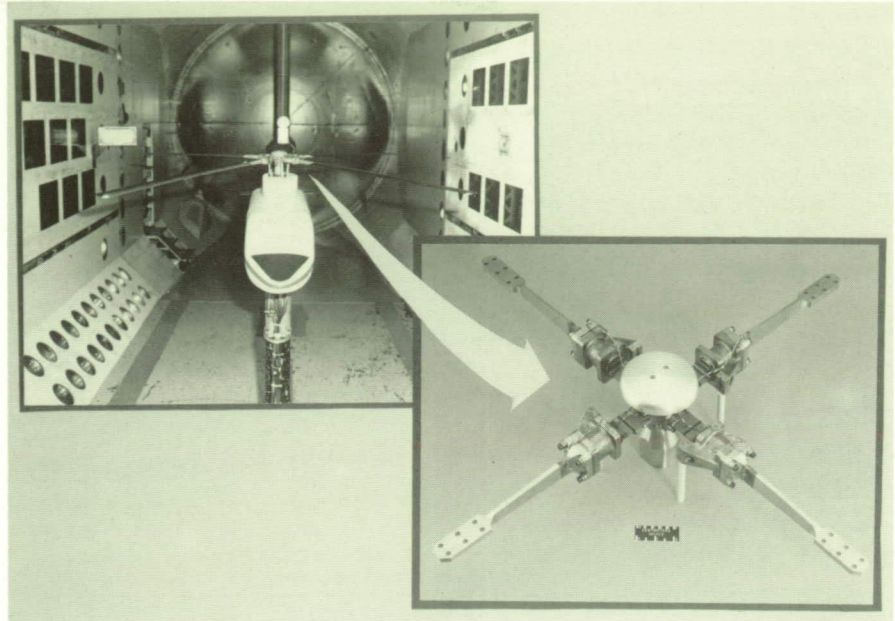
ORIGINAL PAGE
BLACK AND WHITE PHOTOGRAPH

Processing research at Langley Research Center includes the deposition of polymer powder materials on carbon tow in a prototype dry powder prepreg fabrication apparatus. This apparatus is comprised of a pneumatic tow spread tunnel, closed-loop polymer powder recirculation chamber, polymer fusion furnace, resin mass meter, and prepreg windup mechanism. This system improves the quality of prepreg and laminates manufactured with difficult-to-process advanced polymer systems by allowing the application and uniform distribution of very small polymer powder particles into the entire carbon tow bundle. The resultant composite material system promotes resin flow and structural integrity of fully processed composite structures.

(Robert M. Baucom and Joseph M. Marchello, 44252)
Structures Directorate

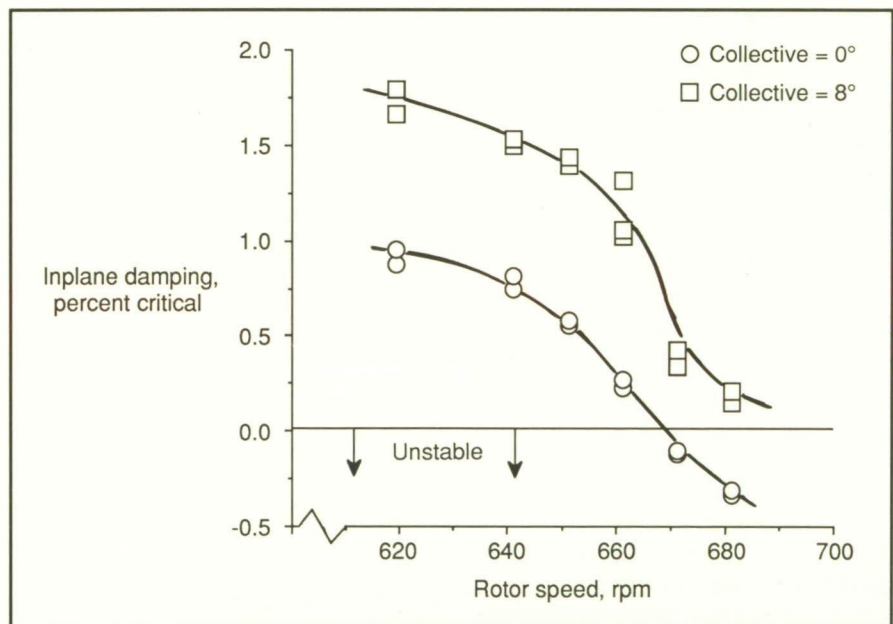
Expanded Aeromechanical Stability Data Base for Parametric Hingeless Rotor

Hingeless rotor designs are attractive for use in advanced rotorcraft designs because they are mechanically simpler than conventional articulated designs and because they offer a convenient means of tailoring the design to provide favorable structural couplings. Although some experimental data are available for hingeless rotors operating in hover, not much data are available for forward flight conditions. Because concern exists about the aeromechanical stability characteristics of hingeless rotor designs and because of the lack of high-quality experimental data for validation of applicable analysis methods, some wind tunnel model studies were conducted in the Transonic Dynamics Tunnel (TDT). A parametric



Hingeless rotor model mounted in TDT.

L-90-7825



Variation of damping with rotor speed in forward flight.

hingeless rotor was tested using the Aeroelastic Rotor Experimental Systems (ARES), which has been developed for use in a variety of rotorcraft wind tunnel forward flight investigations and laboratory hover studies. A photograph of the ARES with the hingeless rotor system is shown in the first figure. The inset

shows the details of the hingeless hub. The design of this system is intended to easily accommodate changes in test parameters.

Testing in hover was conducted at different values of collective pitch over a range of rotor speeds. Testing in forward flight was performed over

a range of advance ratios μ up to 0.35. The moving block method was used to measure rotor inplane damping for determination of aeromechanical stability. Some illustrative forward-flight results in the form of the variation of inplane damping values with rotor speed are shown in the second figure for a value of $\mu = 0.30$. The hover results were similar. The data show a trend of increasing damping with collective pitch. The data also show a decrease in inplane damping with increasing rotor speed with an instability occurring at the higher rotor speeds. Similar results, not shown here, were obtained for configurations incorporating variations in blade droop.

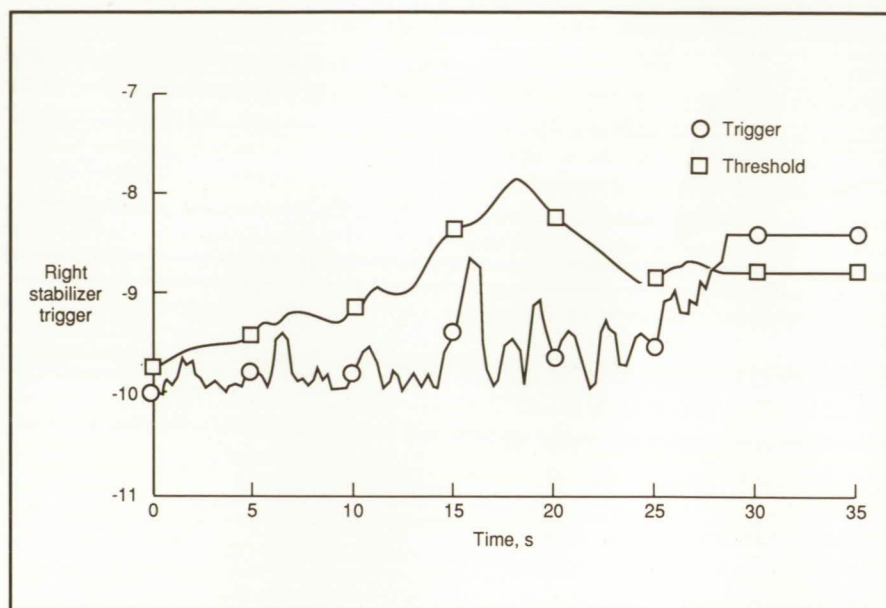
Data obtained during this study significantly expanded the aeromechanical stability data base for the parametric hingeless rotor. Consistent and repeatable measurements of the rotor inplane damping were obtained. Data such as these are vital to provide an understanding of the aeromechanical stability of hingeless rotors and to validate existing analytical methods and new methods under development.

(M.-Nabil H. Hamouda, Jeffrey D. Singleton, and William T. Yeager, Jr., 41266)

Structures Directorate

Adaptive Failure Detection and Isolation System

A methodology has been developed for designing an adaptive Failure Detection and Isolation (FDI) system for detecting control element failures in aircraft control systems in the presence of atmospheric turbulence. Such failures can produce unanticipated, life-threatening flight modes that require corrective action in a timely manner, action that is not always intuitively obvious to the pilot. In many such cases a



Trigger response to right stabilizer failure in turbulence environment.

restructurable flight control system (RFCS) could automatically take the proper corrective action by reconfiguring the flight control system to use other unfailed control effectors if the failure could be properly detected and isolated by the FDI system. A previously developed FDI methodology was based on a decentralized approach that used the best-known redundancy relationships, thereby increasing the robustness of the FDI system in the presence of modeling errors. While evaluation of this approach showed that the system worked well in a no-turbulence environment, a high number of false alarms were produced in the presence of turbulence. A new methodology was developed for designing a decentralized FDI system that estimated the level of the turbulence in flight and then adjusted the thresholds and other FDI system parameters to greatly reduce the number of false alarms without significantly reducing the sensitivity of the system to real failures.

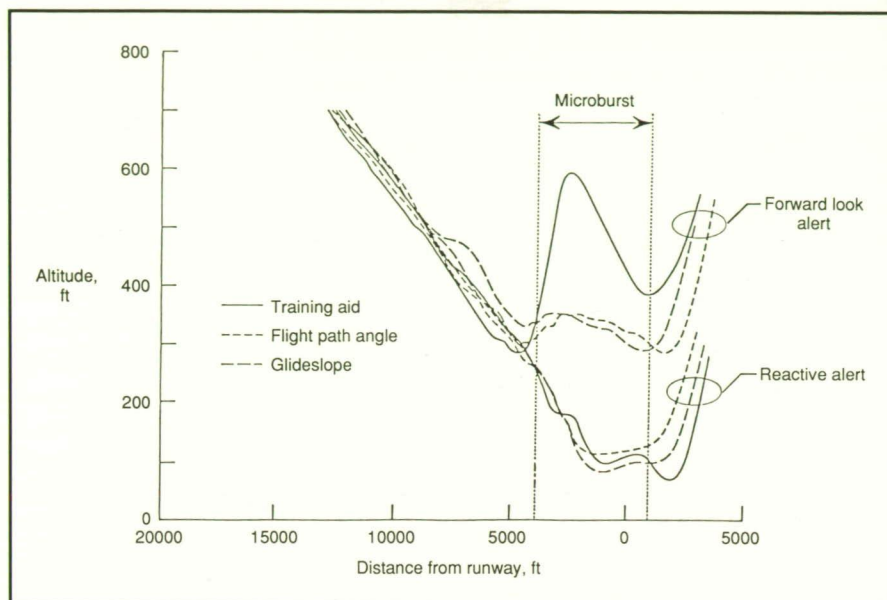
Using this methodology, an FDI system was designed for a hypothetical, modified Boeing 737 airplane and evaluated using a six degree-of-

freedom nonlinear simulation. An example of a right stabilizer failure at 20 percent effectiveness at $t = 22$ s is illustrated in the plot of the trigger signal for the right stabilizer. When this signal exceeds its threshold, it indicates that a failure may have occurred and initiates further processing. Note how the threshold for the right stabilizer adapts as a result of the estimated turbulence. If the threshold had continued at its initial level, the peaks in the trigger signal around $t = 15$ s resulting from turbulence would have triggered a false alarm. The real left aileron failure at $t = 22$ s produced a trigger signal that did exceed the threshold, however, and the failure was correctly detected and isolated.

(W. Thomas Bundick, 44062)
Flight Systems Directorate

Benefits of Forward-Look Wind Shear Detection

Microburst wind shear poses a significant threat to transport aircraft during takeoff and landing. Among



Wind shear recovery trajectories with reactive and forward-look alert system.

the issues concerning the aircraft industry are the safety benefits that can be achieved from forward-look wind shear detection and the distance ahead of an airplane which a sensor must see to ensure microburst escape. To address these issues, computer and piloted simulations of airplane recoveries from microbursts were conducted to evaluate not only the various recovery procedures but also the effect of varying the point at which the recovery was initiated. A Boeing 737-100 airplane model and two microburst models were utilized. A total of 455 simulated microburst encounters were made by 7 pilots during the effort.

The figure shows typical trajectories for three recovery procedures and two alert types (a reactive wind shear alert and a 10-s forward-look alert). The simulation results showed that the factor that caused the greatest improvement in recovery performance was the time at which the recovery was initiated. The difference in recovery performance between the three procedures was not significant, but when the forward-look alert was given, the results were

much improved over the reactive-alert case. All pilots provided very positive comments about the forward-look capability.

These results, which provide the first quantification of the benefits of the use of the forward-look alert system in a piloted environment, have

implications for near-term research on forward-look sensors.

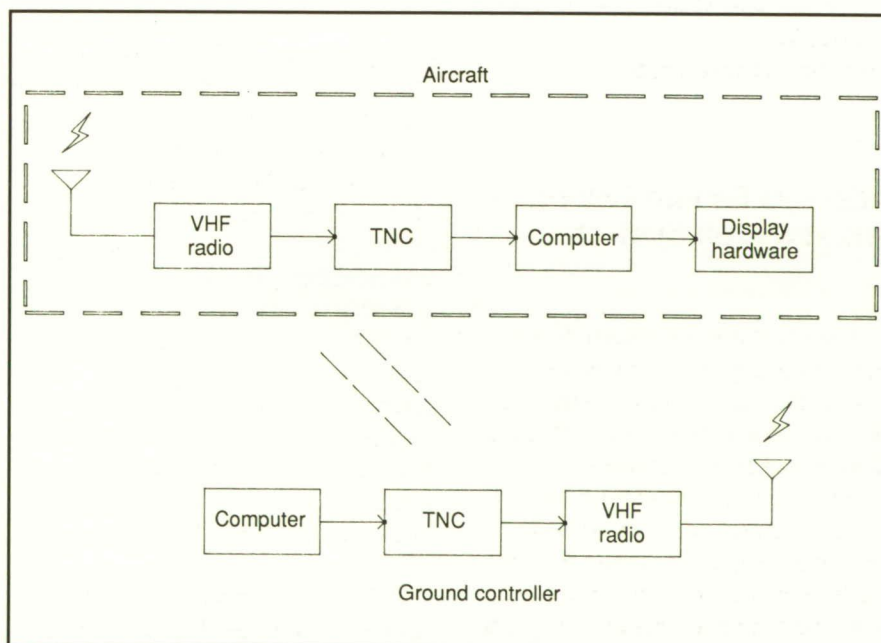
(David A. Hinton, 42040)

Flight Systems Directorate

Aircraft Digital-Packet Up/Down Radio Communications Link

A digital-packet up/down transceiver radio link was developed and utilized for transmitting air traffic control data to and from the Boeing 737 ATOPS (Advanced Transport Operating Systems) research aircraft. By using this type of system, voice channels are less congested, and important aircraft position information is relayed at a faster rate.

The system consists of a digital-packet terminal mode controller (TNC), voice communications transceiver, computer terminal, and graphics display system presently in use in the Boeing 737 ATOPS aft cockpit. A ground controller or a computer outputs a message to the



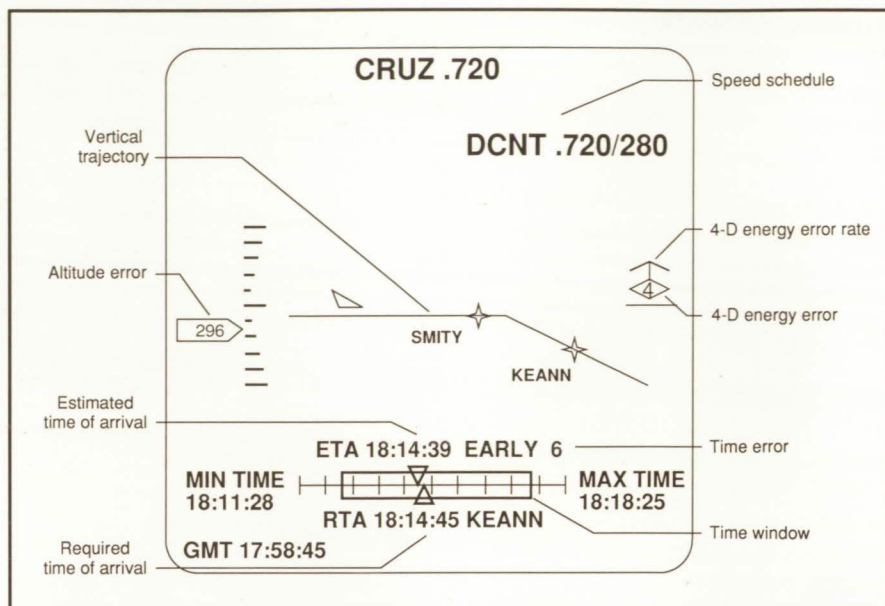
Aircraft digital-packet communications link.

ground TNC, which forms a packet of desired information and sends it out through a very-high frequency (VHF) radio channel. This information contains identifiers that only a particular aircraft will recognize. A typical packet of information would contain information such as altitude change, heading change, and distance measurement equipment (DME) readings. The system may be accessed by many airplanes at the same time due to the fact the information packet contains an identifier that is unique to each aircraft. After a packet is recognized and received by the aircraft, the onboard computer will send this information to a pilot display. The information also can be sent to an automatic pilot system that can control the aircraft. The digital-packet up/down link has been flight qualified and successfully demonstrated to provide reliable communications over a range exceeding 100 nmi using the Boeing 737 and Cessna-402 aircraft. This system also is planned for use in the near future to transmit Doppler weather radar information to the Boeing 737 aircraft for the Wind Shear Research Project.

(J. Otis Riggins, 43807, and Jeffrey J. Massie)
Electronics Directorate

Airborne 4-D Flight Management in Time-Based ATC Environment

Advanced Air Traffic Control (ATC) systems are being developed which contain time-based four-dimensional (4-D) trajectory predictions of aircraft. Airborne flight management systems (FMS) exist or are being developed with similar 4-D trajectory-generation capabilities. Differences between the ATC-generated profiles and those generated by the airborne 4-D FMS may introduce system problems. Signifi-



TSRV Simulator vertical situation display for airborne time guidance (0.720 cruise).

cant design challenges must be addressed to ensure the compatibility of future airborne and ground-based systems.

A simulation experiment was conducted to explore the integration of a 4-D-equipped aircraft into a 4-D ATC system. The Langley Research Center Transport Systems Research Vehicle (TSRV) Simulator cockpit was linked in real time to an Ames Research Center ATC simulation for this effort. Candidate procedures for handling 4-D equipped aircraft were devised, and traffic scenarios were established which required time delays absorbed through speed control alone or in combination with path stretching. A unique vertical situation display, shown in the figure, provided the pilots in the TSRV Simulator cockpit with guidance for flying the 4-D trajectories.

The 4-D procedures and FMS operation were well received by the airline pilots, who achieved an arrival accuracy at the metering fix of 2.9 s standard deviation time error. Dissimilarities between airborne and ATC-generated speed strategies were

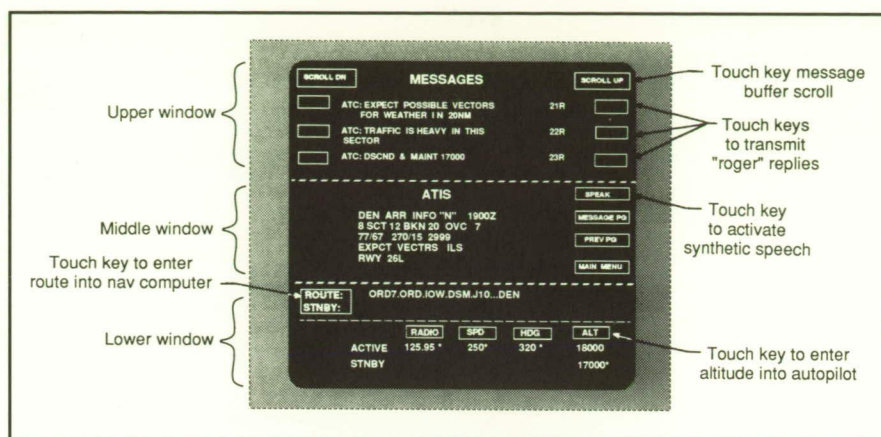
found to be a problem under moderate traffic conditions when most of the traffic remained on established routes. The different cruise speeds of the TSRV Simulator (flying FMS-generated speeds) and the other traffic (flying ATC-generated speeds) produced potential in-trail conflicts that required controller intervention. The TSRV Simulator was found to be more efficient in flying trajectories with speeds that conformed to the ATC strategy when traffic conditions required speed control by the ATC.

Heavy traffic conditions, where time delays forced off-route path stretching, were found to produce the greatest operational benefit of the airborne 4-D FMS. The pilots were able to consistently fly controller vectors to absorb time delays by using their FMS vertical situation display to decide when to turn back on course. This procedure showed a potential for relieving controller work load while improving efficiency. (David H. Williams, 42023)
Flight Systems Directorate

Aircraft ATC Data-Link Information Transfer Simulation

Digital data link (radio transmission of digitized data) is a rapidly maturing technology for ATC information exchange. Increased flight deck utilization of data link will result in increased National Airspace System safety and efficiency by reducing communication errors, relieving congested ATC radio frequencies, and enabling more information transfer between aircraft and ground facilities. A previous Langley Research Center study concluded that key flight deck issues in data-link ATC communication are pilot communication work load, situational awareness, and pilot (instrument and out-of-the-window) vigilance. The primary objective of this effort was to examine methods of using data-link ATC information transfer in combination with conventional voice radio to reduce pilot work load while maintaining situational awareness and minimizing adverse pilot vigilance effects resulting from the switch to a primarily visual ATC communication interface.

This study was conducted in the TSRV Simulator using a 6-in. by 6-in. touch-sensitive center panel, color cathode-ray tube (CRT) as the data-link input/output interface for the pilot (as shown in the figure). To reduce pilot work load, uplinked information (including routes, airspeeds, altitudes, headings, and radio frequencies) could be entered into the aircraft subsystems with a touch input on the data-link interface. To assist the pilots in maintaining situational awareness, weather and traffic information were included in the uplinked ATC messages. To minimize the effects of pilot vigilance, a synthetic voice output capability allowed the pilots to



Three-window touch-sensitive data-link interface.

receive messages without having to view the display.

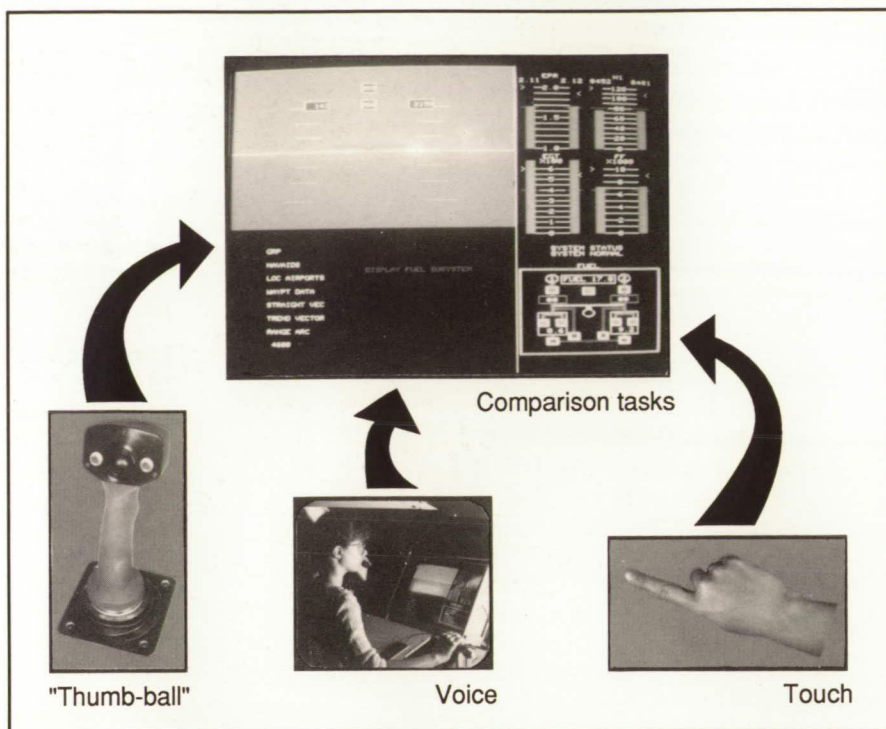
The commercial airline flight crew subjects reported reduced work load attributed to the data-link ATC communication process and to the pilot-initiated automatic input of data into the aircraft subsystems. Synthetic speech reduced the adverse effects on pilot vigilance because they did not have to look at the display to receive messages; however, an increase in the time needed to acknowledge ATC instructions resulted. Pilot situational awareness was improved significantly because of the weather and traffic information added to the data-linked messages. It was demonstrated that, through application of data-link technology in ATC information transfer, reductions in pilot work load can be achieved, while losses in pilot situational awareness can be minimized. (Marvin C. Waller, 42025) **Flight Systems Directorate**

Interactive Management of Large Screen Displays

The rapidly increasing use of computer systems in the cockpit is providing more operational capability

to the transport aircraft crew and, as a consequence, an increase in information that must be managed. Utilization of multiple small-screen color cathode-ray tubes as multimode, multifunction indicators appears to be the current solution to consolidate and integrate this information. An alternate approach being investigated at Langley Research Center is a large-screen, multiwindow, whole-flight deck (WFD) display for the management of aircraft systems. To effectively interact with such a display, user-friendly interface methods must be utilized. The goal of this effort has been to comparatively evaluate three input technology concepts in a simulator environment and determine the qualitative and quantitative advantages of each.

Three promising input technologies were chosen to interface to a WFD display; these technologies include a "thumb-ball" concept, a touch-screen concept, and a voice concept. The "thumb-ball" concept utilized a miniature trackball embedded in a conventional side-arm controller for cursor movements and numerical entry. The touch-screen concept used a capacitive screen for pilot inputs. The voice concept utilized a speech recognition system with input through a headset. Twelve pilots participated in this evaluation in which subjective and objective



Evaluation of three input devices for interactive management of large screen display concept.
L-89-6816

data, including the completion times to perform various tasks, were collected in a simulated, future transport environment.

No single concept was regarded as the most desirable input method for all the evaluated tasks. The quantitative results showed that the completion time differences among the three interfaces varied with the task being performed. Subjective results indicated that the voice concept was the most preferred method of data entry and had the most potential for future applications, assuming further advancements would take place in the recognition capability of speech technology. On the other hand, objective results indicated that, overall, the touch-screen concept was the most effective interface. Generally, the touch-screen concept was well-suited for tasks that operated as an on/off toggle; the voice concept was best-suited for entering a numerical value; and the "thumb-ball" concept was more effective at

handling system failures. Each concept appears to be a plausible candidate as a cockpit input device, especially relative to a specific task. This fact suggests that a combination of input devices and techniques might be the most effective method of providing system inputs in a large-screen, WFD cockpit environment. Multiple devices also may be desirable to serve as backup input systems.

(Denise R. Jones, 42006)
Flight Systems Directorate

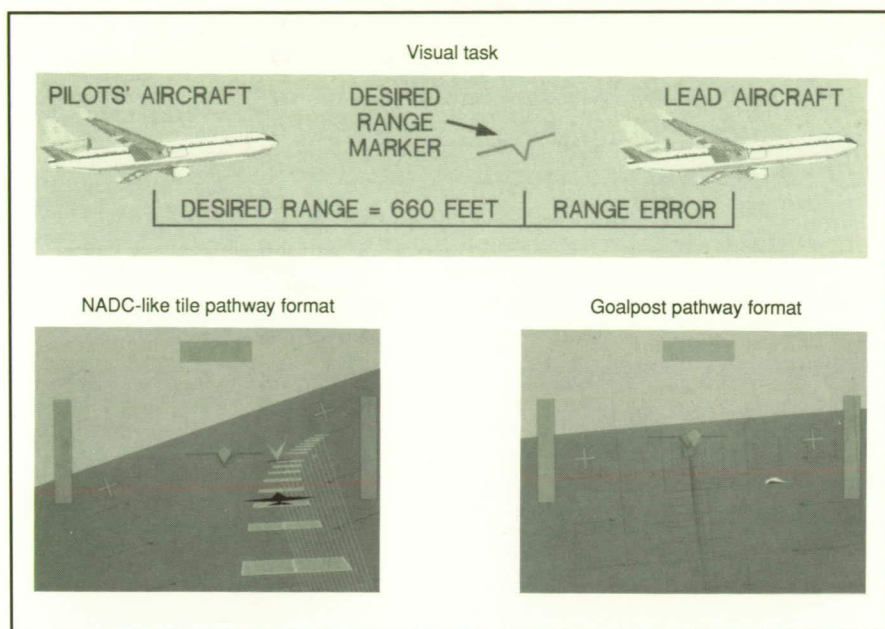
Transport Landing Approach Alternate Pathways and Stereo 3-D Presentation

The power of modern computer graphics generators and advanced avionics and electronics can now provide flight display concepts that

embody real-world three-dimensional (3-D), pictorial displays to the cockpits of advanced aircraft. Flight displays that incorporate pictorial "pathways in the sky" for guidance information are being evaluated at various flight display research laboratories, including Langley Research Center. The introduction of true depth cues via stereopsis techniques offers a means to enhance these displays. The objective of this research has been to determine the effectiveness of two competing pathway formats for landing approach and to investigate the effect of their presentation in stereo versus nonstereo.

A real-time piloted simulation experiment comparing performance in a transport landing-approach-in-turbulence task was conducted. The experiment utilized a tile pathway similar to that used by the Naval Air Development Center (NADC) and a goalpost pathway as the main factors studied. The figure illustrates the visual task chosen for the comparison experiment (i.e., maintaining range separation with a lead aircraft while flying the desired curved, decelerating, descending, landing approach pattern). Separation was regulated with the location of the desired range marker element (a "waterline" symbol). This range marker also provides a nonstereo range cue in that when the lead aircraft is at the desired range, the wingspan of the aircraft is the same width as the ownship symbol (the desired range marker).

Data analyses were made for the mean standard deviation of path error results from 7 U.S. Air Force transport pilots, who each flew 20 approaches with each display format. The variation in vertical path error as indicated by the standard deviation was 10 percent less for the tile format, the variation in lateral path error was 11 percent less for the goalpost format, and the difference in



Pilot's visual range—tracking task and alternate pathway formats.

variation in range path error was not statistically significant. The comparison of the mean range error standard deviation for the stereo condition versus the nonstereo control condition revealed that the inclusion of stereo depth cues improved performance by 18 percent over the nonstereo control condition.

Subjective pilot opinion paralleled the objective data results, with most pilots preferring the tile format for vertical control and the goalpost format for lateral control maneuvering. All pilots preferred the enhanced range and rate-of-closure cues provided by the stereo version of the format. Stereopsis cueing offers a means of displaying complex information in a natural way to enhance situational awareness and provide increases in pilot/vehicle performance.

(Anthony M. Busquets, Russell V. Parrish, and Steven P. Williams, 46649)

Flight Systems Directorate

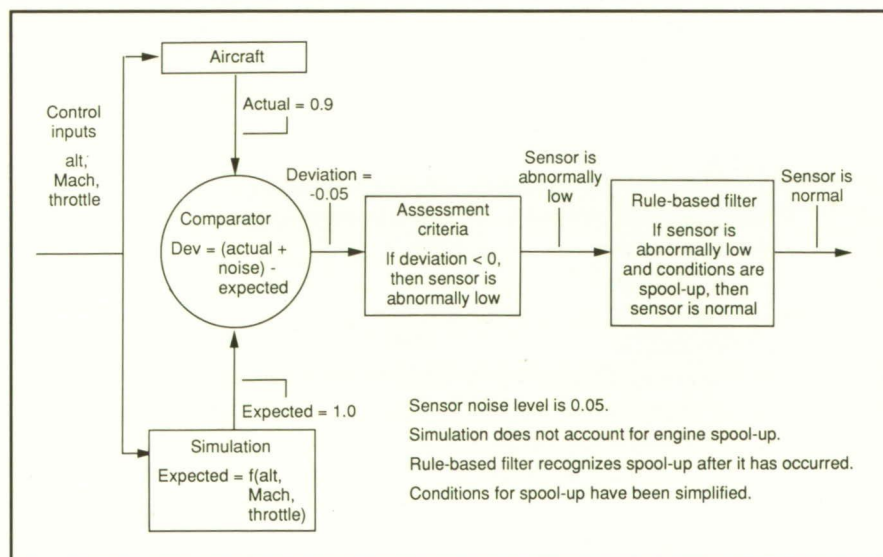
Fault-Monitoring Concept for Application to Aircraft Subsystems

Currently, automation of aircraft subsystem monitoring is limited to the detection of an out-of-tolerance condition. In this type of monitoring, subsystem faults may not be detected immediately. The objective of this

research was to design and implement an automated monitoring system that detects abnormalities earlier than current methods and provides useful information about the health of the aircraft subsystems. This information would be used by other onboard software systems to diagnose faults, generate responses, and alert the crew to potentially dangerous situations.

The performance requirements for the monitor were established by determining the needs of the other systems that would use it. These systems include a fault diagnosis system, which requires the monitor to detect abnormalities with greater sensitivity than conventional methods, and a crew alerting system, which requires a low level of false alarms. Most of the systems that would use the monitor required the information to be interpreted into a more meaningful qualitative form.

Based on these requirements, a conceptual architecture for an onboard subsystem monitoring system was developed and implemented on a Lisp machine in a computer program called MONITAUR. This architecture



Example of MONITAUR architecture as applied to turboprop engine.

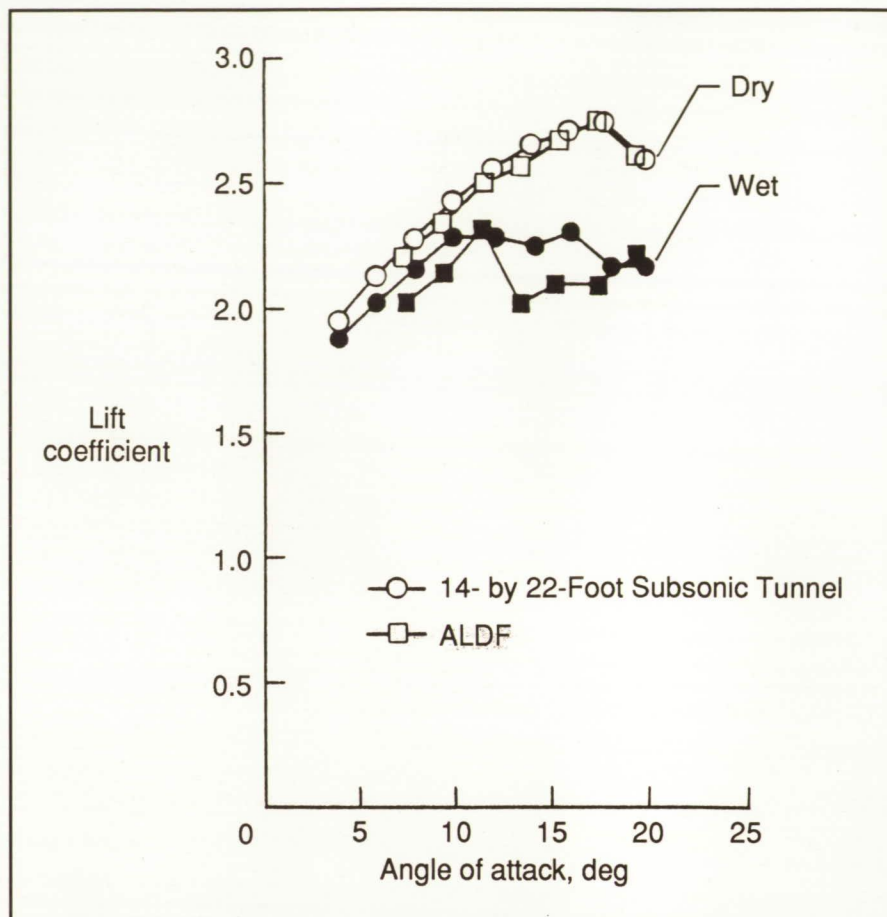
includes a numeric computer simulation of an aircraft subsystem to produce the expected behavior of that subsystem. The MONITAUR program compares the actual behavior to the expectations in order to detect abnormalities. An intelligent comparator filters out sensor noise. Because computer simulations do not perfectly reflect normal subsystem behavior, a rule-based expert system is used to filter potential false alarms before they are submitted to the other onboard computer systems. The assessment process of MONITAUR is used to interpret quantitative data into qualitative data.

(Paul C. Schutte, 42019)
Flight Systems Directorate

Heavy Rain Research

Since 1982, NASA has been studying the influence of heavy rain on airfoil aerodynamic performance. Small-scale airfoil tests in the Langley 14- by 22-Foot Subsonic Tunnel and large-scale airfoil tests at the Aircraft Landing Dynamics Facility (ALDF) showed that a high-intensity rainfall adversely affects airfoil performance. Tests were conducted on an NACA 64-210 wing section mounted in the tunnel and on the ALDF test carriage. Aerodynamic lift data were obtained with and without the rain simulation system turned on for an angle-of-attack range of 7.5° to 19.5° and for rainfall conditions of 9 in/hr and 40 in/hr.

The results obtained at the 9 in/hr rainfall condition indicate a small reduction in maximum lift and only a slight influence in the stall angle of attack. The test results shown in the figure were obtained at the 40 in/hr rainfall condition, and they show a 15- to 20-percent reduction in observed maximum lift and a reduction from a dry air stall angle of



Effect of rain on lift performance of NACA 64-210 airfoil with high-lift flap system.

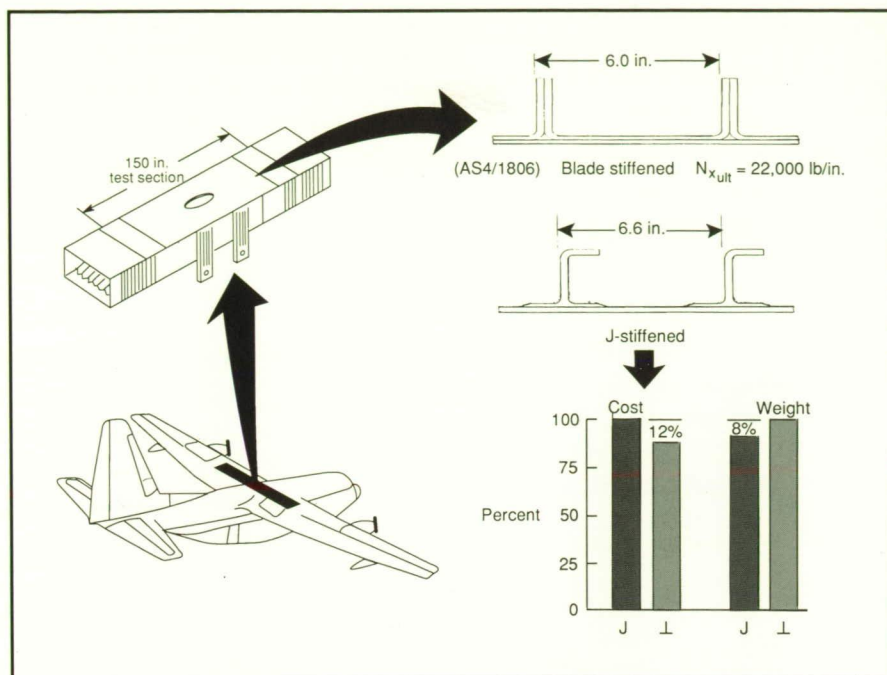
approximately 6° . These results compare well with the previous small-scale wind tunnel results for the same airfoil section. Primary scale effects appear not to be large, and the wind tunnel research technique can be used to predict rain effects on airplane performance. **(Gaudy M. Bezos and Bryan A. Campbell, 45055)**
Aeronautics Directorate

Influence of Design Concept on Composite Wing Structure Weight and Cost

The Advanced Composites Technology (ACT) program is developing

an integrated technology data base to support the introduction of composites into the primary structure of future aircraft. Design and manufacturing integration studies are in progress at Lockheed Aeronautical Systems Company to understand trade-offs between the cost and weight of a composite wing structure. The center wing box beam of the C-130 aircraft has been selected as the baseline to represent a typical piece of heavily loaded wing structure. Various composite structural concepts have been designed for this application and compared on the basis of weight and cost.

The figure illustrates a result from these studies for the upper cover panel of the box beam. The panel carries an ultimate compressive load of 22 000 lb/in. In this case, a simple



Comparison of composite wing structure weight and cost.

blade-stiffened panel concept is compared with a J-stiffened panel; both are fabricated of AS4 graphite fibers in 1806 epoxy matrix. The J-stiffened panel is more efficient in regard to weight, but it is more costly. The effort required to form the more-efficient concept is costlier than that required for the less-efficient concept.

Design and manufacturing integration is providing an understanding of weight and manufacturing cost trade-offs for composite structures. This type of information will lead to the capability to design cost-effective composite structures that offer improved performance over aluminum structure.

(John G. Davis, Jr., 42936, and Mark J. Shuart)
Structures Directorate

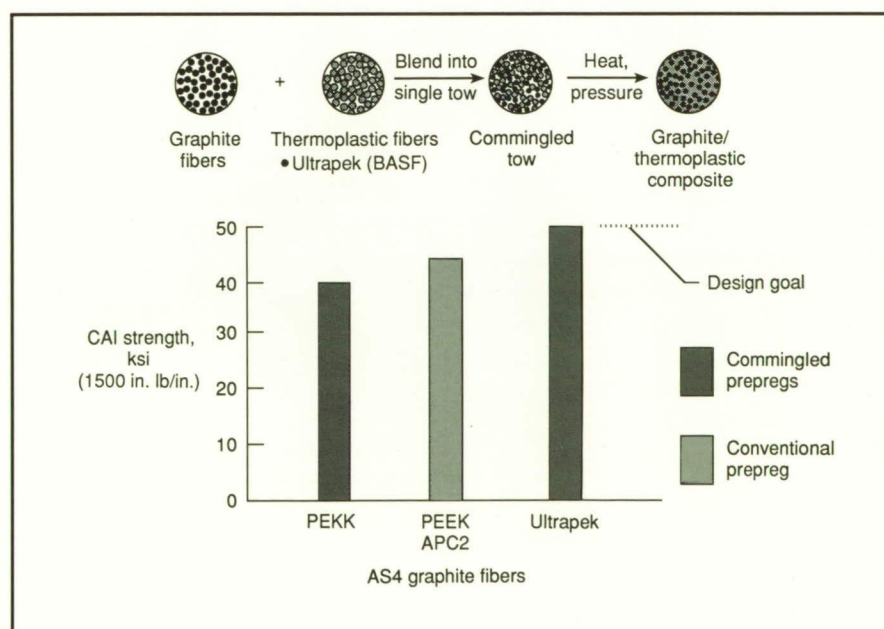
Superior Compression-After-Impact Performance by Commingled Graphite/Thermoplastic Composite

Graphite composite materials are attractive candidates for aircraft structures (because of their weight

savings potential due to low weight-to-strength/stiffness properties) when compared to more conventional structural materials; however, fabrication costs and low-tolerance-to-projectile impact sometimes negate the weight advantages. A new thermoplastic (Ultrapek), which has been developed by BASF under the Advanced Composites Technology program, may prove to be cost effective and impact tolerant enough for aircraft structures.

Ultrapek can be drawn into fibrous form, and, as indicated in the figure, these thermoplastic fibers can be mixed with graphite fibers to form a commingled tow. Subsequent application of heat and pressure melts the Ultrapek fibers and forces the melt to flow around the graphite to form, upon cooling, a graphite/thermoplastic prepreg composite.

Laboratory specimens have been fabricated from AS4 graphite/ Ultrapek for tensile, flexure strength, short-beam shear, and compression-after-impact testing. Tensile, flexure, and short-beam shear strengths are competitive with other composite materials. Compression-after-impact



Compression-after-impact performance of commingled composite.

(CAI) performance of the AS4/Ultrapek, however, is superior to other thermoplastics, as shown by the bar graph in the figure. The 50-ksi design goal noted on the chart is the value that manufacturers judge to be acceptable for commercial transport applications.

The data show that the graphite/Ultrapek commingled product is an excellent candidate for making thermoplastic textile preform composite structures that are impact tolerant.

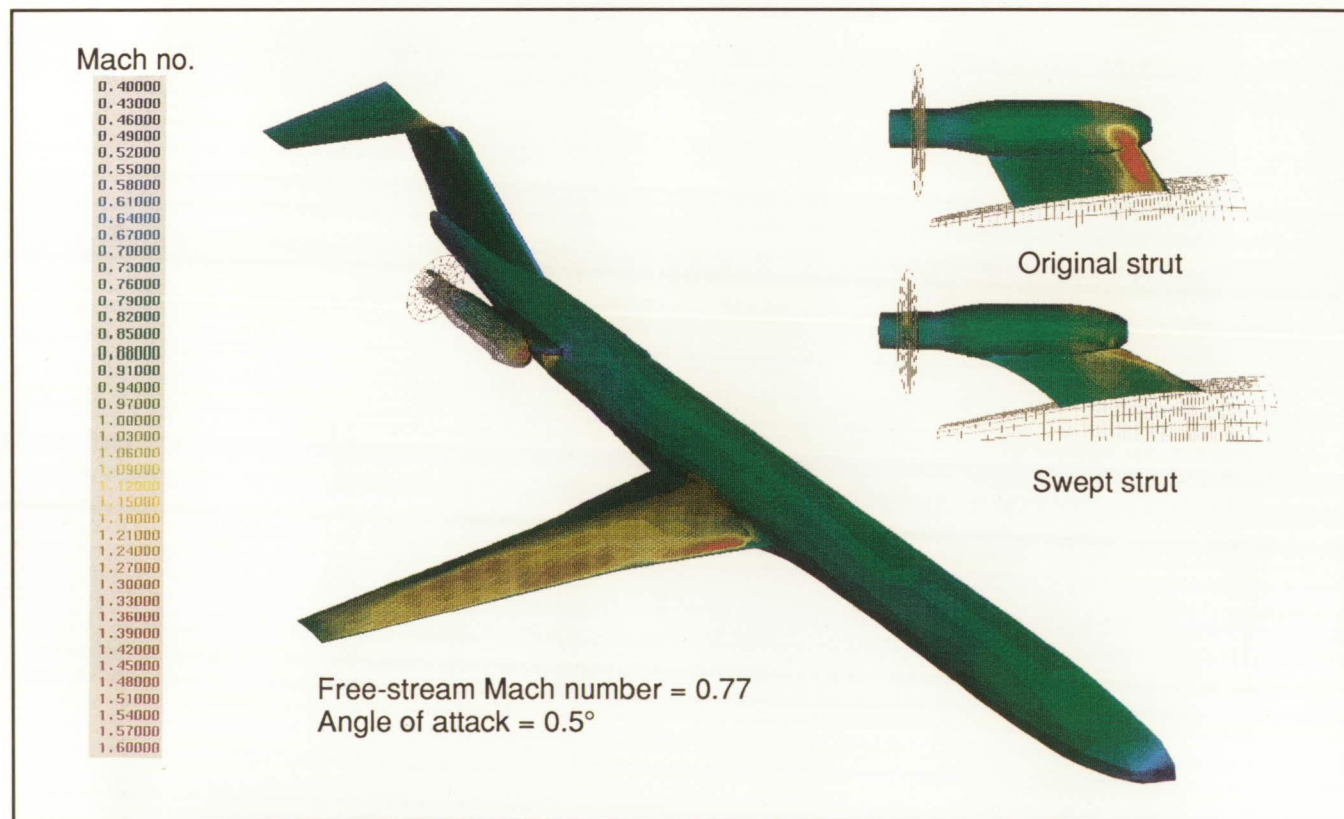
(John G. Davis, Jr., 42936, and Norman J. Johnston)
Structures Directorate

Development of Euler Method for Turboprop Integration

An effective computational capability for the study of turboprop engine-airframe integration has been developed. The approach is to use transonic, three-dimensional, multiblock, multigrid Euler codes for the analyses of complete airplane configurations with either wing-mounted or aft-mounted propfans. A three-dimensional elliptic grid generation code that creates the volume grid from the specified surface grid also has been developed. The propeller power effects are simulated using an actuator disk. On this disk, two choices exist to prescribe boundary conditions. One choice is to designate components of force and work distributions. In the other choice, total pressure, total

temperature, and swirl are prescribed along the disk as boundary conditions for the flow solver. A separate embedded flow solver provides detailed flow characteristics in the vicinity of the propulsive unit. This embedded solver inherits its starting values from the global solution.

The code has been successfully applied to the NASA generic aft-turboprop model shown in the figure. For this example, increasing the sweep of the strut is found to reduce significantly the adverse installation effects of propulsion integration. A typical analysis takes approximately 2 hr on a Cray-2, uses 295 000 grid points, and requires 12 megawords of memory in the single-block mode, or 3 megawords of memory in the multiblock mode. Embedded mesh solutions consume less than 10 min of computation time on the Cray-2.

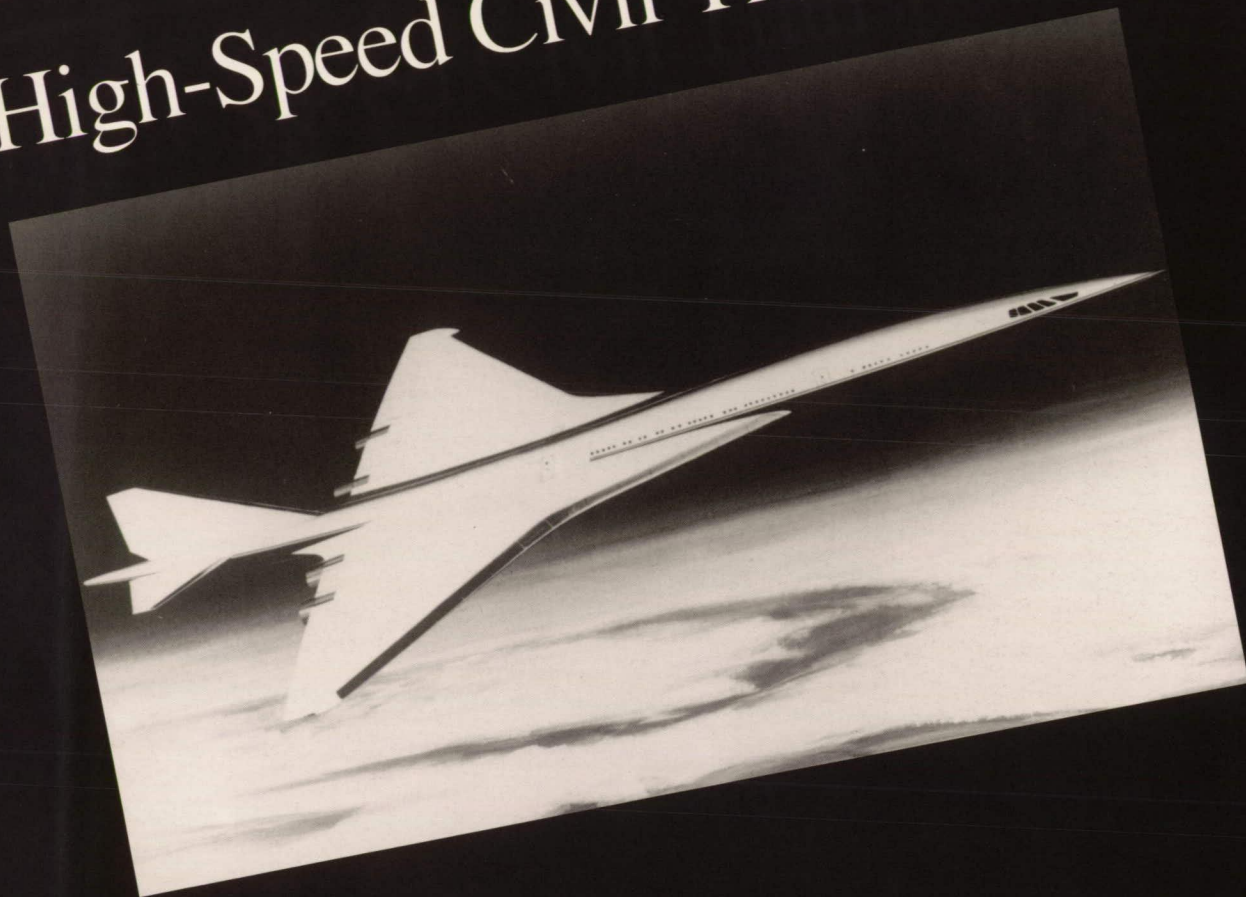


Euler-computed Mach number contours.

The Euler codes that have been developed in this project are an effective tool for propfan engine-airframe integration. Qualitative analysis of the computed solutions has aided in the selection and modification of configurations for quantitative experimental analysis. This experience also is helpful for the extension of this Euler code to the analysis of turbofan/superfan installations.

(D. A. Naik, 43041, N. J. Yu, H. C. Chen, and T. J. Kao)
Aeronautics Directorate

High-Speed Civil Transport



Supersonic Aerodynamic Characteristics of High-Speed Civil Transport

A study has been performed to determine the supersonic aerodynamic characteristics of the Langley Research Center High-Speed Civil Transport (HSCT) configuration. This configuration, which was designed to cruise at Mach 3, is sized to carry 250 passengers for 6500 nmi.

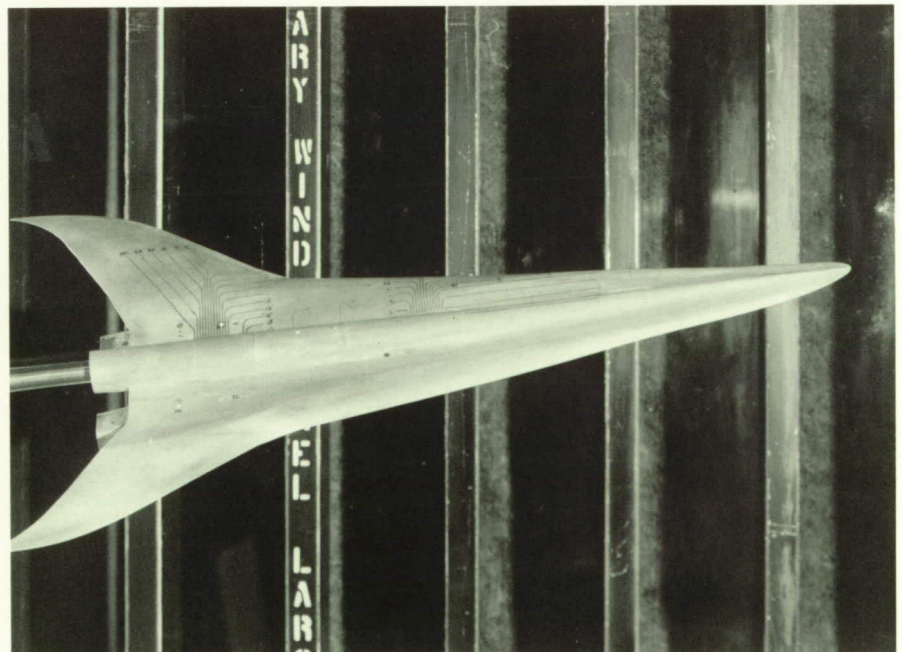
Wind tunnel tests were conducted in the Langley Unitary Plan Wind Tunnel on an 0.01-scale model. The fuselage is blended into the wing, which features a blunt (in planform) parabolic nose, highly swept inboard wing panel, moderately swept outboard wing panel, and curved wing tips. Force and moment, pressure, and flow visualization data were obtained for Mach numbers ranging from 1.6 to 3.6. An alternate configuration, one with straight wing tips, was tested to verify the benefits associated with the curved wing tip. Tests also were conducted to investigate nacelle effects.

The effect of the curved wing tips was to reduce zero lift drag, which yielded a slightly greater maximum lift-to-drag ratio for Mach numbers below 3.0. Typical Mach number and nacelle effects occurred on both the curved and straight tip wings. The configuration was 2 percent less stable than the preliminary linear theory estimates indicated. An unstable break in pitching moment began at a lift coefficient of approximately 0.05; this break was due mainly to nonlinear attached flow effects, although wing tip flow separation also was evident at higher lift conditions.

(G. Hernandez, J. D. Flamm, and P. F. Covell, 45572)
Aeronautics Directorate

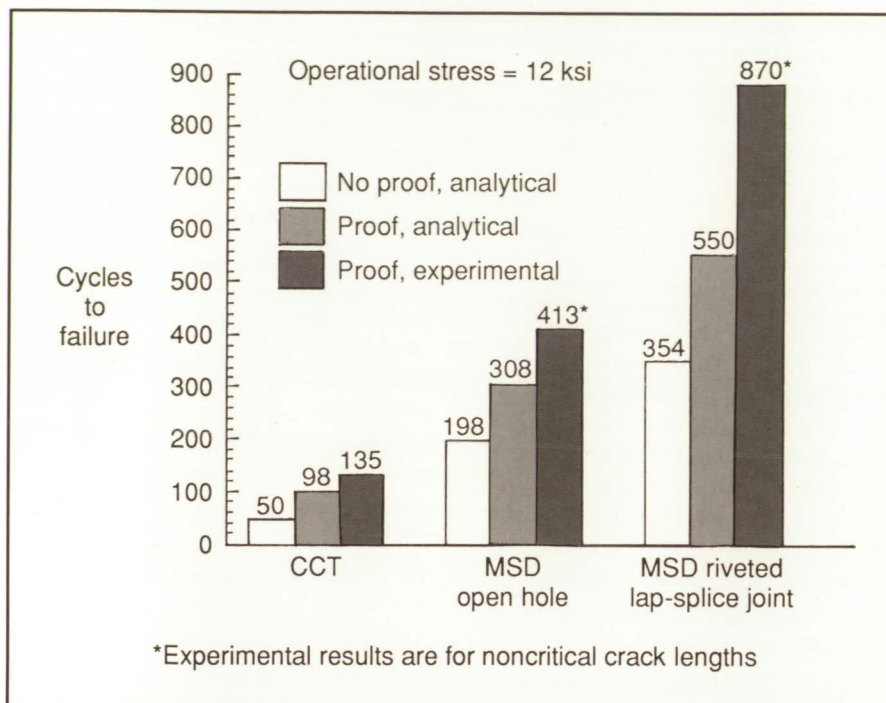
Evaluation of Pressure Proof Test Concept

Several recent incidents involving fatigue cracking have raised concerns about the structural integrity of the aging commercial transport aircraft



HSCT model in Unitary Plan Wind Tunnel.

L-90-8457



Predicted and observed effect of proof stress on life for CCT, open hole, and riveted lap-splice specimens subjected to operational stress of 12 ksi with and without 1.33 proof load.

fleet. The development of multiple-site damage (MSD) in lap-splice joints and other structural components is of great concern to the aerospace community. Multiple-site damage is the formation of a row of cracks, such as along the top line of rivets in a lap-splice joint. The critical size of the individual cracks may be relatively small, thus making their detection with current non-destructive examination (NDE) methods difficult.

The procedure of overpressurizing the fuselage of commercial transport aircraft has been postulated as a proof test that will ensure the continued safe operation of aircraft with MSD fatigue cracks. The concept of pressure proof testing of fuselage structures with fatigue cracks to ensure structural integrity was evaluated from a fracture mechanics viewpoint. A generic analytical and experimental investigation was conducted on uniaxially loaded flat

panels with stress levels typical of longitudinal lap splice joints in commercial transport aircraft fuselages. The specimen configurations (center crack tension (CCT), multiple-open hole, and lap-splice joint with a single row of rivets) were chosen to provide a progression of increasingly more complex configurations and to bring into account the important structural details of MSD and rivet-loading, while at the same time maintaining the simplicity of coupon specimens. A fatigue crack closure model with stress intensity factors corrected for plasticity was used to predict the fatigue crack growth behavior of the experiments.

The fracture mechanics evaluation of the proof test concept required the consideration of the largest possible crack or cracks (just less than critical) which could survive the proof test. The predicted number of cycles that is required to fail each of the three specimen configurations (with the

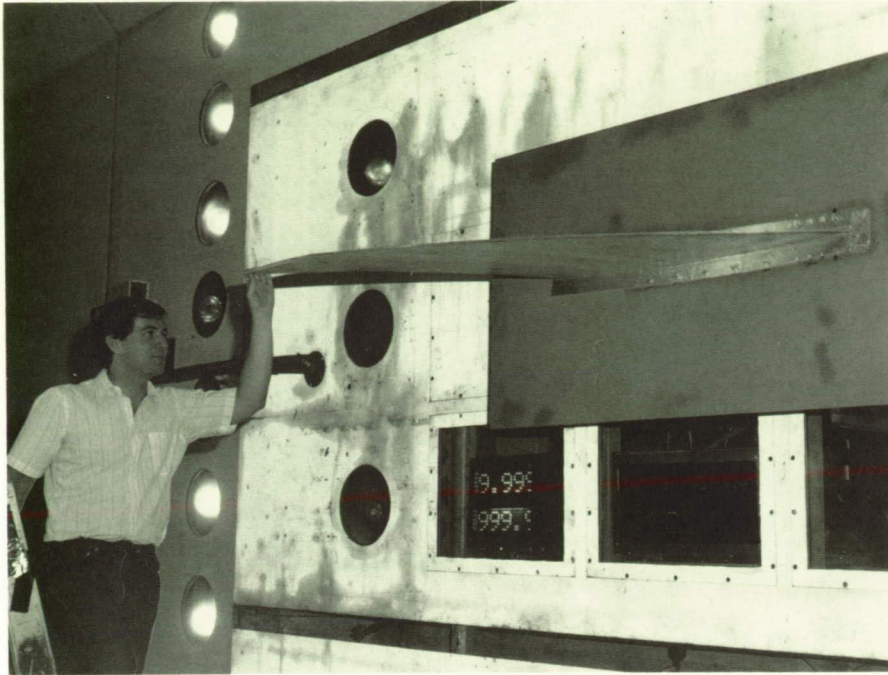
largest possible crack to survive the proof test) is shown in the figure. The corresponding experimental results were consistently higher than the predicted values because it was not practical to take the experiments to stresses that were just at critical conditions. The results revealed that the remaining fatigue life after a proof test was longer than that without the proof test because of crack growth retardation due to increased crack closure. However, based on a crack length that is slightly less than the critical value at the maximum proof stress, the minimum assured life or proof test interval for a lap-splice joint must be no more than 550 pressure cycles for a 1.33 proof load. Also, historically a factor of safety of 2 would be applied to a predicted inspection interval or, in this case, the proof test interval, thereby reducing the interval to well under 300 flights. (D. S. Dawicke, 43477, C. C. Poe, Jr., J. C. Newman, Jr., and C. E. Harris)

Structures Directorate

Determination of Leading-Edge Curvature Effects on Flutter

Swept wings with leading and trailing edges curved in the plane of the wing are attractive for use in HSCT applications because they can provide significant aerodynamic improvements over those obtained by using more conventional planforms. However, because flutter is an important HSCT design consideration and little is known of the effects of planform curvature on wing flutter, the present study was undertaken to determine experimentally the effects of planform curvature on transonic flutter of a series of moderately swept wing models and to compare the experimental results with analytical results.

ORIGINAL PAGE
BLACK AND WHITE PHOTOGRAPH

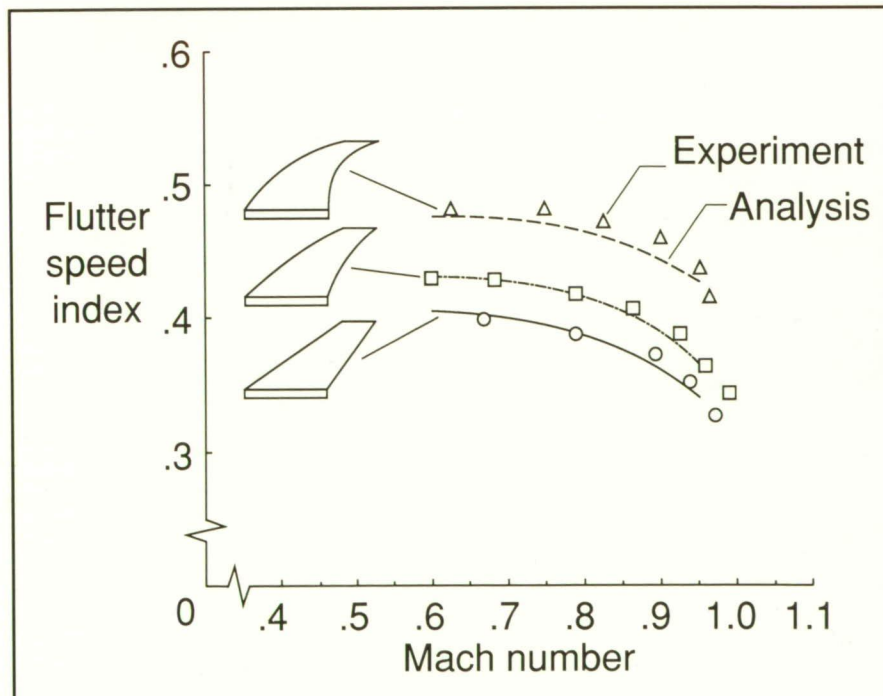


HSCT model mounted on sidewall.

L-89-5086

Three generic flutter models were designed and fabricated to represent the outboard portion of an HSCT wing. The radii of curvature of the leading edges of the three models

were infinity (no curvature), 200 in., and 80 in., respectively. The planform area for all models was the same (900 in^2) as were the length and location of the root and tip chords.



Flutter speed results for three HSCT planforms.

The leading-edge sweep angle of the uncurved wing was 53° . A photograph of the moderately curved model is presented in the first figure.

The flutter boundaries that were obtained over the Mach number range of 0.6 and 1.0 are presented in the second figure as the variation of the Flutter Speed Index (FSI) with Mach number. The FSI is a non-dimensional velocity parameter that is frequently used to correlate flutter results obtained for different models. The FSI value depends on flow conditions, structural stiffness, and planform geometry. The analytical boundaries were calculated using linear subsonic lifting surface (kernel function) unsteady aerodynamic theory. The experimental data show that the FSI increases as the planform curvature is increased. This trend also is seen in the analytical results that agree well with the experimental data. Furthermore, the flutter results for the curved leading-edge configurations do not exhibit any unusual characteristics that would preclude, from a flutter point of view, the use of such configurations on advanced configurations.

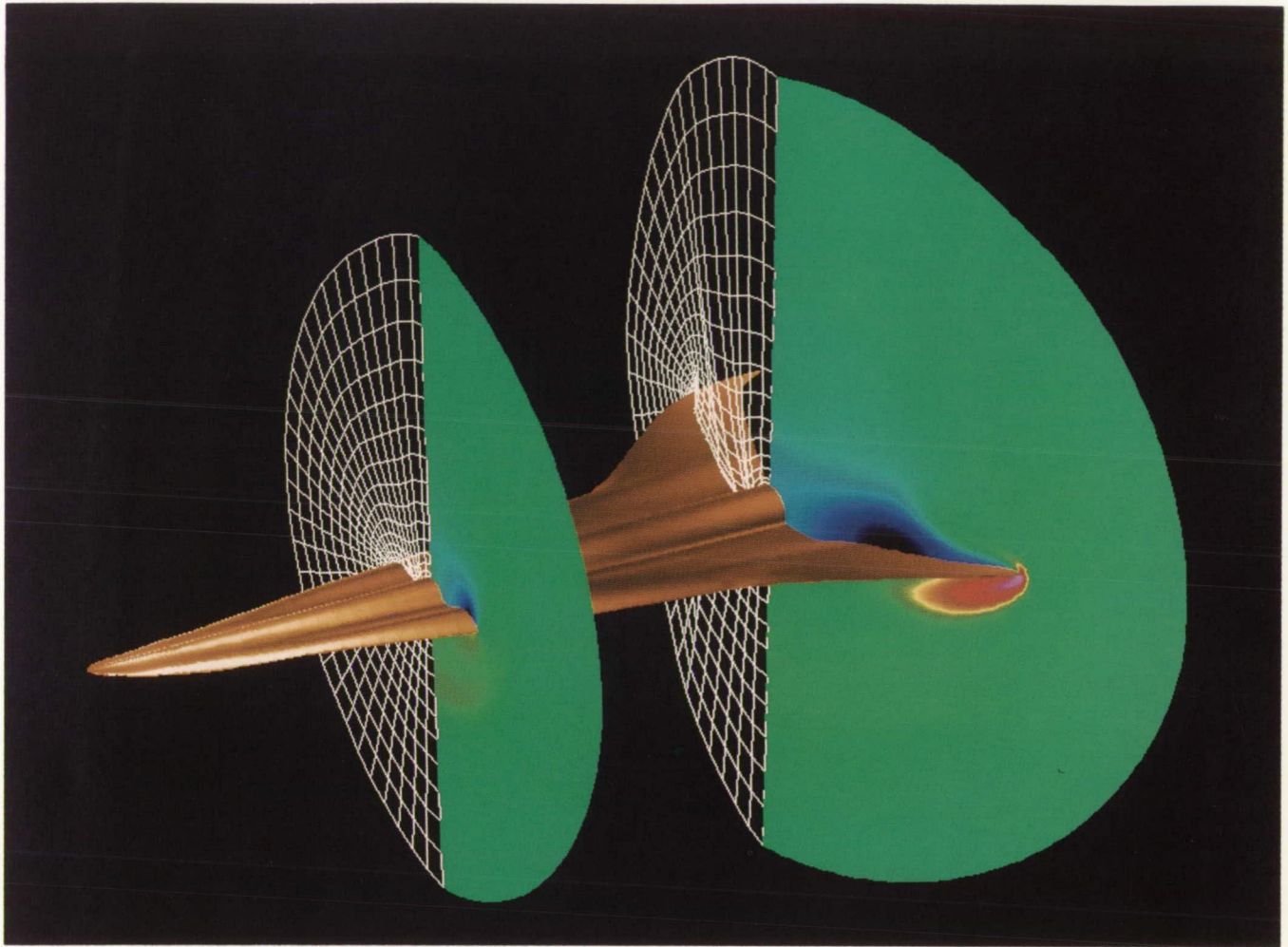
(Donald F. Keller and Maynard C. Sandford, 41259)

Structures Directorate

Grid Generation on and About HSCT Configurations

Computational fluid dynamics (CFD) is being used to study HSCT configurations. Described here is the grid generation on and about the wing-fuselage-tail-nacelle bodies.

The first step in grid generation is to choose a suitable topology that is consistent with the flow conditions and solution algorithm. The initial topology is a single block with grid lines that wrap around the configuration surface. This is the first of



Mach 3 HSCT surface, grid surfaces, and pressure solution.

several topologies that will be applied to the HSCT configurations. Different topologies must be considered to accommodate the wing leading edge, which is rounded near the fuselage and sharp near the wing tip and the engine nacelles. For the initial topology, surface grids have been generated in two- and three-dimensional cross sections using the Aeronautical Surface Topology Routines (ASTAR) tool kit developed at Langley Research Center. These surface grids are designed to be used in several different CFD software packages.

Three-dimensional grids that surround the configuration surface are generated with the aid of the GRIDGEN and EAGLE software,

developed for the U.S. Air Force by General Dynamics Corporation and Mississippi State University, respectively, and the application of transfinite interpolation. The figure shows the shaded surface of an HSCT configuration, a subset of two grid surfaces (one forward and one rearward), and the corresponding pressure solution obtained from an Euler code at Mach 3 and an angle of attack of 2° . The red and yellow regions indicate high pressure, the blue regions indicate low pressure, and the green indicates the free-stream condition.

**(Robert E. Smith, 45774)
Electronics Directorate**

ANOPP Jet Noise Predictions for HSCT

Acceptable jet noise level is one of the key factors in producing an environmentally acceptable HSCT. To support a national effort to develop a U.S. HSCT, the Aircraft Noise Prediction Program (ANOPP) is being adapted to interface with flight simulators so that at the end of a simulated flight a ground contour of the noise produced will be available. This capability will be used to study the effects of high-lift technology and advanced traffic control procedures to try to minimize the impact of aircraft noise on communities. A preliminary study was performed using ANOPP

to evaluate the effects of reduced jet thrust during takeoff on airport community noise levels. Reduced jet thrust can be used by employing high-lift technology in the design and manufacture of an HSCT.

Predictions were made using the ANOPP dual-stream coannular jet noise module for the AST-205-1 aircraft powered by GE21/J11B14A scaled engines. A power setting of 100 percent thrust and a standard lift configuration were used as baselines for this study. Power settings varied from 100 percent to 80 percent maximum thrust, while lift was increased in increments of 15 percent, to a maximum of 60 percent. A constant climb angle of 8° and a rotation rate of $3^\circ/s$ were used. Noise levels were calculated on a 1- by 6-

mile grid consisting of 65 observer positions. Each observer is located at a height of 4 ft above the ground. Noise contours were generated from these observer positions.

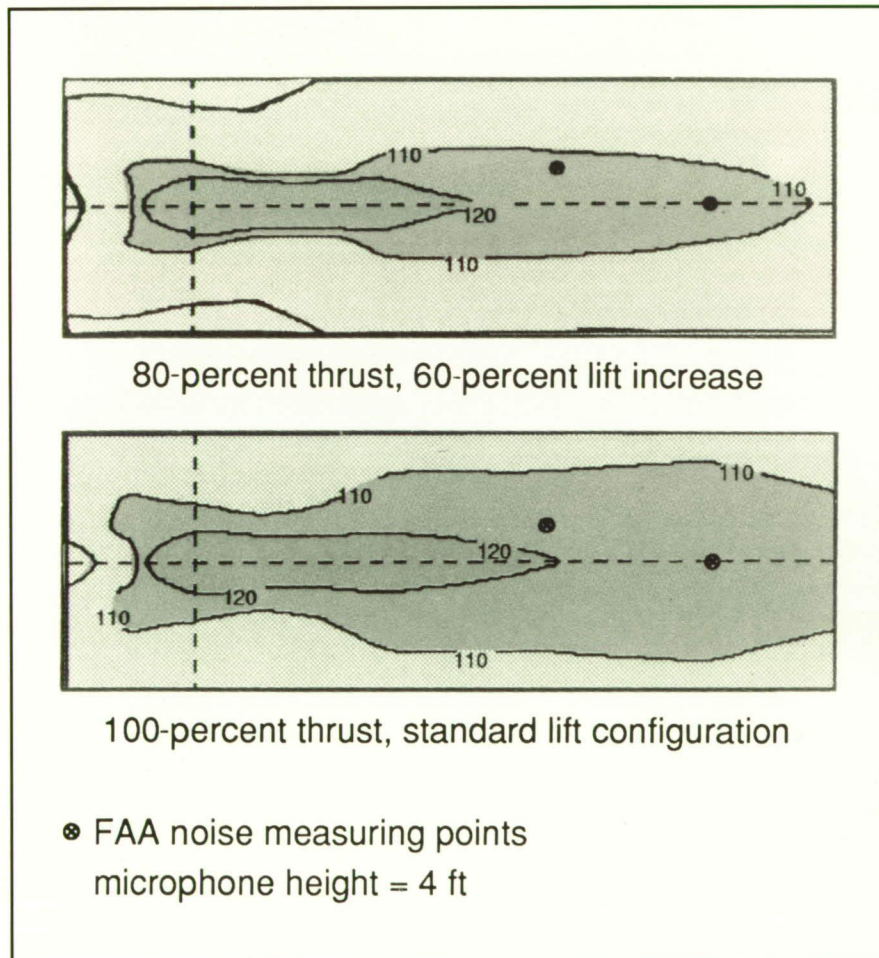
Contours of the 100-percent thrust, standard lift configuration, and the 80-percent thrust/60-percent increased lift cases are shown in the figure. The 110 effective noise level contour (EPNdB) and 120 EPNdB levels are shown. By reducing the thrust level from 100 percent to 80 percent maximum thrust, a 4 EPNdB decrease in the critical sideline effective perceived noise level (EPNL) can be achieved. By using a 60-percent lift increase, the ground roll can be shortened to be within 16 percent of the standard lift configuration. As can be seen when comparing

the two contours presented in the figure, reducing thrust and increasing lift alters the shapes of the contours. In general, as thrust is decreased and lift is increased, the contours shorten in length and become more compact. (Robert A. Golub, John R. Rawls, and Mark Wilson, 45281) Structures Directorate

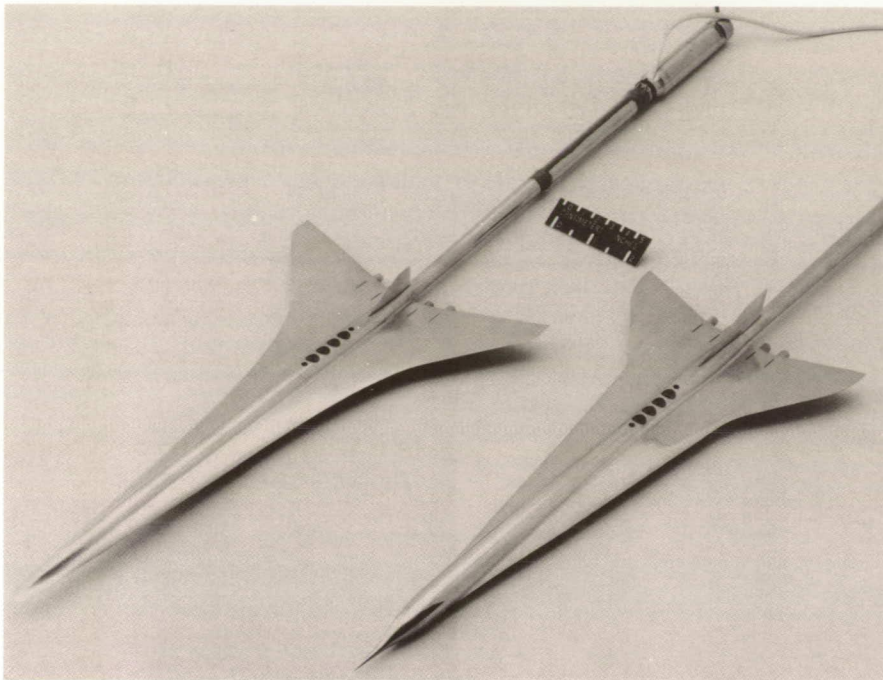
Wind Tunnel Models for Low Sonic Boom Concepts

As part of the research to address environmental concerns of the High-Speed Research Program, two models to evaluate current sonic boom minimization theories have been designed and fabricated. Unlike earlier sonic boom models, the two models have realistic aircraft features that include twist, camber, dihedral, flow-through nacelles, and fins. These models are approximately 1/300-scale representations of the 300-ft configurations designed to cruise 5500 nmi and 6500 nmi with 250 to 300 passengers. The Mach 2 configuration, shown on the left in the figure, was designed to produce a "flat-top" pressure signature with a shock level of 1.0 lb/ft^2 . The Mach 3 configuration, shown on the right, was designed to produce a minimum shock signature in which the bow shock level of 1 lb/ft^2 is followed by an isentropic increase in pressure. Improved propagation methods will allow pressure measurements to be taken nearer to the disturbance source. These models are two to three times larger than any sonic boom models previously tested at Langley Research Center, thus allowing more accuracy and complexity in the design. The models display the typical low sonic boom model characteristics of long lifting length and slender forebody.

Confirmation of sonic boom minimization theories and equivalent area prediction with these complex



ANOPP jet noise prediction for HSCT reduced-thrust takeoff study.



12-in. Mach 2 (left) and Mach 3 (right) low boom sonic boom wind tunnel models. L-90-8266

models will provide the first step to develop an aerodynamically efficient low boom configuration with mission performance comparable to unconstrained configurations.

(Robert J. Mack, 45988, Christine M. Darden, and Kathy E. Needleman)
Aeronautics Directorate

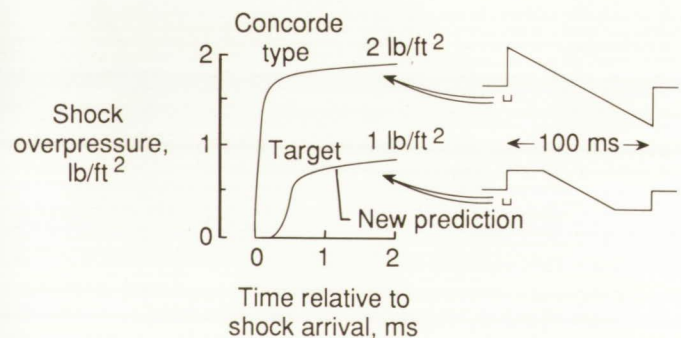
Producing More Acceptable Sonic Booms

Classical sonic boom theory predicts that the disturbance generated by a supersonic aircraft will be led by a very sharp rise in pressure from ambient to the peak over-

pressure. This sharp pressure rise occurs over a time interval that is generally less than 1 percent of the time interval for the total disturbance, yet the annoyance of the sonic boom is probably directly related to this initial pressure rise. This fact has two important consequences. First, the major portion of the sonic boom waveform may be neglected when attempting to determine the effect that the atmosphere has on the sonic boom. Second, and more important, if this sharp pressure rise can be made more gradual, the sonic boom will be more acceptable.

The objective of the current research has been to determine the effect of molecular absorption on the initial portion of the sonic boom. Burgers' equation describes the balance between nonlinear processes and viscous damping on the sonic boom waveform, but in its usual form it does not contain molecular absorption effects. For the current study, Burgers' equation was augmented by the addition of terms describing the molecular relaxation process.

Numerical integration of the augmented Burgers' equation for a range of shock overpressures provided the interesting result that, for



Lower peak overpressure that implies more gentle rise to peak (nonlinear propagation of sonic booms, effects of molecular absorption).

overpressures below 1 lb/ft^2 , the rise in pressure with time, relative to the arrival of the shock, is much more gradual than for higher overpressures (as shown in the figure). The curve labeled Concorde shows the rapid increase in overpressure typical of the sonic booms generated by that aircraft. The second curve labeled target manifests the more gentle pressure rise typically of all shock waves with peak overpressures of 1 lb/ft^2 or less, at least as predicted by the augmented Burgers' equation. This work was accomplished by A. Pierce through a grant at Pennsylvania State University.

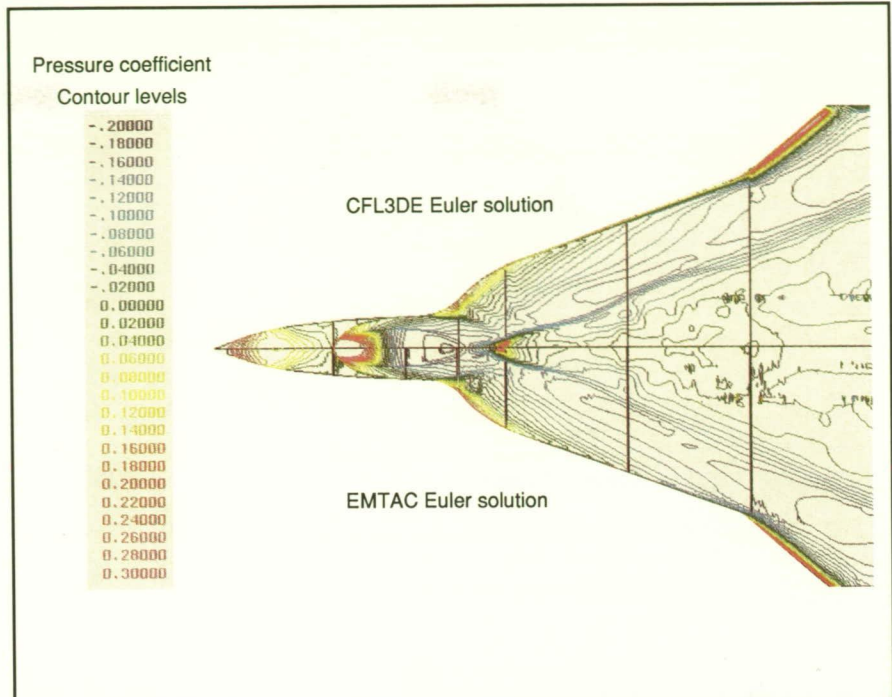
The current theory suggests that the weaker boom is more acceptable not only because the peak overpressure is less, but also because the more gradual pressure rise is more acceptable than the rapid rise typical of higher level booms.

(Gerry L. McAninch, 45269)
Structures Directorate

Numerical Analysis of F-16XL Laminar-Flow Control Configuration

In future projects such as the HSCT, the role of laminar-flow control (LFC) in reducing skin friction drag and skin temperature has been clearly identified. The LFC concept makes use of component shaping for favorable pressure gradient and active control through boundary-layer suction. Computational fluid dynamics has a large role to play in fuselage and wing shaping and the estimation of boundary-layer suction rate requirements.

The F-16XL LFC experiment is aimed at the realization of laminar flow on highly swept supersonic wings. The main features of the flow can be seen by obtaining the inviscid



Pressure coefficient contours on F-16XL wing upper surface at M_∞ of 2 and α of 4° .

solution from an Euler solver. This step is further followed by calculation of the viscous layer through three-dimensional boundary-layer analysis or by solving the full Navier-Stokes equations. The final step is a boundary-layer stability analysis with a parametric variation of suction rates.

The F-16XL base geometry (with no laminar glove) at a Mach number M_∞ of 2 and an angle of attack α of 4° is used as a preliminary study case here. The solution of the Euler equations has been obtained from two codes, the CFL3DE of Langley Research Center and the EMTAC of Rockwell International Corporation. Both codes were run as space-marching Euler solvers with approximately 40 000 mesh points on the body surface and 20 to 30 points in the surface normal direction. Computation is done in seven grid blocks using an upwind-differenced Euler marching scheme and with solution patching at grid interfaces. The solution took approximately 3 hr on

the Cray-2 machine. The figure shows a comparison of the upper-surface pressure coefficient distribution obtained from the two codes. The swept shock originating from the tail end of the canopy will be an important factor in the laminar glove design. The pressure field shown in the figure will be interpolated in the streamwise direction for analysis with a three-dimensional boundary-layer code. The boundary-layer solution then will be used in the stability analysis of the flow. The complete procedure will be repeated for different flight conditions and compared with flight results.
(Venkit Iyer, ViGYAN, Inc., and Julius Harris, 42296)
Aeronautics Directorate

High-Performance Military Aircraft



Acoustics of ASTOVL Aircraft in Ground Effect

Advanced Short Takeoff and Vertical Landing (ASTOVL) aircraft use thrust vectoring to redirect the exhaust flow into the ground, thus providing lift in takeoffs and landings. Interactions between the high-velocity, high-temperature jets and the ground and mutual interactions between the jets make the prediction of the acoustics of the aircraft very difficult. Consequently, direct experimentation is the best way to understand this complicated flow field.

The near-field acoustics and dynamic airframe loading of an ASTOVL aircraft were measured in the NASA Lewis Research Center 9-by 15-Foot Low-Speed Wind Tunnel. The testing was done using a 9.2-percent scale model of the McDonnell Douglas Corporation designed 279-3C aircraft. The objectives of the testing were to characterize ASTOVL acoustics when the aircraft was in ground effect (takeoffs and landings) and to determine the effect of jet exit temperature.

The model was built to evaluate the hot gas ingestion (HGI) character-

istics of the design up to exhaust temperatures of 1000°F. The figure shows the model installed in the wind tunnel. Model geometry parameters that were varied during testing included the nozzle outward splay angle and the Lift Improvement Device (LID) configuration. (The nozzle splay and LID's are used to constrain the development of the exhaust fountain and restrict its area of impingement on the aircraft.)

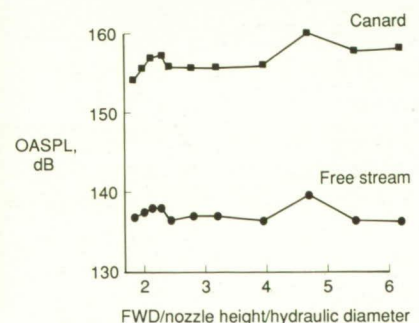
Acoustic data were obtained from a linear array of five free-stream microphones, located parallel to the model centerline. The fluctuating loads on the model were measured with eight dynamic pressure transducers located on the underside of the canard, wing, and aft fuselage. The placement of the inboard canard transducer is illustrated in the figure.

Data were taken for more than 700 combinations of model geometry and test conditions. The data shown illustrate the effect of the normalized nozzle height on the overall sound pressure level (OASPL), as measured by the canard and in the free stream, for a jet temperature of 750°F. As shown by the data, levels up to 160 dB were observed on the model and up to 140 dB in the free stream. At other conditions, levels as high as

Hot gas model in
Lewis 9-by 15-Foot Low-Speed Wind Tunnel



Effect of thrust on noise
Temp. = 750°



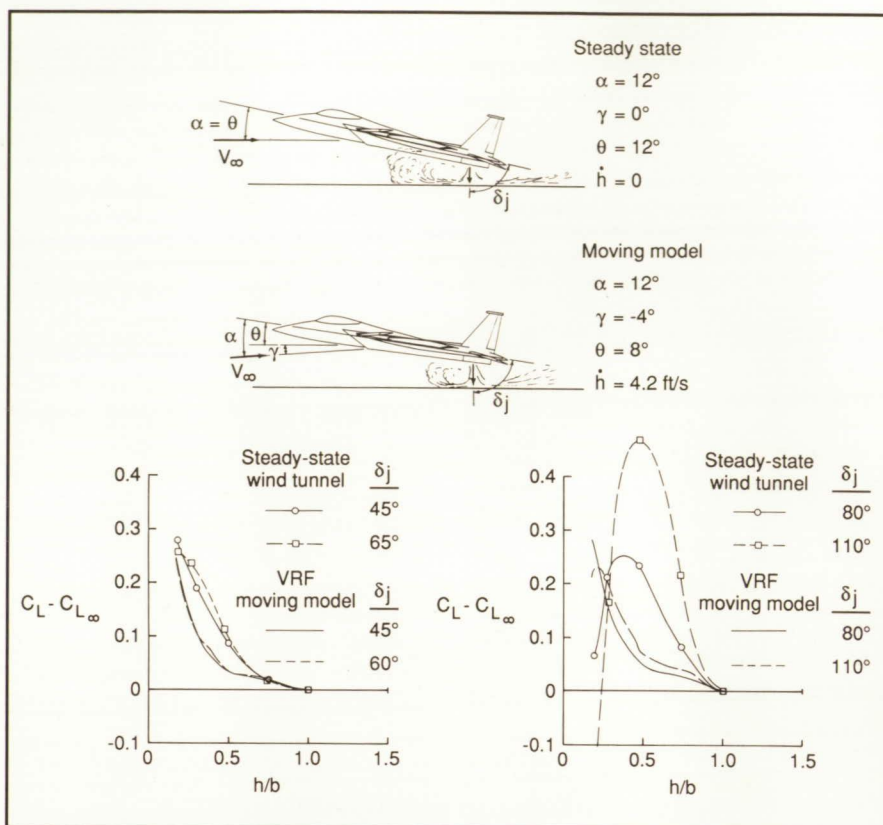
Joint Lewis Research Center and Langley Research Center ASTOVL acoustic loads test. L-90-7569

180 dB, as well as discrete frequency tones 160 dB in amplitude, were measured. These tones were associated with oscillations in the jets as well as feedback between the jets and the ground.

No satisfactory model exists which can predict the acoustics of multiple heated, noncircular jets operating in ground effect in an off-design condition. The data that were acquired in this test will be valuable in understanding both the fundamental physics of jet-impingement and the configuration issues involved in ASTOVL aircraft acoustics.
(L. Kerry Mitchell, 43625)
Structures Directorate

Static and Dynamic Ground Effects

Historically, discrepancies have existed between the ground effects predicted from the wind tunnel tests of many aircraft configurations and those actually experienced in flight. These differences have been greatest on vectored-thrust configurations. A wind tunnel research program has been conducted to determine whether the absence of rate-of-descent \dot{h} simulation in conventional ground-effects testing could be the source of this discrepancy. Early tests, using a model of the F-15 STOL (Short Takeoff and Landing)/Maneuver Technology Demonstrator (S/MTD), confirm the existence of the influence of rate of descent on a configuration of current interest. In general, the data indicate moderate effects on the lift coefficient C_L due to the rate of descent at low thrust vector angles δ_j ; however, much larger differences exist between the results of the two test techniques at higher vector angles. Similar trends were seen in pitching moment.

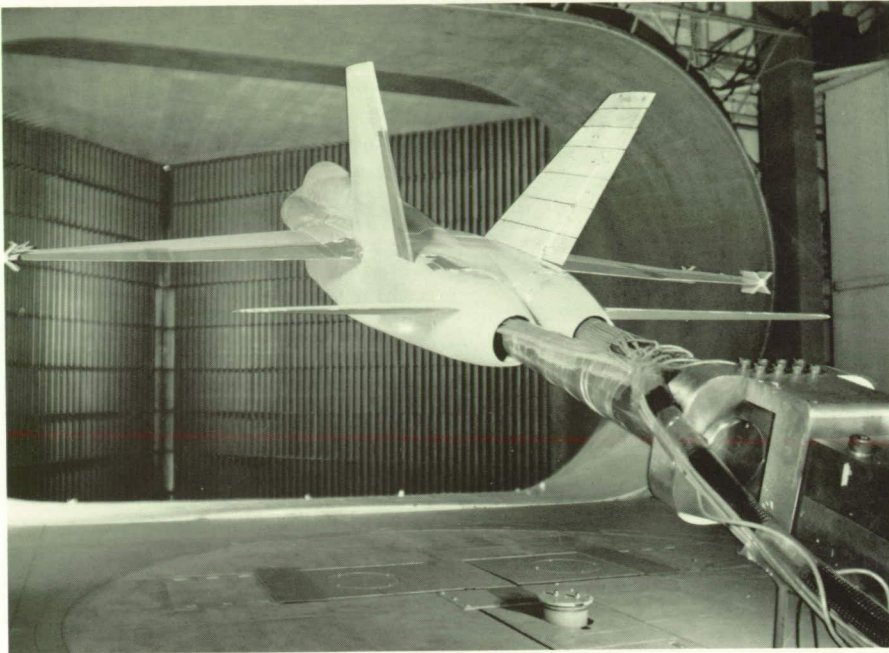


Dynamic ground effects on F-15 S/MTD.

To achieve a simulated rate of descent, an inclined ground board was constructed within the test section of the Langley Vortex Research Facility (VRF). As the model, traveling horizontally through the facility, passed over the inclined ground board, the height of the model above the ground reduced at a constant rate. This rate was the simulated rate of descent. A comparison of these results with those obtained using conventional steady-state ground-effects testing techniques is presented in the figure. In this figure, α is the angle of attack of the model relative to the wind, θ is the angle of incidence of the model relative to the floor, γ is the flight path angle relative to the ground, h is the height of the model above the ground, and b is the wing span of the model. The subscript ∞ indicates conditions in the free stream (away from the ground or model). Similar comparisons have been made for a

variety of other configurations and show conclusively that the effect of sink rate should be represented in predicting ground effects for advanced vehicle designs. Based on the results to date, a special dynamic model support system is being developed for the Langley 14- by 22-Foot Subsonic Tunnel to study dynamic ground effects.
(Guy T. Kemmerly and John W. Paulson, Jr., 45070)
Aeronautics Directorate

ORIGINAL PAGE
BLACK AND WHITE PHOTOGRAPH



Rear view of F-18 model with instrumented tails in Langley 30- by 60-Foot Tunnel. L-90-6772

Tail Buffet Research

The use of the high-energy vortex flows to enhance maneuvering capability has become a widely applied design approach in the development of modern high-performance aircraft. The unsteady nature and high-energy content of these flows can, however, cause unfavorable interactions with airframe components. Recent operational experience has shown that vortical flow fields can induce severe buffeting of vertical tails, which substantially reduces the fatigue life of that structure. A research program is under way to study the effects of vortex flow fields on tail buffet and to explore methods of reducing buffet levels while maintaining the favorable effects that vortex flows may have on high-angle-of-attack aerodynamic characteristics.

Wind tunnel testing has been conducted in the Langley 30- by 60-Foot Tunnel using an 0.16-scale F-18 model equipped with dynamically

scaled, extensively instrumented vertical tails. These tests were conducted to study the vertical-tail flow field and dynamic response and to obtain overall aerodynamic force and moment data for the configuration. The investigation focused on the study of airframe modifications that would alleviate tail buffeting while also improving the lateral-directional stability characteristics at stall and poststall flight conditions.

Results of the study have shown that changes in the wing leading-edge extension (LEX) geometry can appreciably reduce tail buffet levels by repositioning and/or weakening the vortex system, but they also can have a large impact on the overall lift and stability characteristics. Several LEX modifications were identified as providing large reductions in buffeting while having only relatively small effects on the high-angle-of-attack aerodynamic characteristics. Additional studies to evaluate various innovative concepts to further alleviate tail buffeting and to develop ground-to-flight scaling methods are

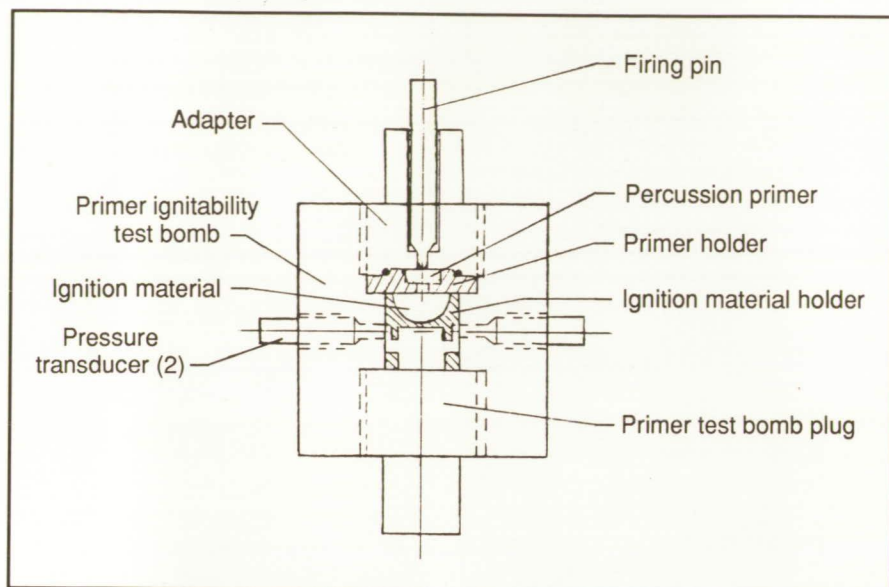
planned. The ultimate goal of this program is to develop a better understanding of vortex/empennage interactions and thereby to allow tail buffet concerns to be addressed early in the design cycle of future high-performance aircraft.

(Gautam H. Shah, Sue B. Grafton, and Jay M. Brandon, 41163)
Aeronautics Directorate

Ignitability Test Method

To overcome serious weaknesses in determining the performance of initiating devices, a novel ignitability test method, representing actual design interfaces and ignition materials, has been developed. Ignition devices, such as percussion primers and the NASA Standard Initiator (NSI), produce heat, light, gas, and burning particles. Because of the dynamic, erratic output of these devices, no generally accepted test methods are available to evaluate ignitability, and, consequently, no specifications exist. Past research methods have evaluated these output parameters individually. Research at Langley Research Center, under U.S. Air Force funding for military aircraft escape system component service evaluation, has developed and demonstrated a test method that combines all these output parameters to provide a quantitative assessment of the function time, ignition performance, effect of cold temperature, and effect of sealing methods on six different types of percussion primers.

The principle of this test method is to fire the initiator onto a bed of ignition material, as shown in the figure, and monitor the gas produced during the initiation and combustion of the ignition material. This gas vents through holes in the ignition material into the lower chamber of the sealed volume (bomb) and pressurizes this volume. This



Cross section of ignitability test method test apparatus for percussion primers.

pressure, detected by the transducers and recorded, produces a signature of the response of the ignition material to the input of the initiator. Each signature is unique to the primer type and provides for the first time a test method for quality assurance, for assessment of changes induced by service, contamination, or variations in initiator material composition, for selection of the optimum initiator for a particular application, and for the evaluation of ignition system inter-

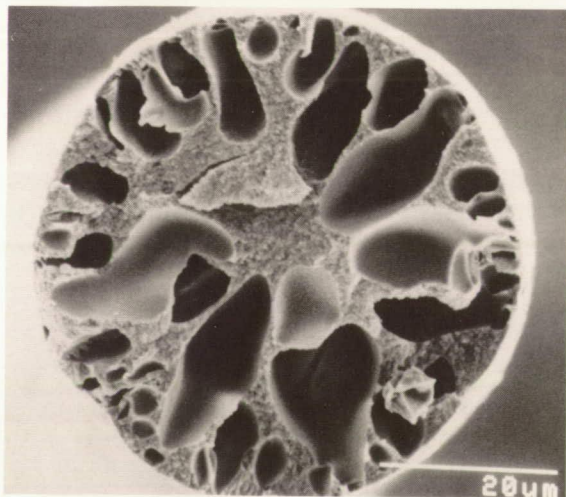
faces (such as geometry and materials).
(Laurence J. Bement, 47084)
Systems Engineering and Operations Directorate

Polyamic Acid and Polyimide Fibers

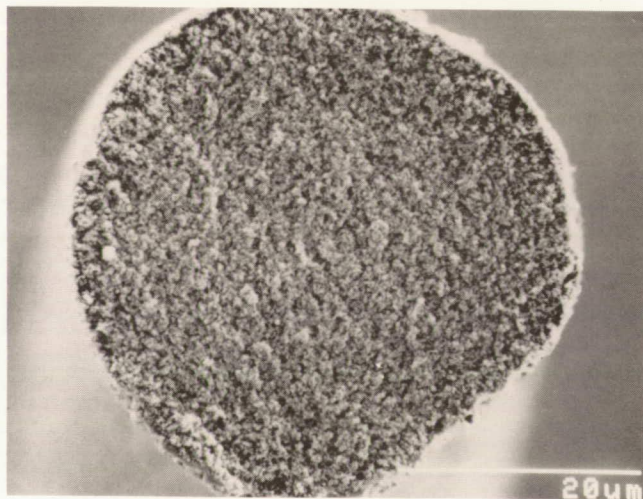
An improved wet-spinning process makes aromatic polyamic acid fibers

that contain no voids and can be converted to polyimide fibers that are also free of voids. When made by prior wet-spinning processes, such fibers contain voids. The elimination of voids has been found to improve tensile strength and other tensile properties. The improved polyimide fibers should prove useful in protective clothing, sealing materials, filters for harsh chemical and/or thermal environments, and other applications that take advantage of their excellent chemical resistance, high thermal stability, and good tensile properties.

The polyamic acid is derived from benzophenone tetracarboxylic dianhydride and oxydianiline dissolved in dimethylacetamide (DMAc) to make the spinning resin. The major differences between the improved process and older processes are in the choice and concentration of the coagulation liquid, inherent viscosity of the resin, and diameter of the resulting filament. Experiments have shown that 100 percent void-free fibers can be produced when the following conditions are provided: the spinning resin should have at least a 1.6 dL/g inherent viscosity and the coagulation liquid into which the polyamic acid is extruded should be



Extruded into 20 percent aqueous DMAc



Extruded into 75 percent aqueous ethylene glycol

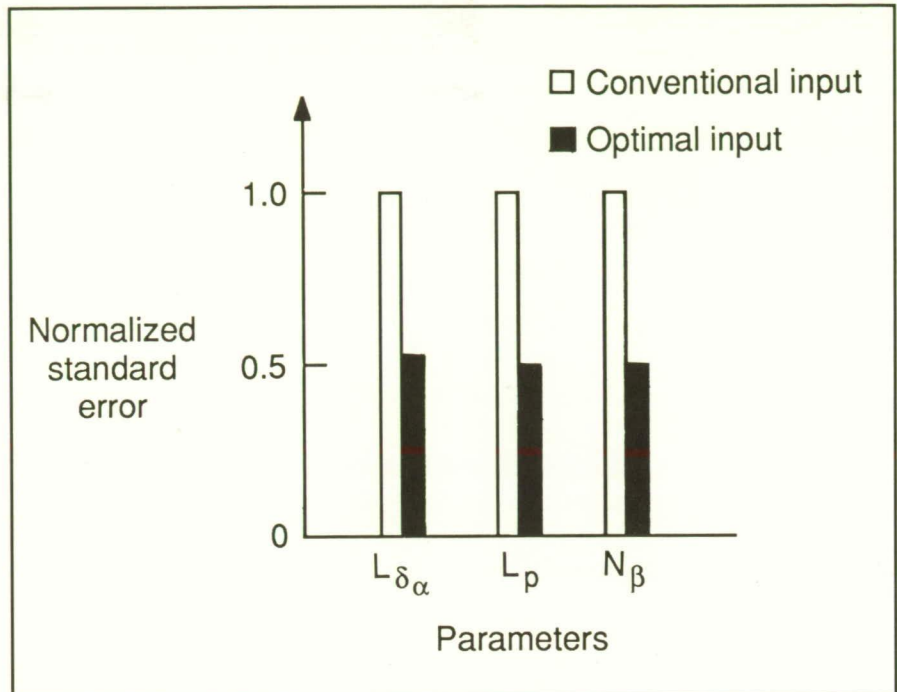
Scanning electron micrographs of polyamic acid fibers.

an aqueous solution of either 70 percent to 75 percent of ethylene glycol or 70 percent to 80 percent of ethanol at a temperature of 20°C. (Anne K. St. Clair, 44242, and William E. Dorogy, Jr.) Structures Directorate

Optimal Input Design for Aircraft Parameter Estimation

Mathematical models of aircraft dynamics typically contain quantities called parameters that depend, in general, on the flight condition and aircraft geometry. It is important to be able to estimate accurately these parameters from aircraft flight data to corroborate wind tunnel parameter estimates, improve aerodynamic calculations, update aircraft dynamic models for flight control system refinement, or predict aircraft responses for realistic flight simulation and ground-based pilot training. In the past, flight test input design for parameter estimation flight experiments was usually based on heuristic rules and experience with similar flight test situations. These methods worked well for conventional aircraft in normal flight conditions with no control augmentation. Today, many fighter aircraft are designed with inherent longitudinal static instability for enhanced maneuverability and performance. These aircraft necessarily employ stability augmentation systems that deflect multiple control surfaces in response to pilot inputs. The object of this research was to develop an algorithm for the design of practical, optimal pilot inputs for aircraft parameter estimation experiments. This algorithm must produce multiple pilot inputs for the estimation of open-loop model parameters from closed-loop flight data.

A general, single pass technique has been developed which allows



Performance comparison for parameter estimation inputs.

global optimization of the flight test input design using a mathematical optimization technique called dynamic programming. Practical constraints on the input form (such as control system dynamics and selected input frequency range exclusions) were included. In addition, the input design was accomplished while imposing output amplitude constraints required by model validity and considerations for safety during the flight test. Multiple pilot input designs were possible, with optional inclusion of a constraint that only one pilot input move at a time. The technique was used to design aileron and rudder inputs for the lateral dynamics of a generic fighter aircraft with 12 model parameters. The improvement in achievable parameter accuracy with the optimal inputs compared to conventional doublet inputs is shown in the figure for three types of parameters (control effectiveness L_{δ_α} , damping L_p , and stability N_β). The achievable standard errors for the conventional doublet input design were normalized to unity for each parameter. Achievable

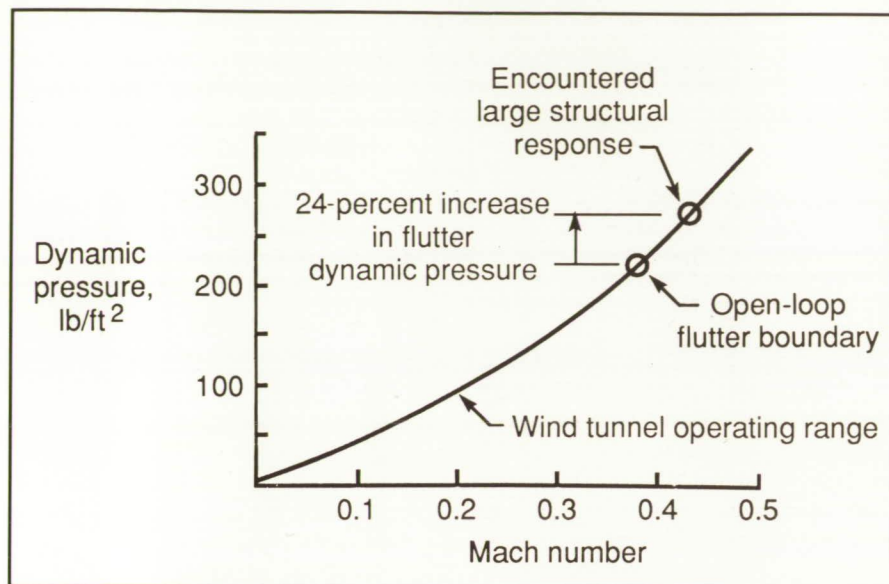
accuracies for all parameters in the model were similarly improved.

In every case studied, the new input design approach showed significant improvement over previous input design methods in terms of achievable parameter accuracies.

(Eugene A. Morelli, 44078)
Flight Systems Directorate

Flutter Suppression on Active Flexible Wing

Design requirements for increased payload and improved fuel efficiency can lead to more flexible aircraft structures with a corresponding increase in the likelihood of encountering flutter. Active flutter suppression can be used to delay the onset of flutter, and it offers a method to expand the flight envelope. The objective of this research has been to design a flutter suppression system (FSS) and experimentally demon-



Wind tunnel test results of flutter suppression system for AFW.

strate the ability to delay significantly the onset of flutter.

A full-span, active flexible wing (AFW) wind tunnel model of an advanced aircraft concept was used as a test bed. A linear mathematical model of the wind tunnel model was developed for use in the design of the FSS. Two flutter modes, one symmetric and one antisymmetric, were predicted to occur during the wind tunnel test. The FSS was designed to stabilize both modes and increase the flutter dynamic pressure by 30 percent. A secondary objective of the designers was to accomplish this with a low-complexity controller. The selected design method employed root locus and Nyquist techniques and relied heavily on a fundamental physical understanding of the flutter mechanism and its relationship to the controller dynamics. Specifically, the design approach placed controller transfer function poles and zeros to take advantage of natural variations in the dynamic properties of the vehicle with changes in dynamic pressure. The AFW model was "flown" in the Transonic Dynamics Tunnel (TDT) at Langley Research Center to evaluate the validity of the mathematical model, identify flutter

boundaries, and test the FSS.

The FSS was shown to successfully stabilize the vehicle, despite inaccuracies in the linear mathematical model used in the design, to a dynamic pressure 24 percent above open-loop flutter. While key aspects of the flutter mechanism were represented in the mathematical model of the AFW, errors existed in the predicted flutter frequency and flutter dynamic pressure. However, the FSS was shown to be robust to these errors, and both symmetric and antisymmetric flutter modes were able to be suppressed. Unfortunately, turbulence in the wind tunnel induced structural deformations in the model that exceeded preset safety limits, and the experiment was terminated before a 30-percent increase in flutter dynamic pressure was attained. At the final test condition, however, the FSS was still stabilizing the flutter modes with commanded control surface deflections and rates well within allowable limits.

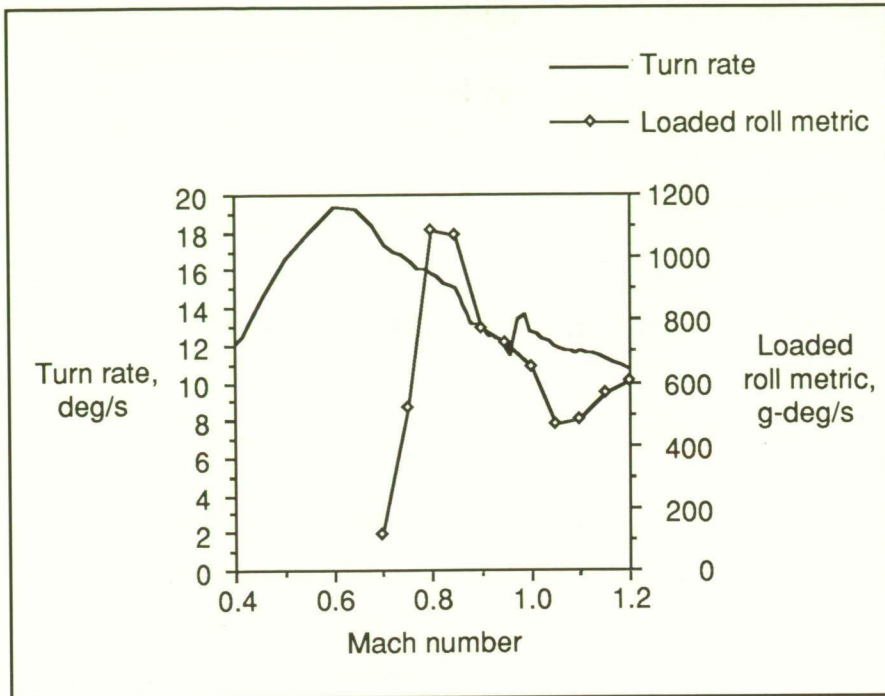
(Martin R. Waszak, 44015)
Flight Systems Directorate

Candidate Control Design Metrics for Agile Fighter

Success in the fighter combat arena of the future will demand increased capabilities from aircraft technology. Enhanced maneuverability and controllability throughout a greatly expanded flight envelope is expected to be one of the major requirements. This enhancement is commonly referred to as agility, and designing to provide agility represents a serious challenge for the flight controls engineer. For example, specialized design techniques capable of translating advanced air combat maneuvering requirements into aircraft control design metrics are needed. The objective of this work is to define agility metrics that might be useful as performance criteria in designing the aircraft flight control system.

As a first step toward developing an agility-based control system design methodology, a large set of potential metrics was identified. Corresponding to each metric, a benchmark maneuver (BKM) was defined. Each BKM is a generic flight task that is used to characterize a particular required capability of interest, e.g., rapid rolling about the velocity vector. Real-time, piloted simulation studies using the postulated metrics and BKM were conducted using the F/A-18 simulation on the Langley Differential Maneuvering Simulator. Additional results were obtained through analytical optimization studies to establish certain dynamic flight conditions.

The primary contributions of this work are the documentation and the evaluation of a large set of potential control design metrics and their corresponding benchmark maneuvers for incorporating agility into advanced fighter designs. These agility metrics provide the aircraft control designer with a tool for comparing different designs or making design



Maximum turn rate and loaded roll capability versus Mach number.

trades within a single system. Also, the numerical evaluations obtained establish an agility benchmark against which new agile designs can be measured. Two metrics are shown as examples in the figure. Through the use of these metrics, the typically competing relationship between loaded roll and flight path turning capability is highlighted. The figure indicates that neither capability is maximized at the same point with respect to Mach number, although this is desirable for agility. This example illustrates one design tradeoff typical in aircraft design and is representative of the metrics studied. These metrics are expected to be of value to control designers in adjusting system dynamics for optimum agility.

(Patrick C. Murphy, 44071)
Flight Systems Directorate

Simulation Study of High-Angle-of-Attack Nose-Down Pitch Control Requirements

A cooperative program between NASA and the U.S. Navy is being conducted to develop high-angle-of-attack nose-down control requirements that can be used as design guidelines for advanced combat aircraft that incorporate relaxed static stability in pitch. Successful application of relaxed static stability in pitch requires design guidelines for nose-down control requirements early in the development process. As part of this research, a piloted simulation study is under way using the Langley Differential Maneuvering Simulator to develop and assess candidate guidelines (as shown in the first figure). The simulation process involves specific assessment maneuvers and pilot rating approaches developed for this application. A key element of the investigation is a study involving systematic variations of critical parameters affecting nose-



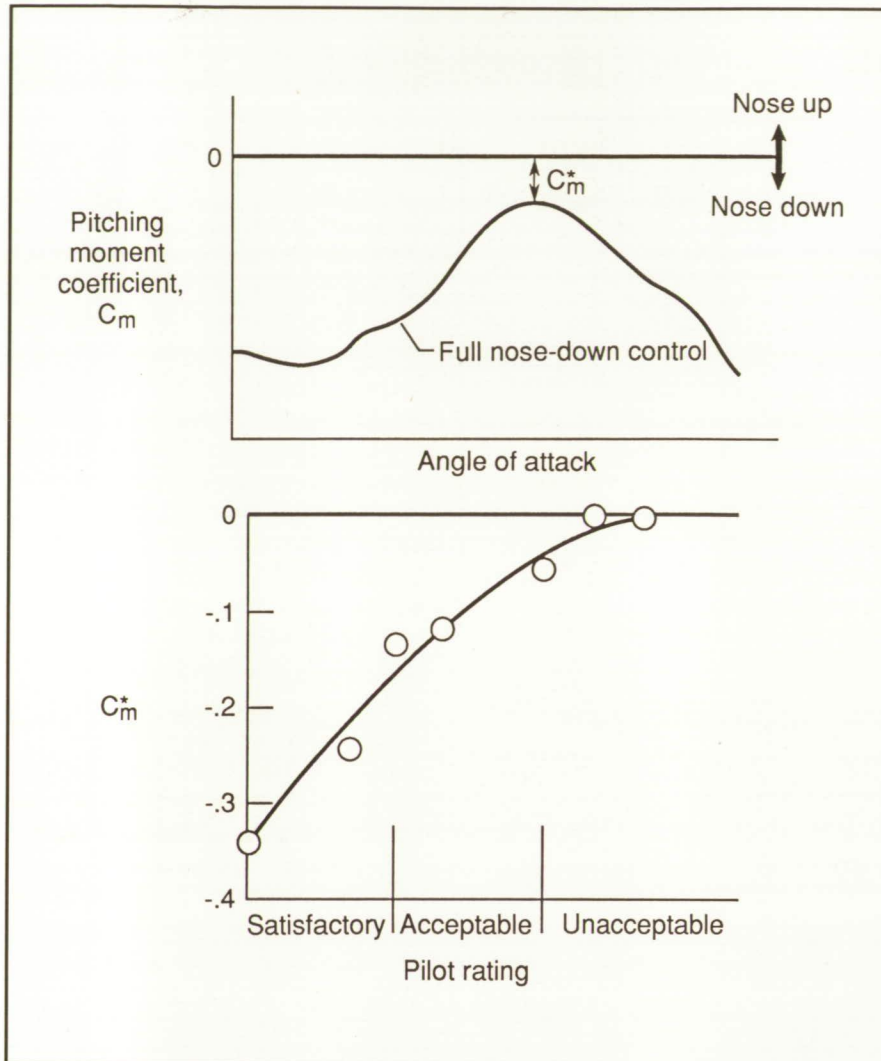
View of Differential Maneuvering Simulator cockpit and visual display.

L-90-5138

Interference Flows About Missile-Sting Assemblies Near and Inside Cavities

The internal carriage of stores by military aircraft offers possible reductions in aerodynamic drag and radar observability. Trade studies of this option should consider the aircraft and the stores together. The Viscous Internal Store Carriage Code (VISCC) has been developed with this motivation. The VISCC consists of a grid generation code, a domain decomposition code, a boundary-layer code, a solver of the flow equations, an interpolation code, and some postprocessing routines. Three-dimensional, Reynolds-averaged, unsteady, compressible, and complete Navier-Stokes equations are solved by an implicit, upwind-biased, approximately factored, finite-volume multigrid method. The domain is decomposed by a hybrid method that utilizes the combined advantages of the overlapped, zonal, and block-structured grids. An algebraic turbulence model is used to represent the Reynolds stresses for the time-accurate computations of these unsteady flows.

Wind tunnel data on two configurations have been obtained for validation of the VISCC code. One configuration consisted of a simple sharp, ogive-nosed cylinder attached to an L-shaped, offset sting. This model was placed first inside then immediately outside of a rectangular cavity. The flow was unsteady and turbulent at $M = 1.65$. The time-averaged computed pressure distributions compared successfully with the experimental data obtained both in the cavity and on the cylinder. Results for the second more complex configuration are shown in the figure. This model consisted of a blunt-nose cylinder with four tail fins attached to a curved, offset sting. The computed pressure distributions are shown to be in excellent agreement with the



Minimum nose-down pitch control (C_m^*) requirements.

down control capability, particularly the minimum level available at high angles of attack.

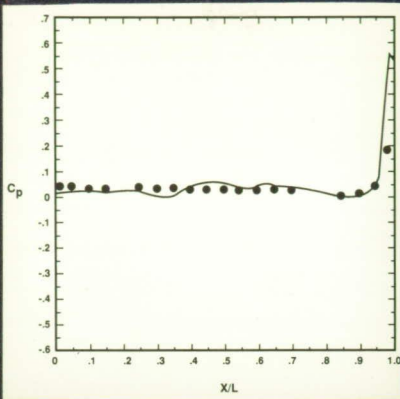
A comprehensive data base of piloted simulation results has been generated to enable the assessment and development of potential guidelines. The results were based on analysis of flight motions and pilot comments and ratings obtained during the parametric study. These results show a strong correlation of pilot rating to the airplane short-term pitch response to nose-down commands applied at high-angle-of-attack conditions (as shown in the second figure). Using these data, candidate

design guidelines are being formulated, assessed, and refined. A limited flight evaluation/validation program on a test F-18 airplane will be conducted, and detailed flight testing of proposed guidelines using the NASA High-Alpha Research Vehicle (HARV) is planned. (Marilyn Ogburn, 41175) Aeronautics Directorate

MACH NUMBER

CONTOUR LEVELS

0.00000
0.20000
0.40000
0.60000
0.80000
1.00000
1.20000
1.40000
1.60000
1.80000
2.00000
2.20000
2.40000
2.60000
2.80000
3.00000
3.20000



2.750 MACH
0.00 DEG ALPHA
 $4.35 \times 10^{+6}$ Re
1.0 TIME
122x40x50 GRID 1
129x17x33 GRID 2
129x33x33 GRID 3
129x17x33 GRID 4
91x31x45 GRID 5

Results for flow past missile model inside cavity.

experimental data. The computed Mach number contours indicate the complex nature of the flow and contribute to the understanding of the physical fundamentals underlying these unsteady, interference flows.

Due to the generality of this computational method, it can be used for many other applications that involve interference flows past multiple and nonsimilar bodies. (Oktay Baysal and David S. Miller, 45568)

Aeronautics Directorate

Forebody Controls Research

One factor that limits the maneuvering effectiveness of current fighter aircraft is the degradation of aerodynamic control effectiveness at stall and poststall angles of attack. As a result, a number of new technologies are being developed, including advanced aerodynamic and propulsive control concepts, to enhance the maneuverability and agility of future fighter aircraft. One of these concepts, the use of actuated strakes on the aircraft forebody, is designed to take advantage of the existence of a powerful forebody vortex flow field at high angles of attack. The actuated forebody strakes are designed to control this strong vortex flow field and provide enhanced yaw control at high angles of attack where a conventional aircraft rudder becomes ineffective.

Research is currently under way to develop and demonstrate this concept during flight tests of the F-18 HARV. The photograph shows a 16-percent scale model of the F-18 which has been modified to include a pair of conformal actuated forebody strakes. Earlier static and free-flight wind tunnel tests conducted in the Langley 30- by 60-Foot Tunnel have shown promising results. During the wind tunnel free-flight tests, the model with the actuated forebody strakes was significantly more maneuverable and was found to be controllable to much higher angles of attack than the model without the actuated strakes. More recently, engineering studies have been conducted to determine the modifications that would be required to implement the actuated strakes on the F-18 HARV aircraft. Additional supporting wind tunnel tests have been conducted to determine the strake hinge moments and airframe loads. The results from these studies



Photograph of 16-percent scale F-18 free-flight model incorporating actuated forebody strakes.

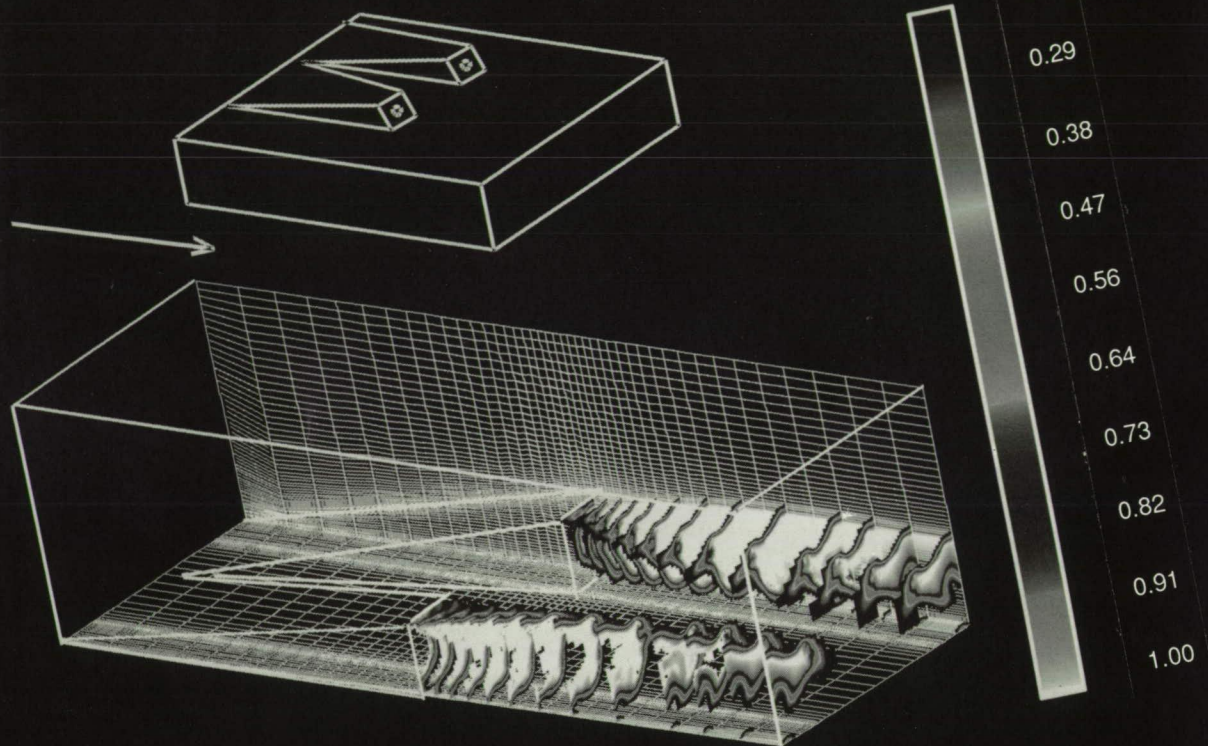
L-88-3358

indicate that it will be possible to modify the F-18 HARV with conformal actuated forebody strakes similar to those tested on the 16-percent scale model.

(Daniel G. Murri, 41160)
Aeronautics Directorate

ORIGINAL PAGE
BLACK AND WHITE PHOTOGRAPH

Hypersonic and Transatmospheric Vehicles



Low-Energy Gamma Ray System for Monitoring Slush Hydrogen

Slush hydrogen is being considered as a propellant for the National Aero-Space Plane (NASP) because it has a low-mass, high-energy content and lower volume than liquid hydrogen. However, no suitable technique currently is available for monitoring the quantity and flow rate of a fluid with a phase configuration that is changing continuously. The feasibility of a low-energy gamma ray system for measuring the quantity (mass) and its rate of change for such a fluid has been demonstrated. The system is based on the theory that the mass attenuation coefficient of gamma rays in any chemical compound is independent of its phase.

Five chemical compounds (water, acetic acid, dibromomethane, bromobenzene, and cetyl bromide) were selected to measure their mass attenuation coefficients in standard narrow beam geometry for Cd^{109} gamma rays. Measurements were made separately in gas, liquid, and solid phases and in mixed phases. These measurements demonstrate that the mass attenuation coefficient

for a gamma ray in any chemical compound is independent of its phase or phase fractions in the case of multiphase mixtures. The results are shown in the figure. On the basis of these data, it can be concluded that a lower energy X-ray system based on Fe^{55} (5.9 keV) will be suitable for monitoring slush hydrogen onboard the NASP.

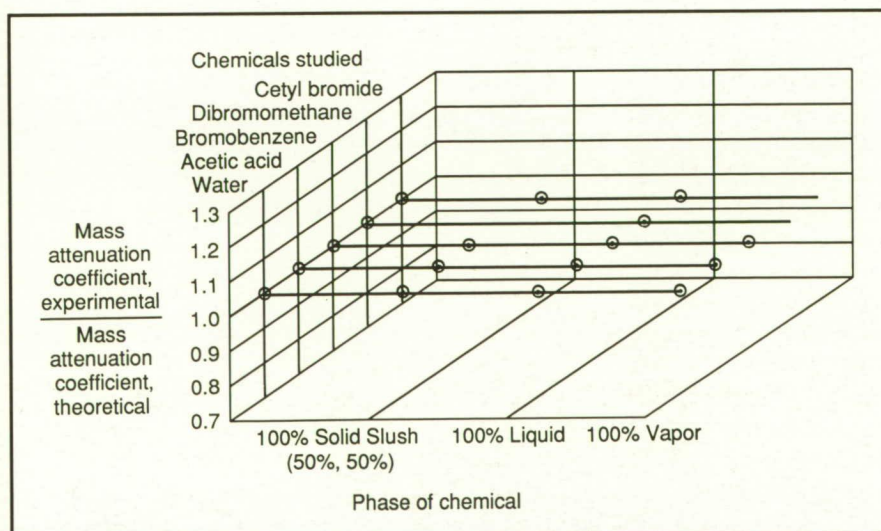
(Jag J. Singh, 44760, and Danny R. Sprinkle)

Electronics Directorate

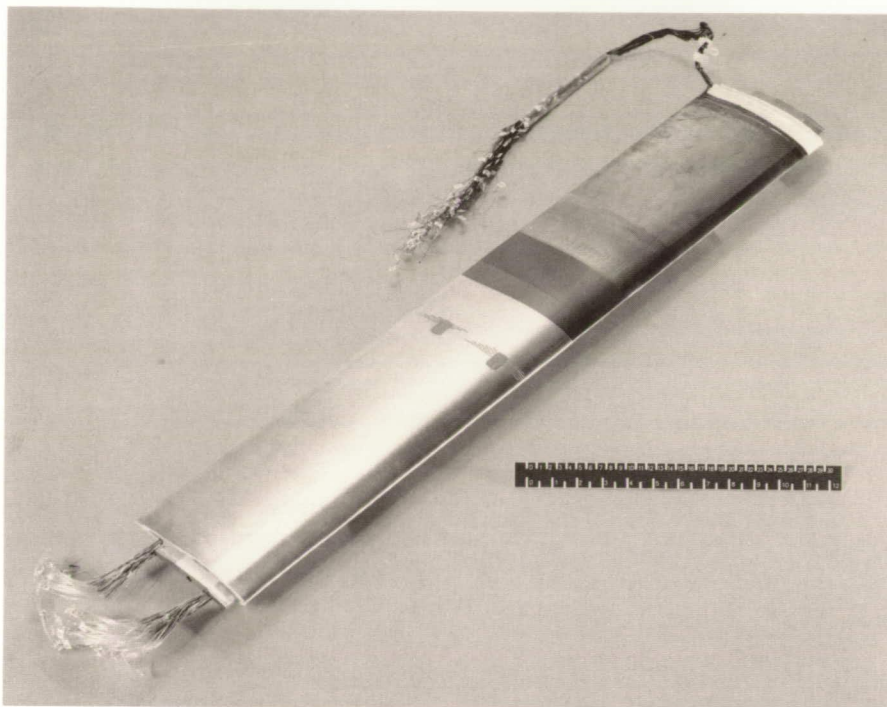
Large Thin-Film Heat-Transfer Sensor Arrays

Significant improvements in the design and fabrication of thin-film heat-transfer-type sensors have been accomplished at Langley Research Center. These improvements have reduced fabrication costs and time and greatly enhanced and broadened wind tunnel flow diagnostics.

Previously, sensors were made individually on separate substrates and attached to the wind tunnel models one at a time. The sensors were mounted in drilled holes at predetermined locations on the



Summary of mass attenuation coefficients in chemicals studied.



Attachable sensor film array for wind tunnel models.

L-88-4881

ing laminar separation and reattachment of a fluid stream (U.S. Patent 4936146). Additionally, these arrays have been used to measure shock-induced laminar separation with and without reattachment; shock-induced turbulent separation with and without reattachment; trailing-edge turbulent separation; leading-edge stagnation; transition location, extent, and intermittency; and boundary-layer instability phenomena, such as Tollmien-Schlichting waves.

(J. Bartlett, 45472)

Systems Engineering and Operations Directorate

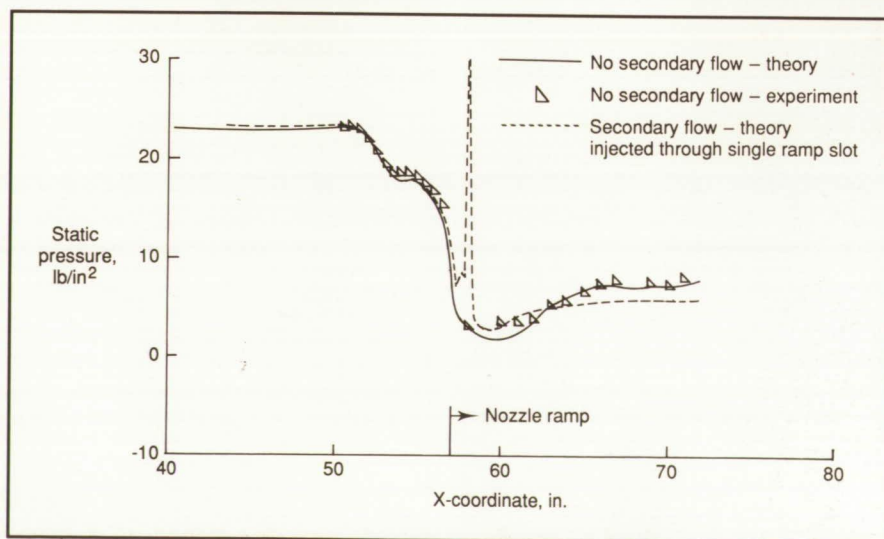
Transonic Numerical Calculations for Nozzle Drag Reduction

model. This technique prevented close spacing of sensors and complicated the change of sensor location or the addition of sensors.

Utilizing computer-aided design (CAD) and microelectronic fabrication technology, thin-film heat-transfer sensors with necessary leads have been produced in an array pattern on a large polymer film. The speed and versatility of CAD enabled significant savings and flexibility in the design and artwork production for sensor array patterns such as lines, grids, sweeps, and arcs. The CAD artwork then was used with microelectronic fabrication technology to produce the pattern in the appropriate thin metal layer on thin polymer films. Significant time and costs also are saved during fabrication because all sensors in a given array are produced simultaneously during one pass through the fabrication process. The completed array can be quickly attached or removed from any two-dimensional model surface in minutes or hours depending upon the attachment procedure.

The rapid design, production, and attachment of these high-density, nonintrusive, specialized arrays have enabled a significant increase in diagnostic power when studying the complex steady and unsteady flow over aerodynamic surfaces. The use of these arrays led to a method and apparatus for simultaneously detect-

Recent tests at the Langley 16-Foot Transonic Tunnel have indicated that generic nozzles applicable to the National Aero-Space Plane suffer from excessive drag at off-design transonic flight conditions. A family of Ames Research Center propulsion codes was obtained from the developers at the Arnold Engineering



Effect of secondary flow on ramp static pressures using PARC3D with Mach number of 1.2 and nozzle pressure ratio of 4.0.

Development Center in order to provide robust computational codes that would be capable of supporting further wind tunnel tests on these and similar configurations. These codes have been verified through comparison of their nozzle ramp static pressures and the just-mentioned wind tunnel data for a number of different nozzle configurations at several transonic Mach numbers and nozzle pressure ratios.

The three-dimensional version of the code, PARC3D, was used for the predictions because the nozzle flow is strongly three dimensional. Areas of secondary blowing from the nozzle ramp, which was the method investigated for drag reduction, were specified as fixed boundaries at appropriate values of temperature and pressure.

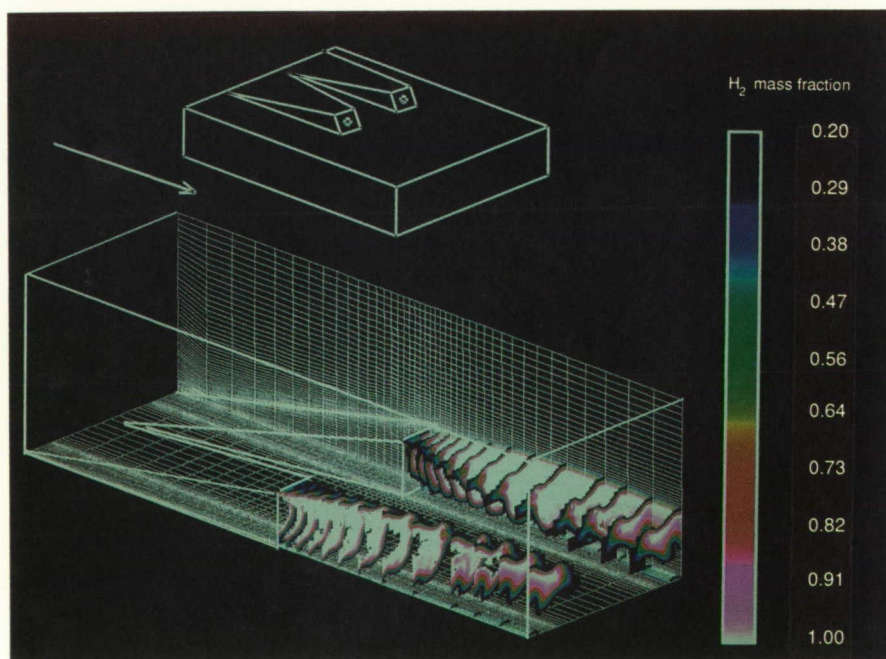
Typical results from this investigation are shown in the figure, in which the secondary blowing is concentrated in a narrow slit spanning the nozzle ramp just downstream of the nozzle exit. The amount of mass flow through the slit is equal to one-quarter of the mass flow through the nozzle, and the slit is choked. The nozzle/ramp configuration for the case shown is a challenging case because the ramp is short and steep and the lack of sidewalls along the ramp makes the flow very three dimensional. With no secondary flow, the agreement between computation and experiment is good, with only a hint of flow separation in the experimental data at the beginning of the ramp. When secondary blowing is introduced, the ramp pressure distribution changes appreciably, even for this modest amount of blowing over such a limited range. In addition to the mass flux, other parameters being considered for model design and test planning are the location of the slit and the total area of mass injection. (Steven F. Yaros, 43050) Aeronautics Directorate

Fuel-Air Mixing Enhancement in Supersonic Combustor

Numerical simulations are used to provide an improved insight into the mechanisms that control the high-speed fuel-air mixing and reacting flows in supersonic combustion ramjet (scramjet) engines. An accurate numerical algorithm is used to solve the equations governing the mixing and chemical reaction of a multicomponent mixture, while a physically realistic chemical kinetics model is used to describe combustion processes occurring in a scramjet combustor. Using knowledge gained from these basic simulations, techniques can be identified and developed for enhancing mixing and reaction in supersonic combustors and improving the overall level of combustion efficiency.

A computer program has been developed that solves the equations governing a multicomponent mixing and reacting flow. This code was

validated against experiments involving both nonreacting and reacting flow fields, and then it was applied in studies of combustor high-speed engine flows. Because mixing is significantly reduced in a scramjet as the combustor Mach number increases with flight Mach number, recent research has been directed toward achieving enhanced fuel-air mixing and combustion efficiency. Alternate combustor fuel injector configurations were designed and studied to evaluate their potential for producing an improved degree of mixing and reaction. One such configuration is shown in the figure. This configuration consists of two swept ramp fuel injectors that introduce gaseous hydrogen fuel from orifices in their bases. The swept ramp sidewalls induce streamwise vorticity into the inlet air passing the ramps, and this vorticity enhances fuel-air mixing downstream of the injectors. The resulting hydrogen-fuel mass-fraction distribution, keyed to the color bar, also is shown in the figure. Without enhancement, the fuel jet would spread only slightly



Enhanced-mixing fuel injector showing computed hydrogen mass fraction. L-90-8035

over the distance studied. With enhancement, however, the fuel jets are captured by the vortices and spread well across the channel downstream of the ramps. This dramatic improvement in fuel-air mixing results in a significant improvement in combustion efficiency.

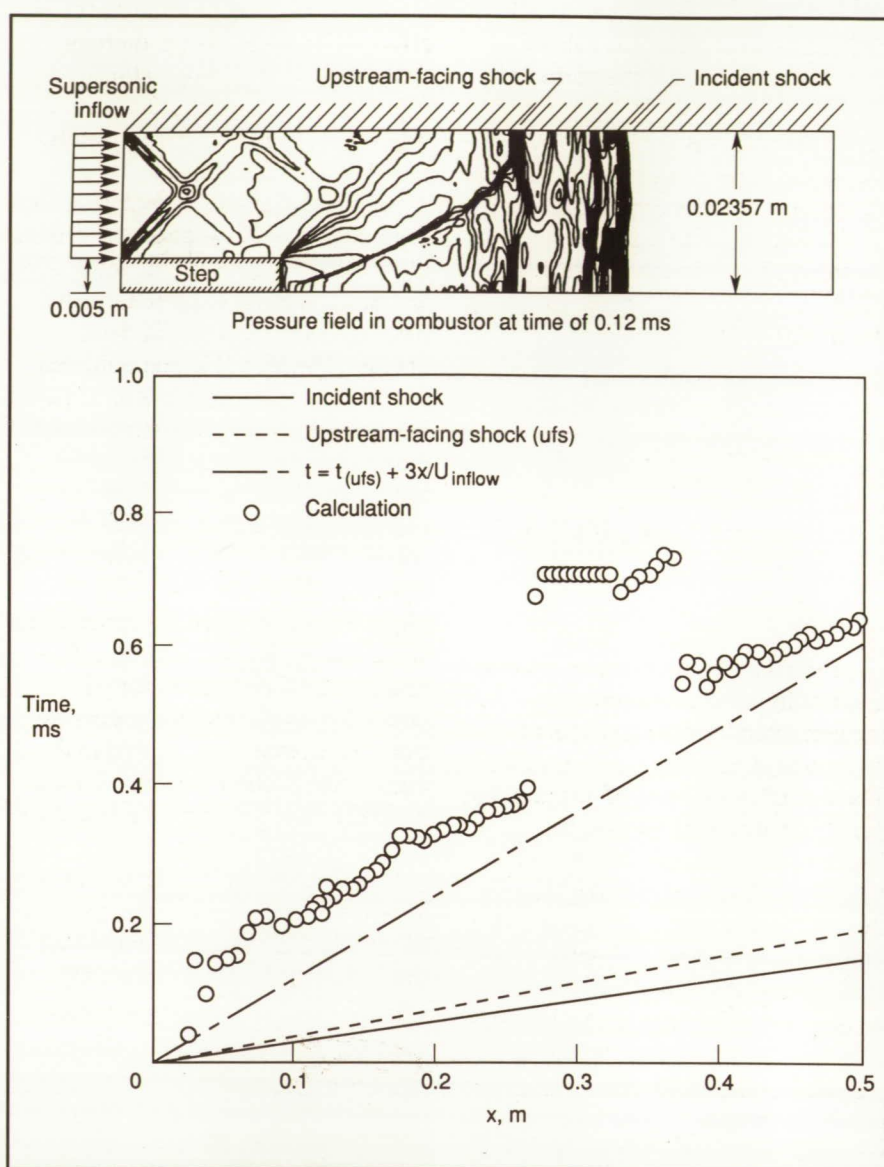
Work is now under way to optimize the degree of enhancement that can be achieved from the fuel injector configuration considered in this study. Other injector configurations that utilize shock excitation and vortex bursting for enhancement also will be examined.

(J. Philip Drummond, 42298, Mark H. Carpenter, and David W. Riggins)
Aeronautics Directorate

Flow Establishment in Generic Scramjet Combustor

Experimental studies of supersonic combustor components and propulsion systems for transatmospheric vehicles must rely on impulse facilities with flow duration times of approximately 1 ms to achieve high-energy air flows to simulate flight at speeds above Mach 8. The quasi-steady nature of the flow is of concern because the flow processes important to the mixing and combustion may not have time to become fully established. The objective of this research is to examine numerically the time for flow establishment in the vicinity of a fuel injector (without injection) for a generic scramjet combustor in a typical shock tunnel facility.

The supersonic laminar flow through a two-dimensional combustor geometry was computed using the time-accurate Navier-Stokes solver



Establishment times for wall heat flux with steady inflow.

SPARK. The dimensions of the combustor, including a rearward-facing step that can serve a fuel injector, are shown in the figure with the calculated static pressure field at 0.12 ms. The flow establishment time was determined for several parameters; these parameters include wall static pressure, boundary-layer thickness at the step, size of the recirculation zone in the step base, and viscous effects (skin friction and heat flux). Generally, wall static pressure is established first, and viscous-dominated features of the

flow (such as heat transfer) require the longest time to establish. As an example, the calculated times at each station in the combustor at which the wall heat flux becomes established are shown by the symbols in the figure. The dashed line represents the passage of the initial starting pulse of test gas through the combustor. The broken line corresponds to events that occur at three times the bulk flow time through the domain, which is the widely used rule of thumb for the flow establishment time. The numerical model indicates

an establishment time for the wall heat flux greater than this rule of thumb, particularly in the region of shock reflection ($x = 0.3$ m). Additional calculations are under way to assess the impact of transient inflow conditions with fuel injection.

(R. C. Roger, 46239, E. H. Weidner, P. A. Jacobs, and R. D. Bittner)

Aeronautics Directorate

Dynamic Response of Initially Deformed Composite Plates Using Finite Elements

The recent interest in the development of hypersonic aircraft has created a need for the analysis of structures at very high temperatures. The dynamic response of aircraft skin panels depends not only on the imposed thermal and mechanical loads but also on any initial deformations. The effect of these parameters on the response must be well understood in order to maximize the fatigue life. The purpose of this work

is to investigate the simultaneous effect of large initial and thermal deformations and temperature-dependent material properties on the free vibration of composite panels.

A finite-element formulation has been developed to analyze the effects of moderately large initial deflections and large thermal deformations on the frequency response of these panels. The Von Kármán nonlinear strain-displacement relations are used to derive the stiffness matrices, and the principle of virtual work is applied to obtain the equations of motion. The resulting system is solved in a two-step procedure. First, a Newton-Raphson iterative technique is used to solve the incremental static system for the thermal deformation based on a given initial deflection and temperature distribution. This result then is used in the eigenvalue problem to solve for the natural frequencies and mode shapes.

Studies were first carried out on aluminum panels to test the accuracy of the approach. The postbuckling deflection due to thermal loading compared favorably with existing

classical solutions. The figure compares the frequency ratios of the panel with various initial deflections and shows that as the initial deflection increases, the decrease in frequency due to a temperature rise vanishes.

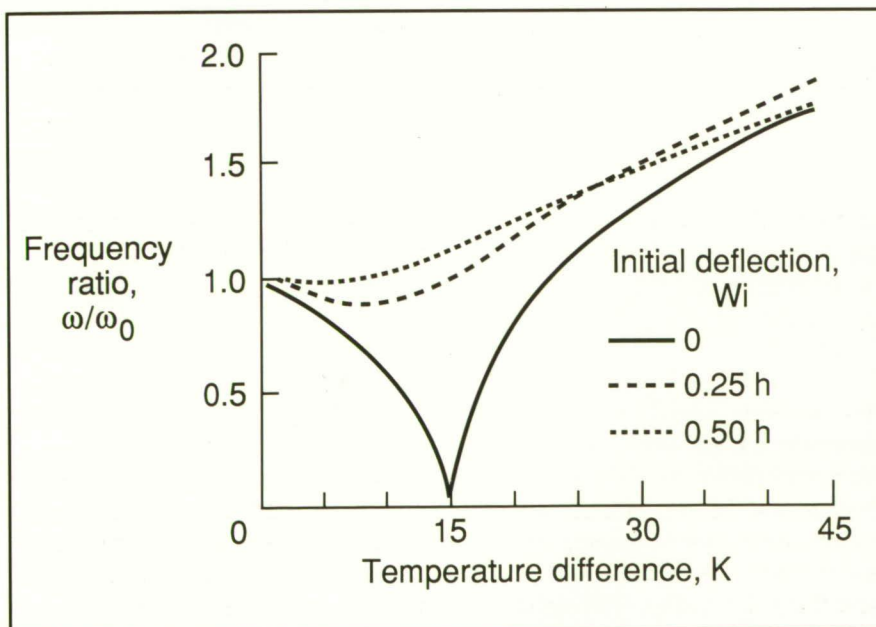
Modification of the formulation is presently under way for the analysis of composite panels. The forced vibration response of these panels due to random acoustic loading then will be analyzed and compared with experimental data obtained from the Thermal Acoustic Fatigue Apparatus (TAFA) at Langley Research Center. The application of this analysis to hypersonic vehicle design will help in maximizing the fatigue life.

(Stephen A. Rizzi, 43599)

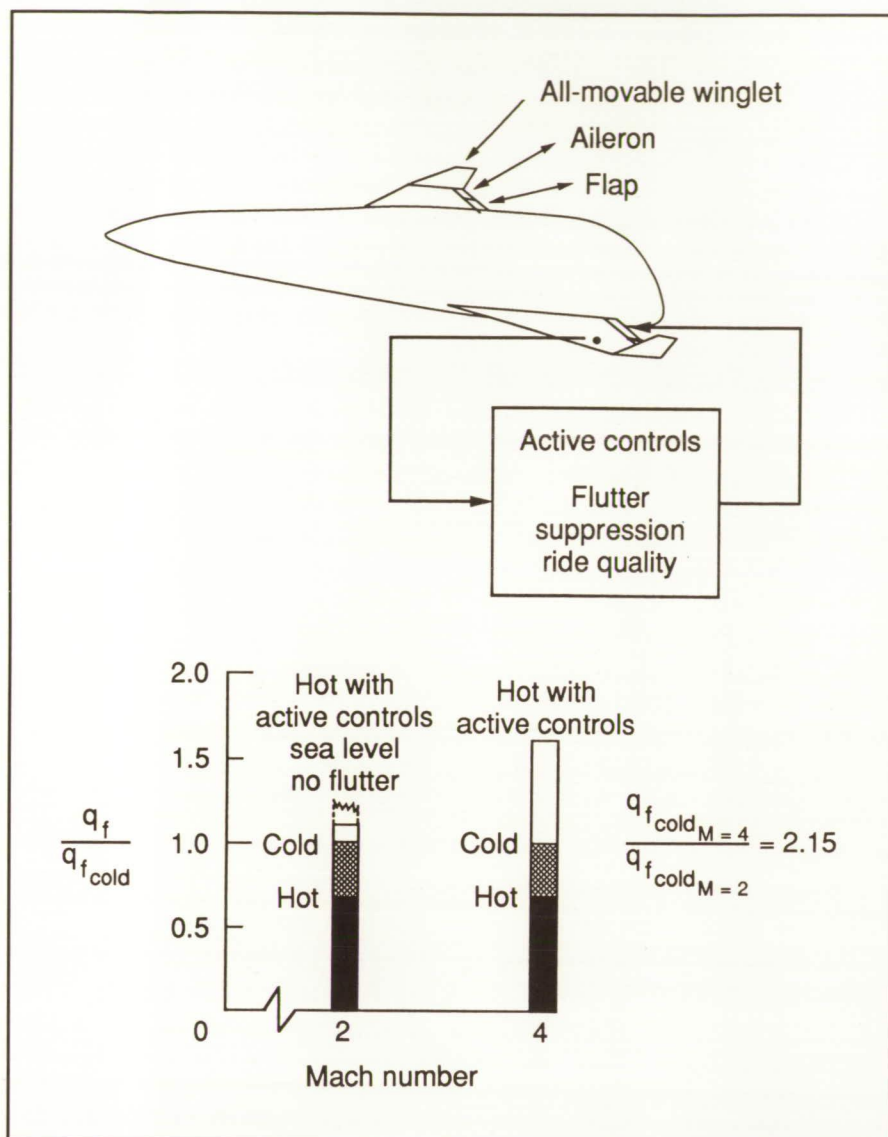
Structures Directorate

Reduction of Thermal Heating Effects on Flutter by Aeroservoelasticity Method

Atmospheric flight at high speeds causes large thermal loads due to aerodynamic heating. These large thermal loads can soften (destiffen) the structure through changes in structural material properties with temperature and through material stress level changes caused by thermal gradients in built-up structural components. Because the more flexible structure can significantly affect the vehicle flutter characteristics and aeroelastic responses, an analysis procedure has been developed to evaluate these concerns. For a given set of thermal loads (radiation equilibrium temperatures) determined for a particular aircraft geometry, the hot and cold vehicle structural stiffnesses are obtained using a finite-



Effect of temperature on natural frequency of panels with initial deflections.



Flutter results for generic hypersonic vehicle. (The symbol q_f is flutter dynamic pressure and $q_{f,cold}$ is flutter dynamic pressure of unheated vehicle.)

vibration mode shapes. Four sets of unsteady generalized aerodynamic forces (Mach 2 cold, Mach 4 cold, Mach 4 hot, and Mach 2 hot using the Mach 4 temperature distribution simulating a vehicle slowing from Mach 4) were computed. The effects of thermal loads on flutter are a 25-percent to 30-percent reduction in flutter dynamic pressure. A flutter suppression active control law was designed to recover the lost flutter dynamic pressure. This control law used wing and fuselage acceleration feedback signals to move the wing flap and aileron to suppress the flutter. The improvement in flutter dynamic pressure using the same control law at both Mach 2 and 4 was dramatic. Because a single control law was found to improve flutter dynamic pressure over a relatively large Mach number range, complex, highly gain-scheduled control laws may not be necessary.

The results of this study clearly show that application of active control technology to hypersonic aircraft can be useful for overcoming adverse structural response and flutter characteristics caused by aerodynamic heating of the vehicle structure.

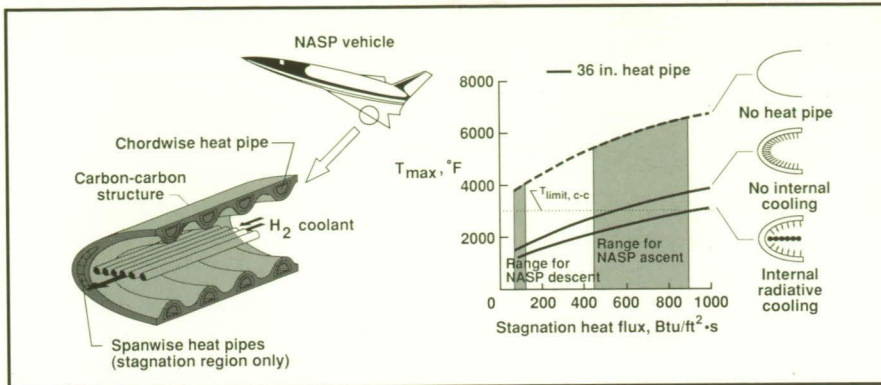
(Michael G. Gilbert, Jennifer Heeg, and Anthony S. Pototzky, 42839) Structures Directorate

element structural model. Structural vibration modes for the hot and cold structure are computed and used with Piston Theory unsteady aerodynamics. Detailed flutter analyses are performed for both the hot and cold structures, and they are compared to determine the changes in flutter dynamic pressure due to the thermal loads. Then, existing aeroservoelastic (ASE) design methods are used to recover the lost flutter dynamic pressure.

Some results obtained by applying this methodology to a generic hypersonic aircraft configuration are shown in the figure. This configuration consists of an elliptical cross-section body with delta wings, flaps, and ailerons. A finite-element model structural representation was developed for the configuration using titanium aluminide structural material properties. Radiation equilibrium temperature distributions were obtained for a Mach 4 flight condition and applied to the finite-element model to determine hot structure

Analysis of Carbon-Carbon/Heat-Pipe Wing Leading Edge

The use of carbon-carbon structures under the high thermal loads in future hypersonic vehicles is limited in today's technology by the oxidation protective coating to temperatures below 2800°F. Concepts developed earlier using embedded heat pipes and radiative cooling have been analyzed in regard to their potential to provide a simple, reliable,



Wing design concepts and analysis results.

L-89-13907

fail-safe, and lightweight wing leading edge to withstand the high heat flux environment.

The use of chordwise heat pipes, smaller spanwise heat pipes, and internal radiative cooling is shown in the figure. Using the Engineering Analysis Language (EAL) and a three-dimensional thermal finite-element model, parametric studies have been performed. The maximum surface temperature T_{\max} of the leading edge as a function of stagnation heat flux is shown in the figure for three cases; these cases include no heat pipes, a heat-pipe-cooled leading edge with no internal cooling, and a heat-pipe-cooled leading edge with internal radiative cooling. Results show that an uncooled heat-pipe concept can reduce peak temperatures for heat fluxes below 500 Btu/ft²·s. At higher heating levels, internal radiative cooling during ascent is required to produce a feasible design. Internal cooling will not be required during descent because the curve for a heat-pipe leading edge with no internal cooling results in maximum temperatures below 2000°F when extrapolated to descent heat flux levels.

The feasibility has been established analytically for a reliable/redundant carbon-carbon/heat-pipe leading-edge design for future

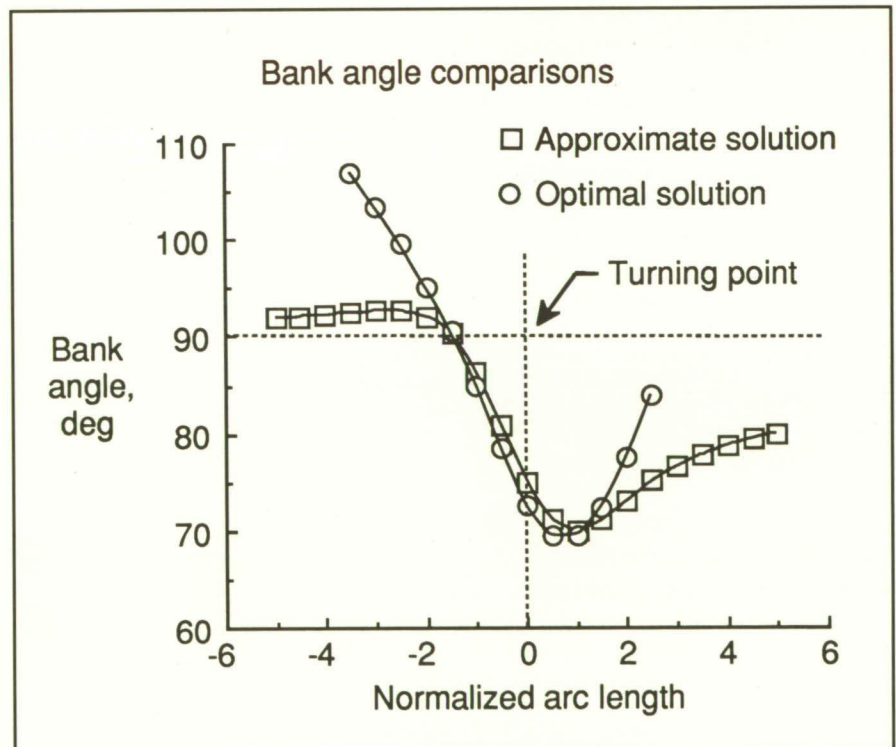
hypersonic vehicles. Further analysis and tests are expected to add to the technology base for advanced aerospace vehicles.

(David E. Glass and Charles J. Camarda, 45436)

Structures Directorate

Guidance Analysis of Aeroglide Orbital Plane Change Maneuver

Both in-plane and out-of-plane aerodynamically assisted orbit transfers have been studied for a number of years because of their fuel efficiency relative to all propulsive (Hohmann) transfers. This research is concerned with the use of aerodynamic lift and bank angle, as opposed to propulsive forces, for orbital plane change maneuvers. In order to realize the full efficiency of these aerodynamic maneuvers, onboard guidance schemes must be developed to steer the vehicle along an approximately optimal path. The purpose of this research was to develop a computationally efficient, sufficiently accurate solution to this problem such that it could be accomplished onboard the orbiting vehicle. The vehicle must use its lift force and bank angle to cause the vehicle to change its heading, corresponding to a desired orbital plane change, while



Comparison of approximate and numerical optimal bank angle controls.

minimizing the amount of energy lost due to aerodynamic drag.

To simplify the solution to this difficult problem, a mathematical approach was developed which uses equation-of-motion simplifications and analytic, singular perturbation techniques of classical mathematics. Development and analysis of the governing equations of motion and optimality conditions led to a particular form of differential equation from which approximately optimal values of bank angle and lift-to-drag ratio could be determined. Asymptotic solutions to this form of differential equation fall under the category of turning point problems in the literature of quantum mechanics.

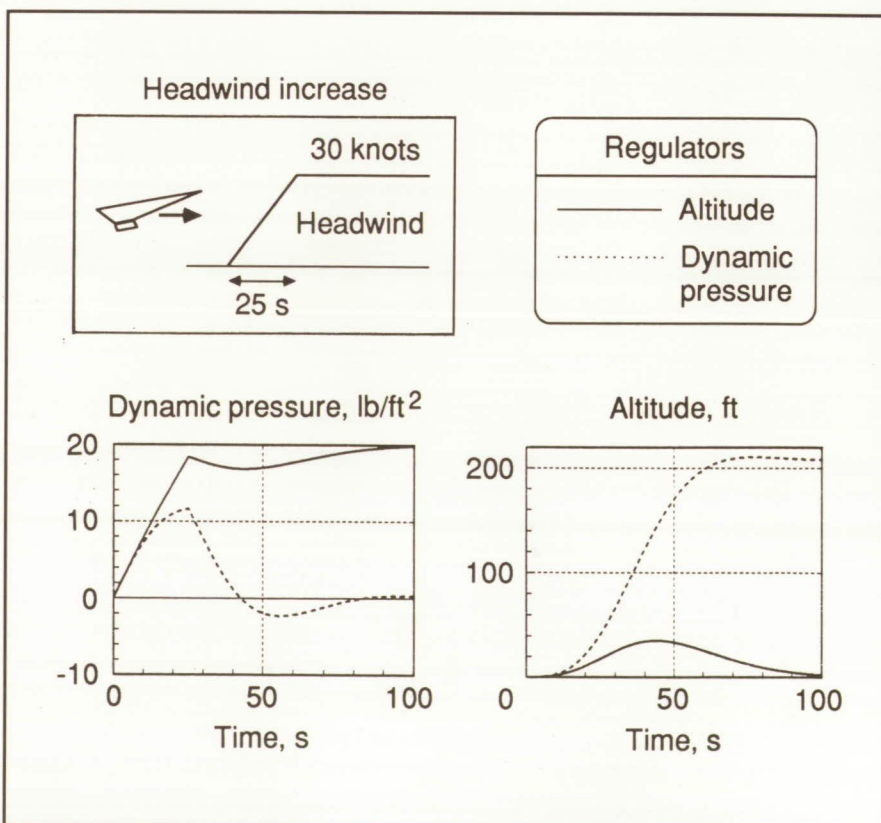
The validity of this problem approach is indicated in the figure in which the optimal bank angle is compared to the approximate bank angle as a function of normalized arc length (one unit corresponds to 3.5° of actual arc length). In the vicinity of a turning point, the approximate solution can be described analytically, and it agrees well with the optimal solution. But, the approximation deteriorates away from the turning point, as predicted by the theory. The theory also predicts that the lift-to-drag ratio asymptotically approaches its maximum value as the vehicle nears the edge of the atmosphere, both at entry and exit. This capability of the theory to analytically and qualitatively describe the optimal control behavior is an important advantage for developing onboard guidance algorithms. These results represent progress toward the simplification of a complicated optimal control problem for changing the orbital plane of a vehicle. (Christopher Gracey, 44019) Flight Systems Directorate

Regulator Designs for Hypersonic Vehicles

The flight and propulsion systems of vehicles operating in the hypersonic regime will be interactively coupled to a greater degree than previously experienced. Effective integration of these systems will, therefore, be critical to vehicle performance. The objective of the present research is to develop the rudiments of several control system designs. These designs are capable of tracking guidance and navigation commands and controlling flight condition perturbations due to atmospheric disturbances such that they remain within propulsion system tolerances.

Integrated control strategies (i.e., those that simultaneously command lift and thrust) were evaluated to investigate the merits of various

feedback combinations. Simulation results demonstrate that selection of control strategy and feedback variables significantly affects the transient behavior of the vehicle in the presence of atmospheric disturbances. Example results in the figure show a comparison of responses to a 30-knot headwind for two regulator designs (one that utilizes altitude error feedback and one that utilizes dynamic pressure error feedback). For the altitude error regulator, the vehicle experiences atmospheric disturbances as essentially unopposed variations in dynamic pressure while modulating lift to hold vertical excursions to a minimum. For the same disturbance, the dynamic pressure regulator acts to modulate lift to cause altitude variations, thus moving the vehicle into regions of different air density, thereby driving dynamic pressure errors to zero. In both cases, thrust modulation controls velocity perturbations. The dynamic



Dynamic pressure and altitude variations in response to headwind.

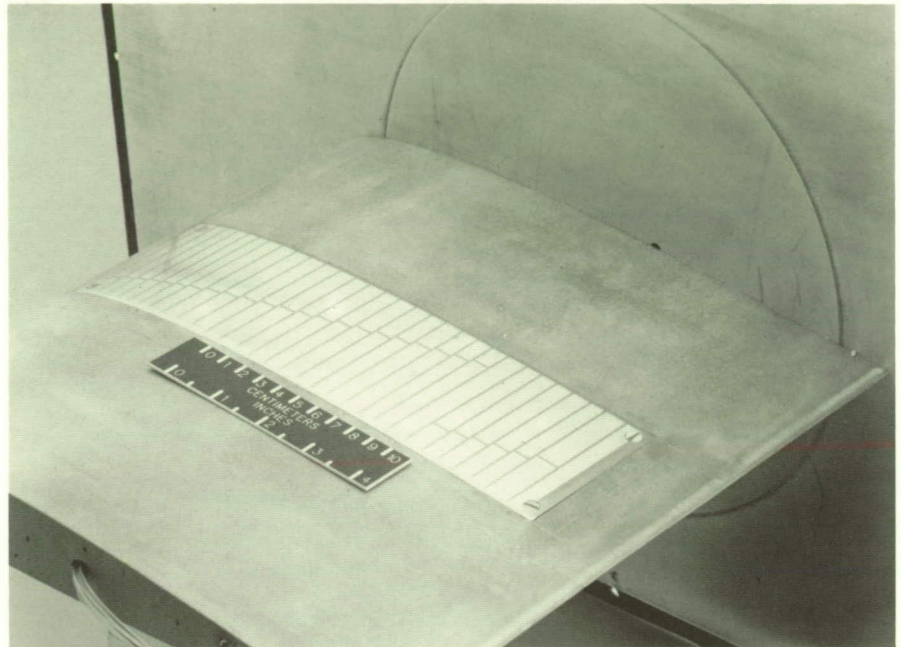
pressure regulators were found to work well in still, ideal atmospheres, but they are excessively active in turbulent conditions; the altitude regulators generally yield a smoother response with smaller transients. Other regulator designs (e.g., with energy and velocity feedback) which show similar advantages and disadvantages were formulated; however, the altitude regulators appear to be the most viable option.

(Frederick J. Lallman, 44020, and David L. Raney)
Flight Systems Directorate

Direct-Deposit Thin-Film Sensors for 3-D Surfaces

Thin-film heat-transfer-type sensors are a powerful, nonintrusive flow diagnostic device for studying complex steady and unsteady flow structures over aerodynamic surfaces. Until recently sensors were made individually on separate substrates and could not be used on three-dimensional (3-D) surfaces at very high Reynolds numbers. The inability to economically produce a contour match on the sensor substrate and the resulting mismatch during installation prevented attainment of the necessary surface smoothness to avoid unwanted flow disturbances at the sensor sites.

Fabrication technology has been developed to enable the direct deposition of thin-film sensors on a model and to avoid the previous fabrication and installation limitations. First, a decomposition technique for a highly uniform, ultra-thin dielectric layer was developed to electrically insulate the sensors from the metal model. Then, the technology to directly deposit sensors on the dielectric layer was developed. The direct-deposit technology also has been used on composite model



Direct-deposit thin-film sensors.

L-87-1747

surfaces and is adaptable to cryogenic test conditions. At present, sensors can be deposited on one-piece models up to 0.3 m in size. Sensors also can be deposited on removable inserts up to 0.3 m in size. These inserts can be used on larger models or used for flight applications.

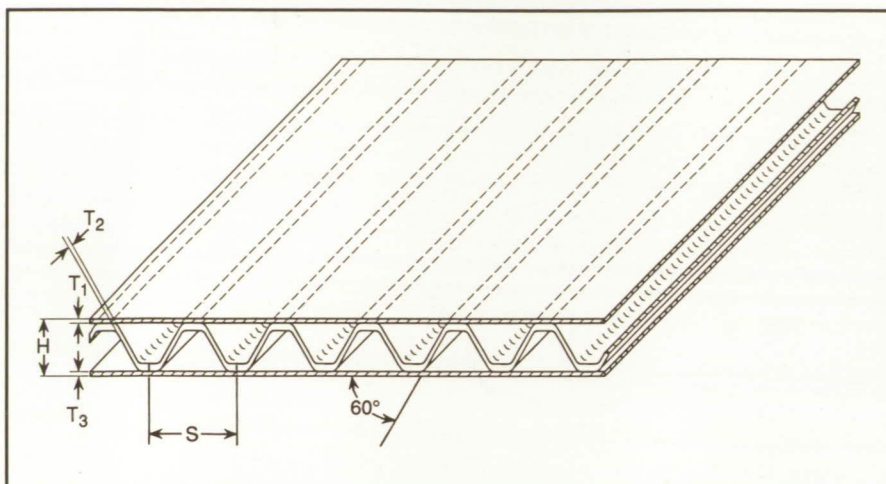
(J. Bartlett, 45472)
Systems Engineering and Operations Directorate

Update and Improvement of Finite-Element Weight Prediction Code

A computer code for structural sizing and weight prediction of conceptual designs for hypersonic vehicles was updated to enhance its capabilities and user friendliness. Previously called NASSIZER, the code was renamed ST-SIZE to better reflect its capability as a structural/thermal sizing tool.

While suitable for all types of aerospace structure, ST-SIZE is designed for hypersonic aircraft in which the critical flight loads are combined with demanding thermal environments. The ST-SIZE code, based on the finite-element method, was improved by including a capability for automatic iteration of the sizing process with the finite-element solution cycle, more detailed reporting of weights and sizing results, and the addition of new or improved structural sections.

Multiple-load cases are fully supported, with each case having its own temperature set. The appropriate temperature-dependent material properties and temperature-induced element loads are combined with mechanical and inertial forces to yield a structural design for each different load case applied. A new set of elemental stiffnesses is computed for the critical (heaviest) load case, and a new finite-element solution may be started to obtain



Truss-core sandwich shown with sizing variables.

revised elemental forces. This procedure may now be automatically iterated for several design cycles before the user intervenes to check the solution.

Enhanced reporting of weights and sizing results was added to assist the user in reviewing the progress of a solution, including the ability to look at individual results for pre-defined components. A fully stressed design is achieved by iterating the solution process until it converges, within the constraints applied by the user.

A number of changes were made to enhance the structural sections available in the code, including the addition of a new section, the truss-core sandwich. The figure illustrates the variables that define the truss-core geometry and provide the basis for its design by the sizing method used in the code. This new section includes strength checks for yield and ultimate stress and stability checks for panel buckling and various forms of local buckling. The stiffness formulation of this element includes membrane, bending, membrane/bending coupling, and transverse shear coupling terms. All of the structural sections, including the truss-core sandwich, may be con-

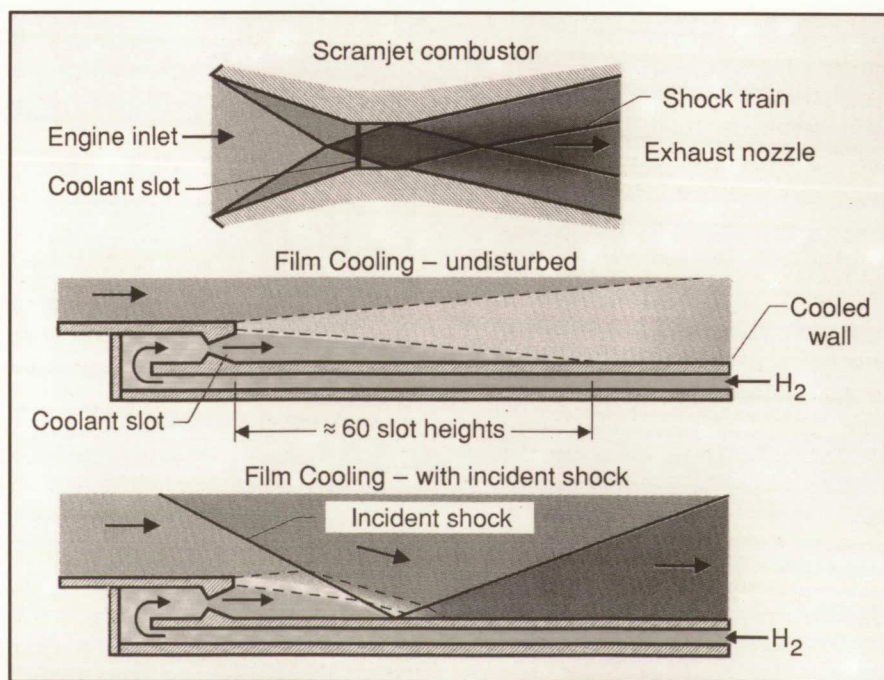
structed of isotropic or composite materials.

The ST-SIZE code is being "beta" tested prior to its first release. Interested U.S. Government agencies and aerospace contractors may obtain copies of the code and documentation upon official request.
(Craig S. Collier and James L. Hunt, 43732)
Aeronautics Directorate

Degradation of Film Cooling Effectiveness by Incident Shocks

For hypersonic atmospheric vehicles, regenerative structural cooling (i.e., the passage of cold hydrogen fuel through the cooling channels in the structure) requires excessive fuel flow at high Mach number operation. Film cooling is a proposed means of reducing the required fuel flow by providing a buffer layer of lower energy fluid between the hotter engine core flow and the structure. When the flow is undisturbed by incident shocks, film cooling is an effective means of reducing heat flux. However, the engine flow will inevitably contain shock waves that impinge on the film-cooling layer. The effect of an incident shock on the cooling effectiveness of a supersonic film cooling layer injected parallel to a scramjet engine combustor structural wall has been examined.

An experimental data base to define film-cooling effectiveness is



Coolant flow undisturbed and with incident shock.

ORIGINAL PAGE
BLACK AND WHITE PHOTOGRAPH

Transatmospheric vehicle model with minimum-drag forebody.

L-89-4825

being developed for film cooling/incident shock interactions in two-dimensional flow without combustion. In tests conducted in the Calspan/University of Buffalo Research Center 48-Inch Hypersonic Shock Tunnel with an air test stream of Mach 6.4, a helium coolant flow of Mach 3, and an adjustable (turning-angle) shock generator, results without shocks show effective downstream cooling for approximately 60 slot heights and a 40-percent degradation at 300 slot heights. When the film cooling is perturbed by an incident shock within the film cooling length, effectiveness is degraded to 40 percent at 19, 10, and 0 slot heights downstream for turning angles of 5° , 7.5° , and 10° , respectively. Film-cooling degradation is the same no matter where the shock interacted with the film-cooling layer within the cooling length.

These results indicate that incident shocks significantly degrade film-cooling effectiveness and suggest that additional downstream film-cooling slots will be required to reestablish the film-cooling layer. The data from these experiments can be used to establish slot spacing criteria for design and trade studies of multiple-slot designs.

(N. R. Baker, George C. Olsen, 42354, Robert J. Nowak, and Michael S. Holden)
Structures Directorate

Experimental Investigation of Transatmospheric Vehicle Concept With Minimum-Drag Forebody

Experimental aerodynamic investigations of a transatmospheric vehicle (TAV) concept incorporating a minimum-wave-drag forebody shape have been performed at Mach numbers of 6 and 10. This study is

part of an ongoing general research effort to determine the effects of Mach number, Reynolds number, density, and wall temperature ratio over a wide range of flow conditions on the hypersonic aerodynamic and aerothermodynamic characteristics of generic TAV configurations. The present force and moment studies were made in the 20-Inch Mach 6 Tunnel and 31-Inch Mach 10 Tunnel at angles of attack from -4° to 20° at sideslip angles of 0° and -2° . Test Reynolds numbers (based on fuselage length) were 1.8×10^6 and 2.4×10^6 at Mach 6 and Mach 10, respectively. The model was designed to facilitate component buildup tests and utilized variable wing incidence for longitudinal trim. Flow-through and blocked-off engine modules also were tested. The model was mounted in the tunnels using a dorsal blade sting arrangement to minimize the effects of support interference on configuration aerodynamics.

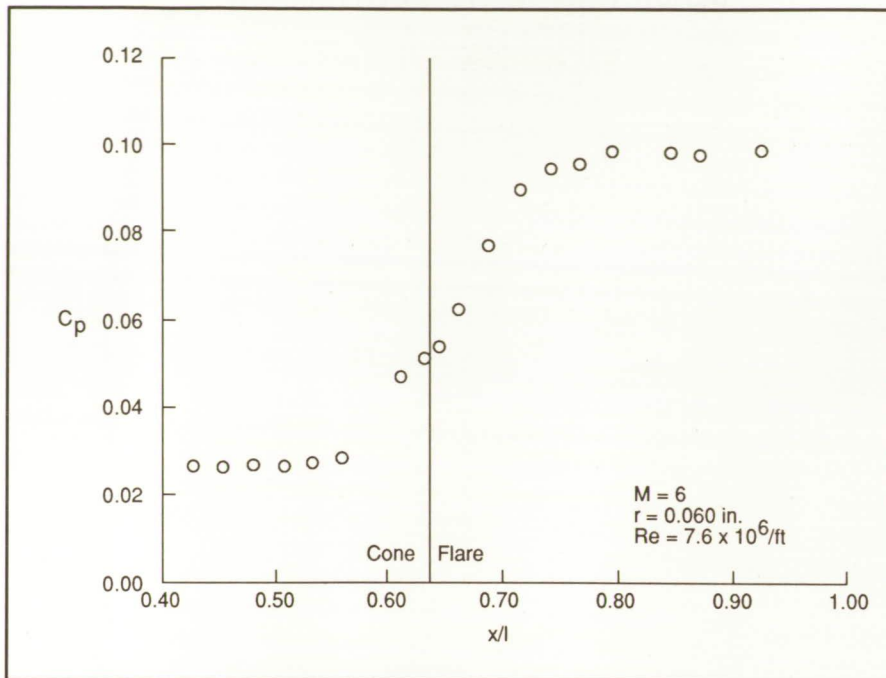
Significant reductions in configuration drag at low angles of attack were realized for the minimum-wave-drag forebody when it replaced a modified one-quarter-power-series forebody. The center-of-pressure location for the baseline TAV configuration (minimum-drag forebody) occurred at approximately the 57-percent model length station at a Mach number of 10. Configuration

buildup test results indicate that incremental drag increases are attributed to the additions of the engine compression ramp, the flow-through engine, and the blocked-off engine. The experimental results of these studies were in agreement with predictions obtained using the Langley Research Center Aerodynamic Preliminary Analysis System (APAS).

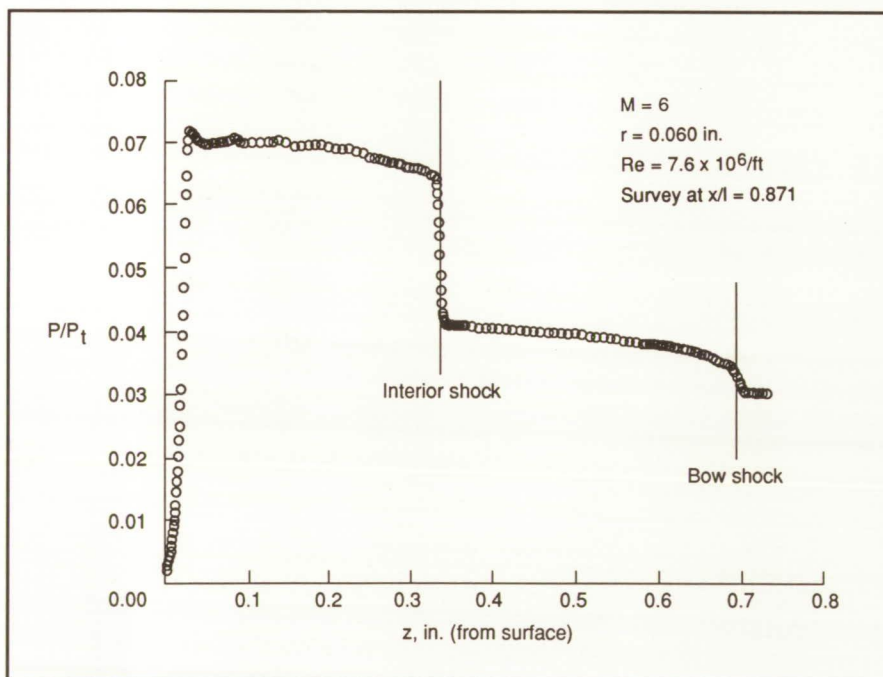
(W. Pelham Phillips, 45239)
Space Directorate

Surface Pressure and Shock-Layer Pitot-Pressure Profiles for $6^\circ/12^\circ$ Cone/Flare at Mach 6 in Air

Surface pressure and shock-layer pitot-pressure profiles were obtained on a $6^\circ/12^\circ$ cone/flare model as part of a National Aero-Space Plane computational fluid dynamics code validation study. Tests were conducted in the 20-Inch Mach 6 Tunnel at Reynolds numbers Re of 2.0×10^6 , 5.9×10^6 , and 7.6×10^6 /ft at an angle of attack of 0° . The 6° cone was approximately 9.5 in. in length l with a 12° flare starting at 6 in. from the nose. Pressure orifices were located in a single line at 22 longitudinal stations (0.25 in. spacing) and at 90°



Surface pressure coefficient on $6^\circ/12^\circ$ coneflare.



Pitot-pressure profile on $6^\circ/12^\circ$ coneflare.

circumferential increments for 4 longitudinal stations. The nose radius was "sharp" for most of the tests. Several runs were made with an 0.060-in. nose radius r .

The pitot-pressure survey was performed with a miniature probe

having a diameter of 0.013 in. The probe entrance was flattened into an oval with a height of approximately 0.007 in. The pressure transducer was water cooled and located approximately 2.5 in. from the probe tip. Surveys were made by traversing from a given orifice on the model

surface through the shock layer. Motion was perpendicular to the model axis.

Preliminary data obtained at a Mach number of 6, Reynolds number of $7.6 \times 10^6/\text{ft}$, and nose radius of 0.060 in. are shown. The plot of the surface pressure coefficient C_p versus nondimensional length x/l (shown in the first figure) indicates a pressure rise before the flare is reached, possibly due to a small separated region in front of the flare moving the associated shock forward. The profile of the ratio of probe pitot-pressure to stagnation pressure P/P_t (shown in the second figure) has three plateau regions (as the probe passes through the boundary layer, at the interior shock from the flare, and at the bow shock). Schlieren photographs also were obtained to aid in interpretation of the data.

(Gregory J. Brauckmann, 45234)
Space Directorate

High-Purity Silica Ceramics for Casting Wind Tunnel Heat-Transfer Test Models

High-purity silica ceramics have been used for casting wind tunnel heat-transfer test models. Such materials have replaced Stycast epoxy for casting aerothermodynamic wind tunnel models at Langley Research Center. The ceramic model has superior insulative properties, thermal expansion characteristics, and survivability up to 2000°F. In the past, epoxy models have been tested in hypersonic tunnels, thermally damaged (charred and warped), and discarded. Cast ceramic models have been tested similarly and then reused in a large test matrix without surface damage or deformation, thus providing improved data quality due to model integrity, reduced lateral conduction, and homogeneous material properties.



Slip-cast silica ceramic wind tunnel heat-transfer test models.

L-89-11811

This casting technology involves an entirely new and innovative use of a material normally used for flask molding of nonferrous metals. The material is a calcium sulphate bonded investment that contains silica, fiberglass, and other specially graded refractory materials. This investment has been found to draw moisture from a ceramic slip similar to plaster and to withstand much higher temperatures than plaster. By unconventional use of this material (as a shell mold), excellent high-purity silica wind tunnel heat-transfer models have been produced.

(P. Vasquez, 45189)

Systems Engineering and Operations Directorate

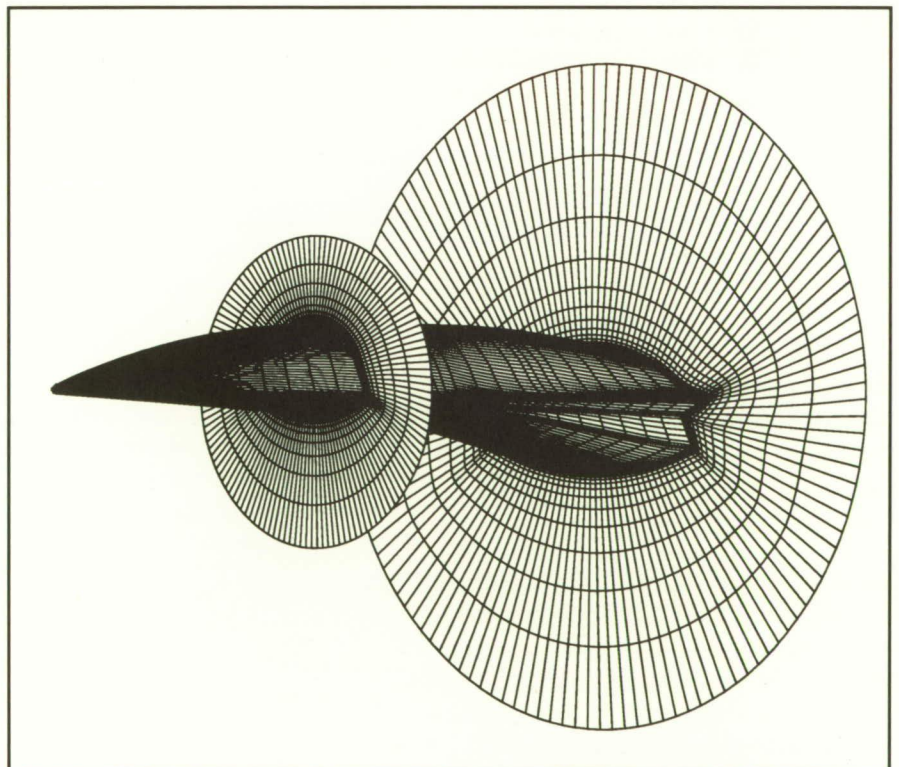
Application of LAURA Code for Slender-Vehicle Aerothermodynamics

Current activity in the National Aero-Space Plane (NASP) program is directed toward the use of computational techniques for basic design and

development tasks. A requirement of this activity is the need for testing and evaluation to better assess the accuracy and applicability of these

techniques. Consequently, a study has been undertaken to demonstrate the application of the LAURA code (Langley Aerothermodynamic Upwind Relaxation Algorithm) to compute the flow over slender hypersonic vehicles and to evaluate the capability for predicting aerodynamic heating. The LAURA code is a three-dimensional, finite-volume, thin-layer Navier-Stokes solver developed at Langley Research Center. The development of this code has been driven primarily by the design requirements of the Aeroassist Flight Experiment (AFE) vehicle and aeroassist vehicles in general. However, the LAURA code can be applied to the spectrum of slender vehicles as well because of the complete geometric generality.

In the present work, the LAURA predictions were compared with ground-based experimental data that enabled an assessment of the code for slender-vehicle applications and contributed to the verification



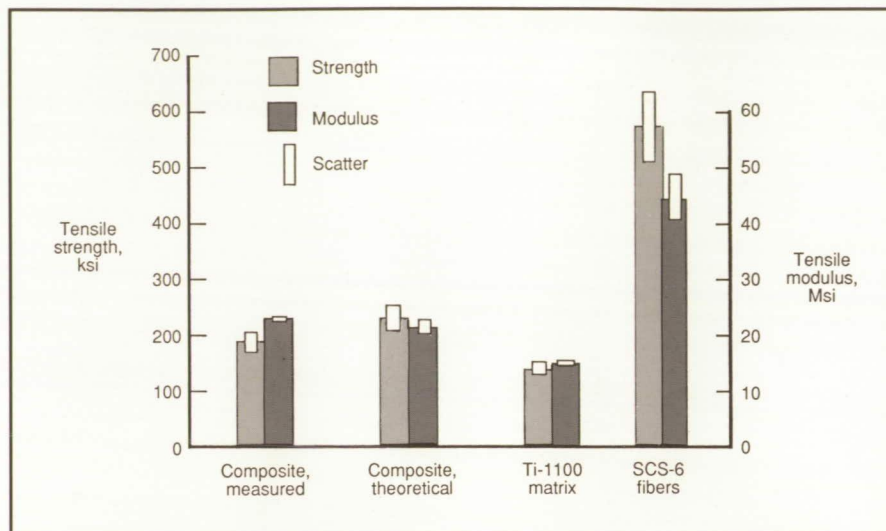
Body surface definition for blended wing-body with typical flow field mesh.

process. The experimental data were obtained by McDonnell Douglas Corporation for a blended wing-body configuration of the NASP from tests in the Calspan 96-Inch Hypersonic Shock Tunnel. These tests provided a data base of pressure, heat transfer, and force measurements on a generic vehicle for validation of computational techniques. Two cases from the experimental tests were selected for study. Flow field grids and a numerical definition of the body surface were generated for the model geometry as shown in the figure. Computations were performed on the Langley Research Center Cray-2S computer, and the predicted results have been compared with the experimental data. Detailed comparisons of predicted and measured heating (and pressure) were made at locations encompassing the entire vehicle. Good to excellent agreement between prediction and measurement was found. Some discrepancies in the comparisons have been noted on the leeside of the vehicle and have been attributed to insufficient grid solution of a region of vortical flow. The results of this research show that the LAURA code is capable of flow field calculation and accurate heat-transfer predictions over slender NASP-like vehicles and should be a useful design tool.

(R. A. Thompson, 44367)
Space Directorate

Potential of Ti-1100 Matrix Composites for Hypersonic Vehicle Applications

Fiber-reinforced titanium matrix composites have the potential to meet some of the projected high-temperature property and stability requirements for hypersonic vehicles. However, matrix alloys with higher temperature capability are required to realize fully the potential of the composite materials. A relatively



Room temperature strength and modulus for 17 volume percent SCS-6 silicon carbide/Ti-1100 composite and constituents.

new titanium alloy, Ti-1100, has shown useful properties at higher temperatures than any currently available titanium alloy. Reinforcing a Ti-1100 matrix with strong SCS-6 silicon carbide fibers has the potential to increase the upper use temperature far beyond 1200°F.

The figure shows the measured and theoretical room temperature strength and modulus for a unidirectional SCS-6/Ti-1100 composite with 17 volume percent fiber reinforcement fabricated at Langley Research Center. Also shown are the properties of the as-received matrix foil and fibers. The measured modulus for the composite is equivalent to the theoretical room temperature value predicted by the rule-of-mixtures model using the as-received constituent properties. The measured strength exceeded 200 ksi and was generally within 20 percent of the theoretical values. Refinements in consolidation techniques are expected to lead to improvements in the composite strength.

Other research sponsored by Langley has shown that potentially

deleterious fiber/matrix reactions proceed at a much slower rate in Ti-1100 matrix composites than in other titanium matrix composites. Studies of reaction kinetics have shown that this fiber-matrix system should have a useful service life several times that of previously demonstrated titanium matrix composites at temperatures typical of hypersonic flight.

(Keith Bird, 43512)

Structures Directorate

New Low-Toxicity, High-Temperature Nadimide End-Capped Thermosetting Polyimide: LaRC-RP46

After 20 years of extensive research by the U.S. government, nadimide end-capped thermoset polyimides such as LaRC-160 are among the leading classes of commercially available high-temperature composite matrix resins. These polyimides are relatively inexpensive and readily processed into high-quality graphite-fiber-reinforced

Property	LaRC-RP46	Standard nadimide end-capped material
Toughness, G_{IC} , J/m ²	392.0	253.0
Glass transition temperature, °C		
Postcured at 316°C for 16 hr	310.0	339.0
Postcured at 371°C for 25 hr	383.0	385.0
Mechanical properties at 25°C		
Flexural strength, ksi	250.0	268.0
Interlaminar shear strength, ksi	19.0	16.0
Thermo-oxidative stability		
After exposure at 316°C for 600 hr		
Interlaminar shear strength at 316°C, ksi	8.5	6.7
Weight loss, percent	1.9	3.1
<ul style="list-style-type: none"> • Nonmutagenic • Easy to process • Scale-up composite fabrication is under way for long-term aging studies • Cost will be volume sensitive (\$5-\$50/lb) 		

Comparison of composite properties.

composites. The composites retain excellent mechanical properties at 316°C, even after service at this temperature for several hundred hours. However, there is an increasing concern about the health hazards of many of these materials because one of the principle chemicals used to prepare them, 4,4'-methylenedianiline (MDA), is a suspected human carcinogen. Current research at Langley Research Center has led to a less toxic composition called LaRC-RP46. This new nadimide end-capped thermoset was prepared by replacing the mutagenic MDA monomer with a nonmutagenic chemical called 3,4'-oxydianiline (m,p'-ODA).

Besides improving environmental safety, the LaRC-RP46 matrix has provided improved composite properties compared with those from standard nadimide end-capped composites such as LaRC-160, as shown in the table. LaRC-RP46 is easier to process because of improved resin flow, and its interlaminar fracture toughness G_{IC} was 55 percent higher than that from standard nadimide compositions. These

improvements are attributed to the greater molecular flexibility of the m,p'-ODA variety compared to that of the MDA. Because m,p'-ODA is less reactive than MDA, LaRC-RP46 requires a higher postcure temperature or time if a comparable glass transition temperature is desired.

The mechanical properties of LaRC-RP46 composites at 25°C compare favorably with those of standard nadimide materials. But, after aging at 316°C for 600 hr, LaRC-RP46 composites exhibit elevated temperature (316°C) mechanical properties and weight loss significantly better than the standard composites, thus suggesting that the modification provides improved thermo-oxidative stability. Further work is under way to scale up the fabrication of LaRC-RP46 composites for long-term (60 000-hr) aging studies. The adhesive and neat resin properties of this improved composition will be evaluated in the near future.

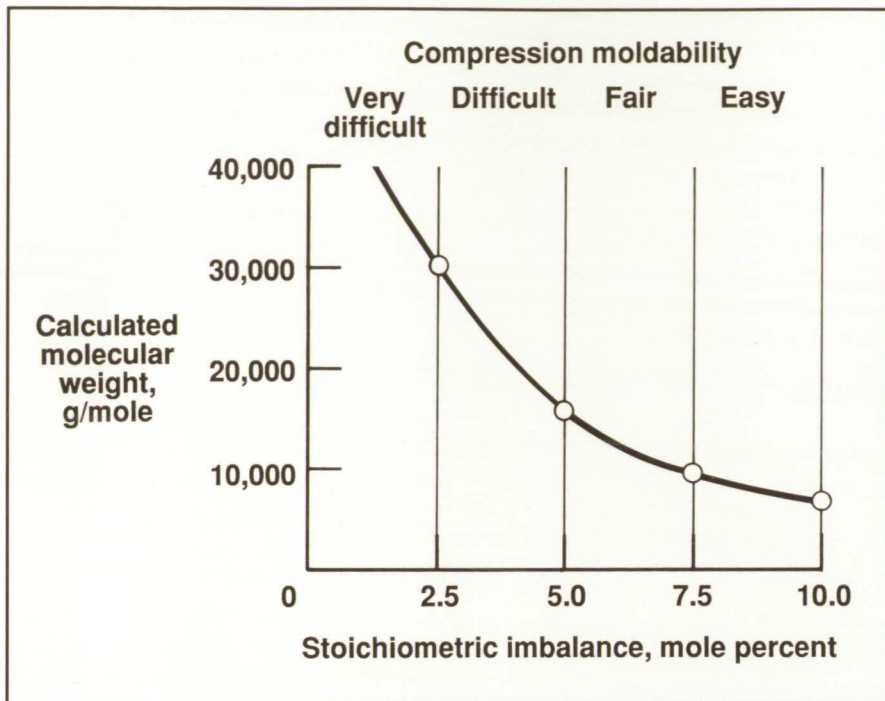
(Ruth Pater, 44227)
Structures Directorate

Improved Processability of LARC-CPI Semicrystalline Polyimide

High-molecular-weight LARC-CPI, a semicrystalline polyimide, has exhibited excellent chemical stability and high mechanical properties in the form of an adhesive, a composite matrix, a film, and a molding at temperatures as high as 232°C. However, the fabrication of well-consolidated adhesive panels, composites, and molding from high-molecular-weight LARC-CPI required a temperature of 400°C and a pressure of 1000 lb/in² for 0.5 hr.

To improve the compression moldability of LARC-CPI, the molecular weight of the polymer was reduced by upsetting the stoichiometry of the monomers used in the synthesis. In addition, stable groups were placed on the ends of the molecules to improve the melt stability at high temperatures. As a result of molecular weight control and end capping, the compression moldability of LARC-CPI was improved considerably, as depicted in the figure.

Unidirectional LARC-CPI laminates using unsized carbon/graphite AS-4 reinforcement fabricated at 375°C under 300 lb/in² pressure for 0.5 hr gave flexural strength and modulus at 23°C of 267 ksi (thousand lb/in²) and 15.0 Msi (million lb/in²) and at 204°C of 196 ksi and 14.4 Msi, respectively. After aging for 100 hr at 316°C in air, the 23°C properties remained the same, while the flexural strength at 204°C increased to 214 ksi. Titanium tensile shear specimens fabricated at 375°C under 200 lb/in² pressure and postcured for 16 hr at 308°C gave strengths of 4830 lb/in² at 23°C, 4820 lb/in² at 177°C, and 4080 lb/in² at 204°C. These preliminary laminate and adhesive properties are excellent



Effect of molecular weight on processability of semicrystalline polyimide.

and indicate the potential for LARC-CPI to be used in high-temperature structural applications. (Paul M. Hergenrother, 44270, and Stephen J. Havens) Structures Directorate

molecular rearrangement under cryogenic conditions leading to hydrogen fuel leakage. The Positron Annihilation Spectroscopy (PAS) has been used to investigate morphologi-

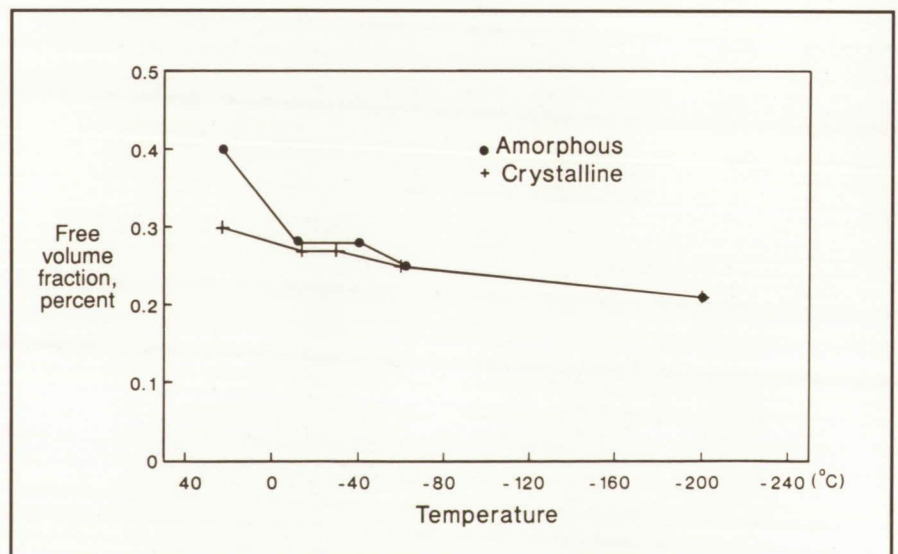
cal features of PEEK as a function of temperature in the range 73 K to 300 K.

Several 250- μ m thick PEEK films (each 10-mil thick) were obtained from ICI Americas, Incorporated. The as-received films were unoriented, noncrystalline, and transparent. Semicrystalline varieties of these films were made by heating them to 435 K and then allowing them to cool down to room temperature. The onset of crystallinity was accompanied by the onset of opacity in the films. The PAS measurements, in both the amorphous and semicrystalline films, were made at room temperature (300 K, 261 K, 233 K, 211 K, and 73 K). The results, illustrated in the figure, indicate that the number of large microvoids, as well as volume fraction associated with them, decreases as the PEEK film temperature is lowered. This result is encouraging because it implies that PEEK will not degrade at cryogenic temperatures.

(Jag J. Singh, 44760, and Abe Eftekhari) Electronics Directorate

Study of Morphological Changes in PEEK at Cryogenic Temperatures

Polyetherether ketone (PEEK), which is an aromatic thermoplastic polymer with excellent properties for a wide range of demanding applications, is a strong candidate for the matrix in the composite materials under consideration for the slush hydrogen fuel tank for NASP. However, some concern exists that PEEK might undergo significant



Free volume fraction versus temperature in PEEK samples.

Integrated Thermal-Structural Analysis With Adaptive Unstructured Meshes

By adjusting the size and location of finite elements, computationally accurate and efficient integrated thermal-structural two-dimensional analysis has been achieved which far surpasses the state-of-the-art procedures. This capability has been demonstrated on an actively cooled leading edge subjected to a steady-state intense localized pressure and an aerodynamic heating rate, which result from a shock-shock interaction, and has been incorporated in the Langley Integrated Fluid-Thermal-Structural (LIFTS) analyzer.

The LIFTS analyzer solves Navier-Stokes flow, thermal energy, and mechanical equilibrium equations for bodies subjected to aerothermostructural loads. The current capability includes development of the independent fluid,

thermal, and structural analyzers with adaptive unstructured remeshing techniques; identification of thermal/deformation coupling that causes changes in aerodynamic flow and in aerothermal loads in a given analysis sequence; and development of the interface requirements for a fully integrated finite-element thermal-structural analysis. For each analyzer, the results from an initial mesh or subsequent remesh provide adaptivity information for a sequence of solutions until desired convergence is obtained; the second derivative of a selected solution variable θ serves as the adaptivity indicator for remeshing; and the nonuniform element size h and distribution are selected by an equidistribution principle, based on the interpolation error for elliptic boundary value problems ($h^2 |d^2 \theta / dx^2| = \text{constant}$). Each disciplinary solution provides input to the next analysis or analysis sequence, as indicated in the figure.

The improvement in integrated analysis has been achieved without

the typical assumptions of isothermal rigid bodies and the requirement for interpolation or extrapolation of disciplinary results between analysis. Thus efficiency with accuracy is achieved.

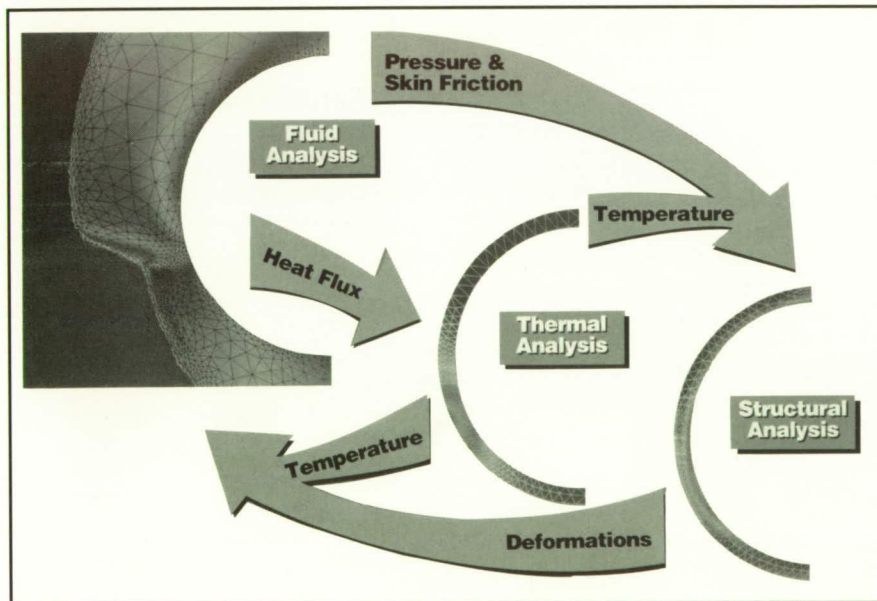
(Pramote Dechaumphai, 41357)
Structures Directorate

Fabrication, Test, and Analysis of Blade-Stiffened Carbon-Carbon Compression Panels

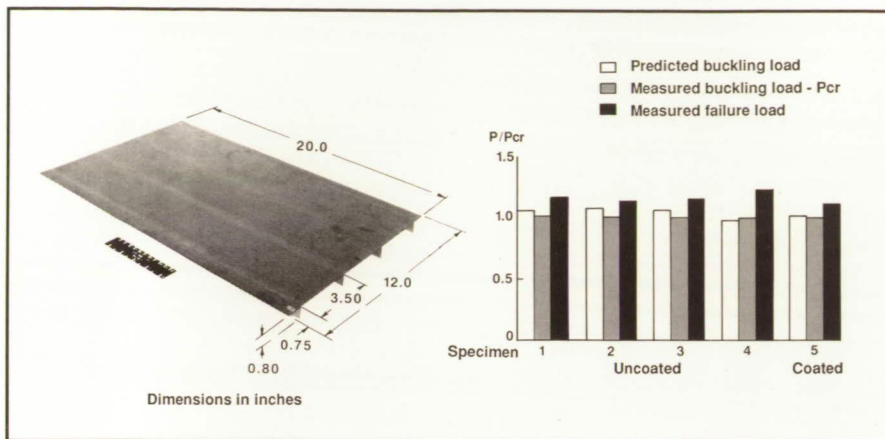
Carbon-carbon composite materials are being considered for use as hot structures on advanced hypersonic vehicles. Stiffened panels are basic to most aerospace vehicle structures, and understanding their behavior in compression is essential for the design of efficient carbon-carbon structural components.

The capability to design, fabricate, and predict the performance of coated and uncoated carbon-carbon blade-stiffened compression panels has been demonstrated. A typical uncoated panel is shown in the figure. Fabrication trials and experimental results show that carbon-carbon panels with integral stiffeners can be fabricated using six plies of woven fabric in a two-dimensional 0/90° cross-ply layup. Analytical buckling, experimental buckling, and experimental failure loads are compared on the graph for both the coated and the uncoated panels. Experimental results show that local skin buckling does not cause panel collapse and that ultimate failure occurs at loads 10 percent to 20 percent above the buckling load. Conventional finite-element analysis adequately predicts the onset of skin buckling.

The demonstrated design-to-performance capability with carbon-carbon compression panels provides



Interactive analysis.



Carbon-carbon panel with test and analysis results.

part of the confidence needed for using carbon-carbon materials in advanced structural components. This capability may be part of the enabling technology for producing advanced hypersonic vehicles. (James Wayne Sawyer, 45432) Structures Directorate

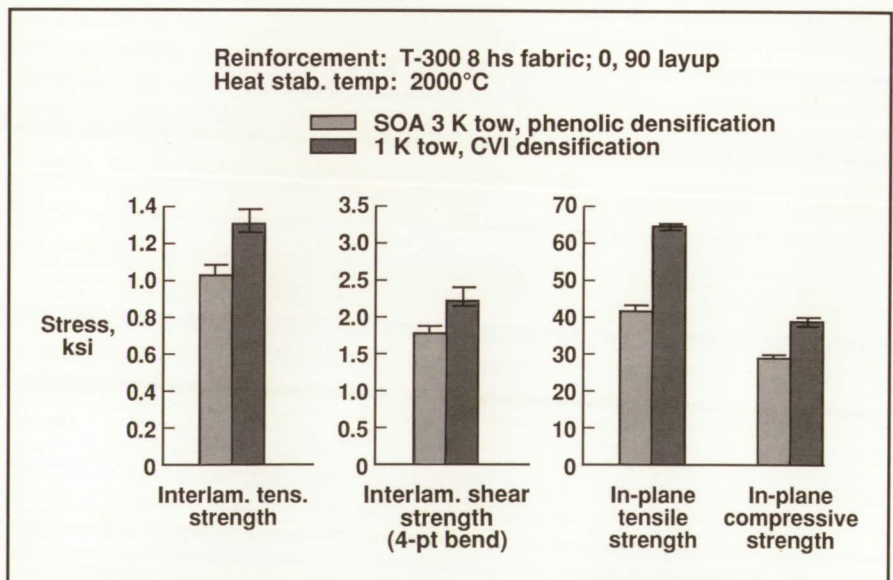
Improved Mechanical Properties of 2-D Carbon-Carbon Composites

A state-of-the art (SOA), high-strength, two-dimensional (2-D) carbon-carbon composite, often used as a baseline material with which to compare emerging carbon-carbon composites, is composed of T-300 carbon fiber reinforcement in a carbon matrix derived entirely from pyrolysis of phenolic resin. Due to the nature of carbon-carbon processing and the requirement for reinforcement in more than one in-plane direction, the fibers are conventionally woven into a fabric for incorporation into the composite. The fabric weave used in the construction of the SOA material is eight-harness satin

(8 hs). The fiber tow bundle used in the SOA material consists of 3000 (3 K) filaments of continuous fiber. The SOA composite has reasonably attractive in-plane mechanical properties; however, taking advantage of these properties to design lightweight hot structures can be somewhat encumbered because interlaminar (cross-ply) strengths are undesirably low. The purpose of the reported research was to improve the

interlaminar strengths without degrading the in-plane properties.

The basic architecture of the SOA material was retained in the newly developed material, i.e., the eight-harness satin weave, but the tow size in the fabric was reduced by reducing the number of filaments to 1000 (1 K). This reduction resulted in a much thinner fabric (from an 0.012-in. to an 0.0075-in. thickness). Also, the method of densifying the initially carbonized composite was changed from phenolic-resin reimpregnation to chemical vapor infiltration (CVI). A comparison of the mechanical properties for the SOA material and the developmental material is shown in the figure. The shaded bars represent the SOA material, and the cross-hatched bars represent the new material. The data show that interlaminar strengths were improved by 30 percent and, at the same time, the in-plane properties also were improved very significantly. Tensile strength was increased by 55 percent, and compressive strength was increased by 35 percent. (P. O. Ransone, 43503) Structures Directorate

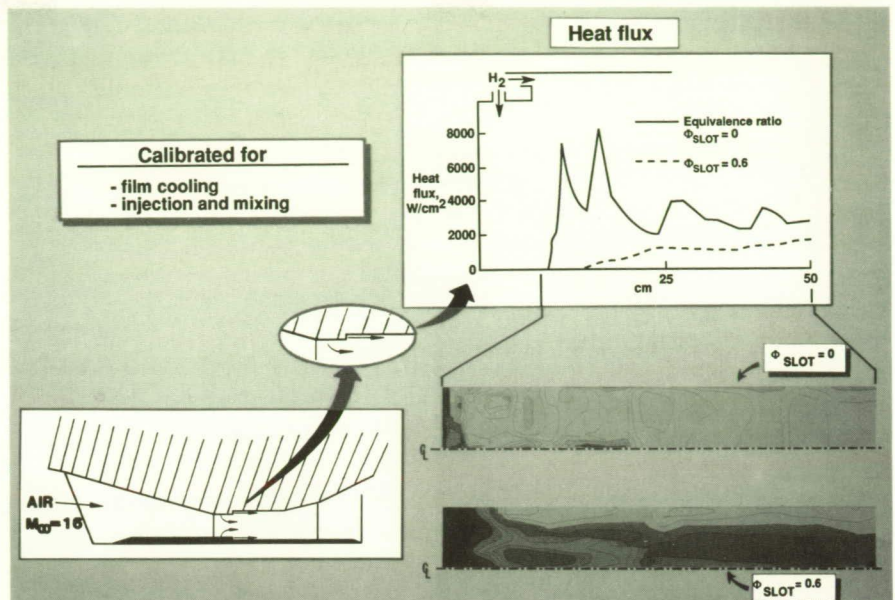


Benefits of fine tow size and CVI densification on selected mechanical properties of 2-D carbon-carbon composites.

Cost-Effective Three-Dimensional Analysis of Scramjet Combustors

A major technological challenge facing the NASP program is the development of the computational tools to calculate the performance of the hydrogen-fueled, airframe-integrated scramjet for flight conditions beyond current ground test capabilities. For the combustor portion of the scramjet, critical design issues are fuel mixing and active cooling of the wall from within the combustor to supplement regenerative cooling on the outside. The SHIP3D code, developed for NASA in the 1970's, has been extensively modified, validated, and demonstrated as a cost-effective tool for the analysis and design studies of film-cooled and transpiration-cooled scramjet combustors.

The strategy adopted in the SHIP3D code to achieve high computational efficiency in these largely supersonic flows is to treat the embedded elliptic (recirculating) flow regions around fuel injectors and step changes in area as parabolic (unidirectional), while ensuring the global conservation of mass, momentum, and energy. The resulting major (factor of 200) reduction in computational resources required is achieved, no doubt, at the cost of a loss of rigor, but without much loss in accuracy. The latter, which has been observed repeatedly in validation studies, is attributed to the fact that these turbulent, reacting flows can be computed to sufficient accuracy if turbulence and turbulent combustion are modeled adequately. The SHIP3D code incorporates several two-equation turbulence models thus allowing more accurate computations of heat transfer and fuel mixing than even elliptic codes (most of which currently use zero-equation (algebraic) turbulence models). For hydrogen-air chemistry, a nonkinetic



Analysis of scramjet film cooling.

step or ramped reaction model is used instead of the vastly more expensive approach of treating generalized chemical kinetics.

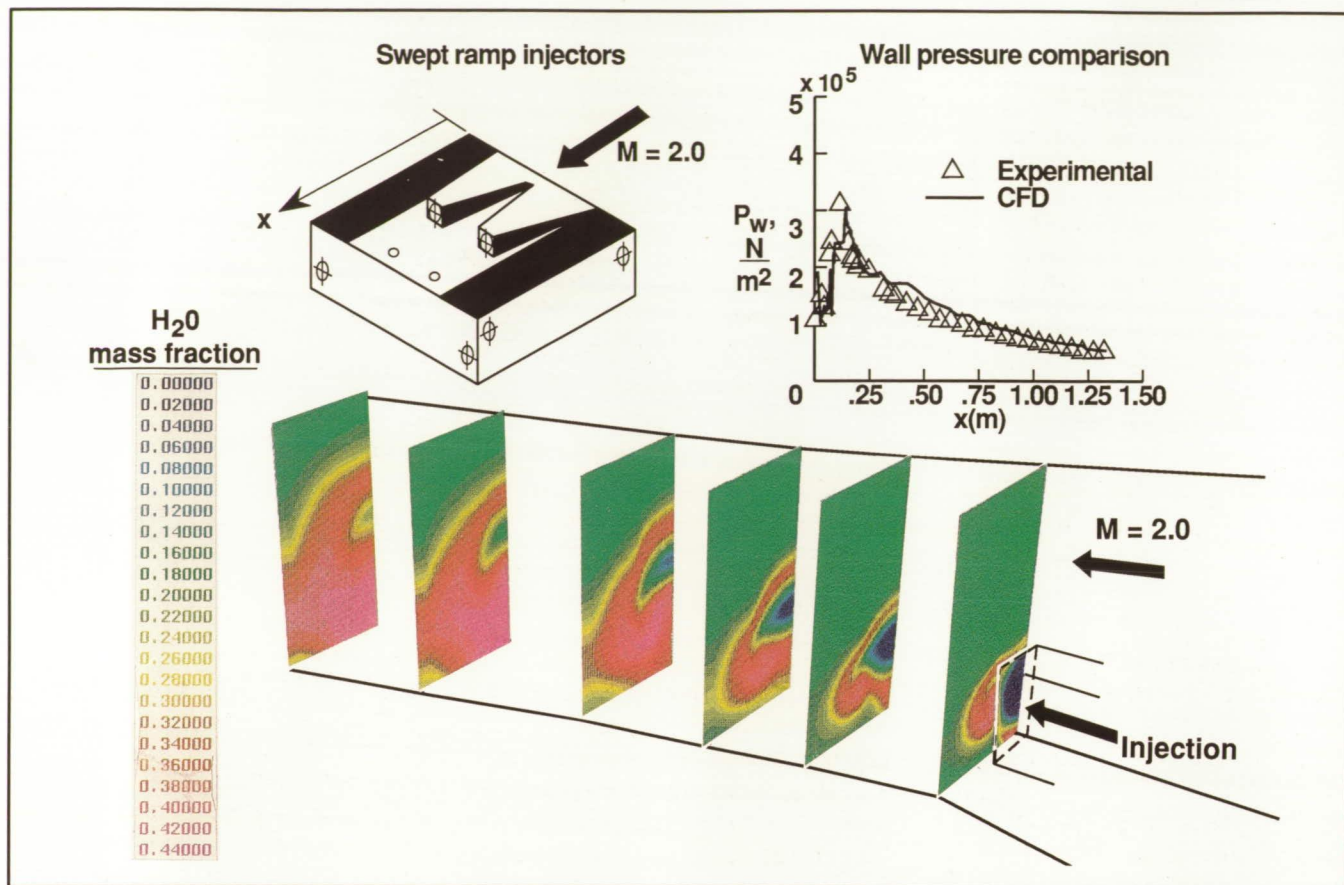
The figure illustrates typical combustor wall heat flux distributions obtained by the SHIP3D code for a film-cooled scramjet combustor operating at simulated Mach 16 flight. The elliptic regions about the primary transverse fuel injectors and downstream of the blunt lip of the film injector are treated as parabolic. The remainder of the supersonic reacting flow and the combustor boundary layer, which largely determine the combustor wall heat-flux distribution and total heat load to the fuel, are parabolic and require no approximation. This procedure is used to provide three-dimensional design information for proposed scramjet configurations.

Thus, the SHIP3D code offers the unique capability of a level of analysis that is a bridge between the one-dimensional cycle analysis used heretofore and the solution of the fully elliptic, time-averaged Navier-Stokes equations in conjunction with

those for nonequilibrium chemistry. (Pradeep S. Kamath, 43736) Aeronautics Directorate

Mixing Enhancement and Flow Losses for Scramjet Combustors

The purpose of this work is to develop three-dimensional numerical techniques for analysis of flow details for supersonic reacting flows such as those that occur in scramjet engines. This technology is critical in the design of efficient hypersonic vehicles (with flight envelopes of Mach 6 to Mach 25). These techniques provide useful information to complement limited measurements obtained in experimental combustor studies and also provide a numerical tool for performing design trade studies (similar to those performed in wind tunnel studies) on fuel injector and combustor geometry. These numerical methods have been extensively calibrated with available experimental data and used to predict complete scramjet combustor flows at



Mixing enhancement with reaction. (P_w is wall pressure.)

flight Mach numbers from 6 to Mach 16. These numerical trades provide solutions that are analyzed in detail to evaluate loss mechanisms in the reacting flow and provide comparisons of combustor performance.

One such computational predicted flow field is depicted for a swept-sided injector ramp mounted in a supersonic combustor. Hydrogen is injected from the base of the ramp, mixes rapidly due to vorticity generated from the ramp, and reacts with high-temperature vitiated air to produce the reaction product water. Predicted water contours are shown in the figure, and they demonstrate the complex swirling nature of the flow and regions of strong reaction (maximum water generation). Comparisons with experimental wall pressures (shown in the figure) and

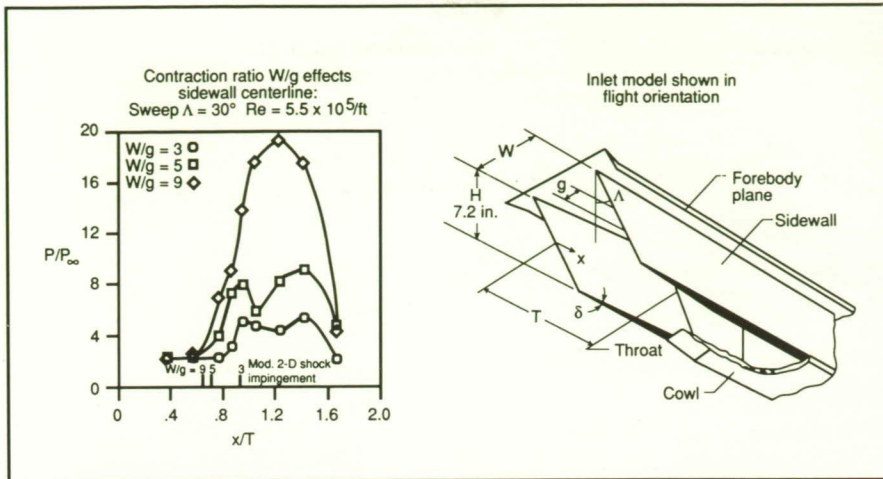
other measurements provide confidence in solutions. Computational studies such as this provide engine performance information (combustion efficiency and combustor thrust) and combustor loads (thermal and pressure). They also provide details of the flow physics, which are essential for combustor design optimization.

(David W. Riggins, Marlon Mao, and Charles McClinton, 43736)
Aeronautics Directorate

Scramjet Inlet Testing at Mach 6

Careful design of primary engine components such as the inlet is

necessary to exploit effectively the potential of propulsion-airframe integration for hypersonic cruise vehicles such as the National Aero-Space Plane (X-30). In order to identify geometric parameters pertinent to improved inlet performance, two existing three-dimensional sidewall compression inlet wind tunnel models with leading-edge sweeps Λ of 30° and 70° have been tested in the Hypersonic CF₄ Tunnel at Mach 6. The models represented moderate to highly swept configurations and were tested over a range of contraction ratios (the ratio of inlet entrance width W to the throat gap g), cowl locations, and Reynolds numbers. The models were instrumented with 42 static pressure orifices distributed on the sidewalls, baseplate, and cowl. Schlieren movies were made of each test for



Three-dimensional sidewall compression scramjet inlet testing at Mach 6 (δ is sidewall compression angle of 6° and H is inlet height of 7.2 in.).

flow visualization of the entrance plane and cowl region.

In order to obtain an approximate characterization of the flow field, a modification to the two-dimensional inviscid oblique shock theory was derived to accommodate the three-dimensional effects of leading-edge sweep. This theory qualitatively predicted the reflected shock structure/sidewall impingement locations (given in the figure as a fraction of the distance from the leading edge to the throat x/T) and the observed increase in spillage with increasing leading-edge sweep. The primary effect of moving the cowl forward was to capture the flow that would have otherwise spilled out ahead of the cowl. Increasing the contraction ratio (moving the sidewalls closer together) increased the number of internal shock reflections and hence incrementally increased the sidewall pressure distribution. Significant Reynolds number effects were noted over a small range of Reynolds numbers.

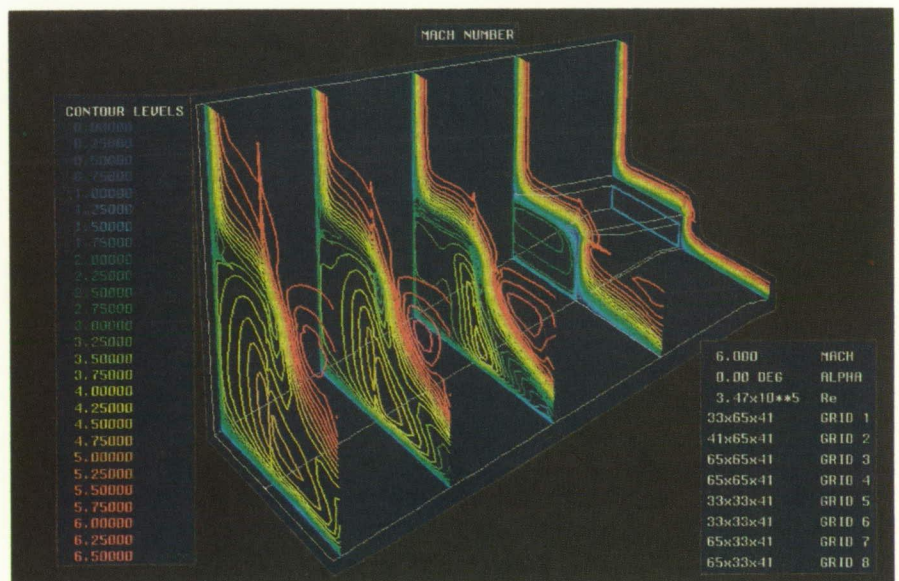
The present work represented the largest model tested in the Hypersonic CF_4 Tunnel to date. In these tests, the tunnel remained started following model injection. Based on

measured static pressures on the tunnel nozzle wall, no significant blockage effects were noted. In addition to evaluating the effects of various geometric parameters on the performance of the inlet, this research provides an enhanced computational fluid dynamics code calibration data base because data for a virial gas environment were obtained. (Scott D. Holland, 45248) Space Directorate

Analysis and Design of Scramjet Nozzle-Afterbody Using Sensitivity Coefficients

The expansion of a Mach 1.7 flow through a scramjet nozzle and its turbulent mixing with a Mach 6 airflow have been simulated numerically. The hot exhaust gases were simulated by matching their specific heat ratio using a cold mixture of Freon-12 and argon. This simulation eliminated the need to include the chemical reactions in the computations that were performed initially in two dimensions, then in three dimensions.

The SPARK code was modified to handle block-structured grids and to include the properties of Freon-12 and argon. The Reynolds-averaged, time-dependent, complete Navier-Stokes equations for compressible, thermally perfect, multispecies gases were solved using the explicit MacCormack scheme. Two-dimensional grids were adapted to the development of the solution to improve the resolution and to reduce the computational errors at regions of high flow gradients. The computed



Mach contours of various cross flow planes for the nozzle-afterbody.

two- and three-dimensional surface pressure distributions agreed with the available wind tunnel data. The feasibility and the accuracy of two different mixing models were evaluated.

Computations also were performed in situations in which the exhaust gases were assumed to be air. The CFL3D code was modified to solve the complete Navier-Stokes equations by an upwind-biased, finite-volume, approximately factored, multigrid method. Two-dimensional results were obtained on flow-adaptive grids. The computed two- and three-dimensional surface pressure distributions and off-surface pitot-pressure surveys compared successfully with the wind tunnel data. The comparisons of these results with the Freon-12/argon mixture will allow a detailed study of the differences in the gas expansion rates, shear-layer spreading rates, and plume shapes.

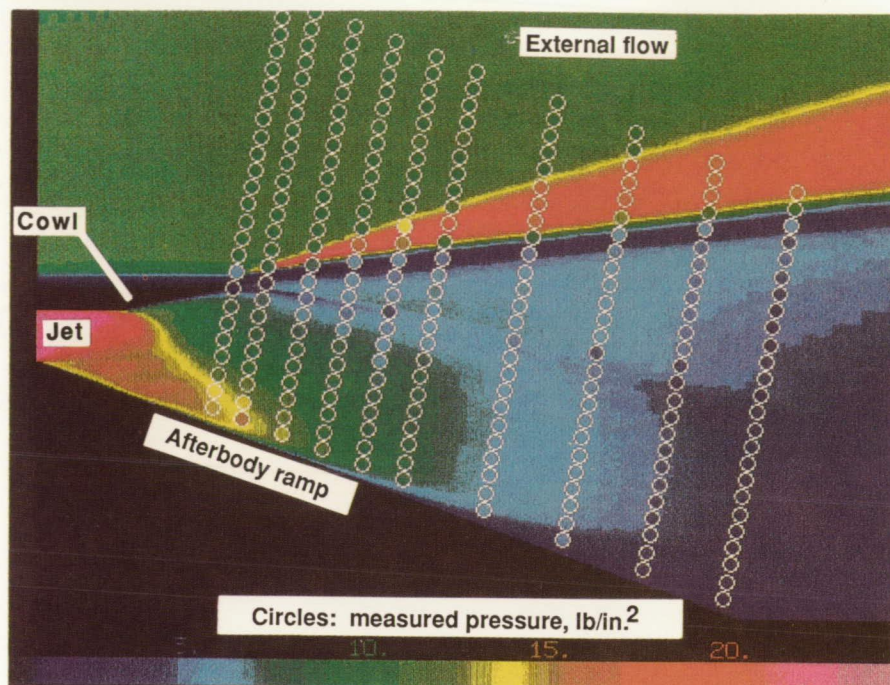
The flow analysis codes have been coupled with an optimization code to maximize nozzle thrust. The sensitivity coefficients are derived to generate the gradients of the objective and the constraint functions as they are needed by the optimization code. Currently, development is in progress for this flow analysis/optimum design/sensitivity code for the longitudinal and lateral nozzle shaping.

(Oktay Baysal, 45570, and David S. Miller)

Aeronautics Directorate

Generic Scramjet Nozzle/Afterbody Studies

Hypersonic, airbreathing vehicles require careful integration of the scramjet propulsion system and the airframe because the airframe afterbody also serves as an external



Two-dimensional General Aerodynamic Simulation Program (GASP) PNS solution compared with measured pitot pressures (lb/in²) for external scramjet nozzle/afterbody (50 percent argon, 50 percent Freon-12 jet, and static nozzle pressure ratio of 26.1).

nozzle surface for the scramjets. Ultimate design goals for such afterbodies are to maximize the thrust obtained while controlling the resultant pitching moment. Performing combustion tests using small-scale wind tunnel models is impractical. Previous studies have shown that a mixture of argon and Freon can be used to simulate the pressure field of hot scramjet exhausts. A generic nozzle/afterbody model was instrumented with surface static pressure taps and tested in the 20-Inch Mach 6 Wind Tunnel. Initial numerical results showed reasonable agreement with the measured static pressures on the afterbody surface.

Further wind tunnel tests now have been conducted with a total pressure rake to measure flow field pressures, both with and without a flow fence for comparison with two- and three-dimensional calculations. As shown in the figure, the rake consisted of 25 pitot tubes extending

across the jet from the afterbody surface out into the free stream. Measurements were made at 10 locations downstream from the cowl trailing edge. Both air and argon/Freon stimulant mixtures were used as the exhaust gases.

The generic model has been numerically modeled using several computational fluid dynamic codes ranging from two- and three-dimensional marching Euler codes to a two-dimensional Parabolized Navier-Stokes (PNS) code, including boundary-layer turbulence. Comparisons with the pressure rake measurements have identified levels of theoretical complexity required to adequately predict scramjet exhaust flow fields. Shown is a comparison of measured pitot pressures superimposed on a two-dimensional turbulent PNS solution from a multizone, multispecies generalized aerodynamic solver developed at Virginia Polytechnic Institute and State

University. While Euler solutions show moderate agreement with measured surface pressures, such features as the locations of multiple shocks and the plume extent are matched only by viscous solutions, such as the one shown.

(Kenneth E. Tatum, 45587, and William J. Monta)

Aeronautics Directorate

Ineffectiveness of Moderate Transpiration Cooling to Reduce Type IV Shock-on-Lip Heat Flux

When an impinging shock produces a Type IV shock/shock interference at a leading edge, such as an engine cowl-lip, a supersonic jet impinges on the structure surface and causes an intense local heat flux that can exceed levels 20 times the normal stagnation point heat flux. The high heat flux, which occurs over a narrow region, can bring large temperature gradients and thermal stresses. An experimental data base is being developed to determine the effect of

transpiration cooling shock/shock interference surfaces. Tests have been conducted in the Calspan 48-Inch Hypersonic Shock Tunnel at Mach 12, using an existing 12-in.-diameter transpiration hemisphere with helium coolant, to establish a fundamental understanding of these phenomena (as shown in the figure).

Results show that without coolant and without shock interference, rough (slotted) transpiration surfaces cause a significant increase in stagnation region heat flux over that predicted by laminar theory. At a coolant-to-free-stream mass flux ratio of 0.16, the overall stagnation region heat flux is reduced to one-half the theory prediction, but the turbulence induced by coolant injection tripled the heat flux near the stagnation point. A higher coolant mass flux reduces the stagnation point heat flux to zero.

Without coolant and with shock interference, the peak heat flux is 21 times that of laminar theory. This factor has been obtained by others on smooth models, thus indicating that surface roughness is not significant with shock/shock interference. With

a coolant-to-free-stream mass flux ratio of 0.31, the stagnation point heat flux is reduced to zero, but the peak heat flux is reduced only 8.3 percent.

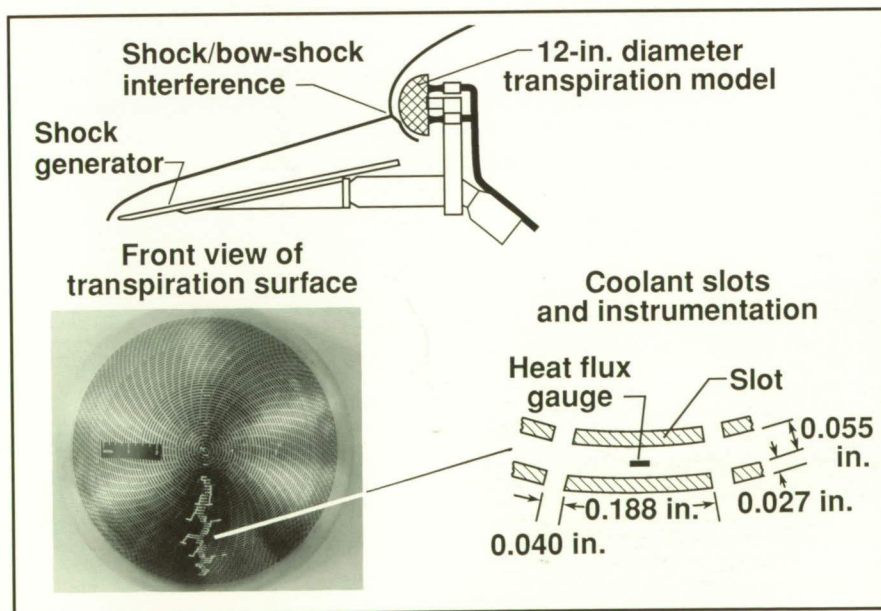
Thus, moderate coolant mass flux is ineffective in protecting against Type IV shock/shock interference. High coolant mass flux is needed in the local region of shock/shock interference.

(Robert J. Nowak, 41391, Allan R. Wieting, and Michael S. Holden)
Structures Directorate

Hydrogen Transport Properties of NASP Materials

The transport properties of hydrogen in candidate materials for NASP must be characterized in order to determine the parameters that affect the mechanical strength of the materials and the hydrogen loss-rate in containment volumes. Titanium aluminide alloys have been identified as candidate materials for NASP because of their high strength-to-weight ratios at elevated temperatures. Unfortunately, these materials are highly reactive to hydrogen. Continual adsorption of hydrogen at the surface and subsequent dissolution into the bulk can substantially affect the mechanical strength, depending on the exposure conditions. Further, concern exists that the hydrogen permeation rate may be too severe for acceptable containment integrity.

Recently, Ti-14Al-21Nb (α_2 aluminide) and Ti-33Al-6Nb-1.4Ta (γ aluminide) have been compared with pure Ti in order to understand the surface composition variations over a 20°C to 1000°C temperature range. These surface characteristics are extremely important because the surface controls the degree of hydrogen uptake. The surface barrier

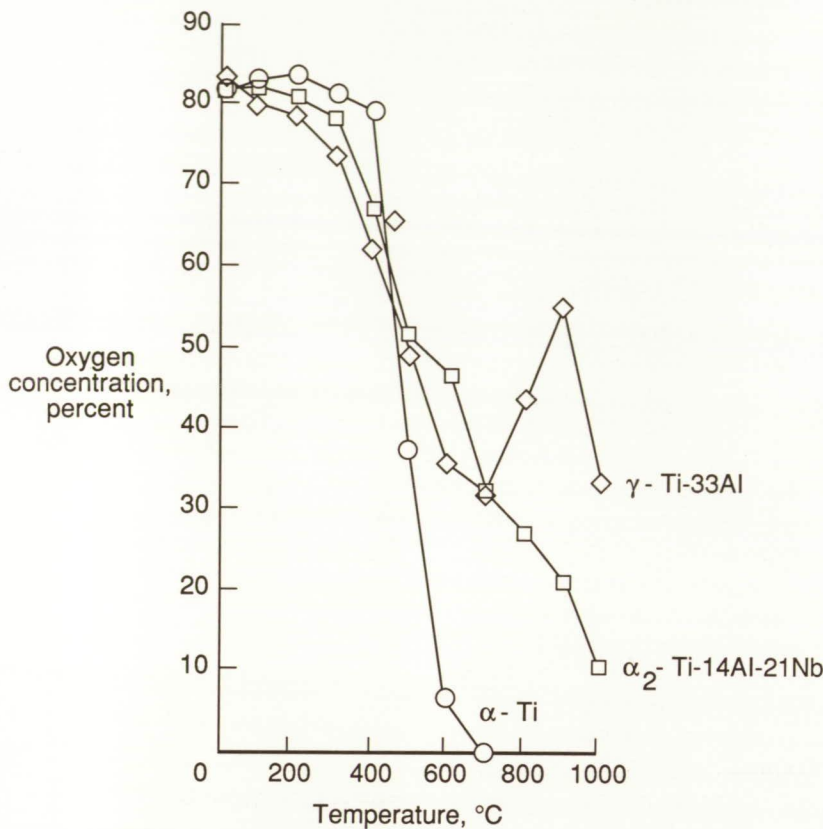


Experimental configuration for shock/bow-shock interference and transpiration cooling.

Analysis of Liquid-Metal-Cooled NASP Engine Cowl Leading Edge

For hypersonic vehicles, one of the most difficult challenges is cooling the leading edge of the engine cowl when the bow shock interacts with the cowl-leading-edge shock, thus causing high, localized heat fluxes approaching 60 000 Btu/ft²·s. The most promising candidate design, a transpiration-cooled leading edge, has several disadvantages. These disadvantages are that performance is difficult to analyze and verify by ground tests, the transpirant can degrade engine performance, the porous leading edge is susceptible to damage, and complex sensors are required to signal the approach of the bow shock. In addition, the thermal effectiveness of internally cooled concepts using cryogenic hydrogen gas is too low to reduce sufficiently the peak temperatures, temperature gradients, and thermal stresses. The feasibility of a liquid-metal convectively cooled concept has been determined analytically as an alternative to transpiration cooling.

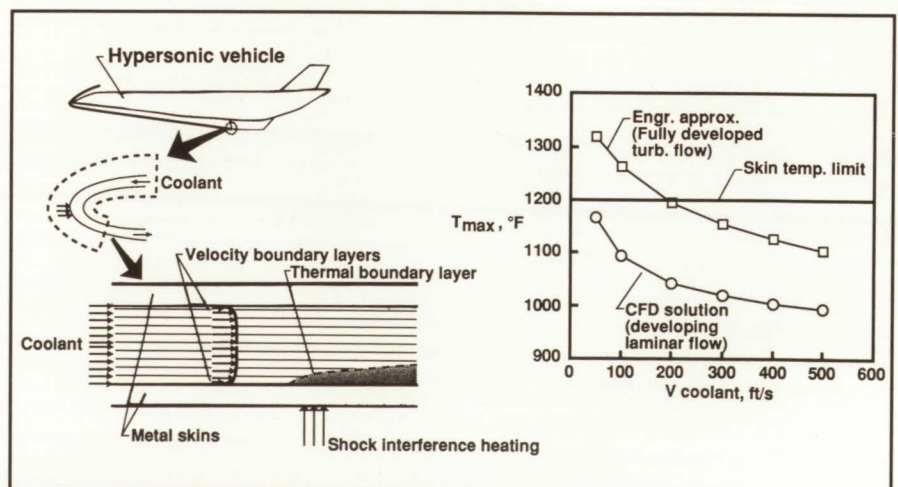
This concept uses a simple flow of sodium around the circumference of the cowl leading edge with a copper skin. A finite-difference code



Surface composition variation of oxygen as a function of temperature for pure Ti, α₂ aluminide, and γ aluminide.

to hydrogen has been found to be directly related to the surface oxide type and thickness. Data are presented in the figure, which shows the variation in surface oxygen concentration as a function of temperature for the aforementioned materials. The data show that pure titanium rapidly dissolves oxygen at temperatures above 400°C and a substantial retention of oxygen by the γ aluminide exists up to 1000°C. Apparently, the oxygen retention is associated with the amount of aluminum in the surface region, which is highest for the γ aluminide. This oxide barrier suggests that there is less hydrogen uptake at elevated temperatures.

(R. A. Outlaw, 41433)
Space Directorate



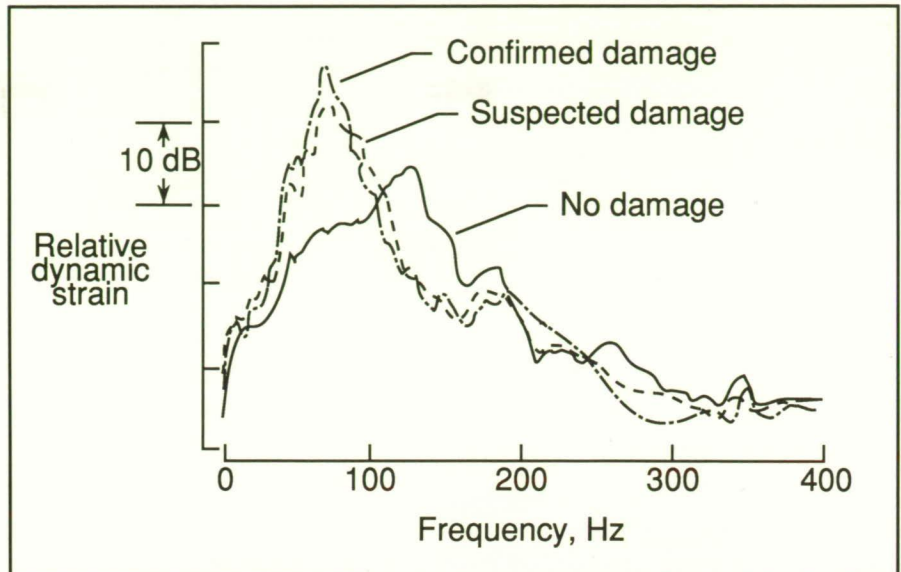
Convective cooling concept and analysis results.

has been developed to solve the coupled computational fluid dynamics (CFD) problem and compute the flow velocities of the liquid metal and the temperatures of both the coolant and skin. A model with 750 000 grid points can be solved in under 10 min on the Langley Research Center Cray-2. Results (shown in the figure) indicate that the liquid-metal-cooled cowl leading edge is feasible for coolant velocities >40 ft/s, assuming a 1200°F limiting temperature for the copper skin. Note that a normal engineering calculation (using published film coefficients for the fluid/skin interface) would result in excessively high predicted temperatures, even assuming turbulent flow with its higher (than laminar flow) heat transfer coefficient and would eliminate the convectively cooled concept from consideration.

An accurate CFD analysis shows that a liquid-metal convectively cooled cowl leading edge is viable from a peak temperature standpoint. If the thermal fatigue life of the concept is also acceptable, this concept may be an attractive alternative to transpiration cooling. (Stephen J. Scotti, 45431) Structures Directorate

Acoustic Testing of High-Temperature Panels

Determination of the sonic fatigue properties of advanced structures at elevated temperature is required to qualify structures for a hypersonic aerospace plane environment. One material considered for NASP structural components is carbon-carbon. However, the sonic fatigue characteristics of this material under thermal-acoustic loading are not well documented. The purpose of this work was to determine the strain response and sonic fatigue behavior of four carbon-carbon panels under



Effect of sonic fatigue damage on carbon-carbon panel strain response.

acoustic and thermal loading. Two flat panels and two blade-stiffened panels (provided by General Dynamics Corporation) were tested in the Thermal Acoustic Fatigue Apparatus at Langley Research Center. One panel of each type was tested at room temperature, and one of each type was tested at elevated temperature (800°F). The panels were mounted in a clamping bar test fixture and were thermally isolated from the fixture. The flat panels were clamped on all four edges; the blade-stiffened panels were on the two edges parallel to the stiffeners. All panels were tested at an applied acoustic level of 160 dB.

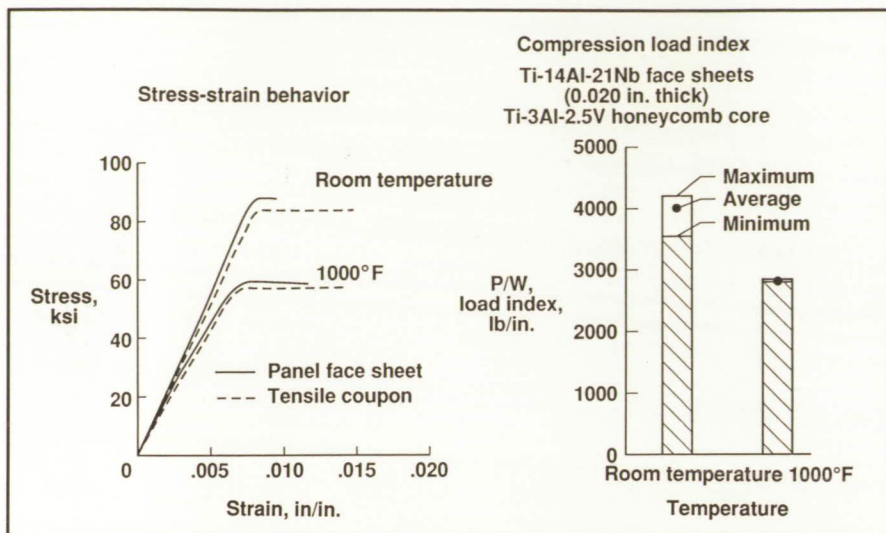
All panels were tested to failure. Panel responses were observed to be nonlinear, and panel strains were lower than expected. As shown in the figure, changes in strain response, such as reduction in first-mode frequency, were indicative of the onset of failure. Failure times ranged from 1 min (blade-stiffened panel tested at room temperature) to 191 min (flat panel tested at elevated temperature). For these tests, the panels tested at room temperature failed much earlier than the corresponding panels tested at elevated

temperature, thus suggesting greater fatigue resistance of carbon-carbon at elevated temperature. This result, however, is based on data from four panels and should be confirmed by additional testing at temperatures closer to the operating limits of carbon-carbon.

(Jack D. Leatherwood, 43591) Structures Directorate

Demonstration of High Structural Efficiency in Honeycomb Core Structure Using Enhanced Diffusion Bonding

One of the main technology drivers for hypersonic vehicles such as NASP is the necessity for lightweight, high-temperature structures. In order to meet the design mass targets while maintaining strength and stiffness, highly efficient structures must be fabricated from low-density, high-temperature materials. One class of materials with the potential for meeting NASP objectives is the titanium aluminide Ti_xAl intermetallics and fiber-reinforced



Edgewise compression of Ti_3Al honeycomb core sandwich panels.

Ti_3Al composites. Previous work has established the potential of Enhanced Diffusion Bonding (EDB) as a joining process suitable for fabricating titanium-based honeycomb core sandwich structure. Further development of the EDB process procedures has focused on improving the properties of sandwich structure fabricated from monolithic Ti-14Al-21Nb (Ti_3Al) face sheets and Ti-3Al-2.5V honeycomb core.

The room and elevated temperature (1000°F) stress-strain curves shown in the figure were generated from an EDB honeycomb core sandwich panel loaded in edgewise compression (EWC). For comparison, the figure also shows the stress-strain behavior from Ti-14Al-21Nb face sheet tensile coupons exposed to simulated EDB processing conditions. The EWC test is used to measure the effectiveness of the core and the face sheet/core bond to stabilize the face sheets in compression. The desired result of the EWC tests is to develop full face sheet (compressive) yield properties. The data in the figure indicate that the face sheets of both specimens yielded prior to specimen failure. Thus, these results show that the EDB honey-

comb sandwich demonstrated panel structural stability beyond the yield strength of the Ti-14Al-21Nb face sheets at both room and 1000°F temperatures.

The figure also shows the room and 1000°F EWC load index for EDB honeycomb core sandwich specimens. The room temperature load

index was approximately 4000 lb/in., highly efficient for a panel weight of 1.25 lb/ft². The 1000°F load index approached 3000 lb/in., demonstrating high-temperature efficiency.

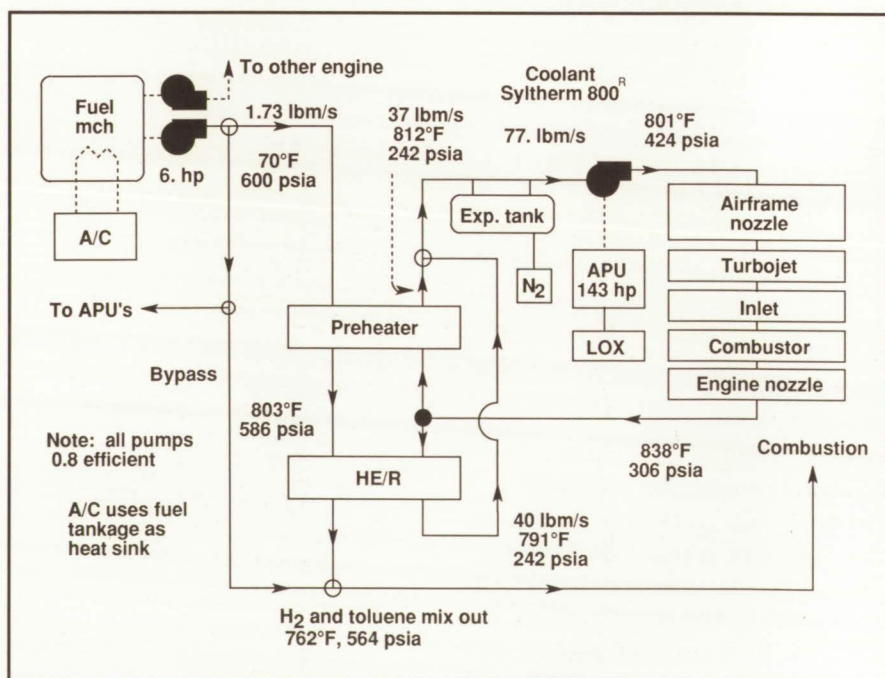
These figures show that the EDB joining process is effective for producing highly efficient structural panels at both room and elevated temperatures.

(Eric K. Hoffman and R. Keith Bird, 43127)

Structures Directorate

Thermal Management for Hypersonics

Hypersonic aircraft (those with flight Mach numbers greater than 5) are subject to aerodynamic heating that is often too severe for an insulated structure to survive without active cooling. The design and analysis of cooling systems and insulation are collectively called thermal management. Detailed studies of local heating leading to the



Cooling system schematic for Mach 5 cruise aircraft that uses endothermic fuel.

design of complete cooling systems have been initiated.

In the past year, a complete cooling system for a Mach 5 cruise aircraft that uses endothermic fuel has been designed. Methylcyclohexane, MCH, or an endothermic fuel, is stored at room temperature and undergoes an energy-absorbing chemical reaction to provide engine cooling. A secondary coolant loop transfers the heat from the engine surfaces to the heat sink. The heat sink is provided by a catalytic reactor operating in parallel with a fuel preheater. The working fluid for the closed loop is a silicone-based liquid polymer (Syltherm 800, a registered trademark of Dow Corning, Inc.). This concept avoids many of the difficulties associated with cryogenic fuels. A Langley Research Center developed high-temperature (4000°F) insulation is used on the engine walls.

The cooling system (with the operating conditions at Mach 5) is shown in the figure. The fuel flows first through the fuel preheater, next through the catalytic reactor (heat exchanger reactor or HE/R) and then is burned. In the closed loop, the heated coolant flow splits after exiting the last cooling panel in the engine nozzle, with almost one-half passing through the preheater and the rest passing through the reactor. After losing heat to the fuel, the flow is remixed at the inlet to the expansion tank. A nitrogen gas blanket fills any unused expansion tank volume. The coolant then is pressurized by the coolant pump and routed back, first to the airframe nozzle cooling panels and then to the engine cooling panels. The cooling panels are arranged in series with the heat load increasing with the direction of coolant flow. The coolant pump is driven by a 143-hp auxiliary power unit (APU). The ambient air at Mach 5 is too hot to use in the APU so a small amount of liquid oxygen

(LOX) is carried for that purpose. (Dennis Petley and Stuart Jones, 43759)

Aeronautics Directorate

NIST Large Temperature Difference Boil-Off Calorimeter

Advanced aerospace vehicles require structures and materials that are exposed to a wide range of temperatures. In support of current vehicle programs, a precision calorimeter has been designed, fabricated, and demonstrated. This calorimeter can accurately measure the thermal conductivity of insulation material from cryogenic to elevated temperatures while sustaining a through-the-thickness temperature (ΔT) of up to 1500°R.

In cooperation with the National Institute for Science and Technology (NIST), an upgraded precision boil-off calorimeter with partial pressures ranging from hard vacuum (10^{-5} torr) to approximately 2 atmospheres in virtually any gaseous medium has

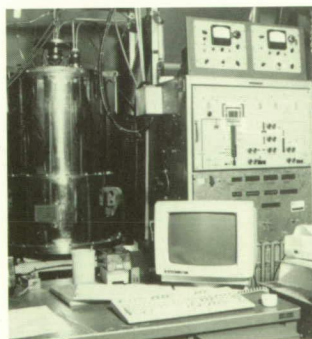
been modified to accommodate large ΔT conductivity measurements, using an electric-resistance, ceramic hot plate. The calorimeter has a closed-loop heat exchanger using liquid neon (LNe), at 48°R, as the refrigerant and liquid hydrogen (LH₂) as the coolant. The boil-off calorimeter now has two capabilities: precision conductivity measurements at LH₂ temperatures and above and a high ΔT measurement capability with a maximum temperature of 2000°R.

The 1500°R ΔT feature has been successfully demonstrated using liquid nitrogen (at 139°R) at the cold face. Conductivity data for two types of Rockwell Shuttle insulators (RSI) are shown in the figure. Note the high ΔT 's sustained and the large variation in conductivities.

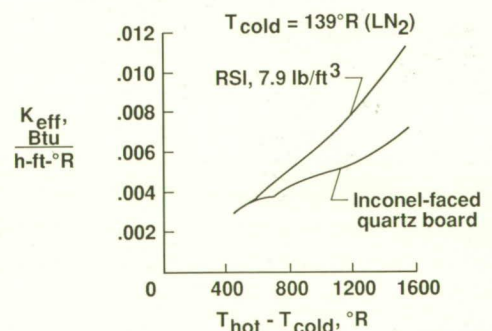
The upgraded boil-off calorimeter provides a unique national capability for precision conductivity measurements and will significantly enhance the ability to evaluate and predict the performance of insulation system and cryogenic structural concepts required in advanced aerospace vehicles.

(Allan H. Taylor, 45428)

Boil-off machine



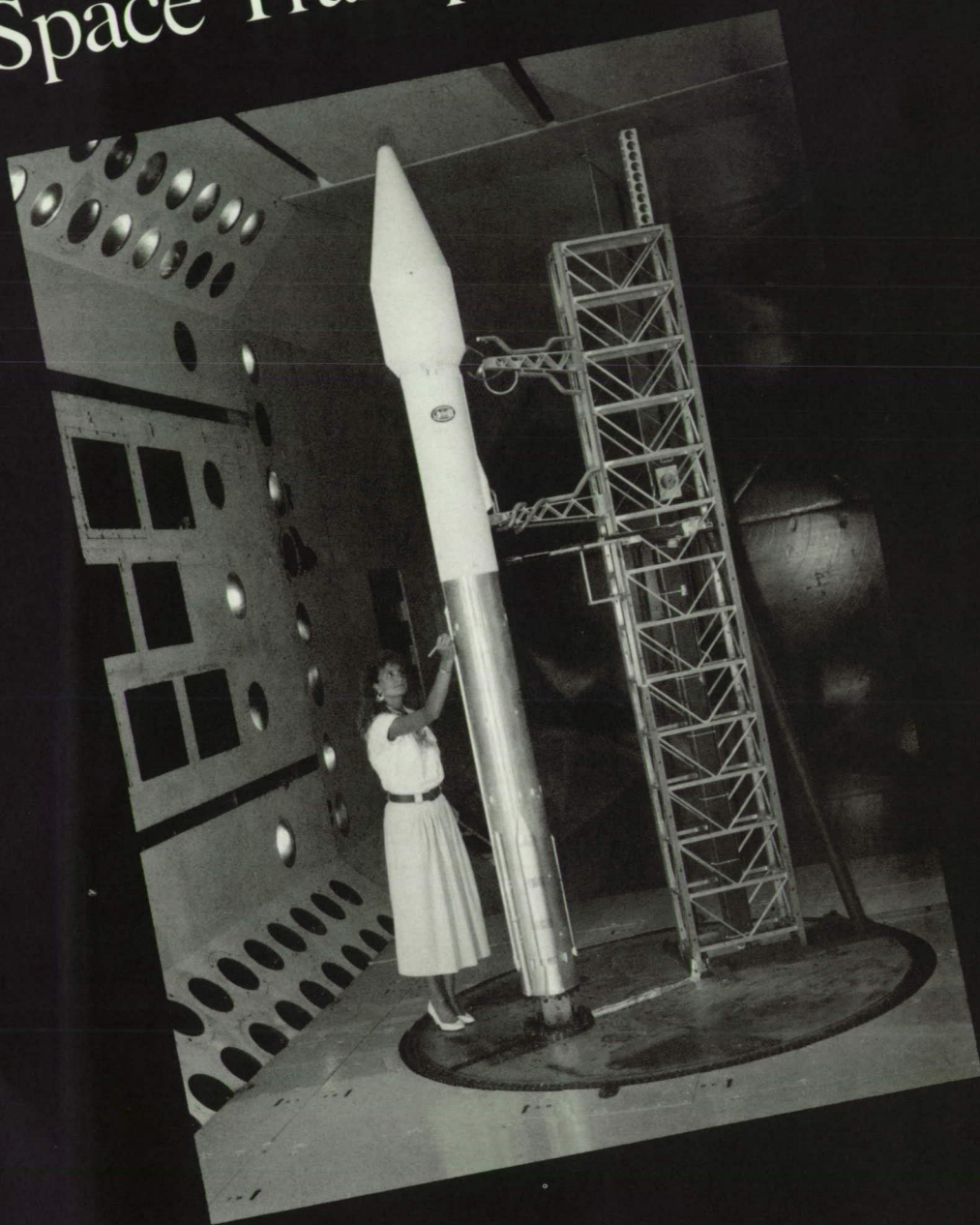
High-gradient measurements



Calorimeter and conductivity measurements.

L-90-1888

Space Transportation



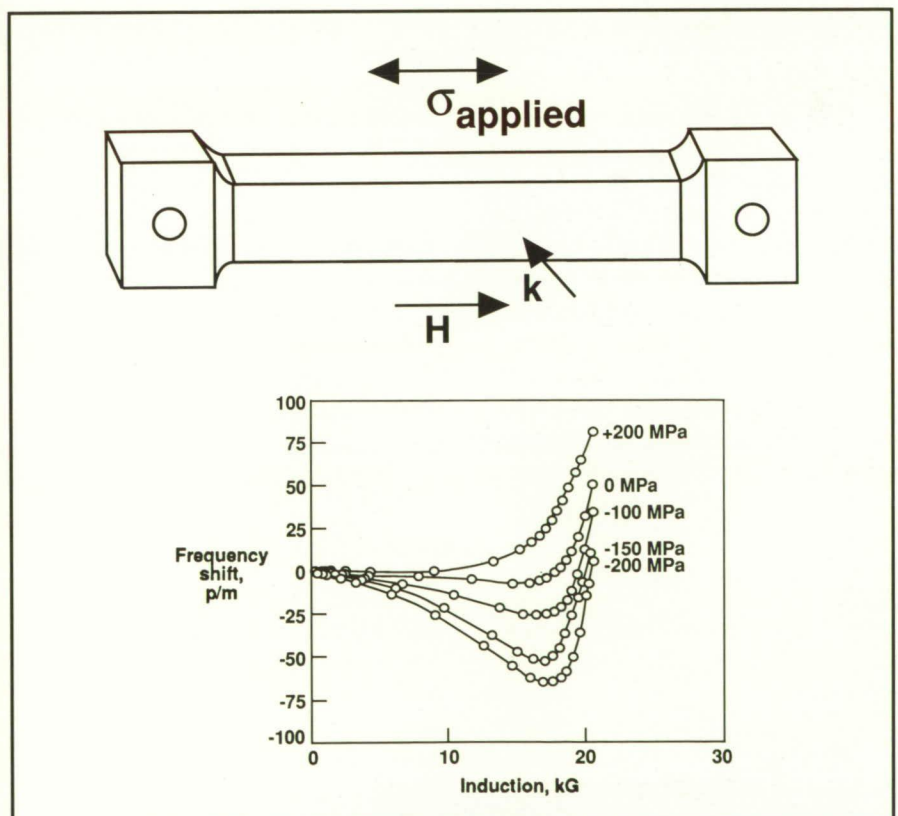
Magnetoacoustic Residual Stress Characterization of SRM D6AC Steel

During a launch, the areas near the Solid Rocket Motor (SRM) joints are under circumferential tensile stress with magnitudes beyond the yield stress of D6AC steel. As a result of repeated launches, some minute deformation occurs, and residual stress builds up near the pinhole areas of the SRM casing. Therefore, residual stress is a factor for SRM safety. The current methods to measure residual stress involve X-ray and neutron diffraction techniques. Both techniques have their shortcomings, and they are not generally suitable for field applications. Magnetoacoustic residual stress characterization has the potential to measure residual stress in D6AC steel and would be suitable for field applications.

Residual stress concerns were investigated by Thiokol Corporation using laboratory X-ray and neutron techniques. This test indicated that the residual compression is on the order of -1200 MPa right at the bottom of an attachment pinhole in a tang region of an SRM.

For a field test of residual stress, however, the neutron diffraction technique is not applicable due to the complexity in the beam source and detector system. The X-ray diffraction technique also suffers some drawbacks, such as extensive sample surface treatment and the range of interrogation being limited only to the surface region. A Langley Research Center developed technique (called magnetoacoustics) for residual stress characterization in a ferromagnet has been performed to demonstrate its feasibility.

The performance of the magnetoacoustic test involves the



Magnetoacoustic measurements at Langley Research Center.

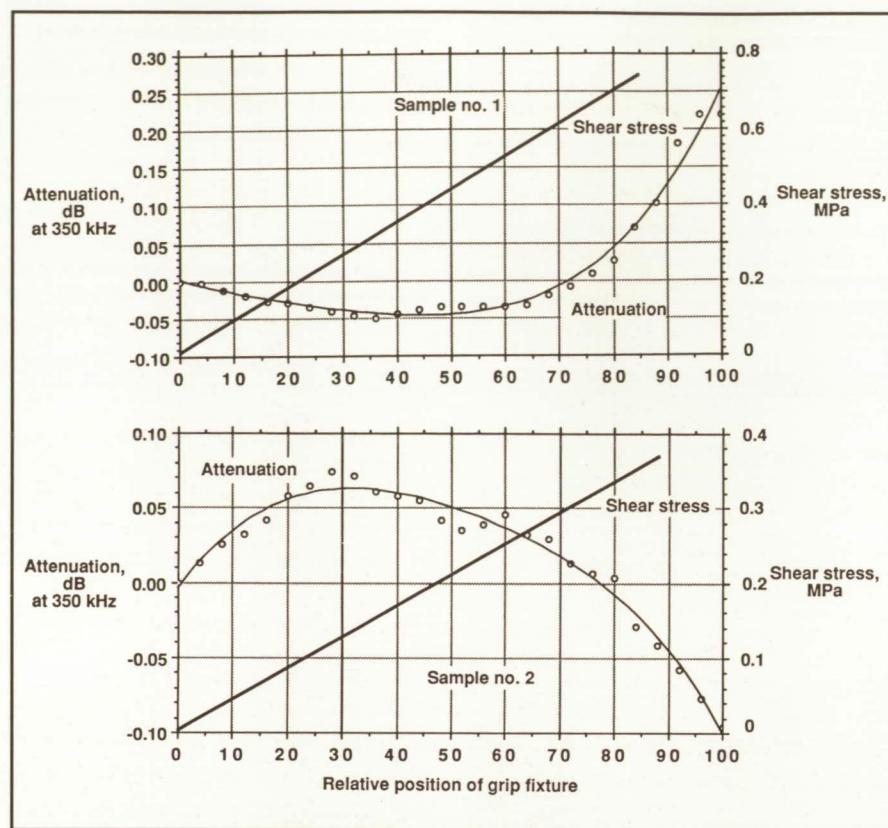
measurement of the fractional changes of acoustic natural velocity as a function of total magnetic induction. The upper part of the figure shows the SRM D6AC sample geometry. An external uniaxial stress σ was applied along the long axis of the sample, while propagating 5 MHz compressional waves k perpendicular to the uniaxial stress axis. In the lower portion of the figure, results of the magnetoacoustic measurements are shown and indicate the various levels of compressive stress state loads by the presence of the negative frequency shifts (the vertical axis) versus the magnetic induction (horizontal axis). The method does not require a calibration standard and shows promise as a new stress measuring technique.

(Min Namkung, 44962)
Electronics Directorate

Measurement and Analysis of Structural Adhesive Bond Strength

During the past year, research efforts have continued in a structural adhesive bond strength evaluation program using ultrasonic techniques. Several important properties of adhesion between an adhesive and a substrate can be studied by inducing shear deformation at the interface. The use of interfacial guided waves provides one convenient method to produce shear stresses at an interface. According to theory, the effective shear modulus of an adhesive can be calculated on the basis of its measured velocity and attenuation parameters and thus can be used to help characterize the effective elastic properties of a multilayered adhesive system.

Presently, attention is being focused on an adhesively bonded steel/adhesive/rubber interface to study the feasibility of future applica-



Variation in attenuation during shear loading.

tions to the case/insulation bond in the Space Shuttle Solid Rocket Motors. Ultrasonic attenuation information is obtained for a transmitted sound wave versus stress loads for several lap shear test samples, and it is shown in the figure. Data were compared for the good and poor bond conditions. Poor bonding was simulated by applying a thin layer of silicone oil on the surface of the steel mounting plate, prior to the application of the adhesive layer.

In the figure, the horizontal scale is defined as the percent of displacement of the load grips with respect to the total displacement at failure. For sample number 1 (top portion of the figure), which was a good bond, a small decrease is seen in the signal attenuation (vertical scale) from zero to a grip displacement of 36 percent (stress load of 0.34 MPa applied load). The figure also shows a significant increase in the signal attenuation beyond 36 percent

displacement. For sample number 2 (bottom portion of the figure), which represents a poor bond, a constant increase is seen in the signal attenuation to a grip displacement of 28 percent (0.12 MPa), followed by a constant decrease in the attenuation to the failure load.

Thus, for the good bond sample, the attenuation initially decreases and then increases, and for the poor bond, the attenuation curve behaves in an opposite manner. Part of this phenomenon can be explained in terms of the failure modes. For the good bond, it was observed that the sample failed within the rubber (cohesive failure) and left the adhesive intact on the mounting plates. In the case of the poor bond, the failure mode was adhesive and left the mounting plate essentially clear of any adhesive material.

This ultrasonic information will be correlated with bond strength to help assess structural adhesive

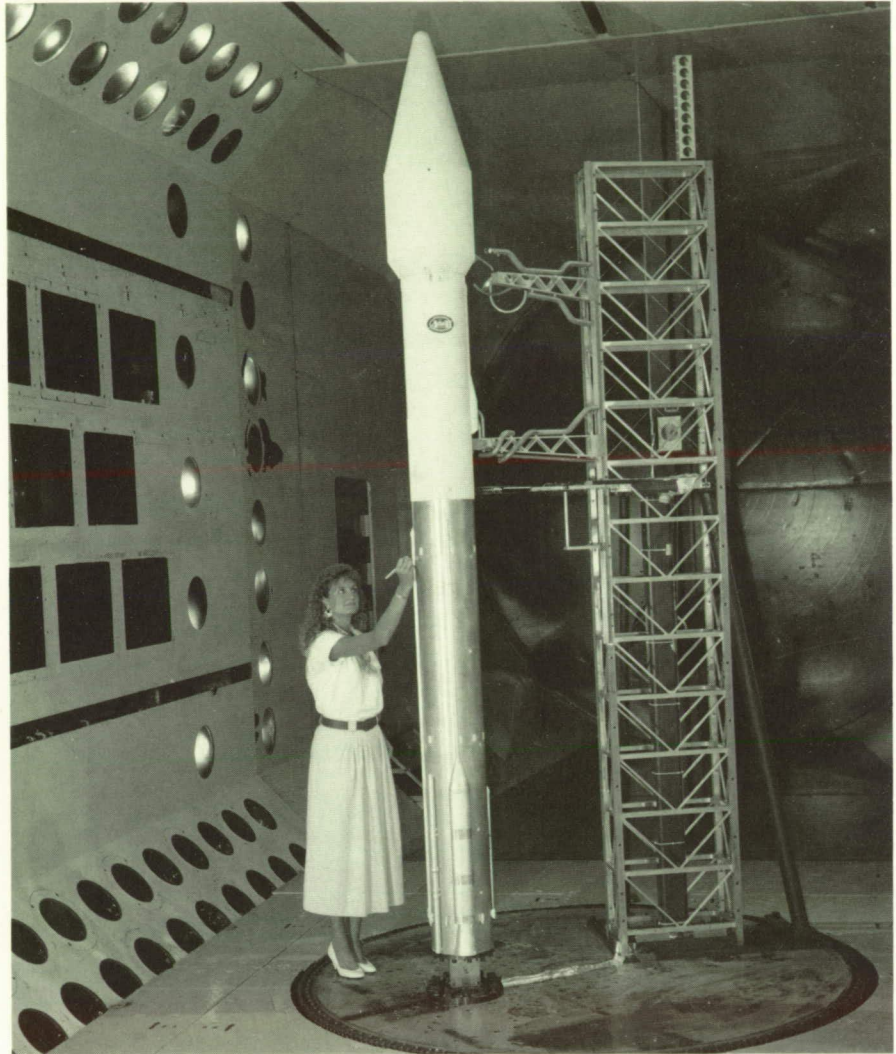
interfacial bonds used in critical applications of aerospace materials. Additional data will be obtained to relate both attenuation and ultrasonic velocity to an effective shear modulus of an interface.

(Alphonso C. Smith, 44961)
Electronics Directorate

Ground Wind Loads Characteristics for Atlas II

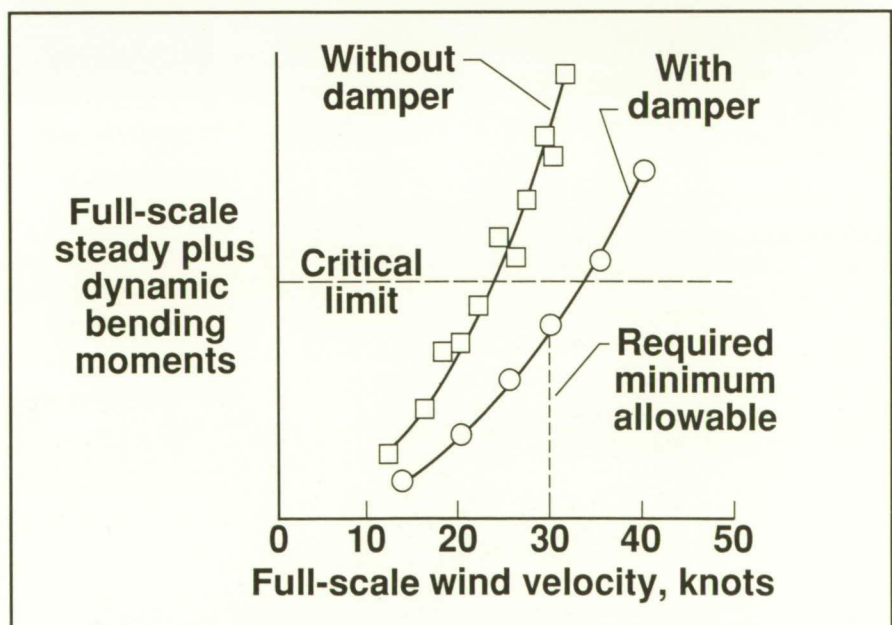
The Atlas II Expendable Booster, which is being developed by General Dynamics Corporation to launch both military and commercial payloads into orbit, is longer than previous Atlas configurations and will be able to launch larger and heavier payloads. As with all launch vehicles, concern exists about ground wind loads while the vehicle is on the launch pad being prepared for launch. The Atlas II is required to withstand loads produced by winds up to 30 knots. Ground wind loads include both steady drag loads and dynamic loads resulting from oscillatory flow around the vehicle. To determine the ground wind loads characteristics of the Atlas II, a 1/12-size dynamically scaled model was tested in the Transonic Dynamics Tunnel. A photograph of the test apparatus is shown in the figure. The model booster and umbilical tower were bolted to a large turntable that could be rotated 360° to simulate ground winds from any compass bearing. The payload fairing shown in the figure simulated a 14-ft-diameter full-scale fairing that will be used for large payloads. A simulated 11-ft-diameter fairing also was tested. The damper that extends out from the gantry to the booster also was simulated in the wind tunnel tests.

The variation of the resultant bending moment (a vector addition of steady and dynamic moments) near the base of the model booster for one



Atlas II ground wind loads model mounted in TDT.

L-89-7023



Atlas II ground wind loads with and without damper.

fuel condition and at a typical wind compass bearing with wind velocity is shown in the figure. The model data have been scaled to the full-scale values. The critical limit bending moment for the full-scale booster also is shown. Data obtained without the damper show that the critical limit is exceeded at approximately 23 knots. With the damper installed, however, the bending moment at 30 knots is less than the critical limit.

These tests have shown that, if final launch procedures are begun only when the weather forecast is good, launches will rarely if ever have to be scrubbed because of

excessive winds after the fueling process has begun.
(Moses G. Farmer, Ellen C. Parker, and Bryan E. Dansberry, 41263)

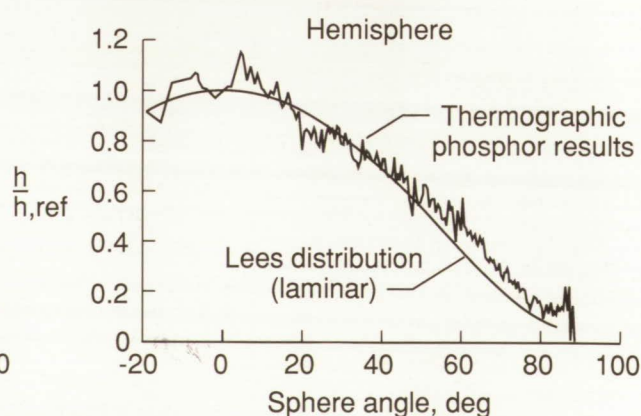
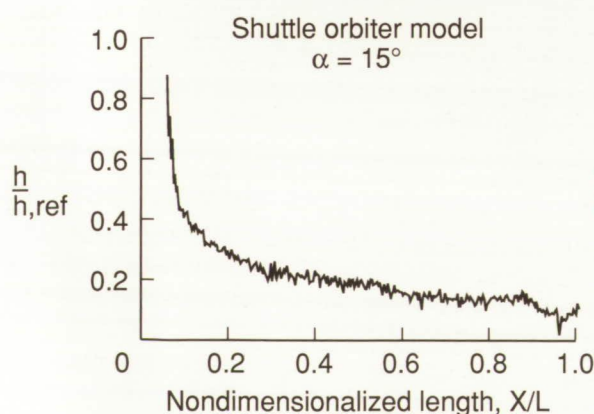
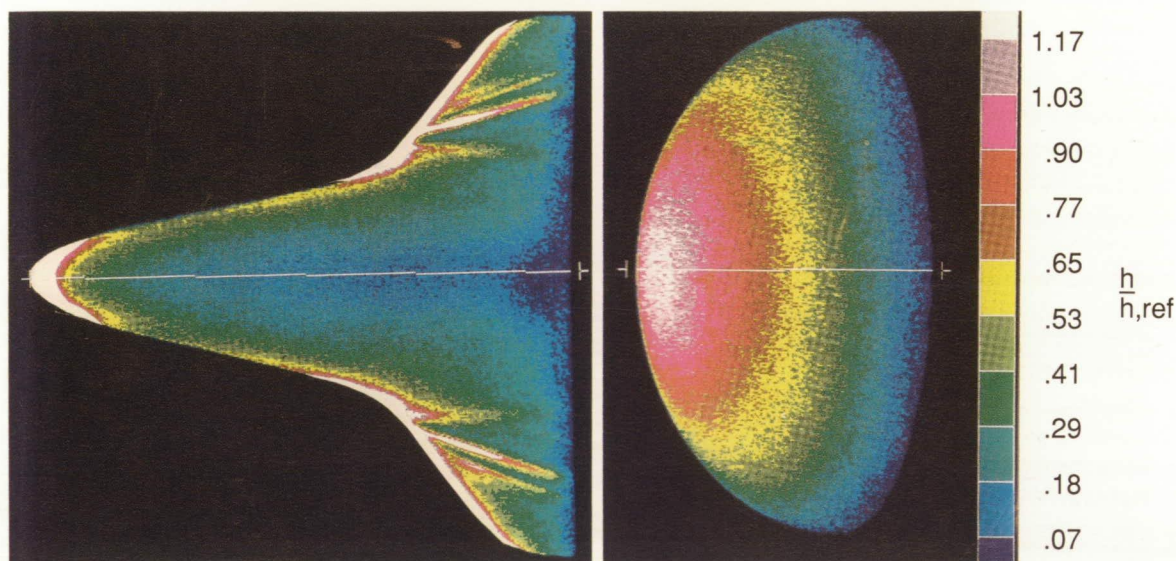
Structures Directorate

Surface Temperature/Heat-Transfer Measurements Using Optical Fluorescence Thermography System

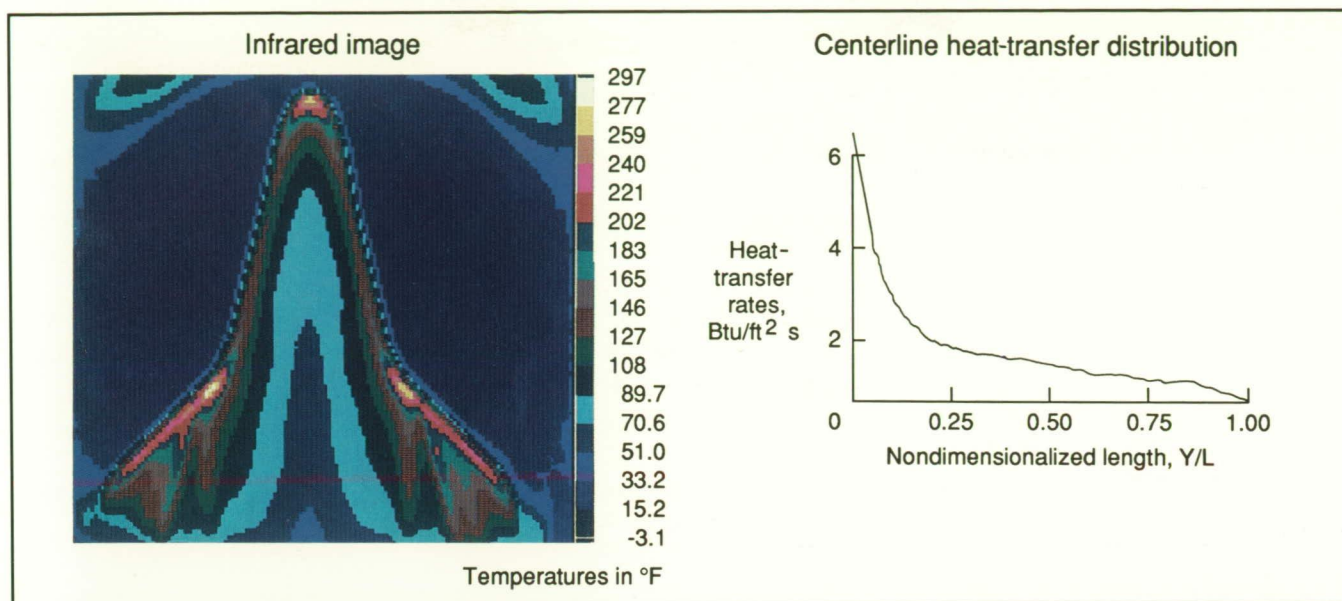
An optical fluorescence thermography (OFT) system has been developed for hypersonic

aerothermodynamic studies using a two-color phosphor technique. Thermal images provide temperature data with time for surface heat-transfer calculations. Temperature-sensitive ceramic coatings, or phosphors, are applied to ceramic base models. When excited by ultraviolet radiation, the model coating fluoresces visually. Test measurements are based on relative wavelength fluorescence.

Aerothermodynamic tests were performed in the 31-Inch Mach 10 Tunnel on a Space Shuttle orbiter model at angles of attack α up to



Surface heating distributions on ceramic phosphor models at Mach 10 in air (Space Shuttle orbiter model, $Re = 1.5 \times 10^6$, and hemisphere model, $Re = 0.4 \times 10^6$).



Surface heating distributions on Space Shuttle orbiter model at Mach 10 in air ($\alpha = 15^\circ$ and $Re = 1.5 \times 10^6$, at a test time of 3 s).

orbiter entry angles to study bow-shock/wing-shock interaction for Reynolds numbers Re from 0.2×10^6 to 1.5×10^6 , based on model length. The OFT system was developed for accurate measurements and improved spatial resolution, such as needed for resolving surface streak heating at shock intersections. Tests also were performed on a ceramic hemisphere to obtain confidence in heat-transfer results. A viewing angle of 18.8° measured from the window normal was used to obtain stagnation point and surface distribution data. As shown, hemisphere data agree quantitatively with the stagnation point theory of Fay and Riddell and tend to follow a laminar heating distribution as predicted by Lee. Surface ceramic coatings were relatively rough, and future fabrication methods are being developed to provide a smoother coating. Ceramic fabrication, coating, and OFT techniques are being developed to provide inexpensive and accurate aerothermodynamic test models. (Gregory M. Buck, 45240) Space Directorate

Evaluation of Infrared Thermography for Hypersonic Heat-Transfer Measurements

Infrared thermography (IRT) techniques were evaluated for providing nonintrusive global heat transfer rate measurements on wind tunnel models in hypersonic flow. Because of recent advances in infrared technology and image processing, a program was initiated to compare IRT with other techniques for providing surface temperature/heat-transfer measurements on various aerodynamic geometries at hypersonic speeds. A commercial infrared imaging system with an $8\text{-}\mu\text{m}$ to $12\text{-}\mu\text{m}$ wavelength bandpass and a video rate of 6.25 frames per second was utilized. A PC-based image processing system capable of real-time digitization, processing, and display of data was used. A zinc selenide window, optimized for 98 percent transmission of the $8\text{-}\mu\text{m}$ to $12\text{-}\mu\text{m}$ range, was utilized for optical access to the wind tunnel test section. The spectral emittance of wind tunnel model material was measured using spectrophotometric techniques.

A series of tests were conducted on a Space Shuttle orbiter model in the 31-Inch Mach 10 Tunnel for model angles of attack α of 0° , 15° , and 30° and Reynolds numbers Re of 0.2×10^6 and 1.5×10^6 based on model length. The infrared images provided real-time qualitative heating patterns such as effects of shock/shock interaction on the model. The time variation of measured surface temperature distributions was used for calculating heat-transfer rates based on the one-dimensional semi-infinite heat-transfer principle.

This IRT thermographic measurement capability has been developed and applied in three hypersonic wind tunnels, the 31-Inch Mach 10 Tunnel, the 20-Inch Mach 6 Tunnel, and the Langley Mach 20 Leg of the High Reynolds Number Helium Tunnel Complex. Initial test results demonstrate a capability to provide nonintrusive heat-transfer measurements in hypersonic facilities using IRT.

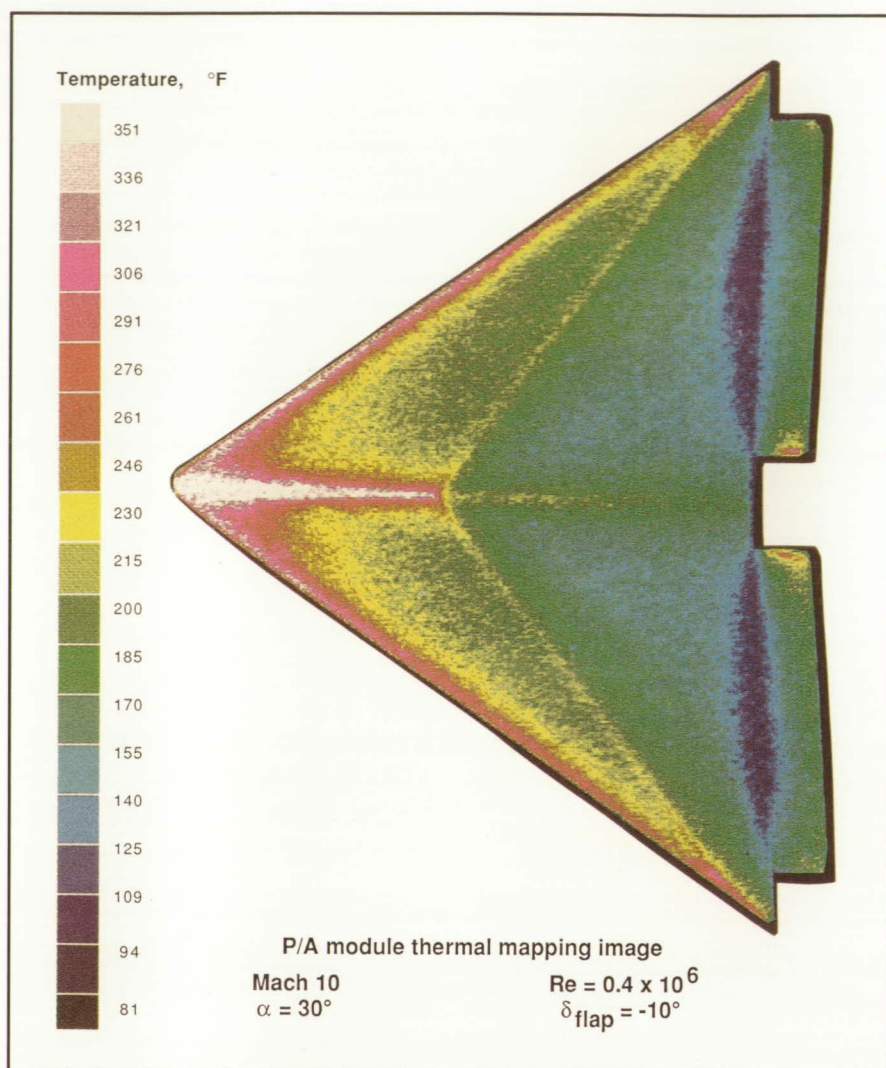
(Kamran Daryabeigi, 44745, and Gregory M. Buck) Space Directorate

Aerothermodynamic and Aerodynamic Testing of Propulsion/Avionics Module

As part of a cooperative agreement between Martin Marietta Corporation Manned Space Systems and Langley Research Center, thermal mapping patterns were determined on a wedge-shaped propulsion/avionics (P/A) module. The wedge-shaped entry vehicle is a proposed reusable carrier for the high-cost propulsion and avionics components of a rocket booster package. Tests were performed in the 31-Inch Mach 10 Tunnel over a Reynolds number range of 0.25×10^6 to 1.3×10^6 and from angles of attack of 0° to 35° .

Thermal mapping images were obtained using a two-color phosphor thermography technique. In this method, ceramic models are coated with phosphor materials that radiate in the visible spectrum according to their temperature when excited by ultraviolet light. A video camera and data acquisition system record, digitize, and store images during a tunnel run. The images later are retrieved for surface temperature analysis. Results from tests in the 31-Inch Mach 10 Tunnel are shown in the figure as surface temperature distributions on the windward side of the model. High surface temperatures are noted on the body nose, leading edges, and windward surface chines. High temperatures reveal the reattachment regions at the trailing edges of the flaps, and the cooler zones at the base of the flaps indicate flow separation.

Further aerodynamic tests to obtain force and moment data are planned for the Hypersonic Facilities Complex. Extensive testing across the hypersonic speed range will establish aerothermodynamic data



Thermal mapping of windward surface of P/A module.

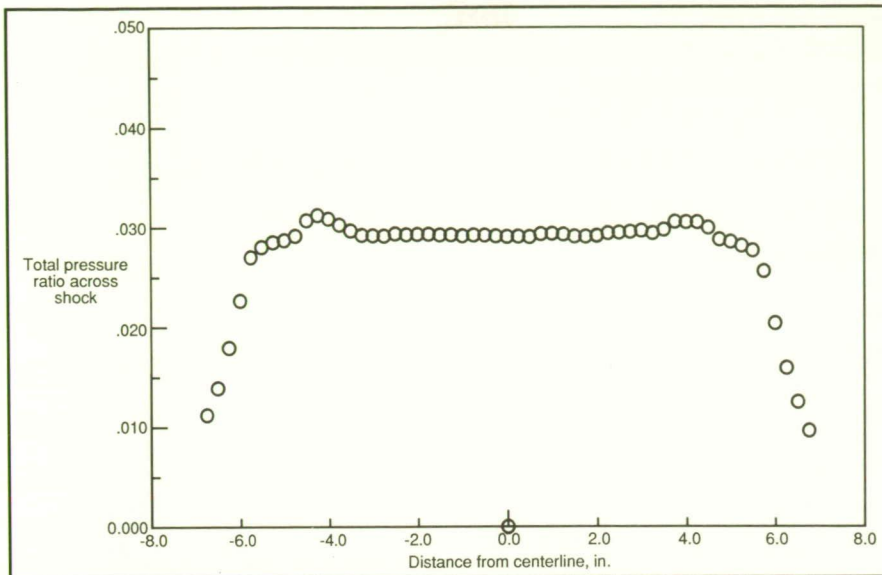
and complement the aerodynamic data already available for the P/A module.

(Charles M. Hackett, 47661)
Space Directorate

Flow Field Calibration of 15-Inch Mach 6 High-Temperature Tunnel

The 15-Inch Mach 6 High-Temperature Tunnel, formerly the Hypersonic Flow Apparatus, was originally designed for Mach 10 flow.

The axisymmetric nozzle was recently modified to provide Mach 6 flow at Reynolds numbers and wall temperature ratios similar to the 31-Inch Mach 10 tunnel. The inviscid contours for the modified nozzle were developed using an inverse method of characteristics procedure; corrections to the wall contour for viscous effects were made using a finite-difference boundary-layer code. The flow field was analyzed by a Navier-Stokes solver to verify the accuracy of the design procedure. Further, the nozzle contour was machined to a tolerance of ± 0.0005 in. in the throat region, ± 0.001 in.



Pitot-pressure profile for 15-Inch Mach 6 High-Temperature Tunnel ($P_0 = 135$ psia and $T_0 = 1230^\circ\text{R}$).

downstream of the inflection region, and ± 0.002 in. throughout the remainder of the nozzle. Such stringent standards help provide higher flow quality.

The tunnel is presently being calibrated; preliminary pitot surveys of the test section have revealed good flow uniformity. As shown in the figure, at a stagnation pressure P_0 of 135 psia and a stagnation temperature T_0 of 1230°R , the center 6 in. of the flow field has less than a ± 2 -percent variation in the ratio of measured pitot pressure to upstream stagnation pressure. The tunnel has been run at stagnation conditions ranging from 45 psia to 135 psia total pressure and 850°R to 1250°R total temperature. Further calibrations are planned over a more extensive operating range. (Jeffrey S. Hodge and Charles M. Hackett, 45237) Space Directorate

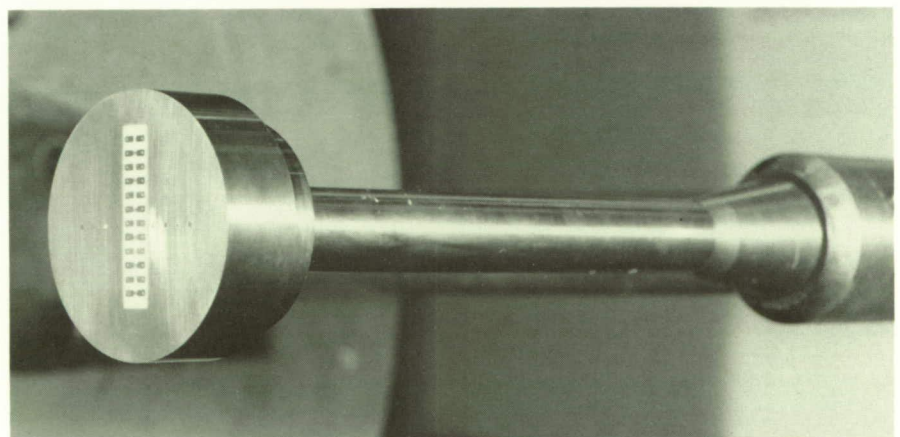
Assessment of Two Heat-Transfer Measurement Techniques

Because of the increased importance of heat-transfer measurements for computational fluid dynamics code validation and the subsequent increased demand for aerothermodynamic models, the Langley Research Center instrumentation capability is being severely taxed in the fabrication and installation of thin-film heat-transfer gauges. To increase the model completion rate,

alternative sensor construction techniques are being explored.

A study is under way in the 31-Inch Mach 10 Tunnel to assess fabrication and installation refinements and requirements for thin-film and coaxial thermocouple heat-transfer sensors. This facility was chosen because of its excellent flow quality and uniformity. The study was designed to compare, for the same test model and free-stream conditions, the sensitivity, repeatability, durability, and accuracy of the two types of sensors and their refinements. Also included in the study was an evaluation of the relative ease of their fabrication and use. The selected models were flat-faced cylinders, instrumented on the front face and aligned normal to the flow. Heat-transfer data were obtained at conditions covering the current operating range of the facility.

Preliminary results indicate that the performance of the gauges that are painted on the model is comparable to that of the gauges that are sputtered. Hand-painted thin-film sensors significantly reduce the time required to instrument a model compared with the current mechanical process of sputtering. In order to translate the response of the thin-film resistance sensor into heating rates, the thermophysical properties of the



Heat-transfer model installed in 31-Inch Mach 10 Tunnel.

L-89-13521

sensor backing or substrate material must be known. A substrate calibration unit has been constructed at Langley Research Center to evaluate substrate properties. This unit is currently being utilized to study substrate properties associated with hand-painted thin-film sensors.

In addition, fast-response coaxial surface thermocouples are being evaluated for possible use in the Hypersonic Facilities Complex. Coaxial thermocouples are attractive from an economical viewpoint because they can be reused many times and are simple to install. The data from the coaxial thermocouples are presently being analyzed to determine their usefulness as heat flux sensors in the hypersonic wind tunnels.

(Thomas J. Horvath, 45236)
Space Directorate

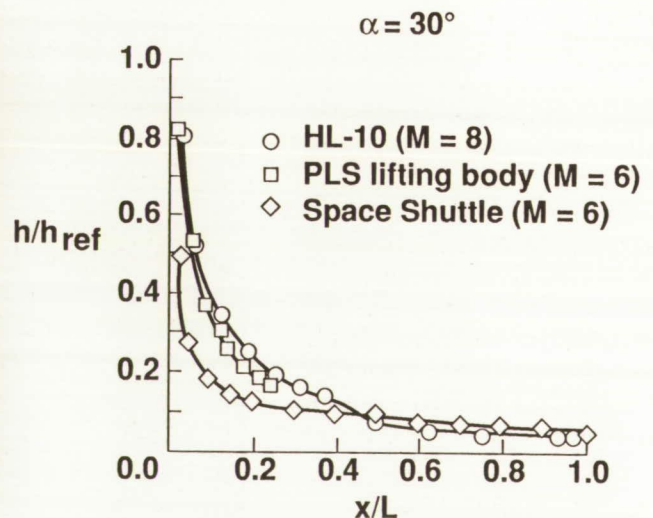
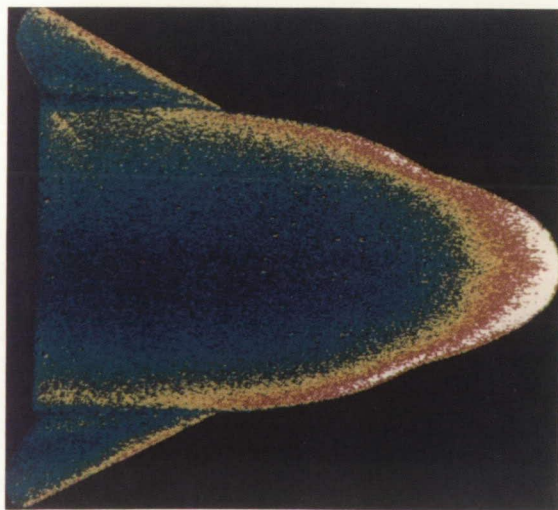
Aerothermodynamic Measurements on Proposed Personnel Launch System Vehicle

Langley Research Center is studying a lifting-body concept as a candidate for the Assured Crew Return Vehicle (ACRV) which would serve as a safeguard for Space Station *Freedom* personnel. This configuration, also being studied as a candidate for the Personnel Launch System (PLS), is similar to the NASA HL-10 and M2-F2 and the U.S. Air Force X-24A lifting-body concepts studied in the 1960's. An 0.02 scale representative of the proposed configuration was tested in the 31-Inch Mach 10 and 20-Inch Mach 6 Tunnels (in air) as well as the Hypersonic CF₄ Tunnel and the Langley Hypersonic Helium Tunnel Facility at Mach 6 and Mach 20, respectively, to develop an experimental aerothermodynamic data base. Thermal mapping patterns, heat-transfer distributions, and surface streamline patterns were obtained at angles of attack of 0° to

40° and unit Reynolds numbers of $0.25 \times 10^6/\text{ft}$ to $8 \times 10^6/\text{ft}$.

As expected, areas that experienced the highest heating were the nose and the tip-fin leading edges. Nondimensionalized windward centerline heating coefficients were compared with those obtained on the HL-10 lifting-body configuration, and the agreement was excellent. For laminar flow, windward centerline heating increased with increasing angle of attack, while no significant effects of compressibility were measured. Transition from a laminar to a turbulent boundary layer resulted in a factor of 3 to 4 increase in windward centerline heating at the highest unit Reynolds number in Mach 6 air.

The planform shape was responsible for streamwise-oriented embedded boundary-layer vortices that resulted in localized striation heating patterns on the windward surface. Shear-layer reattachment on the canopy face was observed at all test conditions and resulted in high



PLS hypersonic aerothermodynamic characteristics.

L-90-6235

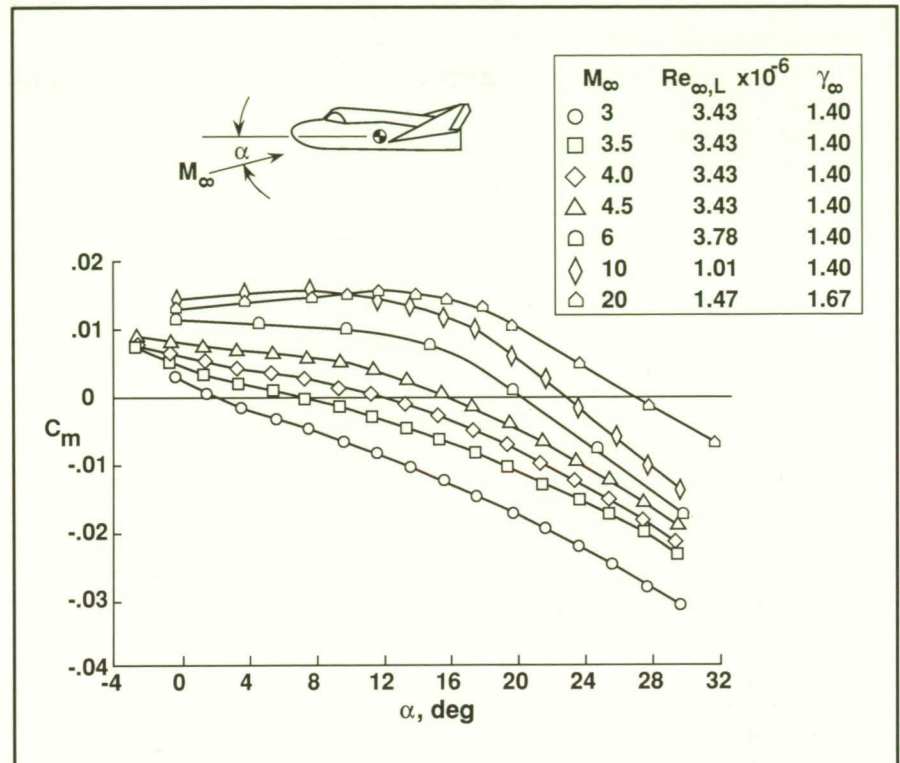
heating rates. Leeward cross flow separation and centerline vortex reattachment were evident across the Reynolds number and angle-of-attack ranges, indicative of a complex flow field. Leeward reattachment near the base of the model, where control surfaces would be located, was observed in both the heating and oil-flow patterns.

(Thomas J. Horvath, 45236)
Space Directorate

Experimental Aerodynamic Characteristics of Proposed PLS Lifting-Body Concept

An extensive aerodynamic data base for the Langley Research Center proposed lifting-body concept for a PLS is being developed at Langley. Aerodynamic measurements for the concept were made over scale models of the proposed 24.6-ft flight vehicle in eight Langley facilities, including four facilities in the Langley Hypersonic Facilities Complex. The present data base was obtained over a Mach number range from 0.1 to 20. Hypersonically, a Reynolds number variation from $0.60 \times 10^6/\text{ft}$ to $7.5 \times 10^6/\text{ft}$ in air and from $0.25 \times 10^6/\text{ft}$ to $0.58 \times 10^6/\text{ft}$ in CF_4 was achieved. The low γ (ratio of specific heats) aspect of a real gas in thermochemical equilibrium was simulated at Mach 6 by testing in ideal air (free-stream $\gamma = 1.4$) and in CF_4 (free-stream $\gamma = 1.22$). The effects of compressibility, viscosity, and real gas on aerodynamic characteristics for the PLS concept were examined. Hypersonic aerodynamic coefficients predicted with the Langley-developed Navier-Stokes solver, LAURA (Langley Aerothermodynamic Upwind Relaxation Algorithm) which was exercised in an inviscid manner, were compared with measurement.

As shown in the figure, results of this study indicate that the proposed



Variation of pitching-moment coefficient with angle of attack for range of Mach number.

lifting-body concept has aerodynamic characteristics that make it an attractive candidate for a PLS. This PLS concept is longitudinally and laterally stable and naturally trimmed (i.e., zero control deflection) in the subsonic, transonic, and hypersonic speed regimes, trimming near maximum lift-to-drag ratio L/D . In the Mach range from approximately 1.5 to 3.0, pitch control input will be necessary to trim to positive lift conditions. Hypersonic L/D values give it sufficient cross range capability, and the subsonic L/D offers the possibility of conventional aircraft-like landing. The aerodynamic data generated from this study are an essential portion of the information needed to define, evaluate, and select a PLS vehicle.

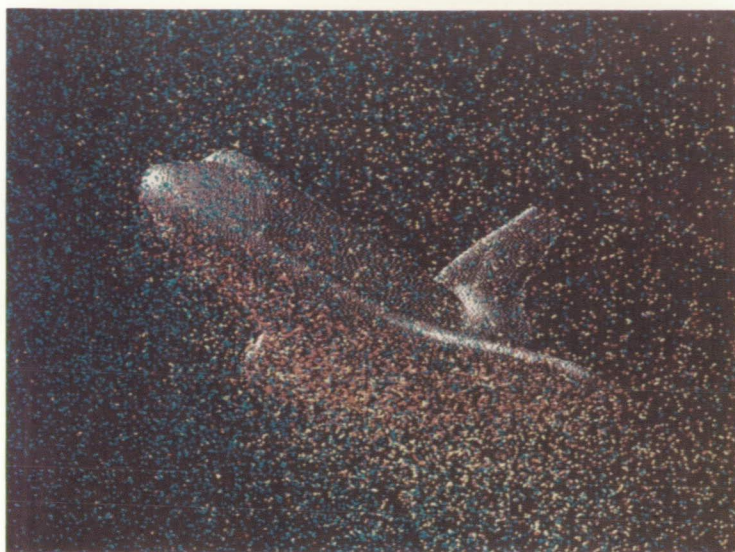
(John R. Micol, 45250, and George Ware)

Space Directorate

New Three-Dimensional DSMC Code

A new fast computer program for the Direct Simulation Monte Carlo (DSMC) method has been developed to more efficiently compute rarefied gas flows about complex three-dimensional shapes. The DSMC method is a technique for the computer modeling of a real gas by thousands of simulated molecules. The velocity components and position coordinates of these molecules are concurrently followed through representative collisions and boundary interactions in simulated physical space. The DSMC method, as developed by Graeme A. Bird, University of Sydney, Australia, is the most widely used method today for simulating rarefied flows in an engineering context.

In this new program developed by Bird, the vehicle body and other



Alt = 120 km

DSMC simulation of flow about Space Shuttle orbiter (altitude of 120 km, V_∞ of 7.5 km/s, and α of 40°).

surfaces are defined by a set of very small rectangular blocks called position elements (PE's). The PE's are set during the initialization process from a tabulated list of the surface coordinates of the vehicle. Thus, the position of a simulated molecule is defined by a single integer for the PE in which it lies rather than by the three components of Cartesian coordinates. Although the vehicle shape is "stepped" at the resolution of the PE's, the exact direction cosines of the corresponding point on the surface are stored with each PE and used in the calculations. This information is used for the surface reflection of the molecules so that the PE model looks smooth to the incident molecules.

The new method has been used to calculate the rarefied gas flow over the Space Shuttle orbiter. The flow over the orbiter at an altitude of 120 km and angle of attack α of 40° is shown in the figure in which the color-coded dots represent different collisional processes. The blue dots

represent stream molecules that are unaffected by the presence of the vehicle, the red dots are molecules that have collided with the vehicle surface, and the yellow dots are the stream molecules that have collided with other molecules, red or yellow.

The new DSMC program reduces the computational time by an order of magnitude when compared with the earlier general DSMC programs. However, just as important is the ease with which flow boundaries may be specified for applications with complex three-dimensional geometry. (J. N. Moss and G. A. Bird, 44379) Space Directorate

Shuttle Infrared Leeside Temperature Sensing Experiment

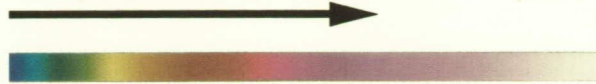
The Shuttle Infrared Leeside Temperature Sensing (SILTS) experiment is designed to obtain

high-spatial-resolution temperature measurements of the leeside surfaces of the Space Shuttle orbiter during atmospheric entry. These measurements are obtained by means of an imaging, infrared radiometer (camera) mounted in an experiment pod atop the vertical tail of the orbiter *Columbia*. The radiometer is mounted in such a way that it may view the leeside surfaces through either of two infrared-transparent windows, one which provides a view of the orbiter fuselage and one which provides a view of the left wing. The infrared detector senses the level of infrared radiation emanating from the surfaces being viewed. Postflight processing of the detector output data provides for determination of the surface temperature.

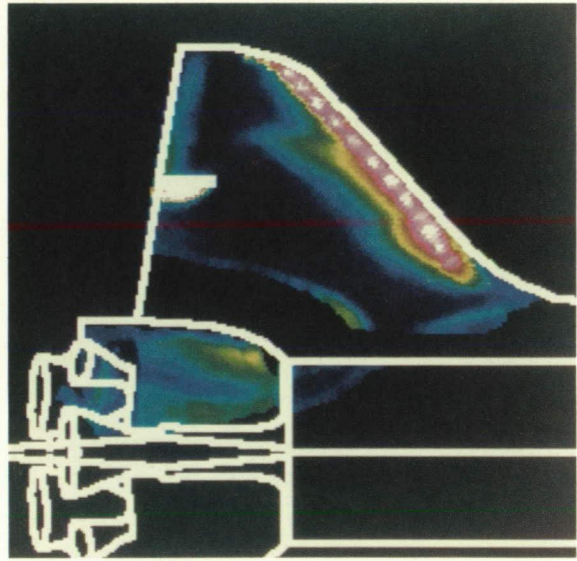
The SILTS experiment obtained high-quality imagery of the left wing of the orbiter during entry on Space Shuttle missions STS-28 and STS-32. The figure contains typical SILTS false-color image data, shown both as they appear from the vantage point of the camera and as projected onto the orbiter planview. Features evident in the image include the wing leading edge, the gap between the inboard and outboard elevons, and the orbital maneuvering system (OMS) pod at the base of the vertical tail. The accuracy of the SILTS-inferred surface temperature data has been validated by comparison with measurements from in situ surface thermocouples. The basic SILTS imagery also has been cast in a time-variable presentation format (movie) which enables observation of the variability of the wing leeside thermal environment throughout the hypersonic portion of entry.

The STS-28 and STS-32 experiment results have provided the first accurate measurements and the leeside surface temperature of an entry vehicle in flight with high spatial resolution. The SILTS results constitute benchmark flight data with which to assess the applicability of

Increasing Temperature



Camera View



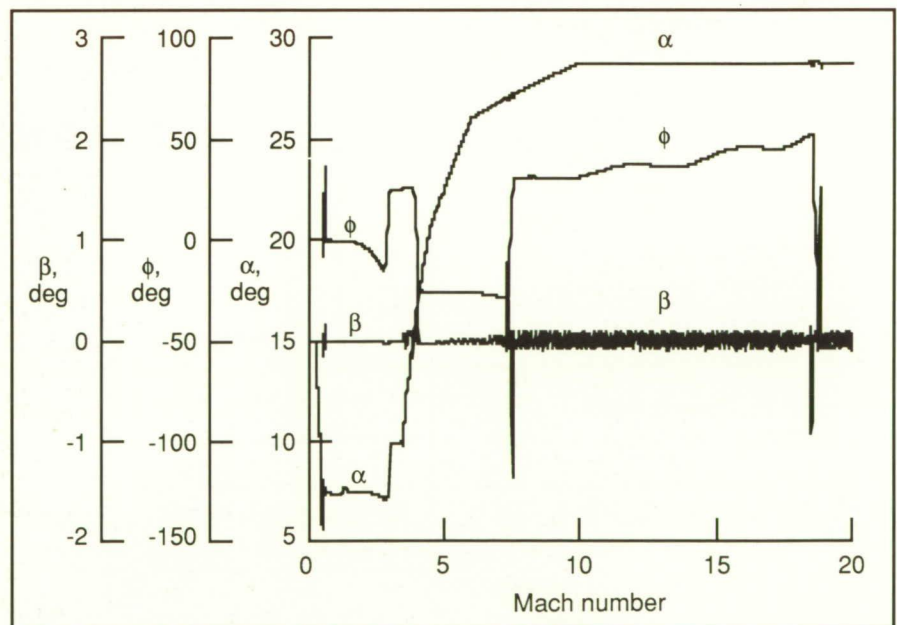
Projection to Planview

Typical SILTS image data from STS-28.

state-of-the-art computational fluid dynamic codes for simulation of the leeside flow field of a lifting vehicle during entry from low-Earth orbit. (D. A. Throckmorton and E. V. Zoby, 44406) Space Directorate

Lifting-Body Personnel Launch System Flyability Analysis

With the advent of Space Station Freedom, the need to augment manned access capability to space will increase. Many alternative approaches to provide this service are being studied. However, the approach that offers the most flexibility is a lifting-body configuration that



Nominal six-degree-of-freedom Personnel Launch System entry profile. (α , β , and ϕ are angle of attack, sideslip, and roll, respectively).

would be launched by an expendable rocket booster. This configuration offers the potential for runway landings at multiple sites and low acceleration during entry. Because of these features, an initial study was performed to establish the feasibility of this concept. This preliminary study established that five landing sites would provide landing opportunities within one orbit after leaving Space Station *Freedom* and, in many cases, multiple landing site selection. In addition, entry deceleration of <2.5 g was demonstrated.

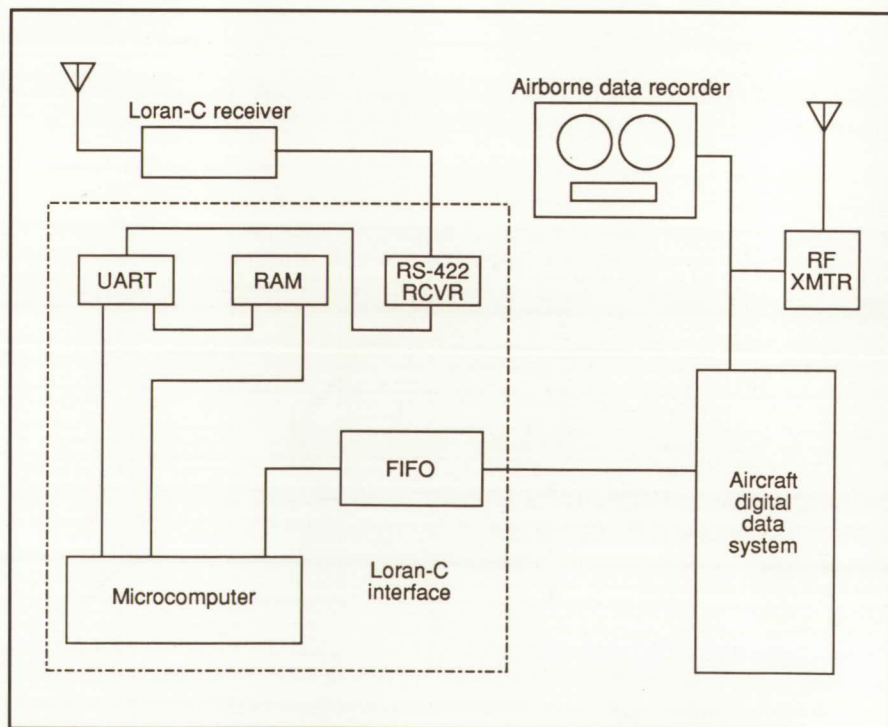
Because of the findings of the initial study, a second-phase, more detailed analysis was conducted, including packaging, center-of-gravity, and mass properties determinations. In addition, a more complete aerodynamic data base was constructed composed of a combination of theoretical and wind tunnel data. These data permitted a six-degree-of-freedom simulation analysis to assess the flyability of the vehicle. The analysis included off-nominal atmospheric conditions (density profiles and steady-state winds) but no turbulence or gusts. The results of the six-degree-of-freedom study completed to date are that precision landings within 400 ft of the nominal and 5 ft of the lateral landing site with touchdown vertical velocities <5 ft/s have been demonstrated and that entries with no lateral center-of-gravity offset consume <40 lb of reaction control system (RCS) propellant. Those entries with a lateral center-of-gravity offset of 0.5 in. consume approximately 200 lb. (Richard W. Powell, 44506) Space Directorate

Aircraft Electronic Subsystem for Acquisition of Loran-C Navigation Data

In order to chart the atmospheric electrical potential at NASA launch sites, the joint Langley Research Center/Marshall Space Flight Center Airborne Field Mills (ABFM) project required acquisition of asynchronous navigation data from the Learjet research aircraft. A microcontroller subsystem was developed to acquire position information from a Loran-C receiver and merge the data into the Learjet digital data acquisition system for onboard recording, which then is telemetered in real time into the launch site ground tracking facility. This development provides a very cost-effective method to acquire aircraft position data without using an expensive inertial navigation system (INS).

Loran-C data are acquired over an RS-422 interface using a universal asynchronous receiver transmitter (UART), a random access memory (RAM) for data capture, and a first-in-first-out (FIFO) buffer, all running under the control of a microcomputer. The navigation parameters are stored in blocks in circular buffers so that the latest Loran-C data sets always are available for output through the telemetry system. Excellent data have been acquired on more than 30 ABFM research flights at Kennedy Space Center. The Loran-C data capture electronics has future flight application to smart aircraft systems with asynchronous serial output such as Global Positioning System (GPS) receivers.

(Daniel R. Norfolk, 43820) Electronics Directorate



Loran-C aircraft position data acquisition electronics.

Built-up Structure for Cryogenic Tanks Using Superplastic Forming

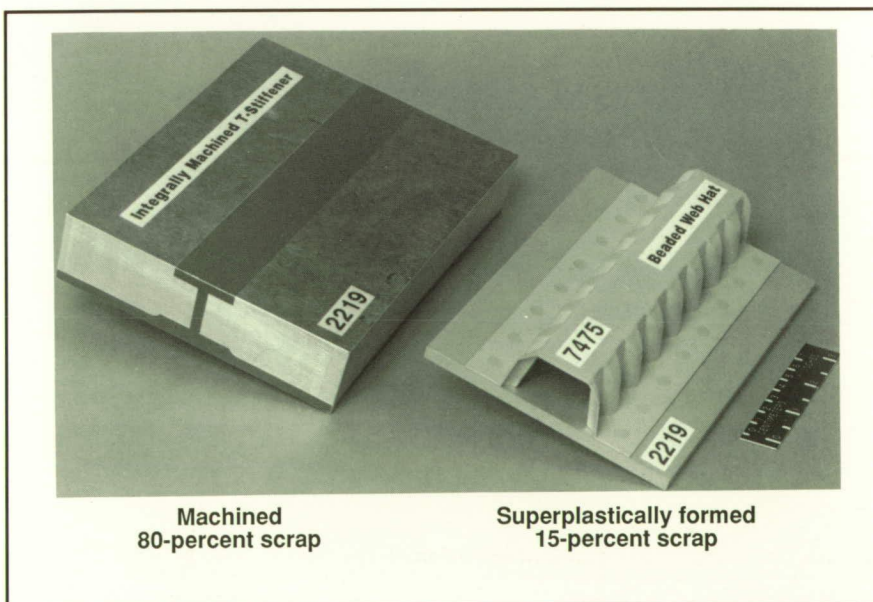
A number of advanced aluminum alloys, when deformed in tension at elevated temperatures, are capable of achieving large, uniform elongation (>500 percent) at low stresses prior to localized thinning and fracture. Such behavior is termed superplasticity and is typically associated with material that has a highly refined grain structure. Due to the large forming strains made possible by superplastic forming (SPF), unique, complex structural shapes can be formed in a single operation that would be difficult or impossible to produce using conventional processes. Because of the low stresses associated with SPF, hat stiffeners such as the beaded web can be molded using simple dies and inert gas pressure to generate the required flow stress to form the part. Results of a previous study conducted at Langley Research Center showed that the structural efficiency of hat stiffeners can be increased by as much as 60 percent

by using more complex stiffener configurations such as the SPF beaded web.

Recent research and development have demonstrated the potential to utilize this forming technique for fabrication of low-cost, lightweight, expendable cryogenic tanks using high-strength/low-density aluminum-lithium alloys and SPF processes in support of the Advanced Launch System program. The Space Shuttle external tank, which represents the state of the art, is fabricated from 2219 aluminum. The external tank is integrally machined and chemically milled from 2-in.-thick plate to form a T stiffened panel. Using this method, approximately 80 percent of the starting plate is machined away as scrap, which prohibits the use of Al-Li alloys that are approximately 5 times the cost of 2219 aluminum. In the built-up structure approach for tank fabrication, superplastically formed stiffeners will be joined to skin material of uniform thickness using resistance spot-welding techniques. The built-up structure approach is estimated to reduce scrap

rate to 15 percent and to significantly lower material costs for fabrication of cryogenic propellant tanks. Furthermore, the decrease in material buy-to-fly ratio afforded by the built-up structure approach will make it cost effective to use low-density aluminum-lithium alloys to reduce tank weight and increase performance.

(John A. Wagner, 43132)
Structures Directorate

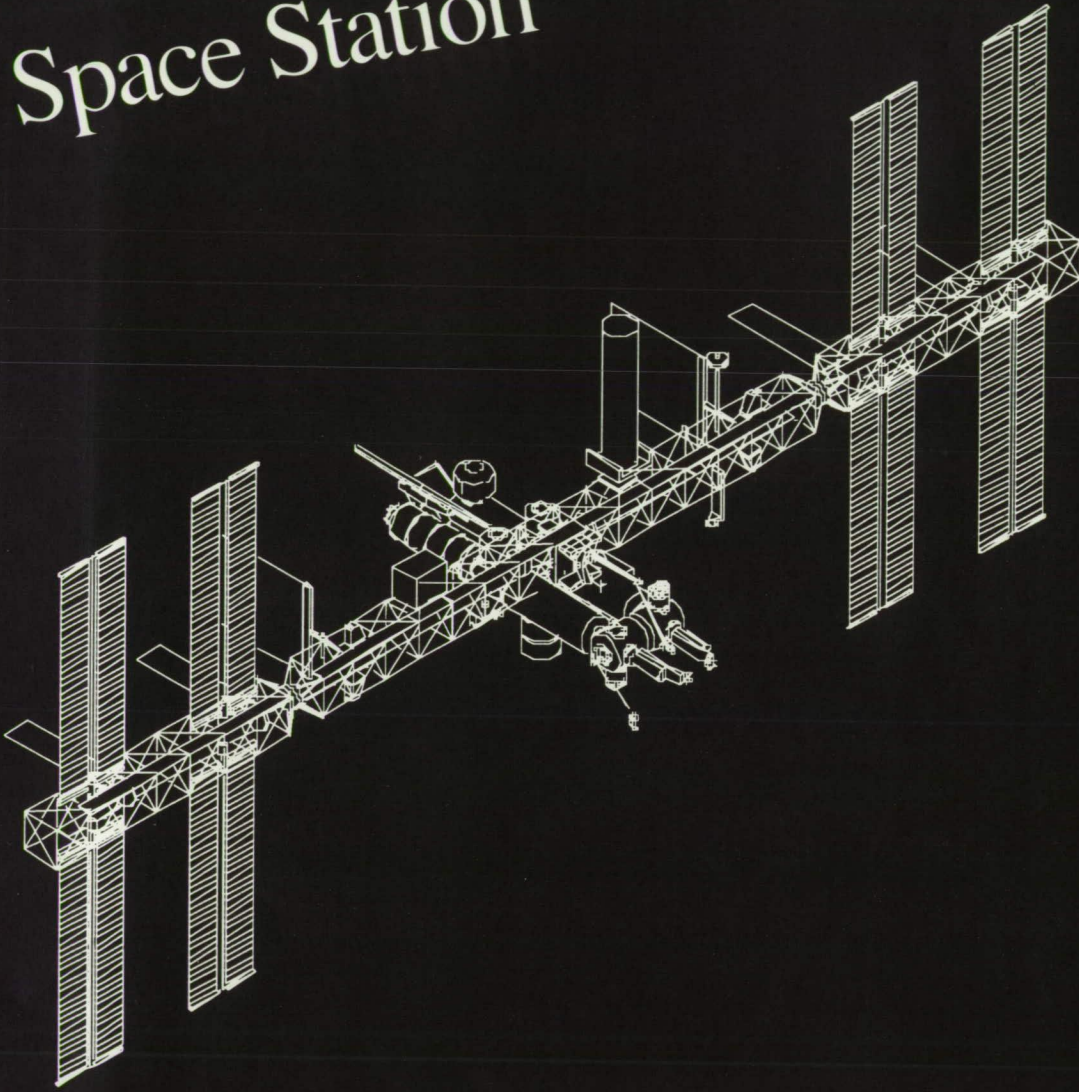


Aluminum cryotank structure.

L-90-2231

ORIGINAL PAGE
BLACK AND WHITE PHOTOGRAPH

Space Station



Noncontacting Motion Monitoring System

A noncontacting motion-sensing system has been developed to monitor a cart moving along a track on the Crew and Equipment Translation Aid (CETA) experiment for the STS-37 flight. The system uses two Hall effect sensors that detect magnets placed at stations along the track to determine the position, velocity, and acceleration of the cart as it moves along a 50-ft track. This motion monitoring system is designed to evaluate different means of propelling personnel and equipment in space. Because of the low frictional force that exists between the cart and the track in orbit, a noncontacting-type sensor is required to avoid affecting the experiment. Other constraints (such as small size and lower power consumption) made the Hall effect sensor the most attractive candidate.

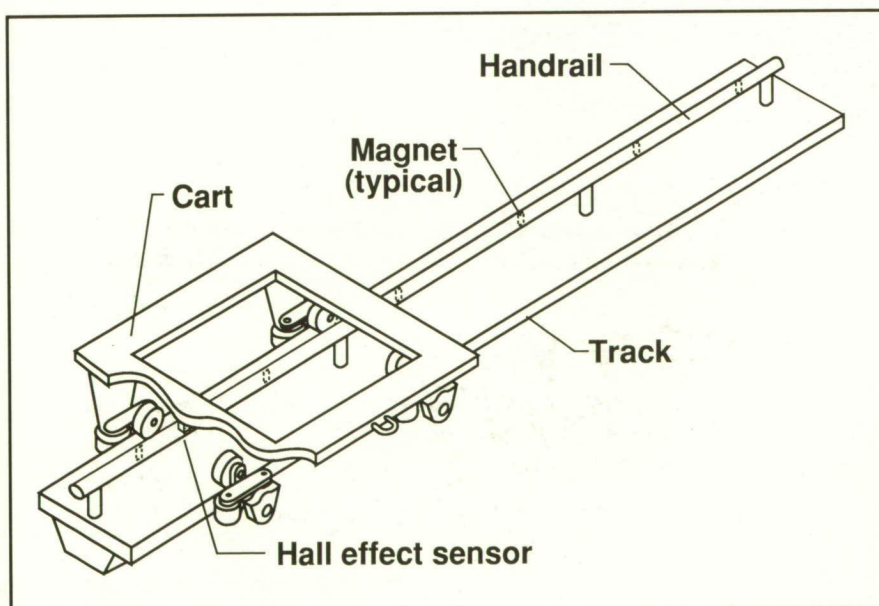
The designed system can measure the velocity of the cart up to 6 ft per second over a wide temperature range, and it will accommodate the movements of the cart in directions

perpendicular to the primary motion axis. The position can be measured at magnet locations within 0.2 in., and the velocity can be calculated within ± 1.6 percent of reading. The system requires little external circuitry and needs no adjustments. This motion sensing system, developed for the CETA project, represents an innovative design to make velocity measurements in space. The simple low-cost design was completed and delivered within a short period of time.

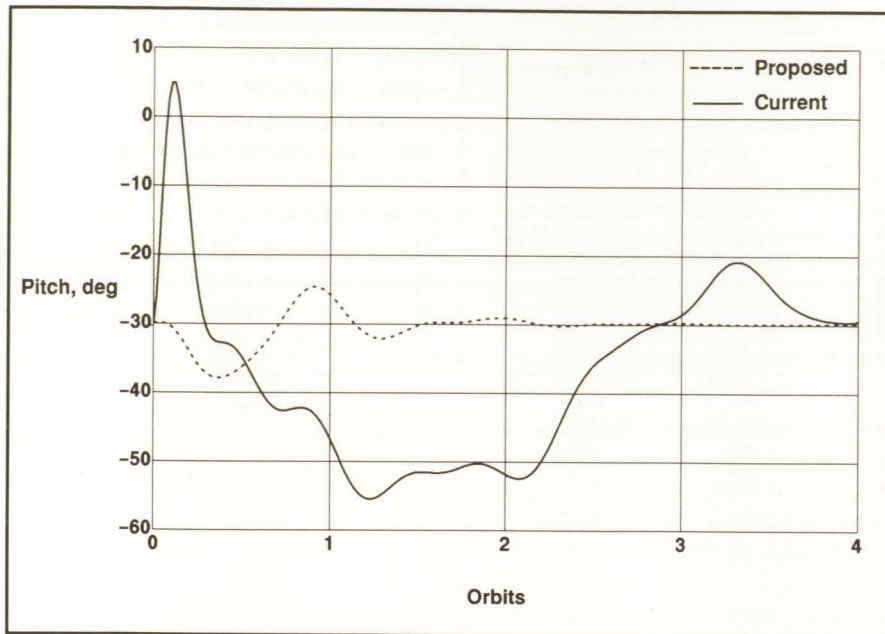
(Tom D. Finley, 44660)
Electronics Directorate

Predicted Torque Equilibrium Attitude Utilization for Space Station Freedom Attitude Control

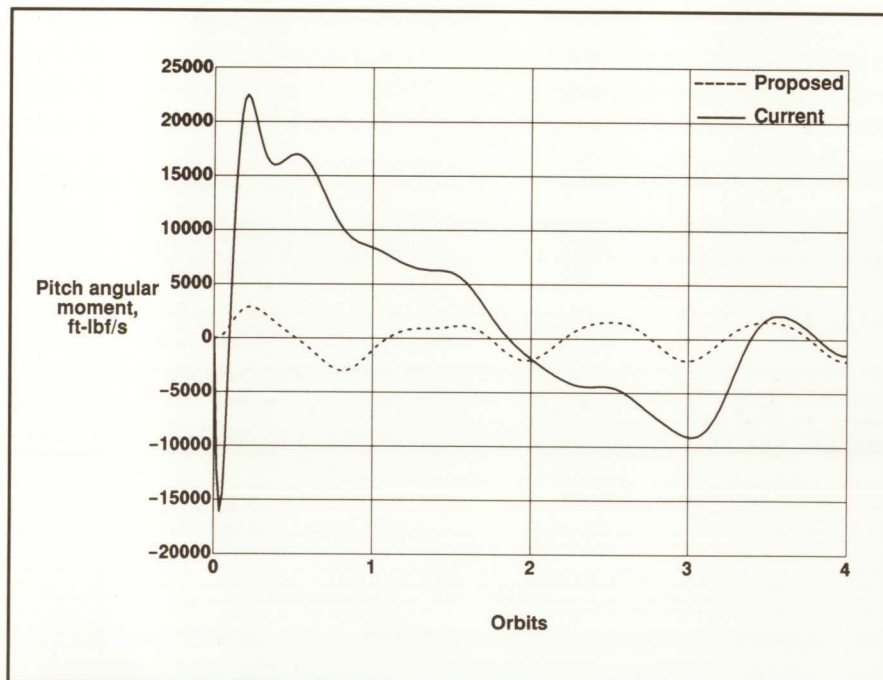
A number of continuous momentum management schemes have been proposed for Space Station *Freedom* attitude control using Control Moment Gyros (CMG's). These schemes exhibit satisfactory performance in the steady-state regime, but the transient behavior may be



CETA motion monitoring system.



Pitch attitude history.



Pitch angular momentum history.

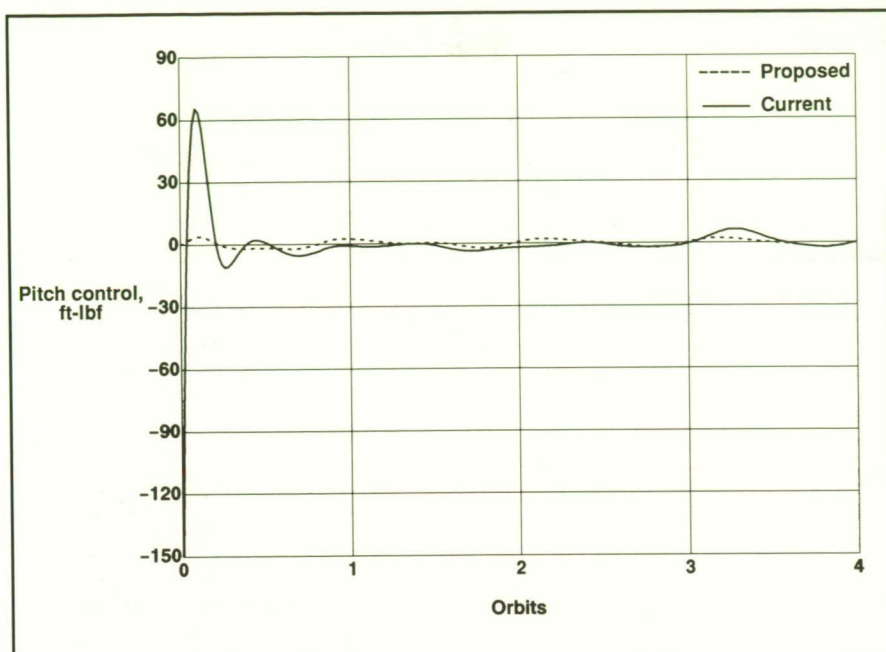
drag caused by solar flare activity, and the changes in solar geometry and configuration geometry. For the four orbit simulations studied, the TEA was considered to be a constant. The disturbing torques arise from aerodynamic and solar radiation pressure forces acting on the spacecraft center of pressure, which in general is offset from the center of mass. A good approximation of the three-axis TEA's can be obtained computationally with the software module Articulated Rigid-body Control Dynamics (ARCD) of the IDEAS² software. This program determines the angular momentum requirements for an articulating spacecraft to maintain a fixed attitude with respect to a local vertical/local horizontal (LVLH) orientation for a given orbit. A rotating Jacchia 1970 (J70) atmospheric density model is used to compute the aerodynamic torque acting on the spacecraft, and the solar pressure effects also are included to obtain realistic environmental effects. The TEA is that value of constant attitude which minimizes the peak angular momentum requirements and has zero or small secular momentum buildup. This attitude is quickly found iteratively.

Alternatively, the three-axis TEA's can be predicted using the software module Attitude Predict (ATTPRED) of the IDEAS² software. The feedback control law with arbitrary values of the TEA's can be used for the first run, and the attitudes about which the spacecraft oscillates in steady state are used as the predicted TEA. If the predicted TEA obtained is small, the equations of motion for the attitude control of the station can be linearized about LVLH and a simple state transformation applied. This process improves the performance of the attitude control/CMG momentum management. For large predicted TEA's, the linearization must be performed about the predicted TEA.

undesirable. The transient peaks of CMG angular momentum and control torque requirements may saturate the CMG's, thus disabling further attitude control. A study has been done of a control scheme that eliminates the undesirable transient

behavior by using a predicted Torque Equilibrium Attitude (TEA).

Under normal conditions, *Freedom's* TEA will change slowly due to the aerodynamic drag increase as the orbit decays, the change in



Pitch control torque history.

All three figures show the pitch attitude, pitch momentum, and control torque histories for a Space Station configuration with large pitch TEA (-29.88°) and small roll-yaw TEA. The linearization was performed about the large pitch TEA and small roll-yaw TEA's, and the gains for a full-state pitch feedback controller were obtained by a pole-placement scheme. The graphs clearly indicate that the proposed scheme shown in broken lines has smaller attitude excursions about the TEA and smaller angular momentum and control torque peaks, and takes a shorter time to reach steady-state conditions. The superiority of the new control law is amplified for large TEA configurations, in comparison to previous methods. The angular momentum requirements and the control effort and attitude oscillation amplitudes about the TEA are reduced drastically.

To operationally take advantage of the proposed control law, the spacecraft would be controlled using the Reaction Control System (RCS) or suitable Space Shuttle orbiter

manipulator arms to the predicted TEA. The CMG mode then would be switched on with the proposed control law for further attitude control about the TEA.

(Renjith R. Kumar, 41950, and Michael L. Heck)
Space Directorate

Space Station Freedom Power Growth Study

Space Station Freedom (SSF) will provide a permanently manned facility in space to support scientific research and, eventually, to provide the capability to accommodate the processing of space exploration vehicles for the lunar/Mars missions. In order to provide the necessary capability to satisfy future mission and user needs, the resources available on SSF must grow beyond that of the Assembly Complete (AC) baseline space station. One of the most critical resources for the accommodation of user needs is power.

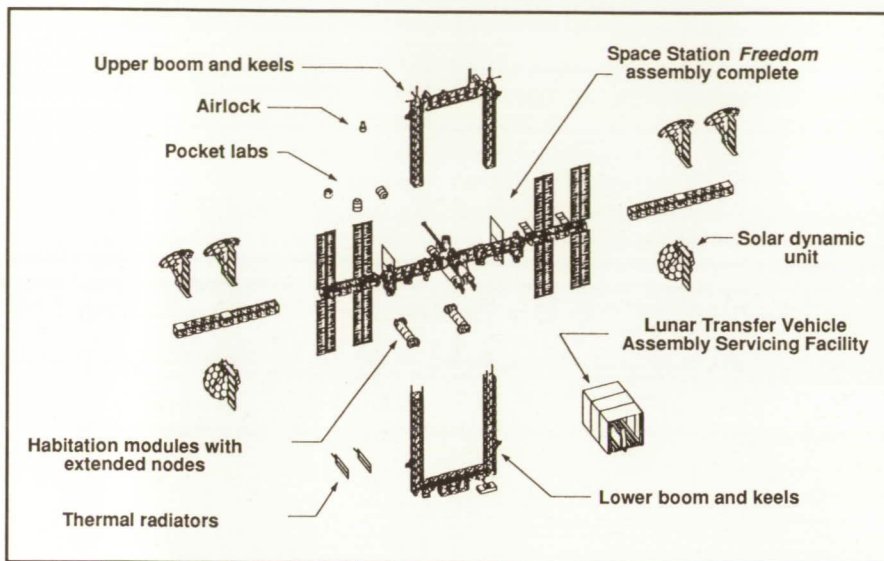
The Space Station Freedom Office/Evolutionary Definition Office conducted an extensive study to determine the growth power requirements and the impacts on the SSF systems resulting from growth of the power system. In all cases, two options were defined: a minimum impact option (lowest up-front costs) and an option that would result in the lowest life cycle costs.

Analysis of user needs derived from data supplied by the NASA Headquarters user representatives and by recent traffic models resulted in a requirement to grow to a 225-kW power system in the final evolution steps of SSF. This number is determined by the necessity to support research and technology experiments for both pure research and for precursor missions for the Space Exploration Initiative (SEI) and by the additional elements that must be added to the AC SSF to accommodate user needs.

System impact studies were conducted for the Electrical Power System (EPS), the Thermal Control System (TCS), the Integrated Truss Assembly (ITA), and the Data Management System (DMS). The results of these studies indicated that the major issues for power growth are associated with the TCS and with the subsystems of the ITA (i.e., structures, Solar Alpha Joint, and utility distribution systems).

Top-level conclusions from the power growth study are that options that result in minimum impact to the AC SSF are available in all cases; minimum impact options are generally at the expense of increased future cost, weight, crew time for EVA, and operational complexity; and growth requirements must be established soon to preserve necessary system "scars" in the baseline.

Additional analyses by the SSF work package organizations are required to verify the conclusions



Growth concept extended operations capability.

reached by the Langley Research Center Power Growth Study and to further define the baseline "scars" for the SSF Preliminary Design Review (PDR).

(Barry D. Meredith, 41960)
Space Directorate

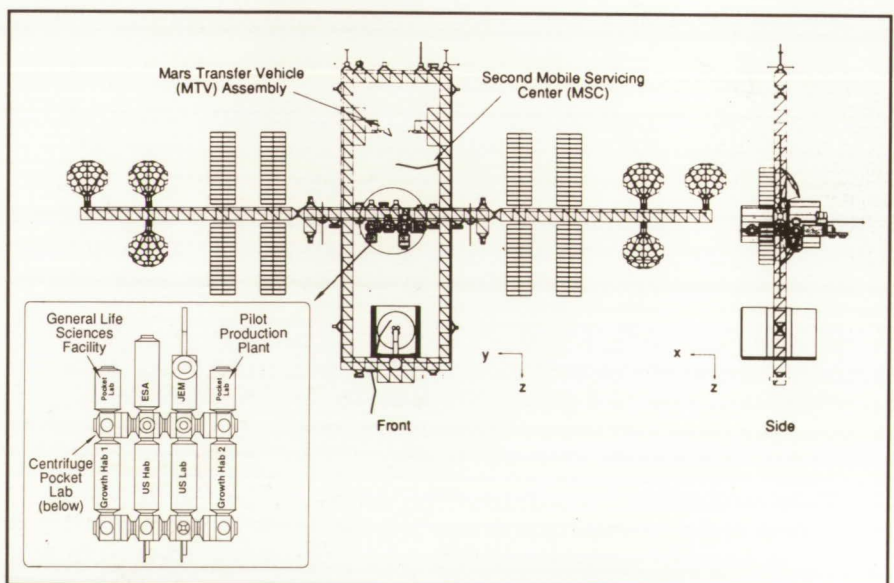
Space Station *Freedom* Evolution to Accommodate Space Exploration Initiative

For several years, the Langley Research Center Space Station *Freedom* Office has been involved in evaluating the role of SSF within the overall low-Earth orbit (LEO) infrastructure required for expanding human presence into the solar system. The office has worked closely with both the Space Station *Freedom* and Space Exploration Initiative (SEI) Programs to define requirements and develop conceptual designs for expanding SSF to serve as a transportation node for processing of lunar and planetary vehicles. This processing would include vehicle assembly, payload integration and checkout, servicing, refurbishment, and repair.

Initial concepts were developed which involved adding vehicle hangars, large propellant tank farms, various amounts of support structure, and power generation hardware to SSF. Later, when it was anticipated that the disturbances from vehicle processing activities would preclude the use of SSF for sensitive science operations such as microgravity research and materials processing, concepts were developed for separate facilities to house and process lunar

and planetary mission vehicles. In more recent studies, it has been shown that through proper scheduling, the often competing requirements of vehicle processing and scientific experiment operations can coexist to a large degree. These latter studies have resulted in an integrated approach to accommodate both SEI requirements and Research and Development (R&D) needs on SSF.

The first figure shows an SSF reference evolution configuration that supports both Lunar Transfer Vehicle (LTV) and Mars Transfer Vehicle (MTV) processing along with all required life science and technology development activities. To support these increased user requirements, two additional pressurized habitat modules, several small life science pocket laboratory modules, and an unpressurized Assembly and Servicing Facility have been added to the baseline Space Station. In order to support these additional facilities, *Freedom's* original power generation capability of 75 kW of photovoltaic arrays has been enhanced by six 25 kW solar dynamic power modules. Before the configuration in the figure is reached, several phases of evolution will occur. These phases and



Lunar and Mars evolutionary configuration.

Station phase	Physical configuration					Servicing
	Labs	Habs	Pocket labs	Airlocks	APAE	
Assembly complete	1 US 2 INT	1	None	1	2	None
Enhanced operations capability (EOC)	1 US 2 INT	2	None	1	6	Space-based OMV and satellite servicing
Lunar vehicle capability (LVC)	1 US 2 INT	2	MTV CLSS test and Large Centrifuge	2	8	Space-based OMV, satellite servicing, and LTV Facility
Extended operations capability (XOC)	1 US 2 INT	3	MTV CLSS test, Large Centrifuge, and Pilot Production Plant	2	9	Space-based OMV, satellite servicing, and LTV Facility
Mars vehicle capability (MVC)	1 US 2 INT	3	Large Centrifuge, Pilot Production Plant, and General Life Science Facility	2	9	Space-based OMV, satellite servicing, LTV Facility, and MTV Facility

Capability summary for growth configurations. APAE is Attached Payload Accommodation Equipment, OMV is Orbital Maneuvering Vehicle, and CLSS is Closed Life Support System.

their associated capabilities are listed in the table shown in the second figure.

(William M. Cirillo, 41938)
Space Directorate

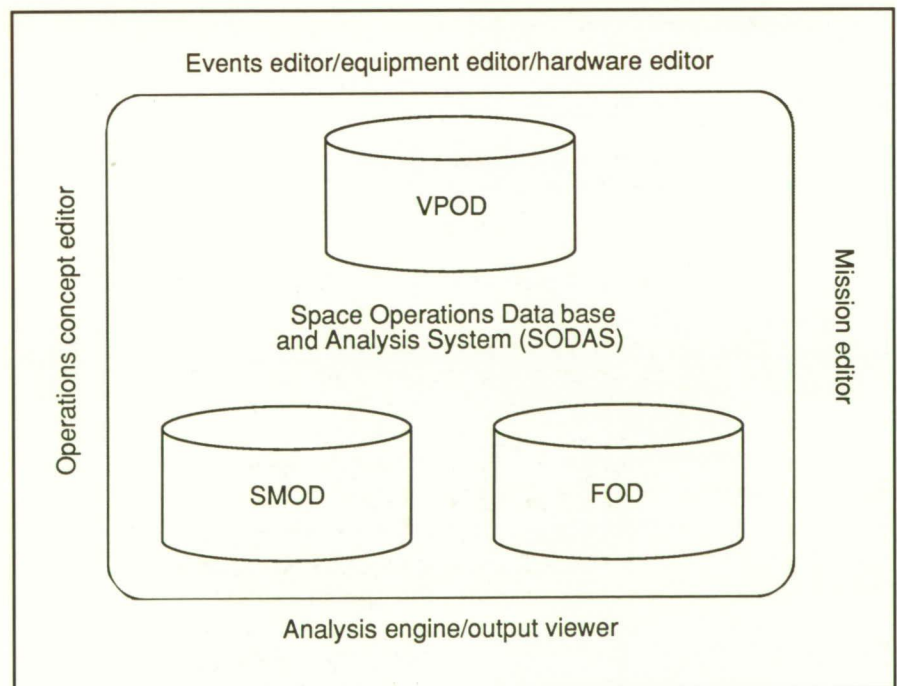
requirements, automated analysis tools are needed.

The Langley Research Center
Space Station Freedom Office/
Evolutionary Definition Office

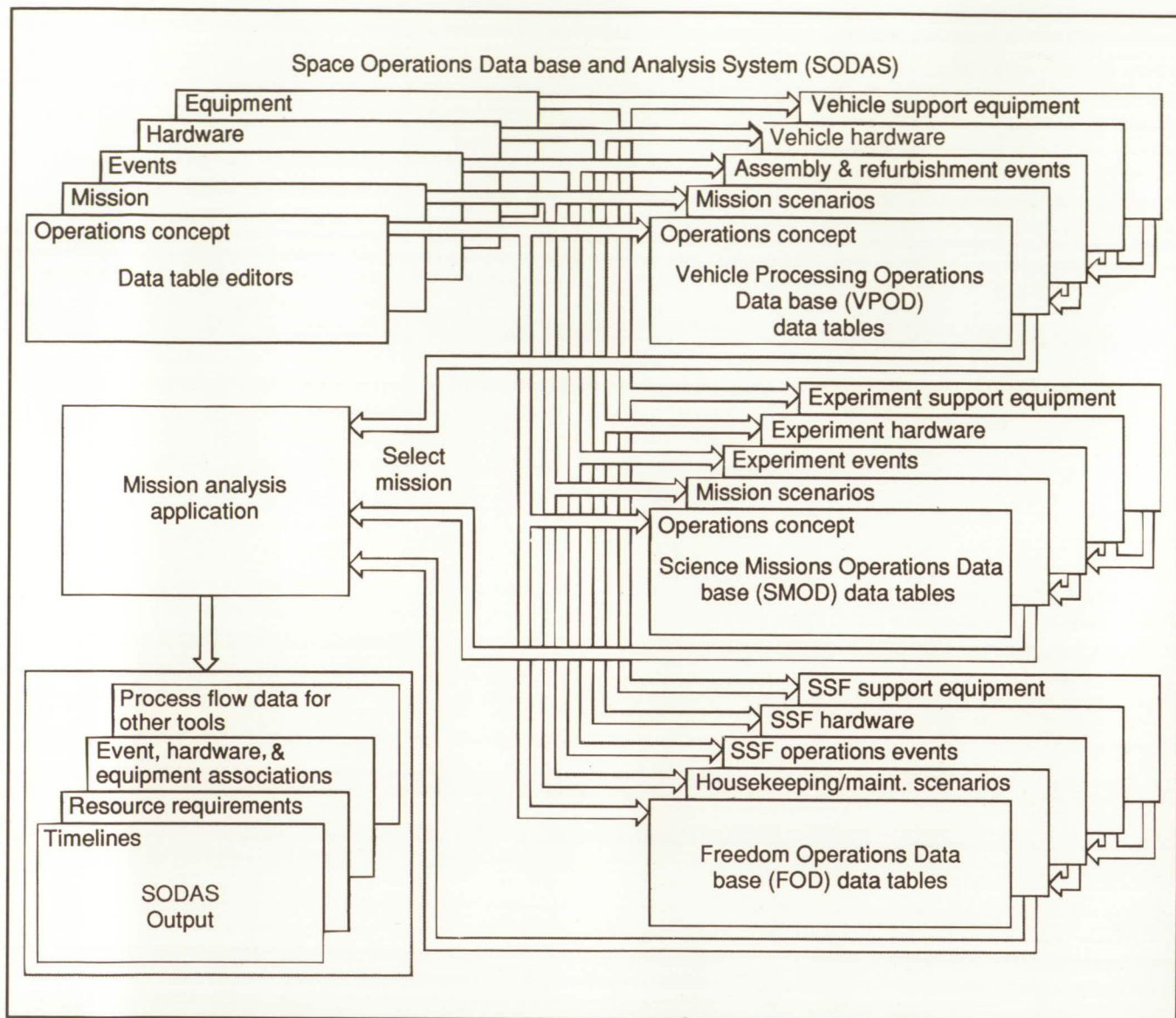
(EDO) and CTA, Incorporated, developed the Space Operations Data Base and Analysis System (SODAS), an automated on-orbit operations analysis tool for *Freedom*-based missions. SODAS can be used to systematically define on-orbit mission scenarios that consist of event process flows and time estimates and to analyze on-orbit crew and ground support personnel requirements. The system can be used to derive estimates of cost and resource loads (such as power, thermal, communications, and fluids) induced by the mission on the *Freedom* infrastructure. SODAS also is applicable to trade studies of automation and robotics alternatives to extravehicular activity (EVA) crew resources and to assess different on-orbit procedures and vehicle or science mission configurations. SODAS includes the Vehicle Processing Operations Data Base (VPOD), the Sciences Missions Operations Data Base (SMOD), the Freedom Operations Data Base (FOD), an analysis engine, and several data editors.

Space Operations Data Base and Analysis System

Space Station *Freedom* is a complex, multifunctional space platform that is designed to evolve and meet the changing needs of the United States and her international partners. Two likely missions that may drive *Freedom* evolution are a transportation node for the assembly, refurbishment, and checkout of interplanetary or lunar vehicles and a scientific platform for microgravity and life sciences. Space operations will be constrained by limited *Freedom* resources, such as equipment, power, communications, thermal control, and on-orbit crew. To anticipate the operational requirements of *Freedom*-based missions and to design *Freedom* to meet these



SODAS that includes Vehicle Processing Operations Data Base, Sciences Missions Operations Data Base, and Freedom Operations Data Base.



SODAS architecture that provides analysis and data editing capability for analysts and master data base administrator.

SODAS combines a formal operations analysis methodology with a data base and a resource requirements assessment capability to provide a comprehensive, automated operations analysis tool for modeling on-orbit resource requirements imposed on *Freedom*. SODAS is currently being used by vehicle processing specialists at Kennedy Space Center (KSC) to analyze the on-orbit assembly of lunar and Mars exploration vehicles. This tool also is being applied by science mission

experts to analyze *Freedom*-based science missions.

Although designed for the SSF environment, the tool is applicable to the analysis of operations in other complex space systems such as the Earth Observing System (EOS) or the Space Shuttle. Many consumable resources in these other systems will be the same, although the available equipment will be different.

SODAS is a powerful automated

analysis tool that is one of several components in the Integrated Space Operations Modeling and Analysis System (ISOMAS). Another component identified for ISOMAS which is currently under development by Langley is the Tool for Operations Modeling and Analysis in Space (TOMAS). TOMAS is a modeling and simulation tool that will dynamically model the events in a mission within the larger and more complex operational environment of *Freedom*. SODAS will provide mission require-

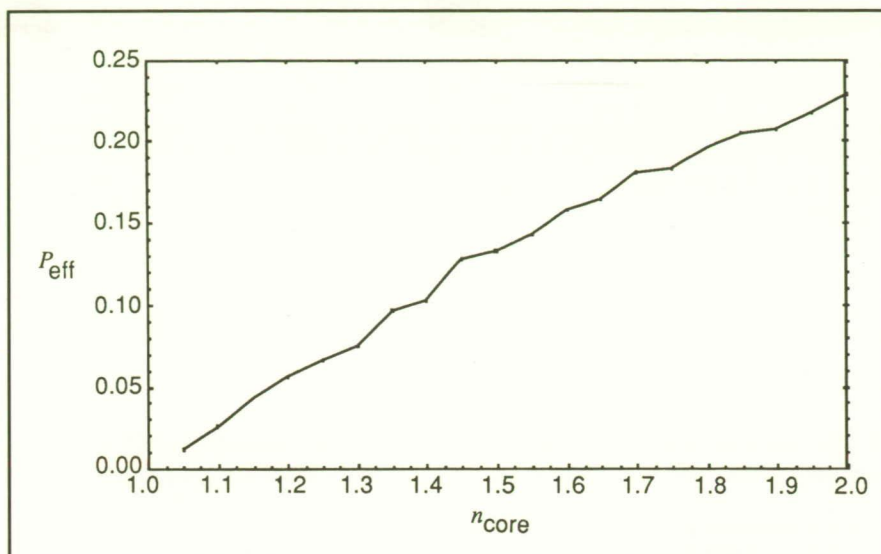
ments as inputs to TOMAS, which will dynamically schedule and simulate missions within constraints imposed by models of *Freedom* resource allocations.

(George G. Ganoe, 41940, and Ray Reaux, CTA, Inc.)
Space Directorate

Smart Structures Research

Survival in the hostile environment of near-Earth orbit presents unique challenges for smart structures technology. Structures containing organic resin (such as graphite/epoxy) are subject to atomic oxygen degradation. Methods for detecting atomic oxygen and monitoring its effects in space structures are being investigated. Light injection efficiency from cladding sources into the core of an optical fiber is being considered. Sources in the outer medium of lower refractive index, the cladding, can inject light into the core, which is the inner medium with a higher refractive index. The sources represent either fluorescent or chemiluminescent substances sensitive to chemical species, such as atomic oxygen.

A computer model has been developed to determine the best configuration of this sensor (a configuration that will allow the highest light injection and, consequently, the highest sensitivity). The results for a bare core fiber coated with a thin film of fluorescent substances $n_{\text{clad}} = 1.0$ are shown in the figure. The relative amount of light captured by the fiber P_{eff} was plotted against the index of refraction of the core n_{core} for a constant ka factor where k is the circular wave number and a is the core radius of the fiber. Due to the unique characteristics of this code, it was possible, for the first time, to determine the variation of P_{eff} with the difference



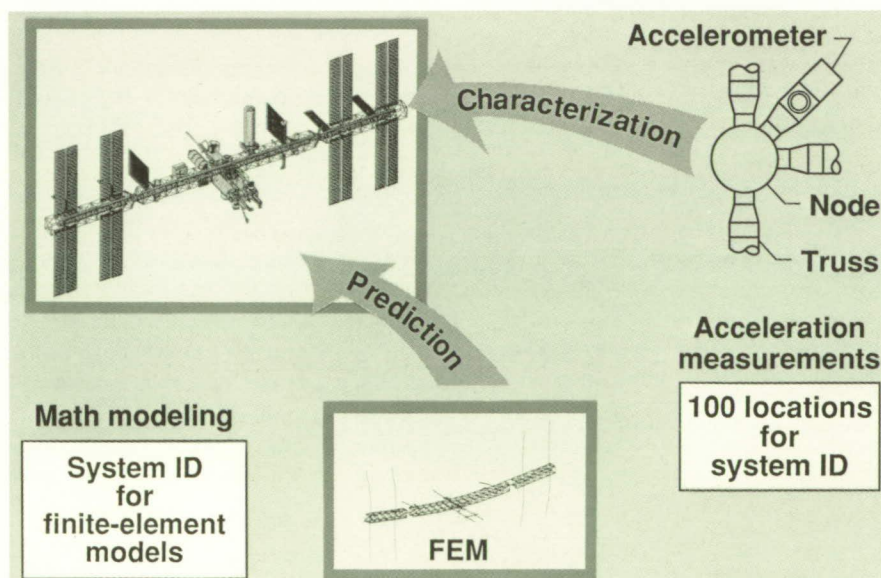
Power injection efficiency P_{eff} versus the index of refraction of the core n_{core} for a constant ka .

$n_{\text{core}} - n_{\text{clad}}$. In the figure, the increase in P_{eff} is due to an increase in the difference $n_{\text{core}} - n_{\text{clad}}$. The experimental verification of this model is under way.

(Claudio O. Egalon, 44788, Robert S. Rogowski, and Alan C. Tai)
Electronics Directorate

Modal Identification Experiment

A study has been conducted for the Office of Aeronautics, Exploration and Technology (OAET) to establish a conceptual design for the Modal Identification Experiment (MIE). The MIE objective is to



On-orbit structural dynamics.

collect on-orbit data to characterize the structural dynamics of Space Station *Freedom* and to develop modeling techniques for large space structures. Space Station *Freedom* offers a unique opportunity for conducting this research on multiple structural configurations during its assembly.

The conclusion has been reached, based on a McDonnell Douglas Space Systems Company study, that the MIE is feasible with minimal impact to Space Station *Freedom* configuration, resources, and operations. The proposed experiment concept, pictured in the figure, requires the excitation derived from Reaction Control System (RCS) thruster firing during reboost, the measurement of acceleration response at approximately 100 locations on the structure, and the use of free-decay modal identification methods to characterize the system. Selective signal-to-noise enhancement, as required to resolve relatively weak modes, may be achieved with the careful modulation of reboost pulses. The Space Station Data Management System will be used for data acquisition and storage. The proposed system has been determined to enable the identification of approximately 20 global structural modes for Space Station *Freedom* configurations selected. Preliminary system design has begun.

(James W. Johnson, 41963)
Space Directorate

In-Space Experiments Data Base

Knowledge of all planned and proposed in-space flight experiments is necessary to reduce duplication of effort between U.S. Government agencies and to provide experimental information for engineering, designing, and utilizing efforts in the Space

Station *Freedom* program. Therefore, as an extension of the Office of Aeronautics, Exploration and Technology's In-Space Technology Experiments Program, the In-Space Experiments (ISE) Data Base was developed as a tool to track and monitor technical characteristics of planned and proposed in-space flight experiments. Flight experiments to be included are all U.S. in-space technology flight experiments independent of carrier vehicle and all in-space flight experiments proposed for Space Station *Freedom* from the United States, Japan, the European Space Agency (ESA), and Canada.

The information in the ISE Data Base is organized into categories such as mission code, experiment title, technology theme, principal investigator and sponsor, carrier vehicle, proposed launch date, physical characteristics (mass volume), and resource requirements (power, thermal, data, crew, and logistics). To provide as thorough a record as possible, the physical characteristics are given for the launch condition, as well as for the deployed configuration. Resource requirements also are given for setup and maintenance, along with operating requirements. The ISE Data Base can be queried by supplying one or more search parameters to locate a specific experiment or set of related experiments. For example, all experiments using Space Station *Freedom* as a carrier can be located, or all the thermal and fluid management technology experiments using the Space Shuttle and using more than 2 W of power can be located. In addition, a report generator and print feature are available during the data base operation.

Anyone with a need to know can be allowed to access the data base on a query-only basis. The experiment data will be updated at least yearly, and changes and enhancements to both the operations and contents of

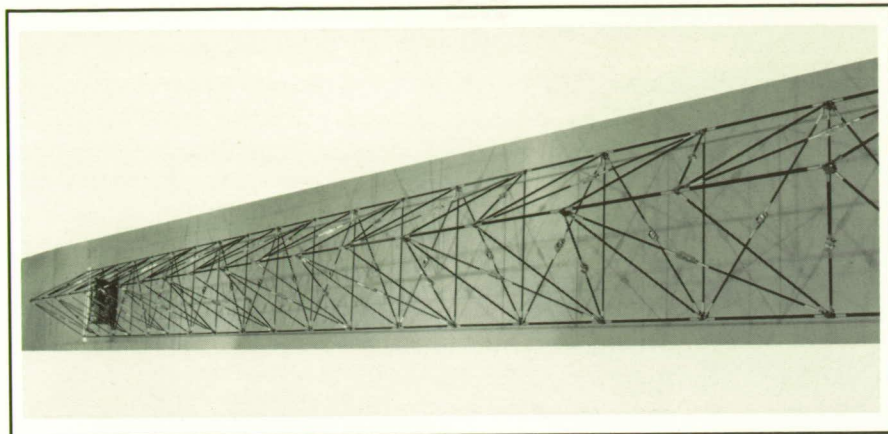
the data base are anticipated to be incorporated in future versions, particularly as experiment and carrier vehicle requirements become better known and as the needs of the users evolve.

(Don E. Avery, 41947)
Space Directorate

Demonstration of Flexible Mini-Mast Control by Guest Investigators

The Controls-Structures Interaction (CSI) Guest Investigator (GI) Program uses a 20-m deployed flight-quality truss, known as Mini-Mast, as an experimental test article. The Mini-Mast provides a realistic space-like structure on which active control concepts for controlling structural response can be evaluated. Pretest simulations are used to ensure the structural integrity of the Mini-Mast by verifying stability of all control laws with an evaluation model and also by checking the percentage of critical load that they impose on the structure before approval is granted to proceed with the experiment.

From a NASTRAN eigensolution that identified 147 natural frequencies between 0 Hz to 100 Hz, 28 modes were selected for the reduced modal representation of the structure in closed-loop simulations. These modes were chosen because they have significant influence on the global response of the structure and correlate well with experimental frequencies and mode shapes. The GI control laws are incorporated into an analog/digital simulation to predict system response to predetermined disturbance signals, with each simulation using only those feedback signals selected by the GI. Predicted responses then are compared with measured responses, as shown in the figure for two representative control laws.



Photograph of Mini-Mast.

L-86-11555

expected to indicate a slightly larger amplitude and a longer time for the amplitude to decay.

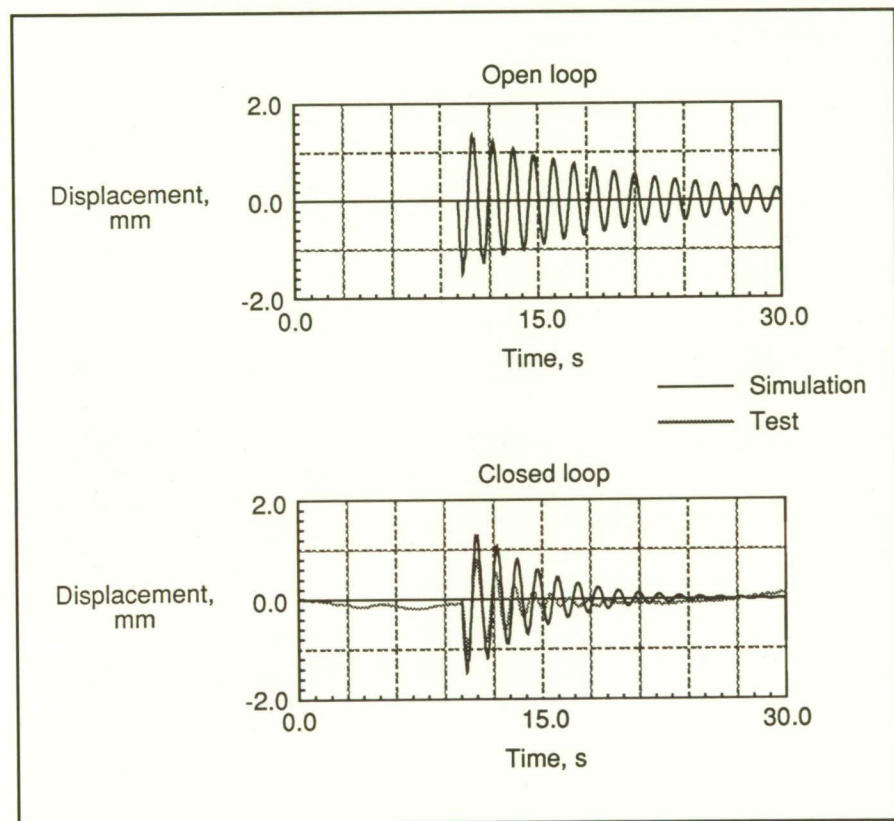
The well-designed analytical simulation process that has been developed not only provides a means of evaluating the risk of using a particular control law design prior to actual tests, but also provides a computationally efficient means for obtaining response data for correlation with experimental results. This simulation capability significantly enhances the use of the Mini-Mast test article for the ground-based evaluation and validation of structural response attenuation control concepts for large space structures.

(S. E. Tanner, L. Horta, and Z. C. Kim, 44353)

Structures Directorate

Middeck 0-Gravity Dynamics Experiment

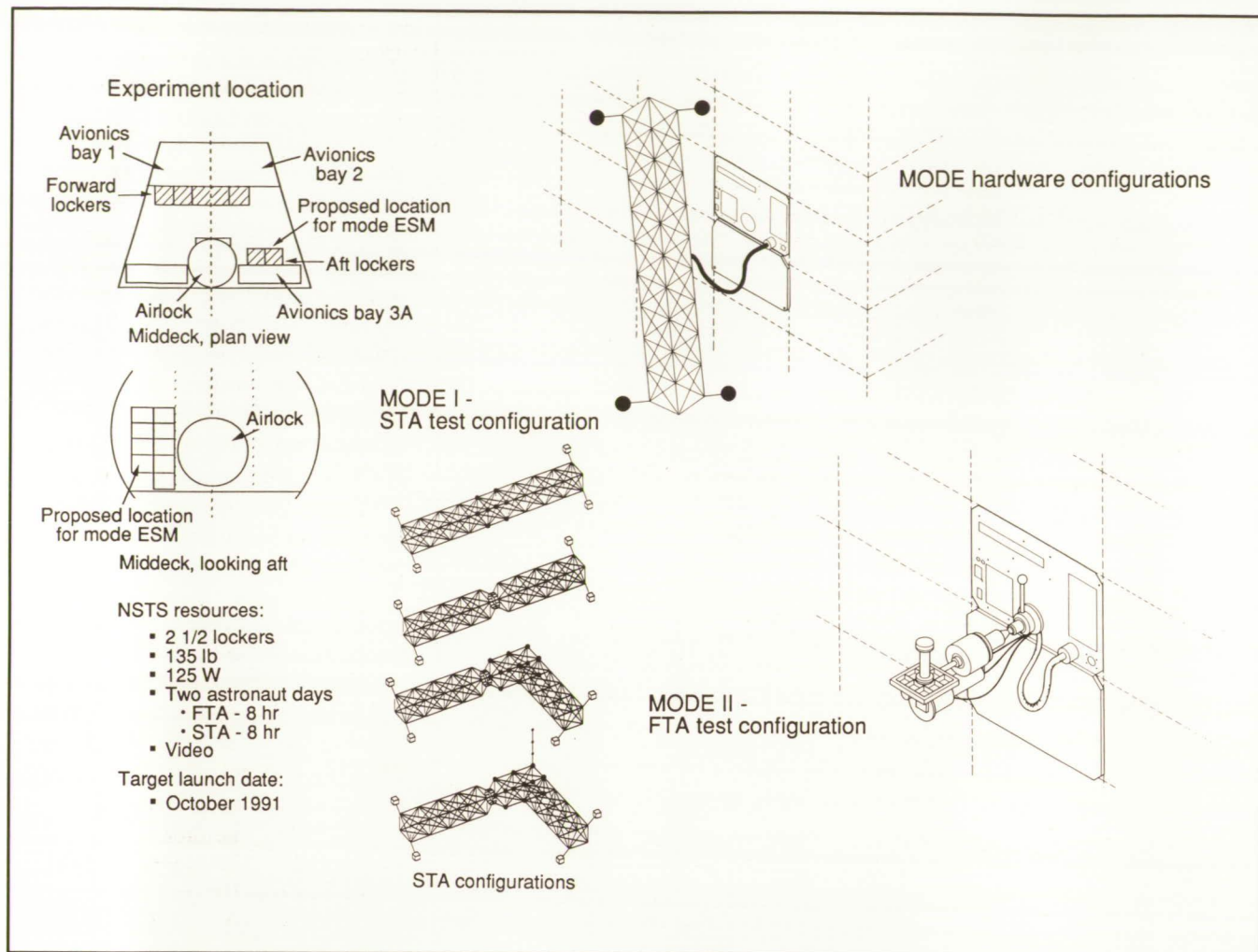
The Middeck 0-Gravity Dynamic Experiment (MODE) is designed to investigate the dynamics of two aspects of nonlinear spacecraft dynamics systems which are altered by the presence or absence of gravity. These two aspects are nonlinear dynamics of jointed truss structures (MODE I) and dynamics of a partially filled fluid tank as it interacts with flexible vehicle motions (MODE II). The engineering science objectives of MODE I are to characterize the fundamental changes in dynamics in 0 g due to the absence of gravity on joints, to quantify the changes due to the absence of suspension and gravity load on structural members, and to obtain quantitative data for correlation with numerical models. The engineering science objective of MODE II is to characterize fundamental 0-g slosh behavior and obtain quantitative data on slosh force and spacecraft response for correlation of numerical models.



Comparison of simulated and experimental control of structural response.

More than 15 digital control laws, from both NASA and the university community, have been efficiently incorporated into this complex simulation that is tailored in each case to the needs of the individual researcher. The stability of the integrated system with each controller design was examined, and predicted responses were compared with

actual responses. Good agreement was attained between predicted and measured responses. Because the Mini-Mast has nonlinearities in damping and frequency as a function of displacement amplitude, some disagreements between the response predicted by using the simulation and the experimental results are to be expected. The simulation would be



MODES I and II on-orbit test configurations.

The MODE hardware has three main components. The Electronics Support Module (ESM) is the electronic brain of the experiment and functions as a semiautonomous test facility. The Fluids Test Article (FTA) consists of a force balance and a small (changeable) fluid tank to investigate the dynamics of fluid-structure interaction in 0 g (MODE II). The Structural Test Article (STA) is a hybrid scale, jointed truss structure of the Space Station *Freedom* boom (variable configuration) to be used to investigate the open-loop dynamics of the configuration (MODE I).

This experiment will be flown as a middeck locker payload. On-orbit,

the test articles will be attached to the ESM and operated in the middeck area for a minimum period of 16 hr. MODE is scheduled for completion and flight certification in August of 1991.

(Sherwin M. Beck, 41966)
Space Directorate

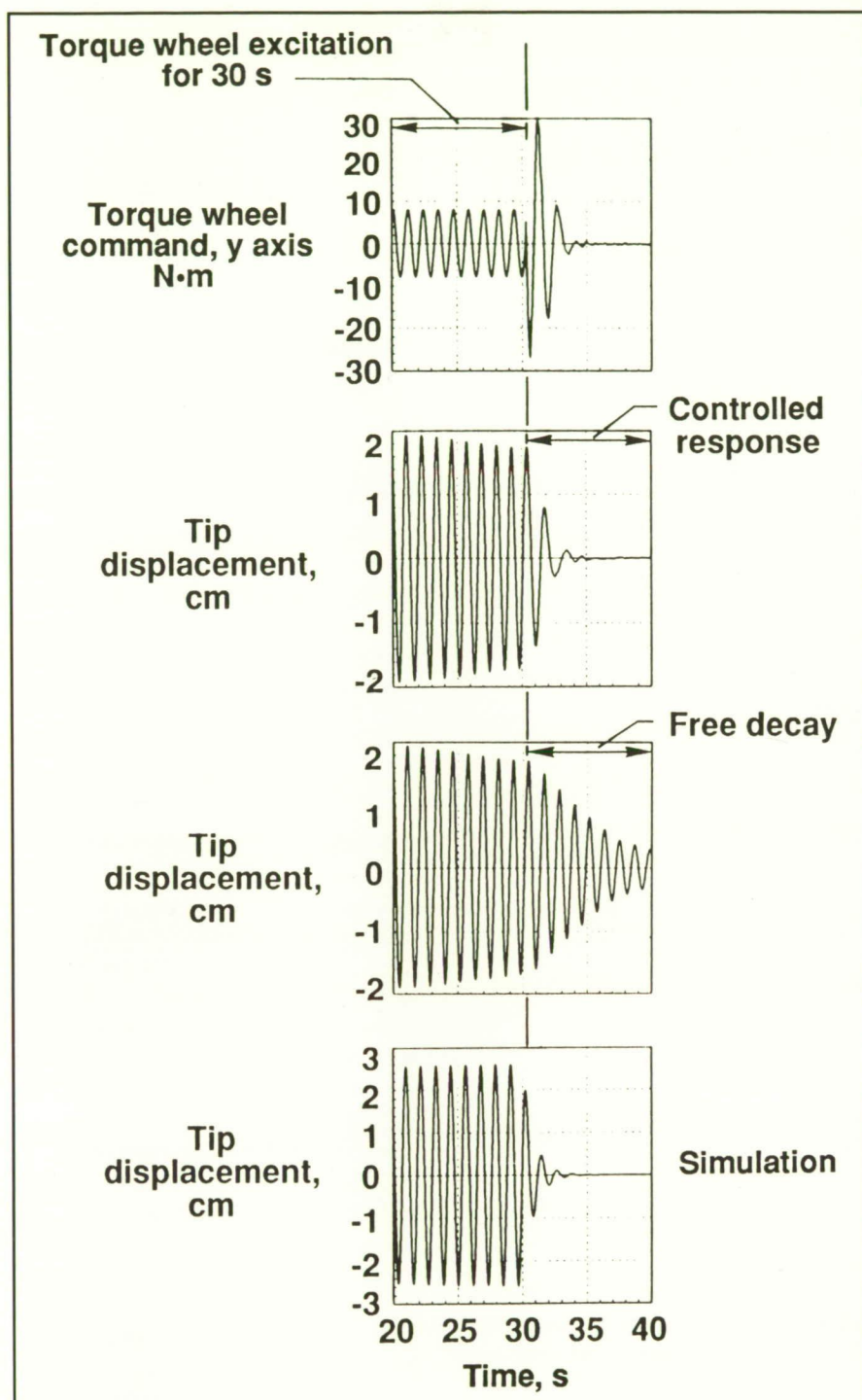
Closed-Loop Control Test on Mini-Mast

The Mini-Mast is a 20 m, joint-dominated, three-longeron beam made of graphite/epoxy tubes with sensors and actuators distributed along its length. The objective of this

research is to develop a high-gain feedback control law for the Mini-Mast and to validate it via simulation and laboratory experiment.

To that end, a modern control law was designed using the ORACLS (Optimal Regulator Algorithms for the Control of Linear Systems) design package, and it was tested in simulations and then in hardware using the Mini-Mast facility.

Open-loop sinusoidal input tests using the torque-wheel actuators (TWA) were made at resonant frequencies of the structure. Data taken from these tests were processed to identify the resonant frequencies, damping coefficients, and control



First active control test on Mini-Mast.

effectiveness of the actuators. A linear quadratic Gaussian (LQG) control law was designed to achieve a 30-percent damping coefficient at the first resonant frequency. This performance was verified in simulation using the identified resonant

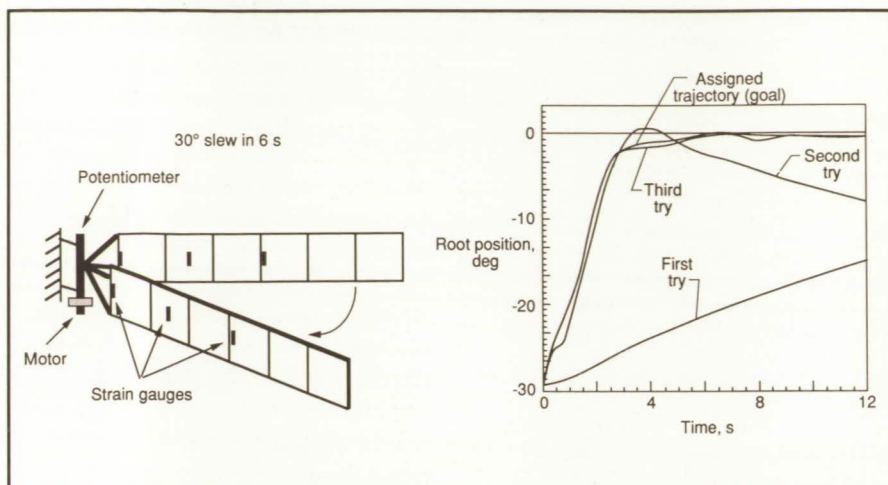
frequencies, damping coefficients, and control effectiveness of the actuators. The control law then was tested using the Mini-Mast facility. The figure contains time histories of tests on the facility and the pretest simulation. For comparison, the next

to the lowest trace was taken from an open-loop test run with start conditions as close as possible to those of the closed-loop test. The top trace is the TWA command input in the Y direction. In this test, excitation of the structure was provided by a 30-s sinusoidal input of the y-axis TWA at the first resonant frequency of the structure. The control law then was engaged. The second trace from the top is the output of a noncontacting displacement sensor at the C-apex of bay 18 of the Mini-Mast. The effectiveness of the control system in providing damping can be noted by comparing the open-loop test (free decay) with the same trace in the closed-loop (controlled response).

This was the first closed-loop control test of the Mini-Mast and as such has developed procedures that will profit future guest investigators that may use the facility. Additionally, torque wheels have been shown to be effective tools for damping large flexible structures.
(Raymond C. Montgomery, 46615)
Flight Systems Directorate

Development and Application of Learning Control Method in Flexible Panel Slewing Analysis

When a command is given to a controlled system, the desired response usually is not precisely obtained because of uncertainties in the mathematical modes of the system used for the control law design. Because the same error in the response is made every time the command is given, the error could be reduced or eliminated by using a control system that can learn from repetitions of the same command or task. Such a system would be useful in many applications because the control system would be tolerant of



Learning control results for slewing panel.

the modeling uncertainties. This tolerance is particularly important in the control of large flexible spacecraft. Such a learning system can be developed by using a control system difference equation representation of the dynamics in a repetition domain instead of the usual time or frequency domains. The repetition domain expresses how changes in the control at any time in performing a task will affect the response of the system during the next execution of the task. The learning control laws developed here make changes in the control operation for the next repetition based on information obtained from a linear combination of the response errors observed in prior repetitions.

A general mathematical framework for learning control design has been developed. The approach has been applied to a slewing flexible panel experiment, and some illustrative results are shown in the figure. The curve marked Assigned Trajectory (Goal) is used as a reference that is to be duplicated through a learning process. To obtain this reference curve, a controller, which uses proportional motor angle and strain feedback, was designed. Because controller designs are usually based on inaccurate system models, an incorrect model of the panel was

used. The incorrect model involved a 25-percent error in the frequency of the first mode and smaller errors in other modes and a 10-percent error in the mass matrix. The curve labeled First Try shows the system behavior obtained by using a controller with only proportional feedback of the motor angle. The performance of this controller is improved through the learning process. The Second Try curve illustrates the performance after the controller has learned from the initial trial only. After three tries, the learning control nearly reproduces the desired response as shown by the Third Try curve.

This is the first application of learning control concepts to the control of flexible structures. This application shows that a controller can be made which can learn to give a desired response after a few trials, in spite of rather large modeling errors. The general framework developed forms a foundation for the application of learning system control to large flexible spacecraft.

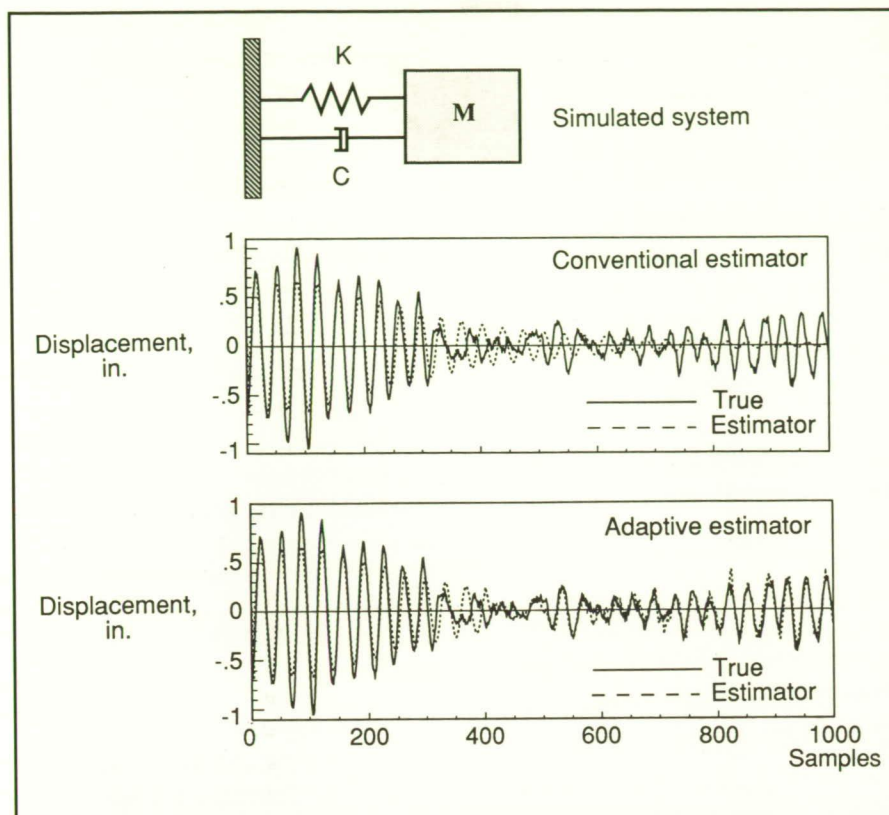
(Minh Phan, Richard W. Longman, and Jer-Nan Juang, 44351)
Structures Directorate

Improved Estimator Performance for Active Control by New Adaptive Modal State Estimator

For precision active control of large flexible structures, an accurate mathematical model of the system dynamics and precise knowledge of the system state are critical items. State estimators, such as the conventional Kalman filter, can be used to estimate the system state based on a limited number of sensors, the mathematical model of the system, and knowledge of statistics of any measurement noise. The objective of this research is to develop efficient state estimators that work well in the presence of unknown system model errors and measurement noise.

A new adaptive modal state estimator has been developed by combining the two disciplines of structural mode parameter identification and state estimation. A linear adaptive predictor, which fits measured output y to input u in a least-squares sense, is used as a complementary predictor to the state estimator. The adaptive predictor produces the impulse response resulting from the predictor plus the system dynamics. This impulse response is used by a system identification method to update the structural mode model and state estimator gain so that the estimator error approximately tracks a reference prediction error that is due primarily to system uncertainties and measurement noise. This method forces the system state estimator to account for unknown system uncertainties and measurement noise.

To illustrate its effectiveness, the new estimator has been applied to a simple numerical example. Some illustrative results are shown in the figure. In this example, the measured signal was purposely contaminated by noise to demonstrate the estimator



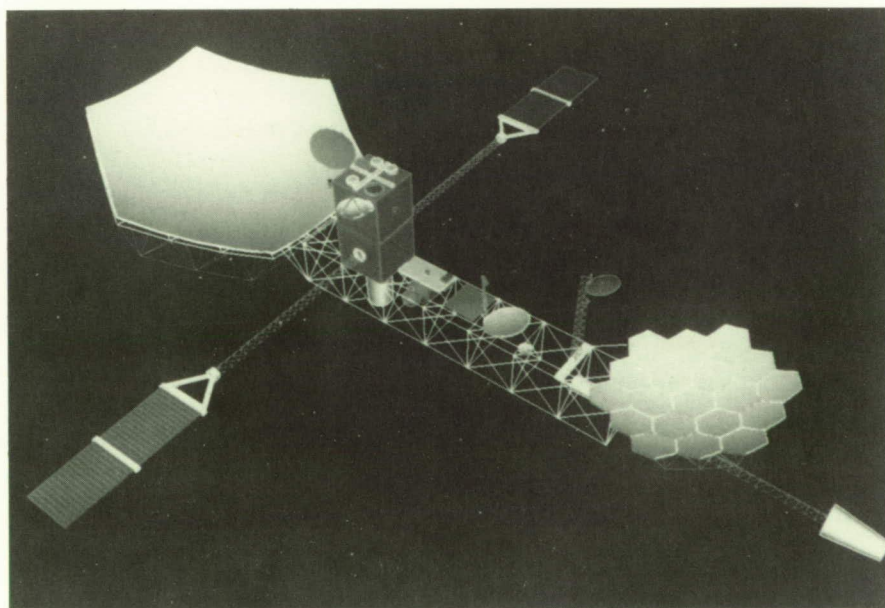
Comparison of adaptive estimator results with Kalman filter results.

performance when accurate forcing input and measurement statistics are not known. In the example, the conventional Kalman estimator (top graph in the figure) does not track the system response well past sample 300 because of error accumulation attributable to the noise statistics error in the Kalman filter design. On the other hand, as shown by the results in the middle graph, the adaptive estimator, which in this example is turned on after 400 time samples, tracks quite well the response, despite the measurement noise error. These results clearly show that the new adaptive estimator performs very well in the presence of model uncertainties and system noise. (Chung-Wen Chen, Jen-Kuang Huang, and Jer-Nan Juang, 44351) Structures Directorate

Integrated Control-Structure Design Methodology Development for Class of Flexible Spacecraft

Future utilization of space will require large space structures in low-Earth and geostationary orbits. The dimensions of such structures will range up to hundreds of meters. For reducing the cost of construction, launching, and operating, the structures should be as light as possible. However, reducing structural masses tends to increase flexibility, thus making control in attitude and shape with a specified precision extremely difficult. In current spacecraft design practice, controller design serially follows the structural design. The objective of this research is to develop a methodology for a concurrent integrated control-structure design for a class of spacecraft which require fine attitude pointing and vibration suppression and which have no articulated payloads.

The approach is to formulate the integrated design problem as a single-objective optimization problem. The design variables of the optimization



Mission to Planet Earth geostationary platform.

L-89-6442

	Objective function	Controlled performance	Structural mass	Actuator mass	Total mass
Initial design	1.0	1.0	1.0	1.0	1.0
Control-optimized design	0.75	1.41	1.0	1.33	1.09
Integrated design	0.32	4.82	0.58	1.97	0.97

Conventional design versus integrated design.

are divided into two groups: structural design variables and control design variables. The geometric properties of the structural members (such as the radius of the cross section and the thickness) are used as structural design variables, while the elements of the position and rate gain matrices are chosen as the control design variables. A constant gain dissipative control law, along with collocated sensors and actuators, is used to guarantee closed-loop stability and provide stability robustness. A function that penalizes both the total mass of the system and the reciprocal of a measure of closed-loop performance is investigated. The optimization constraints include an upper-bound on the total root-mean-square (RMS) pointing error as well as bounds on the structural member sizes.

The integrated design methodology has been applied successfully to a redesign of a large-order, generic model of the geostationary platform shown in the first figure. Results indicate that the integrated design approach can yield a lighter, more flexible spacecraft that has better closed-loop performance as compared to the conventional design (shown in the table in the second figure). In other words, simultaneous

control-structure design has been demonstrated to have substantial benefits over the conventional two-step design.

The versatility of this optimization-based approach in being capable of handling different objectives, as well as accommodating various design constraints and requirements, is highly desirable. The proposed design methodology should play a major role in the design of future spacecraft. Further research is required to extend the integrated design methodology to other classes of spacecraft, such as those involving payload articulations and large-angle slewing maneuvers.

**(Peiman G. Maghami, 46608)
Flight Systems Directorate**

Enhanced Multiprocessor Performance Model

The Algorithm-to-Architecture Mapping Model (ATAMM) has been enhanced to model an increased range of multiprocessor performance for a given data-driven algorithm graph, such as that typically used in processing periodic data inputs for flight control. This enhanced ATAMM, generated by Old Dominion University on a Langley Research Center Cooperative Agreement, deviates from the previous restriction of one token per arc in the Node Marked Graph, which models the READ, PROCESS, and WRITE functions needed for execution of a graph node.

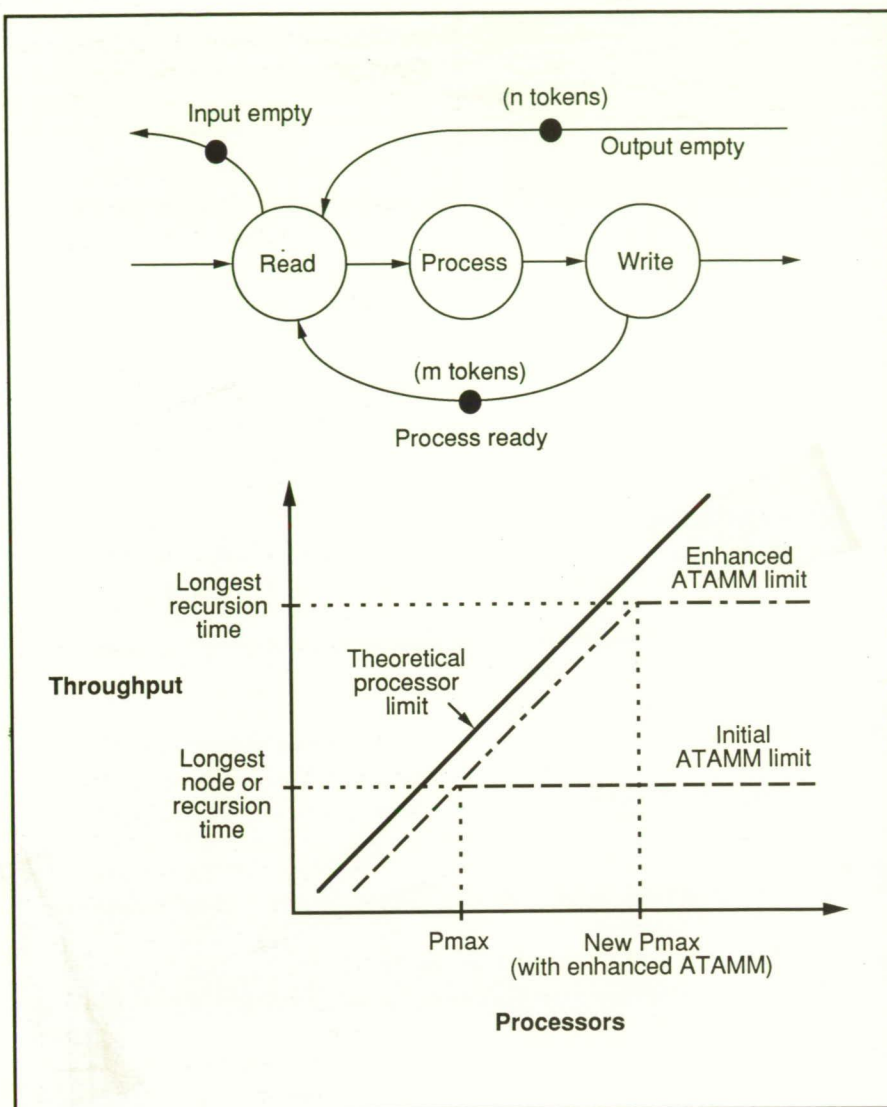
As shown in the figure, the enhanced ATAMM determines the number of simultaneous instantiations (m tokens) of each graph node and the amount of output data buffer space (n tokens) required for the same node. The values of m and n generally are different for each node of an algorithm graph and are graph dependent. The functional impact of the multiple tokens is to enable multiple concurrent executions of the same graph node on different processors with successive data sets and, hence, to facilitate increased throughput. As indicated in the graph of ideal throughput as a function of the number of available parallel processors, the graph-dependent upper limit for throughput is no longer a function of the longest node latency time. Rather, the maximum throughput is substantially increased in the enhanced ATAMM version and only is limited by the longest recursion time in the graph. To ensure that an execution of a graph is deadlock-free and that the data packets are not mixed in order during multiple instantiations of the same node, the data packets must now be tagged to indicate the identity of an input data packet.

Fabrication of Space Crane Articulating Joint Test Bed

NASA's new exploration initiatives will require on-orbit assembly and construction. The space crane articulating joint will provide the large-angle rotation needed to manipulate and position spacecraft components for final assembly in space. A test bed has been designed and fabricated to allow different articulating joint designs to be quantitatively evaluated so that the best design is chosen for a full-scale space crane.

The space crane articulating joint test bed (shown in the figure) uses 1-in. aluminum-tube, erectable truss hardware designed at Langley Research Center. The test bed is cantilevered from the Structures and Materials Laboratory backstop and has a total of eight bays of 1-m truss hardware. The first 1-m bay-size space crane articulating joint candidate has been fabricated and is installed in the third and fourth bays (along the bottom at the bend). This articulating joint design emphasizes commonality with the Space Station *Freedom* truss structure, a minimum number of unique parts, and EVA (extravehicular activity) assembly. The joint design uses three double-hinged nodes, eight single-hinged nodes, and two commercial linear actuators. The linear actuators are electrically driven recirculating ball-screws and have a rated load of 1500.0 lbf. The actuator displacement velocity is variable and can be adjusted from 0.02 in/s to 0.20 in/s. The commercial actuators are very economical and will allow the articulating joint to rotate through a maximum angle of 120° in approximately 2 min and 30 s.

By determining the positioning-accuracy, repeatability, and controllability of space crane articulating joint

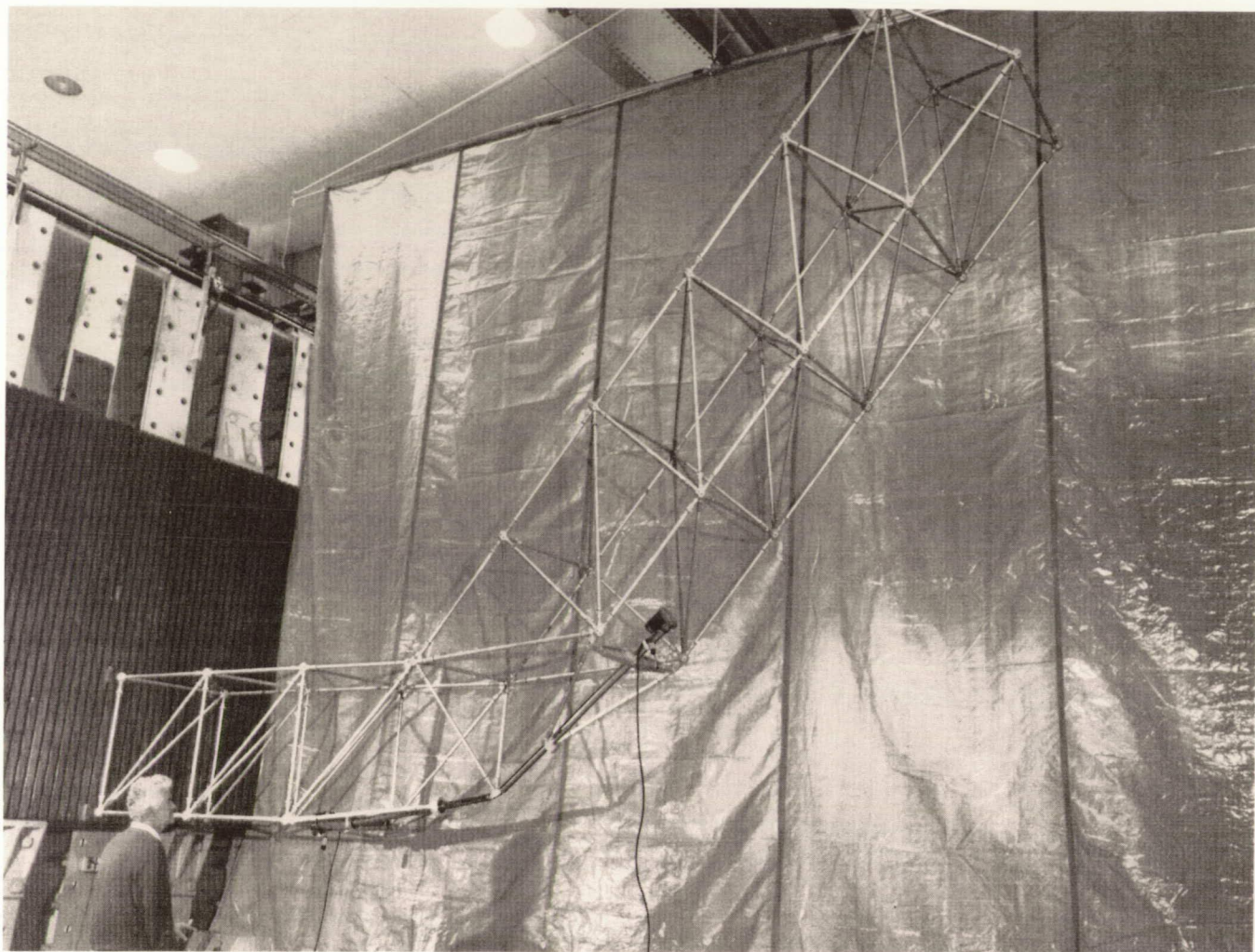


Enhanced ATAMM that provides for multiple tokens and increased throughput performance.

The ATAMM has evolved into a major strategy for modeling the performance of data-driven application algorithms and is currently being implemented and performance evaluated in candidate multiprocessor spaceborne hardware systems.

(Paul J. Hayes and Robert L. Jones, 41491)

Flight Systems Directorate



Space crane test bed with articulating joint installed.

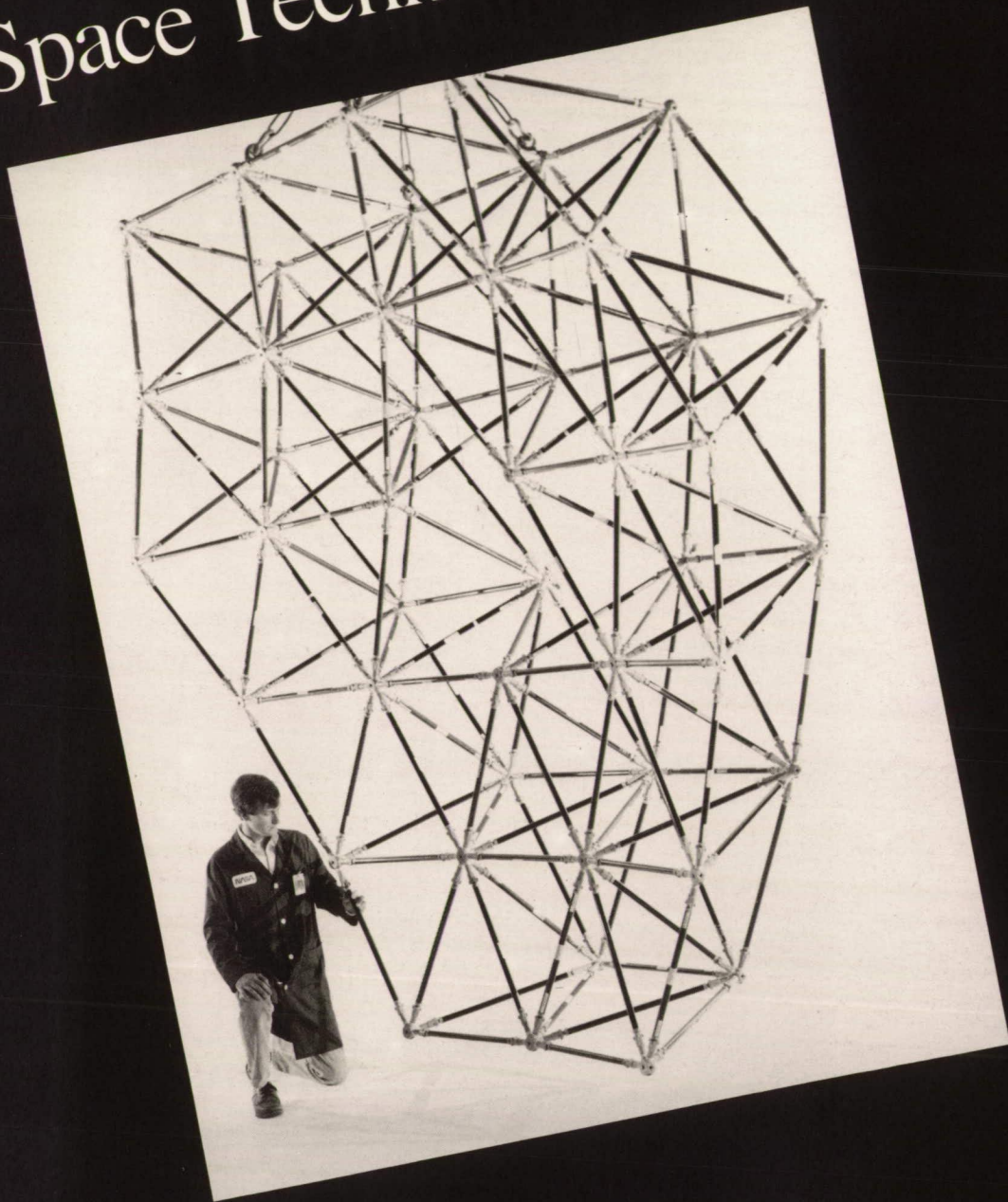
L-90-9160

candidates, the space crane test bed will generate technology to provide a lightweight space crane capable of rapidly positioning payloads in space for final assembly.

(Harold G. Bush, 43109, Thomas R. Sutter, and Richard Wallsom)
Structures Directorate

ORIGINAL PAGE
BLACK AND WHITE PHOTOGRAPH

Space Technology



Experimental Aerodynamics of General-Purpose Heat Source Modules

The hypersonic aerodynamic characteristics for general-purpose heat source (GPHS) modules were determined during a recent study in the 31-Inch Mach 10 Tunnel. The GPHS modules, which are rectangular brick-like shapes containing plutonium oxide pellets, are utilized in the radioisotope thermoelectric generator of the Galileo spacecraft. The objective of this study was to obtain representative hypersonic aerodynamics for the carbon-carbon modules experiencing radical ablation deformations at various angles of attack, sideslip angles, and roll angles. These data were requested by the Department of Energy in order to determine ablative heating and flight trajectories of GPHS modules in the event of reentry of the individual modules following an unanticipated breakup of the Galileo spacecraft.

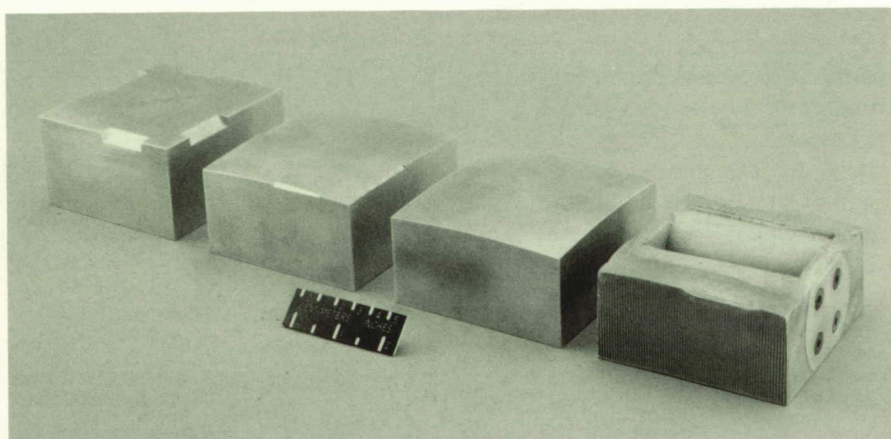
Several full-scale modules were tested (as shown in the figure) which represented successive ablation of the module having one large surface that is oriented normal to the free-stream direction. The ablated GPHS module geometries had been determined from arc jet tests of actual modules at the

Ames Research Center. The module on the left side in the figure is the unablated GPHS module; the module on the right side is an aluminum casting of the most extremely ablated module resulting from the arc jet tests. The two middle bricks in the figure represent intermediately ablated modules. Also tested for comparison with the data from the completely ablated module casting was a simple geometric representation of the completely ablated configuration. Investigation results indicated that the effects of ablation on pitching and yawing moments are much more significant and hence play a larger part in influencing the module trajectories than do variations in axial, normal, and side forces for fixed module orientations.

(W. Pelham Phillips, 45239)
Space Directorate

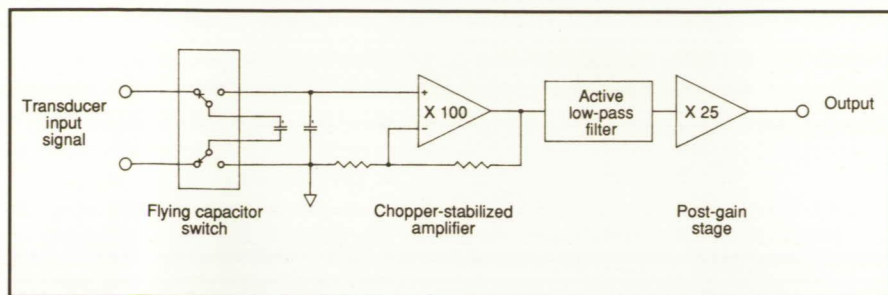
Precision Signal Processing for Micro-Level Flight Measurements

Measurement requirements for the Tethered Dynamics Explorer (TDE) Satellite include the need to resolve very-low-level d.c.-coupled acceleration and strain signals and provide low-temperature drift in a low-power space-saving design. For



General-purpose heat source models.

L-88-13176



Single-channel precision d.c.-coupled high-gain amplifier.

example, a ± 1 -mV signal from an accelerometer representing a ± 1 -milli-g level is required to be amplified by a factor of 2500 to produce a 5-V output signal swing with a low enough residual noise level to be able to resolve inputs in the micro-g range.

State-of-the-art miniature circuit components were utilized to develop a unique signal processing capability. This development allows the project to meet mission requirements using conventional sensors for very sensitive spacecraft measurements. The input signal is coupled to a chopper-stabilized operational amplifier through a flying capacitor switch. This coupling through the switch provides a precision instrumentation amplifier front-end with $<0.1 \mu\text{V}/^\circ\text{C}$ drift and $<1.5 \mu\text{V}$ peak-to-peak (P-P) input noise in a 10-Hz bandwidth. Subsequent low-pass filtering and post-gain stages complete the system. Another added benefit provided by the switched capacitor front-end is elimination of any ground loops from the signal source and a 120-dB rejection of common mode noise over a wide frequency range.

(John K. Diamond, 41668)
Electronics Directorate

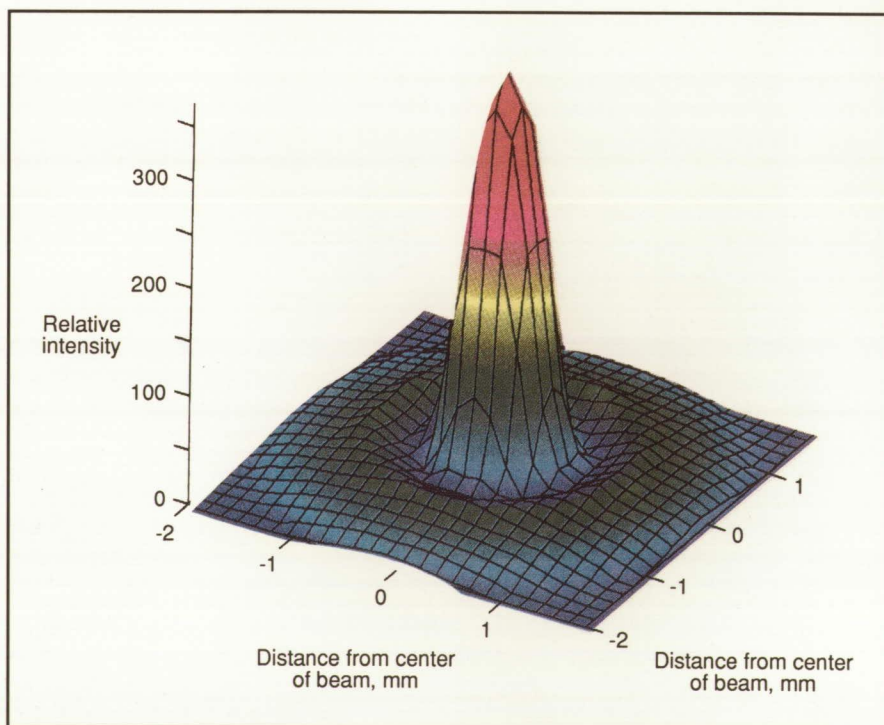
Laser Beam Profile Calculations

High power for space exploration, scientific research, and industrial processing will require new approaches to energy. Remote generation and laser power beaming are being considered to provide energy in a flexible manner. Solar-pumped gas and solid-state lasers and electrically powered diode lasers offer the potential for efficient energy transmission to the user. Critical aspects

of the transmission system are the power and phase profiles of the laser beam.

A computer code has been developed in-house at Langley Research Center to calculate the amplitude and phase of a laser beam. The amplitude and phase distributions at the output aperture of the laser are determined by factors such as the lasing material parameters, laser cavity geometry, gain distribution with the lasant, and characteristics of other optical elements. Huygens' principle provides the physical description of wave propagation within the optical cavity and the basis for mathematical calculation of the required distributions that are reached at steady state.

Steady-state conditions in a typical laser are reached in less than a millionth of a second, but hundreds of wave reflections may occur within this time; each wave is a detailed product of its predecessor. Every microscopic area of a wave projects a



Computer-generated laser beam intensity profile.

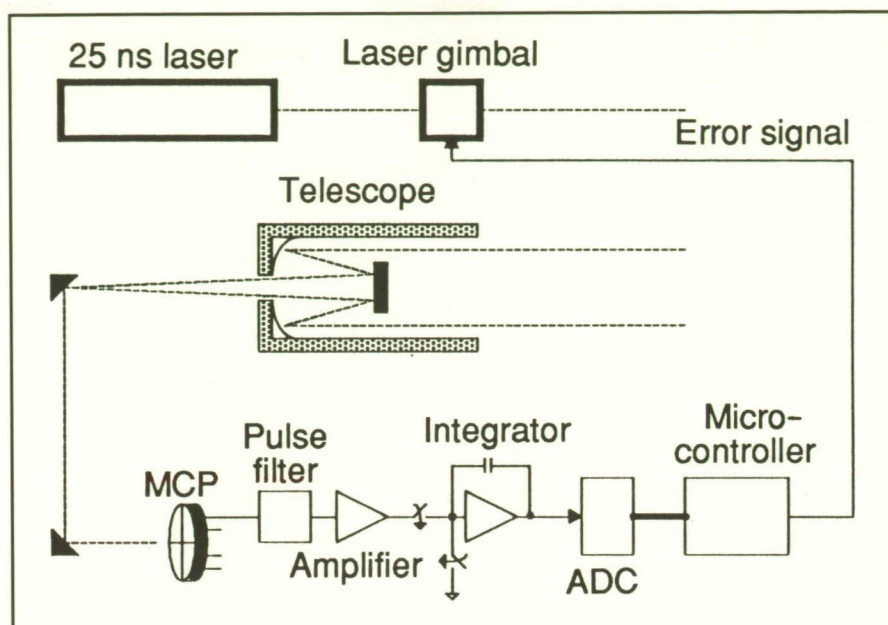
phase and amplitude distribution (as modified by the just-stated factors) over the entire area of its successor, and the contributions of these projections must be summed over microscopic areas in the succeeding wave. Thousands of computer calculations are required per reflection.

The figure, which was generated by the computer code, shows the steady-state spatial intensity distribution of a typical narrowbeam laser. More powerful lasers (using perhaps larger volumes, unstable optical cavities, and inhomogeneous pumping) exhibit much more complicated distributions. The present computer code can account for these and other effects and is currently being modified to include the effect of gain saturation. The code is expected to have a major impact on space laser power-beaming systems design. (M. D. Williams, 41430) **Space Directorate**

Lidar Boresight Alignment Using Four-Quadrant Microchannel Plate Photomultiplier Tube

In lidar research, boresighting is the process of aligning the laser with the field of view of the receiving telescope. In high-altitude spacecraft, severe launch and thermal requirements prevent the use of preflight ground-based alignment. The Lidar In-Space Technology Experiment (LITE) requires alignment to within 10 optical arc seconds. A boresight instrument that utilizes a quadrant microchannel plate photomultiplier tube (MCP) has been designed and built at Langley Research Center to meet the LITE specification.

The LITE boresight block diagram displays the major components of the system. The circular



LITE boresight block diagram.

optical detector used for boresight is divided into four quadrants. The entire atmospheric return from the 25-ns pulsed laser lidar source is used to determine correction factors. Each quadrant has a separate signal processing channel that is multiplexed into a single analog-to-digital converter. A current-fed pulse stretcher limits the rise time of the 25-ns ground return. This filtered signal then is amplified, routed to the integrator, digitized, and passed to the microprocessor. Correct alignment of the laser with the telescope causes the spot size of the laser pulse to be centered on the MCP. Any deviations cause the quadrants to receive unequal amounts of energy. The microprocessor algorithm detects the difference and generates a two-dimensional error signal that feeds back to the laser gimbal mechanism. (C. Antill, 43704)

Electronics Directorate

LDEF Retrieval Mission

The Long Duration Exposure Facility (LDEF), with 57 experiments in its 84 experiment trays, was deployed into Earth orbit in April 1984. Retrieval of the LDEF was required to obtain the data from its experiments because it is a completely passive spacecraft, and all information is obtained from investigations on the ground after it is returned from orbit. The LDEF retrieval mission, STS-32, was launched in January 1990, the LDEF was returned to Earth for processing, and retrieval operations were completed in May 1990.

Three phases of the LDEF retrieval had to be planned and implemented; these were the rendezvous and retrieval from orbit, the return of the spacecraft to the LDEF Processing Facility at the Kennedy Space Center (KSC), and the deintegration of the experiments from the LDEF at KSC for examination, processing, and then shipping to the investigator's laboratory. The first and second phases were carried out



LDEF in LDEF Assembly and Transport System in LDEF Processing Facility at KSC during inspection period. L-90-2273

Spaceflight Optical Disk Drive

Mass data storage requirements of future NASA experiments and facilities on the Earth Observing System (EOS) platforms, Space Shuttle, Space Station *Freedom*, and other missions far exceed current available devices. Of the new technologies, the rewritable optical disk is one of the most promising. A Langley Research Center managed development effort involving three separate contractors culminated in the successful laboratory demonstration of eight-track recording and single-pass erasure at 133 Mbps with a minimum feature size supporting 5 gigabyte capacity on a single side. The conceptual flight packaging of the drive is shown in the figure.

by the Space Transportation System through the Johnson Space Center and the Kennedy Space Center. The deintegration was performed at KSC by Langley Research Center personnel using KSC facilities and support.

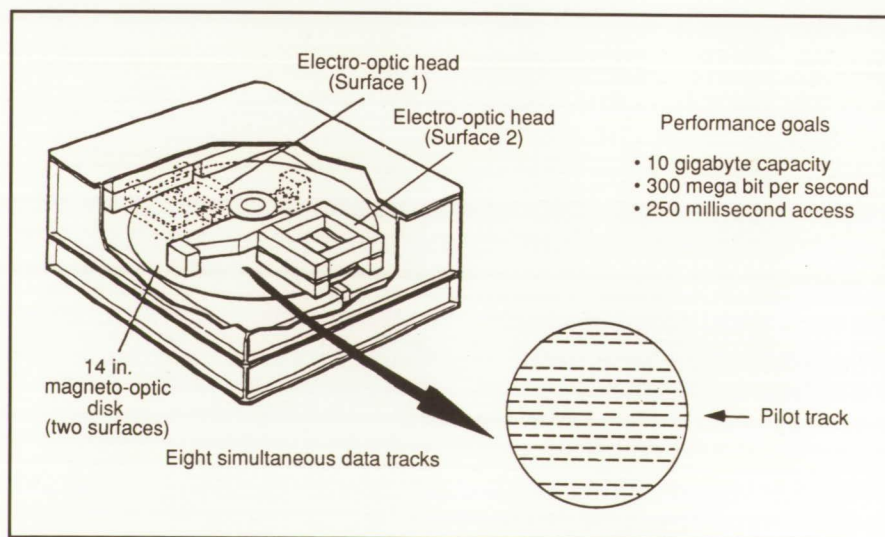
Primary challenges of the retrieval mission were to protect the spacecraft from any environments that might affect the quality of the LDEF experiment data (from the retrieval in orbit through the shipment of the experiments to the LDEF investigators) and to compile a complete and comprehensive photo and visual documentation of the LDEF and its experiments throughout the retrieval process.

Environmental protection included special cleaning of the Space Shuttle orbiter before launch, unique profiles and attitudes during flight, nearly continuous purge capability and contamination protection and monitoring on the ground until the spacecraft was in the LDEF processing facility, and the implementation of special clean room operating

criteria and procedures. Complete photo surveys in orbit and in the clean room at KSC and a full hands-off inspection of the LDEF at KSC by the LDEF investigators were major elements of the photo and visual documentation.

**(E. Burton Lightner, 43772)
Electronics Directorate**

The key technologies that form the basis for the drive are the 14-in. magneto-optic (MO) media developed by 3M, the world's first 10-element diode-laser arrays delivered by the David Sarnoff Research Center, and a multitrack electro-optic head designed by GE Aerospace. A new laser structure was developed for a higher yield line of more efficient



Spaceflight Optical Disk Recorder disk drive packaging concept and performance goals.

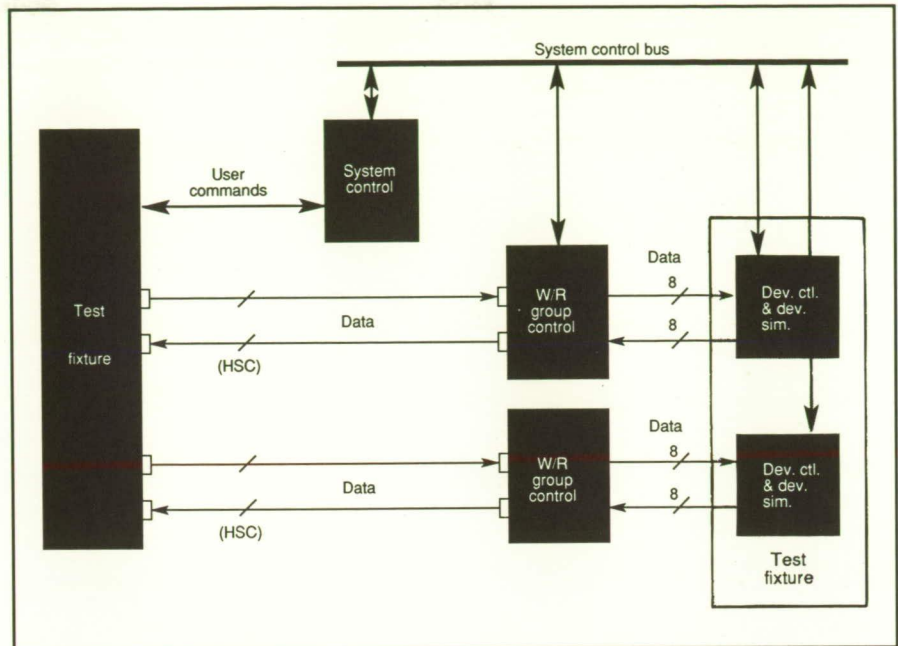
and thus longer-lived devices. Glass substrate was selected instead of aluminum for flight media after testing. The media were tested for outgassing and radiation at Goddard Space Flight Center and underwent vibration testing at Langley.
(T. Shull, 41837)

Electronics Directorate

Spaceflight Optical Disk Recorder Controller Development

In-house development of a versatile, modular controller that will be combined with an externally developed Spaceflight Optical Disk Recorder (SODR) disk drive to provide high-performance mass storage systems that meet NASA high-rate, high-capacity spaceflight needs of the 1990's and beyond is the objective of this effort. This controller will bring the benefits of high-performance random-access storage to spaceborne experiments.

The use of a configurable, expandable system architecture and controller provides application-specific user interfaces and expansion in rate and capacity to satisfy different requirements. The selected architecture also supports development of a generic drive. This architecture enables the controller and drive to be built in parallel. This controller can be used for other storage media as well, not just for optical devices. The controller itself is made up of group control, system control, data port, and matrix switch subsystem elements. Each of these has been developed separately for the breadboard controller using commercially available technology. A top-down hardware and software design approach was selected to enable easy transition to flight VLSI (very-large-scale integrated) electronics during



Top-level breadboard test bed two-port operation with drive simulator.

proposed follow-on phases or commercial application.

The SODR controller performs the usual controller functions plus additional features required of a high-performance optical recorder. The SODR controller supports higher and variable data transfer rates, dynamic reconfiguration, fault tolerance, adaptable file management (from block-oriented devices to file servers), and reprogrammable system algorithms. Also, the command and data ports are separated to achieve the desired reconfigurability and data throughput.

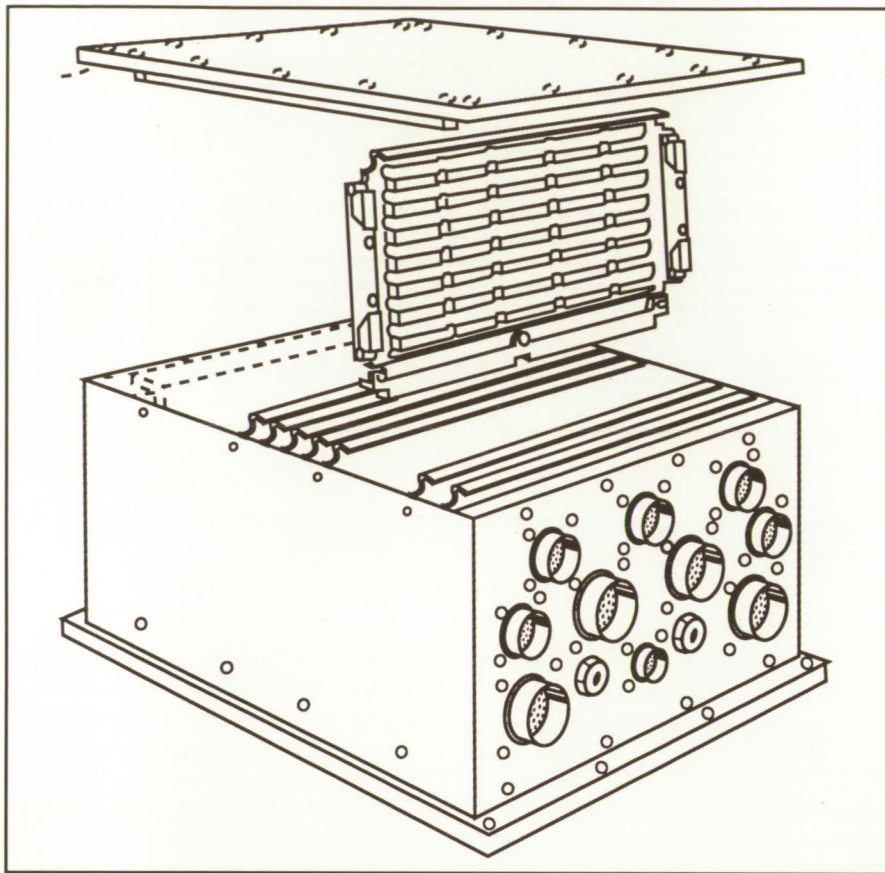
Two-port operation of 150 Mbps simultaneous read and write and 300 Mbps read or write will be demonstrated at an EOS test bed facility at Goddard Space Flight Center. This demonstration includes verification of system concepts, establishment of operational guidelines, and definition of user interfaces and commands.

(S. Jurczyk, 41865)

Electronics Directorate

Multiple Architecture Space Technology 1750A Computer

The Multiple Architecture Space Technology (MAST) 1750A computer was designed and developed in a joint effort by Langley Research Center and SCI Corporation of Huntsville, Alabama. Although this computer was built specifically to solve in real time the computationally complex controls equations, the MAST 1750A also provides a powerful technology for the Space Shuttle, Space Station *Freedom*, and free-flyer use in EOS. This reconfigurable modular computer has 16 available card slots that can hold up to 6 central processor cards for calculation-intensive applications. Other cards developed for the MAST 1750A include 256 K work memory cards (RAM and EPROM), a 13-MFLOP 32-bit array processor with 64-bit double precision floating point to perform fast complex computations and interface cards for sensors, the MIL-STD-1553 bus, and a smart



MAST 1750A flight computer configuration.

programmable interface for general platform use. The MAST computer also can be configured for a 4-M word memory capacity and speeds as high as 150 MIPS.

The system has been packaged to meet flight constraints, and depending upon the configuration, it weighs between 24 lb to 30 lb and uses an average of 25 W to 50 W of power. The MAST has built-in redundancy and error detection and correction to ensure high reliability for long mission life.

The MAST computer successfully completed qualification tests for spaceflight at Marshall Space Flight Center in July. This qualification unit will be installed at Langley as part of the Controls-Structures Interaction Program. It joins previously delivered Government Support Equipment (GSE) that provides full

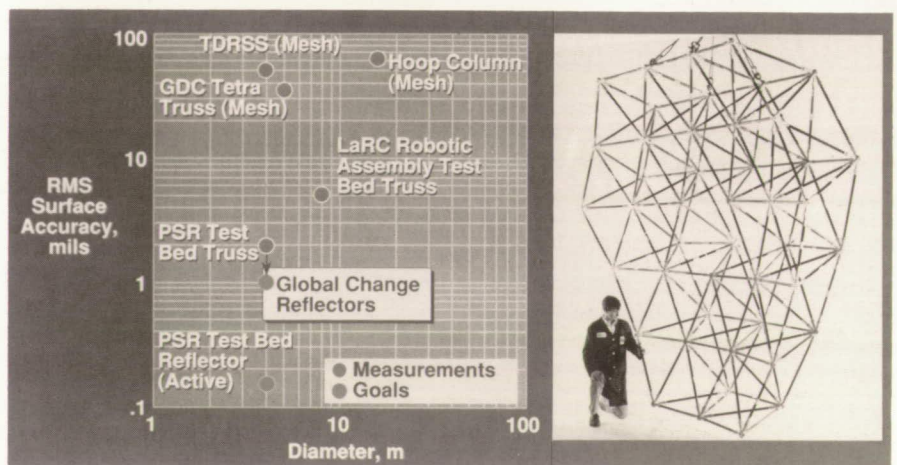
test capability as well as an Ada workstation with all tools needed for software development.

(M. Beatty, 41689)
Electronics Directorate

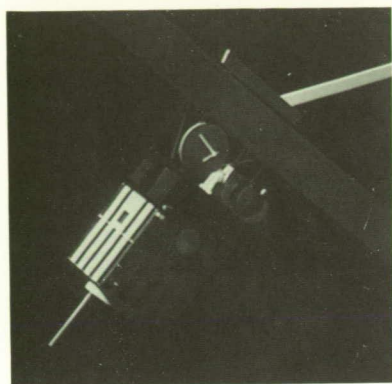
Precision-Segmented Reflector Support Truss

The surface accuracy required for large space reflectors presents a formidable task to develop easy-to-package, erectable structures that, when assembled in space, will have the dimensional compatibility to maintain reflector accuracy. To support Precision-Segmented Reflector (PSR) panel development activities at the Jet Propulsion Laboratory (JPL), an accurate, doubly curved erectable truss for use as a test bed has been developed, and a baseline structural design and fabrication capability has been established at Langley Research Center.

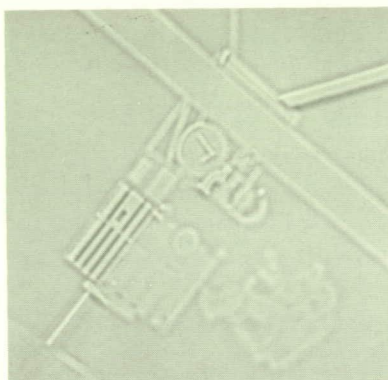
The 4-m tetrahedral truss is designed to accept parabolic panels with a focal length of 2.4 m. The 189-lb assembled truss (shown in the figure) consists of 45 nodes, 150 struts, and 300 joint assemblies. Each core strut of graphite/epoxy (1 in. diameter) is set to a nodal center length of 0.8135 m using a laser interferometer setup. Photogrammetric surface accuracy measurements of the assembled truss show an 0.0028-in. RMS (root-mean-square) surface deviation. As the plotted data show, this accuracy is well within the 0.004-in. PSR goal. The analysis/test



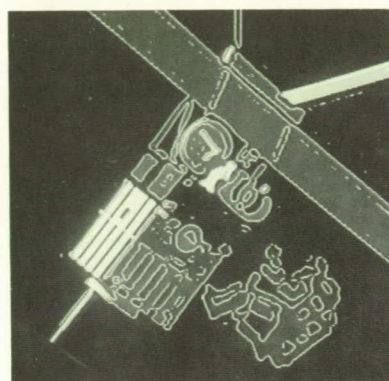
Test bed truss for precision reflector development (RMS surface accuracy of ≈ 2 mil). L-89-13840



Conventional imaging



Local intensity adaptive imaging



Local intensity adaptive imaging reveals astronaut in deep shadow of satellite.

agreement indicates that the test bed truss has a linear, predictable behavior under both static and dynamic loads.

The assembled PSR test bed truss represents a significant design and fabrication milestone demonstrating a start-to-finish capacity for erectable reflector support structure. Geometric accuracy and structural performance of the erectable test bed truss show the validity of the approach for precision reflector applications.

(Harold G. Bush, 43124, Catherine L. Herstrom, Walter L. Heard, Jr., Timothy Collins, and W. B. Fichter)

Structures Directorate

Local Intensity Adaptive Imaging

The human visual system adapts itself very effectively to many orders of magnitude of variations in illumination. This adaptation occurs not only temporally but also locally. Most important, this system is remarkably capable of extracting structure (contour outlines) and reflectance (color) of targets in

shadows as well as in direct illumination.

Tom N. Cornsweet of the University of California, Irvine, recently proposed a surprisingly simple mechanism, referred to as Intensity Dependent Spread (IDS), for this seemingly complex capability. According to this mechanism, when an optical image falls on a photodetector array, then each detector sends a signal into a network, where it spreads out. The special property of the IDS model has to do with the way this spread is controlled. In essence, the magnitude of the signal at the center of its spatial distribution is proportional to the intensity of the light falling on the photodetector, and the spread of the distribution is inversely proportional to this intensity. The total volume under the signal distribution remains constant over many orders of magnitude of changes in intensity. This simple mechanism of image processing has been demonstrated to feature many of the properties of human visual perception.

In a cooperative research and development activity between Odetics, Incorporated, and Langley Research Center, this IDS mechanism

has been successfully implemented in two hardware configurations, both capable of processing 512 by 512 pixel images. One implementation performs the processing in 4 seconds per image, and the other performs at real-time commercial television rate (30 full frames per second). The architecture of the IDS hardware was designed so that it can be implemented both with commercially available electronics for image-processing workstations and with very-large-scale integrated (VLSI) circuits for space imaging systems. In addition, algorithms have been developed for extracting structure and reflectances from the IDS processed signal. This approach provides a uniquely robust and compact method for encoding images in which high structural fidelity is maintained over the wide dynamic range of illuminations that are encountered in space, stretching from deep shadows to highly reflective surfaces in direct sunlight.

(Friedrich O. Huck, 41517, and Rachel Alter-Gartenberg)
Flight Systems Directorate

Thermal Analysis of Solid-State Lasers for DIAL and Doppler Lidar

Solid-state lasers are ideal systems for aircraft- and spacecraft-based remote sensing of atmospheric species and their trajectories. Pumping of these lasers results in thermal loading. Modeling of this loading is required to determine limits imposed by damage to the materials and optical effects including thermal focusing due to the index of refraction and lengths changing with temperature. A Langley Research Center research program has resulted in a model for thermal effects which is being used to design efficient lasers for air and spaceflight remote sensing applications.

The proper thermal design of high-power solid-state laser systems will result in compact efficient systems for use in aircraft and spacecraft. Thermal models are of particular importance for requirements when pulse rates are not constant or where an irregular pulse pattern is required. For a DIAL system, a double-pulse pattern is required to allow rapid

changes from on to off wavelength. The double-pulse operation results in a change in temperature distribution from the first to second pulse because each pulse has a different cooling period. Modeling of the temperature distributions is required to predict the changes in thermal focusing between the pulses and to design the optical system for these changes.

The impact of active and passive cooling on specific laser crystals has been determined for both end and side pumping. Results from the model have been compared to measured data on temperature rise and thermal focusing. A desktop computer program has been made available through the NASA Computer Software Management and Information Center (COSMIC) data base. This program allows the analytic solution of time-dependent temperatures in a short time. The program has been upgraded to process multiple-pulse pair lasers including the Lidar Atmospheric Sensing Experiment (LASE) bread-board laser.

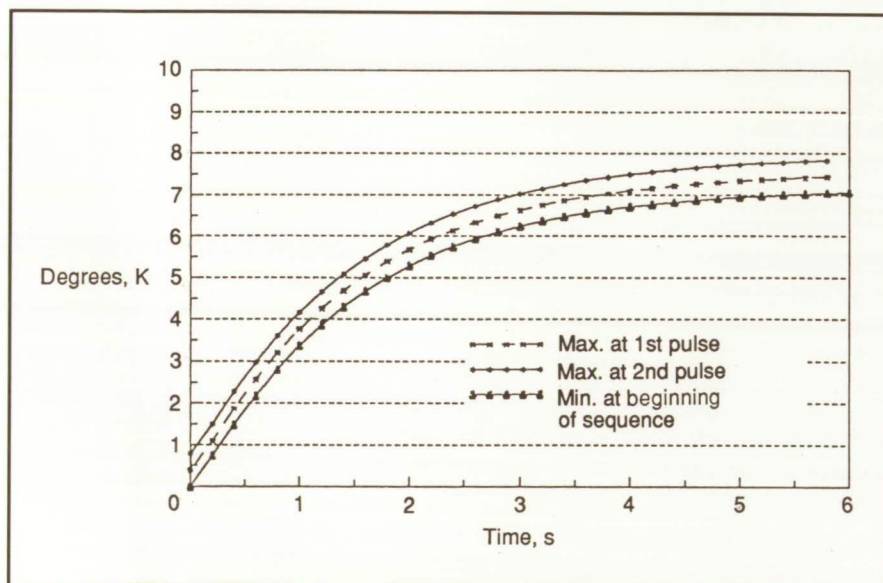
(U. Farrukh and Philip Brockman, 41556)
Electronics Directorate

Modeling of Multiple-Ion-Doped Eye-Safe Solid-State Lasers for DIAL and Doppler Lidar

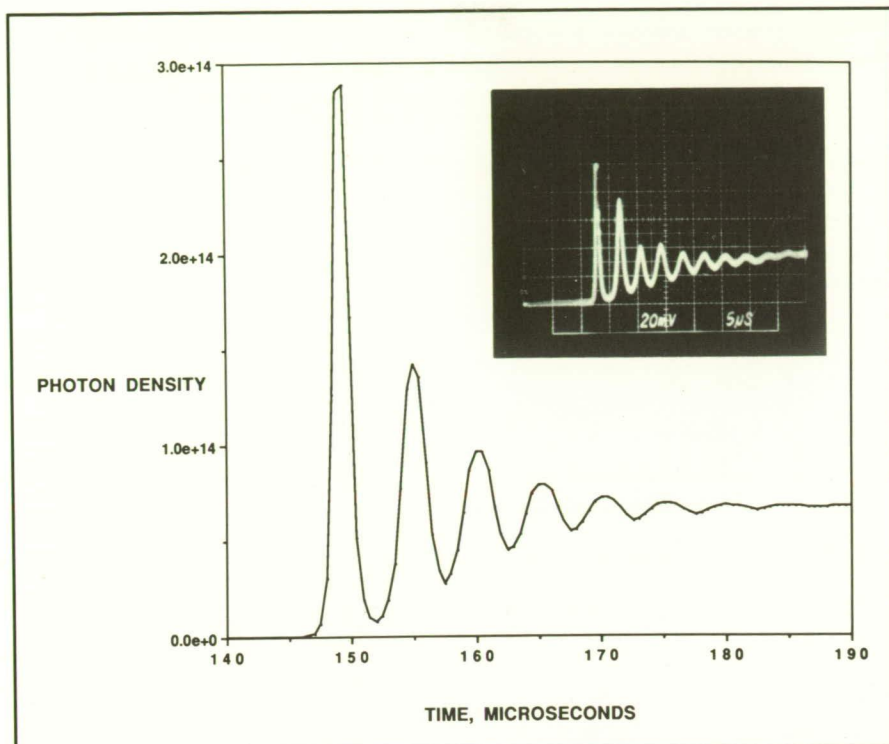
This research program is focused on providing a computer model for optimizing the efficiency of narrowband eye-safe lasers for differential absorption lidar (DIAL) and Doppler lidar remote sensing of atmospheric trace gases and wind velocity. Emphasis has been placed on multiple-ion-doped rare Earth ion solid-state lasers that operate near $2\text{ }\mu\text{m}$, which offers the potential for both high-efficiency frequency conversion into the $2\text{-}\mu\text{m}$ to $5\text{-}\mu\text{m}$ vibration-rotational bands of several key atmospheric constituents or can be used directly for wind velocity/shear sensing.

Laser performance depends critically on many variables, which include mirror reflectivities, cavity losses, type and concentration of lasing and co-dopant ions, and laser pump intensity. To vary these parameters in the laboratory would be difficult, time consuming, and cost prohibitive. By exercising a validated computer model, a detailed understanding of the physical interaction mechanisms can be gained, and predictions can be made to enable the researcher to accurately judge which of the variables to more closely examine in the laboratory.

The detailed rate equation model previously developed to describe energy transfer and laser activity for multiple-ion-doped rare Earth lasers has been upgraded to include several new upconversion interactions. This model has been applied to describe laser performance of a room-temperature thulium and holmium co-doped yttrium aluminum garnet laser (Tm:Ho:YAG) pumped with a chromium-doped gadolinium scandium aluminum garnet (Cr:GSAG) laser simulating diode-laser pumping.



Temperature at center of rod for double pulse (double pulses required for DIAL measurements).



Photon density as function of time for room temperature Tm:Ho:YAG laser.

The rate constants necessary to characterize the Tm-to-Tm and Tm-to-Ho energy transfer processes, as well as the additional upconversion interactions, have been obtained from Langley Research Center spectroscopic measurements. The model has been validated by comparing with experimental results for a variety of rod lengths, pump intensities, output couplers, and dopant concentrations. (Clayton H. Bair, 41556) Electronics Directorate

Spectroscopic Measurements of Energy Transfer Processes in 2- μ m Laser Materials

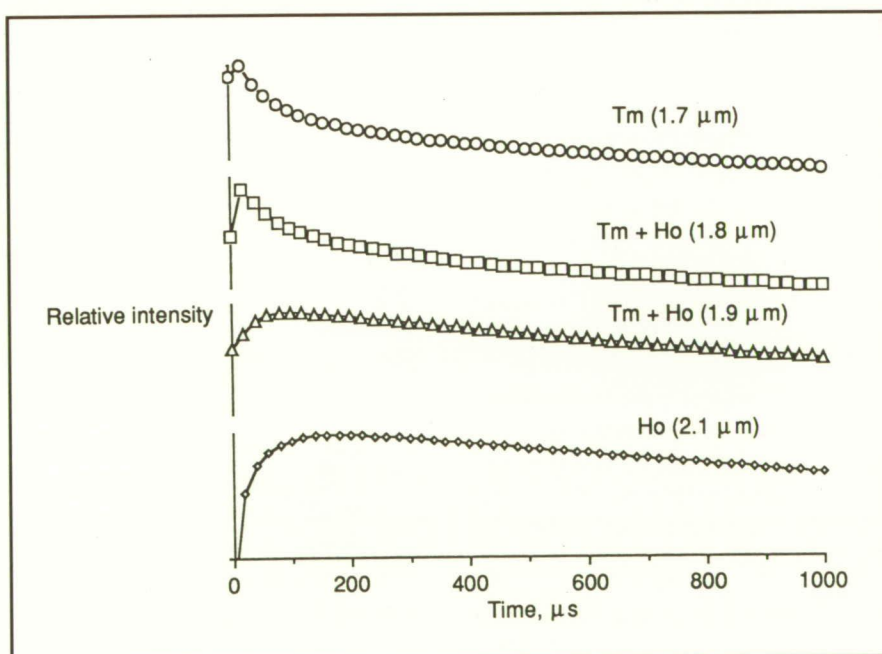
Primary candidates for a 2- μ m solid-state laser are based on thulium (Tm) or holmium (Ho) sensitized with Tm doped into a host material (e.g., yttrium aluminum garnet (YAG) or yttrium lithium fluoride

(YLF). Relatively short pulses are required by laser sources for Doppler lidar wind shear measurements and for remote sensing with differential absorption lidar (DIAL). To obtain

efficient Q-switched operation of these sensitized lasers, it is necessary to have a clear understanding of the interionic processes and their rates, which are responsible for the transport of excitation energy from the primary absorption levels to the upper laser level.

A thorough spectroscopic study of the interionic interactions among Tm and Ho ions in YAG and YLF is under way. Measurements of the steady-state fluorescence spectra and of the temporal response to pulsed excitation have been made. Pulsed sources include short-pulse, low-energy excitation to identify fundamental processes and long-pulse, high-energy sources to simulate lasing conditions under diode-laser or flashlamp pumping.

An analysis of the cross relaxation in Tm-doped YAG and YLF has been completed by measuring the temperature and concentration dependence of the cross-relaxation rate. The interionic interaction between Tm and Ho has been analyzed, and various energy transfer



Rise and decay of Tm and Ho emission for Tm (6 percent), Ho (0.5 percent), and YAG at 300 K.

channels between these two ions have been identified. Some of these channels support the lasing process, and others are loss mechanisms. The energy transfer rates between Tm(3F4) and Ho(517) as functions of temperature and concentration have been measured. Nonlinear effects, including upconversion, have been measured by varying pulsed- and continuous-wave pump intensities.

From the analysis of the spectroscopic data, the fundamental processes responsible for the transport of excitation in Tm and Ho and the rates of these processes as functions of temperature, dopant concentration, and pump intensity have been determined. Information from this study has been incorporated into a model describing the lasing action so that laser efficiency, pulse shape, and wavelength can be predicted.

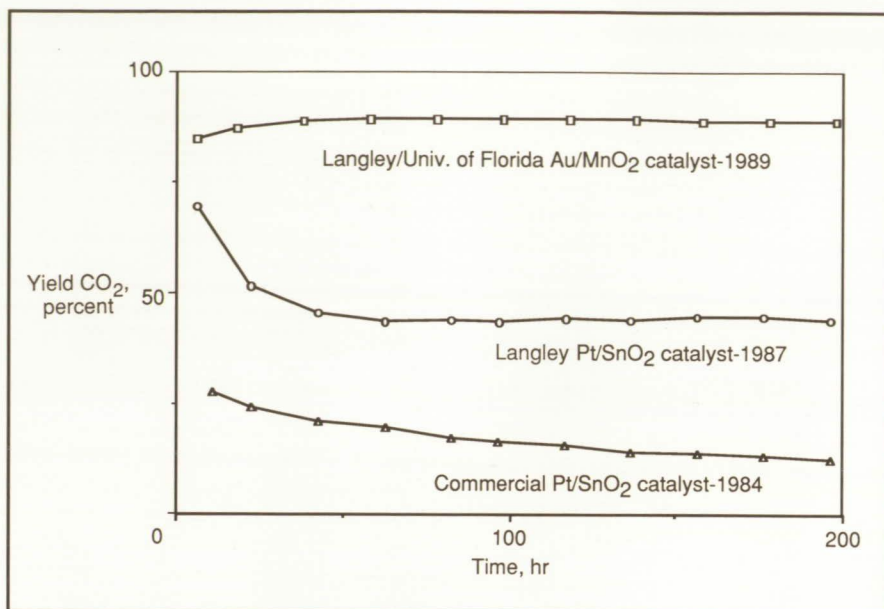
(Clayton H. Bair, 41556, and Guzin Armagan)

Electronics Directorate

CO-O₂ Recombination Catalyst for CO₂ Lasers

Electrically excited pulsed CO₂ lasers undergo some decomposition of CO₂ to CO and O₂ with each pulse. Both the loss of CO₂ and the buildup of O₂ are detrimental to long-life closed-cycle laser operation.

This problem can be overcome by catalytic recombination of CO and O₂ to regenerate CO₂. The CO-O₂ recombination catalysts with high activity at ambient laser temperatures and low oxygen concentrations did not exist until recently. The first such catalyst, based on platinized tin-oxide (Pt/SnO₂), was developed in the United Kingdom and has been significantly improved by research at Langley Research Center. Unfortunately, Pt/SnO₂-based catalysts exhibit significant decay in activity with time. These catalysts lose about



Improvements in CO-O₂ recombination catalysts.

one-half of their activity in a day or two due to surface retention of the product CO₂ and then exhibit a further decay half-life of 6 to 8 months. Techniques to minimize the activity decay of Pt/SnO₂-based catalysts have been studied intensively without significant success.

A new catalyst consisting of gold on manganese-dioxide (Au/MnO₂) has recently been developed by joint Langley/University of Florida research. Extensive tests indicate that this new catalyst is superior to Pt/SnO₂; Au/MnO₂ and Pt/SnO₂ are comparable in initial activity, but Au/MnO₂ undergoes considerably less decay with time.

A sample of Au/MnO₂, which was tested continuously for 5 weeks at 55°C in a stoichiometric CO-O₂ mixture, exhibited an extrapolated half-life of 35 weeks. Another sample tested continuously for 18 weeks at 32°C exhibited no detectable decay.

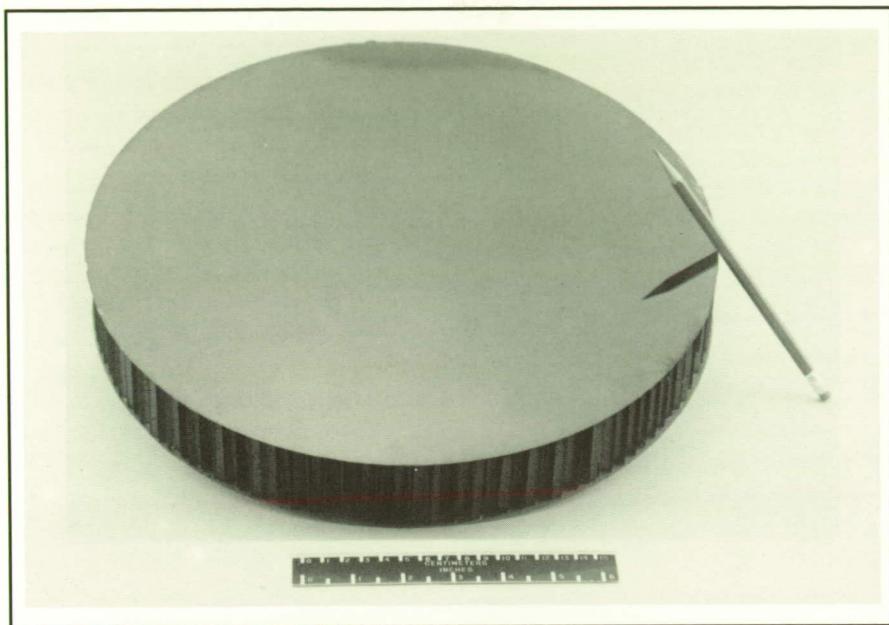
Although Au/MnO₂ has high activity for the stoichiometric CO-O₂ mixtures produced in CO₂ lasers, its activity is significantly higher at high O₂ concentrations, such as in air. Therefore, this catalyst also is being studied for air purification applications as well.

(David R. Schryer, 41576, and Billy T. Upchurch)

Electronics Directorate

Development of Composite Materials for Precision Reflector Panels

Future missions in both astrophysics and optical communications will require large precision reflectors operating in both low circular and highly elliptical Earth orbits. These reflectors will consist of parabolic panels with surface accuracies of a few micrometers and will operate at temperatures as low as -300°F. To provide the enabling technologies for these missions, the NASA Office of



Parabolic composite honeycomb core panel. (Facesheet is P75/930 Gr/Ep [0/45/90/-45]_s laminate with PAEI surface film, core is T300 fabric/phenolic honeycomb, 4.83 cm thick, and panel is parabolic with 2.4 m focal length; areal weight = 4.28 kg/m².)

Aeronautics, Exploration and Technology initiated the Precision Segmented Reflector (PSR) program. A major focus of the PSR program is to develop lightweight composite materials and reflector panels that are durable and stable in the space environment and which maintain both surface figure and required surface accuracy.

A parabolic reflector panel designed and fabricated in-house under the PSR program is shown in the figure. Each constituent material system in the panel meets or exceeds the requirements and collectively forms a panel that meets or exceeds the PSR target requirements. The facesheets are made of a high-modulus graphite/epoxy composite, and the core is made of a graphite/phenolic composite. A recently developed polyarylene ether imidazole (PAEI) thermoplastic polymer film has been added to the surface to

improve surface smoothness and provide resistance to electron radiation.

(S. S. Tompkins, 43096, and T. W. Towell)

Structures Directorate

Functional Margin Demonstration for Pyrotechnics

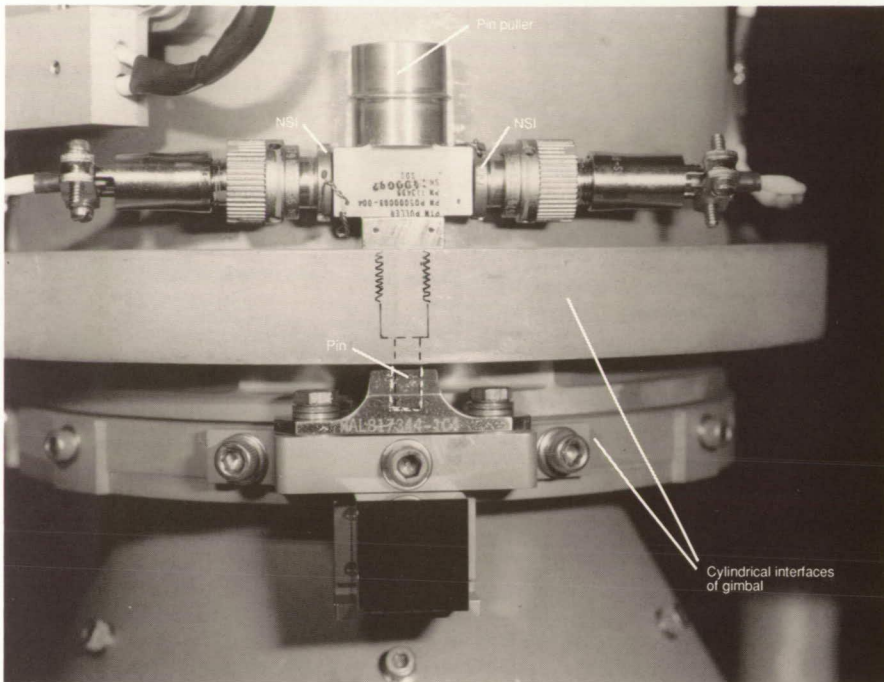
Pyrotechnic mechanisms are used extensively on spacecraft missions for critical functions such as staging and solar panel deployment. Generally, these mechanisms have few requirements to demonstrate functional margins, i.e., how well is a mechanical device, powered by an explosive energy source, actually accomplishing its function? Programs rely almost entirely on go/no-go tests, i.e., repetitive functional

tests of the device which either do or don't work in their final configuration to gain system confidence. However, many subtle factors, such as manufacturing tolerances and variations in combustion efficiencies for the explosive energy source, and manufacturing and assembly tolerances, load paths and friction for the mechanical components, can produce a wide range of performance. Sufficient go/no-go testing to demonstrate system variables requires more test numbers and time than program office budgets generally allow. Therefore, a small number of successful tests are accepted as proof of reliability of a system that could be marginal. New methods have been developed for the Halogen Occultation Experiment (HALOE) gimbal pin pullers to prove functional margin. These principles are applicable to all pyrotechnic mechanisms.

The HALOE gimbal pin puller, as shown in the figure, is designed to withdraw its pin (illustrated in phantom) on firing either of the NASA Standard Initiators (NSI's) to release the gimbals for rotation. Functional evaluation was based on forming a ratio of the energy required to stroke the pin to the energy deliverable by each of the NSI's. A functional margin is achieved if the energy deliverable is larger than the energy required.

The energy required to stroke and lock the retractable pin, obtained by controlled drop tests, was 25 in-lb. The energy deliverable by the NSI, obtained from stroking the pin against calibrated honeycomb, was 125 in-lb to produce a functional margin of 5. Furthermore, an energy-absorbing cup that is mounted internally to the pin puller and is crushed on stroking provides a second verification of energy deliverable in the flight configuration.

This test program produced several additional benefits, including



Pyrotechnic pin puller mounted in HALOE gimbal interface.

L-86-5151

Inspection for flaw size determination was not made prior to installation of three #8-32 fasteners installed on the HALOE flight hardware, and disassembly for inspection was not practical.

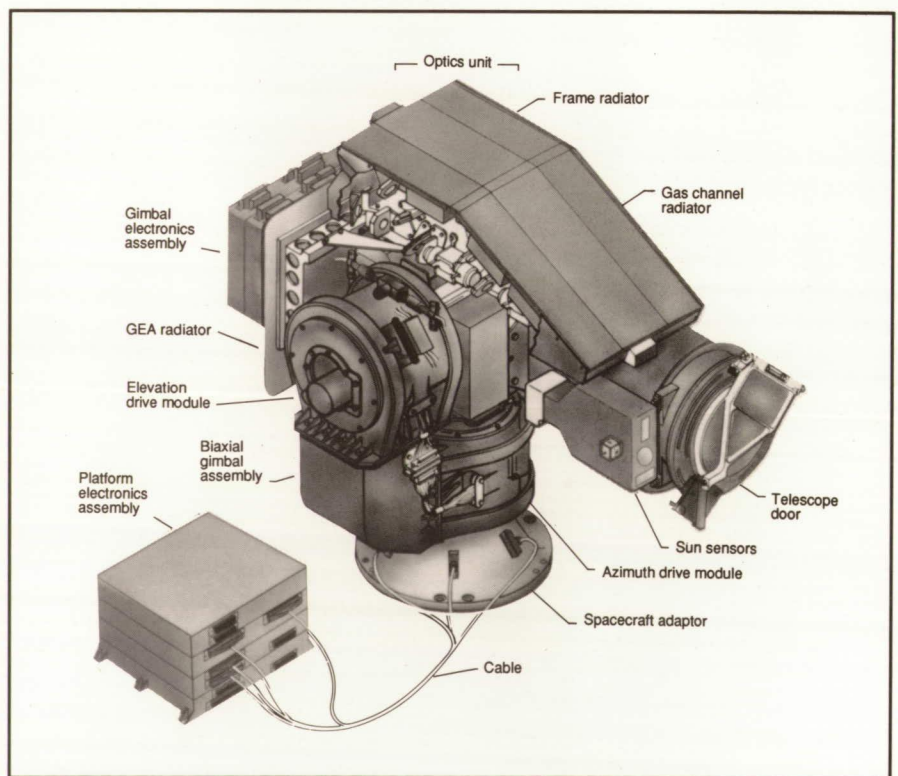
Two series of tests were conducted to demonstrate adequate life of the uninspected screws. In the first series, fasteners with circular flaws of various sizes were fabricated and then torqued to failure. This information was used to establish the largest flaw that could exist in the flight assembly, based upon the torque used for the flight screws. In the second series, a fastener with the determined maximum flaw size was fabricated and installed in a fixture that replicated the stiffness of the flight application. This assembly then was subjected to a cyclic load spectrum that enveloped the loads that the

quantifying the effect of friction, determining that NSI outputs vary considerably among manufacturing lots, and recognizing that the NSI output combustion efficiency is considerably influenced by the mechanical design of the device into which it is fired.

(Laurence J. Bement, 47084)
Systems Engineering and Operations Directorate

Structural Life Assessment of Fasteners Via Test

Concentrations of eight gases in the upper atmosphere will be measured by HALOE to be flown on an STS (Space Transportation System) mission. The HALOE instrument is shown in the figure with the Sun sensor that is attached with three #8-32 fasteners. The method used to demonstrate adequate life of three fasteners after installation without inspection for flaws is presented.



HALOE flight instrument with Sun sensor attached to telescope.

L-86-3584

flight hardware was expected to experience. An additional 3.5×10^6 cycles (many times the expected mission loading) at 2.9 times limit load were applied to the specimen without failure or crack growth. This demonstrated a factor in excess of four on the life of the fastener with a flaw that was as large or larger than could exist on the HALOE flight hardware.

(Thomas C. Jones, 47037, and Dave E. Williams)

Systems Engineering and Operations Directorate

Nonvolatile Residue (NVR) Cleanliness of Clean Room Wipes, Swabs, and Gloves

Nonvolatile residue (usually an organic film) can adversely affect optical transmission, bonding of adhesives and potting compounds, and electrical connections. Solvent (i.e., isopropyl alcohol) cleaning of optics and critical contact surfaces is a fairly standard clean room procedure. Most clean room products (including wipes, swabs, and gloves) are carefully controlled for particle contamination and are well suited for dry handling procedures. However, solvent contact with typical clean room items can leech significant amounts of organic material from these items and leave them as a thin film on critical surfaces. Therefore, it can be very helpful to measure new product nonvolatile residue (NVR) and to know cleaning efficiencies of procedures to remove NVR from items used in critical solvent cleaning.

Organic films strongly absorb far ultraviolet radiation ($<2000\text{\AA}$) due to the electronic transition of hydrogen, moderately to strongly absorb at $3.4\text{ }\mu\text{m}$ due to the carbon-hydrogen (C-H) stretching bond, and moderately absorb between $6\text{ }\mu\text{m}$ to $12\text{ }\mu\text{m}$

New wipe		NVR recovered weight, mgm/ft ²
Texwipe TX309 (cotton)		1.92
Texwipe TX1013 (polyester) 2 wipes		2.75
Kennedy Space Center wipe		1.08
General Electric wipe		3.10
Extracted wipes		
Texwipe TX1013	Soxhlet extracted	0.01
Texwipe TX304	Soxhlet extracted	0.19
Texwipe TX1013	3 x 24 hr isopropyl alcohol (IPA) + H ₂ O rinse	0.08
Texwipe TX309	3 x 24 hr IPA + H ₂ O rinse	0.10
Llulmaloy bagging material		.02

NVR of clean room wipes.

(carbon-hydrogen footprint region). High-resolution-in-transmission measurements of thin films with a Fourier transform infrared (FTIR) spectrometer are used to measure small amounts of NVR extracted from wipes, swabs, or gloves by soaking the test item in high-purity alcohol. The residue left after evaporation of the alcohol is deposited on a thin, preweighed infrared transmitting window. The $3.4\text{-}\mu\text{m}$ C-H absorption spectrum, as well as the residue weight (obtained with a calibrated microbalance), is routinely obtained for each tested item. By measuring the NVR of a sample item before and after cleaning by some procedure, the cleaning efficiency of the procedure can be determined.

New clean room wipes and swabs, which are to be used in critical cleaning with solvents, are routinely cleaned (extracted) either by repetitive warm alcohol soaking and hot water rinsing or by Soxhlet extraction. Soxhlet extraction is the removal of organics by repetitive distillation and flushing with a solvent. Both of these procedures

remove approximately 99 percent of new product NVR from clean room wipes and gloves. The table in the figure lists NVR weights/ft² of both new and extracted clean room wipes. The high potential for NVR contamination by solvent cleaning when using common clean room materials should be recognized. Cleaning procedures should be written to ensure the use of extracted wipes and Teflon gloves for critical optics and bonding and electrical surfaces during assembly and testing of instrument hardware. Because NVR usually becomes mobile in a vacuum, the final cleaning of all space hardware generally should be with extracted wipes and Teflon gloves. (Gale A. Harvey, 46742, and Dewey M. Smith)

Systems Engineering and Operations Directorate

Organic-Film Cleanliness Certification of Environmental Chambers and Clean Rooms

Organic film contamination of critical surfaces can adversely affect optical transmission, materials bonding, and electrical conductivity. Organic films are generally present to some degree because of material outgassing, diffusion, migration, and contact transfer in fabrication, assembly, testing, and transport of aerospace components and experiments. Cleanliness measurement and certification are needed to evaluate contamination hazards and provide efficacious cleaning or protective measures. This is particularly true of environmental chambers because many organic materials that are clean at ambient conditions will heavily outgas under vacuum and/or elevated temperatures.

Organic film contamination of several clean rooms at Langley Research Center now is routinely monitored by optical witness plates and high-integrity solvent-wash plates. Organic film contamination of flight instruments is measured by solvent washes of selected surfaces and alcohol-extracted wipe measurements. Organic films in environmental chambers are measured by extracted-alcohol wipe-measurement, optical witness plates, solvent-wash plates, and residual gas analyzer spectra.

A trial pumpdown and organic-cleanliness recertification of the 8- by 15-Foot Thermal-Vacuum Chamber at the Langley Research Center has been performed recently. This test was the most comprehensive to date organic-cleanliness measurement of any vacuum facility at Langley. Alcohol wipes were taken before and

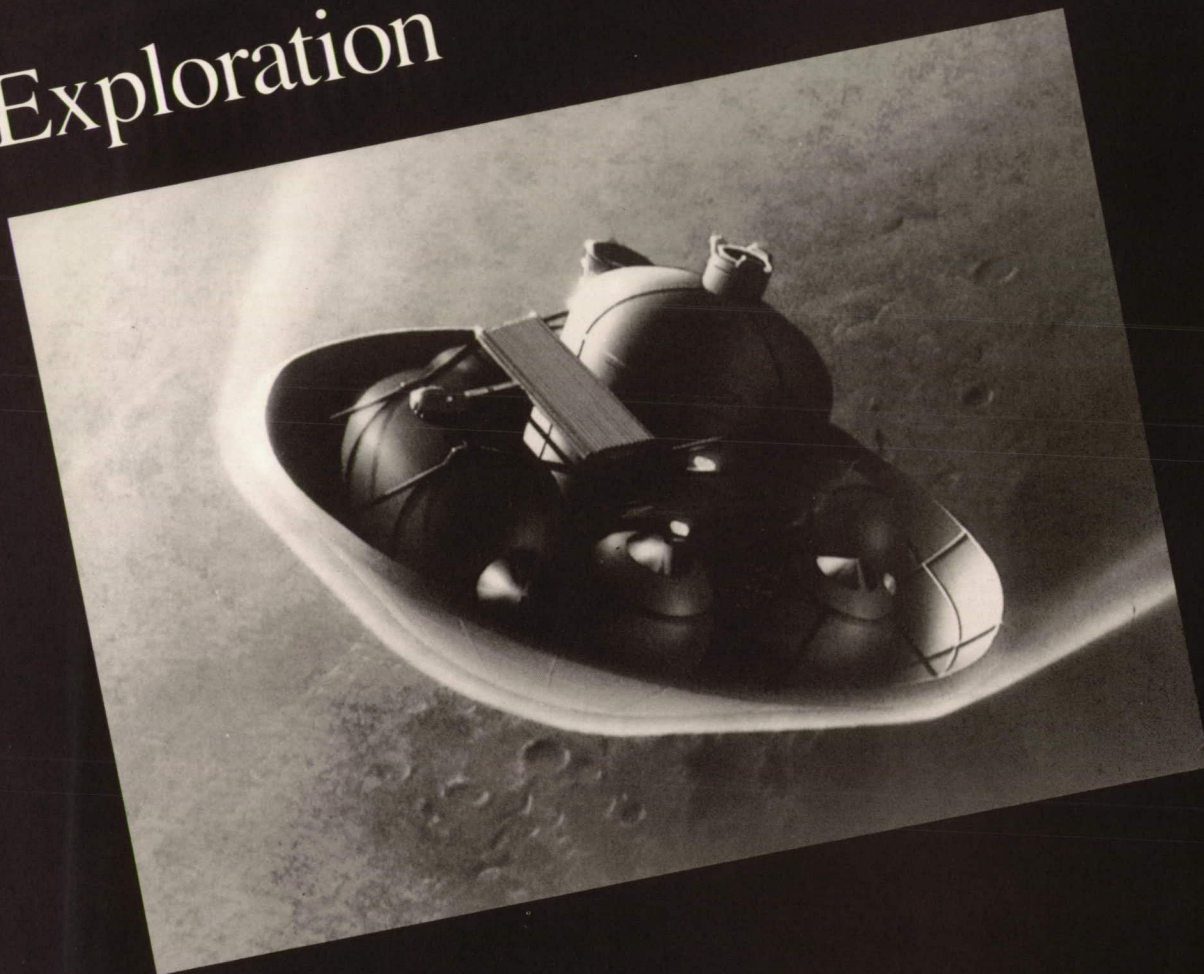
after cleaning and after vacuum exposure. Optical and solvent-wash witness plates were placed in the chamber during vacuum exposure and bakeout. Residual gas analyzer (RGA) spectra were taken during high-vacuum operations. The RGA spectra are listed in the table in the figure.

The unexpected measurements and observations of extremely heavy organic residue film on colder surfaces showed that the black thermal-control paint (painted on the inside of the shrouds) was a very large reservoir of organic contamination. This contamination was similar to the heavy organic contamination of LDEF resulting from outgassing of the black thermal-control paint on the interior of the spacecraft. (Gale A. Harvey, 46742) Systems Engineering and Operations Directorate

Spectrum number	Primary gases	Hydrocarbon products, 50 to 90 amu
1 - 15	H ₂ O, N ₂ , O ₂	$10^{-12} < \text{H-C} < 10^{-11}$ torr
16 - 26	N ₂ , O ₂ , H ₂ O	$10^{-13} < \text{H-C} < 10^{-12}$
27 - 29	N ₂ , O ₂ , CO	$\text{H-C} < 10^{-13}$
30 - 32	He, N ₂ , O ₂	$\text{H-C} < 10^{-13}$
33 - 36	He, N ₂ , O ₂	$10^{-11} < \text{H-C} < 10^{-10}$
37 - 46	He, N ₂ , O ₂	$10^{-12} < \text{H-C} < 10^{-11}$
47 - 59	N ₂ , He, O ₂	$10^{-13} < \text{H-C} < 10^{-12}$
60 - 87	N ₂ , He, O ₂	$\text{H-C} < 10^{-13}$

Residual gas analyzer spectra.

Exploration



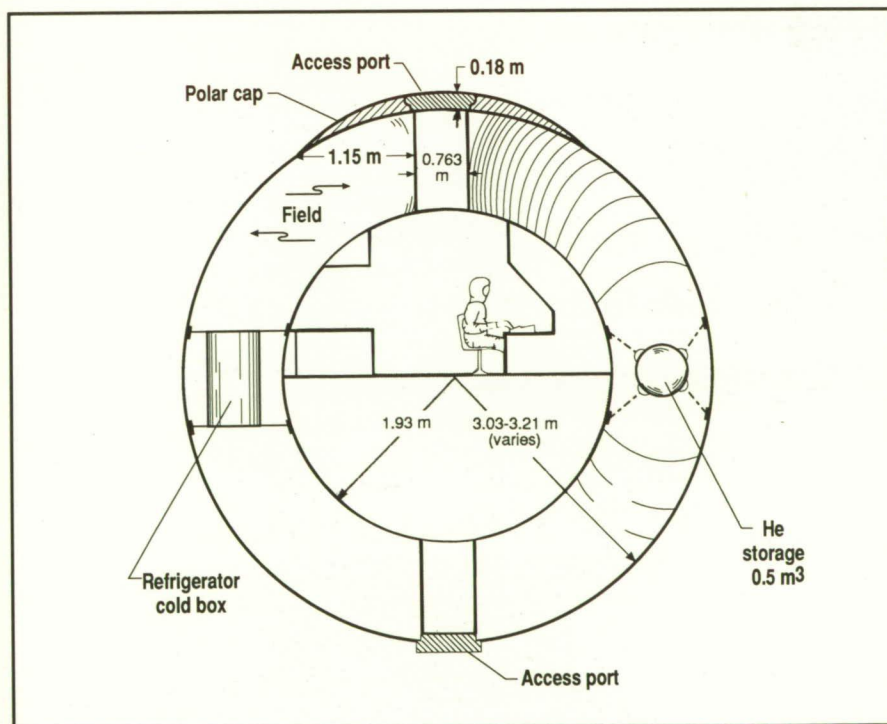
Reevaluation of Magnetic Radiation Shielding for Manned Mars Missions

The effectiveness of a previously proposed concept for shielding a manned Mars vehicle using a confined magnetic-field configuration was evaluated by computing estimated crew radiation exposures resulting from galactic cosmic rays and a large solar flare event. In the study, a hybrid torus configuration proposed in the early 1960's by Avco-Everett Research Laboratory was used. The spacecraft shelter consisted of two concentric spheres with approximate radii of 1.9 m and 3.2 m. The shielded inner sphere housed a crew of up to 10 astronauts. A uniform magnetic field, generated by a set of nested toroidal superconducting coils, was confined to the annular region between the concentric spheres. The magnetic field intensity corresponds to the 200-MeV energy cutoff for protons of 47 MeV/

nucleon for iron, which is one of the abundant species from galactic cosmic rays.

In this work, analysis was performed using a realistic galactic cosmic ray spectrum during solar minimum and the August 1972 solar flare event spectrum as inputs to the deterministic space radiation transport codes developed at Langley Research Center. The calculated exposures demonstrate that magnetic shielding could provide an effective barrier against solar flare protons, but it is virtually transparent to the more energetic galactic cosmic rays. Through the proper selection of materials and shield configuration, it was demonstrated that adequate and reliable bulk materials shielding can be provided for the same total mass as needed to generate and support the more risky magnetic field configuration.

(L. W. Townsend, 41417, J. W. Wilson, and J. L. Shinn)
Space Directorate



Detail of winding cross section, hybrid magnetic shield.

Radiation Dose Estimates for 500-Day Manned Mars Mission

A conceptual manned mission to Mars is analyzed in order to estimate potential ionizing radiation doses that may be incurred by crew members during the course of the mission. The scenario is set for a journey during a solar active period and includes a brief stay on the Martian surface. Propulsion is assumed to be provided by nuclear thermal rocket (NTR) power, and estimates of the dose contributions from the reactors are included. Because of effective shielding of the reactors by large propellant tanks, the incurred doses are principally due to the charged particle natural environment. Recent data (August to December 1989) for large solar proton events are used to simulate the flare environment, while standard models are used for the trapped particle and galactic cosmic ray (GCR) contributions.

The figure indicates the estimated blood-forming organ (BFO) dose contributions from the various

sources. For the reactor firings, previous calculations for this scenario were made at the Idaho National Engineering Laboratory and included a three-burn Earth departure simulation that involved several passes through the trapped radiation belts. Belt transit calculations were made using standard environment models coupled with orbit and incurred dose codes at the Goddard Space Flight Center. The major dose contributions from the solar flares and cosmic rays were evaluated with Langley Research Center developed heavy-ion transport codes. The manned module was assumed to contain a heavily shielded cylindrical compartment (25 g/cm²), which the crew would occupy during solar flare activity. Even in the absence of solar flares, most crew time would be spent in the shielded area. The results show that the cumulative cosmic ray dose comprises the largest fraction of the total dose and varies between 28 cSv and 37 cSv for crew time in the shielded area; this variation occurs between essentially complete occupancy to 16 hr/day. The total 500-day mission dose estimate of 40 cSv to 50 cSv is quite substantial, even though

maximum dose guidelines are not exceeded.

(John E. Nealy, 44412)
Space Directorate

Surface Heating Distributions on Aerobrake-Carrier-Payload Assemblies

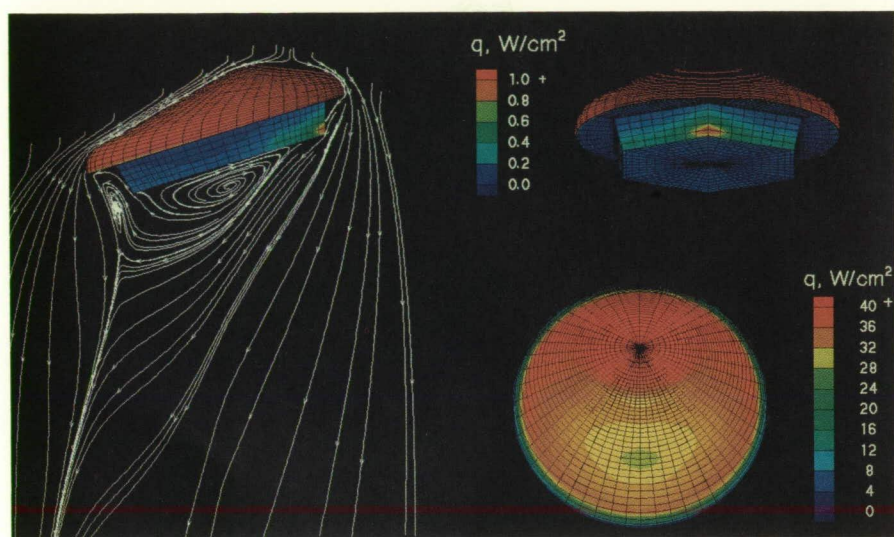
An Aeroassisted Space Transfer Vehicle (ASTV) passes through the upper reaches of a planetary atmosphere and utilizes aerodynamic forces to implement desired orbital adjustments with a minimal expenditure of fuel. This atmospheric interaction with the spacecraft is often referred to as aerobraking or aeromaneuvering. Proposed missions that exploit aerobraking technology include the deceleration of spacecraft returning to low-Earth orbit from Mars, the Earth's moon, and geosynchronous Earth orbit. Exploration of the planet Mars will probably involve an aerobraking maneuver of the arriving spacecraft with the Martian atmosphere.

The ASTV, in its simplest configuration, is composed of an aerobrake, a carrier, and a payload. The aerobrake is typically configured with a large, blunted surface that is designed to take the brunt of the aerodynamic heating and provide acceptable aerodynamic coefficients to implement the required maneuvers. The carrier sits behind the aerobrake and provides the structural support for connecting the payload to the brake and for mission general hardware such as the Reaction Control System. The payload sits behind (or inside) the carrier; its shape and size are mission specific.

The heating distributions on the Aeroassist Flight Experiment (AFE) aerobrake-carrier assembly are shown in the figure, as determined by a

NTR firings	<1.1	cSv
Transit through trapped belts	~1.5	cSv
30-day surface stay (GCR)	<1.0	cSv
Solar flare contribution	7.7	cSv
GCR contribution	27.8-36.7	cSv
Totals	39.1-48.0	cSv
Note: Maximum BFO dose guideline for mission: not to exceed 50 cSv in 12-mo period		

BFO dose estimates for 500-day Mars sprint mission (1 cSv = 1 rem).



AFE surface heating $V_\infty = 9.3$ km/s, $h = 75$ km, and $\alpha = -5^\circ$. L-90-6134

computational analysis using the Langley Aerothermodynamic Upwind Relaxation Algorithm (LAURA). The AFE is designed to obtain critical flight data to improve analysis capability for more general ASTV missions. The heating pattern on the broad front surface of the brake is shown on the lower right. These heating levels are near the limits of current thermal protection system capabilities for reusable material. A hexagonal-shaped carrier sits behind the aerobrake as seen on the upper right. A local hot spot on the carrier is caused by hot gases that spill around the corner of the aerobrake and impinge directly on the carrier. The predicted streamline pattern around the vehicle shown on the left can be used by the designer to position a payload so that aerothermal loads caused by the direct impingement of hot gas are minimized.

(P. A. Gnoffo, 44380)
Space Directorate

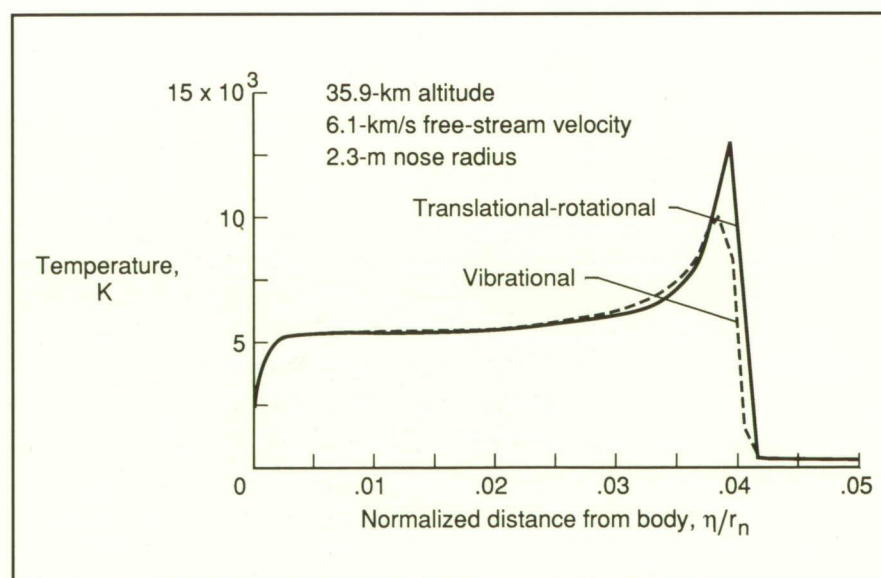
Thermochemical Nonequilibrium for Mars Aerobraking Entry

Renewed interest exists in both manned and unmanned exploration of the planet Mars. To minimize vehicle weight, aerobraking (using aerodynamic drag to obtain the required velocity change) is an effective alternative to an all-propulsive system for atmospheric insertion

at both Mars and on return to Earth. This study concentrated on the development of a computational technique to study the aerothermodynamics of Mars aerobraking with particular emphasis on determining the degree of thermochemical nonequilibrium present in these flows. The study was conducted under a grant by G. V. Candler at the North Carolina State University.

An eight-species chemical kinetics model for the $\text{CO}_2\text{-N}_2$ gas mixture found in the Mars atmosphere was implemented in an existing thermochemical, Navier-Stokes computational technique. The flow about an ellipsoidally blunted 60° cone was studied at two points (a 6.1-km/s velocity at a 36-km altitude and a 7.4-km/s velocity at a 50-km altitude) on a proposed Mars aerobraking trajectory. Two nose radii (2.3 m and 23 m) were used for each trajectory point.

A two-temperature model is used in the thermal nonequilibrium modeling in which the translational and rotational energy modes are assumed to be equilibrated at a translational-rotational temperature and the second temperature is



Mars aerobraking entry stagnation streamline temperatures.

assumed to represent the vibrational energy modes. The temperature profiles along the stagnation streamline for the smaller nose radius at the 6.1-km/s velocity case are shown in the figure. Note that the two temperatures are equal except in the vicinity of the shock region (normalized distance of 0.04).

The results obtained show that thermal equilibrium prevails in all cases computed, except in a small region of the shock. For the low-velocity case (6.1 km/s), the flow is nearly chemically equilibrated; however, significant chemical nonequilibrium exists at the higher velocity (7.4 km/s).

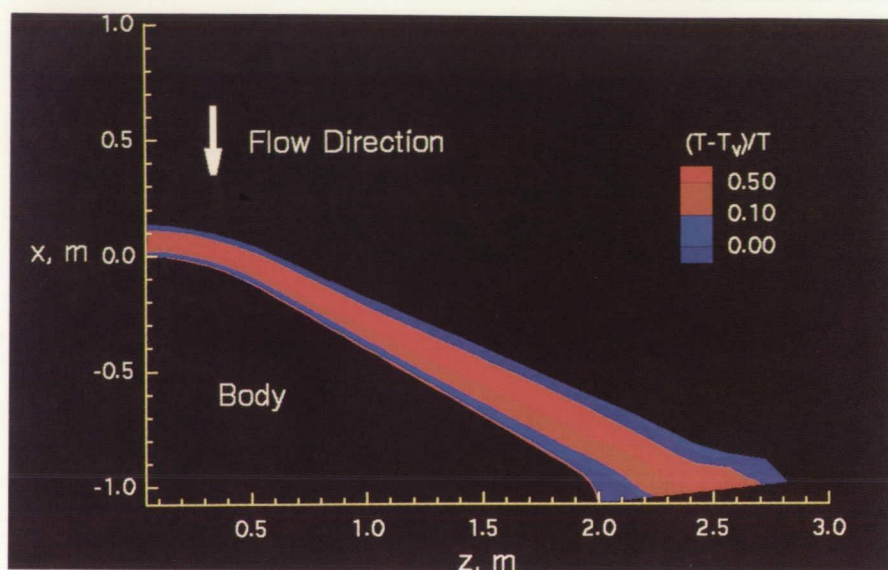
(K. Sutton and G. V. Candler, 44406)

Space Directorate

Thermochemical Nonequilibrium Issues for Earth Reentry of Mars Mission Vehicles

Current manned Mars mission scenarios propose the use of aerobraking during Earth reentry at the end of the mission. The successful use of aerobraking requires accurate prediction of the associated high-energy flow fields. Establishing the degree of thermal and chemical nonequilibrium present in such flow fields is an essential step toward accurate flow field prediction.

Earth entry at 12 km/s was examined using LAURA. Two 60° sphere cones with nose radii of 1.08 m and 3.23 m were each examined at altitudes of 70 km and 80 km. These four test cases bracket the proposed Mars mission scenarios for Earth reentry at this velocity. The thermochemical nonequilibrium LAURA solutions for each case were compared with equilibrium solutions



Thermal nonequilibrium (velocity = 12 km/s and altitude = 80 km). L-90-7425

to establish the degree of nonequilibrium present.

The nonequilibrium effects present in the four test cases ranged from minimal in the near equilibrium case of the 3.23-m nose radius aerobrake at a 70-km altitude to dominant in the smaller 1.08-m nose radius aerobrake at an 80-km altitude. The figure presents contours of the normalized difference between translational temperature T and vibrational temperature T_v from a LAURA solution for the latter, nonequilibrium-dominated case. Regions in which these two temperatures differ indicate the presence of thermal nonequilibrium effects. The remaining two test cases involved significant chemical nonequilibrium effects and, to a lesser degree, thermal nonequilibrium effects.

As system studies of the manned Mars mission further define the aerobrake size and trajectory required for Earth return, these results can be used to predict the degree of thermal and chemical nonequilibrium effects. Knowledge of the degree of nonequilibrium effects present in the flow field assists the aerothermodynamicist in selecting the correct

computational tool to efficiently describe these aerobrake flow fields.

(Robert A. Mitcheltree, 44382)

Space Directorate

Aerodynamic Requirements of Manned Mars Aerobraking Transfer Vehicle

In a manned Mars aerobraking mission, the interplanetary and atmospheric trajectories are inherently coupled. This relationship must be accounted for in the mission and vehicle design processes for an aerobraking transfer. If the emphasis is placed solely on interplanetary transfer, an over-designed aerobrake results. On the other hand, if the design emphasis is purely vehicle oriented, mission flexibility is sacrificed.

The trade-off between aerobrake lift-to-drag L/D ratio (aerodynamic performance and vehicle packaging) and entry velocity (mission opportunity and flexibility) is summarized in the figure, which presents the mini-

imum required Mars aerobrake L/D as a function of entry velocity. Note that this figure is based on the assumptions of a corridor width requirement of 1° , deceleration limit of 5 g, and Mars parking orbit with a period of 24.6 hours (1 Sol). An aerobrake L/D of 0.5 is required for the lowest entry velocity of 6 km/s. As the entry velocity is increased, the vehicle is able to exert a greater degree of lift-induced control; hence, the required aerobrake L/D decreases. A minimum L/D of 0.3 is required for an entry velocity of 7.2 km/s to 7.3 km/s. For an entry velocity above 7.3 km/s, an increased Mars aerobrake L/D is required to compensate for the 5-g deceleration limit. The shallowness of the curve suggests that for a minor increase in aerobrake L/D over 0.3, which is the absolute minimum required, a large entry velocity domain may be considered feasible. Hence, by slightly increasing the vehicle L/D , a major increase in mission flexibility results. For example, although an aerobrake L/D of 0.3 requires a Mars entry velocity in the range of 7.2 km/s to 7.3 km/s, slightly increasing this

L/D to 0.4 significantly expands the range of allowable entry velocities from 6.4 km/s to 8.1 km/s without substantially impacting vehicle packaging concerns.

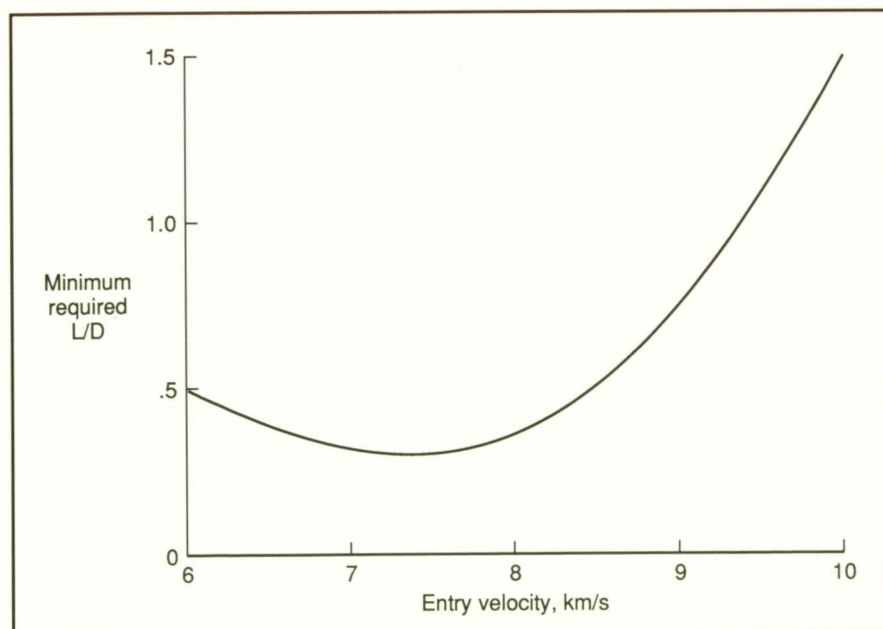
From this figure, a number of facts are apparent. A minimum aerobrake L/D of 1.5 is required for a manned Mars vehicle to successfully aerocapture at entry velocities from 6.0 km/s to 10.0 km/s. Because this aerobrake L/D is feasible over the entire range of entry velocities considered, the configuration is not limited by departure/arrival geometry or trip time. However, selection of an L/D of 1.5 induces numerous vehicle design considerations including significant packaging and aerothermodynamic constraints.

A minimum L/D of 0.5 is required for a manned Mars vehicle to successfully aerocapture at entry velocities between 6.0 km/s and 8.5 km/s. By limiting the Mars entry velocity to values below 8.5 km/s and selecting an aerobrake L/D of 0.5, a compromise is reached between the conflicting interplanetary and

atmospheric trajectory requirements. In this manner, a minor restriction on mission flexibility is induced while alleviating aerothermodynamic and vehicle packaging concerns. However, a configuration with an L/D of 0.5 may still prove difficult to package.

A minimum L/D of 0.3 is required for a manned Mars vehicle to successfully aerocapture. For an L/D of 0.3, the aerocapture must be initiated at an entry velocity between 7.2 km/s and 7.3 km/s. A configuration with $L/D < 0.3$ does not result in enough lift-induced control to be considered feasible. Although an L/D of 0.3 imposes significant constraints on the number of potential mission opportunities, the limitations identified in this investigation may be alleviated by including a Mars entry velocity constraint in the interplanetary trajectory selection or the use of synergistic propulsion. A Mars aerobrake L/D configuration of 0.3 is optimal from a vehicle packaging and assembly standpoint.

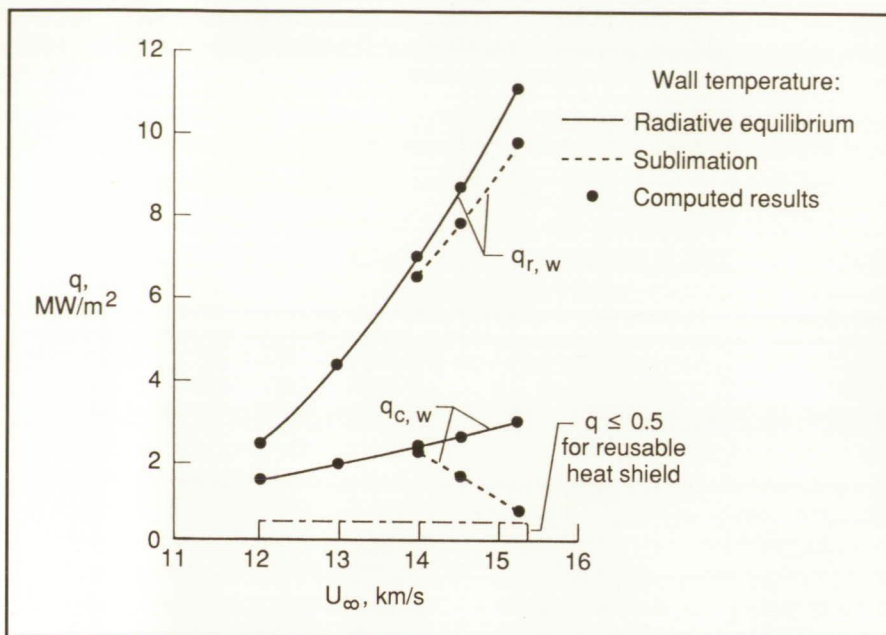
(Robert D. Braun, 44507, and Richard W. Powell)
Space Directorate



Minimum aerobrake L/D for Mars aerocapture (corridor width requirement of 1° , deceleration limit of 5 g, and entry into parking orbit of 1 Sol).

Coupled Radiation Solutions for Earth Aerobraking

Manned and unmanned exploration of the planet Mars has received renewed interest. To minimize the vehicle weight, aerobraking (using aerodynamic drag to obtain the required velocity change) is an effective alternative to an all-propulsive system for atmospheric insertion at both Mars and on return to Earth. This study concentrated on an assessment of aerothermodynamic issues at typical flight conditions for the Earth aerobraking phase. The results are based on flow field



Stagnation-point heat fluxes (altitude = 70 km and $R_N = 3.05$ m).

solutions with coupled radiation and heat shield ablation.

An axisymmetric viscous-shock-layer (VSL) code (HYVIS) was used for the calculations. For the coupled solutions with radiation and ablation injection, a chemical equilibrium version of the code was used. This code was used extensively in the flow field definition for the Pioneer Venus and Galileo entry probes. In addition, a finite-rate chemistry VSL code was used to assess the extent of chemical nonequilibrium. Calculated flow field and surface quantities were obtained at a typical flight condition for a 3-m nose radius R_N body at an altitude of 70 km for free-stream velocities U_∞ from 12 km/s to 15.24 km/s.

The radiative $q_{r,w}$ and convective $q_{c,w}$ components of the stagnation-point heat fluxes are shown in the figure. The heat fluxes are shown for all velocities at the radiative equilibrium wall temperature without ablation. At velocities of 14 km/s and greater, the fluxes also are shown for the sublimation wall temperature

with coupled ablation injection. Also presented as a point of reference is the heat flux limit for current reusable heat shield materials.

The results show that radiation is the dominant heat-transfer component. Both the radiative and convective heat fluxes are greater than the current limit for reusable heat shield materials; thus, an ablation heat shield will be required. The coupled carbon-phenolic ablation rates were of modest values for the higher velocities, and the assumption of sublimation ablation at the lower velocities may not be appropriate. The assumption of equilibrium chemistry was shown to be reasonable for the cases studied.

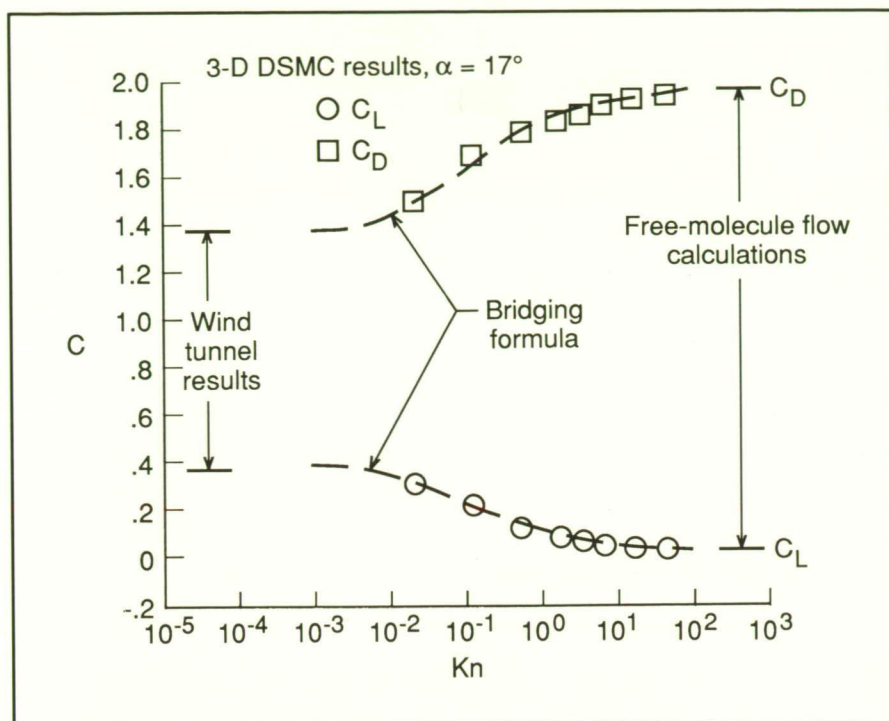
(J. N. Moss and R. N. Gupta, 44379)

Space Directorate

New Bridging Formula for Calculating Rarefied-Flow Aerodynamics of Blunt Bodies

Computations of aerodynamic force and moments in the rarefied-flow regime require many computer hours with state-of-the-art computers using sophisticated fluid dynamic models and surface geometries. This fact is especially true in the rarefied-flow transition regime, that is, between hypersonic continuum and free molecule flow, where the aerodynamics and applicable physical laws undergo a dramatic change. Often, for design purposes, a quick analytical tool to bridge this regime is useful and desirable. The need for this tool is particularly true today with the increased emphasis on aerobraking missions both at Earth and on the planets, e.g., the Manned Mars Program. (The aerobraking mission involves using the drag of the vehicle in the upper atmosphere of the planet to reduce speed and increase payload capabilities). Thus, a quick analytical formula has been developed which can be used to calculate aerodynamic performance parameters in the rarefied-flow transition regime for blunt reentry vehicles.

The development approach consists of using the existing data base to devise an analytical formula to generate quick, accurate aerodynamic data in the rarefied-flow transition regime. A formula was developed which adequately represents the behavior of the aerodynamic force coefficients of the Aeroassist Flight Experiment (AFE) vehicle in the rarefied-flow transition flight regime. A comparison of results using this formula is shown in the figure for the AFE vehicle at an angle of attack α of 17° . Shown are results from four different sources for lift



Comparison of new bridging formula with DSMC calculations.

and drag coefficients C_L and C_D as a function of the rarefaction parameter, Knudsen number Kn , for the AFE vehicle. Values of Kn are small ($<10^{-3}$) in the hypersonic continuum, while values are between 10^{-3} and 10^2 in the transition regime from continuum to free molecule flow. For small values of Kn , i.e., in the hypersonic regime, wind tunnel tests results are indicated. At $Kn > 10^2$, the results of free molecule flow calculations of a three-dimensional model of the AFE vehicle are shown. The transition regime results, $10^{-3} < Kn < 10^2$, were obtained from a three-dimensional simulation using the Direct Simulation Monte Carlo (DSMC) method. The comparison of the new formula with the three-dimensional (3-D) DSMC results in the transition regime shows excellent agreement for both C_D and C_L .

The work is completed, and a favorable comparison between this formula and other existing empirical

bridging techniques has been made, resulting in the inclusion of the formula into the AFE data base. In the near future, flight data from instruments on the AFE vehicle will be collected to verify its validity. (R. C. Blanchard, 44391) Space Directorate

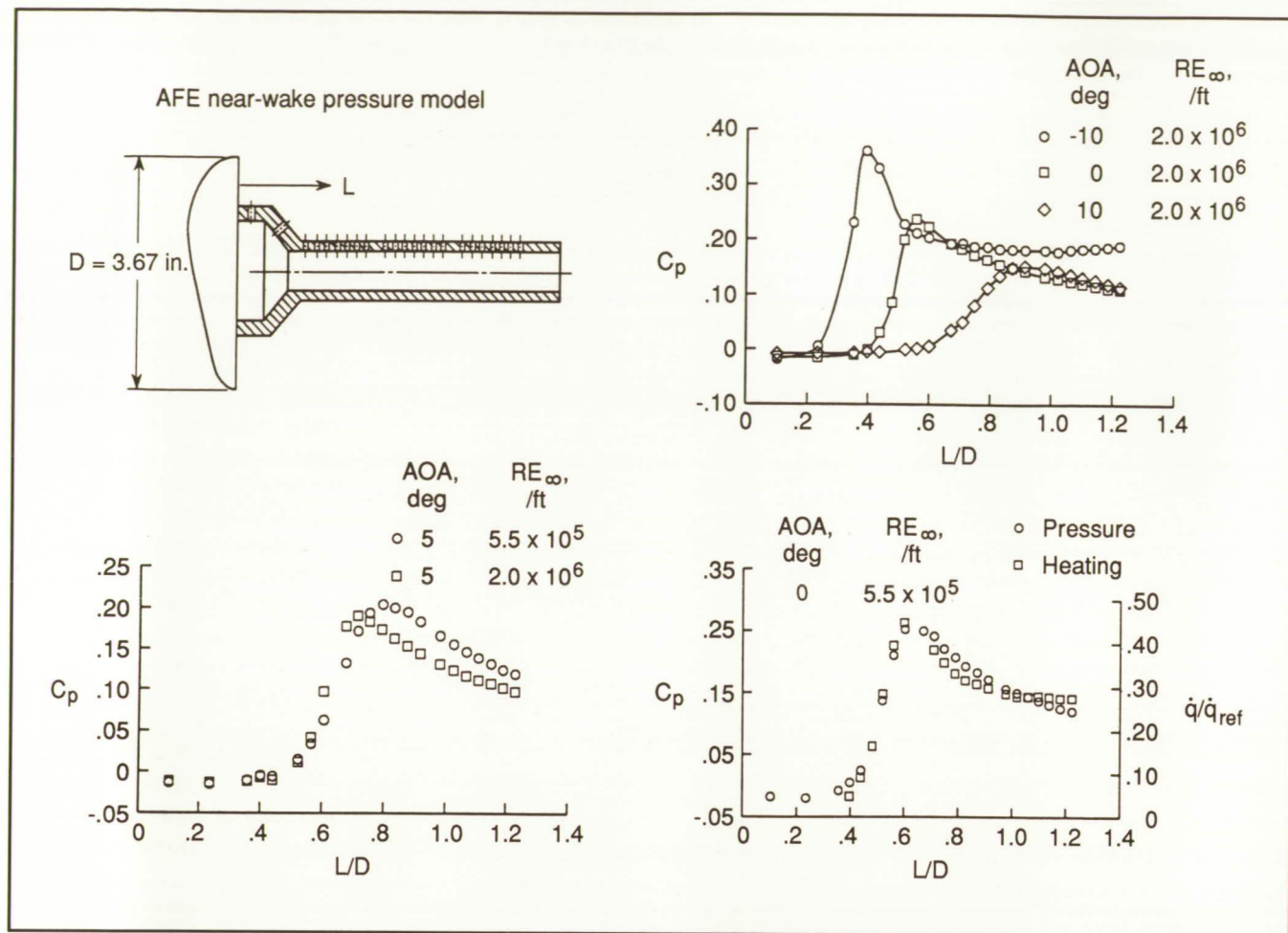
Experimental Investigation of Aerobrake Near Wakes

The near-wake-region flow field behind an Aeroassisted Space Transfer Vehicle (ASTV) is of interest because of its potential influence of any payload and equipment carried by an ASTV in this area. The near-wake region is dominated by a viscous free-shear layer that originates with the boundary layer that separates off the vehicle shoulder around its entire periphery and converges toward the vehicle

centerline in the near-wake region. The impingement of the free-shear layer on a solid surface, such as a payload or rocket motor, can result in high localized surface pressures and heat-transfer rates. Thus, understanding the free-shear layer phenomena is critical in the design of future ASTV's.

In one series of tests conducted in the 20-Inch Mach 6 Tunnel, the magnitude and the distribution of this impingement heating were measured on a simulated payload, a cylinder, located in the near-wake region behind an 0.022-scale model of the Aeroassist Flight Experiment vehicle forebody. More recently, the magnitude and distribution of surface pressures on the payload were measured in the same facility. All testing was for the same model configuration and test conditions. Model angle of attack (AOA) was varied from -10° to $+10^\circ$, and the nominal free-stream unit Reynolds numbers (RE_∞) were $0.55 \times 10^6/\text{ft}$ and $2.0 \times 10^6/\text{ft}$. In conjunction with the surface pressure measurements, an 0.013-in.-diameter traversing pitot-pressure probe was used to perform flow field surveys in the near-wake region between the payload surface and the bow shock with the model at an angle of attack of 0° and a free-stream Reynolds number of $2.0 \times 10^6/\text{ft}$.

Results from the pressure tests show that the distributions do follow the pattern of free-shear layer impingement on the payload. Upstream of the impingement region, in the recirculation region near the base, the pressure is extremely low and constant. In the impingement region, pressure increases substantially and achieves its maximum value (which can be as high as 13 percent of the forebody stagnation pressure). Downstream of the impingement region, the pressure decreased monotonically.



Surface pressure C_p and heating distributions \dot{q}/\dot{q}_{ref} on simulated payload in near-wake flow field behind 0.022-scale model of Aeroassist Flight Experiment vehicle forebody in 20-Inch Mach 6 Tunnel.

The effects of angle of attack and Reynolds number are as follows. As angle of attack increases, the pressure in the base region remains constant, the maximum pressure in the impingement region decreases, and the impingement region moves farther downstream and becomes less localized. As Reynolds number increases, the impingement region moves closer to the base of the forebody.

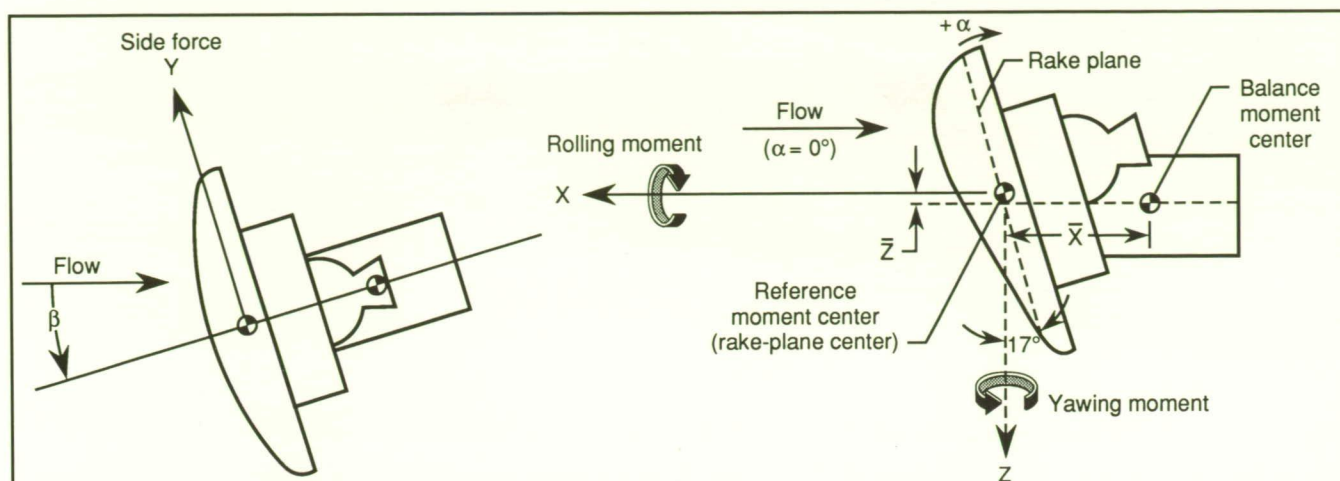
The trends in the heating and pressure distributions are very similar, and both distributions show the same impingement region location. The location of maximum surface pressure and heating rate also is the same. The effect of the free-

shear layer impingement on the heating rates is more localized than its effect on the surface pressure distribution. This effect can be seen in the fact that downstream of the impingement region the heating rate tends toward a constant value much sooner than the surface pressure. Preliminary analysis of the traversing pitot-pressure surveys indicates that the locations of the free-shear layer and the reattachment shock downstream of the impingement region were detected.

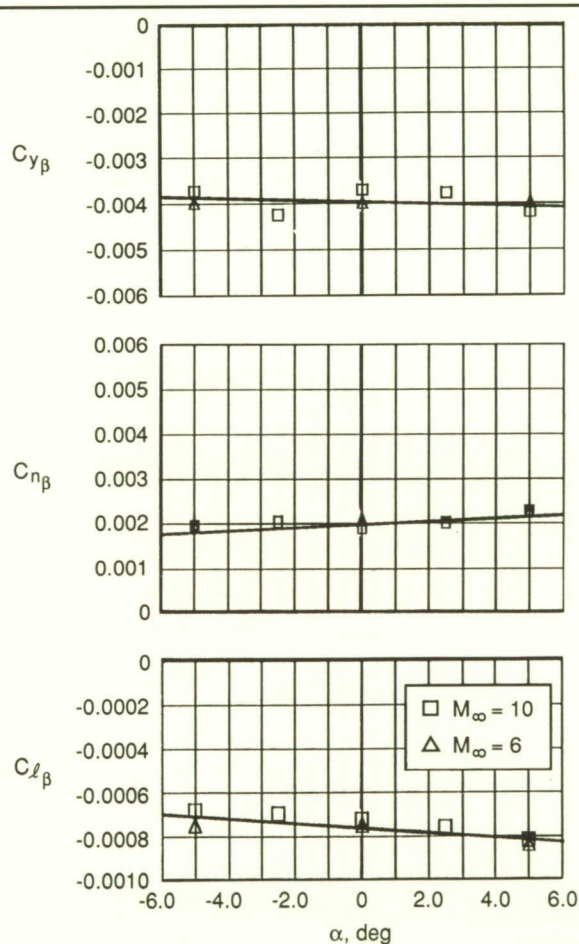
(M. DiFulvio, William L. Wells, and G. C. Ashby, Jr., 45229)
 Space Directorate

Lateral-Directional Stability Characteristics of Aeroassist Flight Experiment (AFE) Vehicle Configuration

As part of an extensive experimental program to develop an aerodynamic and aerothermodynamic data base for the AFE configuration, a test series has been conducted in hypersonic wind tunnels to determine the lateral-directional stability characteristics. These data are of particular significance for this vehicle because trajectory variations are to be accomplished through roll control. Furthermore, relevant computational



Sketch of system of axes used in investigation showing positive direction of forces, moments, velocities, and angles.



Experimental lateral-directional stability characteristics of AFE vehicle. ($C_{y\beta}$, $C_{n\beta}$, and $C_{l\beta}$ are side-force, yaw, and roll lateral and directional stability parameters, respectively.)

fluid dynamics computer programs have not yet matured to the point of considering the effect of sideslip.

Two model sizes, a 2.2-percent scale and a 1.5-percent scale, were tested in air at Mach 6 and at Mach 10, respectively. Tests were conducted with unit free-stream Reynolds numbers of $0.63 \times 10^6/\text{ft}$ and $2.0 \times 10^6/\text{ft}$ at Mach 6, and $1.0 \times 10^6/\text{ft}$ at Mach 10. The tests were conducted over ranges in angle of attack of -5° to 5° and angle of sideslip from -4.5° to 4.5° .

The experimental test results revealed no significant effect of the changes in Mach number, Reynolds number, or model size included in this study. For this investigation, forces and moments are based on a reference moment center located at the center of the rake plane as shown in the first figure. The axis system is the same as that of the original elliptic cone. As illustrated by the stability derivatives presented in the second figure, the configuration remained laterally and directionally stable over the tested range of angle of attack.

(John R. Micol and William L. Wells, 45221)
Space Directorate

Global Change

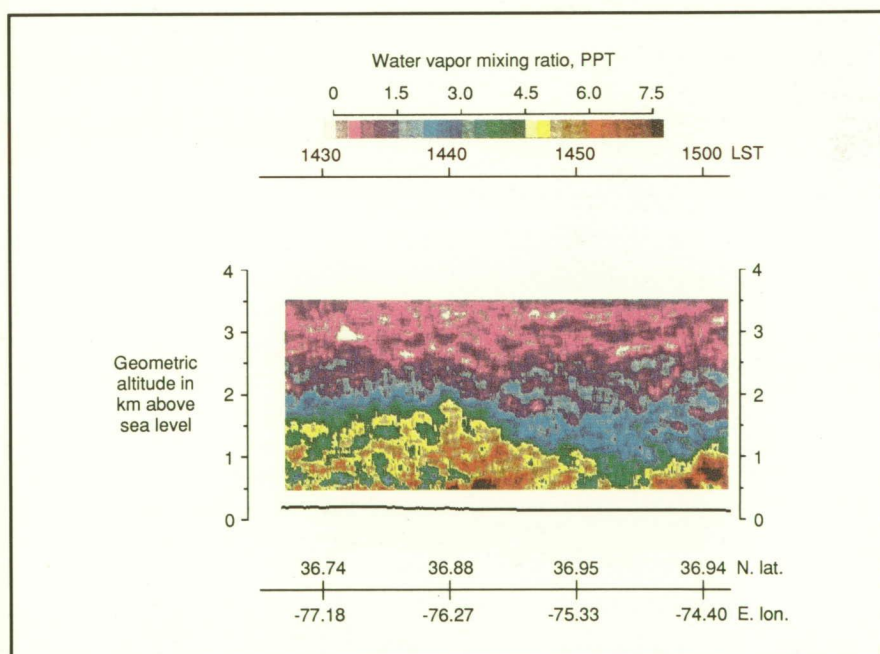


Airborne Lidar Measurements of Atmospheric Water Vapor Distributions

An airborne differential absorption lidar (DIAL) system has been developed at Langley Research Center for the remote measurement of water vapor (H_2O) and aerosols in the lower atmosphere. The DIAL system incorporates advanced solid-state laser technology and extremely accurate diagnostic equipment to achieve high-spatial resolution measurements of H_2O distributions from an airborne platform.

The first extensive observations of H_2O and aerosols in the lower troposphere were made during March and April 1990, with the DIAL system operating in a nadir mode from the NASA Wallops Flight Facility Electra aircraft. Water vapor

measurements were made on flights at night over the ocean, during the day over land and ocean, and across a cold front. An example of the daytime H_2O distribution obtained by the airborne DIAL system as the Electra crosses over the coast of Virginia at approximately $76^\circ E$ longitude is shown in the figure. The H_2O distribution clearly indicates the decrease in the mixed layer depth from approximately 1.7 km over land to less than 1 km over water. The dry atmospheric conditions above the moist mixed layers are readily apparent in the figure. Regions with enhanced H_2O concentrations also were found to have higher aerosol backscattering in the lidar data. The airborne DIAL measurements showed for the first time the detailed H_2O and aerosol structure that occurs in the free troposphere and in the mixed layer over different land and marine regimes. In addition, the first high-spatial resolution distribution of H_2O was obtained across a cold front.



Airborne lidar measurement of daytime water vapor distribution along flight track from land to sea on March 22, 1990. Water vapor mixing ratios in parts per thousand (ppt) are mapped using the color scale at the top of the figure.

The transition from the very dry conditions behind the front to the very moist conditions ahead of the front was seen in detail. These experiments have provided new insights into atmospheric processes involving H_2O , and they will serve as a basis for future investigations, including studies of cloud formation and the effect of H_2O on the climate system of the Earth.

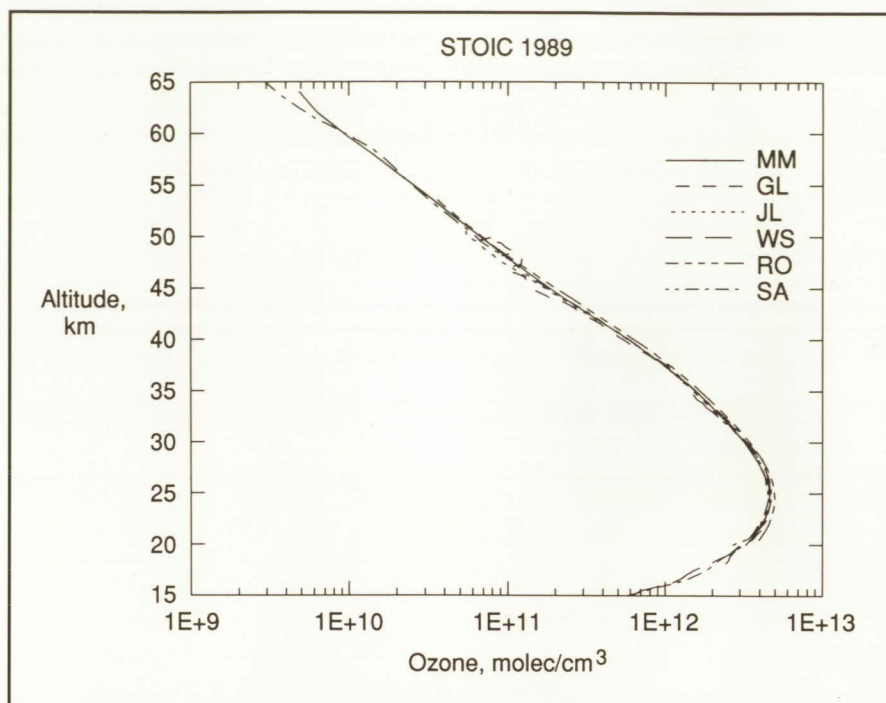
(Edward V. Browell, 41273, and Noah S. Higdon)
Space Directorate

Ground-Based Microwave Monitoring of Stratospheric Ozone

The Network for Detection of Stratospheric Change (NDSC), which is presently being developed, will consist of at least six stations worldwide, each of which will house a suite of complementary instruments measuring temperature, ozone, and other trace species.

The first microwave spectrometer for monitoring ozone profiles for the NDSC was installed at the Table Mountain Facility of the Jet Propulsion Laboratory (JPL) in July 1989. The instrument participated in a 2-wk Stratospheric Ozone Intercomparison (STOIC), along with two ground-based lidars, three series of balloonsondes, Dobson and Brewer spectrophotometers, series of rocketsondes, and the SAGE II satellite instrument. The microwave observations agreed with the average of all observations to within approximately ± 5 percent.

These observations initiated a planned 20-yr program of ozone monitoring with the microwave technique for the NDSC. Further, the observations provided the first comprehensive intercomparison of



Average of STOIC measurements by Langley microwave (MM), Wallops Flight Facility (WFF) balloonsondes (WS), Goddard Space Flight Center lidar (GL), JPL lidar (JL), rocketsondes (RO), and SAGE II (SA).

the microwave measurements with other techniques. The results indicate that such measurements can play an important role in the NDSC.

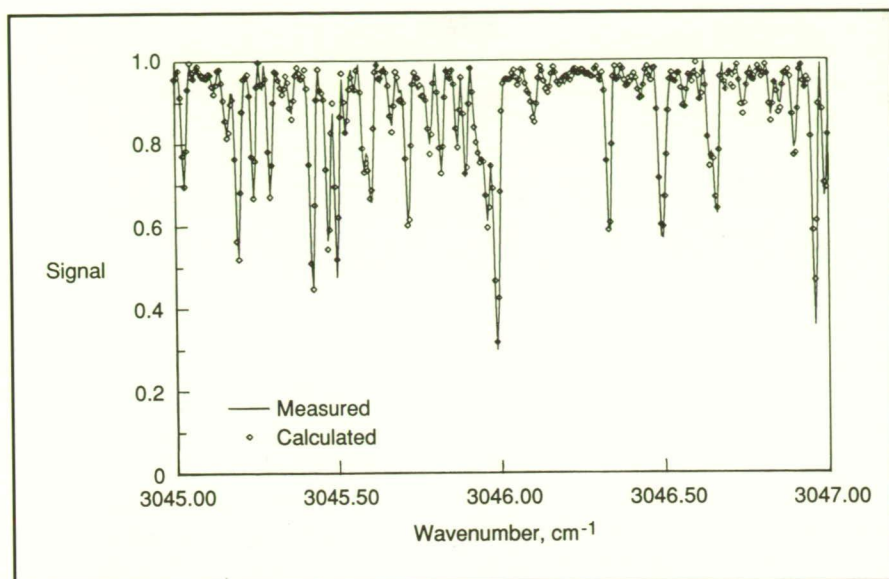
The instrument, which was designed and built by Millitech Corporation, is being operated under a collaborative arrangement involving Langley Research Center, the University of Massachusetts, and JPL. Data analysis and software development are done at Langley. (Brian J. Connor, 45698)
Space Directorate

Laboratory Measurements of Ozone Infrared Spectrum

Detailed knowledge of the infrared spectrum of ozone is needed for accurate calculation of atmo-

spheric heating and cooling rates due to changes in the stratospheric ozone layer. Space-based measurements of atmospheric infrared absorption or emission are used to determine the concentration and distribution of stratospheric ozone on a global scale. The present laboratory investigation has improved knowledge of the ozone spectrum at wavelengths between 2.5 μm and 4.5 μm . These measurements utilized the McMath high-resolution Fourier Transform Spectrometer (FTS) at the National Solar Observatory on Kitt Peak, Arizona. Data analysis was performed primarily at Langley Research Center, and the theoretical interpretation of the results was done in collaboration with investigators at two universities in France.

Results of this work have improved line positions and relative intensities for 10 vibration-rotation bands of the ozone molecule ($^{16}O_3$)



FTS spectrum of ozone, showing absorption features in the $3v_3$ vibration-rotation band of $^{16}\text{O}_3$.

occurring in the 2.5- μm to 4.5- μm region. Although all of these bands appear in atmospheric spectra, only one band (at 3.6 μm) had previously been measured in the laboratory. The spectroscopic constants determined in this study also have been used to calculate the positions and intensities of lines belonging to "hot bands" of ozone in the 4.8- μm and 10- μm spectral regions, which previously had not been analyzed. These laboratory results are being applied in analysis of atmospheric infrared data to improve the accuracy of retrieved concentration profiles of stratospheric ozone.

(Mary Ann H. Smith, 42701)
Space Directorate

Infrared Spectroscopy of Stratosphere: Recent Results of Relevance to Global Change

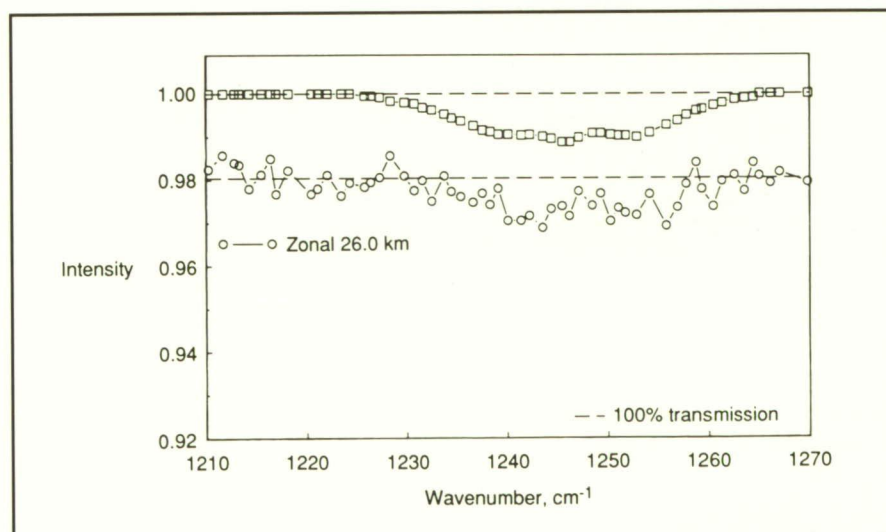
Most of the molecules suspected of affecting our environment through greenhouse warming or depletion of

the stratospheric ozone layer have strong infrared (IR) absorption bands. The IR spectroscopy is a sensitive and accurate technique for measuring these gases, particularly over very long atmospheric paths, such as can be observed from high-altitude balloons and space using the Sun as a source as it rises or sets.

Analysis of high-resolution IR solar absorption spectra recorded by

the University of Denver from balloons since 1979 and by the Jet Propulsion Laboratory (JPL) Atmospheric Trace Molecule Spectroscopy (ATMOS) experiment from the Space Shuttle in 1985 has revealed several trace gases that are increasing rapidly in concentration in the lower stratosphere. For example, the trend in carbonyl fluoride (COF_2), an intermediate in the photodecomposition of the chlorofluorocarbons (CFC's) in the stratosphere, was measured for the first time. A rate of increase of 10.3 ± 1.8 percent per year has been derived. Approximately one-third of the inorganic fluorine column in the stratosphere is contained in COF_2 . Sulfur hexafluoride (SF_6), which is primarily used in high-voltage electrical applications, is estimated to be increasing at a rate of 7.4 ± 1.9 percent per year. SF_6 absorbs strongly in the climatically important 10-mm atmospheric window, but its concentration is too low (only about 2 parts per trillion, 10^{-12} , per volume) to contribute substantially to greenhouse warming.

Nitrogen pentoxide (N_2O_5) is an important temporary reservoir of stratospheric odd nitrogen, which can destroy ozone through catalytic reactions. Analysis of the ATMOS



Simulated (upper plot) and measured (lower plot) N_2O_5 absorption at sunset.

spectra with collaborators at JPL recently has resulted in the first measurement of N_2O_5 at sunset, thus confirming model predictions that not all of this molecule is photodissociated during the day. The weak absorption by N_2O_5 at sunset, approximately 10 times less than at sunrise, is shown in the figure along with a corresponding simulation. (Curtis P. Rinsland, 42699) Space Directorate

CITE-3: Airborne Intercomparison of Tropospheric Instrumentation

Evidence accumulated over the past decade clearly documents that the composition of the Earth's atmosphere is changing. Trace gases such as carbon dioxide, methane, and nitrous oxide have increased significantly. Enhancements of carbon monoxide (CO) and ozone have been observed in both hemispheres. To understand changes in the Earth's atmosphere, the scientific community has stated a need for more refined and better documented (e.g., accuracy and precision) instrumentation for measuring key atmospheric species. In 1983, through its Global Tropospheric Experiment, NASA initiated a program to determine the capabilities of existing and new measurement technology. The Chemical Instrumentation Test and Evaluation (CITE) Program has used airborne investigations and blind intercomparisons of measurements obtained within the same air mass to evaluate measurement capabilities for key species.

The CITE-1 Program evaluated instruments for measuring CO, nitric oxide (NO), and the hydroxyl radical (OH). The CITE-2 Program evalu-

ated instruments for measuring nitrogen dioxide (NO_2), nitric acid (HNO_3), and peroxyacetyl nitrate (PAN). The final CITE expedition (CITE-3), conducted in the summer and fall of 1989, evaluated techniques to measure the major sulfur species: sulfur dioxide (SO_2), dimethylsulfide (DMS), hydrogen sulfide (H_2S), carbonyl sulfide (COS), and carbon disulfide (CS_2). Results from CITE-1 and CITE-2 have demonstrated the capability for airborne measurements of CO, NO, NO_2 , and PAN under a wide range of conditions of interest to the tropospheric chemistry community. New techniques, however, may be needed for measurements of HNO_3 at the very low mixing ratios (e.g., <100 pptv), and the OH intercomparisons clearly demonstrated the need for further instrument development before reliable measurements can be expected. While results from CITE-3 are still being analyzed, preliminary data indicate that concentrations of DMS, H_2S , COS, and CS_2 can be measured at concentration levels expected in the troposphere. The SO_2 results are being reanalyzed to separate ambient SO_2 variations from instrument performance and intercomparison results. (Gerald L. Gregory and James M. Hoell, Jr., 45834) Space Directorate

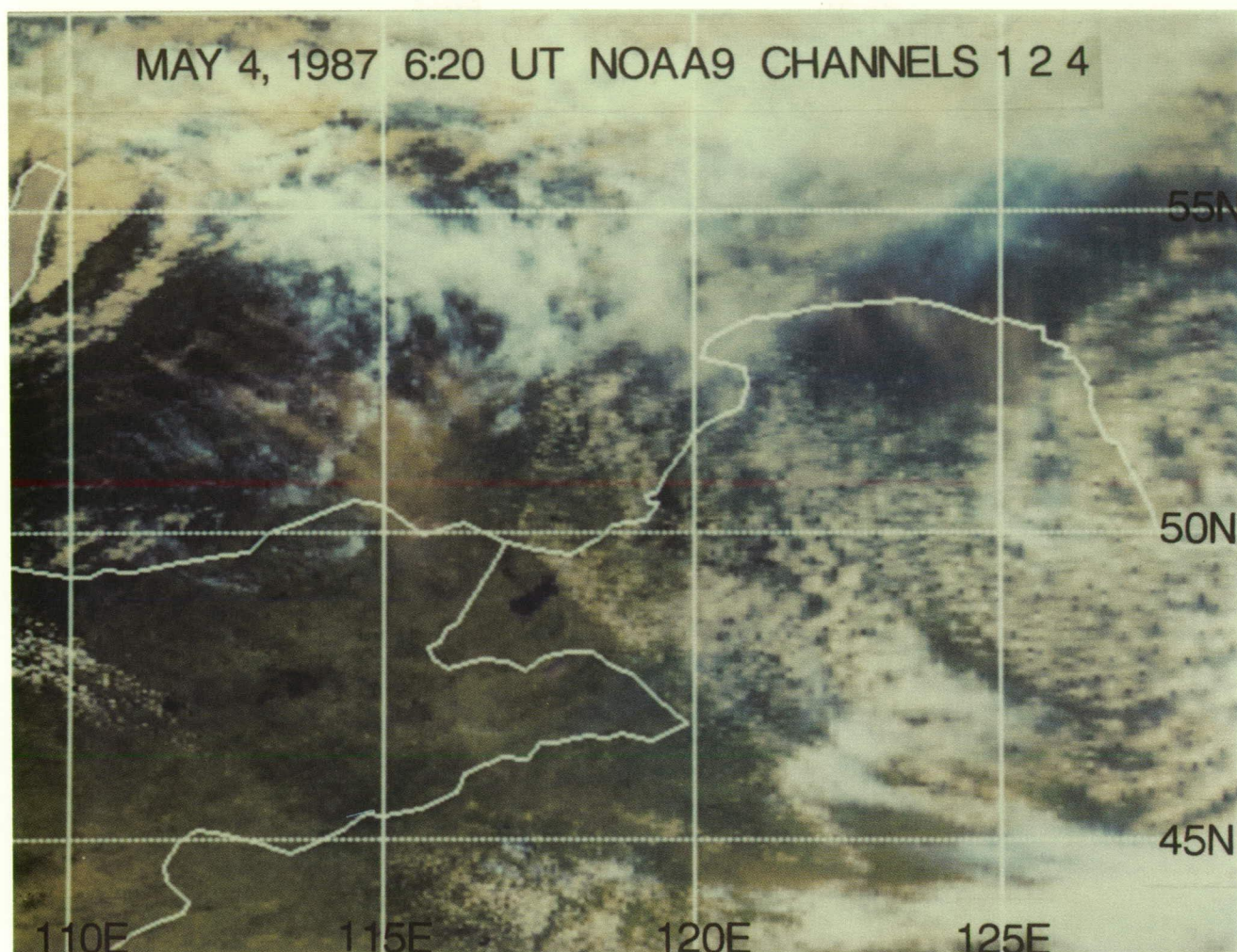
Satellite Estimates of Gases Produced From Biomass Burning

Atmospheric levels of carbon dioxide, carbon monoxide, methane, nonmethane hydrocarbons, and oxides of nitrogen are all increasing with time. The causes for the buildup of these environmentally significant gases are now known. All of these gases are produced by biomass

burning (the burning of the world's forests and savanna grasslands and the burning of agricultural stubble after the harvest).

A new technique has been developed to quantify the gaseous contributions to the atmosphere from global biomass burning. In May 1987, a major fire developed in the boreal forest of China and the neighboring Soviet Union. Images obtained by the NOAA-9 meteorological satellite were analyzed to determine the areal extent of the fire. The analysis indicates that the fire destroyed more than 12 million acres of boreal forest in 21 days, making this fire one of the largest, if not the largest, ever recorded. (For comparison, in 1988, approximately 900 000 acres burned in the Yellowstone National Park in what is believed to be the largest fire ever in a temperate forest.) These results also indicate that extensive burning is not restricted to the world's tropical rain forests as is generally believed.

In 1988, measurements were obtained of the gaseous emissions and other fire characteristics and parameters associated with a large boreal forest fire in Canada, a forest identical to the one that burned in China and the Soviet Union. These measurements were part of an ongoing Langley Research Center research program to quantify the gaseous emissions and burning parameters of fires in diverse ecosystems around the world. The 1988 gaseous and fire measurements were combined with the NOAA-9 images to estimate the production of carbon dioxide, carbon monoxide, and other gases from the 1987 fire. During its 21-day lifetime in May 1987, the Chinese/Soviet Union fire produced approximately 2 percent of the global annual production of carbon dioxide and carbon monoxide. These results represent a new technique to better quantify the role of biomass burning



NOAA-9 image of the Chinese/Soviet Union area of extensive boreal forest burning in May 1987.

as a source of atmospheric gases and to assess the role of biomass burning as a driver for global change.

(Joel S. Levine, 45692, Wesley R. Cofer III, and Donald R. Cahoon, Jr.)

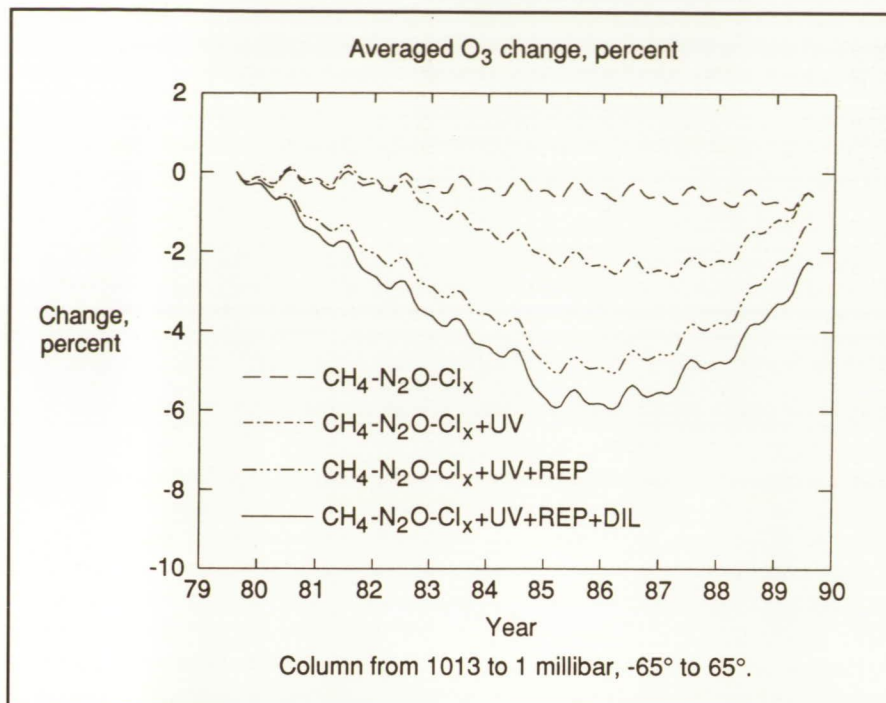
Space Directorate

Global Ozone Changes During 1980's

Two-dimensional photochemical model calculations have been carried out to assess the causes of the unexpectedly large depletion in

global ozone occurring during the 1980's. Effects considered in these calculations include those associated with the increases in trace gases (methane, nitrous oxide, and chlorine-bearing species, $\text{CH}_4\text{-N}_2\text{O-Cl}_x$); the changes in solar ultraviolet flux during the 11-year solar cycle (UV); the dilution (DIL) of global ozone by the seasonal redistribution of ozone following the severe depletions over Antarctica during the late winter and early spring, and the effects of global modulation of nitrogen oxides due to variations of the precipitation of magnetospheric relativistic electrons (REP) associated with the 11-year solar cycle.

The figure illustrates the 11-month running mean percentage changes in ozone averaged from 65°S to 65°N and from the Earth's surface to 48 km, according to the various contributions. These model results indicate that the largest contributor to the global ozone destruction is due to the REP, followed, in order, by UV, DIL, and $\text{CH}_4\text{-N}_2\text{O-Cl}_x$. Natural effects (REP and UV) account for approximately 78 percent of the total. The results illustrate the dominance of natural ozone variations on decadal time scales and also point out the potential importance of newly reported work indicating a significant coupling



Percentage change in O₃ averaged over 65°S to 65°N and from Earth's surface to approximately 50 km shown as it varies with calendar year.

between the state of the magnetosphere and that of the middle atmosphere.

(Linwood B. Callis, 45843, and Robert E. Boughner)
Space Directorate

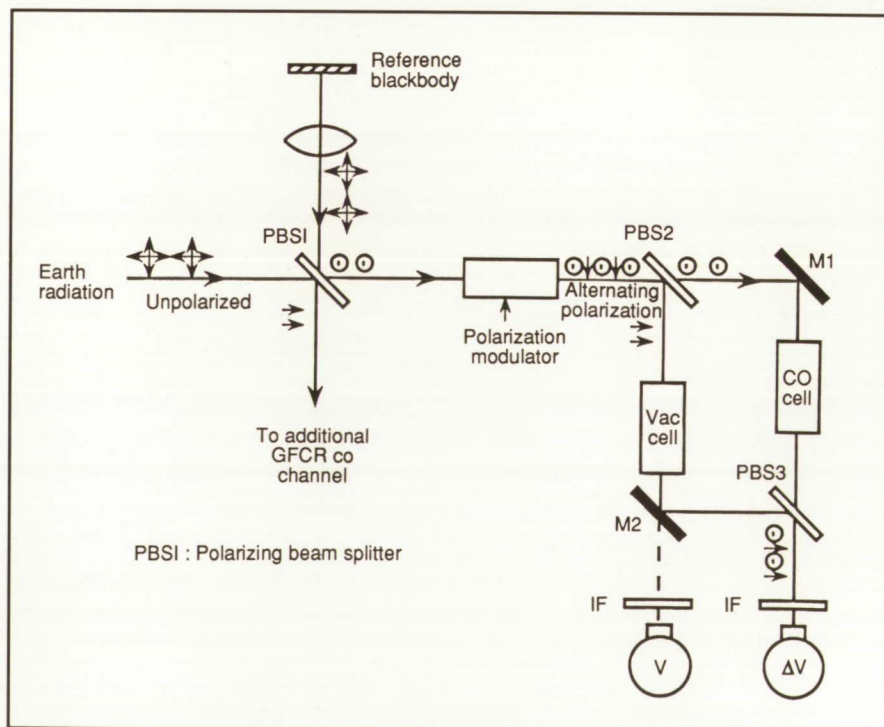
Gas Filter Correlation Radiometer Concept Utilizing Photo-Elastic Modulator

Gas filter correlation radiometers (GFCR's) have made important contributions to our knowledge of the atmosphere by providing remote airborne and spaceborne measurements of atmospheric gases. A new GFCR concept has been successfully developed and tested under the Langley Director's Discretionary Fund. The new GFCR approach uses a polarization modulator in conjunction with polarization sensitive

beamsplitters as a solid-state optical switch to rapidly alternate the path of incoming radiation between two

GFCR optical paths (i.e., the paths containing the gas correlation and vacuum cells). Conventional GFCR's generally are mechanically complex requiring rapidly rotating gas cells or light choppers. In contrast, the new approach does not require rapidly moving mechanical parts and therefore has potential advantages including long operational life (an important consideration for spaceborne applications) and a much higher detection sampling frequency (≈ 100 kHz) which, for a nadir-viewing GFCR, freezes the radiometer's view of the Earth and minimizes $1/f$ noise sources.

This new GFCR concept could be applied for the remote detection of a number of gas species from a satellite platform. Described here, as an important application example, is the remote measurement of atmospheric CO from space. Thermal radiation from the Earth and the atmosphere is collected by a telescope and is polarized by a polarization beamsplitter as it enters the GFCR. The polarized light then is incident on



Simplified diagram of new GFCR technique.

a photo-elastic modulator (PEM) that modulates the output between vertical and horizontal polarization at a rate of ≈ 100 kHz. A second polarization beamsplitter, which transmits vertically polarized light and reflects horizontally polarized light, alternates the light between the two GFCR paths (one having the CO correlation cell and the other having the vacuum cell). The two optical paths carrying the orthogonal polarizations are recombined by a third polarization beamsplitter. The combined light passes through a bandpass filter centered on the $4.7\text{ }\mu\text{m}$ CO band and then is incident on an InSb detector. Using this polarization modulation approach, the detector alternately views the Earth through the correlation CO cell and the vacuum cell at a rapid rate, and a difference signal ΔV between these two paths is obtained. In addition to the ΔV signal, a simple radiometer signal also is measured to normalize the ΔV signal for changes in ground emissivity and temperature. With the measured signals and other parameters including the temperature profile of the atmosphere, a numerical radiative transfer program then may be used to infer an altitude-weighted CO mixing ratio.

A breadboard GFCR using this new concept was built and tested by using a blackbody source to simulate the Earth's radiation, while a cell containing a CO mixture was placed between the blackbody source and the GFCR breadboard to simulate the CO optical depth in the atmospheric column. Laboratory measurements proving the feasibility of this new technique were successfully demonstrated. Future applications of this new concept to flight GFCR instrumentation are being considered. (Glen W. Sachse, 41566, and Liang-guo Wang)
Electronics Directorate

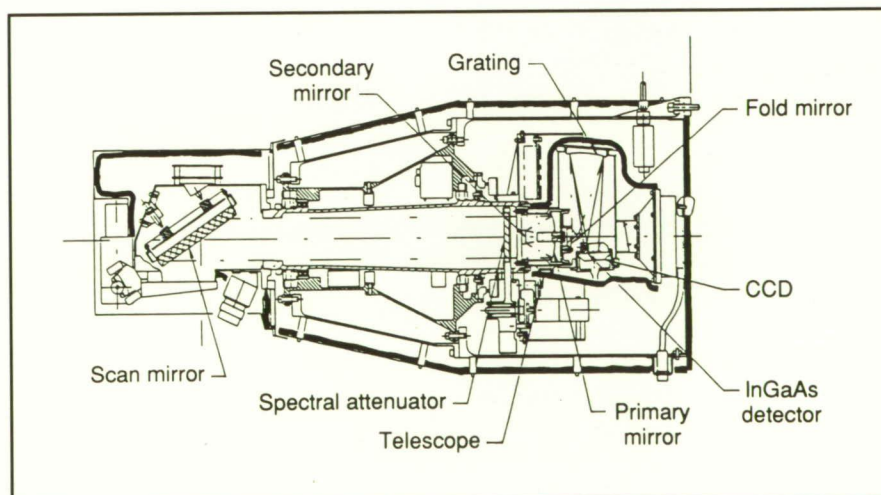
SAGE III

The Stratospheric Aerosol and Gas Experiment III (SAGE III) is an improved extension of the highly successful SAM II, SAGE I, and SAGE II experiments. SAGE III employs the same self-calibrating solar occultation observations and adds lunar occultation observations to measure atmospheric profiles of several key species that are important to achieving a better understanding of the Earth's atmosphere and global climate change. Proposed for the Earth Observing System (EOS) sensor complement to be launched in the late 1990's, SAGE III recently has completed the definition phase activities that have resulted in the selection of a viable instrument conceptual design.

The SAGE III measurement objectives are to retrieve global profiles with 1 km to 2 km vertical resolution of aerosols, clouds, ozone, nitrogen dioxide, water vapor, air density, nitrogen trioxide, and chlorine dioxide in the troposphere, stratosphere, and mesosphere; to investigate the spatial and temporal variability of these species to determine their role in climatological

processes, biogeochemical cycles, and the hydrologic cycle; to characterize tropospheric and stratospheric aerosols and clouds and investigate their effects on the Earth's environment; to continue the SAGE I-II self-calibrating solar occultation data sets enabling the detection of long-term trends; and to provide atmospheric data essential for the calibration and interpretation/correction of other EOS sensors.

SAGE III, which consists of a sensor module and an electronics box, is a limb-viewing spectrometer that performs both solar and lunar occultation measurements in the wavelength region from 290 nm to 1550 nm. The simple optical system consists of a flat scan mirror, an F/2.75 Cassegrain telescope, a stigmatic imaging holographic grating, a 1×450 silicon charge coupled device (CCD) array, and an InGaAs PIN photodiode. Many of the SAGE II subsystems are either identical to or straightforward extrapolations of the SAGE II design. The instrument conceptual design has a mass >40 kg, a volume of $0.3\text{ m} \times 0.3\text{ m} \times 0.7\text{ m}$ (sensor module), an average power of 8 W, and a data rate of 90 kbps. (Lemuel E. Mauldin III, 45382)
Electronics Directorate



SAGE III schematic.

Spaceborne CO and CH₄ Mapper

The Tropospheric Radiometer for Atmospheric Chemistry and Environmental Research (TRACER) is a gas filter correlation instrument for measuring methane (CH₄) and carbon monoxide (CO) in the troposphere. This two-channel instrument (2.33 μm and 4.67 μm) is proposed as part of the Earth Observing System (EOS) complement of sensors that will fly in the late 1990's.

A Definition Phase activity has been completed resulting in a conceptual design that provides four-level CO measurements and total column CH₄ measurements on a global scale. These data will be used to increase the understanding of tropospheric chemistry, reduce the large uncertainties concerning the strengths of the sources of CO and CH₄, define global-scale atmospheric motion, and clarify the interactions between the chemistry and the horizontal and

vertical atmospheric motions.

The simple optical design incorporates an off-axis telescope and two sets of unity-magnification relay optics to focus the upwelling radiance at three locations. These three focal planes provide for the periodic insertion of in-flight calibration blackbodies and gas cells and for a rotating wheel consisting of five calibrated gas cells, three vacuum cells, and a radiometric calibration patch. Gas concentrations are inferred from absorption differences between calibrated cells containing the desired measurement gas and adjacent evacuated cells. Multiple tropospheric layers are mapped by taking radiometric measurements at 2.33 μm and 4.67 μm using separate, radiatively cooled mercury-cadmium-telluride detectors. These two channels share a common optical path through the three focal planes and then are separated by a dichroic beamsplitter into their respective focusing lenses and spectral filters. The detected signals at both wavelengths are amplified and filtered, sampled and digitized, and then

averaged and differenced. An on-board, reprogrammable, central computer controls the data measurement and processing sequence and interfaces with the spacecraft data bus for subsequent relay of the processed data to the ground.

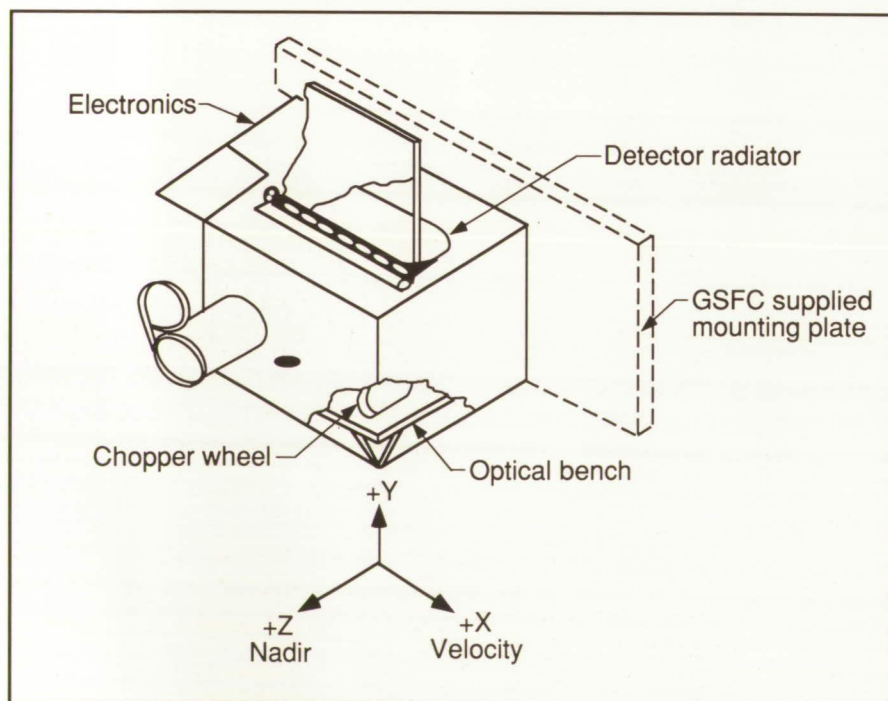
The conceptual design has an estimated mass of 96 kg., measures 75 cm \times 115 cm \times 117 cm, consumes 140 W (average), and has a data rate of 12.5 kbps.

(John C. Fedors, 43771)
Electronics Directorate

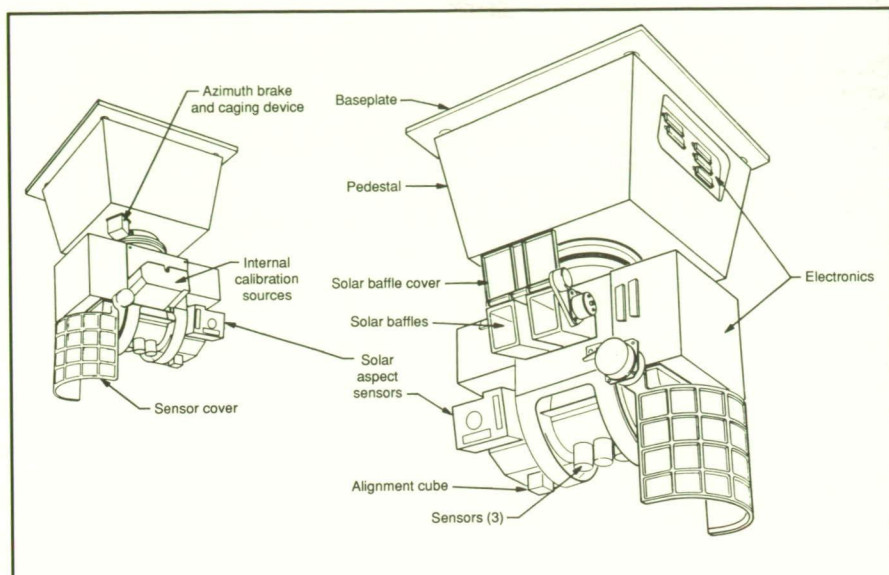
CERES Instrument Definition Studies

The Clouds and Earth's Radiant Energy System (CERES) experiment will provide NASA's Earth Observing System (EOS) of the 1990's with a consistent data base of accurately known fields of radiation and of clouds. The radiation fields will be provided as fluxes at the top of the Earth's atmosphere, at the Earth's surface, and as flux divergences within the atmosphere. Clouds will be provided in terms of measured areal coverage, altitude, condensed water density, and shortwave (SW) and longwave (LW) optical depths.

As part of the EOS program Definition Phase activity, CERES instrument conceptual design studies were completed recently. The CERES instrument is a precision scanning radiometer derived from the successful Earth Radiation Budget Experiment (ERBE) scanner, providing it a space-flight-proven heritage with demonstrated calibration traceability and stability of better than 0.5 percent over 5 years in orbit. The CERES radiometers view the Earth with three co-aligned detector assemblies, each with a different spectral response. The detectors scan back and forth across the Earth from



TRACER.



CERES scanner.

limb to limb and record radiance data. At the extremes of the elevation scan, the detectors view space to establish a zero radiance reference; each detector, tailored to the spectral bandpass of its respective optical train, turns to face internal calibration sources. The three channels will be a total channel ($0.3\ \mu\text{m}$ to $> 50\ \mu\text{m}$), a shortwave channel measuring reflected sunlight ($0.3\ \mu\text{m}$ to $3.5\ \mu\text{m}$), and a long wave channel measuring Earth emitted radiation in the $8\text{-}\mu\text{m}$ to $12\text{-}\mu\text{m}$ region. The field of view near nadir will be approximately 25 km, and the scan cycle back and forth across the Earth will be completed in 6 s. The instrument design includes the capability of operating in a biaxial mode by providing an azimuth oscillating rotation simultaneously with the elevation scanning.

Beginning in the late 1990's, a pair of CERES instruments are proposed to fly on the NASA Polar Platform series (EOS-A and EOS-C) and as Attached Payloads on Space Station *Freedom*, while one instrument is planned for the European Space Agency (ESA) First Polar Mission (ESA-FPM). This multisatellite approach will provide

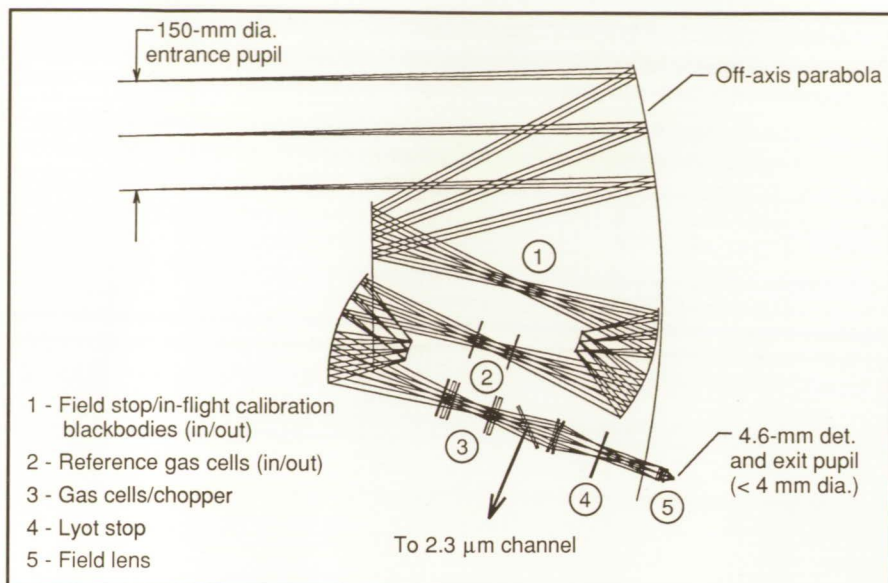
the required temporal sampling to investigate the large diurnal cycle of radiative fluxes. One CERES scanner on each spacecraft will be nominally operated in the cross-track mode to provide maximum spatial coverage from each satellite and for continuity with the previous ERBE measurements. The second scanner on EOS-A and Space Station *Freedom* will be operated in the biaxial mode (i.e., azimuth rotating scan plane) to provide angular sampling for improved radiation Angular Distribution Model (ADM) development and for reduction of errors in the instantaneous radiative flux measurements. Cloud properties will be determined from spectral radiances obtained from companion instruments, such as the Moderate Resolution Imaging Spectrometer (MODIS) on EOS-A, and from geostationary data. The flux divergence within the atmosphere will be provided by radiative transfer calculations based on gridded temperatures and humidities, together with the cloud properties.

The definitive climatology of radiation and clouds provided by this investigation can be expected to

produce a quantum leap in understanding the Earth as a system. This investigation provides data that will allow us to understand the relative importance of different cloud processes, such as frontal clouds, convective activity, and boundary-layer meteorology, and the way that these processes interact with the Earth's climate. These data will allow us to define trends in the clear-sky fluxes and in the impact of clouds and also will be fundamental data for experiments in long-range weather forecasting and climate prediction. (John E. Cooper, 45672) Electronics Directorate

Design, Analysis, and Evaluation of Optical Systems

The need to accurately model a wide variety of complex optical systems and components requires the use of sophisticated software that can aid not only in the design process but also can evaluate the performance of the finished product. A wide variety of such software exists today, and the choice by the optical engineer as to the tools needed for this purpose depends upon the level of design, analysis, and evaluation required. Recent optical designs performed in the Flight Electronics Division for the EOS instruments TRACER and SAFIRE (Spectroscopy of the Atmosphere Using Far-Infrared Emission) required supplementing existing software with other design tools that could extend Langley Research Center's capability. This expanded set of hardware tools now allows complete modeling of instrument performance from concept to testing by using a vast array of program options. For example, the all-reflective optical system design of TRACER and the dual far-infrared/mid-infrared modular concept employed in SAFIRE was success-



TRACER optical system layout.

fully designed, optimized, and analyzed by utilizing a variety of the options available in the software. Initial results indicate that not only will these instruments be capable of meeting imaging requirements but also will be capable of handling signal degrading effects such as scene polarization, stray light, and component motion.

The software packages currently in use for optical design in the Flight Electronics Division are Super Oslo (developed by Sinclair Optics), Code V (a product of Optical Research Associates), and APART (Breault Research Organization). The first two packages are basically known as ray tracing/evaluation programs and have evolved over the years into highly sophisticated software capable of being applied to extremely complex designs. Their output basically provides both geometrical and diffraction-based imaging properties of the optical system, optimization routines for design aid, tolerancing programs for manufacture and assembly, plus many other features. A third program (APART) is used to analyze the stray light properties of the designed systems to determine

overall performance in terms of signal versus noise (stray light). An example of a ray-traced drawing of the TRACER instrument optical path is shown in the figure. The design and performance evaluation were done on both Super Oslo and Code V, and the stray light analyses were done with the APART program.

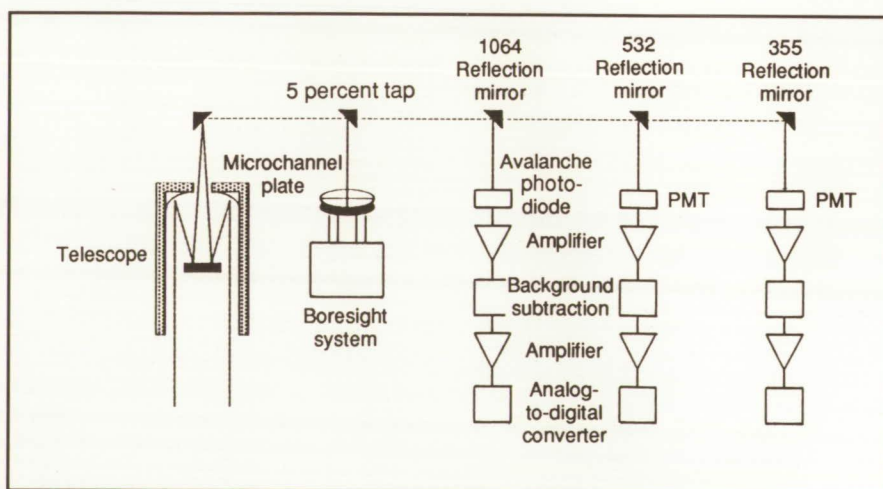
(Don M. Robinson, 41625)
Electronics Directorate

Sensor Research for Lidar Applications

One of the most sensitive sub-systems in lidar instruments is the receiver and supporting electronics that perform detection and amplification of the return laser pulse. The optical receiver must be sensitive to wavelengths ranging from the UV to the near IR, while the electronics must compensate for the wide dynamic range in signal by supplying enormous gains, large bandwidths, and very low noise.

One lidar project currently being developed at Langley Research Center is the Lidar In-Space Technology Experiment (LITE) that will measure numerous atmospheric parameters from the Space Shuttle in the early 1990's. The LITE receiver block diagram displays the major components of the system that was designed to meet the science requirements and derived electronics requirements.

The LITE uses a 25-ns laser pulse from a Nd:YAG laser that has been doubled and tripled. All three wavelengths (1064 nm, 532 nm, and 355 nm) then are sent into the



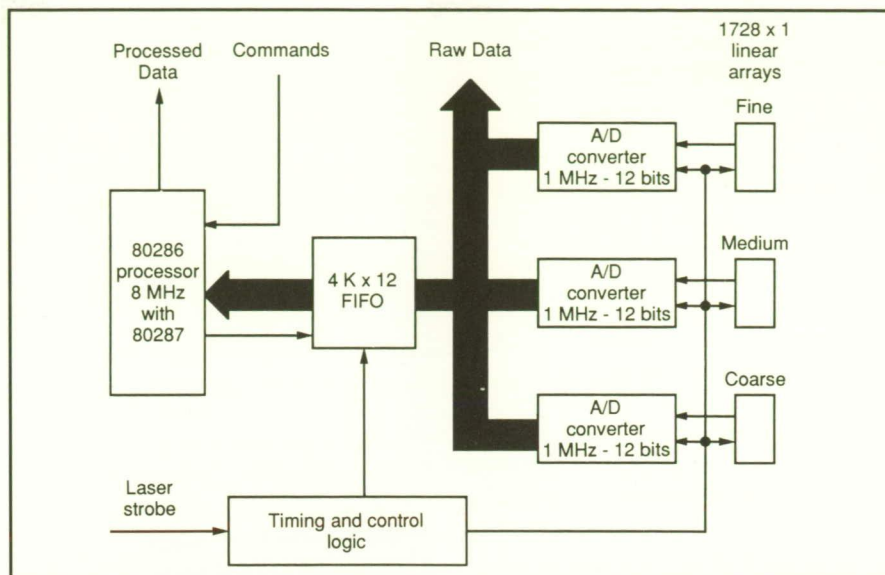
LITE receiver block diagram. (MCP is microchannel plate and APD is avalanche photodiode.)

atmosphere, and the resultant atmospheric backscatter is received by a telescope. During daytime measurements, the background signal can exceed the total atmospheric backscatter return by an order of 10 000. To solve these problems, a separate receiver system was built for each wavelength to optimize the performance of the overall system. A silicon avalanche photodiode was selected to measure the 1064-nm wavelength because of its superior quantum efficiency at that wavelength. After significant analysis and breadboarding, dynode-structured photomultiplier tubes (PMT's) were chosen to measure the two remaining wavelengths because their huge internal gains help reduce external amplifications. In addition, a four-quadrant microchannel plate PMT was selected to align the laser with the telescope. All three detector channels incorporate a background subtraction circuit to increase the overall dynamic range of the system. (C. Antill, 43704)

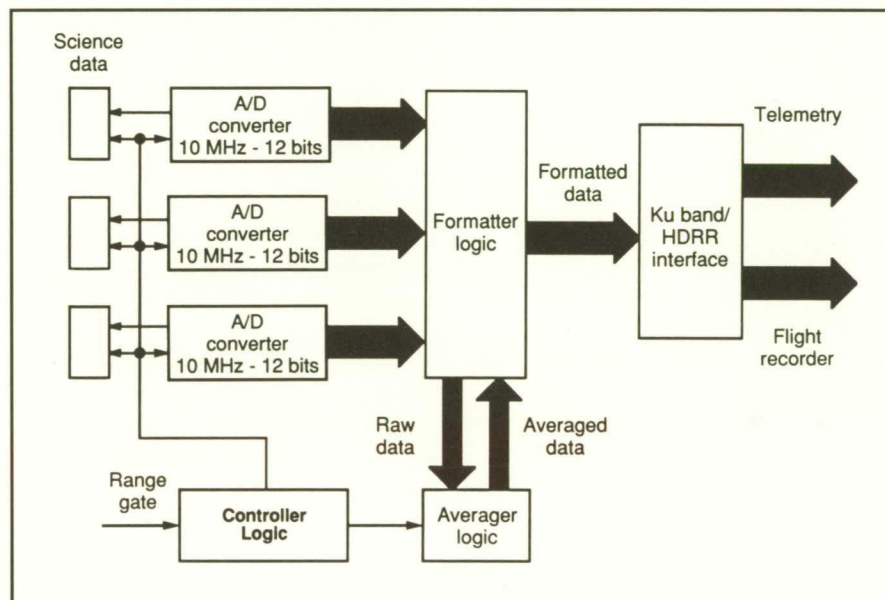
Electronics Directorate

High-Speed Data Acquisition for Lidar Applications

Very high data rates and wide dynamic ranges are common characteristics of lidar experiments. Typically, burst mode data must be sampled at a high rate and resolution to meet mission requirements. Specialized data acquisition electronics are required to capture these signals because nominal analog-to-digital converters (ADC's) controlled by general-purpose processors cannot handle the experiment data throughput. An approach combining state-of-the-art ADC's and first-in-first-out buffers (FIFO's) has been implemented for two laser flight instruments, the Lidar Atmospheric Sensing Experiment (LASE) and



LASE Wave Meter System electronics block diagram.



LITE Digital Data Handling Unit block diagram.

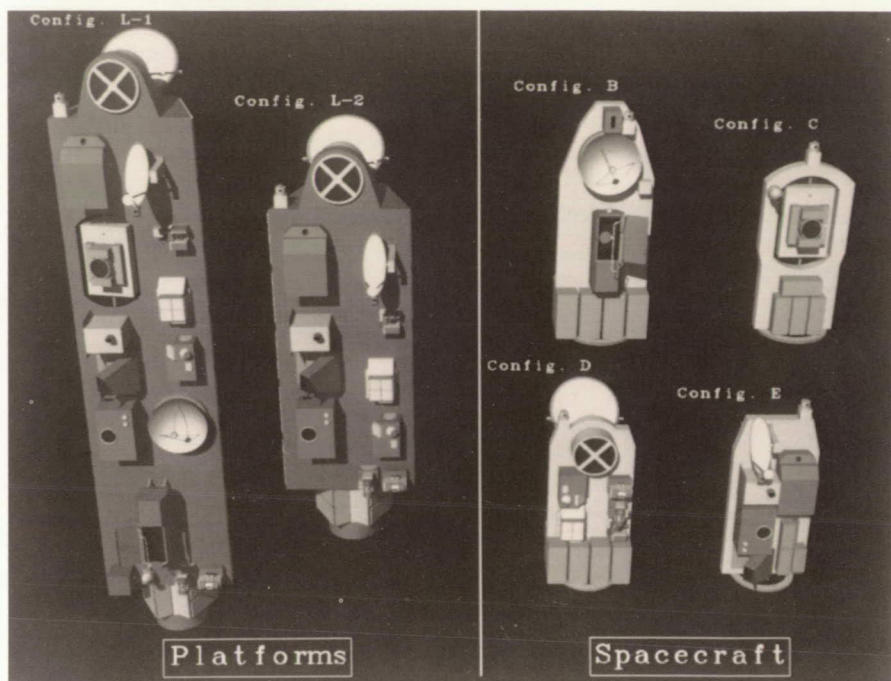
Lidar In-Space Technology Experiment (LITE). The concepts, components, and design tools can be applied to future flight instruments and ground applications with similar data requirements.

The LASE Wave Meter System performs calculations on data generated by a pair of pulsed lasers that fire every 200 ms. This system is composed of optics and electronics as shown in the first figure. One data

acquisition board was designed and built to handle all three channels. The timing for synchronization of the system with the laser firings, linear array exposure times, and rates for data transfer to the ADC's and the central processing unit (CPU) was provided by custom circuitry. The effective data rate realized by this system is on the order of 3 MHz, based on 12-bit ADC's and FIFO's running at 1 MHz.

The LITE Digital Data Handling Unit (DDHU), shown in the second figure, not only digitizes 5500 samples from each of the three science channels simultaneously at a 10 MHz 12-bit rate, but also buffers, averages, and formats data into frames for the Ku band telemetry channel and the high rate flight recorder available on the orbiter. The DDHU also generates system clocks for other LITE subsystems. The electronics is based on 10 MHz ADC's and FIFO's and erasable programmable logic devices to provide flexibility and expansion of control functions. The digital data are presented to the control, averager, and formatter logic at a rate of 2 MHz.

(E. Kist, 41893, and R. Regan)
Electronics Directorate



LEO Earth science systems.

L-90-8972

Global Climate Change Technology Architecture Trades

Systems concepts were developed and technology assessments conducted for science instrument combinations and spacecraft architecture options to measure long-term global climate changes on Earth. An extensive series of atmospheric, land, ocean, and ice; and Earth and solar radiation measurements, to be accumulated over decades, were defined requirements for the study. The need for full global coverage with repeated daily samplings, augmented by near-continuous regional intensive coverage measurements, led to orbit selections at both Sun synchronous low-Earth orbit (LEO) and geostationary Earth orbit (GEO) locations. For global studies, temporal requirements were to sample every 1 hr to 12 hr for atmospheric and radiation parameters and one day or more for most Earth surface measurements.

Spatial resolution needs varied from 1 km for land and ocean surface parameters to 50 km for some atmospheric parameters.

Twenty-seven instrument concepts were selected, with multiple units on duplicate spacecraft, to meet the measurement requirements. The instruments were selected from surveys of existing instruments or developed as new concepts during the study. New concepts include a large soil moisture radiometer and an atmospheric pressure lidar in LEO. New GEO instruments included a high-resolution microwave radiometer for precipitation measurements and several new high-resolution, increased-sensitivity instruments normally associated with LEO missions to meet temporal sampling requirements for < 3 hr. The latter approach was necessary to keep the total number of spacecraft within practical limits.

Several combinations of spacecraft and the large space platform

architecture options were assessed including Delta-launched small LEO spacecraft of the upgraded multimission modular variety and Titan IV-launched large LEO platforms that are new designs with high-performance, high-capacity spacecraft buses. The alternative LEO spacecraft and platform options are shown in the figure. All architectures also included a Titan IV-launched LEO soil moisture radiometer spacecraft and several GEO platforms with optional launch and deployment or on-orbit assembly possibilities. No clear advantage of one architecture over another has emerged to date in the study.

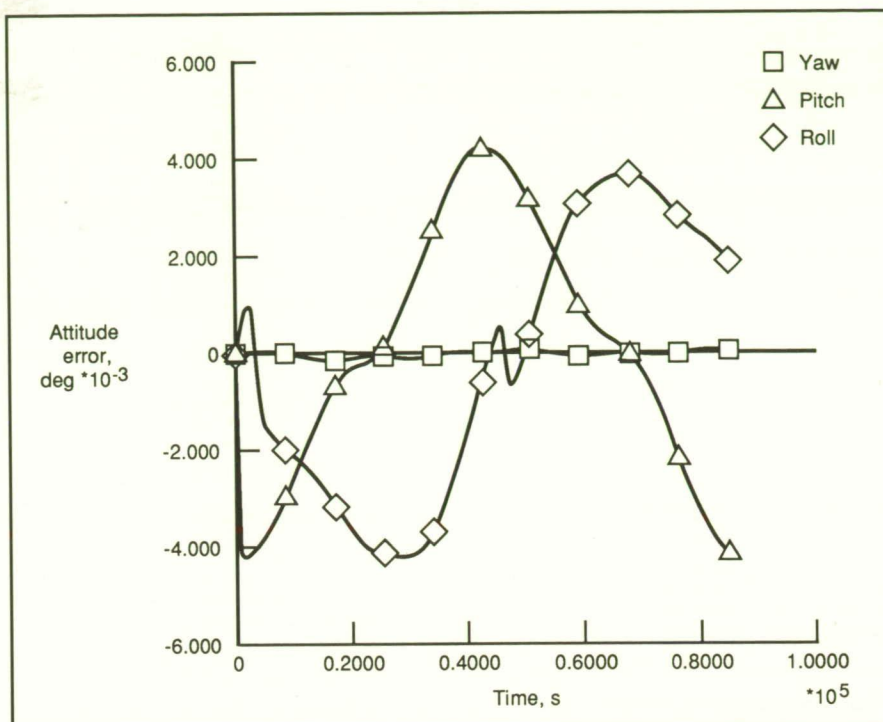
Individual technology development needs in science instrumentation, spacecraft subsystems, and data and information systems were identified. These needs included the new LEO and GEO instruments discussed; large lightweight optics; large antennas; expanded spectral ranges and sensitivities for the detectors; long-life, low-power lasers;

and long-life cryogenic coolers. The spacecraft technologies were precision pointing and control systems, deployable and on-orbit erectable structures, and improved batteries and solar arrays. Data and information systems technology requirements include optical communications, networking, and storage; parallel processing, high-performance computing; and advances in the Tracking and Data Relay Satellite System.

(L. Bernard Garrett, 44425)
Space Directorate

Large Platform Pointing

Large multission platform concepts for the Mission to Planet Earth Initiative have been studied. These concepts generally include large truss structures and oversized microwave radiometer antennas that make the satellites very susceptible to external disturbances such as solar pressure and gravity gradient effects. This problem, coupled with the extremely fine pointing accuracy required of the on-board sensors, questions the feasibility of controlling platforms to low tolerances without the use of additional isolation platforms for certain instruments. A study was performed to verify an 18-arcsec (0.005°) pointing requirement on a modified Ford Aerospace Corporation geostationary platform and a 38-arcsec (0.01°) requirement on a Global Change Technology Initiative (GCTI) geostationary platform. Rigid-body control was to be maintained by implementing off-the-shelf hardware. Flexible characteristics of these platforms were not included because a previous study predicted that they had a minimal effect on attitude control. Reaction wheel assemblies (RWA) were chosen as the primary momentum control devices. The use of RWA, as



Geostationary platform pointing errors over one orbit (required accuracy = 5×10^{-3} deg), attitude error versus time.

opposed to other methods of momentum transfer, was investigated because of their simplicity, relatively light weight, and proven reliability in previous space applications.

The study made use of a software package, Space Systems Integrated Simulation (SPASIS). SPASIS performs a six-degree-of-freedom rigid-body simulation that models disturbances encountered in Earth orbit and calculates their effects on satellites. The program was modified to implement RWA as control devices with RCS (reaction control system) thrusters as RWA desaturation control. A simple proportional plus derivative feedback control law was implemented for each axis to control the spacecraft attitude.

Numerous simulations proved that the modified Ford Aerospace Corporation concept was controllable to better than 18-arcsec on all axes.

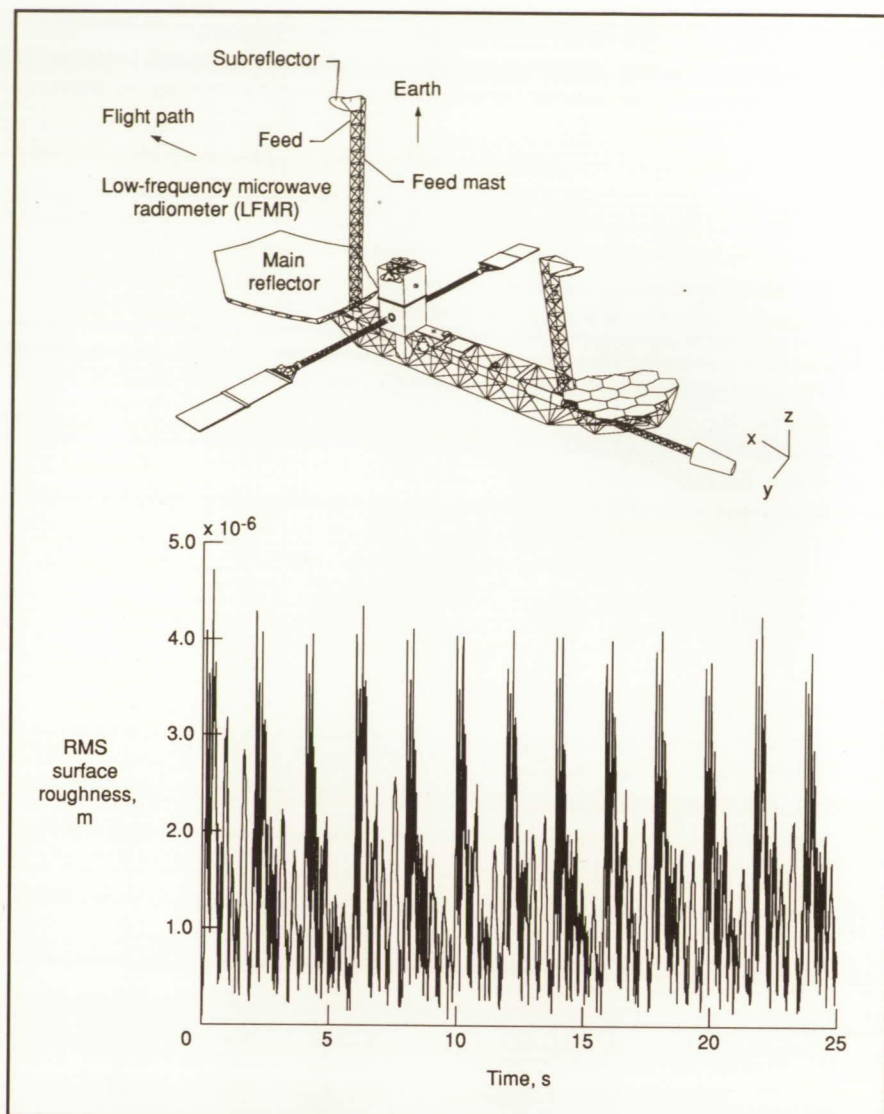
The figure shows the attitude error on the three axes using large momentum capacity reaction wheels designed for the Hubble Space Telescope. The RWA with a smaller momentum and torquing capability also maintained the desired pointing accuracy, but numerous RWA desaturations were required over the course of one orbit. The high frequency of RWA saturation decreases the practicality of employing the smaller RWA on the actual spacecraft. The GCTI platform was not controllable to the desired 38-arcsec with off-the-shelf hardware. Because of the large inertia imbalance of the satellite, a large secular gravity gradient torque affects the spacecraft, and a very large momentum storage and torquing capacity is needed to control the spacecraft to the desired parameters. (James A. Duricy, 44441, and Cheryl C. Jackson)
Space Directorate

Structural-Dynamic Behavior of Earth-Observing Large-Diameter Antenna

The Mission to Planet Earth Initiative is a proposed NASA program to monitor and study the Earth on a global scale. In support of this effort, NASA is proposing technology development programs to produce the sensors to perform the necessary observations and the spacecraft to support these instruments. The low-frequency microwave radiometer (LFMR) is one of the sensing instruments aboard a proposed geostationary platform. The LFMR is an offset-fed Cassegrain antenna with a 15-m-diameter primary reflector and a 19.5-m-long feed mast that supports the subreflector and feed system. The antenna operates at frequencies up to 37 GHz and scans back and forth across the desired area of the Earth. The scanning is performed by rotating the subreflector to redirect the viewing angle of the antenna to the appropriate position.

The electromagnetic performance of an antenna can be affected by numerous factors, among which is the distortion of the antenna structure from its optimum shape. Rotating the subreflector back and forth causes the antenna structure to vibrate and distort. Minimizing the resulting structural distortions (such as surface roughness, pointing error, and defocus) is of extreme importance for high-precision reflector antennas such as the LFMR.

A finite-element model of the LFMR was generated based on current structural technologies. A modal analysis was performed on the model to determine the natural frequencies and mode shapes of the antenna. The scanning maneuver was modeled as orthogonal torque

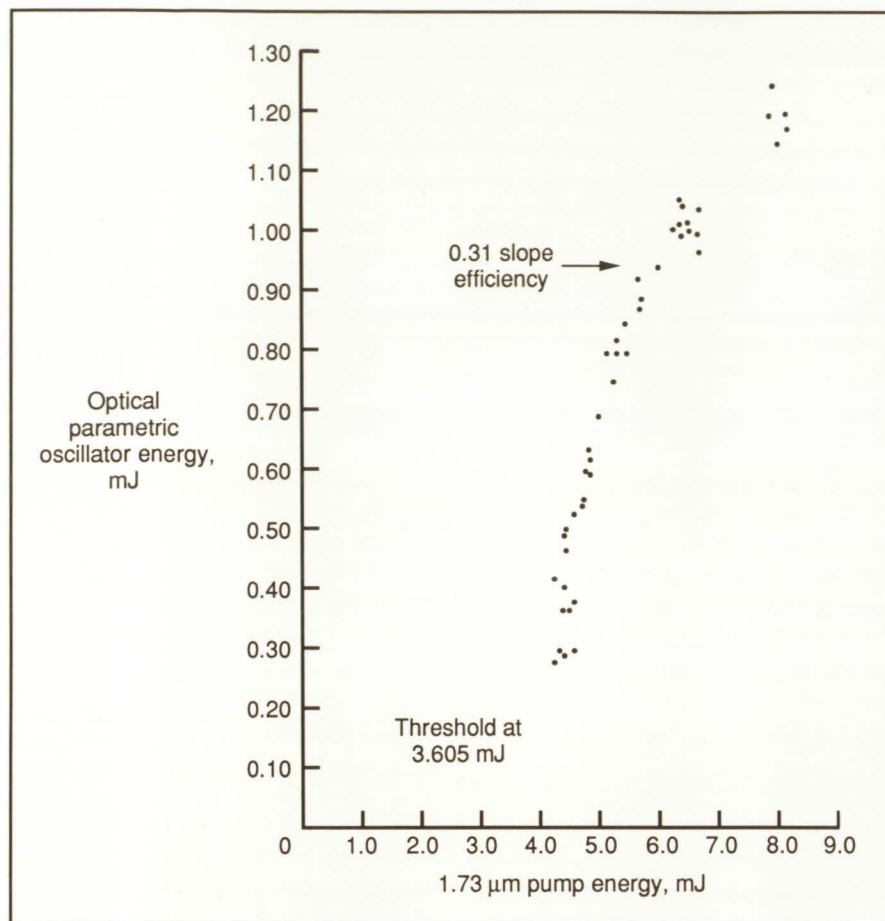


Geostationary platform and sample results curve. Geostationary platform concept (top) and variation of root mean squared (RMS) surface roughness with time (maximum allowable = 8.11×10^{-5} m).

equations that were input to a forced response analysis along the LFMR model and its mode shapes. The resulting dynamic displacements of the antenna nodes then were analyzed to quantify the LFMR surface roughness, pointing error, and defocus. Results show that the scanning maneuver did not induce errors in excess of their specified limits. A sample of the results is shown in the figure, illustrating the variation of surface roughness with time. The results indicate that for dynamic disturbances of the magni-

tude examined, no active control techniques are needed to maintain the shape integrity of this type of antenna.

**(Deborah M. Wahls, 44434)
Space Directorate**



Optical parametric oscillator (70-mm resonator length).

laser. Over 2 mJ of energy have been produced at 3.8 μ m using an approximately 10-mJ pump laser. As higher energy pump lasers become available, the energy output is expected to increase proportionally.

Thresholds and slope efficiencies improved as the length of the resonator decreased. Thresholds and slope efficiencies were measured as a function of the resonator length. Thresholds as low as 3.6 mJ and slope efficiencies as high as 0.31 were achieved with a 70-mm resonator length by using the 3.8- μ m idler as the output. The maximum slope efficiency is set by the ratio of the photon energies (1.73 μ m and 3.82 μ m in this case) at 0.45.

Tuning of the optical parametric oscillator was demonstrated over the range from 2.6 μ m to 5.1 μ m using a single set of mirrors. With other mirrors, further tuning should be possible. Tuning over this range is important as the fundamental resonances of many molecules of interest (including CO, CH₄, CO₂, and O₃) occur in this spectral range. Experimental and derived tuning curves produced good agreement.

Spectral bandwidth was measured and correlated well with a theory developed at Langley to describe the linewidth. A theory was developed which takes into account the spectral bandwidth of the pump, the spectral bandwidth of the nonlinear interaction, and the beam divergence of the pump. Spectral linewidth was found

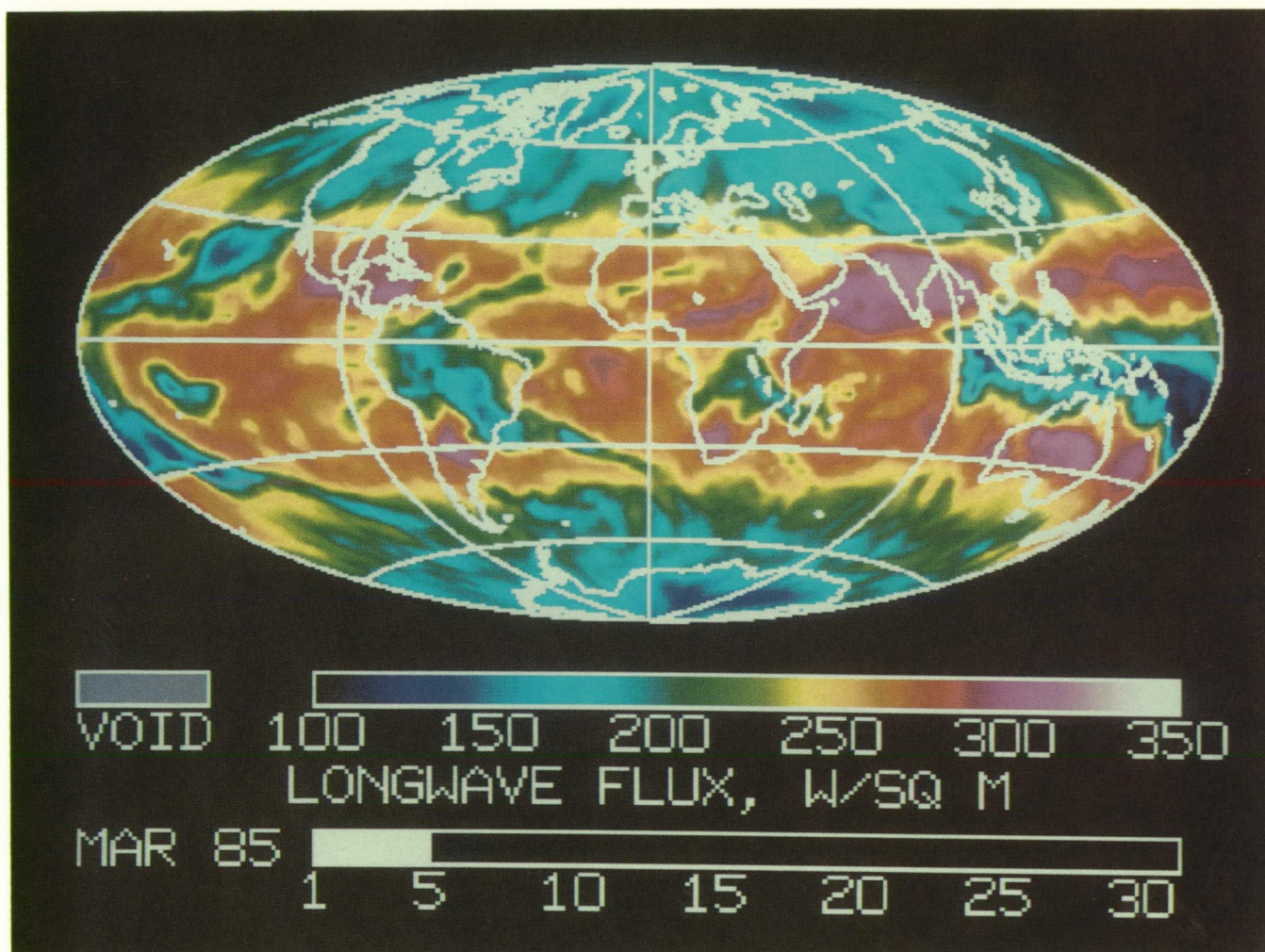
to be limited in this case by the beam divergence of the pump laser.

(Norman P. Barnes, 41630)
Electronics Directorate

Earth Radiation Budget Experiment Movies

The Earth Radiation Budget Experiment (ERBE) consists of an array of radiometric instruments placed in Earth orbit. The purpose of these instruments is to monitor the process by which the Earth receives energy from the Sun and transmits energy back into space. This incoming-outgoing radiant energy transfer process is called the Earth radiation budget. The ERBE instruments quantify the shortwave and longwave components of the Earth radiation budget. The ERBE measurements are vitally important to atmospheric scientists studying the Earth's weather, climate, and the greenhouse effect.

The ERBE data traditionally have been analyzed by examining static pictures containing data from a single day or month. Recently, a software system has been developed which enables the creation of videotapes that detail the temporal dynamics of the ERBE data. The software system first retrieves the ERBE radiation data from archived magnetic tapes. Raster images are created by fitting this daily averaged, hourly averaged, or monthly averaged data to global maps using bilinear spatial interpolation. Next, images representing the times between these data-generated images are derived using time interpolation. The raster metafiles then are transferred to a workstation and are stored on an optical disc. The optical disc image files are recorded directly onto 3/4-in. videotapes, providing an excellent means to animate the image files. The VHS videotapes are then created by



Single frame from ERBE movie depicting the levels of longwave radiation or heat leaving the planet.

copying the 3/4-in. tapes. The VHS tapes are an important new diagnostic tool for the examination of the ERBE data, and they are sent to researchers around the world.

(Brian D. Holeman, 45613)
Space Directorate

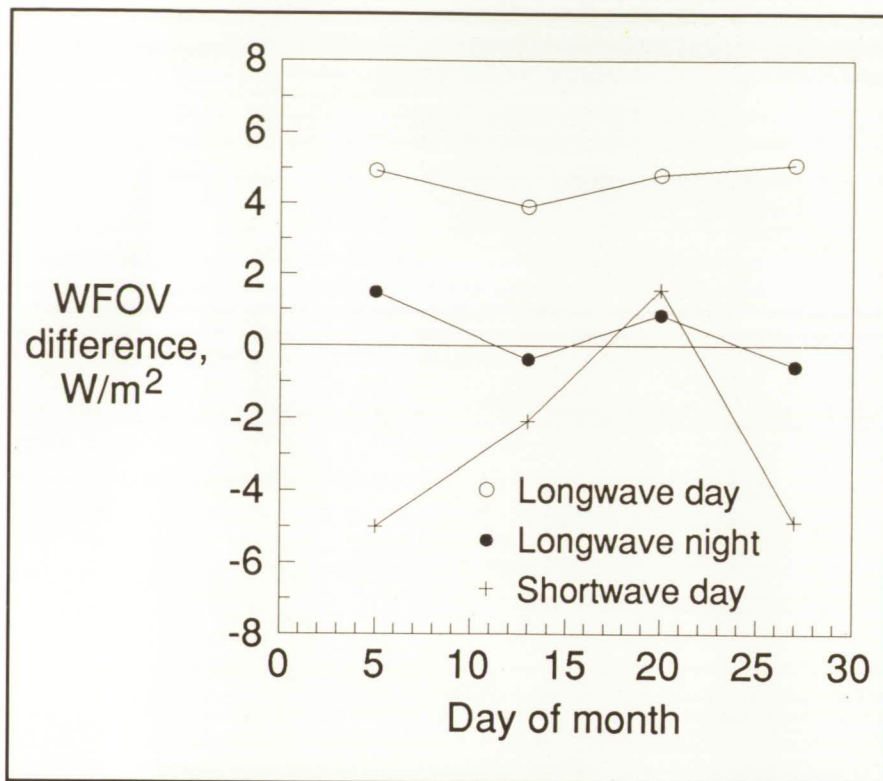
Validation of Earth Radiation Budget Measurements

The Earth Radiation Budget Experiment measures Earth radiation with a scanning radiometer, a medium-field-of-view (MFOV) radiom-

eter, and a wide-field-of-view (WFOV) radiometer. The scanner has a shortwave, a longwave, and a total channel. Both nonscanners have a shortwave and a total channel. These different data sources have been intercompared at satellite altitude for mission validation and quality control. A single, instantaneous nonscanner flux measurement at satellite altitude is compared to an equivalent flux measurement synthesized from the scanner measurements. This comparison is performed every 20° along the orbit over all scene conditions to obtain daily statistics. Possible error sources for this technique are the angular dependence models (ADM's) used to

redirect the scanner radiances, the scene identification algorithm (which selects the appropriate ADM), and the modeled extent of the field of view.

The sensitivity of the technique to possible error sources has been established. The error in synthesizing a single measurement is 1 percent for longwave and 3 percent for shortwave. Errors in synthesizing the average daily measurements are about one-half these amounts. The figure shows the daily variations in the intercomparisons over the month of April 1985. The results for April, July, and October 1985, and January 1986 show that the MFOV total



Earth Radiation Budget Satellite scanner and nonscanner measurement intercomparison for April 1985.

channel and the scanner agree to within 2 Wm^{-2} (2 percent) on the average. The WFOV total channel and scanner agree to within 2 Wm^{-2} (1 percent). For the shortwave channels, the agreement with the scanner is 2 Wm^{-2} (2 percent) for the MFOV and 5 Wm^{-2} (2.5 percent) for the WFOV.

(Richard N. Green, 45684)
Space Directorate

Global Water Vapor Climatology From SAGE II

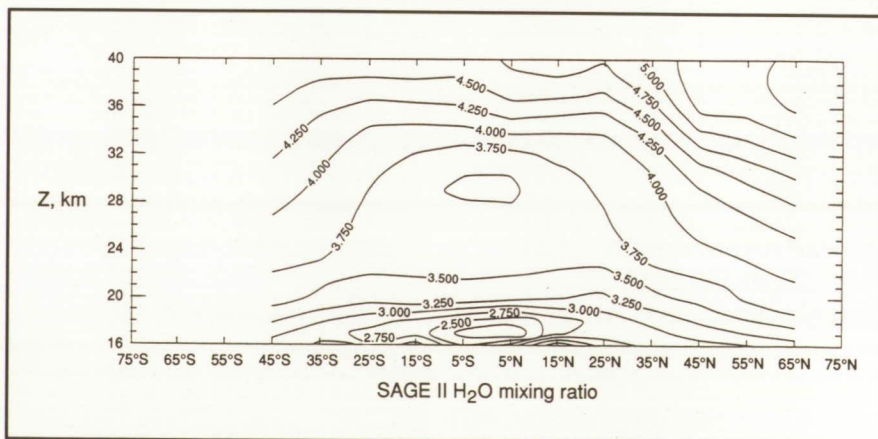
The Stratospheric Aerosol and Gas Experiment (SAGE) II remote sensor onboard the ERBE satellite has been performing water vapor

measurements in the near-infrared wavelengths of $0.94 \mu\text{m}$ since October 1984. Four years (1985 to 1988) of SAGE II water vapor data have been analyzed. Seasonal and annual variations of the water vapor distribution, both in heights and latitudes, have been determined.

The figure shows the zonal mean SAGE II water vapor mixing ratio distribution as a function of altitudes and latitudes for the month of May 1987. The increases of water vapor mixing ratio at higher altitudes confirm the presence of high-altitude water vapor sources originated from the methane oxidation processes. Results from the study of annual variations in the lower stratospheric data indicate the infusion of dry tropical air in the lower stratosphere with subsequent poleward transport during February to March of each year. In addition, high correlation between the region of high humidity in the upper troposphere with the occurrence of high cirrus clouds, as determined from the SAGE II aerosol measurements, has been observed.

In the future, the long-term SAGE II water vapor data can be used for atmospheric dynamics and trends studies.

(W. P. Chu, 42675)
Space Directorate



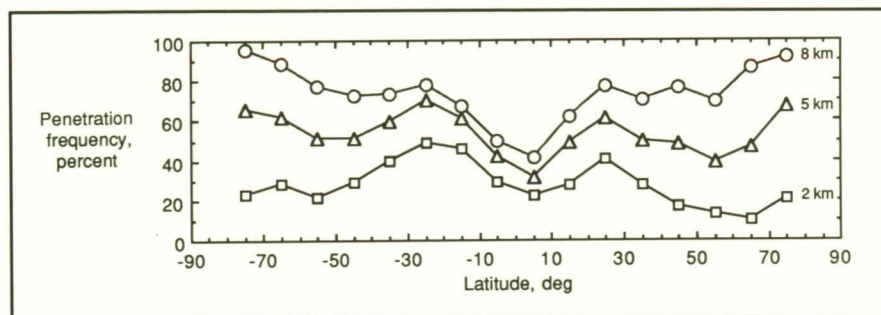
Zonal mean SAGE II water vapor distribution in parts per million volume (ppmv) for May 1987.

Tropospheric Measurements From Space With Solar Occultation Technique

The SAM II, SAGE I, and SAGE II series of solar occultation experiments were designed for the measurement of stratospheric aerosols and gases. In the absence of high-altitude clouds, tropospheric measurements are also possible. These satellite

development of climatologies for aerosol and water vapor in both the stratosphere and the upper troposphere.

The other SAGE II aerosol channels are at shorter wavelengths, and attenuation by aerosols and the molecular atmosphere limits tropospheric penetration. The SAGE II, presently proposed for the EOS, has additional aerosol channels at 1.54 μm and between 0.7 μm and



SAGE II tropospheric penetration frequency in percent of observations down to altitudes of 2 km, 5 km, and 8 km for January to December 1989.

experiments observe the Sun along a horizontal path through the atmosphere and measure the total atmospheric extinction at a number of selected wavelengths over an optical path several hundred kilometers in length. If attenuation of the solar radiation occurs due to clouds, the signal received at the satellite may fall below the threshold of detection. Such occasions, although frequent, do not prevent a significant number of measurement opportunities from occurring well down into the troposphere. The figure shows the frequency of penetration to various altitudes for the SAGE II 1- μm aerosol channel. Over most of the globe, 50 percent penetration down to an altitude of 5 km and 20 percent penetration to an altitude of 2 km are observed. The latitude variation shown in the figure reflects the occurrence of clouds in the atmosphere. A similar penetration frequency is observed at the 0.94- μm water vapor channel, and this penetration frequency permits the

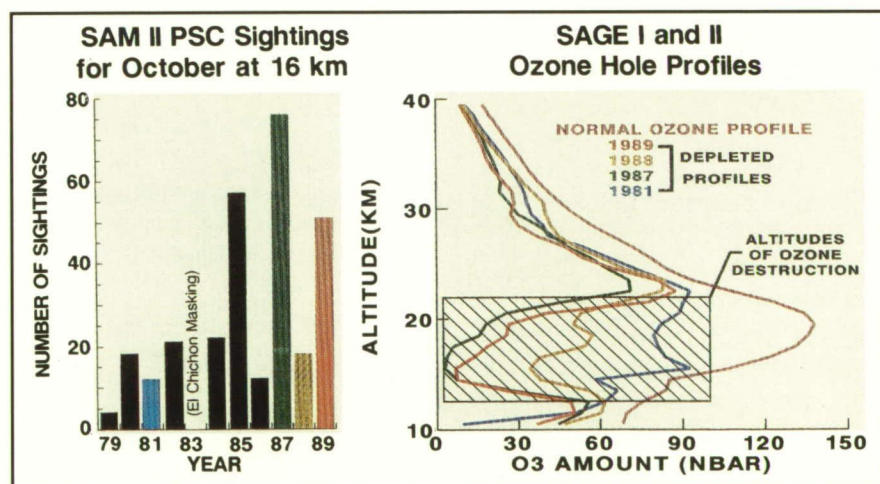
development of climatologies for aerosol and water vapor in both the stratosphere and the upper troposphere.

(L. R. McMaster, 42669)
Space Directorate

Antarctic Ozone Loss Variability Linked to Polar Stratospheric Cloud Abundance

Ongoing observations from satellite-borne Langley Research Center sensors, SAGE I and II, and SAM II show that in 1989 the recurring springtime ozone loss over Antarctica approached the record 1987 levels; these observations support current theories linking ozone destruction to chemical processing by polar stratospheric clouds (PSC's).

Shown in the figure on the left are SAM II Antarctic PSC sightings for the period 1979 to 1989 at 16 km, near the altitude of peak ozone loss. Shown on the right are SAGE measurements of ozone amount versus altitude in early October over Antarctica for 1981 to 1989. The ozone loss region is very obvious in this figure and extends from 12 km to 22 km, altitudes at which PSC's are sighted throughout winter. The greatest ozone loss occurred in 1987 when ozone amounts dropped below 5 nanobars at some altitudes (more than a factor of 25 down from normal values at that altitude). In 1989 the loss was nearly as severe, with ozone



Polar stratospheric cloud sightings at 16 km by SAM II (left) and profiles of ozone measurements by SAGE I and II (right) during October in Antarctica.

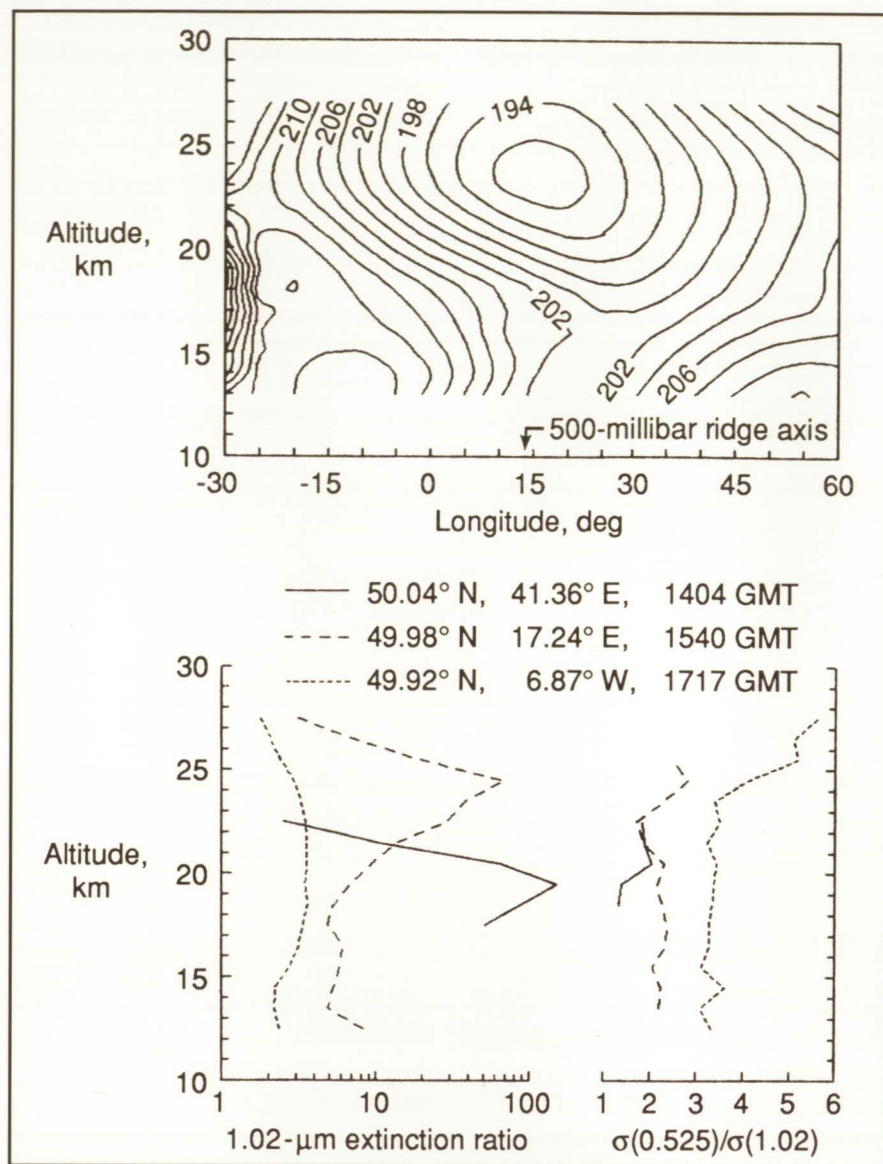
amounts less than 10 nanobars at these altitudes. In contrast, the 1988 ozone profile shows less ozone depletion than either 1987 or 1989. Similarly, PSC sightings in 1989 were near the 1987 levels, while there were considerably fewer sightings in 1988. Some of the year-to-year variability in ozone depletion is probably driven by meteorological factors (e.g., the quasibiennial oscillation) which are not well understood. These factors also may modulate PSC abundances.

Recent Antarctic field studies have shown that PSC's play a crucial role in perturbing the chemistry of the winter polar regions. In particular, it has been established that heterogeneous chemical reactions on PSC surfaces produce large enhancements in reactive chlorine species which can, with the return of sunlight, lead to rapid ozone loss such as that observed during the Antarctic springtime. Because the formation of these clouds requires extremely cold temperatures, variations in stratospheric temperatures from year to year can influence PSC abundances and hence the amount of ozone loss in a given year.

(M. P. McCormick, 42669)
Space Directorate

SAGE II Observations of Polar Stratospheric Clouds Near 50°N

Polar stratospheric clouds (PSC's) have been observed frequently over the last decade during both polar winters and during Antarctic spring. These clouds have recently been established to play a major role in promoting stratospheric ozone loss through the catalysis of heterogeneous (mixed-phase) chemical processes that liberate ozone-destructive chlorine radicals from normally benign reservoir species.



NMC temperatures, in degrees Kelvin, at 50°N (top) and SAGE II extinction profiles (bottom) on February 1, 1989.

The PSC's form only at very cold temperatures (below 195 K to 200 K); hence, their sightings have been confined almost exclusively to very high latitudes (poleward of 65°).

However, PSC's were sighted near 50°N in early February 1989 by the orbiting SAGE II sensor. This unusual episode stemmed from a southward displacement of the Arctic winter vortex, with the edge of the vortex overrunning a strong midtropospheric ridge and producing

local adiabatic cooling to temperatures below the threshold for PSC formation. The figure shows three SAGE II profiles of the 1.02-μm extinction ratio and the ratio of extinction coefficients σ at 0.525 μm and 1.02 μm measured on February 1, 1989, along with temperatures at 50°N for that day provided by the National Meteorological Center (NMC). The SAGE II data near 7°W are typical of the ambient stratospheric aerosol, while those near 17°E and 41°E bear the signature of

PSC's with comparatively much larger particles. The latter two profiles are associated with the cold temperature pocket from 20 km to 25 km overlying the 500-millibar ridge axis. It is noteworthy that these PSC's occurred near the edge of, or even outside, the polar vortex and, more importantly, at a latitude where there was extensive sunlight. Thus, there was an increased likelihood of ozone loss downstream of the area due to enhancements in reactive chlorine produced by heterogeneous chemical processing within the clouds.

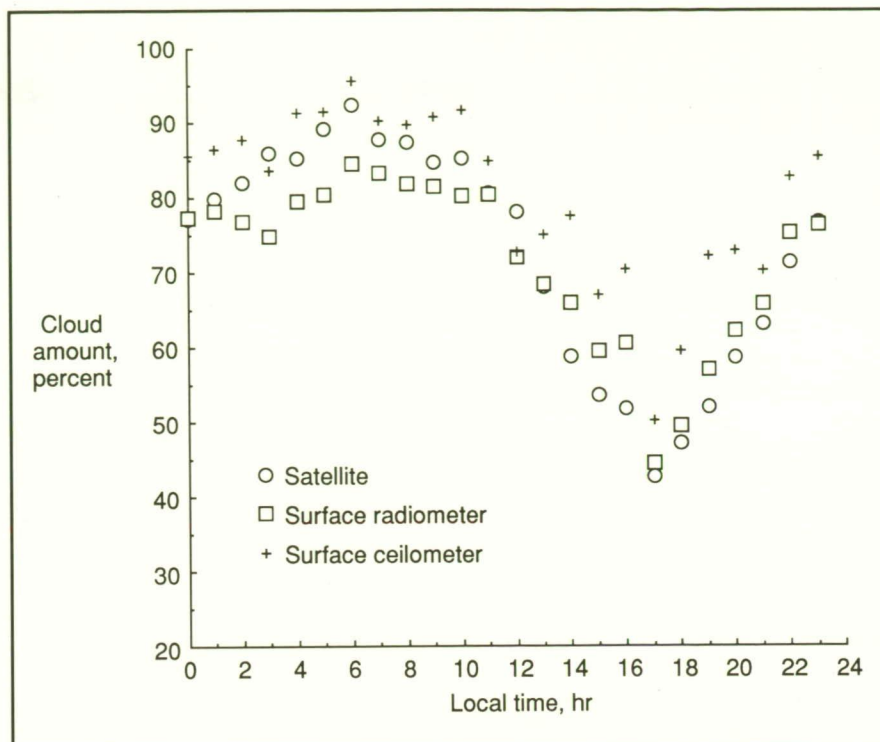
(L. R. Poole, 42689)

Space Directorate

Verification of Satellite Measurements of Stratocumulus Clouds

Marine stratocumulus clouds cover large portions of the oceans. Because these clouds occur at low levels and reflect much of the incident solar energy, they prevent heating of the surface beneath them. This cooling effect casts marine stratocumulus as a critical element in climate change scenarios. Improvements in the current, unreliable, climate-model parameterizations of these clouds rely on accurate satellite observations of stratocumulus properties such as fractional coverage, height, and water content. The accuracy of the satellite techniques for deriving cloud properties is unknown.

The First International Satellite Cloud Climatology Project (ISCCCP) Regional Experiment (FIRE) measured many different aspects of the stratocumulus clouds west of California during July 1987. The observations taken continuously from San Nicolas Island provide a source of ground truth for satellite measure-



Comparison of mean cloud amounts over San Nicolas Island, California, July 1 to 19, 1987.

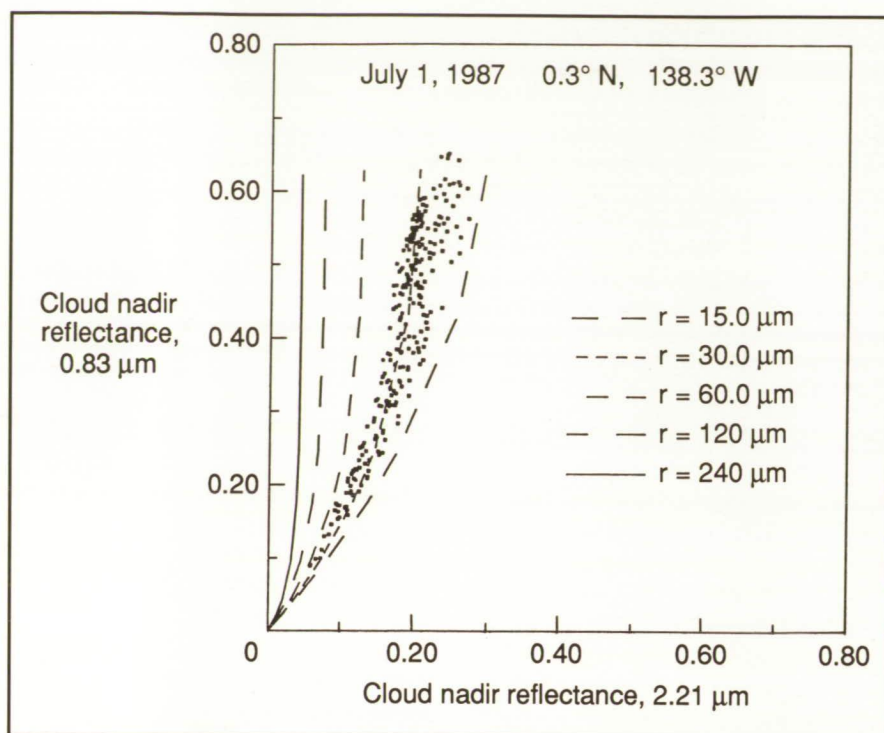
ments of marine stratocumulus. As shown in the figure, the mean fractional cloud coverage derived from the Geostationary Operational Environmental Satellite (GOES) using the hybrid bispectral threshold method generally falls between that derived from two different surface instruments. The mean satellite cloud amounts are as precise as can be measured from the surface, regardless of the time of day. Additional comparisons of GOES- and surface-derived cloud properties indicate that cloud height, thickness, and water content also can be determined with relatively high accuracy using the satellite data. These and other FIRE results are being used to validate the ISCCP results and to provide reliable quantifications of cloud characteristics for the development of improved climate models.

(Patrick Minnis, 45671)

Space Directorate

Determination of Tropical Cirrus Particle Size From Space

Clouds can either warm the Earth/atmosphere system by trapping outgoing thermal infrared radiation (i.e., the greenhouse effect), or they can cool the Earth/atmosphere system by reflecting solar radiation back to space. In addition, these same clouds can vertically redistribute the resulting gain or loss of heat at the surface or within different levels of the atmosphere. Recent studies using global climate models indicate that atmospheric radiative heating by tropical-cirrus clouds may play a critical role in determining the magnitude of the large-scale circulation of the atmosphere. Unfortunately, such models employ necessarily crude models of cloud-radiative properties. For example, little is known concerning the size of cirrus cloud particles needed to model their



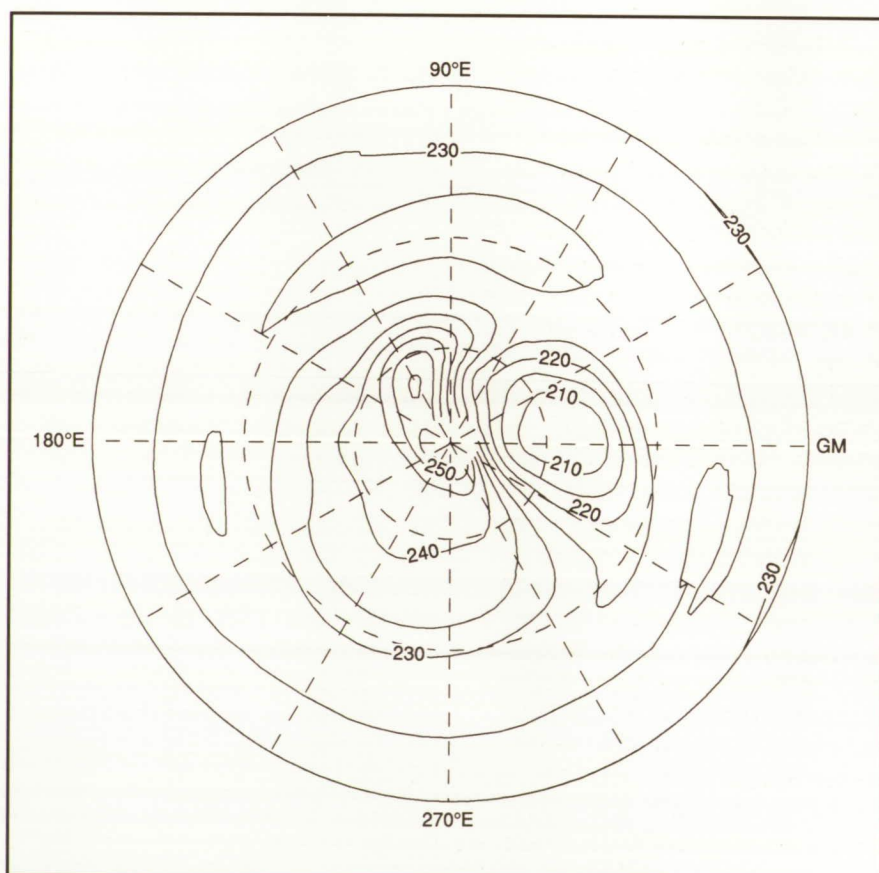
by the solid and dashed lines. Inferred cloud particle radius ranges from 20 μm to 40 μm . For all six cloud fields, the cirrus-particle size is found to range from 20 μm to 120 μm , with most of the observations clustered between 30- μm and 60- μm radius. In general, the data imply that cirrus particle size increases as cloud optical depth (i.e., reflectance at 0.83 μm) decreases. (Bruce A. Wielicki, 45683) Space Directorate

Estimation of Synoptic Fields of Middle Atmosphere Parameters Obtained From Satellite Data Sets

The most widely used version of the Nimbus 7 Limb Infrared Monitor

radiative properties. Cloud particle size can be especially important in determining the relative balance of cirrus cloud warming in the thermal infrared, versus cirrus cloud cooling at solar wavelengths.

Landsat multispectral radiances at wavelengths of 0.83 μm , 1.65 μm , and 2.21 μm have been used to determine cloud particle size for six cases of tropical-cirrus clouds. For each case, measurements were taken over 58.4 km square regions to examine the variation of cloud-particle size in the cirrus-cloud field. Five of the cirrus cases are taken from the eastern Pacific Ocean between 13°N and 15°N latitude and 95°W and 105°W longitude during October 1989. The final case is taken on 0°N, 138°W in the Pacific Ocean on July 1, 1987. The figure shows the data for the case on July 1, 1987. The Landsat-measured nadir reflectances at 0.83 μm and 2.21 μm are shown as points. Theoretical multiple scattering computations for a range of cloud particle radii are given



Polar plot of Northern Hemisphere temperature on the 10-millibar surface for February 9, 1979. Contour interval is 5 K.

of the Stratosphere (LIMS) data set is the set of high-quality, daily, zonal Fourier coefficients which resolve information out to six wavenumbers at 1200 hours Greenwich Mean Time (GMT). A Kalman filter algorithm was applied to the original nonsynoptic LIMS profile data in order to generate those synoptic fields for scientific and archival purposes. Diagnostics also were developed so that the fidelity with which the original profile information was mapped could be judged. As an example, the figure represents the Northern Hemisphere LIMS temperature distribution for February 9, 1979, at 10 millibars (near 30 km altitude in the midstratosphere) that was generated using those Fourier coefficients. The stratosphere at that time was subject to large-scale, high-amplitude, wave activity that induced a significant warming of the polar region, lasting approximately a week.

Similar software is being developed for the generation of the Level 3b globally mapped data product from several experiments as part of the comprehensive Upper Atmosphere Research Satellite (UARS) data set to be developed beginning in 1991. The LIMS results will serve as a test data set in that development, and because the algorithms for both data sets will be very similar, it will be possible to look for global changes in those species which are common to both data sets. It is anticipated that studies (over several decades) of the transport of and/or the chemical depletion of ozone in the middle atmosphere can be determined with high accuracy with the aid of such higher level data products. Furthermore, it should be possible to study the causes and effects of those changes from joint analyses of the many atmospheric species and parameters generated on the common time and space grid. (Ellis E. Remsberg, 45823, Kenneth V. Haggard, and James M. Russell III) Space Directorate

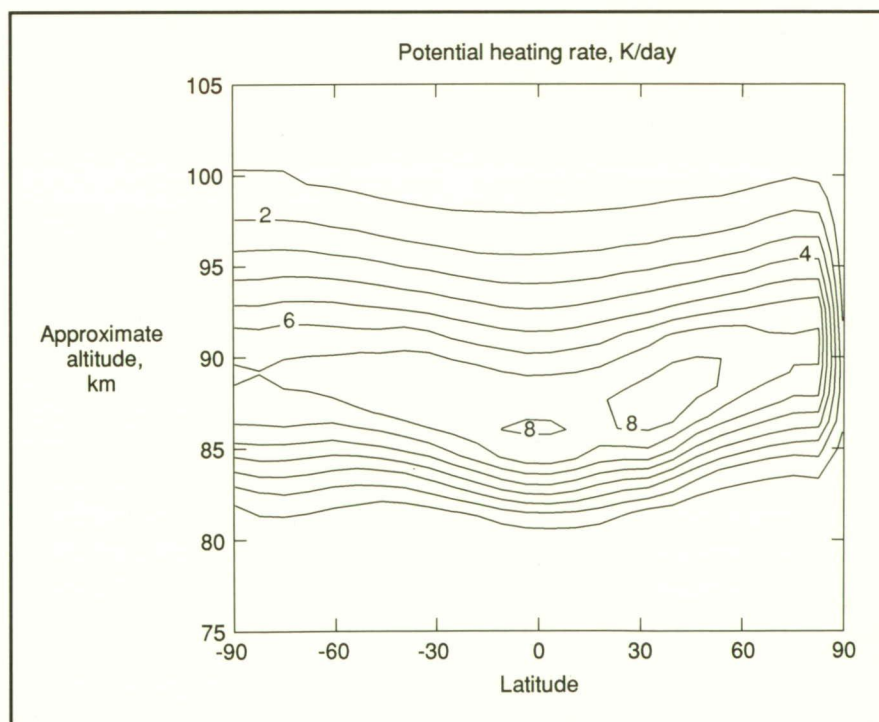
Mesopause Region Heating by Exothermic Chemical Reactions

The mesopause region corresponds to the atmosphere between 80 km and 100 km in altitude. The circulation of the atmosphere at these altitudes is influenced by a number of radiative (solar and terrestrial) and dynamical energy sources. In addition, highly exothermic chemical reactions also may be a significant source of energy at these altitudes. The energy liberated by chemical reaction initially heats the atmosphere, or some fraction of the energy is stored internally in the bonds of the product molecules. The internal energy then may be radiated to space, or it may be converted into heat as the product molecule collides with other molecules, thereby causing a removal of the internal energy.

The reaction of atomic hydrogen (H) and ozone (O₃) which forms the

hydroxyl radical (OH) and molecular oxygen (O₂) is highly exothermic and critically important in the chemistry of the mesopause region. Calculations carried out have shown that the heating rate due to this reaction approaches a maximum of 8.5 K per day at ≈90 km, if all of the available energy goes into heating. The temperature at this altitude varies between 160 K and 190 K, depending on season and latitude. Consequently, it is extremely important to determine the fraction of available energy that goes into heating.

Initial calculations indicate that 30 percent to 65 percent of the available energy goes into heating the mesopause region, resulting in heating rates as large as 3 K to 6 K per day, depending on the rates at which energy is assumed to be removed from the OH molecule by collisions. Heating rates of this magnitude compete with and at times exceed the cooling rate due to infrared emission from carbon



Heating rate (K/day) if all energy liberated by the reaction $H + O_3 \rightarrow OH + O_2$ results in heating the atmosphere, under equinox conditions.

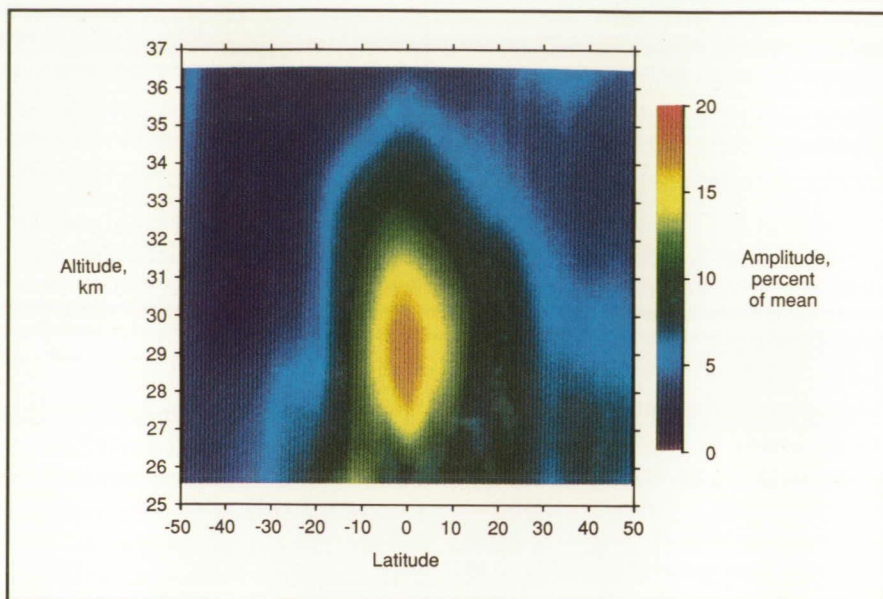
dioxide (CO_2). These results are the first quantitative demonstration of the importance of the exothermic reaction $\text{H} + \text{O}_3 \rightarrow \text{OH} + \text{O}_2$ in heating the atmosphere, and they represent the identification of a potentially significant source of energy in the mesopause region.

(Martin G. Mlynczak, 45695)

Space Directorate

Discovery of QBO Signal in SAGE II NO_2 Data

Initial work on the Study of the Variations in Stratospheric Nitrogen Dioxide (NO_2) using the Solar Mesosphere Explorer (SME) and SAGE Satellite Data has resulted in the discovery of a quasibiennial oscillation (QBO) in stratospheric NO_2 . During the course of this study, researchers from Langley Research Center, the University of Colorado, and New Mexico Institute of Mining and Technology intend to combine the existing stratospheric NO_2 profile data sets into a single data set spanning the period from 1979 to the present. The combined data set then can be used to investigate the response of the Earth's atmosphere to natural perturbations such as the solar cycle and used as a baseline to detect possible effects from anthropogenic sources such as the proposed High-Speed Civil Transport. However, before this data base can be assembled, the natural short and intermediate period variations of NO_2 must be quantified. The seasonal variations in NO_2 generally are well understood, but until now, no single data set had sufficient duration and stability so that the intermediate period variations, such as the QBO, could be studied. Measurements of NO_2 from the SAGE II instrument, currently operating since its launch at the end of 1984, provide the needed stability and duration.



Altitude-latitude variability of the NO_2 QBO amplitude shown in SAGE II data.

The first reported manifestation of the QBO was an oscillation in the equatorial zonal winds between the altitudes of 20 km and 35 km. Eventually, climatologies evolved characterizing the QBO as a quasiperiodic oscillation in the mean zonal winds of the middle and lower stratosphere. The oscillation is not strictly periodic; its period ranges between 23 and 34 months with a mean period near 28 months. An associated QBO in stratospheric temperatures of amplitude 1 K to 2 K has been observed as well as a QBO in ozone. This first-ever measurement of a QBO in NO_2 compares favorably with theory. As shown in the figure, the NO_2 QBO is found primarily in the equatorial region with a peak amplitude of 17 percent (0.8 ppbv) at a 29-km altitude. The observed features of the QBO in NO_2 are notably different from those of ozone (particularly the behavior of the NO_2 column abundances), but they can be understood (in light of relevant photochemistry) to be due to

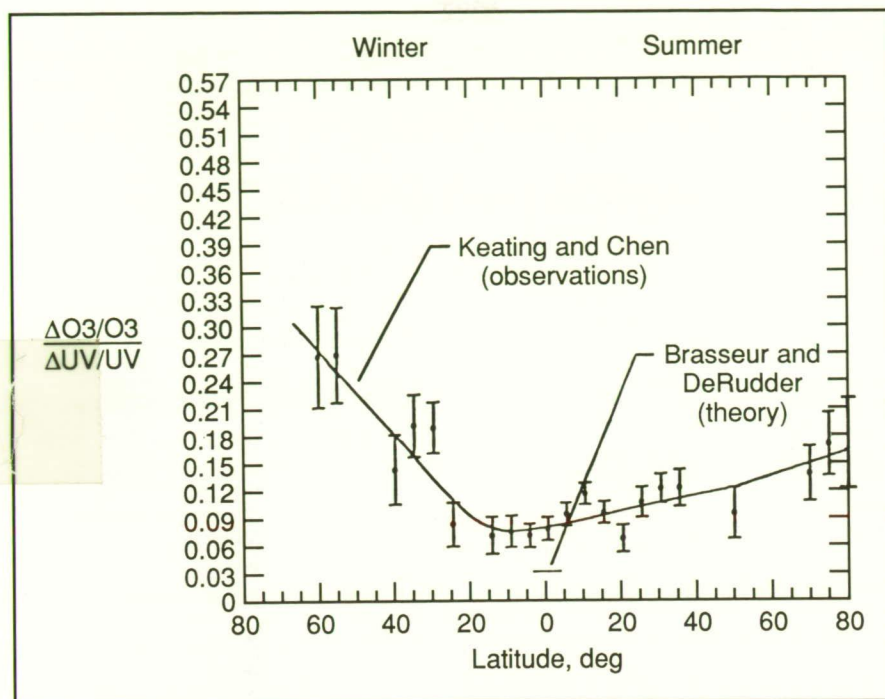
the transport of the long-lived chemical family of oxides of nitrogen (NO_y).

(J. M. Zawodny, 42681)

Space Directorate

Global Change of Total Column Ozone Through Solar Forcing

Of crucial importance when trying to isolate the middle atmosphere changes associated with possible anthropogenic effects is the identification of the magnitude of natural variations in the ozone layer associated with solar ultraviolet (UV) changes. During the period from 1979 to 1986, unexpectedly strong decreases existed in the total column ozone, but this was also the period of decreasing solar activity of the 11-year solar cycle. Direct isolation of the portion of the ozone decreases that are due to the 11-year solar cycle



Short-term response of total column ozone to 27-day variations in solar UV related to rotating Sun (percent increase in total column ozone for 1-percent 205-nm increase, TOMS/UV response from 1979 to 1981).

would require an investigation of a number of solar cycles to be statistically significant, but, unfortunately, the satellite data cover less than two cycles. Therefore, a new approach now has been undertaken by studying the atmospheric response to variations associated with the 27-day rotation of the Sun. The variations in solar UV which drive the 11-year variations have a comparable magnitude on the 27-day time scale. Thus, the response on the 11-year time scale can be estimated studying 27-day variations, and the large number of 27-day variations observed allow accurate statistics to be collected on this solar-terrestrial relationship.

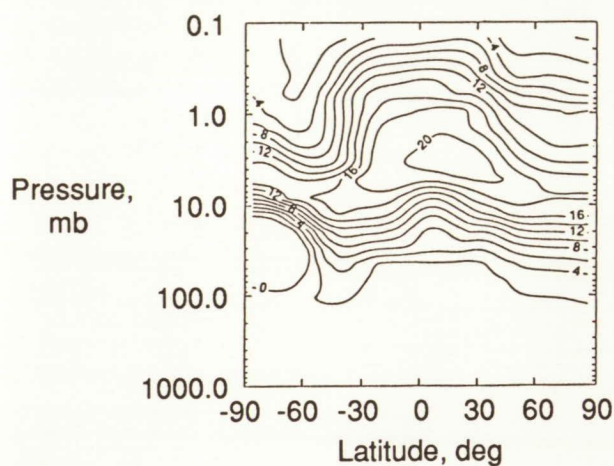
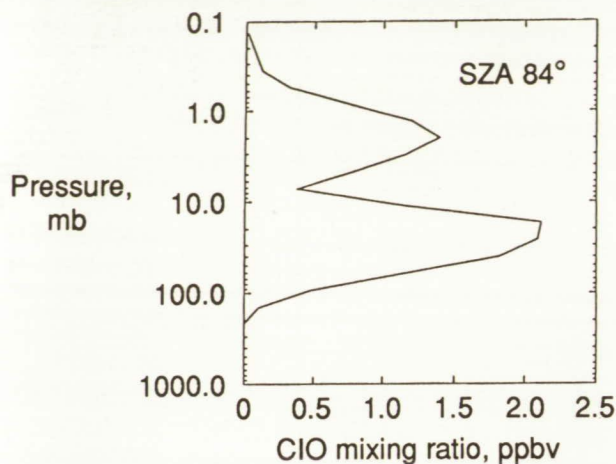
A study of 3 years of Nimbus 7 TOMS (Total Ozone Mapping Spectrometer) total column ozone data reveals an unexpectedly strong response of total column ozone to the 27-day solar variations. Shown in the figure is the percent increase in total

column ozone for winter and summer latitudes for a 1-percent increase in 205 nm solar radiation. For comparison, the calculated response based on a one-dimensional photochemical-radiative time-dependent model also is given. As may be seen, the total column ozone response to solar variability is much stronger than predicted. Thus, solar forcing should play a much more important role than previously expected in the drop in total column ozone from 1979 to 1986, and this reduces the required amplitude of anthropogenic trends. Results intermediate between the winter and summer conditions are found for the spring and fall. (Gerald M. Keating, 45804, and Chaing Chen) Space Directorate

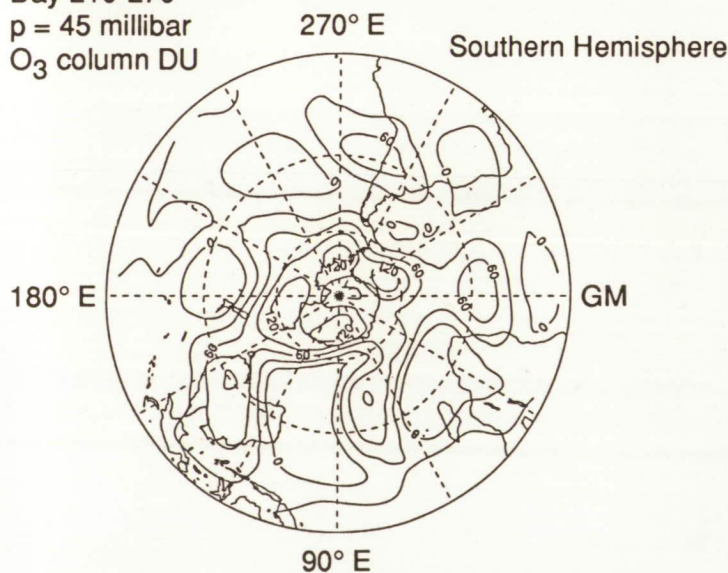
Heterogeneous Chemical Processes and Polar Ozone

Substantial evidence now exists to support the theory that chlorine (and to a lesser extent, bromine) compounds are ultimately responsible for the large reductions in total column ozone observed during austral spring in Antarctica. A key element in the ozone destruction process is thought to be the removal of odd nitrogen through heterogeneous chemical processes on condensed nitric acid trihydrate (NAT) and water particles. A simulation of polar ozone destruction during austral spring has been conducted with the Langley Research Center global three-dimensional atmospheric chemistry/transport model. This model includes a comprehensive representation of gas-phase chemistry, plus a treatment of the gas-to-particle conversion of odd-nitrogen compounds on condensed NAT and water particles. The model simulation has been conducted for 60 days after initialization at the beginning of August. By the beginning of September, the ClO abundance in the lower stratosphere has been enhanced substantially.

The model-predicted values shown in the top figure are in general accord with observations from the Airborne Antarctic Ozone Experiment. The elevated chlorine abundance is a consequence of the denitrification of the lower stratosphere. In the absence of odd nitrogen, conversion of active chlorine into the reservoir species ClONO₂ does not occur. The total odd-nitrogen distribution at the beginning of September is shown in the middle figure. Note the absence of any significant odd nitrogen in the south polar regions between 100 mb and 10 mb. The consequences of the elevated chlorine abundances are evident in the bottom figure, which



Day 210-270
p = 45 millibar
O₃ column DU



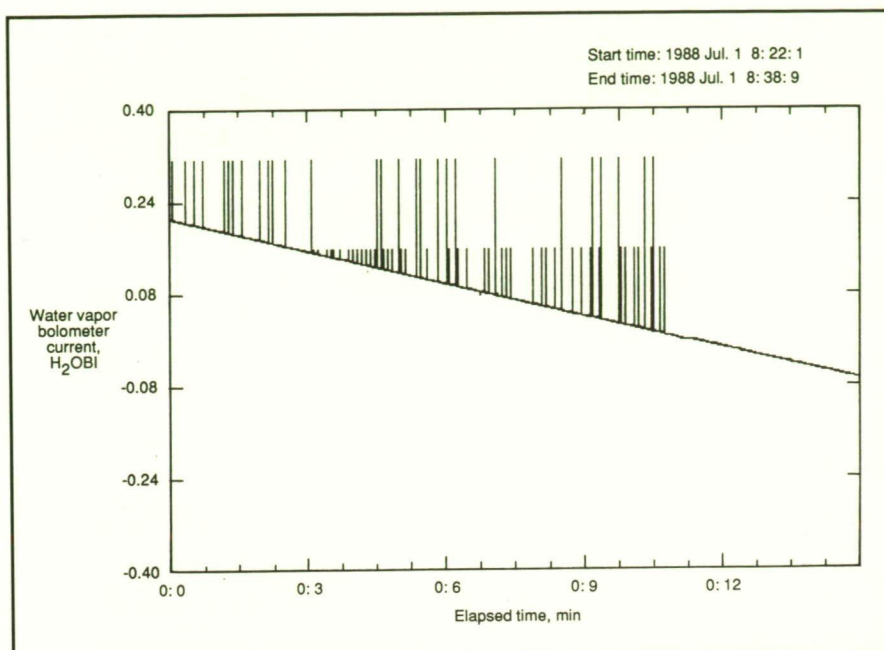
shows the differences in the total column ozone between the beginning of August and the end of September. Differences of 120 Dobson units (DU) are apparent poleward of 60°S. This model represents a significant enhancement for theoretical analyses and interpretation of observations of polar ozone depletion and other potential global change phenomena. (William L. Grose, 45820, Richard S. Eckman, Richard E. Turner, and W. Thomas Blackshear) Space Directorate

Spike Detection Algorithm for HALOE Test Data Analysis

A simple yet effective digital spike detection algorithm was developed as part of the Halogen Occultation Experiment (HALOE) GSE (Ground Support Equipment) computer software Quick-Look system. The technique was originally designed for application during EMI (electromagnetic interference) testing. This software feature was later realized to be an effective way of detecting digital noise spikes, not only during EMI testing, but also during many other testing circumstances. This technique uncovered the HALOE digital noise problem.

The technique consists of establishing a baseline of expected deltas and then comparing expected deltas with actual deltas during a test. The deltas are determined by calculating the average absolute change in a given parameter from one test point to the next. For the HALOE 8 Hz parameters, only 1 Hz calculations were made because these proved sufficient to detect digital noise. A spike was usually defined as any delta exceeding two times the average delta. Any parameters that

CIO mixing ratio (ppbv) versus pressure on model day 250 (September 10) at 75°S latitude (top). Zonally averaged total odd nitrogen (ppbv) versus latitude for model day 250 (middle). Difference of total ozone (Dobson units) at 45 mb between July 30 and September 30 (bottom).



Example of HALOE digital noise.

were determined to have spikes then were plotted and examined more closely.

(William L. Edmonds, 47196)
Systems Engineering and Operations Directorate

HALOE Quick-Look System

Testing of the HALOE instrument presented some challenging requirements for real-time and near-real-time computer GSE software support. The original GSE computer hardware chosen for HALOE consisted of an HP1000 computer and associated IETS (Integrated Electronic Test Set) hardware. During the initial testing at Langley Research Center, a need for greater real-time display and analysis of HALOE data was realized.

A system consisting of several IBM-compatible computers with General-Purpose Interface Buffer (GPB) interfaces was developed.

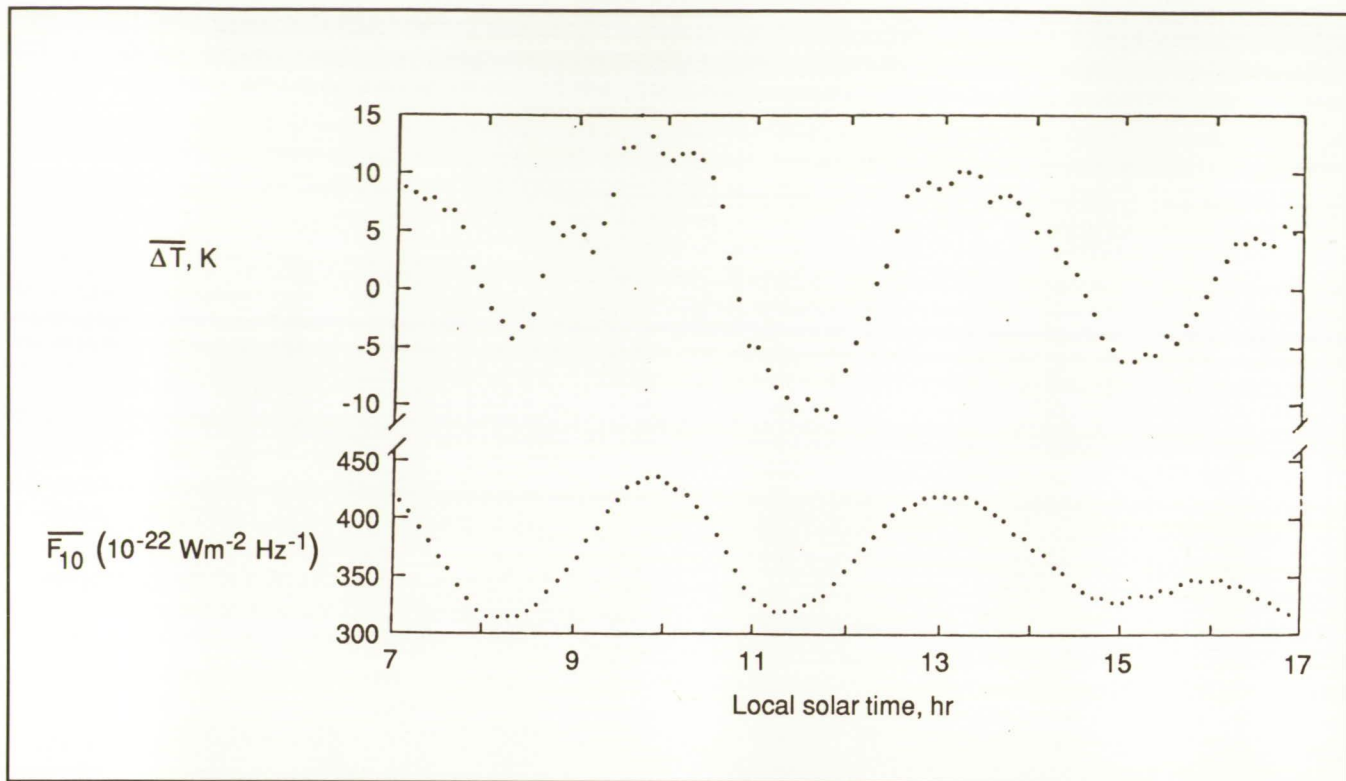
The GPIB interface cards enabled the rapid (near-real-time) transfer of HALOE major frames of data from the HP1000 computer to the IBM compatibles. Software developed in Turbo Pascal then was used to extract over 100 parameters each second. The parameters then were checked against red and yellow limits and displayed in green, yellow, or red on a color monitor. Audible alarms for some of these parameters also were used. Screen plotting and HP color pen plotting capabilities also were important features of this Quick-Look system.

(William L. Edmonds, 47196)
Systems Engineering and Operations Directorate

Venus Cooling Mechanism Isolated-Impact on Mars and Earth

With the arrival of the Pioneer Venus Orbiter at Venus, the dayside atmosphere at 150 km was discovered to be much colder than expected. The only additional mechanisms that were thought to provide a strong enough additional cooling to account for this were the collisional excitation of the CO₂ bending mode by atomic oxygen with subsequent radiation at 15 μ m (O-CO₂ cooling) and downward eddy heat transport (eddy cooling). However, it was not clear which of these mechanisms was the dominant one. A study was performed using the Pioneer Venus Orbiter Atmospheric Drag (OAD) data, and it was discovered that the atmosphere responds to solar extreme ultraviolet variations related to the 27-day rotation of the Sun.

Shown in the figure are the 27-day variations in inferred temperatures relative to mean conditions as a function of local solar time and related to a solar activity index corrected to the Venus location. Detection of these 27-day variations has now led to another finding. It was discovered that in order to have both the observed amplitude 27-day variations and the cool dayside temperatures, the O-CO₂ radiative mechanism had to be the dominant additional cooling mechanism in the Venus upper atmosphere. Over the 11-year solar cycle, this mechanism should act as a thermostat in the Venus upper atmosphere minimizing temperature variations. However, in the upper atmosphere of Mars, where the atomic oxygen to CO₂ ratio is much lower than on Venus, this mechanism will not be as effective, thus resulting in much larger 11-year variations that need to be carefully considered when planning future Mars missions.

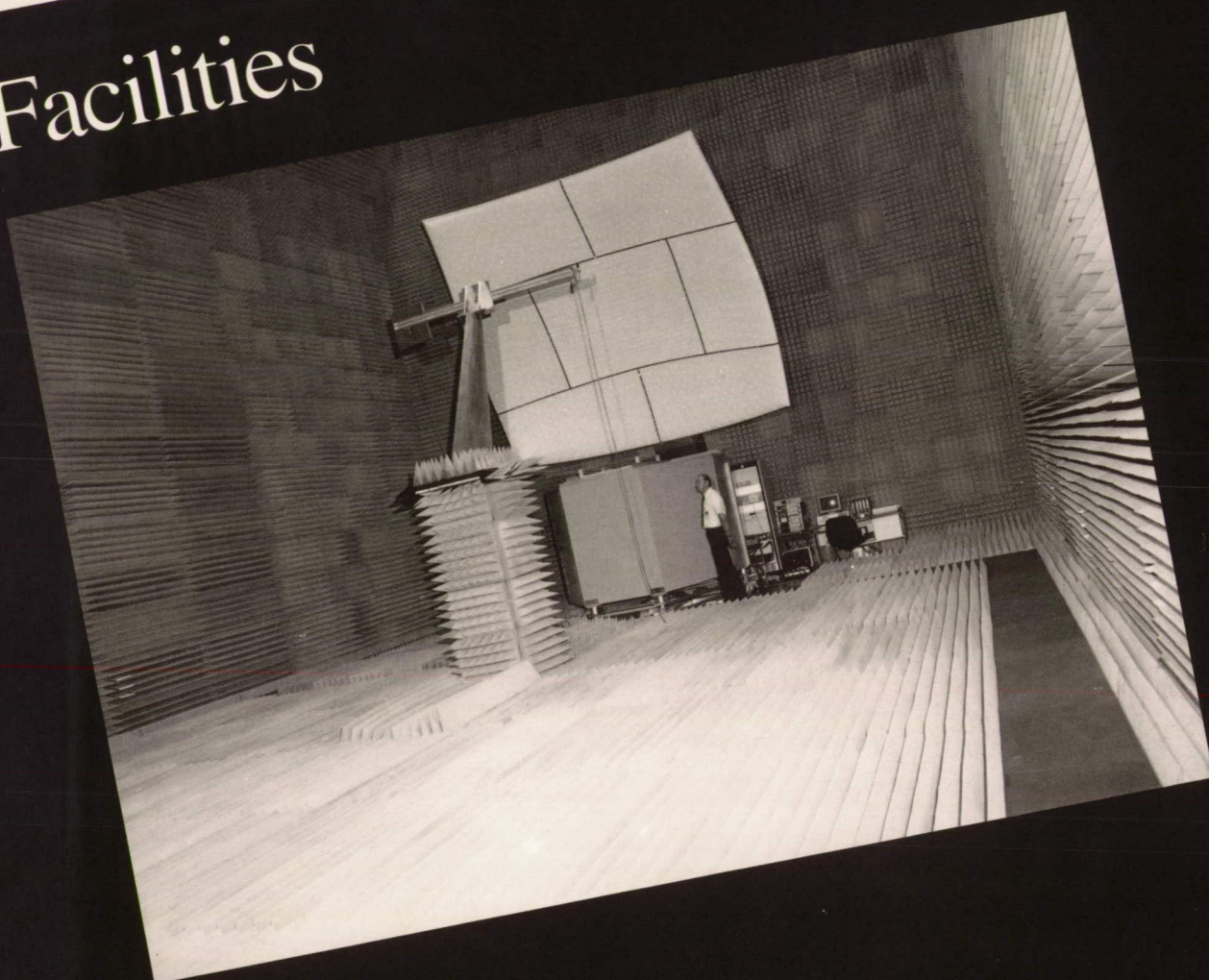


Twenty-seven day variations relative to mean conditions on Venus. Thermospheric temperature residuals ($\overline{\Delta T}$) based on Pioneer Venus OAD data and 10.7-cm solar activity index (\overline{F}_{10}) corrected for the Earth-Sun-Venus angle and Venus-Sun distance. Second diurnal survey (December 5, 1979 to March 6, 1980). 11-day running means.

The O-CO₂ cooling mechanism isolated on Venus also should result in substantial cooling of the Earth's upper atmosphere with the doubling of CO₂ in the next century. Mesospheric temperatures should drop 10°C, and densities at 100 km should drop by a factor of 2.

(Gerald M. Keating, 45804, and S. W. Bougher, Univ. of Arizona)
Space Directorate

Facilities



Bolt Tension Monitor

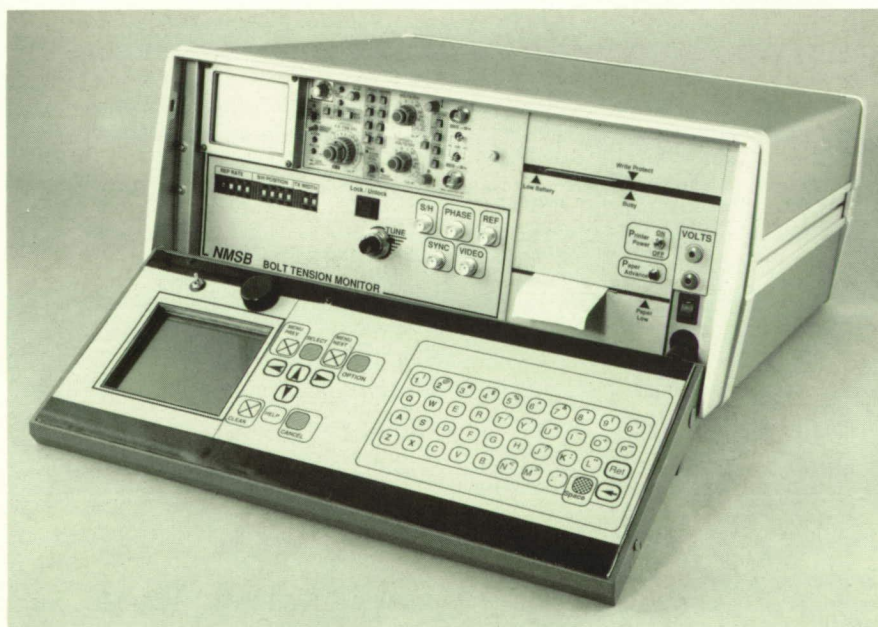
The proper tightening of bolted joints is one of the prime concerns of the aerospace community. The stringent weight-to-strength requirements of aerospace craft often preclude the over-design of critical fasteners to the extent of ground-based systems. Typically, a bolted joint is tightened to a given load by the use of a wrench that is rotated to a specified torque. Unfortunately, the torque required to tighten a bolt primarily represents the work required to overcome frictional forces, not the clamping force applied to the joint. Consequently, any small changes in lubrication or thread geometry may result in drastic changes in bolt load for a given torque.

Researchers at Langley Research Center recently have developed a portable bolt tension monitor (BTM) which uses ultrasonic sound waves to accurately measure bolt load (as shown in the figure). Although several commercial ultrasonic systems are available, the BTM is

unique in that it uses a pulsed phase-locked loop (P2L2) to measure load on a wider range of bolt geometries and with greater accuracy than current systems.

To use the BTM, the operator attaches an ultrasonic transducer to one end of the bolt and tunes the oscillator of the P2L2 to the desired frequency. Next, the system is locked, and an initial frequency is read by the computer. As the bolt is tightened, the speed of sound changes, and the bolt elongates. These two factors alter the effective path length of the ultrasonic signal, and the P2L2 shifts its operating frequency to maintain lock. The frequency shift is directly proportional to the change in load of the bolt. As an example, one class of bolts that has been tested with the BTM shows a frequency shift of more than 42 kHz for a 40 000-lb change in load.

The BTM consists of a computer, display, keyboard, printer, removable storage system, voltmeter, oscilloscope, frequency counter, and P2L2 circuit. The software is menu driven



BTM that uses ultrasonics to monitor load in bolt.

L-90-4503

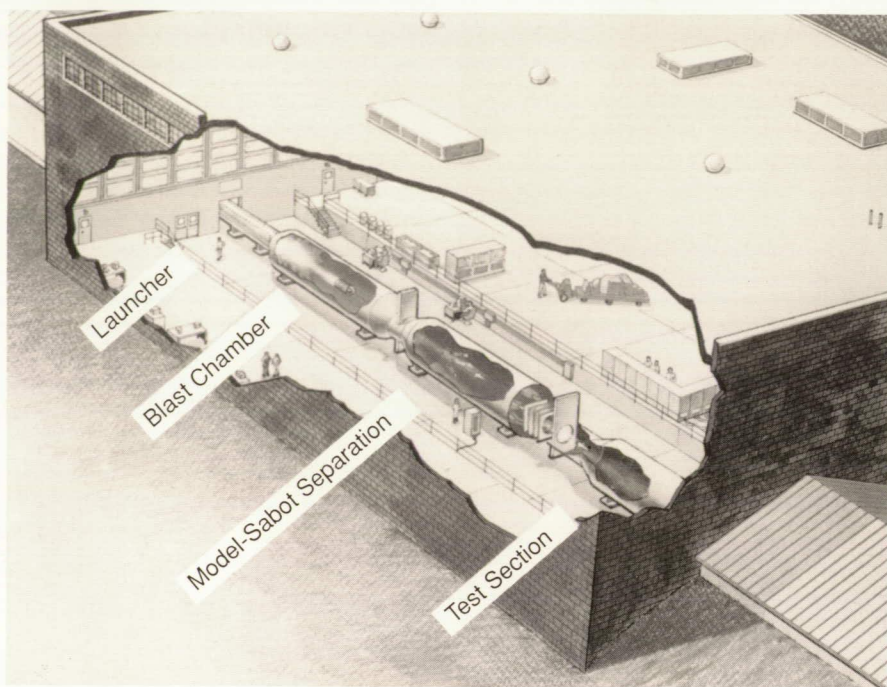
with on-screen help and is designed to allow technicians to use the instrument with a minimum of training. In addition, the BTM provides full data archiving of the tightening procedure and a free-run mode to experiment with different transducer/hardware setups before actual tightening. The system also provides a graphical as well as optional audible indication of load. NASA is currently negotiating the transfer of the BTM technology to industry for commercialization.

(Daniel Perey, 44796)
Electronics Directorate

Technology Developments for Advanced Hypervelocity Aerophysics Facility (AHAF)

Several technology studies have been conducted in support of the effort to develop an advanced hypervelocity test facility for NASA. The facility as proposed by Langley Research Center would be a hypervelocity aeroballistic range utilizing an advanced technology launcher to accelerate large (12-in. to 16-in. diameter) instrumented models to entry flight velocities and densities in a test chamber containing arbitrary gases representative of the Earth's and other planetary atmospheres. The models would be large enough to contain extensive surface pressure and heat-transfer instrumentation as well as onboard accelerometers and gyros.

The primary factor governing the performance of the model launcher (a large light-gas gun, a ram accelerator, or an electromagnetic launcher) is the total launch mass (the model and the sabot, which adapts the model to the bore of the launcher). A model/sabot integration study was conducted utilizing current ballistic range technology. The results of the study



Model launch sequence.

L-90-1292

indicated that the sabot mass could be as high as 10 times the model mass, depending on the model. The launcher performance requirements increased 2.8 times that originally estimated prior to the study. Additional studies of model/sabot mass utilizing advanced kinetic kill weapons technology were initiated with the U.S. Army Research, Development, and Engineering Center at Picatinny Arsenal, New Jersey. The objective of this study is to reduce the model/sabot mass, and consequently the launcher performance requirements. A six-degree-of-freedom lifting-model flight dynamics study was initiated to determine the flight distance required to generate adequate model oscillations for aerodynamic data extraction, the feasibility of launching models at high angle of attack, and the resulting model excursions. Preliminary results indicated that the model completed one oscillation in pitch in 1000 ft and that the flight excursions were within acceptable limits.

Initial results of an in-house study of a large light-gas gun launcher using the Arnold Engineering Development Center (AEDC) Interior Ballistics Code indicate that such launchers can be scaled to large diameters without loss of performance.

A study of the effects of launch bore diameter on the performance of an electromagnetic launcher (EML) by the Los Alamos National Laboratory showed that scaling up to an 18-in. bore diameter was feasible.

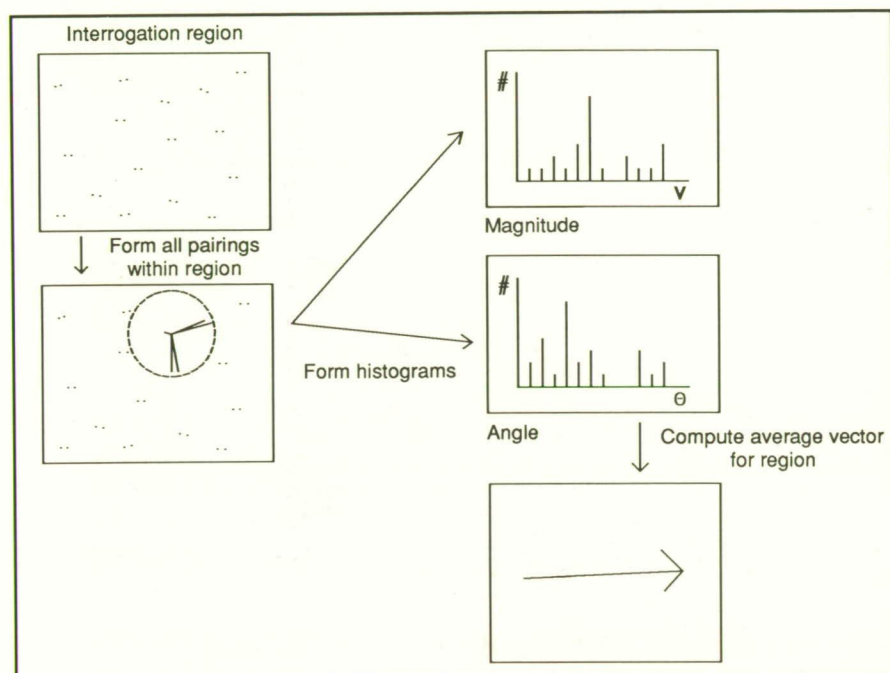
(William I. Scallion, 45235, Robert D. Witcofski, and David J. Carter, Jr.)
Space Directorate

Development of Particle Image Velocimeter for Rapid Global Flow Field Mapping

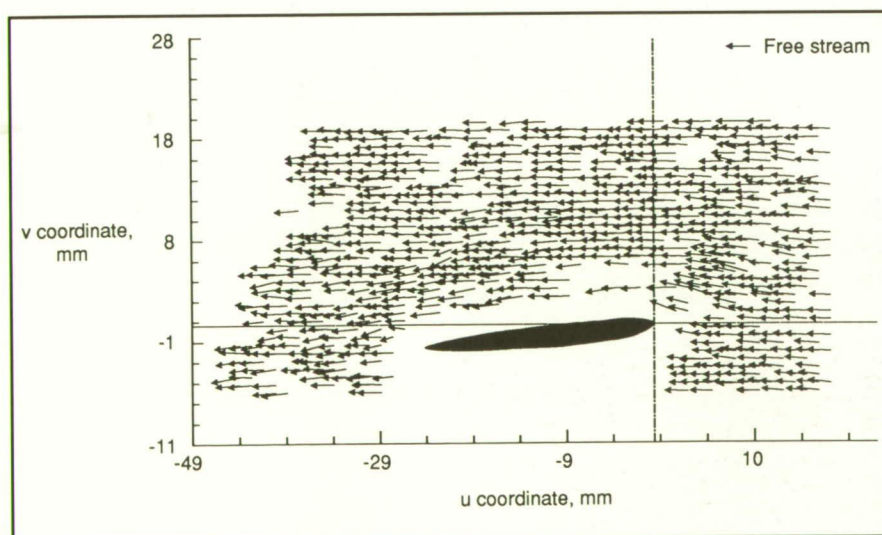
A particle image velocimeter (PIV) system has been developed which allows rapid global flow field mapping. The basic concept of the

system is to obtain velocity vectors at many points in the flow field of interest by tracking the motions of individual tracer particles introduced into the flow. The system consists of two major parts. The first is a data acquisition system capable of producing a photographic negative containing double exposures of imaged tracer particles illuminated by a thin

double pulsed light sheet in the flow field of interest. Two 140-mJ doubled Nd:YAG lasers operating at a wavelength of 532 nm with 10 nS pulse duration are used to produce the pulsed light sheet. The choice of using two lasers allows for control of light sheet pulse separation over a large range, with the separation typically adjusted to yield a tracer particle image separation of 100 μm .



PIV vector extraction technique based on vector histograms.



Flow field around NACA 0012 airfoil.

The second part of the system is an interrogation/data analysis system capable of automatically scanning and detecting individual particle motions to measure flow velocities. The negative obtained with the acquisition system is mounted on an x-y translation stage and interrogated by imaging 1 mm² to 4 mm² regions onto a Charge-Coupled Device (CCD) camera connected to a frame buffer. The frame buffer transfers the images to a minicomputer/array processor system for analysis. A unique feature of the analysis system is the use of a spatial domain technique based on vector histograms to estimate the most likely vector in individual regions of the negative. The technique, illustrated in the first figure, consists of forming a map containing the centroid locations of all particle images in the interrogation region. Each centroid is surrounded by a circular region (determined by the maximum expected velocity) in which all possible pairings between the centroid and all other centroids in the region are made. The ensemble of all pairings is used to generate histograms of vector magnitudes and angles from which the average vector in the interrogation region is extracted. An example vector map of the flow field around an NACA 0012 airfoil at an angle of attack of 5° obtained via particle image velocimetry is shown in the second figure.

(William M. Humphreys, Jr., and William W. Hunter, Jr., 44601)
Electronics Directorate

Calibration and Characterization of Solid-State Cameras

The calibration and the characterization of solid-state video cameras are currently of interest for machine vision, robotics, and video photogrammetric applications, especially when using video frame grabbing boards that may have several synchronization options and varying digitization rates. Several optical bench techniques have been developed at Langley Research Center which are suitable to test solid-state video cameras. These techniques are particularly suited to test for apparent changes in calibration parameters, and they do not suffer the inherent correlations noted for some photogrammetric calibration methods.

In the figure, a laser-illuminated displaced reticle technique is depicted which is used to determine calibration parameters to convert from pixels to engineering units. After the basic sensor/grabber calibration

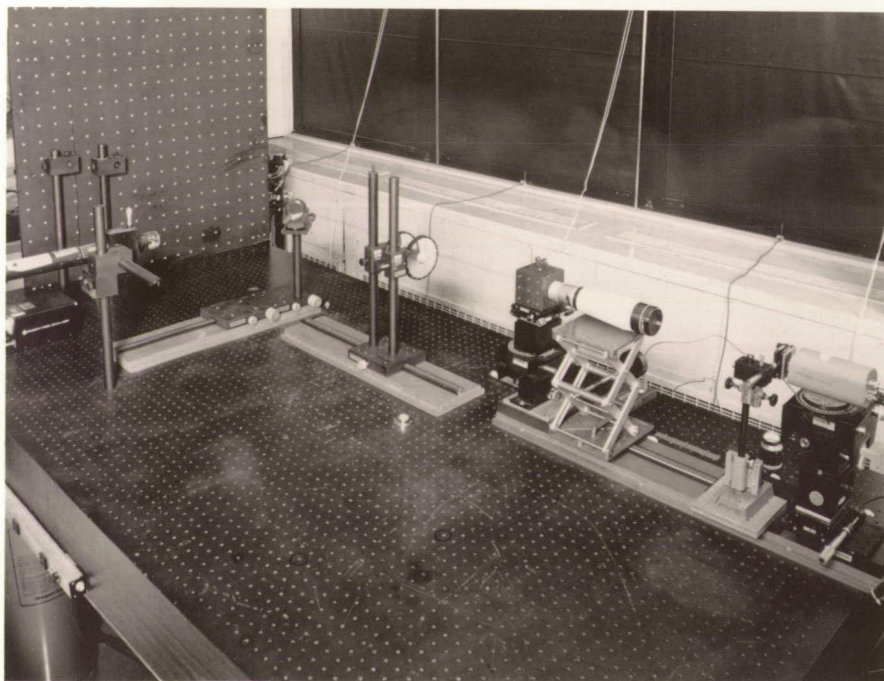
parameters are determined, the lens is replaced on the camera, and the photogrammetric principal point and the point of symmetry are determined. The principal distance and various lens distortion coefficients then are determined from images of a calibrated target plate (as shown in the left side of the figure). The development of these calibration and characterization techniques has contributed to the success of several photogrammetric applications where it was necessary to use video cameras instead of the more traditional film cameras.

(A. W. Burner, W. L. Snow, and W. K. Goad, 44635)
Electronics Directorate

Thermal/Structural Analysis of Shaft Disk Region of National Transonic Facility

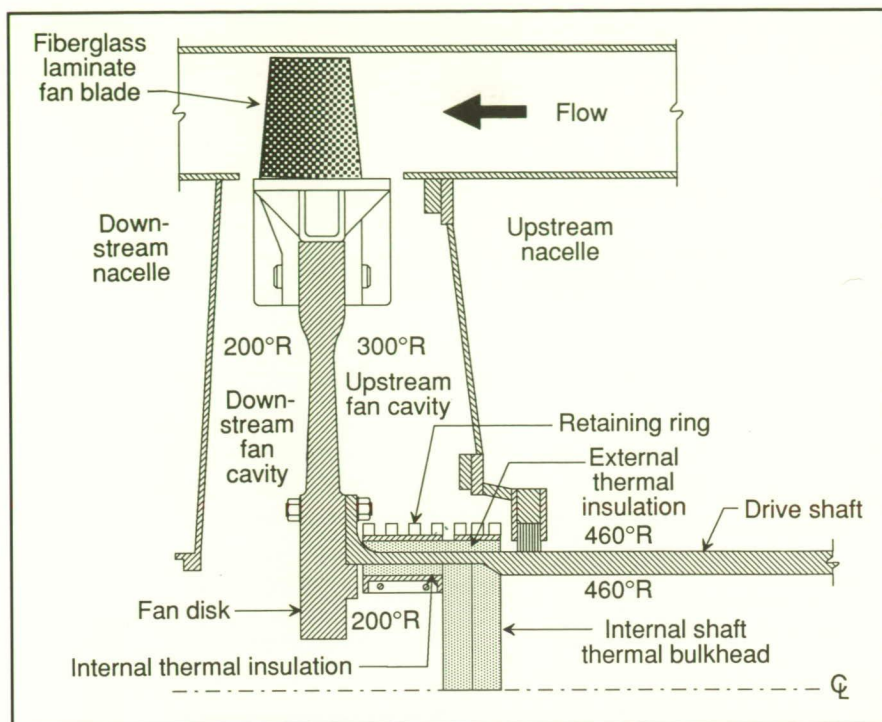
The National Transonic Facility (NTF) wind tunnel at Langley Research Center is a closed-loop cryogenic wind tunnel that uses gaseous nitrogen as a test medium. The 8.2-ft square test section is designed to achieve transonic flow (Mach 0.8 to 1.2) using a fan-driven system as shown in the first figure. The original design of the drive system provided for an external thermal insulation barrier (ETB) around the portion of the drive shaft exposed to the fan cavity to minimize the axial thermal gradients along the shaft. However, due to the high energy associated with rotating systems and the critical location of the insulation system, it became necessary to study the effect of removing and operating without the ETB. The objective of the analysis was to determine what effect removing the ETB would have on the stresses on the shaft, disk, and bolts holding the two together.

To accomplish this, a detailed thermal/structural finite-element analysis of the shaft-disk interface was performed. The maximum stresses on the three components were determined for several configurations and conditions with and without the external thermal insulation. The plot shown in the second figure is of effective stress versus time, with and without the ETB under worst-case conditions. These stress results were compared to the original analyses to assess the effect of removing the external thermal insulation on the proposed future operation of the shaft/disk structures of the fan-driven system. Although the stresses were higher without the external insulation, the stresses did meet all evaluation criteria. In addition, all components have infinite cycle life. Therefore, the structural

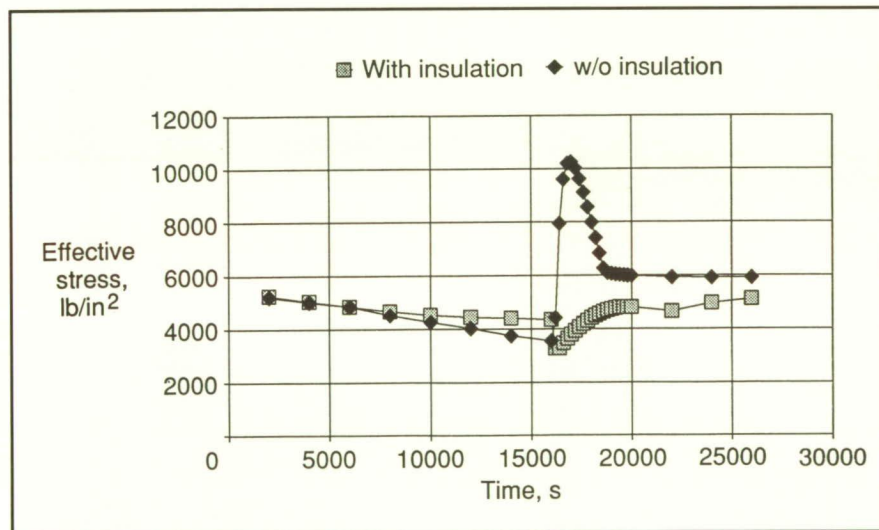


Optical bench setup for calibration of solid-state cameras.

L-90-1220



Cross section of NTF fan region.



Effective stress on the shaft versus time, with and without the external isolation.

integrity of the shaft-disk region has been determined not to be compromised if the external insulation is removed.

(Peyton B. Gregory and Anne D. Holland, 47242)

Systems Engineering and Operations Directorate

Use of Oxygen-Free Contact Tip in GMAW Applications

Standard Gas-Metal Arc Welding (GMAW) contact tips are manufactured from a low-grade, oxygen-impregnated copper. These tips have problems with electrical erosion when used for robotic welding of heavy weldments. Problems resulting from electrical erosion include joint alignment for filler metal deposition and an excessive amount of downtime due to contact tip removal and replacement.

The GMAW contact tips have been fabricated from oxygen-free electron-grade copper. This material has significantly reduced the electrical erosion wear rate. The material used for manufacture of the prototype contact tip was an oxygen-free copper (ASTM F-68-82) commonly used for electronic devices. Twelve prototype tips were manufactured from the oxygen-free electron-grade copper. These tips have been tested in a real-time robotic welder by the Caterpillar Company, Incorporated. Experimental data show that oxygen-free contact tip material has reduced electrical erosion, improved electrical conductivity, and reduced mechanical wear by up to 37.5 percent. Robotic welding productivity has increased, while equipment downtime has been minimal.

This application is intended primarily for users of robotic welders. Utility extends beyond the aerospace industry to the mass production of various types of hardware, including heavy off-highway construction equipment.

(J. F. Pike, 44547)

Systems Engineering and Operations Directorate

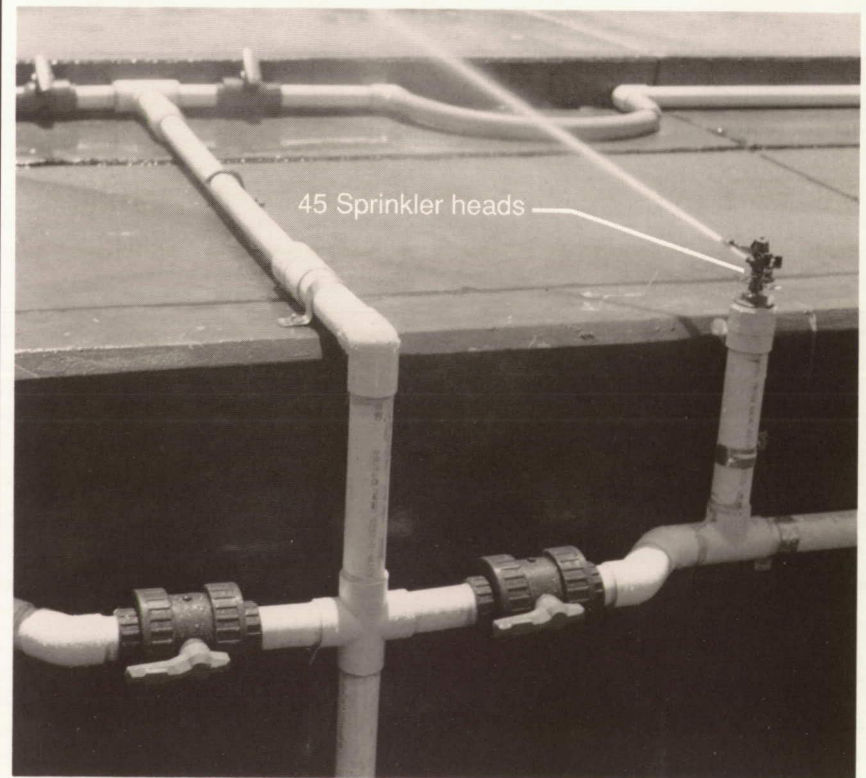
Addition of Automated Wetness System to Aircraft Landing Dynamics Facility

The Aircraft Landing Dynamics Facility (ALDF) is a major facility that provides a relatively low-cost means to study new landing gear concepts and tire designs. The ALDF consists of a large test carriage that is propelled at speeds up to 175 knots by a high-pressure water jet down a specially designed track. Essentially any landing gear can be mounted on the carriage, including exhibiting new concepts, and any runway surface and weather condition can be duplicated on the track.

Because of its uniqueness, this facility is under heavy demand for usage. With the implementation of the joint NASA/Federal Aviation Administration Radial Tire Program on ALDF, facility operation time is in even greater demand. The test schedule for ALDF is completely filled over the next 5 years, and a considerable backlog of research programs for the facility exists. Consequently, it is very desirable to improve the operational efficiency of the facility. One improvement that has been made is the installation of a test runway wetting system using 45 sprinkler heads to wet the entire 1800-ft length of the runway. This system is shown in the figure. The newly installed runway wetting system not only reduces the time needed to get set up for wet-runway tests and the effort to maintain the conditions (for example, on a hot summer day), but also it provides for better test data because it maintains a more consistent wetness condition (i.e., water depth) than the old manual system. This same wetting system can be used in combination with a system of rubber dams to maintain a flooded runway test condition. This modification to ALDF will greatly enhance the productivity of this unique national



L-90-8198



L-90-8199

Wetting system components.

ORIGINAL PAGE
BLACK AND WHITE PHOTOGRAPH

facility and significantly accelerate the development of the data base on radial-belted aircraft tires.

(Robert H. Daugherty and Sandy M. Stubbs, 41309)

Structures Directorate

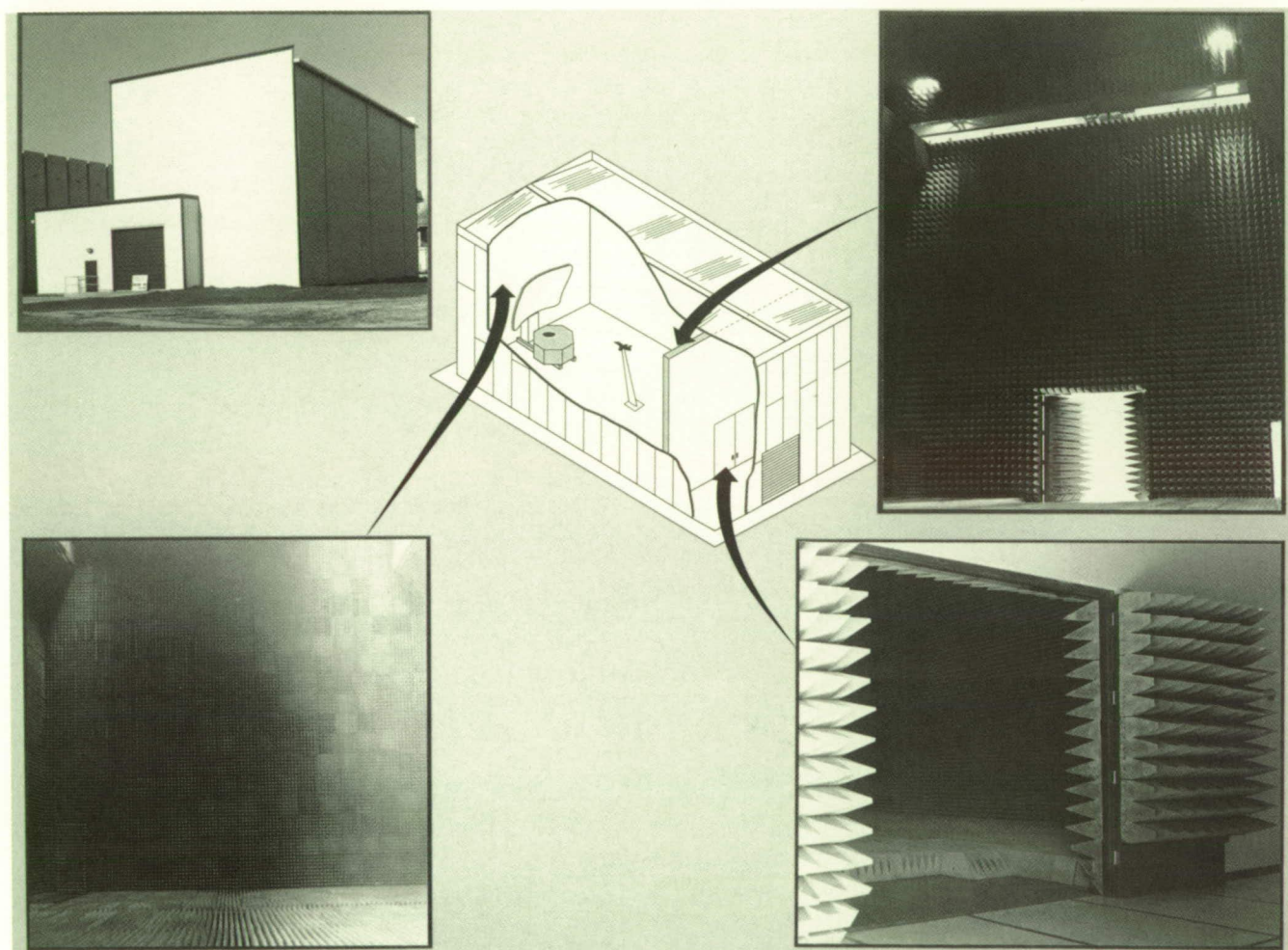
Experimental Test Range

The Experimental Test Range (ETR) is a new facility at Langley Research Center which was needed to conduct research for the advancement of measurement technology in

compact range systems. The ETR consists mainly of a radio frequency (RF) shielded room that is 40 ft wide by 40 ft high by 80 ft long. The need for this new facility was immediate because research was needed in new methods and techniques in compact range technology to meet future requirements.

The facility was completed in such a timely manner early in 1990 that it enabled the immediate assembly and initial testing of the Langley-developed advanced compact range reflector (ACRR) system. The ACRR system, consisting of a

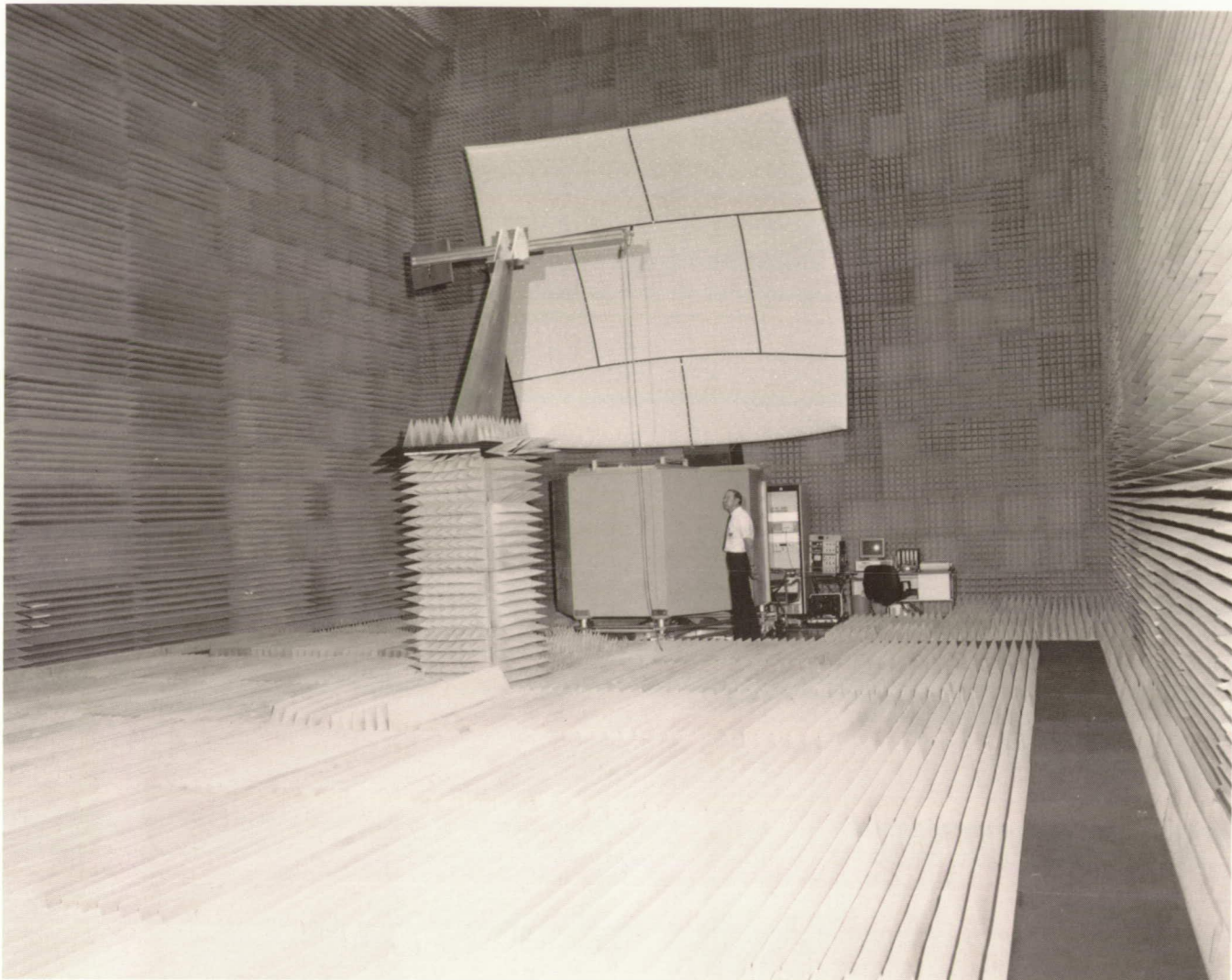
blended-edge main reflector and an ellipsoidal subreflector, was designed and fabricated in-house at Langley. The main reflector, approximately 16 ft by 16 ft, was fabricated in seven separate pieces. Each individual piece had several hundred optical targets installed to permit the use of optical photogrammetry to measure the surface of the total assembled reflector. These data are currently being processed to determine the surface accuracy of the reflector. Currently, testing is under way to complete the electrical alignment of the total system. Once the alignment is completed, an RF evaluation of the



Views of ETR facility.

L-90-8078

ORIGINAL PAGE
BLACK AND WHITE PHOTOGRAPH



ACRR system in ETR.

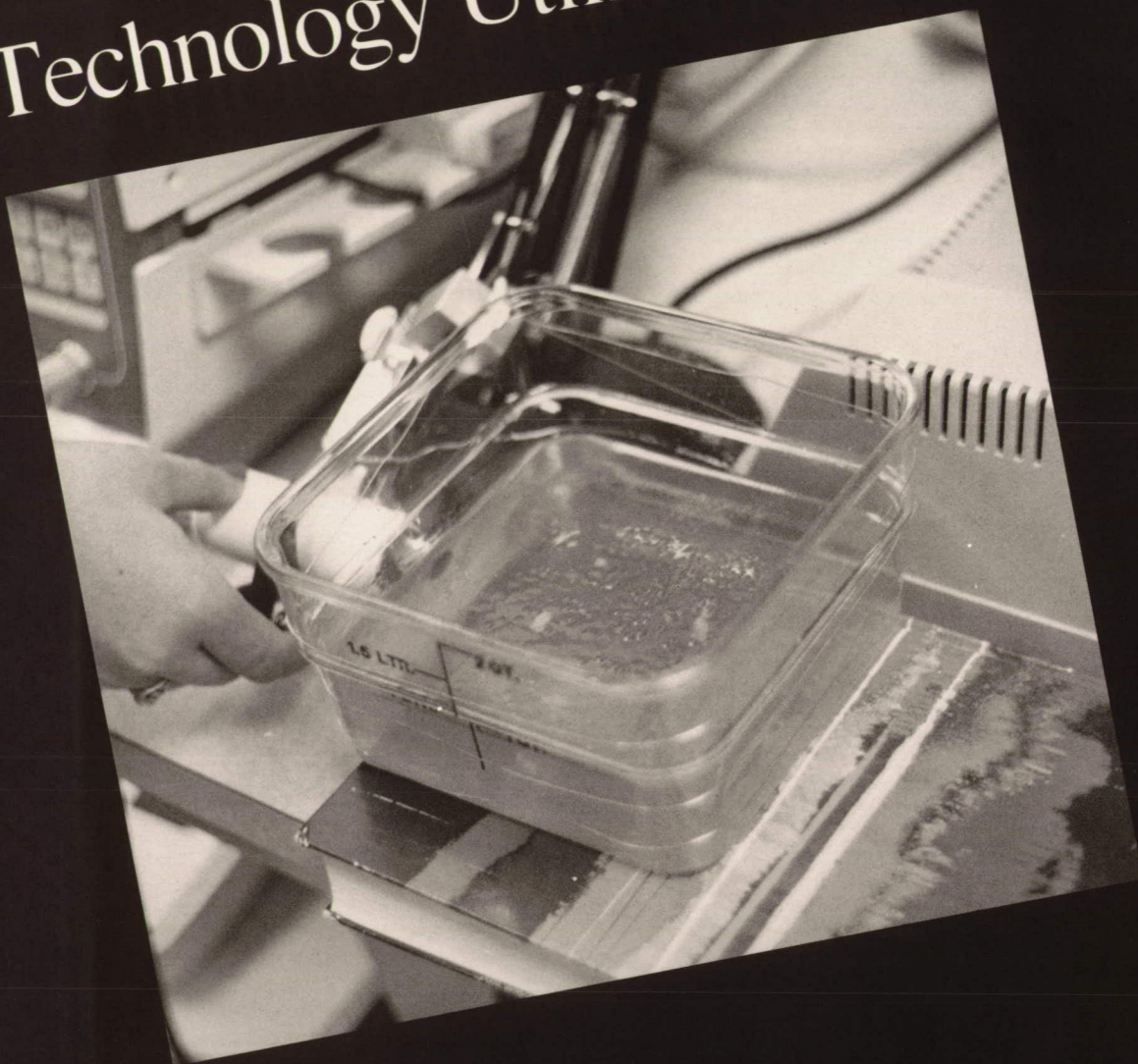
L-90-7956

ACRR system performance will be conducted over the 2 GHz to 18 GHz frequency range.

Information obtained during this evaluation will be utilized to design an optimum larger reflector system for ETR, provide additional design data needed for the proposed Electromagnetic Scattering Laboratory final design, and provide new compact range technology to industry.
(Bruce M. Kendall, 41795)
Flight Systems Directorate

ORIGINAL PAGE
 BLACK AND WHITE PHOTOGRAPH

Technology Utilization



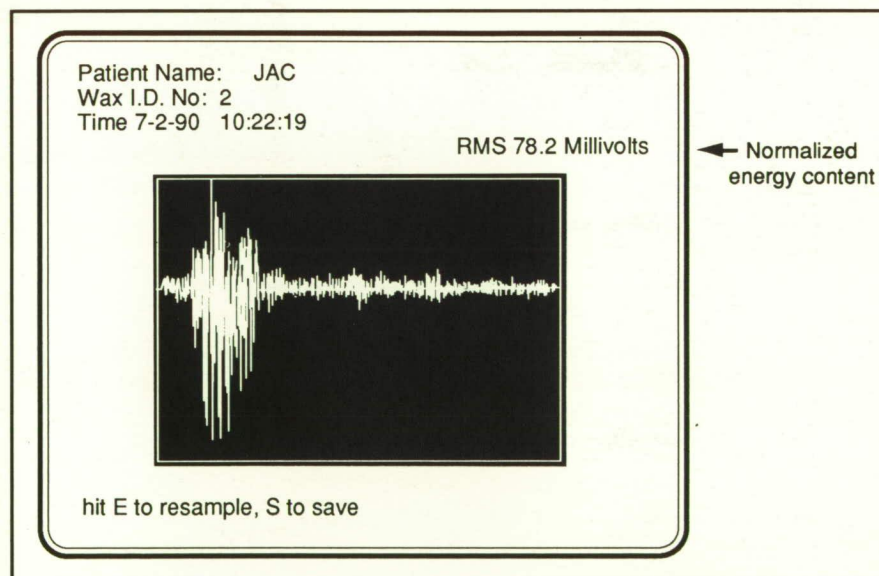
Ultrasonic Tissue Thermometry System

Hyperthermia treatments for cancer involve raising the temperature of a tumor by the application of microwave or ultrasonic radiation. Hyperthermia is a cancer treatment with some potential, but its application has been limited, partially because of the problems of temperature monitoring. The currently used technique for monitoring internal temperatures during hyperthermia involves the insertion of multiple catheters containing thermocouples. The thermocouples are moved back and forth within the catheters to obtain a thermal map of the area as the temperature is elevated. Because this procedure is repeated at intervals over a period of several months, it necessitates considerable trauma to the patient. The risk of infection along the needle tracks and the possibility of encouraging metastasis of the tumor also exist.

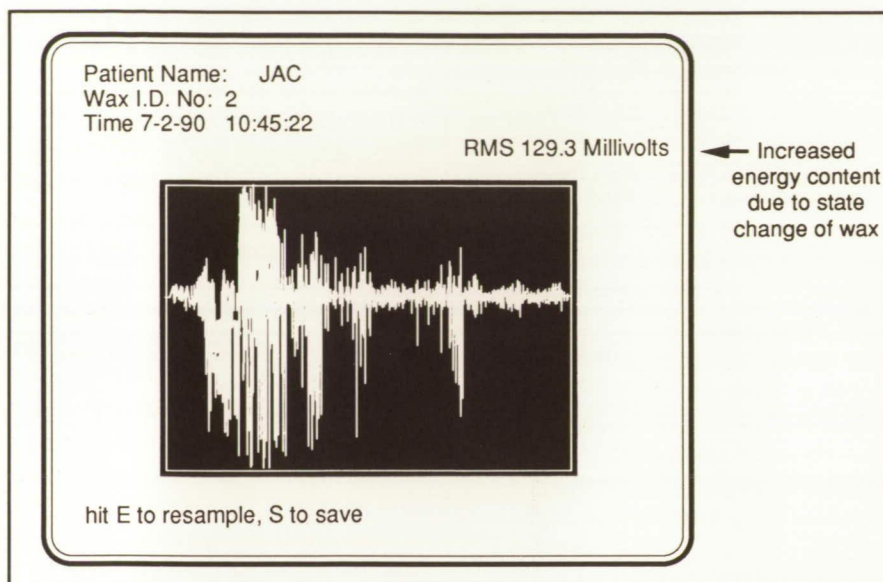
An Ultrasonic Tissue Thermometry System has been developed by

researchers at Langley Research Center which has the potential to provide improved tissue temperature control during hyperthermia treatment. A material has been developed which can be implanted in or around a tumor, via hypodermic needle, in the form of a small bead. This material is nontoxic to the tissues and can be left in place in the body. Because implanting the bead involves only a one-time intrusion into the body, the chance of secondary complications as well as trauma to the patient is considerably reduced.

The implanted material is a waxy substance that has been modified to melt at the desired temperature. Using a medical ultrasound scanner, that change in state can be clearly seen and quantified. When the wax is cool, the ultrasonic response has a characteristic signal and energy level (as shown in the first figure). As the region of the tumor is heated to the desired temperature and the wax melts, the signal and energy level are distinctly different (as shown in the second figure). When the tissue cools, the wax will resolidify.



Screen display of Nondestructive Measurement Science Branch (NMSB) Tissue Thermometry System showing readout from one wax temperature bead implanted in tissue phantom at room temperature (22°C). Main signal is ultrasonic response to cold temperature bead.



Screen display of NMSB Tissue Thermometry System showing readout from same implanted bead after application of microwave radiation has elevated the temperature to approximately 43°C. Signal is ultrasonic response to hot-wax temperature bead and tissue immediately behind it.

The Ultrasonic Tissue Thermometry System now has been transferred to the Radiation Oncology Laboratory, Duke University Medical Center, for further studies. These studies initially will use the Langley-developed high-temperature tissue phantom and later will be used in animals having tumors.

A U.S. Patent No. 4513750 has been granted for the initial concept for this device.
(Eric Madaras, 44993, and Joseph S. Heyman)
Technology Utilization Program

Contact Lens Quality Monitoring System

Contact lenses are widely used by a large segment of the U.S. population, particularly the younger generation. The primary qualifications of a good contact lens polymer are softness, wettability, and high permeability for gases. At present,

no satisfactory quality monitoring system exists for contact lens polymers. Free volume in contact lens samples has been measured using Positron Lifetime Spectroscopy (PLS). These data, in conjunction with measurements of their saturation moisture content and Rockwell Hardness Numbers, have been used to establish acceptable criteria for high-quality contact lens materials.

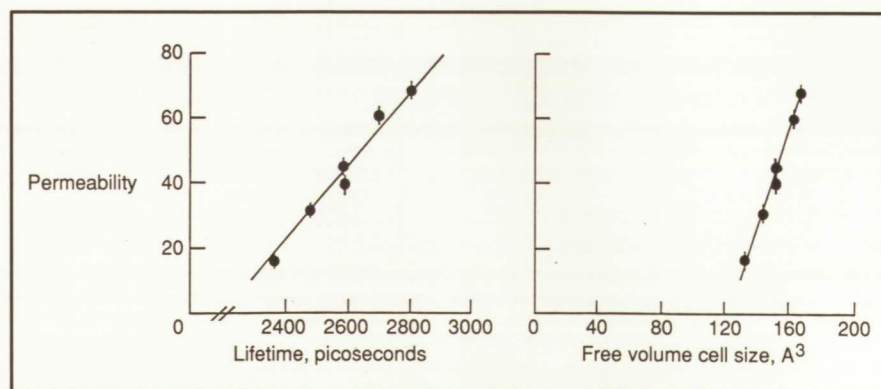
As a result of the extensive series of PLS and associated measurements

in several types of contact lens materials, some interesting conclusions have been drawn. The free volume fraction in contact lens samples containing fluorine atoms is the highest, but these samples pick up the lowest amount of moisture. This fact implies that free volume cells in these samples will not be flooded with eye fluids when in use, and this will facilitate their breathing as well as allow for a natural cleansing process. The samples containing fluorine are the softest, as would be anticipated on the basis of their high free volume fraction. The gas permeabilities are the highest in the samples containing fluorine. Typical results for oxygen are shown in the figure. The present study clearly demonstrates the unique role of PLS in characterizing contact lens polymers.

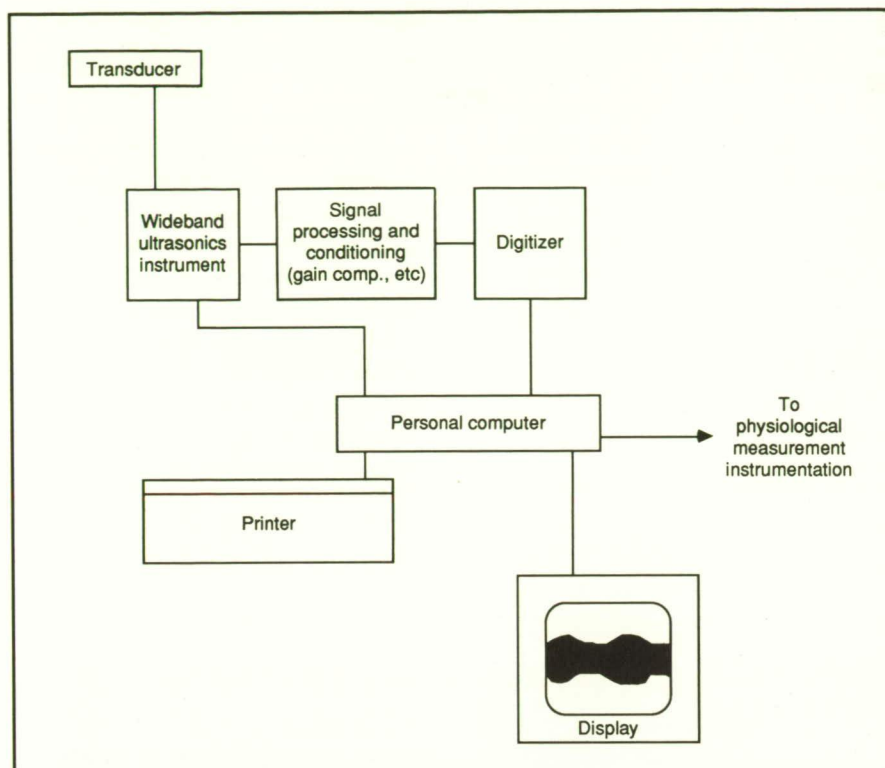
(Jag J. Singh, 44760, and Billy T. Upchurch)
Technology Utilization Program

Diaphragmatic Function Monitor

One of the most pressing problems facing the pulmonologist today is determining when patients, suffering from emphysema or similar breathing disorders, should be removed from their respirators. If the



Oxygen permeability versus PLS parameters in contact lens samples.



Block diagram of diaphragmatic thickness monitor.

patients are removed from the respirators too soon, they can develop respiratory distress. If, on the other hand, their breathing is mechanically assisted for too long, the muscles involved in breathing can lose tone. At present, the judgment as to when patients can be safely removed from respirator support is largely subjective.

To develop a measurement-based criterion for such patients, NASA, in cooperation with physicians at the Veterans Administration (VA) Medical Centers in Hampton and Dallas, initiated a project to apply Langley Research Center high-resolution ultrasonic instrumentation technology (developed for nondestructive evaluation of metals) to a measurement of diaphragmatic thickness. This measurement, in conjunction with other physiological measurements, can serve as a basis for an assessment of diaphragmatic fatigue.

A block diagram of the instrument developed in the Nondestructive Measurement Science Branch to perform this measurement is shown in the figure. As breathing occurs, the diaphragm contracts (and thick-

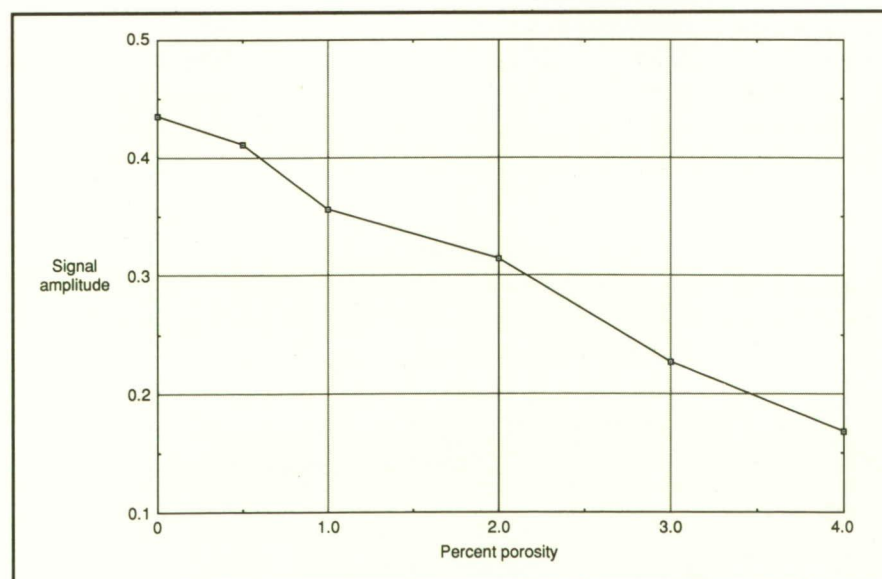
ens), causing it to move downward within the rib cage. By placing the ultrasonic transducer between the ribs, an image of diaphragmatic thickness can be obtained. Changes in thickness with time can be related to muscle tone, and they can be used to aid the pulmonologist in the decision-making process.

At present, the VA investigators are using a quick-look, M-mode device for their clinical studies, but a prototype A-scan device is currently being built. This instrument will be available for clinical testing in 1990. (William T. Yost, 44991)

Technology Utilization Program

Ultrasonic Monitor of Composite Porosity During Pultrusion

Pultrusion of composite parts offers a quick, inexpensive technique for fabrication of large quantities of a part. Currently, the parts are continuously fabricated and subsequently inspected for the presence of porosity and/or delaminations that may have resulted from variations in the



Effect of porosity on ultrasonic signal amplitude in pultruding graphite/epoxy.

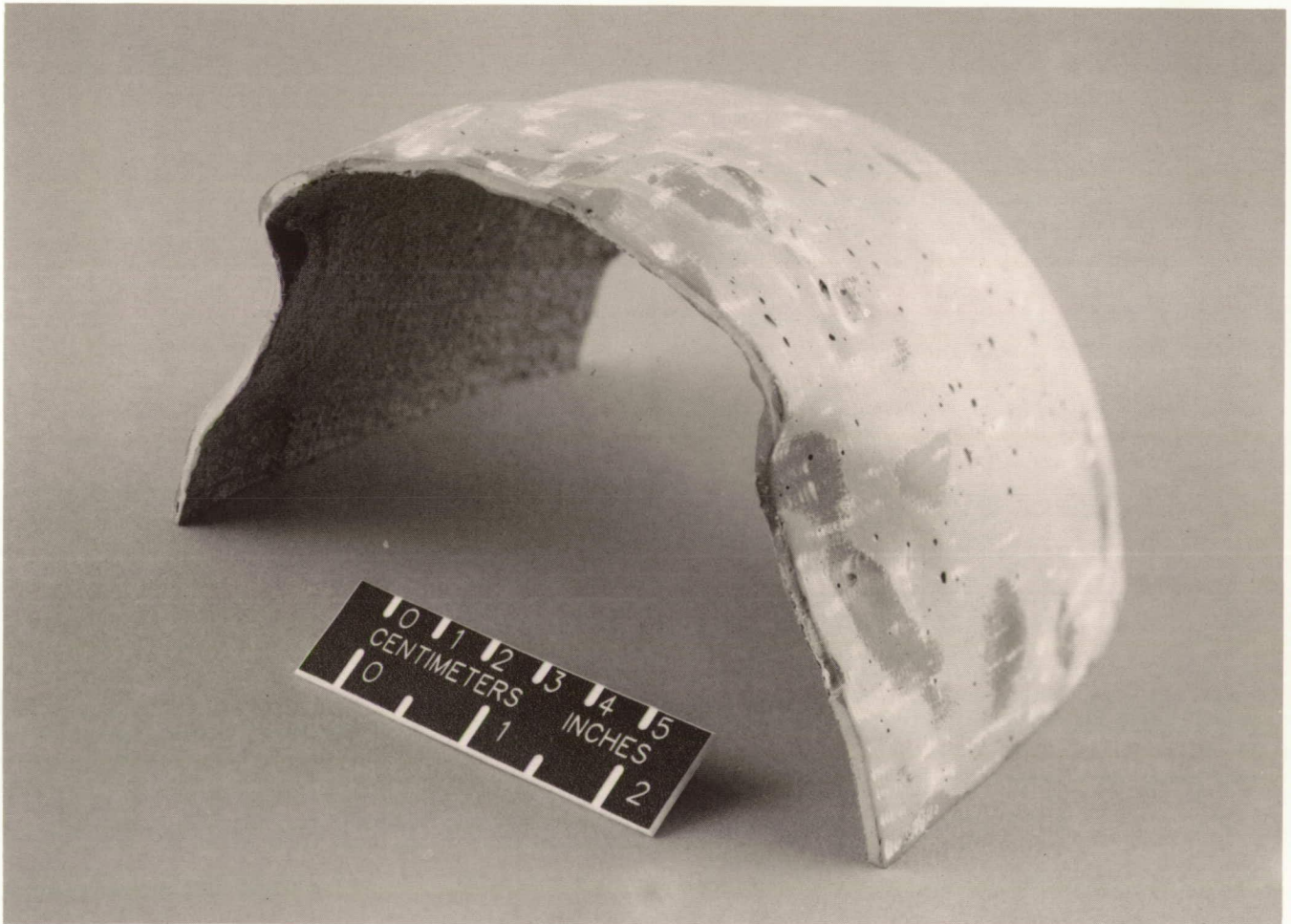
fabrication process. Should there develop a problem in the pultrusion process, the delay between processing and inspection can lead to the fabrication of large amounts of defective materials.

An ultrasonic technique has been developed which is applicable for inspection of the pultruded parts as they are fabricated. This technique consists of a series of special high-temperature ultrasonic transducers that are mounted to the exterior of the pultrusion die and nonintrusively characterize the composite as it moves through the die. Recent studies have shown that it is possible with this technique to detect porosity

levels of 1 percent in the composite during the fabrication process. The figure shows the change in signal level as a function of the induced porosity level measured during the pultrusion of a composite part. This technique offers the possibility of real-time feedback to enable correcting or discontinuing the process before the production of large quantities of defective parts, which subsequently must be rejected. (F. Raymond Parker, 44965)
Electronics Directorate

Custom Cranial Patches

The present method for filling cranial holes resulting from surgical procedures involves the surgeon hand-forming the patches from standard blanks of biocompatible materials. Not only is this procedure very time consuming, but also it results in cranial patches that are neither a perfect fit to the edges of the opening nor have the same interior and exterior surface as the original piece. A method is required by which customized cranial patches can be generated from CAT scans taken before and after surgery.



Automated custom cranial patch.

L-90-9404

ORIGINAL PAGE
BLACK AND WHITE PHOTOGRAPH

A program has been developed which uses a CAD/CAM-like approach to convert CAT scan data of human crania to data sets appropriate for machining cranial patches. A custom cranial patch has not yet been machined but cranial sections with realistic interior and exterior surfaces have been generated. This computer program will be refined, and work will be done with Ted McFadden (a retired neurosurgeon, formerly with the Eastern Virginia Medical School (EVMS)) to produce acceptable custom cranial patches. Once this ability is achieved, the program will be turned over to EVMS for clinical testing and further refinement, and a copy of the program will be sent to the Computer Software Management and Information Center (COSMIC). Currently, biocompatible materials that have the required strength and that can be molded and/or machined are being sought. During fiscal year 1991, a search will be initiated for a company interested in commercializing the custom cranial patch program. (Franklin H. Farmer, 42490)

Technology Utilization Program

Contributing Organizations

Aeronautics Directorate

The Aeronautics Directorate is composed of approximately 350 scientists and engineers engaged in basic and applied research in the various aeronautics disciplines and includes research wind tunnels, aircraft, and computers with a replacement value exceeding 1 billion dollars. The directorate is organized into four research divisions, a hypersonic technology office, and a facilities planning office, which conduct aeronautical research to advance the state of the art throughout the complete aerodynamic speed range.

The research divisions of the Aeronautics Directorate form a team whose mission is to develop advanced technology for future civil and military aircraft. Each division plays a unique role through application of wind tunnel testing, flight experiments, theoretical research, and computational efforts to advance the state of the art in aeronautics. The Advanced Vehicles Division conducts multidisciplinary advanced aeronautical vehicle studies to assess the benefits of discipline research advances and to identify potential new research thrusts. The Applied Aerodynamics Division conducts research on subsonic through hypersonic aerodynamics including propulsion integration using computational fluid dynamics techniques and a variety of wind tunnels including the 14- by 22-Foot Subsonic Tunnel, the National Transonic Facility, the 16-Foot Transonic Tunnel, and the Unitary Plan Wind Tunnel. The Flight Applications Division utilizes research aircraft to conduct experiments that complement the ground-based research effort of the Center with an emphasis on flight experiments, flight dynamics, and aviation safety. The Fluid Mechanics Division conducts theoretical, computational, and experimental research to advance the

state of knowledge in fluid mechanics as it applies to the design of advanced aircraft and missiles across the speed range and to hypersonic propulsion systems. The Hypersonic Technology Office coordinates broad-scope hypersonic vehicle research and technology programs including those involving the National Aero-Space Plane (NASP).

The Aeronautics Directorate has had a number of significant accomplishments this past year. Comprehensive flight, wind tunnel, and computational evaluations of a vortex flap applied to the Langley Research Center F-106 airplane have validated the concept for dramatically increasing climb lift-to-drag ratios. The extremely successful Boeing 757 hybrid laminar-flow control (LFC) flight experiment achieved extensive runs of laminar flow (back to 50 percent chord at Mach 0.81) the first time the LFC system was activated. Lift and drag changes on a two-dimensional wing section due to heavy rain were quantified in large-scale, simulated rain environment testing at the Aircraft Landing Dynamics Facility, and these impacts were evaluated in ground-based piloted simulations to develop safe operating procedures in adverse weather. Increased fuel mixing for scramjet engines was achieved with wall-mounted ramp injectors in a supersonic stream. The first comprehensive measurements of a complete flow field mapping in a real combustor flow were made using coherent anti-Stokes Raman spectroscopy. High-Speed Civil Transport studies show that composite structures potentially offer the largest weight reduction and economic advantage of any single technology.

Electronics Directorate

The Electronics Directorate is responsible for planning, directing, and evaluating research and applications programs in the areas of measurements and computer science which will benefit the Center's aerospace activities. This directorate also manages the Center's instrumentation, data acquisition, and data processing resources through the four divisions, each of which has specific support functions.

The Analysis and Computation Division is responsible for the development and application of mathematical and computer theory to the solution of computational problems arising from theoretical and experimental aerospace research activities performed at Langley Research Center. Additional responsibilities include conception, design, implementation, and management of advanced centralized data processing systems, flight software systems, flight simulators, and advanced communications and networking technology, as well as providing consultation on Langley Research Center application of computer technology.

The Instrument Research Division provides instrumentation and measurement for experimental aerospace research activities performed at Langley Research Center, with primary responsibility for the instrumentation of ground-based facilities. This division conducts research and development programs in instrument areas in which present measurement capabilities are deficient or nonexistent to satisfy both current and future aerospace test program requirements. Additional responsibilities include providing engineering and application expertise to support computer-based data acquisition and control requirements, developing and maintaining measurement standards, calibrating and

repairing instruments, and managing an instrument pool.

The Flight Electronics Division is responsible for the development and application of electronic and electro-optical systems for aerospace flight and flight-related projects. This division conducts research and development programs in electronics, optics, lasers, and related disciplines to provide measurement, communication, and data processing systems. Additional responsibilities include design, testing, and operation of ground and flight electronic equipment and instrumentation.

The Projects Division is responsible for the implementation and management of the Langley Research Center participation in major NASA projects. These projects include four Earth Observing System (EOS) instruments (three of which have completed phase A-B and the fourth that is currently in the definition phase) and the development of NASA's first spaceflight lidar (laser-radar), the Lidar In-Space Technology Experiment (LITE). In addition, this division is responsible for mature projects, such as the Scout launch vehicle, which can place a 400-lb class payload in a low-Earth orbit, and retrieval of the Long-Duration Exposure Facility (LDEF).

The accomplishments of the Electronics Directorate over the past year are as diverse as the directorate itself. Significant advances have been realized in applied research for remote sensing of the Earth's atmosphere and nonintrusive diagnostic measurements for Center-wide ground facilities. Some examples of these advances include an improved catalyst material that recombines oxygen and carbon monoxide to greatly extend the lifetime of carbon dioxide lasers, a solid-state tunable titanium-doped sapphire laser for

Differential Absorption Lidar, an eye-safe 2- μ m laser for detecting wind shear, advanced techniques for monitoring slush hydrogen, and nondestructive evaluation (NDE) techniques applied to Space Shuttle rocket motors. The NDE research has led to strong cooperative programs with several aerospace companies. In addition, the directorate brought to full power the use of all vector processors in a Cray supercomputer in creating a production computational fluid dynamics code that won recognition by receiving a GigaFlop Performance Award.

Flight Systems Directorate

The Flight Systems Directorate, which consists of three research divisions and two project offices, conducts basic research and development in the broad, multidisciplinary area associated with aerospace flight systems. This includes systems hardware and software architecture concepts and design guidelines, validation and verification methods for reliable flight control systems, advanced cockpit interfaces, advanced airborne systems technology, aircraft operating procedures, fundamental electronics research, automation and robotics technology, and aircraft and spacecraft guidance and control system design methods, guidelines, and criteria. A special multidirectorate, multicenter research activity addressing controls-structures interaction (CSI) issues associated with large flexible space systems also is managed and participated in by directorate personnel.

In the past year, the Flight Systems Directorate had a significant number of accomplishments across a wide range of technical areas. Of special note were the activities associated with the NASA/FAA Airborne Wind Shear Detection and Avoidance program. Important accomplishments included continued developments in wind shear modeling, flight management techniques utilizing advanced warning information to avoid a wind shear, and progress in development and testing of the three major candidates for an airborne sensor that will provide early detection of wind shears. Also of note was the opening of a new Experimental Test Range facility that will enhance research efforts in compact range measurement technology. A series of manned simulation efforts were conducted that addressed the basic technology development and benefits of advanced displays utilizing stereo 3-D. The CSI research accomplished this past year

included the first closed-loop control of Mini-Mast and the development of an integrated design methodology for a class of flexible space platforms that require fine attitude pointing and vibration suppression. A full set of flight test programs was completed this year in the Directorate's Transport Systems Research Vehicle (B-737) including successful tests of a new aircraft-ATC data-link concept and initial evaluation of an infrared wind shear sensor.

Space Directorate

The Space Directorate is responsible for research in atmospheric sciences, advanced transportation systems, and energy conversion for space applications. In addition, the Directorate is the focal point for conceptual design activities for large space systems technology, Space Station *Freedom*, and the Space Exploration Initiative.

Major advances were made by the Space Systems Division in the development of the Langley Research Center lifting-body candidate configuration for the Personnel Launch System (PLS). A detailed data base was defined, the configuration was tested through the speed regime, and computational fluid dynamics (CFD) solutions were completed at critical flight conditions. Six-degree-of-freedom and man-in-the-loop simulations were completed, and they show that minimal controls are needed from reentry to landing. The weight of the conservative structural design was verified by finite-element and failure mode analysis. Current technology subsystems were sized to meet the two design reference missions, Space Station *Freedom* crew changeout, and assured access to space. Total vehicle weight was well within the launch limits of the Titan IV and the National Space Transportation System. The design and construction of a full-scale mock-up was completed by North Carolina State University and North Carolina Agriculture and Technical State University.

Several important experiments designed to provide new insight into chemical and dynamical processes in the atmosphere were accomplished by the Atmospheric Sciences Division. The Global Tropospheric Experiment (GTE), which was conducted in South America, established the ability of airborne instruments to measure the important

species in the global sulfur cycle. Airborne lidar observations of the ozone and polar stratospheric clouds in the winter Arctic stratosphere provided the first direct evidence of Arctic ozone depletion. Estimates of the gaseous emissions of carbon dioxide, methane, and nitrous oxide from the very large boreal forest fire of 1987 along the Chinese-Russian border were made using both satellite and aircraft data. Extensive model studies of the chemistry of the Arctic stratosphere were performed and demonstrated the rapidity with which the composition of the stratosphere is altered by exposure to polar stratospheric clouds. Good agreement was obtained between the model and observed results obtained by the NASA ER-2 aircraft. A full year of Earth Radiation Budget Satellite (ERBS) data was analyzed, and clouds were found to have a net cooling effect on the Earth for all seasons.

Structures Directorate

The Structures Directorate conducts basic research and develops technology in the areas of advanced aerospace materials and structures, structural loading, dynamics and aeroelasticity, noise generation by aircraft propulsion systems and its interaction with structures, and methodologies for interdisciplinary design, optimization, and vibration control. This technology development is directed toward reduction in both weight and cost of aircraft and space structures along with an increase in their reliability and service life.

Research results from the Materials Division include a new low-toxicity high-temperature nadimide end-capped thermosetting polyimide and Ti-1100 (titanium) matrix composites that show promise for hypersonic vehicle applications. Materials applications studies have shown that stitching improves the damage tolerance of carbon/epoxy composites with impact damage and that an integrally woven hat-stiffener preform eliminates the stiffener/skin separation failure mode. Processing research has developed an apparatus to prepare powder-coated prepreg that improves the quality of both the prepreg and the produced laminate, and the development of composite materials for precision reflector panels demonstrated close tolerance surface accuracies.

Research results from the Structural Mechanics Division include an accurate global/local stress analysis procedure that was developed for detailed stress distribution calculations by adjusting the size and location of finite elements, and an integrated thermal-structural analysis with adaptive unstructured meshes which has achieved efficiencies and computational accuracies that far surpass state-of-the-art procedures. In the space structures area, a space

crane articulation joint test bed was fabricated along with a precision segmented reflector support truss which demonstrated high surface accuracy and good structural behavior. Work involving the influence of a design concept on the composite wing structure weight and cost and a carbon-carbon/heat-pipe wing leading edge that was analyzed with spanwise cooling pipes and radiative cooling are typical of the aircraft structures research.

Leading-edge curvature effects on flutter were determined by the Structural Dynamics Division, and flutter control was demonstrated using the Active-Flexible-Wing wind tunnel model. The aeromechanical stability data base for a parametric hingeless rotor was expanded in the Transonic Dynamics Tunnel in which ground wind loads characteristics for Atlas II were determined. Tire analysis codes were validated with experimental measurements on the Space Shuttle nose gear tire. An automated wetness system was added to the Aircraft Landing Dynamics Facility, and an integrated controls-structures optimization was demonstrated which has application to both Space Station *Freedom* and to the Mission to Planet Earth.

The Acoustics Division evaluated the acoustics of an ASTOVL (Advanced Short Takeoff and Vertical Landing) aircraft in ground effect as part of a cooperative program with the Lewis Research Center. A pressure-instrumented main rotor noise test was conducted in the Duits-Nederlandse Windtunnel (DNW) as part of a cooperative government (Langley and Ames Research Centers and the U.S. Army) and industry research program. Interior noise control in fuselage structures was demonstrated using piezoceramic actuators. A study showed that

producing more acceptable sonic booms may result if a more gradual pressure rise in the far-field sonic boom is generated. Another highlight was that acoustic testing of high-temperature panels has obtained the first sonic fatigue properties of advanced carbon-carbon structure at the elevated temperatures in which the National Aero-Space Plane will operate.

Systems Engineering and Operations Directorate

The prime function of the Systems Engineering and Operations (SE&O) Directorate is to support the ongoing aeronautic and space research at Langley Research Center. This Directorate is organized into five divisions and one office with specific support functions in a wide variety of engineering and technical disciplines. The Systems Engineering Division is responsible for the design, development, analysis, and testing of aerospace hardware and wind tunnel models. The Facilities Engineering Division is responsible for the design, construction, and modification of institutional and research facilities and hardware. The Fabrication Division's function is to produce hardware, components, and systems for aerospace projects and research facilities. The Operations Support Division provides maintenance services and operates the wind tunnels and research equipment and facilities, and the Systems Safety, Quality, and Reliability Division ensures the integrity of hardware and facilities as well as manages the environmental health programs. The Facilities Program Development Office is responsible to the Directorate.

Because of the unique requirements of much of the research performed at the Center, engineers and technicians of the SE&O Directorate are involved in applied research to solve engineering and fabrication problems. These problems relate to the design and fabrication of hardware and software necessary to provide the various components and experimental systems requested by the researchers.

In pyrotechnics, a method was developed for quantitative assessment of the ignitability of initiation devices. Another technique was

developed to determine functional margins of pyrotechnic mechanisms. A Quick-Look data system was developed to provide real-time data display and analysis for the Halogen Occultation Experiment (HALOE). Also, from the contamination work on HALOE, two sources of contaminants, nonvolatile residue and organic film residue, were identified as were methods of dealing with them on optical instruments. A digital spike detection algorithm was developed to detect digital noise spikes present in electronic circuits. A Direct Simulation Monte Carlo method was developed to predict radiation from a shock representative of the flows that might be experienced by spacecraft such as the Aeroassist Flight Experiment.

Technology Utilization

One of the Congressionally mandated responsibilities of NASA is to promote economic and productivity benefits to the Nation by facilitating the transfer of aerospace-generated technology to the public domain. NASA's means of meeting this objective is its Technology Utilization Program, which provides a link between the developers of aerospace technology and those in either the public or private sectors who might be able to employ the technology productively. The *NASA Tech Briefs Journal*, which has over 170 000 subscribers, has been an effective method of announcing new technology generated by NASA.

Another important facet of the NASA Technology Utilization Program is its applications engineering projects, which involve the use of NASA expertise to redesign and re-engineer aerospace technology to solve the problems delineated by federal agencies or other public-sector institutions. Applications engineering projects originate in various ways; some stem from requests for NASA assistance from other government agencies and some are generated by NASA engineers and scientists who perceive possible solutions to public-sector problems through the adaptation of NASA technology. Additionally, NASA employs a multidisciplinary applications team that maintains a liaison with public-sector agencies, medical and public-health institutions, professional organizations, and academia to uncover significant problems in diverse fields such as health care, public safety, transportation, environmental protection, and industrial processes that might be amenable to solution by the application of NASA technology.

A Technology Utilization applications project is considered successful when the technology developed under the project is used or when the technology, if patented, is licensed and manufactured for the market.

Index

- A**
- Acoustics 32, 77, 78
 - Active control 47, 54, 55, 75, 94, 138, 141, 142, 188
 - Adhesive 103, 118, 160
 - Aeroassist Flight Experiment 42, 101, 166, 170, 171, 172
 - Aeroballistic range 206
 - Aerobrake 166
 - Aeroelastic 23, 24, 27, 28, 46, 57, 93
 - Aeromechanical 57, 58
 - Aeroservoelasticity 93
 - Aerosol 175, 181, 192, 193, 194
 - Air combat maneuvering 82
 - Aircraft 210, 211
 - Control systems 58
 - Dynamic models 81
 - Parameter estimation 81
 - Subsystems 61, 63
 - Tires 26, 211
 - ALDF 64, 210
 - Aluminum 3, 21, 47, 65, 93, 112, 128, 145, 149, 152, 156
 - Antarctic Ozone Experiment 199
 - Assured Crew Return Vehicle 124
 - ASTOVL 77, 78
 - Atomic oxygen 137, 201
- B**
- Biomass burning 178, 179
 - Blade 17, 32, 46, 47, 58, 65, 99, 105, 113
 - Deflection 46
 - Loads 46, 47
 - Pressures 32
 - Buckling 56, 93, 98, 105
 - Buffers 128, 185, 186
- C**
- Calibration 109, 118, 122-124, 181, 182, 183, 208
 - Cancer 47, 215
 - CAP-TSD 23
 - Carbon monoxide 178, 182
 - Catalyst 157, 158
 - CFL3D 6, 15, 27, 28, 75, 110
 - Climate 176, 181, 183, 186, 190, 195
 - Clouds 181, 182, 183, 192, 193, 194, 195, 196
 - Cockpit 36, 59, 60, 61, 62, 83
 - Collimated optics 38
 - Combustor 91, 92, 98, 107, 108
 - Composite 2, 3, 17-22, 26, 44-46, 55-57, 64-66, 93, 97-106, 114, 158, 159, 217, 218
 - Computational fluid dynamics (CFD) 15, 41, 46, 51, 71, 75, 99, 109, 113, 123, 172
 - Computational mechanics 16, 26
 - Concurrent integrated control 143
 - Conditional factoring 36
 - Contact lens 216
 - Control
 - Design metrics 82
 - Element failures 58
 - Law 25, 49, 94, 132, 133, 138-144, 187
 - Converters 185
 - Cracks 19, 20, 21, 53, 54, 70
 - Crash 17, 18
 - Cray 6, 11, 16, 41, 42, 46, 66, 75, 102, 113
 - Crew alerting system 63
 - Cryogenic tanks 128, 129
 - CSI 43, 44, 138
- D**
- Damage 2, 3, 18, 44, 45, 70, 100, 112, 113, 155
 - Damping 23, 31, 44, 58, 74, 81, 139, 140, 141
 - Data acquisition 122, 128, 138, 185, 207
 - Delamination 3, 18, 19, 56, 217
 - Depth perception 39
 - Depth-viewing volume 37, 38
 - DFP-ATP 46
 - Differential Maneuvering Simulator 82, 83
 - Digital 139
 - Signal 10
 - Signal processing 49
 - Direct
 - Numerical simulations 9
 - Simulation Monte Carlo 42
 - Drag 13, 69, 84, 90, 91, 96, 99, 119, 125, 132, 167, 168, 169, 170, 171
 - Ducts 54, 55, 160, 162
 - Dynamic
 - Loads 119, 153
 - Programming 81
 - Response 23, 28, 79, 93
 - Dynamics 119, 123, 134, 139, 149, 167, 173, 206, 210
- E**
- ERBE 182, 190, 191
 - Electroluminescent 36, 37, 50
 - EOS 136, 151, 153, 181, 182, 183, 193
 - Epoxy 3, 16, 17, 19, 22, 23, 44, 45, 55, 56, 65, 100, 137, 140, 153, 158
 - Erasable programmable logic 186
 - Euler 5, 7, 8, 11, 26, 27, 28, 29, 66, 67, 72, 75, 110, 111
- F**
- Failure
 - Behavior 17, 18, 20, 34
 - Detection 58
 - Mode 22, 56, 118
 - Fasteners 159, 205
 - Fatigue
 - Behavior 19, 113
 - Cracking 69
 - Fault 33, 34, 35, 63, 152
 - Fault tolerant 34, 36
 - Fighter aircraft 4, 81, 85
 - Film cooling 98, 99, 107
 - Finite element 26, 29-31, 93, 105
 - FIRE (First International Satellite Cloud Climatology Regional Experiment) 195
 - Fire 159, 178, 185
 - Flight
 - Data 45, 81, 127, 167, 171
 - Displays 37, 39
 - Management systems 60
 - Flutter
 - Analysis 27, 28
 - Control 25
 - Fourier 3, 26, 42, 51, 160, 176, 197
 - Fracture mechanics 21, 70
 - Fuel
 - Injector 91, 92, 107
 - Mixing 107
 - Tank 104

Fuselage 6, 18, 23, 24, 46, 47, 69,
70, 71, 72, 75, 94, 99, 126

G

Galileo 149, 170
Geostationary operational 195
Geostationary platform 143, 144,
187, 188
Global Tropospheric Experiment
(GTE) 178
Gold 158
Grid 5-8, 11, 17, 26-28, 41, 42, 66,
71-75, 84, 90, 102, 109-113

H

Hall effect 131
Heat
 Pipe 94, 95
 Source modules 149
 Transfer 92, 102, 107, 113, 121
Heat pipe cooled 95
Helicopter 32, 45, 46
Helmet 38
High angle of attack 4, 28
High-Alpha Research Vehicle 84
High-performance aircraft 28, 79
High-Speed Civil Transport 38, 69,
198
Holmium 156
Hypersonic 9, 13, 19, 93-114, 120-
126, 149, 170-172
Hyperthermia 215

I

Image processing 121, 154
Imaging 2, 54, 121, 126, 154, 155,
181, 183, 184, 207
In-space flight experiments 138
Infrared 54, 55, 121, 126, 160, 176,
177, 183, 189, 192, 195, 196, 197
Integration, engine-airframe 66, 67
Ion 36, 37, 156

J

Jointed truss 139, 140

K

Kalman filtering 49

L

Landsat 196
Large space platform 186
Lasers 150, 155, 156, 157, 158, 185,
186, 190, 207
LAURA 101, 102
LDEF 151, 152, 162
Lidar 150, 155, 156, 175, 176, 184-
186, 189

M

Magnetoacoustics 117
Mapping 37, 55, 122, 124, 144, 199,
207
Mass storage 152
Mechanical response 16
Mesopause 197, 198
Mesosphere 181, 198
Metal 17, 18, 53, 90, 97, 101, 112,
113, 209, 217
Methane 89, 178, 179, 182, 192
Microburst 58, 59
Microchannel 150, 184, 185
Microstructure 2
Mini-Mast 138, 139, 140, 141
Modal Identification Experiment 137
Multiprocessor 144, 145

N

NASTRAN 46, 138
National Aero-Space Plane 89, 90,
99, 101, 108
Navier-Stokes 4-7, 9-10, 14-15, 75,
84, 92, 101, 105, 107, 109-110,
122, 125
Navigation 128
Nitrogen dioxide 178, 181, 198
Nozzle 8, 13, 15
Nuclear 166
Numerical methods 5, 8, 10

O

ONERA 6, 27

Optical

 Fiber 137
 Systems 82
Optics 38, 160, 161, 182, 184-186
Optimal
 Control 43, 96
 Input design 81
Optimization 32, 33, 42, 43, 44, 81,
82, 143, 144, 184
Ozone 176, 177, 178, 179, 181, 193,
194, 195, 197, 198, 199, 200

P

Parabolic panels 153, 158
Parallel architectures 33
Personnel Launch System (PLS) 124
Perturbation 11, 23, 198
Phosphor 36, 37, 120, 122
Photogrammetry 50, 211
Photomultiplier 150, 185
Piloted simulation 62
Planform 69, 70, 71, 124
Polyamic acid fibers 80
Polyimide 80
Polymer 56, 57, 158, 216
Porosity 217, 218
Positron 216
Prepreg 3, 22, 56, 57, 65
Processors 144
Propellant 128, 129, 134, 166

R

Radiation budget 182, 190, 191, 192
Rain 64
Reacting 91, 107, 108
Reflectors 153, 158
Regulator 49, 96, 97, 140
Reliability 153, 159, 187
Remote sensing 155, 156, 189
ROTONET 46
Rotor 57, 58
Rotorcraft vibration 29

S

SAFIRE 183
Seed 189
Shear 55, 56, 58-60, 65, 98, 103,
110, 118, 119, 124, 156, 171, 172

Shock 53, 73-75, 90-93, 98-102,
105, 109-112, 121, 168
Shuttle 16, 26, 115, 133, 136, 138,
118, 120, 121, 126, 129, 151, 153,
177, 184
Skin friction 75, 92
Slush hydrogen 89, 104
Smart structures 137
Solid state 50, 150, 155, 156, 175,
180, 208
Sonic boom 73, 74, 75
Space experiments 138
Space Station 124, 127, 131, 133,
134, 135, 138, 140, 145, 151, 153,
183
Spectroscopic 156, 157, 177
Speech 61, 62
Stereo 62, 63
Stochastic 49
Stratosphere 177, 181, 192, 193,
197, 198, 200
Stratospheric Aerosol and Gas
Experiment (SAGE) 181, 192
Stress 117
Subsonic 7, 27, 64, 71, 78, 125
Superplastic 128, 129
Supersonic 69, 91
Supersonic combustion ramjet 91

T

Tail buffet 79
Telemetry 128, 186
Temperature monitoring 215
Tension monitor 205
Thermal
Loads 93, 94, 105, 167
Management 114
Thermal-structural analysis 105
Thermoplastic 55, 56, 65, 66, 104,
158
Thulium 156
Tile pathway 62
Tire 26
Titanium
Aluminide 94, 111, 113
Matrix 19
Topology 8, 27, 71, 72
Transatmospheric vehicle (TAV) 99
Transition 13-17, 39, 51-53, 90, 103,

124, 152, 160, 170, 171, 176
Transonic flow 6, 11, 15, 208
Transport
Aircraft 58, 61, 69, 70
Landing-approach-in 62
Systems research 41, 60
Transportation node 134, 135
Tumor 215, 216
Turboprop 52, 66

U

Ultrasonic
Attenuation 118
Sound waves 205
USM3D 11

V

Validation 4, 10, 26
Vector processors 41
Velocimeter 10, 207
Venus 170, 201, 202
VGRID3D 11
Vibration 29, 31, 43, 44, 93, 94, 152,
156
Suppression 143
Viscous 4, 6, 7, 8, 31, 74, 75, 84, 92,
111, 122, 170, 171
Visual perception 154
Voice amplitude 40, 41
Vortex detection 50, 52
Vortical flows 4, 28

W

Wake vortex 52
Water vapor 175, 181, 192, 193
WBPPW 12
Wing 4-8, 11-13, 24-25, 27-29, 64
Workstation 35, 153, 155, 190

Report Documentation Page

1. Report No. NASA TM-4243		2. Government Accession No.		3. Recipient's Catalog No.	
4. Title and Subtitle Research and Technology 1990 Langley Research Center		5. Report Date February 1991			
		6. Performing Organization Code			
7. Author(s)		8. Performing Organization Report No. L-16860			
		10. Work Unit No.			
9. Performing Organization Name and Address NASA Langley Research Center Hampton, VA 23665-5225		11. Contract or Grant No.			
		13. Type of Report and Period Covered Technical Memorandum			
12. Sponsoring Agency Name and Address National Aeronautics and Space Administration Washington, DC 20546-0001		14. Sponsoring Agency Code			
		15. Supplementary Notes			
16. Abstract The mission of the NASA Langley Research Center is to increase the knowledge and capability of the United States in a full range of aeronautics disciplines and in selected space disciplines. This mission will be accomplished by performing innovative research relevant to national needs and Agency goals, transferring technology to users in a timely manner, and providing development support to other United States Government agencies, industry, and other NASA centers. This report contains highlights of the major accomplishments and applications that have been made during the past year. The highlights illustrate both the broad range of the research and technology activities at NASA Langley Research Center and the contributions of this work toward maintaining United States leadership in aeronautics and space research. For further information concerning the report, contact the Chief Scientist, Mail Stop 105-A, NASA Langley Research Center, Hampton, Virginia 23665, (804) 864-6062.					
17. Key Words (Suggested by Authors(s)) Research and technology Electronics Aeronautics Flight systems Space Technology utilization Structures Engineering Materials Aerodynamics			18. Distribution Statement Unclassified—Unlimited Subject Category 99		
19. Security Classif. (of this report) Unclassified	20. Security Classif. (of this page) Unclassified	21. No. of Pages 245	22. Price A11		